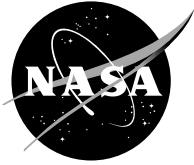# Jet Noise Modeling for Coannular Nozzles Including the Effects of Chevrons

James R. Stone, Eugene A. Krejsa, and Bruce J. Clark
Modern Technologies Corporation, Middleburg Heights, Ohio

The NASA STI Program Office . . . in Profile

Since its founding, NASA has been dedicated to the advancement of aeronautics and space science. The NASA Scientific and Technical Information (STI) Program Office plays a key part in helping NASA maintain this important role.

The NASA STI Program Office is operated by Langley Research Center, the Lead Center for NASA's scientific and technical information. The NASA STI Program Office provides access to the NASA STI Database, the largest collection of aeronautical and space science STI in the world. The Program Office is also NASA's institutional mechanism for disseminating the results of its research and development activities. These results are published by NASA in the NASA STI Report Series, which includes the following report types:

- TECHNICAL PUBLICATION. Reports of completed research or a major significant phase of research that present the results of NASA programs and include extensive data or theoretical analysis. Includes compilations of significant scientific and technical data and information deemed to be of continuing reference value. NASA's counterpart of peer-reviewed formal professional papers but has less stringent limitations on manuscript length and extent of graphic presentations.

- TECHNICAL MEMORANDUM. Scientific and technical findings that are preliminary or of specialized interest, e.g., quick release reports, working papers, and bibliographies that contain minimal annotation. Does not contain extensive analysis.

- CONTRACTOR REPORT. Scientific and technical findings by NASA-sponsored contractors and grantees.

- CONFERENCE PUBLICATION. Collected papers from scientific and technical conferences, symposia, seminars, or other meetings sponsored or cosponsored by NASA.

- SPECIAL PUBLICATION. Scientific, technical, or historical information from NASA programs, projects, and missions, often concerned with subjects having substantial public interest.

- TECHNICAL TRANSLATION. English-language translations of foreign scientific and technical material pertinent to NASA's mission.

Specialized services that complement the STI Program Office's diverse offerings include creating custom thesauri, building customized databases, organizing and publishing research results . . . even providing videos.

For more information about the NASA STI Program Office, see the following:

- Access the NASA STI Program Home Page at *http://www.sti.nasa.gov*

- E-mail your question via the Internet to help@sti.nasa.gov

- Fax your question to the NASA Access Help Desk at 301–621–0134

- Telephone the NASA Access Help Desk at 301–621–0390

- Write to:
  NASA Access Help Desk
  NASA Center for AeroSpace Information
  7121 Standard Drive
  Hanover, MD 21076

NASA/CR—2003-212522
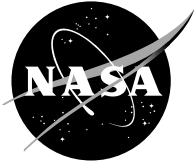
Jet Noise Modeling for Coannular Nozzles Including the Effects of Chevrons

James R. Stone, Eugene A. Krejsa, and Bruce J. Clark
Modern Technologies Corporation, Middleburg Heights, Ohio

National Aeronautics and
Space Administration

Glenn Research Center

September 2003

Acknowledgments

Contents

Nomenclature

2DME	Two-dimensional mixer ejector
A	Nozzle area, m^2
ANOPP	NASA LaRC's *Aircraft Noise Prediction Program*
BPR	Bypass ratio, ratio of outer stream to inner stream mass flow rates, dimensionless
C	Coefficient in mixing noise correlation relations, dB
c	Sonic velocity, m/sec
CVP	Conventional velocity profile (inner stream velocity higher than outer stream velocity)
D	Diameter, m
f	1/3-Octave-band center frequency, Hz
$F(\theta - \theta_M)$	Function of directivity angle minus Mach angle for shock noise component, dB
FAA	Federal Aviation Administration
FOOTPR	Noise prediction code originally developed by NASA LeRC
GE	General Electric
GRC	NASA John H. Glenn Research Center at Lewis Field
IVP	Inverted velocity profile (outer stream velocity higher than inner stream velocity)
L_{ch}	Chevron length, m
L_I	Inner nozzle extension (beyond outer nozzle exit plane), m
L_P	Plug length (beyond inner nozzle exit plane), m
LaRC	NASA Langley Research Center
LeRC	NASA Lewis Research Center (now the John H. Glenn Research Center at Lewis Field)
LSF	Linear scale factor, dimensionless
M	Mach number, V/c, dimensionless
MTC	The Modern Technologies Corporation
N	Slope in mixing noise correlation relations, dimensionless
N_{ch}	Number of chevron elements, dimensionless
n_c	Coefficient in convection Mach number relations, dimensionless
NASA	The National Aeronautics and Space Administration
OASPL	Overall sound pressure level, dB re 20 μPa

P	Total pressure, Pa
R	Source to observer distance, m
r_{pt}	Plug tip radius, m
Rdg	Reading number
S	Strouhal number for noise component, fD/V, dimensionless
SPL	1/3-Octave-band sound pressure level, dB re 20 μPa
T	Total temperature, K
UOL	Overall sound pressure level, uncorrected for refraction, dB re 20 μPa
V	Velocity, m/sec
V_e	Effective velocity for noise component, m/sec
X_S	Axial source location downstream of outer-stream nozzle exit plane, m
α_J	Jet angle of attack, deg (For all cases herein, $\alpha_J = 0$.)
β	Shock strength, dimensionless
γ	Specific heat ratio, dimensionless
ρ	Density, kg/m^3
θ	Directivity angle, deg (Note that in some automated notations on charts, "thet" is used for θ.)
θ_M	Mach angle (context should clarify that Subscript does not refer to merged region), deg
θ'	Effective directivity angle for noise component, deg
ω	Density exponent in noise component correlations, dimensionless
ψ	Directivity angle corrected for angle of attack, deg
<u>Subscripts:</u>	(Note that in some automated notations on charts, subscripts appear as regular text.)
amb	Ambient
c	Convection
component	Component (general)
cor	Corrected (for source location effects)
D	Downstream merged shock quantity
d	Design value
EE	Experimental/extracted quantity
exp	Experimental value
eq	Equivalent

f	Flight (or simulated flight)
h	Hydraulic
I	Inner stream property, or inner stream mixing region
INC	Inner nozzle chevron effect
ISA	International Standard Atmosphere
I/O	Maximum of inner or outer stream value
jet	Jet property (general)
M	Merged mixing region
MAX	Maximum value of effect
mix	Mass-averaged mixed property
Norm	Normalized value
O	Outer stream property, or outer shear layer
ONC	Outer nozzle chevron effect
P	Inner stream plug separation region
Pred	Predicted value
sh	Shock noise
T	Total
1	Inner boundary of stream
2	Outer boundary of stream

Introduction

For a balanced approach to aircraft propulsion system design, noise must be considered from the outset. Commercial aircraft have stringent noise certification requirements, and military aircraft must be designed to minimize the adverse impacts of noise on flight-line personnel as well as on the communities near military installations. To conduct the necessary trade studies, the system designer needs a versatile noise prediction tool, and the National Aeronautics and Space Administration (NASA) uses state-of-the-art system noise prediction codes to analytically calculate the noise levels of aircraft. Federal Aviation Administration (FAA) certification noise levels, airport-vicinity noise footprints, climbout, and en route noise levels all may be calculated with these computer models using a variety of noise metrics. These analysis tools (namely NASA Langley's *Aircraft Noise Prediction Program (ANOPP)* (Ref. 1) and NASA Glenn's *FOOTPR/RADIUS* (Ref. 2) codes) compute spectral, one-third octave band sound pressure levels from several aircraft noise sources for both static and in-flight conditions. The source noise models are generally semi-empirical, using real physical scaling laws that are calibrated with measured test data. The coded prediction structure is flexible enough that new methods may easily be added to the system. A new source noise model that more accurately predicts jet noise and that incorporates new features is the focus of this task. As stated by Goldstein in the Introduction of Reference 3, "Current jet noise prediction methods are largely empirical and are only completely satisfactory for round jets. They are incapable of predicting the changes in the sound field resulting from detailed changes in the flow and are therefore unable to account for the effects of complex nozzle geometry." The approach used in developing this model might be called "hybrid experimental/empirical," but relevant elements of theory are utilized to the extent considered practical.

Turbofan engines with coannular exhaust nozzles are employed on both subsonic and supersonic cruise aircraft, although under quite different operating conditions. Current interest in near-sonic cruise begins to blur the distinctions previous between regimes: high bypass ratio (BPR) engines with conventional-velocity-profile (CVP) exhausts for subsonic application and low BPR engines with inverted-velocity-profile (IVP) exhausts for supersonic application. More advanced concepts such as blended wing body aircraft and exoskeletal engines further broaden the range of interest for potential coannular nozzle applications. A methodology is needed which applies seamlessly to coannular nozzles of whatever geometric configuration or aero/thermodynamic conditions and includes all the appropriate noise generation mechanisms present in such complex systems.

The *FOOTPR* framework has been used by MTC in developing new models for NASA and the industry, including the two-dimensional mixer ejector (2DME) noise model (e.g., Ref. 4) and the recent high bypass ratio (BPR) nozzle model including chevron effects (Ref. 5-6). The approach MTC has employed in these tasks is to use an initial prediction model based on analogy to a relatively simple semi-empirical model derived mainly from the theory of Lighthill (Refs. 7-8) for circular jets. We assume that even for complex geometries subsonic jet noise will correlate in a manner analogous to the classical model (also taking into account the theoretical developments of Ffowcs-Williams (Ref. 9) and Goldstein and Howes (Ref. 10)), if the proper characteristic velocity and characteristic

length can be established. For supersonic jet cases, we assume that the subsonic mixing noise relations may be extrapolated and that the additional shock/turbulence interaction noise can be correlated with a model similar to that of Harper-Bourne and Fisher (Ref. 11), again assuming that characteristic velocity and characteristic length can be established. These initial models are used to estimate the <u>relative</u> contributions of each noise component at each frequency and angle, and the resulting corrections are applied to the experimental data, yielding what we refer to as "experimental/extracted" spectra at each angle. These experimental/extracted results are then correlated empirically to yield models more accurate than those originally used. Repeating this process starting with the already improved models further improves the ultimate accuracy of the final predictive model; sometimes several iterations are worthwhile. (This iterative process is an informal application of Bayesian logic, e.g. see Ref. 12.)

Development of good predictive models for jet noise has always been plagued by the difficulty in obtaining good quality data over a wide range of conditions in different facilities. Viswanathan (Ref. 13) has recently demonstrated and documented these issues very carefully. We consider such issues very carefully in selecting data to be used in developing our model. Flight effects are of critical importance, and none of the means of determining them are without significant problems. Free-jet flight simulation facilities are very useful, and can provide meaningful data so long as they can be analytically transformed to the flight frame of reference. In this report we show that different methodologies used by NASA and industry to perform this transformation produce very different results, especially in the rear quadrant; this compels us to rely largely on static data to develop our model, but we show reasonable agreement with simulated flight data when these transformation issues are considered. A persistent problem in obtaining good quality data is noise generated in the experimental facility upstream of the test nozzle: valves, elbows, obstructions, and especially the combustor can contribute significant noise, and much of this noise is of a broadband nature, easily confused with jet noise. Muffling of these sources is costly in terms of size as well as expense, and it is particularly difficult in flight simulation facilities, where compactness of hardware is very important, as discussed by Viswanathan (Ref. 13). We feel that the effects of jet density on jet mixing noise may have been somewhat obscured by these problems, leading to the variable density exponent used in most jet noise prediction procedures including our own. We investigate this issue, applying "Occam's razor," (e.g., Ref. 14), in a search for the simplest physically meaningful model that adequately describes the observed phenomena. In a similar vein, we see no reason to reject the Lighthill approach; it provides a very solid basis upon which to build a predictive procedure, as we believe we demonstrate in this report. Another feature of our approach is that the analyses are all conducted with <u>lossless</u> spectra, rather than Standard Day spectra, as is often done in industry. We feel that it is important to isolate the effects of as many physical processes as practical. Atmospheric attenuation can then be included using the relations developed for NASA by Shields and Bass (Ref. 15), which are available in both *FOOTPR* and *ANOPP*.

The current approach to coannular jet noise prediction used in *FOOTPR* is reported in Reference 16, which updates the earlier conventional-velocity-profile (CVP, Ref. 17) and inverted-velocity-profile (IVP, Ref. 18) models. The CVP model utilizes a set of frequency shift and level corrections, based on the earlier work of Olsen and Friedman

(Ref. 19) and Williams, et al. (Ref. 20), updated from the original NASA *ANOPP* interim model (Ref. 21) for jet mixing noise. The IVP model uses a more fundamental approach in breaking down jet mixing noise into premerged (higher frequency) and merged (lower frequency) components. Shock noise is calculated for the inner and outer streams separately in both cases. The approach of the current task, as in References 4 to 6, is to use an initial model to separate the experimental noise spectra into the individual components and then update the model based on minimizing the errors between the experimental and predicted noise components. Based on recent analyses and past experience, seven potential source mechanisms must be assessed and preliminary models are available: merged mixing noise (the lowest frequency component), outer shear layer mixing noise (mid-to-high frequency), inner stream mixing noise (modeled as shear layer, but contributes over a broad frequency range in some cases), inner-stream plug separation noise (high-frequency), downstream (beyond plug tip) shock noise (mid-to-high frequency, Ref. 22), outer-stream shock noise (mid-to-high frequency), and inner-stream shock noise (mid-to-high frequency). Shock noise is included if the appropriate Mach number exceeds 1.0.

Predictive Model

The noise prediction and component separation approach developed in References 5 and 6 is modified for use in this task. The general dual-stream nozzle geometry and the mixing noise generation regions modeled are illustrated in Figure 1. Inner stream flow separation from the plug was also found to be a significant source in References 5 and 6. When the exhaust conditions of either or both streams are supersonic shock noise can become a very important source. Figure 2 (from Ref. 23) illustrates a coannular plug nozzle case where the outer stream is supersonic, creating shocks in the outer part of the exhaust near the nozzle exit, and the termination of the plug creates shocks in the merged region downstream of the plug. Turbulence interacting with these shock structures, and also with that of the inner stream when it is supersonic, can be sources of significant noise.

Experimental jet noise measurements are typically made at a distance far enough from the nozzle to be in the far field of any individual noise source region, but not far enough away to treat the entire exhaust plume as a point source at the center of the nozzle exit plane, as is usually assumed in determining the directivity angle, θ. In general the prediction procedures must take this difference into account. The method of References 5 and 6 is used herein to approximate these source location effects for the external mixing noise sources. The geometric relations for noise sources downstream of the nozzle exit plane are given in Figure 3. The relationship of the actual (corrected) source-to-observer distance, R_{cor}, to its apparent value, R, for a source at a distance X_s downstream of the exit plane is as follows:

$$(R_{cor}/R)^2 = 1 + (X_s/R)^2 + 2 (X_s/R) \cos \theta \tag{1}$$

The relationship of the corrected angle, θ_{cor}, to its apparent value, θ, is then

$$\theta_{cor} = \cos^{-1}[(R/R_{cor}) \cos \theta + X_s/R_{cor}] \tag{1a}$$

$$\Delta\theta = \theta_{cor} - \theta \tag{1b}$$

$$\Delta SPL = -20 \log (R_{cor}/R) \tag{1c}$$

In reality the noise received at any point in the far field comes from multiple locations within the source region as a function of frequency, but reasonably accurate predictions can be made with a simple model wherein the source location variation with frequency is assumed to be less important than the variation with angle. Essentially the model accounts for the location, for each component, from which the peak of the noise spectrum at that angle appears to radiate. These corrections differ for each component, because the source positions are different. The simplification of assuming no change in source location as a function of frequency at each far field angle is generally adequate because each component contributes only over a limited frequency range. (This is an area where future improvement is quite feasible, as done for the 2DME in Ref. 4. This is particularly important for future modeling of airframe installation effects and reflections.) Source location relations are given for each component. For the recent GRC/GE data (Ref. 24), the directivity angle θ is referenced to the origin at the center of the fan nozzle exit plane, whereas for the earlier LeRC data (Refs. 25), θ is referenced to the origin at the center of the core nozzle exit plane.

Merged Mixing Noise

The merged jet region is treated as the round jet of an area equal to the sum of the two stream areas at fully-mixed conditions. The underlying philosophy of our approach is dealt with in more detail here than for the other noise components, where similar reasoning is also used.

For the merged region the overall level, uncorrected for refraction, UOL_M, is given by the following:

$$UOL_M = C_M + 10 \log [(\rho_{amb}/\rho_{ISA})^2 (c_{amb}/c_{ISA})^4] + 10 \log (A_M/R^2) + 10 \, \omega_M \log (\rho_M/\rho_{amb})$$
$$+ N_M \log (V_{e,M}/c_{amb}) - 10 \log [1 - M_f \cos \psi] - 15 \log [(1 + M_{c,M} \cos \theta_{cor,M})^2$$
$$+ 0.04 \, M_{c,M}^2] \tag{2}$$

Where C_M is the coefficient and N_M the slope, both determined experimentally and then correlated, A_M is the total outer-stream and inner-stream nozzle exit area ($A_O + A_I$), and ρ_M is the mass-averaged fully-expanded jet density. The effective velocity for noise generation, $V_{e,M}$, is calculated as follows:

$$V_{e,M} = V_{mix} [1 - M_f (c_{amb}/V_{mix}) \cos \alpha_J]^{1/2} \tag{2a}$$

Where the mass-averaged jet velocity V_{mix} is calculated as follows:

$$V_{mix} = (\rho_I A_I V_I^2 + \rho_O A_O V_O^2)/(\rho_I A_I V_I + \rho_O A_O V_O) \tag{2b}$$

The expression for $V_{e,M}$ (Eq. (2a)) has evolved from earlier relations wherein jet noise was assumed to vary with relative jet velocity to a relatively high power, typically 5th or 6th, times absolute jet velocity to a somewhat lesser power, typically 2nd or 3rd, preserving the overall 8th power of velocity expected from Lighthill (Refs. 7-8). Most of our earlier relations (e.g., Ref. 16) split the velocity effect as 2/3 relative and 1/3 absolute; the current even split is somewhat more conservative, yielding a smaller in-flight reduction of jet noise than the earlier relations. The effect of jet temperature or density on noise has also been a matter of contention, and is rather complicated even for a single subsonic

static round jet, as discussed by Lilley in Session 1 of Reference 3 in reviewing the state of jet noise models. It is generally accepted that in the case of the hot jet the noise generated is due to two source terms: quadrupole and dipole, with the dipole term contributing more strongly as jet temperature increases (or as density decreases) and as jet velocity is reduced. Thus for cold jets the 8th power velocity effect is observed even to low velocity, while for hot jets at low velocity the jet velocity dependence reduces to a 5th or 6th power. Although such behavior can be explained on a theoretical basis, in an experiment it is difficult to separate this relative increase in noise with increasing temperature at low velocity from the contamination from upstream noise sources. This problem has long been recognized (e.g., Ref. 26) and must still be dealt with (e.g., Ref. 13); it is further complicated for the dual stream case where two fluid supply systems must be quieted and becomes especially difficult for flight simulation facilities where upstream hardware must be compact and externally streamlined. The approach to quantifying this effect, as suggested by Ahuja and Bushell (Ref. 26), has been to assume that the density effect on noise can be correlated by a variable exponent ω as a function of velocity, i.e., OASPL $\propto$ 10 ω log (ρ_{jet}/ρ_{amb}), where ω is tabulated as a function of nondimensionalized jet velocity, V_{jet}/c_{amb}.

In our earlier work we have used a simple algebraic expression for this density exponent, in this case for the merged region, as follows:

$$\omega_M = 3 \, (V_{e,M}/c_{amb})^{3.5}/[0.6 + (V_{e,M}/c_{amb})^{3.5}] - 1 \qquad (2c)$$

However, in this investigation we consider other approaches where ω_M is considered constant, with the idea that breaking the noise down into different components, potentially having different velocity and density sensitivities, a simpler set of predictive relations might result.

The convective Mach number, $M_{c,M}$, is calculated from the following relation:

$$M_{c,M} = n_{c,M} \, [(V_{mix}/c_{amb}) - M_f \cos \alpha_J] \qquad (2d)$$

Initially $n_{c,M}$ is assumed constant at 0.62, as has been assumed in many early models including our own. Any changes in $n_{c,M}$ could be related to flow-acoustic interaction, or "flow shielding." These considerations are explored more thoroughly by Gliebe, et al. (Ref. 27).

The directivity angle ψ corrected for angle of attack α_J is given by the following:

$$\psi = \theta - \alpha_J \qquad (2e)$$

The jet angle of attack, α_J, is defined in Figure 4. However, all the experimental data are for $\alpha_J = 0.0$; this term is included as a preliminary estimate of the angle of attack effect.

The effect of refraction is incorporated in the spectral directivity relations in an empirical manner, but crudely in the direction suggested by theory. The relative sound pressure level, $SPL_M - UOL_M$, is correlated as a function of the effective directivity angle, θ'_M, and the logarithmic Strouhal number, log S_M, where the Strouhal number is calculated as follows:

$$S_M = (f \, D_M/V_{e,M}) \, (T_{mix}/T_{amb})^{0.4 \, (1 + \cos \theta'_M)} [1 - M_f \cos \psi] \qquad (3)$$

Where D_M is the equivalent diameter based on total fan plus core area and T_{mix} is the mass-averaged total temperature, calculated as follows:

$$T_{mix} = (\rho_I A_I V_I T_I + \rho_O A_O V_O T_O)/(\rho_I A_I V_I + \rho_O A_O V_O) \tag{3a}$$

The effective angle, to account for refraction effects, is calculated as follows:

$$\theta'_M = \theta_{cor,M} (V_{mix}/c_{amb})^{0.1} \tag{3b}$$

It is by use of this effective directivity angle that in a very simple and approximate way refraction is accounted for. It is assumed that the spectra for widely differing jet velocities are similar at this adjusted angle rather than at the same geometric angle. This approach, in conjunction with the analytically modeled convection effect in Eq. (2), correlates the variation of SPL with frequency and angle rather well, as shown later herein. The resulting spectral directivity tables are developed iteratively as further discussed later in this report.

The source location for merged region noise, $X_{s,M}$, is as follows:

$$X_{s,M} = [L_I + (4 + \theta/30)\, D_M]/LSF \tag{4}$$

LSF is the linear scale factor, full-scale dimension divided by model-scale dimension. As with the other components, but with greater impact here, the uncorrected angle, θ, is used here to start the correction process in closed form. Even though the experimental data are scaled to the correct size for comparisons, the linear scale factor is used in conjunction with the experiment geometry to correct the predictions for each component for the effect of source location.

Outer Shear Layer Mixing Noise

For the outer shear layer the overall level, uncorrected for refraction, UOL_O, is given by the following:

$$UOL_O = C_O + 10 \log [(\rho_{amb}/\rho_{ISA})^2 (c_{amb}/c_{ISA})^4] + 10 \log (A_O/R^2) + 10\, \omega_O \log (\rho_O/\rho_{amb})$$
$$+ N_O \log (V_{e,O}/c_{amb}) - 10 \log [1 - M_f \cos \psi] - 15 \log [(1 + M_{c,O} \cos \theta_{cor,O})^2$$
$$+ 0.04\, M_{c,O}^2] \tag{5}$$

Where C_O is the coefficient and N_O the slope, both determined experimentally and then correlated, and A_O is the fan nozzle (outer stream) exit area. The density exponent, ω_O, the convective Mach number, $M_{c,O}$, and the effective velocity, $V_{e,O}$, are calculated as follows:

$$\omega_O = 3 (V_{e,O}/c_{amb})^{3.5}/[0.6 + (V_{e,O}/c_{amb})^{3.5}] - 1 \tag{5a}$$

$$M_{c,O} = n_{c,O} [(V_O/c_{amb}) - M_f \cos \alpha_J] \tag{5b}$$

$$V_{e,O} = V_O [1 - M_f (c_{amb}/V_O) \cos \alpha_J]^{1/2} \tag{5c}$$

Initially $n_{c,O}$ is assumed constant at 0.62, the same as for $n_{c,M}$. For the outer and inner shear layer region analogous models are used with the appropriate characteristic velocities and lengths. Somewhat similar relations, but with significant modifications, are used for inner stream plug separation noise.

The relative sound pressure level, $SPL_O - UOL_O$, is correlated as a function of the effective directivity angle θ'_O and the logarithmic Strouhal number log S_O, where the Strouhal number is calculated as follows:

$$S_O = (f\, D_{2,O}/V_{e,O})\, (T_O/T_{amb})^{0.4\,(1+\cos\theta'_O)}\,[1 - M_f \cos\psi] \tag{6}$$

Where $D_{2,O}$ is the fan (outer stream) nozzle outer diameter and T_O is the fan (outer stream) total temperature. The effective angle, to account for refraction effects, is calculated as follows:

$$\theta'_O = \theta_{cor,O}\,(V_O/c_{amb})^{0.1} \tag{6a}$$

These spectral directivity tables are developed iteratively as discussed later in this report.

The source location for outer shear layer noise, $X_{s,O}$, is as follows:

$$X_{s,O} = (\theta/45)\,D_{2,O}/LSF \tag{7}$$

Again, note that the uncorrected angle, θ, is used here to start the correction process in closed form.

Inner Stream Mixing Noise

For the additional effect of the inner stream, modeled as a shear layer effect, but perhaps influencing the lower frequency region, where merged noise is generally expected to dominate, as well, the overall level, uncorrected for refraction, UOL_I, is given by the following:

$$\begin{aligned} UOL_I = &\; C_I + 10 \log\left[(\rho_{amb}/\rho_{ISA})^2\,(c_{amb}/c_{ISA})^4\right] + 10 \log\,(A_I/R^2) + 10\,\omega_I \log\,(\rho_I/\rho_O) \\ &+ N_I \log\,(V_{e,I}/c_{amb}) - 10 \log\,[1 - M_f \cos\psi] - 15 \log\,[(1 + M_{c,I}\cos\theta_{cor,I})^2 \\ &+ 0.04\,M_{c,I}{}^2] \end{aligned} \tag{8}$$

Where C_I is the coefficient and N_I the slope, both determined experimentally and then correlated, and A_I is the core nozzle (inner stream) exit area. The choice of ρ_O and c_{amb} to nondimensionalized density and sonic velocity, respectively, is arbitrary and is a matter which could be investigated carefully in follow-on studies. The density exponent, ω_I, the convective Mach number, $M_{c,I}$, and the effective velocity, $V_{e,I}$, are calculated as follows:

$$\omega_I = 3\,(V_{e,I}/c_O)^{3.5}/[0.6 + (V_{e,I}/c_O)^{3.5}] - 1 \tag{8a}$$

$$M_{c,I} = n_{c,I}\,[(V_I/c_{amb}) - M_f \cos\alpha_J] \tag{8b}$$

$$V_{e,I} = V_O\{(1 - V_I/V_O)^2\}^{1/4} \tag{8c}$$

As discussed later herein, this expression for $V_{e,I}$ may not be appropriate, and alternatives are considered. Formulations of the sort, $V_{e,I} = V_I\,[(V_I - V_O)^2/V_I{}^2]^{1/4}$, were explored in Reference 5 with the initial assumption $N_I = 75$, which yielded $C_{I,exp}$ values from about 130 at high $V_{e,I}/c_{amb}$ to over 200 at low $V_{e,I}/c_{amb}$. As discussed in Reference 5 and later herein, the component being investigated at that point was ultimately attributed to plug separation. It is interesting to note that, based only on static test results, Fisher, et al. (Refs. 28-29) also find a coannular nozzle noise component in this frequency range that depends simply on the primary velocity. It might be worthwhile to explore a correlation as a function of the momentum difference between the two streams, analogous to the

Mani-Gliebe-Balsa model (Ref. 27), but without experimental data including some extreme conditions to highlight presumed effects it would be difficult to determine what the appropriate parameter is, since so many parameters increase in a similar manner with engine power.

The relative sound pressure level, $SPL_I - UOL_I$, is correlated as a function of the effective directivity angle θ'_I and the logarithmic Strouhal number log S_I, where the Strouhal number is calculated as follows:

$$S_I = (f\,D_{2,I}/V_{e,I})\,(T_I/T_O)^{0.4\,(1+\cos\theta'_I)}\,[1 - M_f \cos \psi] \qquad (9)$$

Where $D_{2,I}$ is the inner stream nozzle outer diameter and T_I is the core (inner stream) total temperature. The effective angle, to account for refraction effects, is calculated as follows:

$$\theta'_I = \theta_{cor,I}\,(V_{e,I}/c_{amb})^{0.1} \qquad (9a)$$

These spectral directivity tables are developed iteratively as discussed later in this report.

The source location for inner stream mixing noise, $X_{s,I}$, is as follows:

$$X_{s,I} = [L_I + (\theta/45)\,D_{h,I}]/LSF \qquad (10)$$

Again, note that the uncorrected angle, θ, is used here to start the correction process in closed form.

Inner Stream Plug Separation Noise

For the inner stream plug separation noise, the overall sound pressure level uncorrected for refraction effects, UOL_P, is calculated first. Then the spectral directivity effects, including source location, are calculated, resulting in a matrix of SPL_P values as a function of frequency, f, and directivity angle, θ. For the inner stream the overall level, uncorrected for refraction, UOL_P, is given by the following:

$$UOL_P = C_P + 10 \log [(\rho_{amb}/\rho_{ISA})^2 (c_{amb}/c_{ISA})^4] + 10 \log (A_I/R^2) + 10\,\omega_P \log (\rho_I/\rho_O)$$

$$+ N_P \log (V_{e,P}/c_O) - 10 \log [1 - M_f \cos \psi] - 15 \log [(1 + M_{c,P} \cos \theta_{cor,P})^2$$

$$+ 0.04\,M_{c,P}^2] \qquad (11)$$

Where C_P is the coefficient and N_P the slope, both determined experimentally and then correlated, c_O is at fan (outer stream) temperature. As for inner stream mixing, the choice of ρ_O and c_O to nondimensionalized density and sonic velocity, respectively, is arbitrary and could be a fruitful area for further investigation. The density exponent ω_P, and the convective Mach number, $M_{c,P}$, are calculated as follows:

$$\omega_P = 3\,(V_{e,P}/c_O)^{3.5}/[0.6 + (V_{e,P}/c_O)^{3.5}] - 1 \qquad (11a)$$

$$M_{c,P} = 0.62\,[(V_{e,P}/c_O) - M_f \cos \alpha_J] \qquad (11b)$$

The determination of the effective velocity, $V_{e,P}$, for this component is quite difficult, as discussed in more detail in References 5 and 6, and the following simple relation is currently employed:

$$V_{e,P} = V_I \qquad (11d)$$

Behavior of this sort would be consistent with plug separation noise, which Olsen and Karchmer (Ref. 30) found to be potentially significant for plug nozzles. The relative sound pressure level, $SPL_P - UOL_P$, is correlated as a function of the effective directivity angle θ'_P and the logarithmic Strouhal number log S_P, where the Strouhal number is calculated as follows:

$$S_P = (2\, f\, r_{pt}/V_{e,P})\, (T_I/T_O)^{0.4\,(1\,+\,\cos\,\theta'_P)}\, [1 - M_f \cos \psi] \tag{12}$$

Where r_{pt} is the inner stream nozzle plug tip radius and T_I is the core (inner stream) total temperature. The effective angle, to account for refraction effects, is calculated as follows:

$$\theta'_P = \theta_{cor,P}\, (V_{e,P}/c_{amb})^{0.1} \tag{12a}$$

These spectral directivity tables are developed iteratively as discussed later in this report.

The source location for inner stream plug separation noise, $X_{s,P}$, is as follows:

$$X_{s,P} = [L_I + L_P + 2\, (\theta/45)\, r_{pt}]/LSF \tag{13}$$

Again, note that the uncorrected angle, θ, is used here to start the correction process in closed form.

Inner Stream Shock Noise

The relationship used to predict inner stream shock noise $OASPL_{I,sh}$, for $M_I \geq 1.0$, is as follows:

$$OASPL_{I,sh} = C_{I,sh} + 10 \log [(\rho_a/\rho_{ISA})^2(c_a/c_{ISA})^4] + 10 \log (A_I/R^2) + 10 \log \{\beta_I^4/(1 + \beta_I^4)\} -$$

$$40 \log (1 - M_f \cos \psi) - F (\theta - \theta_{M,I}) \tag{14}$$

Where β_I is the inner stream shock strength, the ambient property and area/distance terms also used in the internal mixing noise relations have the same meaning. Where $\theta_{M,I}$ is the Mach angle. (Note on terminology: θ_M will always have an additional subscript; otherwise the subscript M on other variables refers to the merged region.) The shock strength parameter β_I is calculated differently depending on whether the primary nozzle is over-expanded or under-expanded, as follows:

$$\beta_I = (M_I^2 - M_{I,d}^2)^{1/2} \qquad \text{for } M_I > M_{I,d}$$
$$\left.\vphantom{\begin{array}{c}a\\b\end{array}}\right\} \tag{14a}$$
$$\beta_I = (M_I^2 - 1)^{1/2} \qquad \text{for } 1.0 < M_I \leq M_{I,d}$$

Where M_I is the inner stream nozzle Mach number expanded to ambient conditions and $M_{I,d}$ is the design Mach number. The intercept $C_{I,sh}$ may be dependent on geometry and also on whether the primary nozzle is under-expanded or over-expanded. In order to avoid a discontinuity about the design point, it is expected that below a value of M_I to be determined for convergent divergent nozzles, and probably dependent on $M_{I,d}$, the simpler $\beta_I = (M_I^2 - 1)^{1/2}$ will be used with a different values as a function of $M_{I,d}$; β_I will then be calculated from both relations (Eq. 14a) and the larger value used. This problem for convergent-divergent nozzles near the design point remains to be resolved in follow-on development and may be more complicated than anticipated.

The Mach angle is denoted by $\theta_{M,I}$, calculated as follows:

$$\theta_{M,I} = 180 - \sin^{-1}(1/M_I) \qquad \text{(in degrees)} \qquad (14b)$$

The term $F(\theta - \theta_{M,I})$ is calculated as follows:

$$
\left.
\begin{array}{ll}
F(\theta - \theta_{M,I}) = 0.0 & \text{for } \theta < \theta_{M,I} \\[1em]
F(\theta - \theta_{M,I}) = 0.75(\theta - \theta_{M,I}) & \text{for } \theta \geq \theta_{M,I}
\end{array}
\right\} \qquad (14c)
$$

Spectral directivity effects are calculated next. The relative sound pressure level, $SPL_{I,sh} - OASPL_{I,sh}$, is given in tabular form as a function of the directivity angle θ and the logarithmic Strouhal number $\log S_{I,sh}$. The Strouhal number is calculated as follows:

$$S_{I,sh} = (f\beta_I D_{h,I}/0.7V_I)(1 - M_f \cos\psi)\{[1+(0.7V_I/c_{amb})\cos\theta]^2 + 0.04(0.7V_I/c_{amb})^2\}^{1/2} \quad (15)$$

It may very well be that the tables developed will be different for under-expanded and over-expanded cases.

The source location for inner stream shock noise, $X_{s,I,sh}$, is as follows:

$$X_{s,I,sh} = [L_I + 2 D_{h,I}(M_I^2-1)^{1/2}]/LSF \qquad (16)$$

Outer Stream Shock Noise

The relationship used to predict outer stream shock noise $OASPL_{O,sh}$, for $M_O \geq 1.0$, is as follows:

$$OASPL_{O,sh} = C_{O,sh} + 10\log[(\rho_a/\rho_{ISA})^2(c_a/c_{ISA})^4] + 10\log(A_O/R^2) + 10\log\{\beta_O^4/(1+\beta_O^4)\}$$

$$- 40\log(1 - M_f\cos\psi) - F(\theta - \theta_{M,O}) \qquad (17)$$

Where β_O is the outer stream shock strength, the ambient property and area/distance terms also used in the internal mixing noise relations have the same meaning. Where $\theta_{M,O}$ is the Mach angle. The shock strength parameter β_O is calculated differently depending on whether the primary nozzle is over-expanded or under-expanded, as follows:

$$
\left.
\begin{array}{ll}
\beta_O = (M_O^2 - M_{O,d}^2)^{1/2} & \text{for } M_O > M_{O,d} \\[1em]
\beta_O = (M_O^2 - 1)^{1/2} & \text{for } 1.0 < M_O \leq M_{O,d}
\end{array}
\right\} \qquad (17a)
$$

Where M_O is the inner stream nozzle Mach number expanded to ambient conditions and $M_{O,d}$ is the design Mach number. The intercept $C_{O,sh}$ is dependent on geometry and may also be dependent on whether the primary nozzle is under-expanded or over-expanded. As for the inner stream shock noise, in order to avoid a discontinuity about the design point, it is expected that below some value of M_O, and probably dependent on $M_{O,d}$, the simpler $\beta_O = (M_O^2 - 1)^{1/2}$ will be used with a different values as a function of $M_{O,d}$; β_O will then be calculated from both relations (Eq. 17a) and the larger value used. Again, this problem for convergent-divergent nozzles near the design point remains to be resolved in follow-on development and may be more complicated than currently anticipated.

The Mach angle is denoted by $\theta_{M,O}$, calculated as follows:

$\theta_{M,O} = 180 - \sin^{-1}(1/M_O)$ (in degrees)   (17b)

The term F is calculated as follows:

$F(\theta - \theta_{M,O}) = 0.0$ for $\theta < \theta_{M,O}$ ⎫

                                           ⎬   (17c)

$F(\theta - \theta_{M,O}) = 0.75(\theta - \theta_{M,O})$ for $\theta \geq \theta_{M,O}$ ⎭

Spectral directivity effects are calculated next. The relative sound pressure level, $SPL_{O,sh}$ – $OASPL_{O,sh}$, is given in tabular form as a function of the directivity angle θ and the logarithmic Strouhal number $\log S_{O,sh}$. The Strouhal number is calculated as follows:

$$S_{O,sh} = (f\beta_O D_{eq,O}/0.7V_O)(1 - M_f \cos \psi)\{[1 + (0.7V_O/c_{amb})\cos \theta]^2 + 0.04(0.7V_O/c_{amb})^2\}^{1/2} \quad (18)$$

Note that the characteristic length used is the outer nozzle <u>equivalent</u> diameter, $D_{eq,O}$. It may very well be that the tables developed will be different for under-expanded and over-expanded cases.

The source location for outer stream shock noise, $X_{s,O,sh}$, is as follows:

$$X_{s,O,sh} = [2 D_{h,O}(M_O^2 - 1)^{1/2}]/LSF \quad\quad\quad\quad\quad\quad\quad\quad (19)$$

Downstream Merged Shock Noise

For the merged region downstream of the plug an analogous model is used with the appropriate characteristic velocities and lengths. The relationships are based on Reference 22.

The relationship used to predict downstream merged shock noise $OASPL_{D,sh}$, for $M_D \geq 1.0$, is as follows:

$$OASPL_{D,sh} = C_{D,sh} + 10 \log [(\rho_a/\rho_{ISA})^2 (c_a/c_{ISA})^4] + 10 \log (A_D/R^2)$$

$$+ 10 \log \{\beta_D^4/(1 + \beta_D^4)\} - 40 \log (1 - M_f \cos \psi) - F(\theta - \theta_{M,D}) \quad (20)$$

The ambient property and area/distance terms also used in the internal mixing noise relations have the same meaning, and the effective area $A_D = A_M$. As suggested by Janardan, et al. (Ref. 23), the <u>effective</u> pressure ratio P_D/P_{amb}, Mach number M_D, and shock strength β_D, are calculated differently depending on the stream pressure ratio, P_O/P_I. When $P_O/P_I \geq 1.00$, the inner stream actually appears to control the downstream shock structure, but when $P_O/P_I < 1.00$ there is an interaction which complicates matters, as follows:

$P_D = P_I$ for $P_O/P_I \geq 1.00$ ⎫

                                        ⎬ (20a)

$P_D = P_I(A_I/A_M) + P_O(A_O/A_M)$ for $P_O/P_I < 1.00$ ⎭

The Mach number M_D is then calculated based the effective pressure ratio P_D/P_{amb} and the corresponding specific heat ratio, $\gamma_D = \gamma_I$ for $P_O/P_I \geq 1.00$ or $\gamma_D = \gamma_M$ for $P_O/P_I < 1.00$. The Mach angle $\theta_{M,D}$ and the merged stream shock strength β_D are then based on this effective Mach number M_D, as follows:

$$\beta_D = (M_D^2 - 1)^{1/2} \quad\quad\quad\quad\quad\quad\quad\quad\quad\quad (20b)$$

The intercept $C_{D,sh}$ may also be dependent on whether the primary nozzle is under-expanded or over-expanded.

Spectral directivity effects are calculated next. The relative sound pressure level, $SPL_{D,sh}$ – $OASPL_{D,sh}$, is given in tabular form as a function of the directivity angle θ and the logarithmic Strouhal number log $S_{D,sh}$. The Strouhal number is calculated as follows:

$$S_{D,sh} = (f\beta_D D_{h,O}/0.7V_D)(1-M_f \cos \psi)\{[1+(0.7V_D/c_{amb})\cos\theta]^2+0.04(0.7V_D/c_{amb})^2\}^{1/2} \qquad (21)$$

Note that the characteristic length used is the outer nozzle <u>hydraulic</u> diameter, $D_{h,O}$. Where the effective downstream velocity is calculated from the effective Mach number and the appropriate effective sonic velocity, $c_D = c_I$ for $P_O/P_I \geq 1.00$ or $c_D = c_M$ for $P_O/P_I < 1.00$, as follows:

$$V_D = M_D c_D \qquad (21a)$$

The source location for downstream merged shock noise, $X_{s,D,sh}$, is as follows:

$$X_{s,D,sh} = [L_I + L_P + 2 D_{h,O}(M_D^2-1)^{1/2}]/LSF \qquad (22)$$

Component Extraction Examples

Four sample cases over a wide range of conditions are included to illustrate the mechanics of the process and how well it works.

<u>Untypical Low Velocity Ratio</u>

In developing the model of References 5 and 6, based entirely on experimental conditions along feasible engine cycle lines, it was reasoned that since the velocity difference across the outer shear layer was always greater than that across the inner shear layer, the inner stream mixing noise contribution should be minor. Consequently, the correlations developed therein do not account for any inner stream mixing noise contribution and, as further consequence, may slightly over-predict the outer shear layer and perhaps even merged noise contributions. To determine inner stream mixing noise, it seems likely that cases where $V_O/V_I < 0.5$ should be appropriate, and such data were obtained in the early LeRC tests reported in 1979 (Ref. 25). This case is for a coplanar nozzle without plug at BPR = 2.7, A_O/A_I = 1.94, V_O/V_I = 0.37, and normalized fully mixed velocity V_{mix}/c_{amb} = 0.938; this is not likely representative of any realistic engine cycle but was taken specifically to help clarify noise mechanisms. (Note that the "Rdg." Reading number is assigned for current purposes only and is not to be found in the reference.)

Component noise separation is shown in Figure 5 at three far-field locations: forward quadrant, θ = 46 deg (Fig. 5(a)), sideline, θ = 95 deg (Fig. 5(b)), and near the peak noise angle in aft quadrant at θ = 139 deg (Fig. 5(c)). The measured noise spectra ($SPL_{T,exp}$) are shown by the × symbols connected by a solid curve; the merged noise spectra ($SPL_{M,EE}$) are indicated by the $\bigcirc$ symbols connected by the dashed curve, the outer shear layer noise spectra ($SPL_{O,EE}$) are indicated by the $\square$ symbols connected by the dotted curve, and the inner stream noise spectra ($SPL_{I,EE}$) are indicated by the $\diamondsuit$ symbols connected by the dot-dash curve; since there is no plug, plug separation noise is not considered. The experimental/extracted component SPLs are obtained by subtracting as a "correction" the predicted amount by which that component falls below the total predicted SPL at that frequency and angle. Data are not usually plotted if $SPL_{compnent,EE}$ -

$SPL_{T,exp} \leq -10.0$ dB, since such data are not meaningful; where such low values are shown, it is simply to show that the particular component does not contribute significantly at that angle. Comparisons are only meaningful for the dominant component at each frequency and angle. It should be noted that regardless of whether or not component levels are plotted, using this method of extraction, the antilogarithmic sum of the components always equals the total SPL, whether experimental or predicted. Comparing the plots at the three different angles shows that the various components have different directivity effects.

The magnitude of the correction applied to the experimental data can be seen by comparing the extracted component spectra with the total. At low enough frequency, the difference between the merged and the total becomes very small, but in the region where the merged noise is expected to peak the corrections become significant, so these data will be most useful in establishing the low frequency roll-off characteristics of the merged mixing noise. There is a broad mid-frequency range where the difference between the total and the extracted inner stream mixing noise is very small (essentially 0.0 over a wide frequency range at $\theta = 139$ deg (Fig. 5 (c)). Thus this test is useful in establishing the peak region and much of the high-frequency roll-off for this component. On the other hand the outer shear layer noise appears to be dominant only over a very limited high frequency range. As will be developed in more detail herein, where the extracted component SPL is within 4.0 dB of the total, the data are correlated in normalized spectral form.

Once the noise spectra have been broken down into their components, the experimental/ extracted components can be compared with prediction, as shown in Figure 6, for the same case as in Figure 5. The same symbols are used for each component as in Figure 5, but now the corresponding curves are the predicted values. The coefficients for the various components, C_M, C_O, etc., are adjusted to minimize the average error (experimental minus predicted) at all angles where the data are considered valid, over the frequency range where that component is most important. Extensive comparisons of experimental/extracted and predicted components are shown later herein on a normalized basis to illustrate the agreement of the model with experiment and show where improvements are needed. Reasonably good agreement between experimental/extracted and predicted spectra can be seen at all angles, but areas of potential improvement can be seen.

Very High Bypass Ratio Cycle

The next sample, for a very high bypass ratio (BPR = 14.9) simulated flight ($M_f = 0.20$) case is selected from a recent NASA/GE test series conducted in the anechoic free-jet facility at GRC (Ref. 24). The component separation/extraction process is illustrated at θ = 60 deg (Fig. 7 (a)), 90 deg (Fig. 7 (b)), 120 deg (Fig. 7 (c)), 135 deg (Fig. 7 (d)), 150 deg (Fig. 7 (e)), and 165 deg (Fig. 7 (f)). The total, merged, outer shear layer and inner shear layer terms are denoted as in figure 5, and inner stream plug separation noise ($SPL_{P,EE}$) is now added, as are indicated by the $\triangle$ symbols connected by the double-dot-dash curve. This plug separation noise can be seen to be a very important component for these conditions. The inner stream mixing noise is shown in each figure for a limited range of frequencies for reference purposes even though it is significant only at $\theta \geq 150$

deg (Fig. 7 (e) – (f)). Issues of data quality are apparent here in the forward quadrant, and our judgment is that the low frequency data for $\theta \leq 90$ deg (e.g., Fig. 7 (a) – (b)) are likely contaminated by extraneous noise, so these data are not considered further. At $\theta \geq$ 150 deg (Fig. 7 (e) – (f)) there are clearly problems with the high frequency data, and at θ = 165 deg (Fig. 7 (f)) there is a very suspicious dip in the spectrum at the 160 Hz band; none of these suspect data are used in further analyses. Similar judgments are made for each data set used in developing and calibrating this model. Although this process is time consuming, we consider it an important part of the process. In the high and low frequency ranges the differences between merged and plug separation noises (respectively) from the total is quite small, but in the middle range, where the outer shear layer term appears to be most important, corrections of 0.5 to 1.0 dB are seen even at the peak level. These data are useful for spectral directivity relations of these three components, but with a little less precision for the outer shear layer.

Comparisons of the resulting component spectra with the predictions are shown for this same case in Figure 8. These comparisons use only the experimental data judged to be valid, as pointed out in the discussion of Figure 7. The experimental/extracted data support the predicted spectral directivities rather well for $\theta \leq 135$ deg (e.g., Fig. 8 (a) – (d)), with some modest disagreement at more aft angles; this is not at all unexpected in view of the flight transformation issues.

Typical Moderate BPR Subsonic Cycle

The same process is next applied to a lower bypass (BPR = 4.85), higher specific thrust, static case also from Reference 24. The experimental total and extracted component spectra are shown in Figure 9 for directivity angles θ from 60 to 160 deg. It appears that neither the inner stream mixing noise, so evident in Figure 5, nor the inner stream plug separation noise clearly seen in Figure 7, appears to contribute significantly in this case. This allows the differing spectral directivity characteristics of the merged and outer shear layer components to be more readily observable, and it can be seen that these effects are significantly different for the two. Because of the dominance of the merged noise over most of the frequency range, it is again difficult to determine at just what frequency the outer shear layer noise peaks at most angles.

Comparisons of the resulting component spectra with the predictions are shown for this same case in Figure 10. Agreement is rather good at all angles for the two dominant components. The comparisons for the other sources are not really significant in terms of accuracy and are shown only as evidence that their expected contribution is being accounted for.

Inverted Velocity Profile

The final sample shown (from Ref. 25) is a low-bypass high specific thrust case with outer-stream to inner-stream velocity ratio $V_O/V_I = 2.1$. The experimental total and extracted component spectra are shown for directivity angles $\theta = 95$ deg (Fig. 11 (a)) and $\theta = 139$ deg (Fig. 11 (b)). At both angles the low frequency region is completely dominated by merged mixing noise, but the situation is more complicated for the inner and outer stream terms. At $\theta = 95$ deg (Fig. 11 (a)) it is difficult to separate the contributions based on the initial spectral directivity model, while at $\theta = 139$ deg

(Fig. 11 (b)) the high frequency peak appears to correlate with the outer shear layer mixing, while the inner stream mixing may be dominant in a few mid-frequency bands.

Comparisons of the resulting component spectra with the predictions are shown for this same case in Figure 12. The experimental/extracted merged noise appears to agree reasonably well with prediction at both angles. The inner stream and outer shear layer mixing components are in fairly good agreement at $\theta = 95$ deg (Fig. 12 (a)), but one or the other, or both to a lesser degree are under-predicted by 3 dB. At $\theta = 139$ deg (Fig. 12 (b)), the inner stream mixing noise may be predicted fairly well and the errors at higher frequency may be due entirely to under-prediction of outer shear layer mixing noise.

First Generation Correlation

The same extraction and coefficient adjustment approach demonstrated in the foregoing section was applied to a more extensive set of data from References 24 and 25. This section presents the correlation of these coefficients and spectral directivities to establish the first generation prediction procedure. It is important to note that these data are not arbitrarily adjusted except for the experimental determination of the component coefficients; they are simply normalized and correlated using the expressions presented herein. Even though the model sizes differ and the acoustic facility for the more recent tests (Ref. 24) is much more sophisticated, no facility corrections are applied.

Merged Region Mixing Noise

The normalized overall level for merged mixing noise, UOL_M, is obtained by rearranging Eq. (2), as follows:

$$UOL_{M,Norm} = UOL_M - 10 \log [(\rho_{amb}/\rho_{ISA})^2 (c_{amb}/c_{ISA})^4] - 10 \log (A_M/R^2) - 10 \, \omega_M \log$$
$$(\rho_M/\rho_{amb}) + 10 \log [1 - M_f \cos \psi] + 15 \log [(1 + M_{c,M} \cos \theta_{cor,M})^2 +$$
$$0.04 \, M_{c,M}^2] = C_M + N_M \log (V_{e,M}/c_{amb}) \tag{23}$$

Plots of UOL_M versus $\log (V_{e,M}/c_{amb})$ were made for the seven configurations (Refs. 24-25) using several different density effect assumptions: $\omega_M = 0.0, 1.0, 2.0$ and the variable value from Eq. (2c). It was found that slope $N_M = 75$ appeared reasonable for all cases, but there was also an additional effect of velocity ratio, which in turn was dependent on configuration; it also appeared that the $\omega_M = 2.0$ assumption, which is in concord with Lighthill's theory (Refs. 7-8) was at least as good as, if not better than the other assumptions. (As discussed later herein, this approach is rejected in the final model.) The coefficients C_M (under the assumptions that $\omega_M = 2.0$ and $N_M = 75$) are plotted against the geometric and velocity ratio parameter, $\log [1 + (V_O/V_I)^2 (L_I/D_{2,I})]$ in Figure 13. The three data sets identified by area ratio are from the more recent relatively high BPR coannular plug nozzle tests (Ref. 24), while the data sets identified by velocity ratio are from the older tests (Ref. 25) for plugless coannular nozzles. The first generation correlation expression obtained is

$$C_M = 143.0 - 5 \log [1 + (V_O/V_I)^2 (L_I/D_{2,I})] \tag{24}$$

Although the velocity and density effects are modified in the final relations, the geometry/velocity ratio term is retained.

Normalized merged mixing noise spectra are shown for several ranges of effective merged directivity angles θ'_M (corrected for source location effects as well as for V_{mix}/c_{amb}) in Figure 14. Each SPL is normalized to the predicted overall level at $\theta'_M = 90$ deg based on the experimental value of C_M. For $\theta'_M \cong 41$ deg (Fig. 14 (a)) data are shown for three test runs from the earlier data set for $A_I/A_O = 1.94$ (Ref. 25); readings 05 and 07 are CVP cases and reading 10 is IVP. (The configuration notation for the Ref. 25 data is "GS" (for the authors' last initials) followed by approximate area ratio and then type of velocity profile; e.g., Conf. GS-1.9C refers to the CVP conditions for $A_O/A_I = 1.94$.) While the agreement is not perfect, it is rather good for this type comparison. For $\theta'_M \cong 50$ deg (Fig. 14 (b)) representative data from Reference 24 are shown; 3 static cases for $A_O/A_I = 2.75$ (BPR $\cong 5$) are shown at high, intermediate and low mixed jet velocity, along with one simulated flight case for $A_I/A_O = 6.53$ (BPR $\cong 14$) at a relatively high mixed velocity for such a high bypass ratio, but which is in the lower end of the velocity range for the lower BPR nozzle. (For the Ref. 24 data, Conf. 3BB, 5BB and 7BB denote $A_O/A_I = 2.75$. 3.74 and 6.53, respectively.) The agreement is even better than that seen for the older data at the lower angle (Fig. 14 (a)), which is not surprising since the newer data were obtained in an anechoic chamber and the older data were obtained in an outdoor test stand with nominally free-field spectra requiring the merger of analytically-corrected ground and pole-mounted microphone data. Further comparisons (not shown) at $\theta'_M \cong 60$ and $\theta'_M \cong 70$ deg are quite similar to those at 50 deg (Fig. 14 (b)). At $\theta'_M \cong 80$ deg (Fig. 14 (c)) a large data set is available from the two sources; only a few data points from the old test series fall outside the predicted ± 1.5 dB band, and by combining all these data sets over a wide range of geometries and test conditions a large range of Strouhal parameter is covered. For $\theta'_M \cong 90$, 100 and 120 deg (not shown) and $\theta'_M \cong 110$ deg (Fig. 14 (d)), only the Reference 24 data are available, and the agreement is fairly good. As θ'_M increases further the variations as a function of angle increase, so plots of this type show more scatter. At $\theta'_M \cong 130$ deg (Fig. 14 (e)) and $\theta'_M \cong 140$ deg (Fig. 14 (f)) data are available from both references, and although there is some scatter the predicted trends are reasonably supported by the experimental data. At the most aft angles, $\theta'_M \cong 150$ deg (not shown) and $\theta'_M \cong 157$ deg (Fig. 14 (g)), the available data, all from the more recent test (Ref. 24) again reasonably support the predicted trends even in this range where the effects of angle are very strong. It can be concluded that these first generation spectral directivity relations are in quite good overall agreement with the experimental data. Only minor adjustments are made in developing the final relations.

Outer Shear Layer Mixing Noise

The experimental outer shear layer noise coefficients C_O, utilizing four different density effect assumptions were plotted against the logarithmic effective velocity parameter for data from the seven geometric configurations over a fairly extreme range of test conditions. The density effect assumptions examined were $\omega_O = 0.0$, 1.0, 2.0 and the variable value from Eq. (5a); it was further assumed that $N_O = 70$. As for merged mixing noise, it appeared that the $\omega_O = 2.0$ assumption, which is in concord with Lighthill's theory (Refs. 7-8) was at least as good as, if not better than the other assumptions. Outer shear layer coefficients C_O, assuming $\omega_O = 2.0$ and $N_O = 70$, are plotted against the logarithmic effective velocity parameter $\log(V_{e,O}/c_{amb})$ in Figure 15. In the initial

analysis there was an error in producing the Reference 24 data sets labeled "Uncor.," which resulted in the interim correlation relation, with $N_O = 75$ and $C_O = 136.0$. After these analyses were completed, including the extensive comparisons in the next major section, the error was found and the data corrected. The corrected results for Reference 24 data are shown by the unconnected symbols labeled "Crct'd;" it appears that the slope should be increased somewhat. As shown later herein, both the velocity and density relations have been changed in the final model. This is not surprising, since the outer shear layer numerical values are almost always influenced significantly by contributions from other components.

Normalized outer shear layer mixing noise spectra are shown for several ranges of effective outer shear layer directivity angles θ'_O (corrected for source location effects) in Figure 16. Each SPL is normalized to the predicted overall level at $\theta'_O = 90$ deg based on the experimental value of C_O. For $\theta'_O \cong 43$ deg (Fig. 16 (a)) data are shown from CVP test runs from the earlier data set for $A_I/A_O = 1.94$ (Ref. 25); readings 05 and 07. The limited range where data are available near the peak is in reasonable agreement, but it appears that the high-frequency prediction should roll-off more rapidly with increasing frequency. For $\theta'_O \cong 50$ deg (Fig. 16 (b)) representative data from Reference 24 are shown; 3 static cases for $A_I/A_O = 2.75$ (BPR $\cong 5$) are shown at high, intermediate and low mixed jet velocity, along with one simulated flight case for $A_I/A_O = 6.53$ (BPR $\cong 14$) case at a relatively high mixed velocity for such a high bypass ratio, but which is in the lower end of the velocity range for $A_I/A_O = 2.75$ (BPR $\cong 5$); also included is one IVP case from Reference 25. The experimental data from this diverse set agree surprisingly well with each other; the increased scatter compared with that seen for the merged noise in the forward quadrant is probably due to the fact that there is always a significant contamination of the outer shear layer noise by other components. Again there is reasonable agreement near the peak, but it appears that the high-frequency prediction should roll-off more rapidly with increasing frequency. At $\theta'_O \cong 80$ deg (Fig. 16 (c)) and $\theta'_O \cong 90$ deg (Fig. 16 (d)) data are available from both test series. At $\theta'_O \cong 80$ deg (Fig. 16 (c)), where the 2 cases from Reference 25 are for CVP, almost all the data fall within the ± 1.5 dB scatter band from the prediction; whereas at $\theta'_O \cong 90$ deg (Fig. 16 (d)), where IVP data are included, the scatter increases substantially. At $\theta'_O \cong 130$ deg (Fig. 16 (e)), with the newer (Ref. 24) data and 2 CVP cases from the older tests (Ref. 25), reasonably good agreement is seen over a wide frequency range. However, at $\theta'_O \cong 140$ deg (Fig. 16 (f)) there is significant disagreement with the IVP cases. The good agreement at $\theta'_O \cong 157.5$ deg (Fig. 16 (g)) is not surprising since there is such a limited amount of data to be correlated. These aft angle difficulties and the IVP problems at $\theta'_O \cong 90$ deg (Fig. 16 (d)) may be due at least in part to the difficulty in separating the contributions of the inner stream mixing and outer shear layer mixing components as well as the plug separation noise where it is a factor. Some adjustments based on these comparisons are included in the final model.

Inner Stream Mixing Noise

The inner stream mixing component has proven very illusive and difficult to correlate. In unpublished MTC-funded analyses of the Reference 25 data preliminary to the GE/NASA funded work of References 5 and 6 a crude correlation was developed.

However, the contribution of this component was not clearly identifiable in the analyses (Refs. 5-6) of the Reference 24 data; instead a somewhat higher frequency component was found that appeared to be function of inner stream velocity alone, with no significant effect of the outer stream velocity and with the only flight effect being the expected convective amplification. This component was eventually attributed to inner stream flow separation from the plug, and the correlations of References 5 and 6 do not include inner stream mixing noise. To attempt to sort out this issue we reanalyze the older (Ref. 25) data using the new (Ref. 6) models for merged and outer shear layer components and find that there was still a definite need to include an inner stream mixing term. A very crude ("zeroth" generation) model resulted that is then used in a re-analysis of the Reference 24 data. Because of the difficulty in identifying and extracting this component, relatively large scatter is found in the various plots made in correlation attempts. It is finally determined that as an interim approach setting $\omega_I = 0.0$ and $N_I = 30$ offers the best prospects of correlating the additional effects of velocity ratio and inner nozzle extension, as shown in Figure 17. This correlation is not aesthetically pleasing, and a more satisfactory relationship is evolved in the final model.

Normalized inner stream mixing noise spectra are shown for a three ranges of effective inner stream mixing directivity angles θ'_I (corrected for source location effects) in Figure 18. Only data from Reference 25 are shown since this component appears to be rather marginal in all the Reference 24 cases analyzed. Each SPL is normalized to the predicted overall level at $\theta'_I = 90$ deg based on the experimental value of C_I. For $\theta'_I \cong 43$ deg (Fig. 18 (a)) both IVP and CVP data show good agreement with the prediction. For $\theta'_I \cong 90$ deg (Fig. 18 (b)) there is some scatter, but the basic spectral shape appears to be well modeled. Finally, over a rather broad range around $\theta'_I = 134$ deg (Fig. 18 (c)), again the spectral shape agrees fairly well but with some disagreement in level.

Inner Stream Plug Separation Noise

This component is not as difficult to identify as the inner stream mixing term, but is still difficult to correlate with precision because it occurs at high frequencies where data acquisition is inherently more difficult. Preliminary comparisons, assuming $N_P = 35$ indicated that $\omega_P = 1.0$ offered the best prospects for correlating the results. Resulting values of the coefficient C_P are plotted versus the logarithmic effective velocity parameter $\log (V_{e,P}/c_O)$ in Figure 19. It appears that a slightly higher slope is needed, resulting in the first generation relation where $\omega_P = 1.0$, $N_P = 40$ and $C_P = 138.5$.

Normalized inner stream plug separation noise spectra are shown for several ranges of effective inner stream plug separation directivity angles θ'_P (corrected for source location effects) in Figure 20. Only data from Reference 24 are shown since the Reference 25 configurations did not have plugs. Each SPL is normalized to the predicted overall level at $\theta'_P = 90$ deg based on the experimental value of C_P. For $\theta'_P \cong 60$ deg (Fig. 20 (a)) within the scatter expected for these high frequency data, the agreement is not bad but may be improvable, especially since the peak level appears to be a little over-predicted and the experimental data may peak at S_P lower than predicted. At $\theta'_P \cong 70$ to 120 deg, but shown only at $\theta'_P \cong 90$ deg (Fig. 20 (b)) the spectral shapes agree well and the scatter is less. At $\theta'_P \cong 130$ (Fig. 20 (c)) the scatter begins to increase and peak frequency agreement is not universally good. As θ'_P increases the low frequency sources become

more dominant, making it more difficult to obtain good resolution at high frequency, so these problems become worse at $\theta'_P \cong 140$, $\theta'_P \cong 150$ (Fig. 20 (d)) and $\theta'_P \cong 160$. With the scatter and experimental difficulties the experimental data are in reasonable agreement with the predictive model.

Comparisons and Implications

The correlation relations developed in the preceding section are now applied to the experimental cases on an absolute basis to demonstrate the validity of the first generation model and show where improvements are most needed. When all the sources are put together, there is a tendency to over-predict, due mainly to contributions of components not originally thought to be significant in a particular case. In these comparisons the biggest issues are created by the inner shear layer noise, which was assumed to be less significant than the first generation correlation now indicates. The first generation model appears to be weakest at low values of specific thrust or V_{mix}/c_{amb}, so the presentation will be in order of increasing V_{mix}/c_{amb}.

The lowest mixed velocity case analyzed is Reading 1262 for $A_O/A_I = 6.53$ (BPR $\cong$ 14, with $M_f = 0.20$ and $V_O/V_I = 0.84$ (Ref. 24). The agreement of the experimental OASPL directivity with prediction, shown in Figure 21, is good for 70 deg $\leq \theta \leq$ 135 deg. From the OASPL plot it is difficult to determine which component or components are causing the problem at higher and lower θ; it should also be noted that the aft quadrant problems may very well be related to the flight transformation procedure used in reducing the data, as discussed in Reference 6. The spectral comparisons shown in Figure 22 shed further light on the problem areas. In a global sense, the agreement is not bad and the spectral directivity effects appear to be modeled with reasonable accuracy. In the forward quadrant, as shown at $\theta = 60$ deg in Figure 22 (a), it appears that the main problem is due to the inner stream mixing, which is not surprising since this was not expected to be a significant component when the experimental/extracted levels were determined on which the correlations are based. It also appears that the outer shear layer noise is over-predicted. At $\theta = 90$ deg (Fig. 22 (b)) the same tendencies are present but not as strong; here the high frequency plug separation noise appears to be under-predicted, and there may be a slight over-prediction of the merged mixing noise except for 63 Hz, where the experimental data exhibit an apparent tone. The problems at $\theta = 120$, 135 and 150 deg (Fig. 22 (c) – (e)) are essentially the same as at $\theta = 90$ deg. Even at the extreme aft angle $\theta = 165$ deg (Fig. 22 (f)), where the experimental data exhibit clear problems at $f = 160$ Hz and $f \geq 2$ kHz, the agreement is surprisingly good. It is encouraging that the problems seen in Figures 21 and 22 are primarily over-predictions; this is indirect evidence that the experimental data are at least not grossly contaminated by upstream noise even though the jet velocity is low and the free jet is flowing at $M_f = 0.20$.

Two static cases for $A_O/A_I = 2.75$ (BPR $\cong$ 5) have near equal mixed jet velocities, with $V_{mix}/c_{amb} = 0.633$ for Reading 565 and with $V_{mix}/c_{amb} = 0.635$ for Reading 378. The main difference between these two cases is velocity ratio; $V_O/V_I = 1.07$ (IVP) for Reading 565, and $V_O/V_I = 0.92$ (CVP) for Reading 378. Comparisons are shown for the IVP case Figure 23 (OASPL directivity) and Figure 24 (spectra). The OASPL agreement shown in Figure 23 is not as good as in the previous case: $OASPL_{I,Pred} > OASPL_{M,Pred}$ over wide angular range, whereas it had earlier been presumed that $OASPL_{I,Pred} << OASPL_{O,Pred} <$

$OASPL_{M,Pred}$. The spectral directivity agreement shown in Figure 24 would be rather good except for the over-predicted contribution of inner stream mixing noise, and to a lesser degree outer shear layer mixing noise. However, since in all likelihood there should be some contribution from the inner stream mixing, it may very well be that the predicted levels for the outer shear layer and the merged region should be reduced somewhat also. For the CVP case (Figs. 25-26) the agreement is considerably better, obviously because the predicted inner stream mixing noise is relatively less. Even so, the inner stream mixing term still creates problems, but not so severe. The experimental OASPL directivity (Fig. 25) essentially agrees with the prediction for merged noise alone. At $\theta = 60$ deg (Fig. 26 (a)) it would help if all the noise component predictions were reduced. This is also true at $\theta = 90$ deg (Fig. 26 (b)), but the importance of the inner stream mixing term is reduced. At $\theta = 120$ deg (Fig. 26 (c)), $\theta = 135$ deg (Fig. 26 (d)) and $\theta = 145$ deg (Fig. 26 (e)) there are only slight over-predictions, which could be minimized with a slight reduction in the predicted merged and outer shear layer components. At $\theta = 155$ deg (Fig. 26 (f)) the same holds true, except that the inner stream mixing prediction should also be reduced. From these two sets of comparisons (Figs. 23-26), it appears that the inner stream mixing noise model should be revised to give relatively lower levels for the IVP case.

Another static comparison at only slightly higher velocity, $V_{mix}/c_{amb} = 0.725$, is shown in Figure 27 for the much older (1979) LeRC tests (Ref. 25), with $V_O/V_I = 0.69$ and BPR = 2.8. Comparisons are shown at $\theta = 46$ deg (Fig. 27 (a)), $\theta = 95$ deg (Fig. 27 (b)) and $\theta = 139$ deg (Fig. 27 (c)). Considering that these data were obtained in an outdoor facility using ground and pole microphones with spectra analytically combined, the agreement is quite good, although not perfect. Since this is a much different geometry, a coplanar nozzle with relatively small area ratio, the agreement seen here is quite encouraging in terms of the generality of the prediction procedure.

Comparisons for the largest area ratio nozzle of the older test series (Ref. 25), $A_O/A_I = 3.27$ and BPR = 4.6, are shown at $\theta = 95$ deg (Fig. 28 (a)) and 139 deg (Fig. 28 (b)) at $V_{mix}/c_{amb} = 0.839$ and $V_O/V_I = 0.37$. Generally good agreement is seen, with regions near the peak agreeing rather well at both angles. At $\theta = 95$ deg there is a slight under-prediction, and at $\theta = 139$ deg there is an under-prediction at low frequency and an over-prediction at high frequency.

An OASPL directivity comparison is shown in Figure 29 for $V_{mix}/c_{amb} = 0.87$ and $M_f = 0.00$ (Reading 1015, $A_O/A_I = 3.74$, $V_O/V_I = 0.69$ and BPR = 6.9). This is the lowest mixed velocity case where the peak OASPL is under-predicted (by 1.8 dB); from $\theta = 55$ to 120 deg the experimental and predicted OASPLs agree within ± 1.0 dB. The corresponding spectral comparisons are shown in Figure 30; from $\theta = 60$ to 120 deg the agreement is quite good, while at higher angles the merged noise is slightly under-predicted, while the outer shear layer (and possibly inner stream mixing at $\theta = 160$ deg) noises are over-predicted a little. The general agreement of the prediction with all aspects of the experimental results is good in this case.

At higher velocity, $V_{mix}/c_{amb} = 0.938$ and $M_f = 0.00$ ($V_O/V_I = 0.37$ and BPR = 2.7, Ref. 25), good spectral agreement is seen at $\theta = 46$ deg (Fig. 31 (a)), $\theta = 95$ deg (Fig. 31 (b))

and θ = 139 deg (Fig. 31 (c)). Note that for this case and the others with V_O/V_I = 0.37, the most important component is inner stream mixing noise.

At again slightly higher velocity, V_{mix}/c_{amb} = 0.949 and M_f = 0.00 (Reading 1017, A_O/A_I = 3.74, V_O/V_I = 0.62 and BPR = 6.6) in Figure 32 we see the lowest velocity case where the OASPL is under-predicted at all angles. (This is the highest velocity where data are available for this configuration.) The peak OASPL, at θ = 145 deg, is under-predicted by 1.4 dB, and the largest under-prediction is 2.7 dB at θ = 135 deg. For $\theta \leq 115$ deg the average over-prediction is 1.0 dB or less. The spectral agreement is fairly good at θ = 60 deg (Fig. 33 (a)) with modest under-predictions at low frequencies and over-predictions at high frequencies. At θ = 90 deg (Fig. 33 (b)) the agreement is about as good as is likely to be seen. At θ = 120 deg (Fig. 33 (c)) it appears that the merged noise is under-predicted by 1.5 to 2.0 dB, while the agreement at high frequency is very good. At θ = 135 deg (Fig. 33 (d)), where the OASPL discrepancy is greatest, it appears that the merged noise is under-predicted and the outer shear layer is over-predicted. At θ = 150 deg (Fig. 33 (e)) and θ = 160 deg (Fig. 33 (f)) the low-frequency noise is predicted fairly well, and there is an increasing over-prediction with increasing frequency. The problems with the experimental SPLs at 1 and 5 kHz are not enough to cause significant problems with the OASPL comparisons, but they are indicative of the difficulty in obtaining good experimental data at high frequencies and aft angles. Note that the 1 kHz tone exceeds the level of the adjacent bands by about 25 dB.

The highest velocity comparisons for the newer data set (Ref. 24), for V_{mix}/c_{amb} = 1.09 and M_f = 0.00 (A_O/A_I = 2.75, V_O/V_I = 0.65 and BPR = 4.8) are shown in terms of OASPL directivity in Figure 34. The results are qualitatively similar to those shown in Figure 32 for a somewhat lower velocity, but the disagreements here are greater. The peak OASPL, at θ = 145 deg, is under-predicted by 3.1 dB, and the largest disagreement is the 3.5 dB under-prediction at θ = 135 deg. The under-prediction is 1.0 dB or less for $\theta \leq 115$ deg, and the agreement is exact at θ = 160 deg. At θ = 60 deg (Fig. 35 (a)) the spectral agreement is fairly good with a small under-prediction at low frequency and a small over-prediction at high frequency. At θ = 90 deg (Fig. 35 (b)) the agreement is very good, while at θ = 120 deg (Fig. 35 (c)) the disagreements are small and similar to those at θ = 60 deg. At θ = 135 deg (Fig. 35 (d)), where the OASPL disagreement is worst, the merged noise appears to be under-predicted by 3 to 4 dB. The low frequency under-prediction decreases at θ = 150 deg (Fig. 35 (e)) and 160 deg (Fig. 35 (f)), but there is an increase in the over-prediction at high frequency.

Figure 36 shows comparisons for the highest shock-free mixed velocity case from Reference 25, V_{mix}/c_{amb} = 1.63 for the 1.94 area-ratio coplanar nozzle, with V_O/V_I = 1.11 and BPR = 2.20. The agreement is not bad at θ = 46 deg (Fig. 36 (a)) with a slight under-prediction in the middle frequencies and some over-prediction at the high and low frequencies. At θ = 95 deg (Fig. 36 (b)) the agreement at low frequency may be slightly better, but there is a significant region of under-prediction at middle-to-high frequency, by as much as 5.0 dB at 12.6 kHz. At θ = 139 deg (Fig. 36 (c)) there is an over-prediction averaging about 1 dB at low frequency, followed by a region of more significant over-prediction, as much as 6.8 dB at 2.5 kHz; the agreement at high frequencies is fairly good.

<u>Implications</u> – Considering the wide range of conditions correlated, this is a very good start. Even so there are some systematic overall trends that can be addressed in setting up the next version of this model. For both merged mixing noise and outer shear layer mixing noise there is a tendency to over-predict at low velocity and under-predict at high velocity; to move in this direction we could increase N_M from 75 to 80 and N_O from 70 to 80 with no change in C_M and C_O. It also appears that at low velocities N_I should perhaps be increased, but this component definitely needs further study.

Improved Correlations

The adjustments suggested at the end of the preceding section are incorporated, and adjusted spectral directivity relations developed. These tables are given for merged mixing noise in Table I, for outer shear layer mixing noise in Table II, for inner stream mixing noise in Table III, for inner stream plug separation noise in Table IV, for downstream merged shock noise in Table V, for outer stream shock noise in Table VI, and for inner stream shock noise in Table VII.

The process of coefficient adjustment and component extraction is repeated in the same manner as for the first iteration. New correlations for the coefficients are developed in this section and experimental/extracted spectral directivities are compared with the predicted values (Tables I-VII). In Table IV at corrected directivity angles of 0 and 10 deg, it was intended that the levels be 1.0 dB lower, and in Table VI at corrected directivity angles of 0, 10, 20 and 30 deg, it was intended that the peak values be –12.1, –11.6, –11.1 and –10.6, respectively. These changes will be made at the outset of any further development of this methodology.

Note that the effects of inner nozzle chevrons and of combined inner nozzle and outer nozzle chevrons are found only to influence the levels and not the spectra, so simple "delta" correlations are all that is justified at present of the observed reductions in merged noise at the expense of small increases in the higher frequency components. It is also assumed, for correlation purposes, that the effects of outer nozzle chevrons is additive to that for inner nozzle chevrons. The chevron design is described by two variables: the number of chevrons N_{ch} and the length L_{ch}, with half of the length being upstream of the exit plane of the unmodified nozzle and the other half being a downstream extension to a point. The chevron contour is a smooth continuation of the contour upstream of the original exit plane. An additional chevron design variable is the penetration of the chevron into the flow; at present designers consider this variable to be proprietary, although it is acknowledged to be on the order of the boundary layer thickness. At present the optimum penetration must be determined experimentally. The only chevron results shown are from Reference 24, Conf. 3IB with the 12 in-flip chevrons on the core nozzle, and Conf. 3IC which has 12 in-flip chevrons on the core nozzle and 24 fan chevrons. The relations are formulated in cognizance of data for a higher BPR nozzle with core chevrons not having the in-flip feature (Ref. 6), which exhibited only small effects. These effects are calculated only if there are chevrons, so the "delta" relations are not forced to zero for no chevrons.

<u>Merged Mixing Noise</u>

The normalized geometry corrected overall level, $UOL_{M,Norm}$ (Eq. (23)) – 5 log [1 + $(V_O/V_I)^2$ $(L_I/D_{2,I})$] is plotted against the logarithmic effective velocity parameter,

log ($V_{e,M}/c_{amb}$), in Figure 37 for several different assumptions regarding the density exponent ω_M. Because of the range of test conditions included there is a significant range of temperature and velocity, and the method of correlating density effects is quite significant. Figure 37 (a) gives results for $\omega_M = 0.0$; Figure 37 (b) gives results for $\omega_M = 1.0$; Figure 37 (c) gives results for $\omega_M = 2.0$; and Figure 37 (d) gives results for variable ω_M (from Eq. (2c)). To get a good correlation using any of the constant ω_M approaches requires a three-segment approach (three regions having different slopes versus velocity), while for the variable ω_M formulation, for up to log ($V_{e,M}/c_{amb}$) = 0.10 (low supersonic) the slope is constant at 90, and as expected at higher supersonic conditions the slope decreases. Therefore, our crude application of "Occam's Razor" implies that the variable exponent is preferred, and this is used in the finalized prediction model. Since there is a velocity effect included in the ω_M formulation, the small deviation from the 80 slope of Lighthill's theory (Refs.7-8) is quite reasonable. The finalized prediction for merged mixing noise is to use Eq. (2) with the following relation for C_M and N_M:

$$C_M = 141.5 - 5 \log [1 + (V_O/V_I)^2 (L_I/D_{2,I})] \text{ and } N_M = 90; \log (V_{e,M}/c_{amb}) \leq 0.10$$

$$C_M = 145.0 - 5 \log [1 + (V_O/V_I)^2 (L_I/D_{2,I})] \text{ and } N_M = 55; \log (V_{e,M}/c_{amb}) > 0.10$$

(25)

Spectral directivity comparisons are shown in Figure 38. In comparison with the first generation relations (Fig. 14) it appears that the scatter has increased, but this is the result of plotting data over a much wider range of test conditions, especially some of the older data for very extreme conditions that was taken only to allow limiting behavior to be reasonably well modeled (Ref. 25). In order to achieve this degree of agreement, it is necessary to introduce a variable ratio of convection velocity to relative velocity $n_{c,M}$ in Eq. (2d), as follows:

$$n_{c,M} = 1/(1+\{V_O/V_I\}^{0.5}) \tag{26}$$

As mentioned earlier, this term may approximate some aspects of "flow shielding," as discussed more definitively by Gliebe, et al. (Ref. 27). The only changes in the merged spectral directivity relations from Figure 14 are smoothing of the high-frequency and low-frequency roll-offs to give consistent angle-to-angle variations.

As was shown in more extensive comparisons (Ref. 6), the chevrons appear only to influence the levels and not the spectral directivities, so it is necessary only to correlate the level changes. The effects of mixing enhancement chevrons on the inner and outer nozzle exits are shown in Figure 39, using the same variable density coefficient relation as in Figure 37 (d). The effects are very similar to those found in the more extensive comparisons (Ref. 6), leading to the conclusion that no more complicated relation is justified than a configuration-dependent reduction for both inner nozzle chevrons and combined inner and outer nozzle chevrons.

For this configuration the inner nozzle chevron penetration was optimized experimentally. Due to the very limited data available the following simple relation is suggested:

$$\Delta UOL_{M,INC} = \Delta UOL_{INC,MAX} + 6.5 \log [\{1 + 26.6 (L_{ch,I}/D_{2,I})^2\} \{(1 + [(N_{ch,I}/24) - 1]^2\}] \tag{27}$$

Where

$\Delta UOL_{INC,MAX} = -2.0$ for $A_O/A_I \le 2.75$ $\left.\right\}$

$\Delta UOL_{INC,MAX} = -2.0 + [A_O/A_I - 2.75]$ for $A_O/A_I > 2.75$ (27a)

The effect of outer nozzle chevrons is available only as an added effect to that of the inner nozzle chevrons, and perhaps because of this, the additional effect is small. The outer nozzle chevrons had no penetration into the mixing layer. The following simple relation is suggested:

$$\Delta UOL_{M,ONC} = \Delta UOL_{ONC,MAX} + 1.5 \log [\{1 + 92.5(L_{ch,O}/D_{2,O})^2\}\{1 + [(N_{ch,O}/12) - 1]^2\}] \quad (28)$$

Where

$\Delta UOL_{ONC,MAX} = -0.5$ for $A_O/A_I \le 2.75$ $\left.\right\}$

$\Delta UOL_{ONC,MAX} = -0.5 + 0.25 [A_O/A_I - 2.75]$ for $A_O/A_I > 2.75$ (28a)

Note that these expressions produce a reduction in the benefit of chevrons away from the optimum design point, which is consistent with the relatively sparse published information; this conservative approach is recommended until further results for other configurations are published and analyzed.

Outer Shear Layer Mixing Noise

The normalized geometry corrected overall level $UOL_{O,Norm}$ is plotted against the logarithmic effective velocity parameter $\log (V_{e,O}/c_{amb})$ in Figure 40, where

$$UOL_{O,Norm} = UOL_O - 10 \log [(\rho_{amb}/\rho_{ISA})^2 (c_{amb}/c_{ISA})^4] - 10 \log (A_O/R^2) - 10 \omega_O \log$$
$$(\rho_O/\rho_{amb}) + 10 \log [1 - M_f \cos \psi] + 15 \log [(1 + M_{c,O} \cos \theta_{cor,O})^2 +$$
$$0.04 M_{c,O}^2] = C_O + N_O \log (V_{e,O}/c_{amb}) \quad (29)$$

There is not enough independent variation of outer stream velocity and temperature in the experimental data to really determine the best approach to correlating density effects. Therefore, since the variable ω_M relation was found appropriate for merged mixing noise, the analogous assumption is made here, and the variable ω_O is calculated from Eq. (5a). A relatively simple correlation results, with

$C_O = 133.0$ (30a)

$N_O = 75$ (30b)

A correlation with only slightly more scatter is obtained assuming $\omega_O = 2.0$ with the same velocity dependence, so the issue of density effects is not really resolved, but the current expression is certainly adequate.

Spectral directivity comparisons for outer shear layer mixing noise are shown in Figure 41. As was the case for the merged region, we believe the scatter appears comparable to that of the first generation relations (Fig. 16) primarily because of the wider range of test conditions. It is also worth noting that because the total noise levels from which these component spectra are extracted always have a significant contribution from other components, errors are amplified. Analogous to the merged case, in order to achieve this degree of agreement, it is necessary to introduce a variable ratio of convection velocity to relative velocity $n_{c,O}$ in Eq. (5b), as follows:

$$n_{c,O} = 1/(1+\{V_O/V_I\}^{0.5}) \tag{31}$$

Like the merged noise case and again as was shown in more extensive comparisons (Ref. 6), the chevrons appear only to influence the levels and not the spectral directivities for outer shear layer noise, so it is necessary only to correlate the level changes. The effects of mixing enhancement chevrons on the inner and outer nozzle exits are to increase outer shear layer noise, as shown in Figure 42.

The effect of the inner nozzle chevrons can be correlated simply, under the assumption that the length of the chevrons is the key parameter as follows:

$$\Delta UOL_{O,INC} = 13 \log(1 + L_{ch,I}/D_{2,I}) \tag{32}$$

Similarly the additional effect of outer nozzle chevrons can be expressed as:

$$\Delta UOL_{O,ONC} = 13 \log(1 + L_{ch,O}/D_{2,O}) \tag{33}$$

Inner Stream Mixing Noise

A significant change from the earlier model is made here; it is found that much better agreement is obtained if the characteristic velocity $V_{I/O}$ is taken to be the larger of V_O and V_I:

$$V_{I/O} = MAX\ (V_O,\ V_I) \tag{34}$$

The expressions in Eqs. (8b) and (8c) should also be replaced as follows:

$$M_{c,I} = n_{c,I}\ [(V_{I/O}/c_{amb}) - M_f \cos \alpha_J] \tag{8bb}$$

$$V_{e,I} = V_{I/O}\ [1 - (V_f/V_{I/O})]^{1/2} \tag{8cc}$$

It appears that the overall level correlates reasonably well with $\omega_I = 0.0$ and $N_I = 75$ with an additional BPR effect, as shown in Figure 43. The relatively large scatter is due mainly to this component being only a minor contributor in many cases, thus magnifying errors. Because of the earlier problems with having predicted levels much higher than expected, the coefficients are plotted even for cases where the contribution is not predicted to be very significant; otherwise the final prediction might yield coefficients much higher than experimentally indicated. The following simple two-segment relation is suggested:

$$
\left.
\begin{aligned}
C_I &= 124.5 + 25 \log (1 + BPR) \qquad \text{for } \log (1 + BPR) \leq 0.3 \\[2mm]
C_I &= 135.0 - 10 \log (1 + BPR) \qquad \text{for } \log (1 + BPR) > 0.3
\end{aligned}
\right\} \tag{35}
$$

Spectral directivity relations are shown in Figure 44. Nearly all the data are from Reference 25, some at rather extreme conditions, but some data from Reference 24 are included where this component does appear to contribute within 4 dB of the total. As for the merged and outer shear layer regions, a variable ratio of convection velocity to relative velocity $n_{c,I}$ is used in Eq. (8bb), as follows:

$$n_{c,I} = 1/(1+\{V_O/V_I\}^{0.5}) \tag{36}$$

Any effects of chevrons on this component are not significant for the chevron configurations and cycle conditions tested, where this component is not a major contributor. Additional testing would be required to quantify any effects.

Inner Stream Plug Separation Noise

With the improvement in the other component models, the contribution of what we term inner stream plug separation noise can be better correlated. Comparisons strongly indicate that better correlation is obtained for $\omega_P = 2.0$. With this density effect, the normalized geometry corrected overall level corrected for nondimensionalized plug length, $UOL_{P,Norm} + 50 \log (1 + L_P/D_{2,I})$, is plotted against the logarithmic effective velocity parameter $\log (V_{e,P}/c_O)$ in Figure 45, where

$$UOL_{P,Norm} = UOL_P - 10 \log [(\rho_{amb}/\rho_{ISA})^2 (c_{amb}/c_{ISA})^4] - 10 \log (A_I/R^2) - 10 \omega_P \log (\rho_I/\rho_O)$$
$$+ 10 \log [1 - M_f \cos \psi] + 15 \log [(1 + M_{c,P} \cos \theta_{cor,P})^2 + 0.04 M_{c,P}^2]$$
$$= C_P + N_P \log (V_{e,P}/c_O) \tag{37}$$

For the three configurations tested with plugs at GRC (Ref. 24), the data agree reasonably well, and a simple correlation expression is obtained, as follows:

$$C_P = 158.0 - 50 \log (1 + L_P/D_{2,I}) \tag{38a}$$

$$N_P = 50 \tag{38b}$$

This expression shows significantly better agreement than the first generation relation (Fig.19).

Normalized inner stream plug separation noise spectra are shown for several ranges of effective directivity angles θ'_P shown in Figure 46, for experimental data from Reference 24. Each SPL is normalized to the predicted overall level at $\theta'_P = 90$ deg based on the experimental value of C_P. For $\theta'_P \cong 60$ deg (Fig. 46 (a)), the agreement is not quite as good as appears to be the case for the first generation (Fig. 20 (a)), which may be due to the somewhat different set of experimental data selected and is not bad within the scatter expected for these high frequency data; in general there is a slight tendency to over-predict SPLs in this angular range. At $\theta'_P \cong 70$ to 120 deg, but shown only at $\theta'_P \cong$ 80 deg (Fig. 46 (b)) the spectral shapes agree well and the scatter is less. At $\theta'_P \cong 120$ (Fig. 46 (c)) the scatter begins to increase and peak frequency agreement is not universally good. As θ'_P increases the low frequency sources become more dominant, making it more difficult to obtain good resolution at high frequency, so these problems become worse at $\theta'_P \cong 140$ (Fig. 46 (d)). With the scatter and experimental difficulties the experimental data are in reasonable agreement with the predictive model.

As with the merged noise and outer shear layer noise, and again as was shown in more extensive comparisons (Ref. 6), the chevrons appear only to influence the levels and not the spectral directivities for inner stream plug separation noise, so it is necessary only to correlate the level changes. The effects of mixing enhancement chevrons on the inner and outer nozzle exits are to increase outer shear layer noise, as shown in Figure 47.

The correlations are based not only on these data, but also the more extensive comparisons of Reference 6. The effect of the inner nozzle chevrons can be correlated simply, under the assumption that the length of the chevrons is the key parameter as follows:

$$\Delta UOL_{P,INC} = 20 \log(1+L_{ch,I}/D_{2,I}) \tag{39}$$

Similarly the additional effect of outer nozzle chevrons can be expressed as:

$$\Delta UOL_{P,ONC} = 13 \log(1+L_{ch,O}/D_{2,O}) \tag{40}$$

Outer Stream Shock Noise

Outer stream shock noise coefficient is shown as a function of outer nozzle diameter ratio in Figure 48, with different relations depending on whether or not the inner stream is also supersonic. The relations recommended are:

$$C_{O,sh} = 168.0 - 60 \log [1 + (D_{1,O}/D_{2,O})^2] \qquad \text{for Inner Stream Supersonic}$$

$$C_{O,sh} = 163.5 - 45 \log [1 + (D_{1,O}/D_{2,O})^2] \qquad \text{for Inner Stream Subsonic} \tag{41}$$

Normalized outer stream shock noise spectra are shown for two ranges of corrected directivity angle are shown in Figure 49. In the forward quadrant, at $\theta_{O,sh,cor} \cong 45$ deg (Fig. 49 (a)), this component can be quite dominant, and a spectral range of more than 1.5 decades is covered. Although the agreement is less than perfect, it is reasonable and the sharp low frequency rise with subsequent slower high-frequency roll-off is certainly qualitatively in agreement. Near the equivalent flyover point, $\theta_{O,sh,cor} \cong 93$ deg (Fig. 49 (b)), somewhat less spectral range can be extracted, but the agreement is reasonably good. Shock noises are generally not very important contributors at higher angles.

Inner Stream Shock Noise

Inner stream shock noise is shown to correlate reasonably well with a constant coefficient for the plugless configurations of Reference 25. Previous experience indicates that nozzle diameter ratio is a factor, so the relation recommended is as follows:

$$C_{I,sh} = 158.0 - 50 \log[1 + (D_{1,I}/D_{2,I})^2] \tag{42}$$

Normalized inner stream shock noise spectra are shown for two ranges of corrected directivity angle are shown in Figure 50. In the forward quadrant, at $\theta_{I,sh,cor} \cong 44$ deg (Fig. 50 (a)), this component can be dominant over a significant spectral range, about one decade for these cases. The spectral range is very limited $\theta_{I,sh,cor} \cong 92$ deg (Fig. 50 (b)), so the apparent slight over-prediction may not be significant. As already mentioned, shock noises are generally not very important contributors at higher angles.

Downstream Merged Shock Noise

This area still needs investigation, so the initial model is retained at present. Reference 23 contains a very significant shock noise database and should be utilized, but corrections are required since an early free-jet to flight transformation methodology was used that is now recognized to introduce artificial increases in SPL approaching 1.5 dB at higher frequency. Ultimately criteria must be established as to the conditions under which the merged shock noise comes into play and the separate stream contributions suppressed. Until these analyses are performed and this model calibrated, it is recommended that the outer and inner stream shock components be calculated as described herein.

Comparisons with Improved Model

The correlation relations upgraded in the preceding are now applied to the experimental cases on an absolute basis to demonstrate the validity of the final model and show where

improvements or future work are still needed. As mentioned in regard to the first generation comparisons, when all the sources are put together, there is a tendency to over-predict. This second iteration should reduce such problems. Comparisons are made with data from three different NASA facilities: the old LeRC outdoor static dual-stream hot jet rig, the current GRC relatively large anechoic free jet facility, and the current LaRC relatively small anechoic free jet facility. Each has unique strengths and weaknesses with regard to producing high quality data over a wide range of conditions, but as we have mentioned throughout, practical trade-offs make it extremely unlikely that a flight simulation facility can be developed that does not have similar limitations. Comparing data for similar conditions and geometries in different facilities enables a better understanding of these problems and creates more confidence in the predictive model developed.

Influence of Flight Transformation Methodology on Comparisons

As has been discussed throughout this report, analytical transformation is required to put experimental data taken with microphones outside the free jet into a flight frame of reference. The recent GRC (Ref. 24) and LaRC (Ref. 31) data sets were processed using the "Amiet" technique, essentially a ray acoustics approach wherein neither source location nor source type has any effect; the actual code was developed for NASA by Lockheed-Georgia (Ref. 32). Recent supersonic jet noise suppressor analyses conducted by MTC for GE and NASA (e.g., Ref. 4) utilized data from GE's anechoic free jet facility that was transformed using GE's "Mani" procedure, an earlier version of which is documented in Reference 23. The Mani procedure takes into account source type. We are concerned that the influence of source location may be the cause of some of the disagreement between and experimental and predicted values. For example, using the Amiet/Lockheed method (Ref. 32) for the GRC facility of Reference 24 with $M_f = 0.28$, movement of the source location 10 diameters downstream would change the angular displacement calculated for the shear layer by as much as 7 deg in the rear quadrant, where the sensitivity to angle is great.

The differences between the two flight transformation procedures are greater at high jet velocity conditions and high free jet Mach number; the example shown is for the nominal BPR = 5 nozzle of Reference 24 at $V_{mix}/c_{amb} = 1.087$ and $M_f = 0.28$. OASPL comparisons are shown in Figure 51 for the same raw data processed by the two techniques and compared with the final prediction. In terms of OASPL the agreement between the two methodologies is quite good for 80 deg $\leq \theta \leq$ 120 deg, and both fall somewhat below the prediction, which of course has been adjusted to provide good agreement with a wide range of test data rather than optimized to this case. At low angles the Mani levels are higher and rise above the prediction. At aft angles, $\theta > 120$ deg, the differences become large and neither conforms as well as desired with the prediction, whose general character has evolved over decades of comparisons with both simulated flight and full scale flight data (e.g., see Ref. 17). The Amiet-transformed data indicate that the OASPL continues to increase with increasing angle even at $\theta = 165$ deg, which is certainly not the expected trend. On the other hand, the Mani-transformed data exhibit qualitatively the expected trends but with much sharper rise and fall and a relatively higher peak. To deal with the uncertainties such comparisons create, in developing our model, only data for $\theta \leq 140$ deg are utilized in adjusting the component coefficients for

simulated flight data, whereas static data are used for $\theta \leq 160$ deg except for ranges of data excluded because of data quality considerations.

The difficulties and differences are further illustrated in the spectral comparisons over a wide range of angles shown in Figure 52. At $\theta = 60$ deg (Fig. 52 (a)) the Mani levels are fairly consistently ~ 1.5 dB above the Amiet levels except at very high frequency, where the Mani levels increase sharply. A speculative explanation is that this sharp increase at high frequency may be due to the Mani approach deducing that the source has relatively high monopole or dipole content, whereas the bulk of the spectrum is likely interpreted as quadrupole. In this frequency range inner stream plug separation noise is predicted to contribute significantly, and its velocity dependence is more consistent with dipole than quadrupole characteristics. A difficulty in developing an accurate prediction procedure results from the fact that it is in simulated flight this component contributes most strongly, while the flight transformation issues cause uncertainties in the transformed data. At $\theta = 90$ deg (Fig. 52 (b)) and $\theta = 120$ deg (Fig. 52 (c)) the disagreement is small except at high frequency, where the same behavior seen at $\theta = 60$ deg is repeated, but to a lesser degree. In general it is the middle frequency range, where outer shear layer noise is predicted to dominate, where the greatest disagreement, about 2 dB over-prediction at $\theta = 90$ deg, occurs. At $\theta = 120$ deg, the agreement of the Mani-transformed data, with its high-frequency turn-up, with prediction is almost exact. At $\theta = 135$ deg (Fig. 52 (d)) more significant differences appear, and the Mani levels in the region of the low frequency peak exceed the Amiet levels (and the prediction) by as much as 5 dB, while at middle and high frequencies the behavior is much the same as at lower angles. Here the agreement of the Amiet-transformed data with prediction is extremely good except for the two highest frequency bands. At $\theta = 150$ deg (Fig. 52 (e)) and $\theta = 165$ deg (Fig. 52 (f)) the differences progress from very significant to gross; with such disagreements it is difficult to ascribe any confidence to comparisons between experimental and predicted levels, although optimistically it can be stated that the agreement of the Mani-transformed data with prediction is excellent at $\theta = 150$ deg.

<center>GRC/GE Nominal BPR = 5 Coannular External Plug Nozzle</center>

A lower jet velocity, $V_{mix}/c_{amb} = 0.635$, static case for the same configuration as Figures 51 and 52 is shown for comparison. OASPL directivity comparisons are shown in Figure 53 and show rather good agreement between experiment and prediction. Merged mixing noise is predicted to be dominant at all angles, but the contributions of other components are significant. There is a tendency to under predict by as much as 2 dB that is greatest for $\theta \cong 120$ deg.

Spectral comparisons over a wide range of angles are shown in Figure 54. At $\theta = 60$ deg (Fig. 54 (a)) the general agreement is good with a very small under-prediction at low frequency and a more significant over-prediction at high frequency. At $\theta = 90$ deg (Fig. 54 (b)) the under-prediction at low frequency is slightly increased, but at higher frequencies the agreement is extremely good. At $\theta = 120$ deg (Fig. 54 (c)) there is a general under-prediction, which is least in the middle frequencies. At $\theta = 135$ deg (Fig. 54 (d)) the general agreement is good except for an under-prediction at low frequency; the small high frequency over-prediction is probably not significant. Essentially the same comments are appropriate for $\theta = 145$ deg (Fig. 54 (e)) except that

the experimental data appear to exhibit a tone at 631 Hz, and the highest frequency does not appear to give meaningful data. At θ = 155 deg (Fig. 54 (f)), the highest angle for which data are available in this case, the agreement is very good except in the vicinity of 631 Hz where evidence of a tone was more evident at θ = 145 deg and at the two highest frequency bands, where the data do not appear reliable.

GRC/GE Nominal BPR = 8 Coannular External Plug Nozzle

With increasing BPR the mixed velocity range tends to be shifted to lower values. Comparisons are shown for two static cases.

OASPL directivity comparisons for V_{mix}/c_{amb} = 0.613 are shown in Figure 55. The general agreement is comparable to, but not quite as good as seen in Figure 53 for the lower BPR nozzle. The corresponding spectral comparisons over a wide range of angles are shown in Figure 56. At θ = 60 deg (Fig. 56 (a)) the general agreement is good with a small under-prediction at low frequency and a smaller over-prediction at high frequency. At θ = 90 deg (Fig. 56 (b)) there is under-prediction at both low and high frequencies with very good agreement in the vicinity of 1000 Hz. At θ = 120 deg (Fig. 56 (c)) there is under-prediction at all frequencies, and the same is true but to a lesser degree at θ = 135 deg (Fig. 56 (d)). The agreement is very good at the more aft angles of θ = 145 deg (Fig. 56 (e)) and θ = 155 deg (Fig. 56 (f)) except for the problem-prone very high frequencies.

For higher power, V_{mix}/c_{amb} = 0.949, OASPL directivity comparisons are shown in Figure 57. The agreement is rather good except for the region near the peak noise angle, which may be due attempting to accommodate simulated flight data in the model at angles $\theta \leq$ 140 deg. The corresponding spectral comparisons over a wide range of angles are shown in Figure 58. Agreement is rather good for θ < 135 deg (Figs. 58 (a) – (c)) except for slight under-predictions at low frequency. At θ = 135 deg (Fig. 58 (d)) there is a significant under-prediction at low frequency and good agreement at higher frequencies except for the highest two bands. At θ = 150 deg (Fig. 58 (e)) and θ = 160 deg (Fig. 58 (f)), the general agreement is good except for the low frequency under-prediction.

GRC/GE Nominal BPR = 14 Coannular External Plug Nozzle

For this ultra-high BPR nozzle, static data are not reported at low power, so comparisons are shown for V_{mix}/c_{amb} = 0.591 and M_f = 0.20. OASPL directivity comparisons are shown in Figure 59. The agreement is in general good, with a slight over-prediction in the vicinity of θ = 100 deg and a somewhat larger under-prediction at high θ. It is interesting to note that in this case, in contrast to the previous comparisons in this section, plug separation noise is predicted to be dominant over most of the range. The corresponding spectral comparisons over a wide range of angles are shown in Figure 60. At θ = 60 deg (Fig. 60 (a)) both prediction and experiment show that the SPL peak occurs at high rather than low frequency, and the agreement between the two is fairly good. At θ = 90 deg (Fig. 60 (b)) the agreement is excellent in the higher frequency range, while there is an under-prediction at low frequency, but the major cause of this low frequency problem may be the tone at about 63 Hz, which might also influence neighboring bands. Similar observations can be made at θ = 120 deg (Fig. 60 (c)) and θ = 135 deg

(Fig. 60 (d)) where at $\theta = 120$ deg the 63 Hz tone is not so obvious, but may be accompanied by a harmonic at 126 Hz, while at $\theta = 135$ deg there is hardly any tone evidence. At $\theta = 150$ deg (Fig. 60 (e)) there is a significant under-prediction, but this is in the range where the transformation procedure may cause problems. Such problems are even more evident at $\theta = 165$ deg (Fig. 60 (f)) where general quality of the experimental data looks poor.

For the only static test reported for this configuration, at fairly high power, $V_{mix}/c_{amb} = 0.766$, OASPL directivity comparisons are shown in Figure 61. The agreement is much better than for the lower power simulated flight case (Fig. 59). Merged mixing noise is predicted to predominate except in the region near $\theta = 90$ deg. The corresponding spectral comparisons over a wide range of angles are shown in Figure 62. At $\theta = 60$ deg (Fig. 62 (a)) agreement is good for $f < 1$ kHz, but the high frequency region is over-predicted. At $\theta = 90$ deg (Fig. 62 (b)) the spectrum peaks at high frequency and the agreement is better, with a small under-prediction at low frequency and a small over-prediction at high frequency. Agreement is not quite as good, although qualitatively similar, at $\theta = 120$ deg (Fig. 62 (c)). At $\theta = 135$ deg (Fig. 62 (d)), $\theta = 150$ deg (Fig. 62 (e)) and $\theta = 160$ deg (Fig. 62 (f)), where the low frequency merged mixing peak is dominant, agreement is reasonably good except for the high frequency region, where the over-prediction is significant.

LeRC 1.3 Area-Ratio Extended-Core Coannular Nozzle

Spectral comparisons for a CVP case with both streams subsonic (Ref. 25) are shown in Figure 63 for an unlikely practical, extreme case with $V_O/V_I = 0.37$ where the inner stream mixing component becomes quite significant and $V_{mix}/c_{amb} = 1.04$. At $\theta = 95$ deg (Fig. 63 (a)) there is a small under-prediction at high (inner stream) and low (merged region) frequencies, with a larger under-prediction occurring in the region where both components are important. At $\theta = 139$ deg (Fig. 63 (b)) the situation is similar but with slightly worse agreement. So although the agreement could be better here, at least approximately the right limits are approached at low V_O/V_I.

Spectral comparisons for an IVP case ($V_O/V_I = 2.14$) with both streams subsonic and $V_{mix}/c_{amb} = 1.17$ are shown in Figure 64 at $\theta = 95$ deg (Fig. 64 (a)) and at $\theta = 139$ deg (Fig. 64 (b)). The agreement at low frequencies, where merged mixing noise is predicted to be dominant, is quite good. In the middle and high frequency regions, predicted to be dominated by outer shear layer mixing noise, there is some over-prediction, as great as 3 dB at $\theta = 95$ deg and 5 dB at $\theta = 139$ deg. The fact that the prediction comes this close at such extreme conditions is encouraging.

Spectral comparisons for a CVP case with supersonic inner stream and subsonic outer stream at $V_{mix}/c_{amb} = 1.04$ and $V_O/V_I = 0.45$, spectral comparisons are shown at $\theta = 46$ deg (Fig. 65 (a)), at $\theta = 95$ deg (Fig. 65 (b)) and at $\theta = 139$ deg (Fig. 65 (c)). At $\theta = 46$ deg shock noise is predicted to dominate more than half the spectrum, and the experimental data are in reasonably good agreement. The screech tone, most evident at $\theta = 95$ deg, in the experimental data may influence the mixing process and the resulting broadband noise components, but investigating such matters is beyond the scope of this effort. In spite of this problem, the agreement is rather good, except at $\theta = 139$ deg,

where the noise is under-predicted by more than 5 dB if the experimental data are considered valid.

LeRC 1.4 Area-Ratio Coannular Nozzle

For a very high velocity IVP case with both streams supersonic, V_{mix}/c_{amb} = 2.04, V_O/V_I = 1.33 and BPR = 1.35, spectral comparisons are shown at θ = 46 deg (Fig. 66 (a)), at θ = 95 deg (Fig. 66 (b)) and at θ = 139 deg (Fig. 66 (c)). At θ = 46 deg outer stream shock noise is predicted to dominate two decades of the spectrum. Agreement is good in the low frequency (merged) range and in the middle frequency range where outer stream shock noise is predicted to be the dominant source; however, at high frequency it appears that inner stream and possibly outer shear layer mixing noises are over-predicted. At θ = 95 deg shock noise dominates only a few bands and the general agreement is quite good, with a slight over-prediction at high frequency, related mainly to the inner stream component. At θ = 139 deg the general agreement is good, but with about a 2 dB over-prediction of merged mixing noise.

LeRC 1.9 Area-Ratio Coannular Nozzle

Spectral comparisons are shown in Figure 67 for a low power case with V_O/V_I = 0.69, BPR = 2.83, V_{mix}/c_{amb} = 0.725 and both streams subsonic. The agreement is fairly good at θ = 46 deg (Fig. 67 (a)) and θ = 95 deg (Fig. 67 (b)) with an under-prediction of 1 to 2 dB. However, at θ = 139 deg (Fig. 67 (c)) although the spectral shape is predicted fairly well, it is about 5 dB low. This may indicate a weakness in the current empirical modification to the convection model, since n_c = 0.546 for merged, inner and outer components in the current prediction rather than the previous 0.62 that would produce higher levels at θ = 139 deg.

Spectral comparisons are shown in Figure 68 for a fairly high velocity IVP case with only the outer stream supersonic. This is a complicated situation wherein all four potential components are predicted to be dominant at some frequencies for at least one angle. In general the agreement is fairly good, with the poorest agreement being at θ = 46 deg (Fig. 68 (a)) where the peak frequency for outer stream shock noise is apparently higher than predicted.

Spectral comparisons are shown in Figure 69 for a very high velocity IVP case with both streams supersonic, V_{mix}/c_{amb} = 2.08, V_O/V_I = 1.33 and BPR = 2.07. This is a rather unique case where all five potential components, merged, inner stream, outer shear layer, outer stream shock and inner stream shock noises all contribute, at least marginally. The agreement is quite good at all three angles shown.

LeRC 3.3 Area-Ratio Coannular Nozzle

Spectral comparisons for a very high velocity IVP case with both streams supersonic, V_{mix}/c_{amb} = 2.13 and V_O/V_I = 1.33, spectral comparisons are shown at θ = 46 deg (Fig. 70 (a)), at θ = 95 deg (Fig. 70 (b)) and at θ = 139 deg (Fig. 70 (c)). At θ = 46 deg outer stream shock noise is predicted to dominate two decades of the spectrum, and the experimental data agree very well. The agreement at the other two angles is also reasonably good.

LaRC Nominal BPR = 5 Coannular External Plug Nozzle

The LaRC data are reported in Reference 31; all comparisons are for the lowest free jet Mach number for which data are available, $M_f = 0.10$. These data were not used to develop the component correlations, and so represent an independent check.

An OASPL directivity comparison at relatively low velocity, for $V_{mix}/c_{amb} = 0.835$, is shown in Figure 71, and the agreement is encouragingly good in view of the relatively close-in microphone array and the transformation issues. The agreement is excellent at the aft angles near the peak OASPL. Spectral comparisons are shown for $\theta = 58$ deg (Fig. 72 (a)), $\theta = 92$ deg (Fig. 72 (b)), $\theta = 117$ deg (Fig. 72 (c)), $\theta = 136$ deg (Fig. 72 (d)) and $\theta = 157$ deg (Fig. 72 (e)). Agreement in all cases is very good except at high frequency, where inner stream plug separation noise is predicted to be dominant; if there is any contribution at all, it is about 10 dB lower than predicted.

An OASPL directivity comparison at somewhat higher velocity, for $V_{mix}/c_{amb} = 0.989$, is shown in Figure 73. Agreement is nearly as good as at the lower velocity, again with the best agreement being in the aft angle region near the peak OASPL. Spectral comparisons are shown in Figure 74. Generally, except for the high frequency region where plug separation noise is significantly over-predicted, the agreement is fairly good, but with a tendency to over-predict the outer shear layer noise except at the highest and lowest angles.

The relatively good spectral directivity agreement for merged mixing noise with the close-in microphone array is evidence that the source location model currently in the prediction is at least reasonably valid. The angular shifts produced by the Amiet transformation are much less than for the previously discussed GRC case at $M_f = 0.28$ because of the much lower $M_f = 0.10$ here; thus any effect of not accounting for the downstream source location in the transformation procedure is much less. (Source location is accounted for in the prediction.)

LaRC Nominal BPR = 5 Coannular Internal Plug Nozzle

An OASPL directivity comparison at relatively low velocity, for $V_{mix}/c_{amb} = 0.809$ is shown in Figure 75. The relative directivity trends are in excellent agreement, but there is a consistent under-prediction of 1 to 1.5 dB. The spectral comparisons in Figure 76 indicate that the under-prediction is of the low frequency merged mixing noise. The outer shear layer noise appears to be predicted very well at all angles. This is even true to the highest frequencies for this configuration with no external plug (and thus no plug separation noise). Comparing the experimental data at high frequencies with the external plug configuration at nearly the same conditions (Fig. 72), a slight up-turn can be seen with the external plug at $\theta = 58$ deg and 92 deg, while at 117 deg the very high frequency SPLs level out while for the external plug while they do not for the internal plug. This weakly supports the presence of plug separation noise for the external plug, but at significantly lower levels than predicted based on data from GRC (Ref. 24).

Higher velocity comparisons, at $V_{mix}/c_{amb} = 0.967$, are shown in Figure 77 for OASPL directivity and Figure 78 for spectra at several angles. The directivity trends are in reasonably good agreement, with small over-prediction in the vicinity of $\theta = 100$ deg and

some under-prediction at high and low angles. At all angles except $\theta = 117$ deg (Fig. 78 (c)) the merged mixing noise is somewhat under-predicted. The outer shear layer and inner stream components are slightly over-predicted except at the furthest aft angles (Fig. 78 (e)). Comparisons with the external plug configuration (Fig. 74) again indicate, although even more weakly than at lower jet velocity, that there may be a small contribution of plug separation noise, but certainly at lower levels than currently predicted.

As with the external plug configuration, the relatively good spectral directivity agreement for merged mixing noise with the close-in microphone array is evidence that the source location model currently in the prediction is at least reasonably valid.

LaRC Nominal BPR = 8 Coannular External Plug Nozzle

An OASPL directivity comparison at very low velocity, for $V_{mix}/c_{amb} = 0.671$, is shown in Figure 79. The agreement is good near the peak noise angle, but the experimental levels exceed the prediction increasingly as θ decreases, approaching 3 dB at low θ. At $\theta = 67$ deg (Fig. 80 (a)) there is some evidence of a tone in the 500 Hz band with a harmonic in the 1000 Hz band; otherwise the low and middle frequency levels fall 2 to 3 dB above the prediction. At high frequency, it appears that plug separation noise, if present, is over-predicted. At $\theta = 92$ deg (Fig. 80 (b)) the agreement is not too bad even though there is some tone evidence at 1000 Hz, but is low by 1.5 to 2 dB at low frequency and high by as much as 4 dB at the very high frequencies where plug separation noise is predicted. Qualitatively similar agreement is seen at the more aft angles (Figs. 80 (c) – (e)) with differences even smaller for some. In comparing high frequency experimental levels with the internal plug case, essentially no differences are seen at any angle, which implies that if plug separation noise is present it is at too low a level to contribute to the total SPL even at the highest frequencies.

An OASPL directivity comparison at somewhat higher velocity, for $V_{mix}/c_{amb} = 0.828$, is shown in Figure 81. The agreement is generally quite good except at low angles where the experimental data do not decrease with decreasing angle as expected. At $\theta = 67$ deg (Fig. 82 (a)) there is some evidence of a tone in the 500 Hz band; at higher frequencies agreement is good over most of the spectrum except at very high frequencies where plug separation noise is predicted. At $\theta = 92$ deg (Fig. 82 (b)) and higher (Figs. 82 (c) – (e)) the agreement is very good except for the very high frequency prediction of plug separation noise. As at lower velocity, in comparing high frequency experimental levels with the internal plug case, essentially no differences are seen at any angle, which implies that if plug separation noise is present it is at too low a level to contribute to the total SPL even at the highest frequencies.

LaRC Nominal BPR = 8 Coannular Internal Plug Nozzle

An OASPL directivity comparison at very low velocity, for $V_{mix}/c_{amb} = 0.676$, is shown in Figure 83. Only at the angles near the peak is there even approximate agreement, and the prediction falls below the experimental data at all angles. The spectral comparisons in Figure 84 somewhat elucidate the problems. At $\theta = 67$ deg (Fig. 84 (a)) there is a very strong tone evident in the f = 500 Hz band, and for the low and middle frequencies the experimental data fall about 5 dB above the prediction. In addition, at the highest

frequency the experimental data flatten or even rise a little with increasing frequency, even though this configuration has no external plug to produce separation noise. At θ = 92 deg (Fig. 84 (b)) and θ = 117 deg (Fig. 84 (c)) the low and middle frequency disagreement is reduced to about 3 dB, but the high frequency problem is worse. Essentially the same observations hold for θ = 130 deg (Fig. 84 (d)), but here the tone in the 500 Hz band is again evident, raising that band 5 dB higher than the average of the two adjacent bands. For higher angles, as shown for θ = 142 deg (Fig. 84 (e)) and θ = 157 deg (Fig. 84 (f)), the agreement is rather good except at the high frequencies, which show the same type problem at all other angles.

An OASPL directivity comparison at somewhat higher velocity, for V_{mix}/c_{amb} = 0.840, is shown in Figure 85, and the agreement is much better than at lower velocity. At θ = 67 deg (Fig. 86 (a)) there is some evidence of possible tone contamination in the 400 and 500 Hz bands; otherwise the experimental data fall smoothly about 3 dB above the prediction. At θ = 92 deg and aft (Fig. 86 (b) – (e)) the agreement is quite good except for high frequency problems similar to those seen at lower velocity (Fig. 84), but of smaller magnitude. Comparing the differences between high and low velocity cases, it is possible that both high and low frequency background noise may become issues as velocity, and consequently test noise levels are decreased. Recall that Viswanathan (Ref. 13) showed that in trying to obtain high quality uncontaminated data it is not sufficient to show that the measured spectra have the shape generally expected for mixing noise. Since GRC data (Ref. 24) at similar conditions show better agreement with prediction, it may be reasonable to suspect background noise in the LaRC facility, but this is not a conclusive argument and further investigation is certainly warranted.

LaRC Nominal BPR = 11 Coannular Internal Plug Nozzle

An OASPL directivity comparison at very low velocity, for V_{mix}/c_{amb} = 0.592, is shown in Figure 87. The same type problems are seen as for the lower bypass case (Fig. 83), but the level of disagreement is greater. At θ = 67 deg (Fig. 88 (a)) there is a tone in the 500 Hz band that is so high it influences the adjacent bands also, and there is some evidence of the harmonic in the 1000 Hz band. At θ = 92 and 117 deg (Fig. 88 (b) – (c)) the disagreement is similar in nature to that in Figure 84, but of greater magnitude. At θ = 130 deg (Fig. 88 (d)) the 500 Hz tone is evident. At θ = 157 deg (Fig. 88 (e)) the agreement is not bad except at the high frequencies.

An OASPL directivity comparison at somewhat higher velocity, for V_{mix}/c_{amb} = 0.800, is shown in Figure 89. In the forward quadrant the experimental results fall above the prediction, but in the rear quadrant reasonable agreement is obtained. At θ = 67 deg (Fig. 90 (a)) there is evidence of a tone in the 500 Hz and a broadband under-prediction of 3-4 dB up to around 10000 Hz. At θ = 92 deg and beyond (Fig. 90 (b) – (e)) the agreement is rather good, with some small problems at the highest frequencies.

LaRC Nominal BPR = 14 Coannular Internal Plug Nozzle

For this ultra-high BPR configuration OASPL directivity comparison at high power but relatively low mixed velocity (on an absolute basis), V_{mix}/c_{amb} = 0.635, is shown in Figure 91. The disagreement is similar to that shown earlier herein for other low velocity cases. At θ = 67 deg (Fig. 92 (a)) there is a tone in the 500 Hz band that is so high it

influences the adjacent bands also, and there is some evidence of the harmonic in the 1000 Hz band. At θ = 92 deg and 117 (Fig. 92 (b) – (c)) the middle and low frequency data fall broadly somewhat above the prediction, and at high frequency the "roll-up" problem is evident. The low and middle frequency differences are less as angle increases, but the high frequency problem remains. The agreement is better at θ = 136 deg (Fig. 92 (d)), but the high frequency "roll-up" persists. At θ = 157 deg (Fig. 92 (e)), the agreement is quite good except for the high frequency "roll-up."

GRC/GE Nominal BPR = 5 Coannular External Plug Nozzle with Inner Stream Chevrons

As mentioned earlier herein, the chevron effects correlations developed in Reference 6 is updated herein, and a limited number of comparisons is shown.

An OASPL directivity comparison at static conditions and high mixed velocity, V_{mix}/c_{amb} = 1.04, is shown in Figure 93, with rather good agreement shown, although the peak level is under-predicted by about 2 dB. At θ = 60 deg (Fig. 94 (a)) the middle and high frequencies are somewhat over-predicted, while at the low frequency, the rather sharp peak exhibited by the experimental data at 100 Hz is under-predicted. As the angle increases to θ = 90 deg (Fig. 94 (b)) and θ = 120 deg (Fig. 94 (c)) the agreement improves. The agreement remains fairly good at θ = 135 - 160 deg (Fig. 94 (d) – (f)).

GRC/GE Nominal BPR = 5 Coannular External Plug Nozzle with
Inner and Outer Stream Chevrons

An OASPL directivity comparison at static conditions and high mixed velocity, V_{mix}/c_{amb} = 1.04, is shown in Figure 95, with rather good agreement shown, very similar to that for the core chevrons alone (Fig. 93). At θ = 60 deg (Fig. 96 (a)) the agreement is better than for the core chevrons alone (Fig. 94 (a)), with a lesser tendency to under-predict at low frequencies and a modest over-prediction at middle frequencies. At θ = 90 and 120 deg (Fig. 96 (b) – (c)) the agreement is very good at high and low frequencies (except the very highest), with an over-prediction approaching 3 dB at the middle frequencies. The agreement is fairly good at the more aft angles, θ = 135, 150 and 160 deg (Figs. 96 (d) – (f)).

Discussion

In view of all the issues with the analysis of simulated flight data and the possible contamination of data at low noise levels, the comparisons shown in this section are very encouraging, but by no means conclusive. The issue of plug separation noise is certainly an open one, in view of the differences between the GRC and LaRC data. The inner stream noise model is based primarily on very old data from a non-anechoic facility without flight simulation. The same is true at present for all the shock noise models, but here a significant body of data exists (e.g., Ref. 23) that can be analyzed if interest revives in supersonic aircraft. We also believe this approach is applicable to a wide range of suppressor concepts, not just chevrons; again pursuit of this topic would be particularly applicable to supersonic aircraft. Another item of concern is the crude empirical models for convection velocity for the mixing noise components, where further investigation is suggested to accurately cover the wide range of velocity ratios.

The most outstanding issues, however, are flight effects, the simulation of flight effects and the prediction of flight effects. A thorough analysis of recent flight data for configurations of interest could be compared with similar smaller scale model simulated flight data. It would be desirable to investigate both the Mani and Amiet approaches with an accounting for source location and investigating parametric variations in the models. It may be that neither the Mani nor Amiet approaches is adequate, and it might be worthwhile to utilize the Mani-Gliebe-Balsa model (Ref. 27) to investigate these issues. Only when such analyses have been made can the accuracy of the flight noise model be evaluated.

Concluding Remarks

A prediction model is presented that is more consistent and robust than that previously available in the NASA/MTC *FOOTPR* code, which was based on an interim coupling of older separate codes for conventional and inverted-velocity-profile coannular jets. The new model also includes a limited-range prediction of the effects of mixing-enhancement nozzle-exit chevrons on jet noise. Most of the validation comparisons are focused on recent NASA Glenn Research Center (GRC) data for relatively high bypass ratio (~5 ≤ BPR ≤ ~14) cases with both streams subsonic, but more limited comparisons are made with older NASA data that extend to much lower bypass ratios and higher velocities, including either or both streams supersonic. The development of this predictive model is heavily dependent on having good quality experimental data available to work with and data quality is carefully considered throughout this task. Uncertainties in the interpretation of simulated flight data cloud the validation of the procedure, but the comparisons shown herein are at least encouraging.

The finalized procedure is also compared with data from another test facility, at NASA Langley Research Center (LaRC) with its own unique characteristics; these comparisons establish the general validity of the new methodology over a wide range of conditions including the effects of flight, and identify issues or areas needing further improvement. The improved finalized model is incorporated into MTC's version *FOOTPR* code and a user's guide is provided. MTC also supports the adaptation of this code for incorporation in the NASA LaRC *Aircraft Noise Prediction Program (ANOPP)*.

Issues that particularly need further attention are as follows:

    (1)   Shear layer corrections for simulated flight data,

    (2)   Validation of models with actual flight data,

    (3)   Further development of shock noise and inner stream mixing noise models,

    (4)   Assessment of plug separation noise differences,

    (5)   Refinement of the current very arbitrary and preliminary models for mixing noise convection effects,

    (6)   Extension of model to wider range of suppression concepts.

References

1. Zorumski, W.E., "Aircraft Noise Prediction Program Theoretical Manual," NASA TM–83199, Parts 1 and 2, February 1982.

2. Clark, B.J., "Computer Program to Predict Aircraft Noise Levels," NASA TP–1913, September 1981.

3. "Proceedings of the Jet Noise Workshop," NASA/CP—2001-211152, November 2001.

4. Stone, J.R., and Clark, B.J., "Development of a Noise Prediction Code for 2–D Mixer Ejector Nozzle Systems, I – Effects of Principal Geometric Variables," Modern Technologies Corporation Report to General Electric Aircraft Engines, December 30, 1996. (Subject to limited exclusive rights under Government Contract Number NAS3–27235 until December 30, 2001.)

5. Stone, J.R., Krejsa, E.A. and Clark, B.J., "Jet Noise Source Separation and Improved Correlation Using Separate Flow Nozzle Data," MTC Report to GE Aircraft Engines, June 15, 2001. (Correction of October 6, 2000 Report) (Currently subject to limited exclusive rights under Government Contract Number NAS3–27720 until June 15, 2006; but with release by NASA planned before completion of this task.)

6. Stone, J.R., "Separate Flow Nozzle Jet Noise Source Separation and Correlation Extension to Enhanced Mixing Configurations," MTC Report to GE Aircraft Engines, June 22, 2001. (Currently subject to limited exclusive rights under Government Contract Number NAS3–27720 until June 22, 2006; but with release by NASA planned before completion of this task.)

7. Lighthill, M.J., "On Sound Generated Aerodynamically. I. General Theory," Proc. Roy. Soc. (London), Ser. A, vol. 211, No. 1107, March 1952, pp. 564–587.

8. Lighthill, M.J., "On Sound Generated Aerodynamically. II. Turbulence as a Source of Sound," Proc. Roy. Soc. (London), Ser. A, vol. 222, No. 1148, February 1954, pp. 1–32.

9. Ffowcs Williams, J.E., "Some Thoughts on the Effects of Aircraft Motion and Eddy Convection on the Noise from Air Jets," USAA Report 155, Southampton University, Great Britain, 1960.

10. Goldstein, M.E. and Howes, W.L., "New Aspects of Subsonic Aerodynamic Noise Theory," NASA TN D–7158, 1973.

11. Harper-Bourne, M. and Fisher, M.J., "The Noise from Shock Waves in Supersonic Jets," Noise Mechanisms, AGARD Conference Proceedings No. 131, 1974, Paper No. 11.

12. Jaynes, E.T, "Bayesian Methods: General Background," Presented at the Fourth Annual Workshop on Bayesian/Maximum Entropy Methods, University of Calgary, August 1984; also in Proceedings Volume, *Maximum Entropy and*

Bayesian Methods in Applied Statistics, J.H. Justice, Editor, Cambridge University press, 1985, pp. 1–25.

13. Viswanathan, K., "Quality of Jet Noise Data: Issues, Implications and Needs," AIAA 2002–0365, January 2002.

14. Heylighen, F., "Occum's Razor," http://pespmcl.vub.ac.be/OCCAMRAZ.html, July 1997.

15. Bass, H.E. and Shields, F.D., "Atmospheric Absorption of High Frequency Noise and Application to Fractional Octave Bands," NASA CR–2760, 1977.

16. Stone, J.R., Zola, C.L. and Clark, B.J., "An Improved Model for Conventional and Inverted-Velocity-Profile Coannular Jet Noise," AIAA–99–0078, January 1999.

17. Stone, J.R., Groesbeck, D.E., and Zola, C.L., "Conventional Profile Coaxial Jet Noise Prediction," AIAA J., Volume 21, Number 3, March 1983, pp. 336–342 (supersedes NASA TM–82712).

18. Stone, J.R., "An Empirical Model for Inverted-Velocity-Profile Jet Noise Prediction," NASA TM–73838, December 1977.

19. Olsen, W.A., and Friedman, R., "Jet Noise from Coaxial Nozzles over a Wide Range of Geometric and Flow Parameters," AIAA Paper 74–-3, January 1974.

20. Williams, T.J., Ali, M.R.H., and Anderson J.S., "Noise and Flow Characteristics of Coaxial Jets," J. Mechanical Engineering Science, Vol. 11, April 1969, pp. 133–142.

21. Stone, J.R., "Interim Prediction Method for Jet Noise," NASA TM–71618, November 1974.

22. Stone, J.R., "Supersonic Jet Shock Noise Reduction," AIAA Paper 84–2278, October 1984 (also NASA TM–83799).

23. Janardan, B.A., Yamamoto, K., Majjigi, R.K., and Brausch, J.F., "Experimental Investigation of Shock-Cell Noise Reduction for Dual-Stream Nozzles in Simulated Flight," NASA CR-3846, November 1984.

24. Janardan, B.A., Hoff, G.E., Barter, J.W., Martens, S., and Gliebe, P.R. (GEAE), and Mengle, V. and Dalton, W.N. (Allison Engine Co.), "AST Critical Propulsion and Noise Reduction Technologies for Future Commercial Subsonic Engines – Separate-Flow Exhaust System Noise Reduction Evaluation," Final Report: NAS3–27720, Area of Interest 14.3, General Electric Report R98AEB152, May 1998.

25. Goodykoontz, J.H. and Stone, J.R., "Experimental Study of Coaxial Nozzle Exhaust Noise," AIAA Paper 79–0631, March 1979.

26. Ahuja, K.K. and Bushell, K.W., "An Experimental Study of Subsonic Jet noise and Comparison with Theory," J. Sound Vibration, Vol. 30, No. 3, 1973, pp.317–341.

27. Gliebe, P.R., Brausch, J.F., Majjigi, R.K. and Lee, R., "Jet Noise Suppression," NASA RP–1258, Vol. 2 (WRDC Technical Report 90–3052), August 1991, pp.207–269.

28. Fisher, M.J., Preston, G.A. and Bryce, W.D., "A Modelling of the Noise from Simple Co-axial Jets," AIAA–93–4413, October 1993.

29. Fisher, M.J., Preston, G.A. and Mead, C.J., "A Modelling of the Noise from Simple Coaxial Jets, Part II—With Heated Primary Flow," AIAA–96–1666, 1996.

30. Olsen, W. and Karchmer, A., "Lip Noise Generated by Flow Separation from Nozzle Surfaces," AIAA–76–3, January 1976. (Also NASA TM X–71859)

31. Posey, J.W., Norum, T.D., Brown, M.G. and Bhat, T.R.S., "Jet Noise from Ultra-High Bypass Turbofan Engines," 143rd Meeting of the Acoustical Society of America, Pittsburgh, PA, June 3–7, 2002.

32. Ahuja, K.K., Tester, B.J. and Tanna, H.K., "The Free Jet as a Simulator of Forward Velocity Effects on Jet Noise," NASA CR–3056, October 1978.

Table I - Spectral Directivity Relations for Merged Mixing Noise
(a) Corrected Effective Directivity Angle, $\theta'_{M,cor}$, from 0 to 100 deg

Frequency parameter, log S_M — Normalized sound pressure level, $SPL_M - UOL_M$, dB vs. corrected effective directivity angle

Corrected effective directivity angle, $\theta'_{M,cor}$, deg

log S_M	0	10	20	30	40	50	60	70	80	90	100
-3.6	-93.8	-93.7	-93.6	-93.5	-93.4	-93.3	-93.2	-93.1	-92.9	-92.9	-92.9
-2.2	-51.8	-51.7	-51.6	-51.5	-51.4	-51.3	-51.2	-51.1	-50.9	-50.9	-50.9
-2.1	-48.8	-48.7	-48.6	-48.5	-48.4	-48.3	-48.2	-48.1	-47.9	-47.9	-47.9
-2.0	-45.8	-45.7	-45.6	-45.5	-45.4	-45.3	-45.2	-45.1	-44.9	-44.9	-44.9
-1.9	-42.8	-42.7	-42.6	-42.5	-42.4	-42.3	-42.2	-42.1	-41.9	-41.9	-41.9
-1.8	-40.0	-39.9	-39.8	-39.7	-39.6	-39.5	-39.4	-39.3	-39.1	-39.1	-39.1
-1.7	-37.4	-37.3	-37.2	-37.1	-37.0	-36.9	-36.8	-36.7	-36.5	-36.5	-36.5
-1.6	-34.9	-34.8	-34.7	-34.6	-34.5	-34.4	-34.3	-34.2	-34.0	-34.0	-34.0
-1.5	-32.5	-32.4	-32.3	-32.2	-32.1	-32.0	-31.9	-31.8	-31.6	-31.6	-31.6
-1.4	-30.2	-30.1	-30.0	-29.9	-29.8	-29.7	-29.6	-29.5	-29.3	-29.3	-29.3
-1.3	-28.0	-27.9	-27.8	-27.7	-27.6	-27.5	-27.4	-27.3	-27.1	-27.1	-27.1
-1.2	-25.8	-25.7	-25.6	-25.5	-25.4	-25.3	-25.2	-25.1	-24.9	-24.9	-24.9
-1.1	-23.6	-23.5	-23.4	-23.3	-23.2	-23.1	-23.0	-22.9	-22.7	-22.7	-22.7
-1.0	-21.5	-21.4	-21.3	-21.2	-21.1	-21.0	-20.9	-20.8	-20.6	-20.6	-20.6
-0.9	-19.5	-19.4	-19.3	-19.2	-19.1	-19.0	-18.9	-18.8	-18.6	-18.5	-18.5
-0.8	-17.6	-17.5	-17.4	-17.3	-17.2	-17.1	-17.0	-16.9	-16.7	-16.5	-16.5
-0.7	-15.8	-15.7	-15.6	-15.5	-15.4	-15.3	-15.2	-15.1	-14.9	-14.6	-14.6
-0.6	-14.3	-14.2	-14.1	-14.0	-13.9	-13.8	-13.7	-13.6	-13.4	-13.1	-13.0
-0.5	-13.2	-13.1	-13.0	-12.9	-12.8	-12.7	-12.6	-12.5	-12.3	-12.0	-11.9
-0.4	-12.4	-12.3	-12.2	-12.1	-12.0	-11.9	-11.8	-11.7	-11.5	-11.2	-11.1
-0.3	-11.9	-11.8	-11.7	-11.6	-11.5	-11.4	-11.3	-11.2	-11.0	-10.7	-10.6
-0.2	-11.6	-11.5	-11.4	-11.3	-11.2	-11.1	-11.0	-10.9	-10.7	-10.4	-10.3
-0.1	**-11.4**	**-11.3**	**-11.2**	**-11.1**	**-11.0**	**-10.9**	**-10.8**	**-10.7**	**-10.5**	**-10.2**	**-10.0**
0.0	-11.6	-11.5	-11.4	-11.3	-11.2	-11.1	-11.0	-10.8	-10.6	-10.4	-10.2
0.1	-12.0	-11.9	-11.8	-11.7	-11.6	-11.4	-11.3	-11.2	-11.0	-10.8	-10.6
0.2	-12.5	-12.4	-12.3	-12.2	-12.1	-11.9	-11.8	-11.7	-11.5	-11.4	-11.2
0.3	-13.4	-13.3	-13.2	-13.1	-13.0	-12.8	-12.7	-12.6	-12.4	-12.3	-12.0
0.4	-14.6	-14.5	-14.4	-14.3	-14.2	-14.0	-13.9	-13.8	-13.6	-13.5	-13.2
0.5	-16.2	-16.1	-16.0	-15.9	-15.8	-15.6	-15.5	-15.3	-15.1	-15.0	-14.7
0.6	-17.8	-17.7	-17.6	-17.5	-17.4	-17.2	-17.1	-16.9	-16.7	-16.6	-16.3
0.7	-19.4	-19.3	-19.2	-19.1	-19.0	-18.8	-18.7	-18.5	-18.3	-18.2	-17.9
0.8	-21.0	-20.9	-20.8	-20.7	-20.6	-20.4	-20.3	-20.1	-19.9	-19.8	-19.5
0.9	-22.6	-22.5	-22.4	-22.3	-22.2	-22.0	-21.9	-21.7	-21.5	-21.4	-21.1
1.0	-24.2	-24.1	-24.0	-23.9	-23.8	-23.6	-23.5	-23.3	-23.1	-23.0	-22.7
1.1	-25.8	-25.7	-25.6	-25.5	-25.4	-25.2	-25.1	-24.9	-24.7	-24.6	-24.3
1.2	-27.4	-27.3	-27.2	-27.1	-27.0	-26.8	-26.7	-26.5	-26.3	-26.2	-26.0
1.3	-29.0	-28.9	-28.8	-28.7	-28.6	-28.4	-28.3	-28.1	-27.9	-27.8	-27.7
1.4	-30.6	-30.5	-30.4	-30.3	-30.2	-30.0	-29.9	-29.7	-29.5	-29.4	-29.4
1.5	-32.2	-32.1	-32.0	-31.9	-31.8	-31.6	-31.5	-31.3	-31.1	-31.0	-31.1
1.6	-33.8	-33.7	-33.6	-33.5	-33.4	-33.2	-33.1	-32.9	-32.7	-32.6	-32.8
1.7	-35.4	-35.3	-35.2	-35.1	-35.0	-34.8	-34.7	-34.5	-34.3	-34.2	-34.5
1.8	-37.0	-36.9	-36.8	-36.7	-36.6	-36.4	-36.3	-36.1	-35.9	-35.8	-36.2
1.9	-38.6	-38.5	-38.4	-38.3	-38.2	-38.0	-37.9	-37.7	-37.5	-37.4	-37.9
2.0	-40.2	-40.1	-40.0	-39.9	-39.8	-39.6	-39.5	-39.3	-39.1	-39.0	-39.6
3.6	-62.6	-62.5	-62.4	-62.3	-62.2	-62.0	-61.9	-61.7	-61.5	-61.4	-63.4
$OASPL_M - UOL_M$	-1.1	-1.0	-0.9	-0.8	-0.7	-0.6	-0.5	-0.4	-0.2	0.0	0.2

Table I (Concluded) - Spectral Directivity Relations for Merged Mixing Noise
(b) Corrected Effective Directivity Angle, $\theta'_{M,cor}$, from 100 to 250 deg

Frequency parameter, log S_M | Normalized sound pressure level, SPL_M-UOL_M, dB vs. corrected effective directivity angle. Corrected effective directivity angle, $\theta'_{M,cor}$, deg

Frequency parameter, log S_M	110	120	130	140	150	160	170	180	190	200	250
-3.6	-92.9	-90.1	-85.0	-80.5	-79.1	-80.3	-80.4	-81.9	-83.4	-84.9	-92.4
-2.2	-50.9	-48.1	-43.0	-38.5	-37.1	-38.3	-39.8	-41.3	-42.8	-44.3	-51.8
-2.1	-47.9	-45.2	-40.1	-35.6	-34.4	-35.7	-37.2	-38.7	-40.2	-41.7	-49.2
-2.0	-44.9	-42.2	-37.2	-32.9	-31.8	-33.2	-34.7	-36.2	-37.7	-39.2	-46.7
-1.9	-41.9	-39.3	-34.5	-30.3	-29.3	-30.8	-32.3	-33.8	-35.3	-36.8	-44.3
-1.8	-39.1	-36.6	-31.9	-27.8	-26.9	-28.5	-30.0	-31.5	-33.0	-34.5	-42.0
-1.7	-36.5	-34.0	-29.4	-25.4	-24.6	-26.2	-27.7	-29.2	-30.7	-32.2	-39.7
-1.6	-34.0	-31.5	-27.0	-23.1	-22.3	-23.9	-25.4	-26.9	-28.4	-29.9	-37.4
-1.5	-31.6	-29.1	-24.7	-20.8	-20.0	-21.7	-23.2	-24.7	-26.2	-27.7	-35.2
-1.4	-29.3	-26.8	-22.4	-18.5	-17.8	-19.6	-21.1	-22.6	-24.1	-25.6	-33.1
-1.3	-27.1	-24.5	-20.1	-16.3	-15.7	-17.6	-19.1	-20.6	-22.1	-23.6	-31.1
-1.2	-24.9	-22.2	-17.9	-14.2	-13.7	-15.7	-17.2	-18.7	-20.2	-21.7	-29.2
-1.1	-22.7	-20.0	-15.8	-12.2	-11.8	-14.1	-15.6	-17.1	-18.6	-20.1	-27.6
-1.0	-20.6	-17.9	-13.8	-10.3	-10.2	-12.2	-13.7	-15.2	-16.7	-18.2	-25.7
-0.9	-18.5	-15.9	-11.9	-8.7	-8.7	-10.7	-12.2	-13.7	-15.2	-16.7	-24.2
-0.8	-16.5	-14.0	-10.3	-7.2	-7.4	-9.4	-10.9	-12.4	-13.9	-15.4	-22.9
-0.7	-14.7	-12.4	-8.8	-5.9	-6.5	-8.5	-10.0	-11.5	-13.0	-14.5	-22.0
-0.6	-13.1	-10.9	-7.5	-5.0	-5.8	-7.8	-9.3	-10.8	-12.3	-13.8	-21.3
-0.5	-11.7	-9.6	-6.6	-4.3	**-5.5**	**-7.5**	**-9.0**	**-10.5**	**-12.0**	**-13.5**	**-21.0**
-0.4	-10.5	-8.7	-5.9	**-4.0**	-6.3	-8.3	-9.8	-11.3	-12.8	-14.3	-21.8
-0.3	-9.7	-8.0	**-5.6**	-4.8	-7.8	-9.8	-11.1	-12.6	-14.1	-15.6	-23.1
-0.2	-9.3	**-7.7**	-6.2	-6.3	-10.2	-12.2	-13.5	-15.0	-16.5	-18.0	-25.5
-0.1	**-9.0**	-8.1	-7.1	-8.3	-13.1	-15.1	-16.4	-17.9	-19.4	-20.9	-28.4
0.0	-9.3	-8.7	-8.3	-10.5	-16.0	-18.1	-19.4	-20.9	-22.4	-23.9	-31.4
0.1	-9.9	-9.4	-9.8	-12.7	-18.9	-21.1	-22.4	-23.9	-25.4	-26.9	-34.4
0.2	-10.6	-10.4	-11.4	-14.9	-21.8	-24.1	-25.4	-26.9	-28.4	-29.9	-37.4
0.3	-11.8	-11.5	-13.1	-17.1	-24.7	-27.1	-28.4	-29.9	-31.4	-32.9	-40.4
0.4	-13.1	-12.8	-15.1	-19.4	-27.6	-30.1	-31.4	-32.9	-34.4	-35.9	-43.4
0.5	-14.6	-14.4	-17.1	-21.7	-30.5	-33.1	-34.4	-35.9	-37.4	-38.9	-46.4
0.6	-16.2	-16.2	-19.2	-24.0	-33.4	-36.1	-37.4	-38.9	-40.4	-41.9	-49.4
0.7	-17.8	-18.1	-21.3	-26.3	-36.3	-39.1	-40.4	-41.9	-43.4	-44.9	-52.4
0.8	-19.4	-20.0	-23.4	-28.6	-39.2	-42.1	-43.4	-44.9	-46.4	-47.9	-55.4
0.9	-21.1	-21.9	-25.5	-30.9	-42.1	-45.1	-46.4	-47.9	-49.4	-50.9	-58.4
1.0	-22.8	-23.8	-27.6	-33.2	-45.0	-48.1	-49.4	-50.9	-52.4	-53.9	-61.4
1.1	-24.5	-25.7	-29.7	-35.5	-47.9	-51.1	-52.4	-53.9	-55.4	-56.9	-64.4
1.2	-26.2	-27.6	-31.8	-37.9	-50.8	-54.1	-55.4	-56.9	-58.4	-59.9	-67.4
1.3	-27.9	-29.5	-33.9	-40.3	-53.7	-57.1	-58.4	-59.9	-61.4	-62.9	-70.4
1.4	-29.6	-31.5	-36.0	-42.7	-56.6	-60.1	-61.4	-62.9	-64.4	-65.9	-73.4
1.5	-31.3	-33.5	-38.2	-45.1	-59.5	-63.1	-64.4	-65.9	-67.4	-68.9	-76.4
1.6	-33.0	-35.5	-40.4	-47.5	-62.4	-66.1	-67.4	-68.9	-70.4	-71.9	-79.4
1.7	-34.7	-37.5	-42.6	-49.9	-65.3	-69.1	-70.4	-71.9	-73.4	-74.9	-82.4
1.8	-36.5	-39.5	-44.8	-52.3	-68.2	-72.1	-73.4	-74.9	-76.4	-77.9	-85.4
1.9	-38.3	-41.5	-47.0	-54.7	-71.1	-75.1	-76.4	-77.9	-79.4	-80.9	-88.4
2.0	-40.1	-43.5	-49.2	-57.1	-74.0	-78.1	-79.4	-80.9	-82.4	-83.9	-91.4
3.6	-68.9	-71.5	-80.0	-90.7	-120.4	-126.1	-127.4	-128.9	-130.4	-131.9	-139.4
$OASPL_M-UOL_M$	0.7	1.9	3.5	4.6	2.9	0.9	-0.6	-2.1	-3.6	-5.1	-12.6

Table II - Spectral Directivity Relations for Outer Shear Layer Mixing Noise
(a) Corrected Effective Directivity Angle, $\theta'_{O,cor}$, from 0 to 100 deg

Normalized sound pressure level, $SPL_O - UOL_O$, dB vs. corrected effective directivity angle

Frequency parameter, $\log S_O$	Corrected effective directivity angle, $\theta'_{O,cor}$, deg										
	0	10	20	30	40	50	60	70	80	90	100
-3.6	-253.5	-253.5	-253.5	-253.5	-253.5	-253.5	-253.5	-253.5	-253.5	-253.8	-253.6
-2.2	-169.5	-169.5	-169.5	-169.5	-169.5	-169.5	-169.5	-169.5	-169.5	-169.8	-169.6
-2.1	-163.5	-163.5	-163.5	-163.5	-163.5	-163.5	-163.5	-163.5	-163.5	-163.8	-163.6
-2.0	-157.5	-157.5	-157.5	-157.5	-157.5	-157.5	-157.5	-157.5	-157.5	-157.8	-157.6
-1.9	-151.5	-151.5	-151.5	-151.5	-151.5	-151.5	-151.5	-151.5	-151.5	-151.8	-151.6
-1.8	-145.5	-145.5	-145.5	-145.5	-145.5	-145.5	-145.5	-145.5	-145.5	-145.8	-145.6
-1.7	-139.5	-139.5	-139.5	-139.5	-139.5	-139.5	-139.5	-139.5	-139.5	-139.8	-139.6
-1.6	-133.5	-133.5	-133.5	-133.5	-133.5	-133.5	-133.5	-133.5	-133.5	-133.8	-133.6
-1.5	-127.5	-127.5	-127.5	-127.5	-127.5	-127.5	-127.5	-127.5	-127.5	-127.8	-127.6
-1.4	-121.5	-121.5	-121.5	-121.5	-121.5	-121.5	-121.5	-121.5	-121.5	-121.8	-121.6
-1.3	-115.5	-115.5	-115.5	-115.5	-115.5	-115.5	-115.5	-115.5	-115.5	-115.8	-115.6
-1.2	-109.5	-109.5	-109.5	-109.5	-109.5	-109.5	-109.5	-109.5	-109.5	-109.8	-109.6
-1.1	-103.5	-103.5	-103.5	-103.5	-103.5	-103.5	-103.5	-103.5	-103.5	-103.8	-103.6
-1.0	-97.5	-97.5	-97.5	-97.5	-97.5	-97.5	-97.5	-97.5	-97.5	-97.8	-97.6
-0.9	-91.5	-91.5	-91.5	-91.5	-91.5	-91.5	-91.5	-91.5	-91.5	-91.8	-91.6
-0.8	-85.5	-85.5	-85.5	-85.5	-85.5	-85.5	-85.5	-85.5	-85.5	-85.8	-85.6
-0.7	-79.5	-79.5	-79.5	-79.5	-79.5	-79.5	-79.5	-79.5	-79.5	-79.8	-79.6
-0.6	-73.5	-73.5	-73.5	-73.5	-73.5	-73.5	-73.5	-73.5	-73.5	-73.8	-73.6
-0.5	-67.5	-67.5	-67.5	-67.5	-67.5	-67.5	-67.5	-67.5	-67.5	-67.8	-67.6
-0.4	-61.5	-61.5	-61.5	-61.5	-61.5	-61.5	-61.5	-61.5	-61.5	-61.8	-61.6
-0.3	-55.5	-55.5	-55.5	-55.5	-55.5	-55.5	-55.5	-55.5	-55.5	-55.8	-55.6
-0.2	-49.5	-49.5	-49.5	-49.5	-49.5	-49.5	-49.5	-49.5	-49.5	-49.8	-49.6
-0.1	-43.5	-43.5	-43.5	-43.5	-43.5	-43.5	-43.5	-43.5	-43.5	-43.8	-43.6
0.0	-37.6	-37.6	-37.6	-37.6	-37.6	-37.6	-37.6	-37.6	-37.6	-37.8	-37.6
0.1	-32.6	-32.6	-32.6	-32.6	-32.6	-32.6	-32.6	-32.6	-32.6	-32.8	-32.6
0.2	-28.1	-28.1	-28.1	-28.1	-28.1	-28.1	-28.1	-28.1	-28.1	-28.3	-28.1
0.3	-24.1	-24.1	-24.1	-24.1	-24.1	-24.1	-24.1	-24.1	-24.1	-24.3	-24.1
0.4	-20.6	-20.6	-20.6	-20.6	-20.6	-20.6	-20.6	-20.6	-20.6	-20.8	-20.6
0.5	-17.5	-17.5	-17.5	-17.5	-17.5	-17.5	-17.5	-17.5	-17.5	-17.6	-17.6
0.6	-15.0	-15.0	-15.0	-15.0	-15.0	-15.0	-15.0	-15.0	-15.0	-15.1	-15.1
0.7	-13.0	-13.0	-13.0	-13.0	-13.0	-13.0	-13.0	-13.0	-13.0	-13.1	-13.1
0.8	-11.5	-11.5	-11.5	-11.5	-11.5	-11.5	-11.5	-11.5	-11.5	-11.6	-11.6
0.9	-10.5	-10.5	-10.5	-10.5	-10.5	-10.5	-10.5	-10.5	-10.5	-10.6	-10.6
1.0	-9.8	-9.8	-9.8	-9.8	-9.8	-9.8	-9.8	-9.8	-9.8	-9.9	-9.9
1.1	**-9.5**	**-9.5**	**-9.5**	**-9.5**	**-9.5**	**-9.5**	**-9.5**	**-9.5**	**-9.5**	**-9.6**	**-9.6**
1.2	-9.7	-9.7	-9.7	-9.7	-9.7	-9.7	-9.7	-9.7	-9.7	-9.8	-9.8
1.3	-10.0	-10.0	-10.0	-10.0	-10.0	-10.0	-10.0	-10.0	-10.0	-10.1	-10.1
1.4	-10.4	-10.4	-10.4	-10.4	-10.4	-10.4	-10.4	-10.4	-10.4	-10.5	-10.6
1.5	-11.0	-11.0	-11.0	-11.0	-11.0	-11.0	-11.0	-11.0	-11.0	-11.1	-11.3
1.6	-11.7	-11.7	-11.7	-11.7	-11.7	-11.7	-11.7	-11.7	-11.7	-11.8	-12.2
1.7	-12.6	-12.6	-12.6	-12.6	-12.6	-12.6	-12.6	-12.6	-12.6	-12.7	-13.2
1.8	-13.6	-13.6	-13.6	-13.6	-13.6	-13.6	-13.6	-13.6	-13.6	-13.7	-14.2
1.9	-14.7	-14.7	-14.7	-14.7	-14.7	-14.7	-14.7	-14.7	-14.7	-14.8	-15.4
2.0	-15.8	-15.8	-15.8	-15.8	-15.8	-15.8	-15.8	-15.8	-15.8	-15.9	-16.6
3.6	-31.2	-31.2	-31.2	-31.2	-31.2	-31.2	-31.2	-31.2	-31.2	-31.3	-33.4
$OASPL_O - UOL_O$	0.2	0.2	0.2	0.2	0.2	0.2	0.2	0.2	0.2	0.0	0.0

Table II (Concluded) - Spectral Directivity Relations for Outer Shear Layer Mixing Noise
(b) Corrected Effective Directivity Angle, $\theta'_{O,cor}$, from 110 to 250 deg

Normalized sound pressure level, SPL_O-UOL_O, dB vs. corrected effective directivity angle

Frequency parameter, log S_O	Corrected effective directivity angle, $\theta'_{O,cor}$, deg										
	110	120	130	140	150	160	170	180	190	200	250
-3.6	-253.6	-254.7	-256.9	-253.5	-256.0	-260.0	-264.0	-268.0	-272.0	-276.0	-296.0
-2.2	-169.6	-170.7	-172.9	-169.5	-172.0	-176.0	-180.0	-184.0	-188.0	-192.0	-212.0
-2.1	-163.6	-164.7	-166.9	-163.5	-166.0	-170.0	-174.0	-178.0	-182.0	-186.0	-206.0
-2.0	-157.6	-158.7	-160.9	-157.5	-160.0	-164.0	-168.0	-172.0	-176.0	-180.0	-200.0
-1.9	-151.6	-152.7	-154.9	-151.5	-154.0	-158.0	-162.0	-166.0	-170.0	-174.0	-194.0
-1.8	-145.6	-146.7	-148.9	-145.5	-148.0	-152.0	-156.0	-160.0	-164.0	-168.0	-188.0
-1.7	-139.6	-140.7	-142.9	-139.5	-142.0	-146.0	-150.0	-154.0	-158.0	-162.0	-182.0
-1.6	-133.6	-134.7	-136.9	-133.5	-136.0	-140.0	-144.0	-148.0	-152.0	-156.0	-176.0
-1.5	-127.6	-128.7	-130.9	-127.5	-130.0	-134.0	-138.0	-142.0	-146.0	-150.0	-170.0
-1.4	-121.6	-122.7	-124.9	-121.5	-124.0	-128.0	-132.0	-136.0	-140.0	-144.0	-164.0
-1.3	-115.6	-116.7	-118.9	-115.5	-118.0	-122.0	-126.0	-130.0	-134.0	-138.0	-158.0
-1.2	-109.6	-110.7	-112.9	-109.5	-112.0	-116.0	-120.0	-124.0	-128.0	-132.0	-152.0
-1.1	-103.6	-104.7	-106.9	-103.5	-106.0	-110.0	-114.0	-118.0	-122.0	-126.0	-146.0
-1.0	-97.6	-98.7	-100.9	-97.5	-100.0	-104.0	-108.0	-112.0	-116.0	-120.0	-140.0
-0.9	-91.6	-92.7	-94.9	-91.5	-94.0	-98.0	-102.0	-106.0	-110.0	-114.0	-134.0
-0.8	-85.6	-86.7	-88.9	-85.5	-88.0	-92.0	-96.0	-100.0	-104.0	-108.0	-128.0
-0.7	-79.6	-80.7	-82.9	-79.5	-82.0	-86.0	-90.0	-94.0	-98.0	-102.0	-122.0
-0.6	-73.6	-74.7	-76.9	-73.5	-76.0	-80.0	-84.0	-88.0	-92.0	-96.0	-116.0
-0.5	-67.6	-68.7	-70.9	-67.5	-70.0	-74.0	-78.0	-82.0	-86.0	-90.0	-110.0
-0.4	-61.6	-62.7	-64.9	-61.5	-64.0	-68.0	-72.0	-76.0	-80.0	-84.0	-104.0
-0.3	-55.6	-56.7	-58.9	-55.5	-58.0	-62.0	-66.0	-70.0	-74.0	-78.0	-98.0
-0.2	-49.6	-50.7	-52.9	-49.5	-52.0	-56.0	-60.0	-64.0	-68.0	-72.0	-92.0
-0.1	-43.6	-44.7	-46.9	-43.5	-46.0	-50.0	-54.0	-58.0	-62.0	-66.0	-86.0
0.0	-37.6	-38.7	-40.9	-38.5	-41.0	-45.0	-49.0	-53.0	-57.0	-61.0	-81.0
0.1	-32.6	-33.7	-35.9	-34.0	-36.5	-40.5	-44.5	-48.5	-52.5	-56.5	-76.5
0.2	-28.1	-29.2	-31.4	-30.0	-32.5	-36.5	-40.5	-44.5	-48.5	-52.5	-72.5
0.3	-24.1	-25.2	-27.4	-26.5	-29.0	-33.0	-37.0	-41.0	-45.0	-49.0	-69.0
0.4	-20.6	-21.7	-23.9	-23.5	-26.0	-30.0	-34.0	-38.0	-42.0	-46.0	-66.0
0.5	-17.6	-18.7	-20.9	-21.0	-23.5	-27.5	-31.5	-35.5	-39.5	-43.5	-63.5
0.6	-15.1	-16.2	-18.4	-19.0	-21.5	-25.5	-29.5	-33.5	-37.5	-41.5	-61.5
0.7	-13.1	-14.2	-16.4	-17.5	-20.0	-24.0	-28.0	-32.0	-36.0	-40.0	-60.0
0.8	-11.6	-12.7	-14.9	-16.5	-19.0	-23.0	-27.0	-31.0	-35.0	-39.0	-59.0
0.9	-10.6	-11.7	-13.9	-15.8	-18.3	-22.3	-26.3	-30.3	-34.3	-38.3	-58.3
1.0	-9.9	-11.0	-13.2	**-15.5**	**-18.0**	**-22.0**	**-26.0**	**-30.0**	**-34.0**	**-38.0**	**-58.0**
1.1	**-9.6**	**-10.7**	**-12.9**	-15.8	-18.3	-22.3	-26.3	-30.3	-34.3	-38.3	-58.3
1.2	-9.8	-10.9	-13.1	-16.4	-18.9	-22.9	-26.9	-30.9	-34.9	-38.9	-58.9
1.3	-10.2	-11.4	-13.7	-17.3	-19.8	-23.8	-27.8	-31.8	-35.8	-39.8	-59.8
1.4	-10.8	-12.0	-14.4	-18.5	-21.0	-25.0	-29.0	-33.0	-37.0	-41.0	-61.0
1.5	-11.6	-12.8	-15.3	-19.9	-22.4	-26.4	-30.4	-34.4	-38.4	-42.4	-62.4
1.6	-12.7	-14.0	-16.5	-21.3	-23.8	-27.8	-31.8	-35.8	-39.8	-43.8	-63.8
1.7	-13.8	-15.2	-17.8	-22.7	-25.2	-29.2	-33.2	-37.2	-41.2	-45.2	-65.2
1.8	-15.0	-16.4	-19.1	-24.1	-26.6	-30.6	-34.6	-38.6	-42.6	-46.6	-66.6
1.9	-16.2	-17.7	-20.4	-25.5	-28.0	-32.0	-36.0	-40.0	-44.0	-48.0	-68.0
2.0	-17.4	-19.0	-21.8	-26.9	-29.4	-33.4	-37.4	-41.4	-45.4	-49.4	-69.4
3.6	-34.2	-37.2	-41.5	-49.3	-51.8	-55.8	-59.8	-63.8	-67.8	-71.8	-91.8
$OASPL_O-UOL_O$	-0.2	-1.3	-3.6	-6.3	-8.8	-12.8	-16.8	-20.8	-24.8	-28.8	-48.8

Table III - Spectral Directivity Relations for Inner Stream Mixing Noise
(a) Corrected Effective Directivity Angle, $\theta'_{I,cor}$, from 0 to 100 deg

Frequency parameter, $\log S_I$ — Normalized sound pressure level, $SPL_I - UOL_I$, dB vs. corrected effective directivity angle

Corrected effective directivity angle, $\theta'_{I,cor}$, deg

$\log S_I$	0	10	20	30	40	50	60	70	80	90	100
-3.6	-212.2	-211.4	-210.8	-210.4	-210.2	-210.6	-205.0	-205.5	-206.0	-204.5	-199.5
-2.2	-128.2	-127.4	-126.8	-126.4	-126.2	-126.6	-121.0	-121.5	-122.0	-120.5	-115.5
-2.1	-122.2	-121.4	-120.8	-120.4	-120.2	-120.6	-115.0	-115.5	-116.0	-114.5	-109.5
-2.0	-116.2	-115.4	-114.8	-114.4	-114.2	-114.6	-109.0	-109.5	-110.0	-108.5	-103.5
-1.9	-110.2	-109.4	-108.8	-108.4	-108.2	-108.6	-103.0	-103.5	-104.0	-102.5	-97.5
-1.8	-104.2	-103.4	-102.8	-102.4	-102.2	-102.6	-97.0	-97.5	-98.0	-96.5	-91.5
-1.7	-98.2	-97.4	-96.8	-96.4	-96.2	-96.6	-91.0	-91.5	-92.0	-90.5	-85.5
-1.6	-92.2	-91.4	-90.8	-90.4	-90.2	-90.6	-85.0	-85.5	-86.0	-84.5	-79.5
-1.5	-86.2	-85.4	-84.8	-84.4	-84.2	-84.6	-79.0	-79.5	-80.0	-78.5	-73.5
-1.4	-80.2	-79.4	-78.8	-78.4	-78.2	-78.6	-73.0	-73.5	-74.0	-72.5	-67.5
-1.3	-74.2	-73.4	-72.8	-72.4	-72.2	-72.6	-67.0	-67.5	-68.0	-66.5	-61.5
-1.2	-68.2	-67.4	-66.8	-66.4	-66.2	-66.6	-61.0	-61.5	-62.0	-60.5	-55.5
-1.1	-62.2	-61.4	-60.8	-60.4	-60.2	-60.6	-55.0	-55.5	-56.0	-54.5	-49.5
-1.0	-56.2	-55.4	-54.8	-54.4	-54.2	-54.6	-49.0	-49.5	-50.0	-48.5	-43.5
-0.9	-50.2	-49.4	-48.8	-48.4	-48.2	-48.6	-43.0	-43.5	-44.0	-42.5	-37.5
-0.8	-44.2	-43.4	-42.8	-42.4	-42.2	-42.6	-37.0	-37.5	-38.0	-37.5	-32.5
-0.7	-38.2	-37.4	-36.8	-36.4	-36.2	-36.6	-32.0	-32.5	-33.0	-32.5	-28.0
-0.6	-33.2	-32.4	-31.8	-31.4	-31.2	-31.6	-27.5	-28.0	-28.5	-28.0	-24.0
-0.5	-28.7	-27.9	-27.3	-26.9	-26.7	-27.1	-23.5	-24.0	-24.5	-24.0	-20.5
-0.4	-24.7	-23.9	-23.3	-22.9	-22.7	-23.1	-20.0	-20.5	-21.0	-20.5	-17.5
-0.3	-21.2	-20.4	-19.8	-19.4	-19.2	-19.6	-17.0	-17.5	-18.0	-17.5	-15.0
-0.2	-18.2	-17.4	-16.8	-16.4	-16.2	-16.6	-14.5	-15.0	-15.5	-15.0	-13.0
-0.1	-15.7	-14.9	-14.3	-13.9	-13.7	-14.1	-12.5	-13.0	-13.5	-13.0	-11.5
0.0	-13.7	-12.9	-12.3	-11.9	-11.7	-12.1	-11.0	-11.5	-12.0	-11.5	-10.5
0.1	-12.2	-11.4	-10.8	-10.4	-10.2	-10.6	-10.0	-10.5	-11.0	-10.5	-10.0
0.2	-11.2	-10.4	-9.8	-9.4	-9.2	-9.6	-9.5	-10.0	-10.5	-10.0	**-9.8**
0.3	-10.7	-9.9	-9.3	-8.9	-8.7	-9.1	**-9.3**	**-9.8**	**-10.3**	**-9.8**	-10.0
0.4	**-10.5**	**-9.7**	**-9.1**	**-8.7**	**-8.5**	**-8.9**	-9.5	-10.0	-10.5	-10.0	-10.4
0.5	-10.7	-9.9	-9.3	-8.9	-8.7	-9.1	-9.9	-10.4	-10.9	-10.4	-11.0
0.6	-11.1	-10.3	-9.7	-9.3	-9.1	-9.5	-10.5	-11.0	-11.5	-11.0	-12.2
0.7	-11.7	-10.9	-10.3	-9.9	-9.7	-10.1	-11.7	-12.2	-12.7	-12.2	-13.4
0.8	-12.9	-12.1	-11.5	-11.1	-10.9	-11.3	-12.9	-13.4	-13.9	-13.4	-14.6
0.9	-14.1	-13.3	-12.7	-12.3	-12.1	-12.5	-14.1	-14.6	-15.1	-14.6	-15.8
1.0	-15.3	-14.5	-13.9	-13.5	-13.3	-13.7	-15.3	-15.8	-16.3	-15.8	-17.0
1.1	-16.5	-15.7	-15.1	-14.7	-14.5	-14.9	-16.5	-17.0	-17.5	-17.0	-18.2
1.2	-17.7	-16.9	-16.3	-15.9	-15.7	-16.1	-17.7	-18.2	-18.7	-18.2	-19.4
1.3	-18.9	-18.1	-17.5	-17.1	-16.9	-17.3	-18.9	-19.4	-19.9	-19.4	-20.6
1.4	-20.1	-19.3	-18.7	-18.3	-18.1	-18.5	-20.1	-20.6	-21.1	-20.6	-21.8
1.5	-21.3	-20.5	-19.9	-19.5	-19.3	-19.7	-21.3	-21.8	-22.3	-21.8	-23.0
1.6	-22.5	-21.7	-21.1	-20.7	-20.5	-20.9	-22.5	-23.0	-23.5	-23.0	-24.2
1.7	-23.7	-22.9	-22.3	-21.9	-21.7	-22.1	-23.7	-24.2	-24.7	-24.2	-25.4
1.8	-24.9	-24.1	-23.5	-23.1	-22.9	-23.3	-24.9	-25.4	-25.9	-25.4	-26.6
1.9	-26.1	-25.3	-24.7	-24.3	-24.1	-24.5	-26.1	-26.6	-27.1	-26.6	-27.8
2.0	-27.3	-26.5	-25.9	-25.5	-25.3	-25.7	-27.3	-27.8	-28.3	-27.8	-29.0
3.6	-44.1	-43.3	-42.7	-42.3	-42.1	-42.5	-44.1	-44.6	-45.1	-44.6	-45.8
$OASPL_I - UOL_I$	-0.8	0.0	0.6	1.0	1.2	0.8	0.5	0.0	-0.5	0.0	0.0

Table III (Concluded) - Spectral Directivity Relations for Inner Stream Mixing Noise
(b) Corrected Effective Directivity Angle, $\theta'_{I,cor}$, from110 to 250 deg

Frequency parameter, $\log S_I$

Normalized sound pressure level, $SPL_I - UOL_I$, dB vs. corrected effective directivity angle

Corrected effective directivity angle, $\theta'_{I,cor}$, deg

$\log S_I$	110	120	130	140	150	160	170	180	190	200	250
-3.6	-198.3	-191.3	-178.5	-174.0	-173.0	-172.0	-169.0	-168.5	-168.5	-169.0	-189.5
-2.2	-114.3	-107.3	-94.5	-90.0	-89.0	-88.0	-85.0	-84.5	-84.5	-85.0	-105.5
-2.1	-108.3	-101.3	-88.5	-84.0	-83.0	-82.0	-79.0	-78.5	-78.5	-79.0	-99.5
-2.0	-102.3	-95.3	-82.5	-78.0	-77.0	-76.0	-73.0	-72.5	-72.5	-73.0	-93.5
-1.9	-96.3	-89.3	-76.5	-72.0	-71.0	-70.0	-67.0	-66.5	-66.5	-67.0	-87.5
-1.8	-90.3	-83.3	-70.5	-66.0	-65.0	-64.0	-61.0	-60.5	-60.5	-61.0	-81.5
-1.7	-84.3	-77.3	-64.5	-60.0	-59.0	-58.0	-55.0	-54.5	-54.5	-55.0	-75.5
-1.6	-78.3	-71.3	-58.5	-54.0	-53.0	-52.0	-50.5	-50.5	-51.0	-52.0	-69.5
-1.5	-72.3	-65.3	-52.5	-48.0	-47.0	-46.0	-46.0	-46.5	-47.5	-49.0	-68.0
-1.4	-66.3	-59.3	-46.5	-42.0	-41.0	-41.0	-41.5	-42.5	-44.0	-46.0	-66.5
-1.3	-60.3	-53.3	-40.5	-36.0	-36.0	-36.5	-37.5	-39.0	-41.0	-43.5	-65.0
-1.2	-54.3	-47.3	-34.5	-31.0	-31.5	-32.5	-34.0	-36.0	-38.5	-41.5	-64.0
-1.1	-48.3	-41.3	-29.5	-26.5	-27.5	-29.0	-31.0	-33.5	-36.5	-40.0	**-63.5**
-1.0	-42.3	-35.3	-25.0	-22.5	-24.0	-26.0	-28.5	-31.5	-35.0	-39.0	-63.8
-0.9	-36.3	-30.3	-21.0	-19.0	-21.0	-23.5	-26.5	-30.0	-34.0	**-38.5**	-64.6
-0.8	-31.3	-25.8	-17.5	-16.0	-18.5	-21.5	-25.0	-29.0	**-33.5**	-38.8	-65.8
-0.7	-26.8	-21.8	-14.5	-13.5	-16.5	-20.0	-24.0	**-28.5**	-33.8	-39.6	-67.3
-0.6	-22.8	-18.3	-12.0	-11.5	-15.0	-19.0	**-23.5**	-28.8	-34.6	-40.8	-69.1
-0.5	-19.3	-15.3	-10.0	-10.0	-14.0	**-18.5**	-23.8	-29.6	-35.8	-42.3	-71.2
-0.4	-16.3	-12.8	-8.5	-9.0	**-13.5**	-18.8	-24.6	-30.8	-37.3	-44.1	-73.3
-0.3	-13.8	-10.8	-7.5	**-8.5**	-13.8	-19.6	-25.8	-32.3	-39.1	-46.2	-76.3
-0.2	-11.8	-9.3	**-7.0**	-8.8	-14.6	-20.8	-27.3	-34.1	-41.2	-49.2	-79.3
-0.1	-10.3	-8.3	-7.3	-9.6	-15.8	-22.3	-29.1	-36.2	-44.1	-52.2	-82.3
0.0	-9.3	**-7.8**	-8.1	-10.8	-17.3	-24.1	-31.2	-39.0	-47.0	-55.2	-85.3
0.1	**-8.8**	-8.1	-9.2	-12.3	-19.1	-26.2	-33.9	-41.8	-49.9	-58.2	-88.3
0.2	-9.1	-8.9	-10.8	-14.1	-21.2	-28.8	-36.6	-44.6	-52.8	-61.2	-91.3
0.3	-9.8	-10.0	-12.4	-16.2	-23.7	-31.4	-39.3	-47.4	-55.7	-64.2	-94.3
0.4	-10.8	-11.6	-14.2	-18.3	-26.2	-34.0	-42.0	-50.2	-58.6	-67.2	-97.3
0.5	-12.3	-13.3	-16.1	-20.4	-28.7	-36.6	-44.7	-53.0	-61.5	-70.2	-100.3
0.6	-13.8	-15.1	-18.1	-22.5	-31.2	-39.2	-47.4	-55.8	-64.4	-73.2	-103.3
0.7	-15.3	-16.9	-20.2	-24.7	-33.7	-41.8	-50.1	-58.6	-67.3	-76.2	-106.3
0.8	-16.8	-18.7	-22.4	-27.0	-36.2	-44.4	-52.8	-61.4	-70.2	-79.2	-109.3
0.9	-18.3	-20.5	-24.6	-29.3	-38.7	-47.0	-55.5	-64.2	-73.1	-82.2	-112.3
1.0	-19.8	-22.3	-26.8	-31.6	-41.2	-49.6	-58.2	-67.0	-76.0	-85.2	-115.3
1.1	-21.3	-24.1	-29.0	-33.9	-43.7	-52.2	-60.9	-69.8	-78.9	-88.2	-118.3
1.2	-22.8	-25.9	-31.2	-36.2	-46.2	-54.8	-63.6	-72.6	-81.8	-91.2	-121.3
1.3	-24.3	-27.7	-33.4	-38.5	-48.7	-57.4	-66.3	-75.4	-84.7	-94.2	-124.3
1.4	-25.8	-29.5	-35.6	-40.8	-51.2	-60.0	-69.0	-78.2	-87.6	-97.2	-127.3
1.5	-27.3	-31.3	-37.8	-43.1	-53.7	-62.6	-71.7	-81.0	-90.5	-100.2	-130.3
1.6	-28.8	-33.1	-40.0	-45.4	-56.2	-65.2	-74.4	-83.8	-93.4	-103.2	-133.3
1.7	-30.3	-34.9	-42.2	-47.7	-58.7	-67.8	-77.1	-86.6	-96.3	-106.2	-136.3
1.8	-31.8	-36.7	-44.4	-50.0	-61.2	-70.4	-79.8	-89.4	-99.2	-109.2	-139.3
1.9	-33.3	-38.5	-46.6	-52.3	-63.7	-73.0	-82.5	-92.2	-102.1	-112.2	-142.3
2.0	-34.8	-40.3	-48.8	-54.6	-66.2	-75.6	-85.2	-95.0	-105.0	-115.2	-145.3
3.6	-55.8	-65.5	-79.6	-86.8	-101.2	-112.0	-123.0	-134.2	-145.6	-157.2	-187.3
$OASPL_I - UOL_I$	0.0	0.8	1.6	0.1	-5.0	-10.0	-15.0	-20.0	-25.0	-30.0	-55.0

Table IV - Spectral Directivity Relations for Inner Stream Plug Separation Noise
(a) Corrected Effective Directivity Angle, $\theta'_{P,cor}$, from 0 to 100 deg

Frequency parameter, log S_P											

Normalized sound pressure level, SPL_P-UOL_P, dB vs. corrected effective directivity angle
Corrected effective directivity angle, $\theta'_{P,cor}$, deg

log S_P	0	10	20	30	40	50	60	70	80	90	100
-3.6	-193.2	-190.2	-188.2	-185.2	-182.2	-179.2	-176.0	-172.8	-171.1	-169.5	-169.3
-2.2	-137.2	-134.2	-132.2	-129.2	-126.2	-123.2	-120.0	-116.8	-115.1	-113.5	-113.3
-2.1	-133.2	-130.2	-128.2	-125.2	-122.2	-119.2	-116.0	-112.8	-111.1	-109.5	-109.3
-2.0	-129.2	-126.2	-124.2	-121.2	-118.2	-115.2	-112.0	-108.8	-107.1	-105.5	-105.3
-1.9	-125.2	-122.2	-120.2	-117.2	-114.2	-111.2	-108.0	-104.8	-103.1	-101.5	-101.3
-1.8	-121.2	-118.2	-116.2	-113.2	-110.2	-107.2	-104.0	-100.8	-99.1	-97.5	-97.3
-1.7	-117.2	-114.2	-112.2	-109.2	-106.2	-103.2	-100.0	-96.8	-95.1	-93.5	-93.3
-1.6	-113.2	-110.2	-108.2	-105.2	-102.2	-99.2	-96.0	-92.8	-91.1	-89.5	-89.3
-1.5	-109.2	-106.2	-104.2	-101.2	-98.2	-95.2	-92.0	-88.8	-87.1	-85.5	-85.3
-1.4	-105.2	-102.2	-100.2	-97.2	-94.2	-91.2	-88.0	-84.8	-83.1	-81.5	-81.3
-1.3	-101.2	-98.2	-96.2	-93.2	-90.2	-87.2	-84.0	-80.8	-79.1	-77.5	-77.3
-1.2	-97.2	-94.2	-92.2	-89.2	-86.2	-83.2	-80.0	-76.8	-75.1	-73.5	-73.3
-1.1	-93.2	-90.2	-88.2	-85.2	-82.2	-79.2	-76.0	-72.8	-71.1	-69.5	-69.3
-1.0	-89.2	-86.2	-84.2	-81.2	-78.2	-75.2	-72.0	-68.8	-67.1	-65.5	-65.3
-0.9	-85.2	-82.2	-80.2	-77.2	-74.2	-71.2	-68.0	-64.8	-63.1	-61.5	-61.3
-0.8	-81.2	-78.2	-76.2	-73.2	-70.2	-67.2	-64.0	-60.8	-59.1	-57.5	-57.3
-0.7	-77.2	-74.2	-72.2	-69.2	-66.2	-63.2	-60.0	-56.8	-55.1	-53.5	-53.3
-0.6	-73.2	-70.2	-68.2	-65.2	-62.2	-59.2	-56.0	-52.8	-51.1	-49.5	-49.3
-0.5	-69.2	-66.2	-64.2	-61.2	-58.2	-55.2	-52.0	-48.8	-47.1	-45.5	-45.3
-0.4	-65.2	-62.2	-60.2	-57.2	-54.2	-51.2	-48.0	-44.8	-43.1	-41.5	-41.3
-0.3	-61.2	-58.2	-56.2	-53.2	-50.2	-47.2	-44.0	-40.8	-39.1	-37.5	-37.3
-0.2	-57.2	-54.2	-52.2	-49.2	-46.2	-43.2	-40.0	-36.8	-35.1	-33.5	-33.3
-0.1	-53.2	-50.2	-48.2	-45.2	-42.2	-39.2	-36.0	-32.8	-31.1	-29.5	-29.3
0.0	-49.2	-46.2	-44.2	-41.2	-38.2	-35.2	-32.0	-28.8	-27.1	-25.5	-25.3
0.1	-45.2	-42.2	-40.2	-37.2	-34.2	-31.2	-28.0	-24.8	-23.1	-21.5	-21.3
0.2	-41.2	-38.2	-36.2	-33.2	-30.2	-27.2	-24.0	-20.8	-19.1	-17.5	-17.3
0.3	-37.2	-34.2	-32.2	-29.2	-26.2	-23.2	-20.0	-16.8	-15.3	-14.0	-13.8
0.4	-34.0	-31.0	-29.0	-26.0	-23.0	-20.0	-16.9	-13.8	-12.3	-11.2	-11.2
0.5	-31.6	-28.6	-26.6	-23.6	-20.6	-17.6	-14.5	-11.5	-10.2	-9.4	-9.5
0.6	**-30.4**	**-27.4**	**-25.4**	**-22.4**	**-19.4**	**-16.4**	**-13.4**	**-10.4**	**-9.1**	**-8.4**	**-8.5**
0.7	-30.8	-27.8	-25.8	-22.8	-19.8	-16.8	-13.8	-10.8	-9.5	-8.8	-8.9
0.8	-31.4	-28.4	-26.4	-23.4	-20.4	-17.4	-14.4	-11.4	-10.1	-9.4	-9.5
0.9	-32.6	-29.6	-27.6	-24.6	-21.6	-18.6	-15.6	-12.6	-11.3	-10.6	-10.7
1.0	-33.8	-30.8	-28.8	-25.8	-22.8	-19.8	-16.8	-13.8	-12.5	-11.8	-11.9
1.1	-35.0	-32.0	-30.0	-27.0	-24.0	-21.0	-18.0	-15.0	-13.7	-13.0	-13.1
1.2	-36.2	-33.2	-31.2	-28.2	-25.2	-22.2	-19.2	-16.2	-14.9	-14.2	-14.3
1.3	-37.4	-34.4	-32.4	-29.4	-26.4	-23.4	-20.4	-17.4	-16.1	-15.4	-15.5
1.4	-38.6	-35.6	-33.6	-30.6	-27.6	-24.6	-21.6	-18.6	-17.3	-16.6	-16.7
1.5	-39.8	-36.8	-34.8	-31.8	-28.8	-25.8	-22.8	-19.8	-18.5	-17.8	-17.9
1.6	-41.0	-38.0	-36.0	-33.0	-30.0	-27.0	-24.0	-21.0	-19.7	-19.0	-19.1
1.7	-42.2	-39.2	-37.2	-34.2	-31.2	-28.2	-25.2	-22.2	-20.9	-20.2	-20.3
1.8	-43.4	-40.4	-38.4	-35.4	-32.4	-29.4	-26.4	-23.4	-22.1	-21.4	-21.5
1.9	-44.6	-41.6	-39.6	-36.6	-33.6	-30.6	-27.6	-24.6	-23.3	-22.6	-22.7
2.0	-45.8	-42.8	-40.8	-37.8	-34.8	-31.8	-28.8	-25.8	-24.5	-23.8	-23.9
3.6	-65.0	-62.0	-60.0	-57.0	-54.0	-51.0	-48.0	-45.0	-43.7	-43.0	-43.1
$OASPL_P-UOL_P$	-22.2	-19.2	-17.2	-14.2	-11.2	-8.2	-5.2	-2.2	-0.8	0.0	-0.1

Table IV (Concluded) - Spectral Directivity Relations for Inr. Str. Plug Separation Noise
(b) Corrected Effective Directivity Angle, $\theta'_{P,cor}$, from 110 to 250 deg

Frequency parameter, log S_P	Normalized sound pressure level, SPL_P-UOL_P, dB vs. corrected effective directivity angle Corrected effective directivity angle, $\theta'_{P,cor}$, deg										
	110	120	130	140	150	160	170	180	190	200	250
-3.6	-169.8	-170.0	-172.2	-175.2	-181.2	-182.8	-185.8	-188.8	-191.8	-194.8	-209.8
-2.2	-113.8	-114.0	-116.2	-119.2	-125.2	-126.8	-129.8	-132.8	-135.8	-138.8	-153.8
-2.1	-109.8	-110.0	-112.2	-115.2	-121.2	-122.8	-125.8	-128.8	-131.8	-134.8	-149.8
-2.0	-105.8	-106.0	-108.2	-111.2	-117.2	-118.8	-121.8	-124.8	-127.8	-130.8	-145.8
-1.9	-101.8	-102.0	-104.2	-107.2	-113.2	-114.8	-117.8	-120.8	-123.8	-126.8	-141.8
-1.8	-97.8	-98.0	-100.2	-103.2	-109.2	-110.8	-113.8	-116.8	-119.8	-122.8	-137.8
-1.7	-93.8	-94.0	-96.2	-99.2	-105.2	-106.8	-109.8	-112.8	-115.8	-118.8	-133.8
-1.6	-89.8	-90.0	-92.2	-95.2	-101.2	-102.8	-105.8	-108.8	-111.8	-114.8	-129.8
-1.5	-85.8	-86.0	-88.2	-91.2	-97.2	-98.8	-101.8	-104.8	-107.8	-110.8	-125.8
-1.4	-81.8	-82.0	-84.2	-87.2	-93.2	-94.8	-97.8	-100.8	-103.8	-106.8	-121.8
-1.3	-77.8	-78.0	-80.2	-83.2	-89.2	-90.8	-93.8	-96.8	-99.8	-102.8	-117.8
-1.2	-73.8	-74.0	-76.2	-79.2	-85.2	-86.8	-89.8	-92.8	-95.8	-98.8	-113.8
-1.1	-69.8	-70.0	-72.2	-75.2	-81.2	-82.8	-85.8	-88.8	-91.8	-94.8	-109.8
-1.0	-65.8	-66.0	-68.2	-71.2	-77.2	-78.8	-81.8	-84.8	-87.8	-90.8	-105.8
-0.9	-61.8	-62.0	-64.2	-67.2	-73.2	-74.8	-77.8	-80.8	-83.8	-86.8	-101.8
-0.8	-57.8	-58.0	-60.2	-63.2	-69.2	-70.8	-73.8	-76.8	-79.8	-82.8	-97.8
-0.7	-53.8	-54.0	-56.2	-59.2	-65.2	-66.8	-69.8	-72.8	-75.8	-78.8	-93.8
-0.6	-49.8	-50.0	-52.2	-55.2	-61.2	-62.8	-65.8	-68.8	-71.8	-74.8	-89.8
-0.5	-45.8	-46.0	-48.2	-51.2	-55.2	-56.8	-59.8	-62.8	-65.8	-68.8	-83.8
-0.4	-41.8	-42.0	-44.2	-47.2	-51.2	-52.8	-55.8	-58.8	-61.8	-64.8	-79.8
-0.3	-37.8	-38.0	-40.2	-43.2	-47.2	-48.8	-51.8	-54.8	-57.8	-60.8	-75.8
-0.2	-33.8	-34.0	-36.2	-39.2	-43.2	-44.8	-47.8	-50.8	-53.8	-56.8	-71.8
-0.1	-29.8	-30.0	-32.2	-35.2	-39.2	-40.8	-43.8	-46.8	-49.8	-52.8	-67.8
0.0	-25.8	-26.0	-28.2	-31.2	-35.2	-36.8	-39.8	-42.8	-45.8	-48.8	-63.8
0.1	-21.8	-22.0	-24.2	-27.2	-31.2	-33.6	-36.6	-39.6	-42.6	-45.6	-60.6
0.2	-17.8	-18.5	-20.7	-24.0	-28.0	-31.2	-34.2	-37.2	-40.2	-43.2	-58.2
0.3	-14.8	-15.9	-18.1	-21.6	-25.6	**-30.0**	**-33.0**	**-36.0**	**-39.0**	**-42.0**	**-57.0**
0.4	-12.6	-13.9	-16.1	**-20.4**	**-24.4**	-30.4	-33.4	-36.4	-39.4	-42.4	-57.4
0.5	-11.1	**-12.9**	**-15.1**	-20.8	-24.8	-31.0	-34.0	-37.0	-40.0	-43.0	-58.0
0.6	**-10.1**	-13.3	-15.5	-21.4	-25.4	-32.2	-35.2	-38.2	-41.2	-44.2	-59.2
0.7	-10.5	-13.9	-16.1	-22.6	-26.6	-33.4	-36.4	-39.4	-42.4	-45.4	-60.4
0.8	-11.1	-15.1	-17.3	-23.8	-27.8	-34.6	-37.6	-40.6	-43.6	-46.6	-61.6
0.9	-12.3	-16.3	-18.5	-25.0	-29.0	-35.8	-38.8	-41.8	-44.8	-47.8	-62.8
1.0	-13.5	-17.5	-19.7	-26.2	-30.2	-37.0	-40.0	-43.0	-46.0	-49.0	-64.0
1.1	-14.7	-18.7	-20.9	-27.4	-31.4	-38.2	-41.2	-44.2	-47.2	-50.2	-65.2
1.2	-15.9	-19.9	-22.1	-28.6	-32.6	-39.4	-42.4	-45.4	-48.4	-51.4	-66.4
1.3	-17.1	-21.1	-23.3	-29.8	-33.8	-40.6	-43.6	-46.6	-49.6	-52.6	-67.6
1.4	-18.3	-22.3	-24.5	-31.0	-35.0	-41.8	-44.8	-47.8	-50.8	-53.8	-68.8
1.5	-19.5	-23.5	-25.7	-32.2	-36.2	-43.0	-46.0	-49.0	-52.0	-55.0	-70.0
1.6	-20.7	-24.7	-26.9	-33.4	-37.4	-44.2	-47.2	-50.2	-53.2	-56.2	-71.2
1.7	-21.9	-25.9	-28.1	-34.6	-38.6	-45.4	-48.4	-51.4	-54.4	-57.4	-72.4
1.8	-23.1	-27.1	-29.3	-35.8	-39.8	-46.6	-49.6	-52.6	-55.6	-58.6	-73.6
1.9	-24.3	-28.3	-30.5	-37.0	-41.0	-47.8	-50.8	-53.8	-56.8	-59.8	-74.8
2.0	-25.5	-29.5	-31.7	-38.2	-42.2	-49.0	-52.0	-55.0	-58.0	-61.0	-76.0
3.6	-44.7	-48.7	-50.9	-57.4	-61.4	-68.2	-71.2	-74.2	-77.2	-80.2	-95.2
$OASPL_P-UOL_P$	-1.6	-4.5	-6.7	-12.2	-16.2	-21.8	-24.8	-27.8	-30.8	-33.8	-48.8

Table V - Spectral Directivity Relations for Downstream Merged Shock Noise
(a) Corrected Directivity Angle, $\theta_{D,sh,cor}$, from 0 to 90 deg

Frequency parameter log $S_{D,sh}$	Normalized sound pressure level, $SPL_{D,sh}-UOL_{D,sh}$, dB vs. corrected directivity angle Corrected effective directivity angle, $\theta_{D,sh,cor}$, deg									
	0	10	20	30	40	50	60	70	80	90
-3.6	-188.2	-187.8	-187.4	-187.0	-186.6	-186.2	-185.8	-185.4	-180.0	-179.6
-2.2	-118.2	-117.8	-117.4	-117.0	-116.6	-116.2	-115.8	-115.4	-110.0	-109.6
-2.1	-113.2	-112.8	-112.4	-112.0	-111.6	-111.2	-110.8	-110.4	-105.0	-104.6
-2.0	-108.2	-107.8	-107.4	-107.0	-106.6	-106.2	-105.8	-105.4	-100.0	-99.6
-1.9	-103.2	-102.8	-102.4	-102.0	-101.6	-101.2	-100.8	-100.4	-95.0	-94.6
-1.8	-98.2	-97.8	-97.4	-97.0	-96.6	-96.2	-95.8	-95.4	-90.0	-89.6
-1.7	-93.2	-92.8	-92.4	-92.0	-91.6	-91.2	-90.8	-90.4	-85.0	-84.6
-1.6	-88.2	-87.8	-87.4	-87.0	-86.6	-86.2	-85.8	-85.4	-80.0	-79.6
-1.5	-83.2	-82.8	-82.4	-82.0	-81.6	-81.2	-80.8	-80.4	-75.0	-74.6
-1.4	-78.2	-77.8	-77.4	-77.0	-76.6	-76.2	-75.8	-75.4	-70.0	-69.6
-1.3	-73.2	-72.8	-72.4	-72.0	-71.6	-71.2	-70.8	-70.4	-65.0	-64.6
-1.2	-68.2	-67.8	-67.4	-67.0	-66.6	-66.2	-65.8	-65.4	-60.0	-59.6
-1.1	-63.2	-62.8	-62.4	-62.0	-61.6	-61.2	-60.8	-60.4	-55.0	-54.6
-1.0	-58.2	-57.8	-57.4	-57.0	-56.6	-56.2	-55.8	-55.4	-50.0	-49.6
-0.9	-53.2	-52.8	-52.4	-52.0	-51.6	-51.2	-50.8	-50.4	-45.0	-44.6
-0.8	-48.2	-47.8	-47.4	-47.0	-46.6	-46.2	-45.8	-45.4	-40.0	-39.6
-0.7	-43.2	-42.8	-42.4	-42.0	-41.6	-41.2	-40.8	-40.4	-35.0	-34.6
-0.6	-38.2	-37.8	-37.4	-37.0	-36.6	-36.2	-35.8	-35.4	-30.0	-29.6
-0.5	-33.2	-32.8	-32.4	-32.0	-31.6	-31.2	-30.8	-30.4	-25.0	-24.6
-0.4	-28.2	-27.8	-27.4	-27.0	-26.6	-26.2	-25.8	-25.4	-20.0	-19.6
-0.3	-23.2	-22.8	-22.4	-22.0	-21.6	-21.2	-20.8	-20.4	-15.0	-14.6
-0.2	-18.2	-17.8	-17.4	-17.0	-16.6	-16.2	-15.8	-15.4	-10.0	-9.6
-0.1	-13.2	-12.8	-12.4	-12.0	-11.6	-11.2	-10.8	-10.4	**-8.0**	**-7.6**
0.0	**-11.2**	**-10.8**	**-10.4**	**-10.0**	**-9.6**	**-9.2**	**-8.8**	**-8.4**	-9.0	-8.6
0.1	-12.2	-11.8	-11.4	-11.0	-10.6	-10.2	-9.8	-9.4	-10.0	-9.6
0.2	-13.2	-12.8	-12.4	-12.0	-11.6	-11.2	-10.8	-10.4	-11.0	-10.6
0.3	-14.2	-13.8	-13.4	-13.0	-12.6	-12.2	-11.8	-11.4	-12.0	-11.6
0.4	-15.2	-14.8	-14.4	-14.0	-13.6	-13.2	-12.8	-12.4	-13.0	-12.6
0.5	-16.2	-15.8	-15.4	-15.0	-14.6	-14.2	-13.8	-13.4	-14.0	-13.6
0.6	-17.2	-16.8	-16.4	-16.0	-15.6	-15.2	-14.8	-14.4	-15.0	-14.6
0.7	-18.2	-17.8	-17.4	-17.0	-16.6	-16.2	-15.8	-15.4	-16.0	-15.6
0.8	-19.2	-18.8	-18.4	-18.0	-17.6	-17.2	-16.8	-16.4	-17.0	-16.6
0.9	-20.2	-19.8	-19.4	-19.0	-18.6	-18.2	-17.8	-17.4	-18.0	-17.6
1.0	-21.2	-20.8	-20.4	-20.0	-19.6	-19.2	-18.8	-18.4	-19.0	-18.6
1.1	-22.2	-21.8	-21.4	-21.0	-20.6	-20.2	-19.8	-19.4	-20.0	-19.6
1.2	-23.2	-22.8	-22.4	-22.0	-21.6	-21.2	-20.8	-20.4	-21.0	-20.6
1.3	-24.2	-23.8	-23.4	-23.0	-22.6	-22.2	-21.8	-21.4	-22.0	-21.6
1.4	-25.2	-24.8	-24.4	-24.0	-23.6	-23.2	-22.8	-22.4	-23.0	-22.6
1.5	-26.2	-25.8	-25.4	-25.0	-24.6	-24.2	-23.8	-23.4	-24.0	-23.6
1.6	-27.2	-26.8	-26.4	-26.0	-25.6	-25.2	-24.8	-24.4	-25.0	-24.6
1.7	-28.2	-27.8	-27.4	-27.0	-26.6	-26.2	-25.8	-25.4	-26.0	-25.6
1.8	-29.2	-28.8	-28.4	-28.0	-27.6	-27.2	-26.8	-26.4	-27.0	-26.6
1.9	-30.2	-29.8	-29.4	-29.0	-28.6	-28.2	-27.8	-27.4	-28.0	-27.6
2.0	-31.2	-30.8	-30.4	-30.0	-29.6	-29.2	-28.8	-28.4	-29.0	-28.6
3.6	-47.2	-46.8	-46.4	-46.0	-45.6	-45.2	-44.8	-44.4	-45.0	-44.6
$OAL_{D,sh}-UOL_{D,sh}$	-3.6	-3.2	-2.8	-2.4	-2.0	-1.6	-1.2	-0.8	-0.4	0.0

Table V (Concluded) - Spectral Directivity Relations for Downstream Merged Shock Noise
(b) Corrected Directivity Angle, $\theta_{D,sh,cor}$, from 90 to 180 deg

Frequency parameter log $S_{D,sh}$	Normalized sound pressure level, $SPL_{D,sh}-UOL_{D,sh}$, dB vs. corrected directivity angle Corrected effective directivity angle, $\theta_{D,sh,cor}$, deg								
	100	110	120	130	140	150	160	170	180
-3.6	-179.6	-179.6	-179.6	-179.6	-179.6	-179.6	-179.6	-179.6	-179.6
-2.2	-109.6	-109.6	-109.6	-109.6	-109.6	-109.6	-109.6	-109.6	-109.6
-2.1	-104.6	-104.6	-104.6	-104.6	-104.6	-104.6	-104.6	-104.6	-104.6
-2.0	-99.6	-99.6	-99.6	-99.6	-99.6	-99.6	-99.6	-99.6	-99.6
-1.9	-94.6	-94.6	-94.6	-94.6	-94.6	-94.6	-94.6	-94.6	-94.6
-1.8	-89.6	-89.6	-89.6	-89.6	-89.6	-89.6	-89.6	-89.6	-89.6
-1.7	-84.6	-84.6	-84.6	-84.6	-84.6	-84.6	-84.6	-84.6	-84.6
-1.6	-79.6	-79.6	-79.6	-79.6	-79.6	-79.6	-79.6	-79.6	-79.6
-1.5	-74.6	-74.6	-74.6	-74.6	-74.6	-74.6	-74.6	-74.6	-74.6
-1.4	-69.6	-69.6	-69.6	-69.6	-69.6	-69.6	-69.6	-69.6	-69.6
-1.3	-64.6	-64.6	-64.6	-64.6	-64.6	-64.6	-64.6	-64.6	-64.6
-1.2	-59.6	-59.6	-59.6	-59.6	-59.6	-59.6	-59.6	-59.6	-59.6
-1.1	-54.6	-54.6	-54.6	-54.6	-54.6	-54.6	-54.6	-54.6	-54.6
-1.0	-49.6	-49.6	-49.6	-49.6	-49.6	-49.6	-49.6	-49.6	-49.6
-0.9	-44.6	-44.6	-44.6	-44.6	-44.6	-44.6	-44.6	-44.6	-44.6
-0.8	-39.6	-39.6	-39.6	-39.6	-39.6	-39.6	-39.6	-39.6	-39.6
-0.7	-34.6	-34.6	-34.6	-34.6	-34.6	-34.6	-34.6	-34.6	-34.6
-0.6	-29.6	-29.6	-29.6	-29.6	-29.6	-29.6	-29.6	-29.6	-29.6
-0.5	-24.6	-24.6	-24.6	-24.6	-24.6	-24.6	-24.6	-24.6	-24.6
-0.4	-19.6	-19.6	-19.6	-19.6	-19.6	-19.6	-19.6	-19.6	-19.6
-0.3	-14.6	-14.6	-14.6	-14.6	-14.6	-14.6	-14.6	-14.6	-14.6
-0.2	-9.6	-9.6	-9.6	-9.6	-9.6	-9.6	-9.6	-9.6	-9.6
-0.1	**-7.6**	**-7.6**	**-7.6**	**-7.6**	**-7.6**	**-7.6**	**-7.6**	**-7.6**	**-7.6**
0.0	-8.6	-8.6	-8.6	-8.6	-8.6	-8.6	-8.6	-8.6	-8.6
0.1	-9.6	-9.6	-9.6	-9.6	-9.6	-9.6	-9.6	-9.6	-9.6
0.2	-10.6	-10.6	-10.6	-10.6	-10.6	-10.6	-10.6	-10.6	-10.6
0.3	-11.6	-11.6	-11.6	-11.6	-11.6	-11.6	-11.6	-11.6	-11.6
0.4	-12.6	-12.6	-12.6	-12.6	-12.6	-12.6	-12.6	-12.6	-12.6
0.5	-13.6	-13.6	-13.6	-13.6	-13.6	-13.6	-13.6	-13.6	-13.6
0.6	-14.6	-14.6	-14.6	-14.6	-14.6	-14.6	-14.6	-14.6	-14.6
0.7	-15.6	-15.6	-15.6	-15.6	-15.6	-15.6	-15.6	-15.6	-15.6
0.8	-16.6	-16.6	-16.6	-16.6	-16.6	-16.6	-16.6	-16.6	-16.6
0.9	-17.6	-17.6	-17.6	-17.6	-17.6	-17.6	-17.6	-17.6	-17.6
1.0	-18.6	-18.6	-18.6	-18.6	-18.6	-18.6	-18.6	-18.6	-18.6
1.1	-19.6	-19.6	-19.6	-19.6	-19.6	-19.6	-19.6	-19.6	-19.6
1.2	-20.6	-20.6	-20.6	-20.6	-20.6	-20.6	-20.6	-20.6	-20.6
1.3	-21.6	-21.6	-21.6	-21.6	-21.6	-21.6	-21.6	-21.6	-21.6
1.4	-22.6	-22.6	-22.6	-22.6	-22.6	-22.6	-22.6	-22.6	-22.6
1.5	-23.6	-23.6	-23.6	-23.6	-23.6	-23.6	-23.6	-23.6	-23.6
1.6	-24.6	-24.6	-24.6	-24.6	-24.6	-24.6	-24.6	-24.6	-24.6
1.7	-25.6	-25.6	-25.6	-25.6	-25.6	-25.6	-25.6	-25.6	-25.6
1.8	-26.6	-26.6	-26.6	-26.6	-26.6	-26.6	-26.6	-26.6	-26.6
1.9	-27.6	-27.6	-27.6	-27.6	-27.6	-27.6	-27.6	-27.6	-27.6
2.0	-28.6	-28.6	-28.6	-28.6	-28.6	-28.6	-28.6	-28.6	-28.6
3.6	-44.6	-44.6	-44.6	-44.6	-44.6	-44.6	-44.6	-44.6	-44.6
$OAL_{D,sh}-UOL_{D,sh}$	0.0	0.0	0.0	0.0	0.0	0.0	0.0	0.0	0.0

Table VI - Spectral Directivity Relations for Outer Stream Shock Noise
(a) Corrected Directivity Angle, $\theta_{O,sh,cor}$, from 0 to 90 deg

Frequency parameter $\log S_{O,sh}$	Normalized sound pressure level, $SPL_{O,sh}-UOL_{O,sh}$, dB vs. corrected directivity angle

Frequency parameter $\log S_{O,sh}$	0	10	20	30	40	50	60	70	80	90
-3.6	-184.6	-184.6	-184.6	-184.6	-187.1	-186.6	-186.1	-185.6	-180.1	-179.6
-2.2	-114.6	-114.6	-114.6	-114.6	-117.1	-116.6	-116.1	-115.6	-110.1	-109.6
-2.1	-109.6	-109.6	-109.6	-109.6	-112.1	-111.6	-111.1	-110.6	-105.1	-104.6
-2.0	-104.6	-104.6	-104.6	-104.6	-107.1	-106.6	-106.1	-105.6	-100.1	-99.6
-1.9	-99.6	-99.6	-99.6	-99.6	-102.1	-101.6	-101.1	-100.6	-95.1	-94.6
-1.8	-94.6	-94.6	-94.6	-94.6	-97.1	-96.6	-96.1	-95.6	-90.1	-89.6
-1.7	-89.6	-89.6	-89.6	-89.6	-92.1	-91.6	-91.1	-90.6	-85.1	-84.6
-1.6	-84.6	-84.6	-84.6	-84.6	-87.1	-86.6	-86.1	-85.6	-80.1	-79.6
-1.5	-79.6	-79.6	-79.6	-79.6	-82.1	-81.6	-81.1	-80.6	-75.1	-74.6
-1.4	-74.6	-74.6	-74.6	-74.6	-77.1	-76.6	-76.1	-75.6	-70.1	-69.6
-1.3	-69.6	-69.6	-69.6	-69.6	-72.1	-71.6	-71.1	-70.6	-65.1	-64.6
-1.2	-64.6	-64.6	-64.6	-64.6	-67.1	-66.6	-66.1	-65.6	-60.1	-59.6
-1.1	-59.6	-59.6	-59.6	-59.6	-62.1	-61.6	-61.1	-60.6	-55.1	-54.6
-1.0	-54.6	-54.6	-54.6	-54.6	-57.1	-56.6	-56.1	-55.6	-50.1	-49.6
-0.9	-49.6	-49.6	-49.6	-49.6	-52.1	-51.6	-51.1	-50.6	-45.1	-44.6
-0.8	-44.6	-44.6	-44.6	-44.6	-47.1	-46.6	-46.1	-45.6	-40.1	-39.6
-0.7	-39.6	-39.6	-39.6	-39.6	-42.1	-41.6	-41.1	-40.6	-35.1	-34.6
-0.6	-34.6	-34.6	-34.6	-34.6	-37.1	-36.6	-36.1	-35.6	-30.1	-29.6
-0.5	-29.6	-29.6	-29.6	-29.6	-32.1	-31.6	-31.1	-30.6	-25.1	-24.6
-0.4	-24.6	-24.6	-24.6	-24.6	-27.1	-26.6	-26.1	-25.6	-20.1	-19.6
-0.3	-19.6	-19.6	-19.6	-19.6	-22.1	-21.6	-21.1	-20.6	-15.1	-14.6
-0.2	-14.6	-14.6	-14.6	-14.6	-17.1	-16.6	-16.1	-15.6	-10.1	-9.6
-0.1	-9.6	-9.6	-9.6	-9.6	-12.1	-11.6	-11.1	-10.6	**-8.1**	**-7.6**
0.0	**-7.6**	**-7.6**	**-7.6**	**-7.6**	**-10.1**	**-9.6**	**-9.1**	**-8.6**	-9.1	-8.6
0.1	-8.6	-8.6	-8.6	-8.6	-11.1	-10.6	-10.1	-9.6	-10.1	-9.6
0.2	-9.6	-9.6	-9.6	-9.6	-12.1	-11.6	-11.1	-10.6	-11.1	-10.6
0.3	-10.6	-10.6	-10.6	-10.6	-13.1	-12.6	-12.1	-11.6	-12.1	-11.6
0.4	-11.6	-11.6	-11.6	-11.6	-14.1	-13.6	-13.1	-12.6	-13.1	-12.6
0.5	-12.6	-12.6	-12.6	-12.6	-15.1	-14.6	-14.1	-13.6	-14.1	-13.6
0.6	-13.6	-13.6	-13.6	-13.6	-16.1	-15.6	-15.1	-14.6	-15.1	-14.6
0.7	-14.6	-14.6	-14.6	-14.6	-17.1	-16.6	-16.1	-15.6	-16.1	-15.6
0.8	-15.6	-15.6	-15.6	-15.6	-18.1	-17.6	-17.1	-16.6	-17.1	-16.6
0.9	-16.6	-16.6	-16.6	-16.6	-19.1	-18.6	-18.1	-17.6	-18.1	-17.6
1.0	-17.6	-17.6	-17.6	-17.6	-20.1	-19.6	-19.1	-18.6	-19.1	-18.6
1.1	-18.6	-18.6	-18.6	-18.6	-21.1	-20.6	-20.1	-19.6	-20.1	-19.6
1.2	-19.6	-19.6	-19.6	-19.6	-22.1	-21.6	-21.1	-20.6	-21.1	-20.6
1.3	-20.6	-20.6	-20.6	-20.6	-23.1	-22.6	-22.1	-21.6	-22.1	-21.6
1.4	-21.6	-21.6	-21.6	-21.6	-24.1	-23.6	-23.1	-22.6	-23.1	-22.6
1.5	-22.6	-22.6	-22.6	-22.6	-25.1	-24.6	-24.1	-23.6	-24.1	-23.6
1.6	-23.6	-23.6	-23.6	-23.6	-26.1	-25.6	-25.1	-24.6	-25.1	-24.6
1.7	-24.6	-24.6	-24.6	-24.6	-27.1	-26.6	-26.1	-25.6	-26.1	-25.6
1.8	-25.6	-25.6	-25.6	-25.6	-28.1	-27.6	-27.1	-26.6	-27.1	-26.6
1.9	-26.6	-26.6	-26.6	-26.6	-29.1	-28.6	-28.1	-27.6	-28.1	-27.6
2.0	-27.6	-27.6	-27.6	-27.6	-30.1	-29.6	-29.1	-28.6	-29.1	-28.6
3.6	-43.6	-43.6	-43.6	-43.6	-46.1	-45.6	-45.1	-44.6	-45.1	-44.6
$OAL_{O,sh}-UOL_{O,sh}$	0.0	0.0	0.0	0.0	-2.5	-2.0	-1.5	-1.0	-0.5	0.0

Table VI (Concluded) - Spectral Directivity Relations for Outer Stream Shock Noise
(b) Corrected Directivity Angle, $\theta_{O,sh,cor}$, from 90 to 180 deg

Normalized sound pressure level, $SPL_{O,sh}-UOL_{O,sh}$, dB vs. corrected directivity angle

Frequency parameter $\log S_{O,sh}$	Corrected effective directivity angle, $\theta_{O,sh,cor}$, deg								
	100	110	120	130	140	150	160	170	180
-3.6	-179.6	-179.6	-179.6	-184.6	-189.6	-189.6	-189.6	-189.6	-189.6
-2.2	-109.6	-109.6	-109.6	-114.6	-119.6	-119.6	-119.6	-119.6	-119.6
-2.1	-104.6	-104.6	-104.6	-109.6	-114.6	-114.6	-114.6	-114.6	-114.6
-2.0	-99.6	-99.6	-99.6	-104.6	-109.6	-109.6	-109.6	-109.6	-109.6
-1.9	-94.6	-94.6	-94.6	-99.6	-104.6	-104.6	-104.6	-104.6	-104.6
-1.8	-89.6	-89.6	-89.6	-94.6	-99.6	-99.6	-99.6	-99.6	-99.6
-1.7	-84.6	-84.6	-84.6	-89.6	-94.6	-94.6	-94.6	-94.6	-94.6
-1.6	-79.6	-79.6	-79.6	-84.6	-89.6	-89.6	-89.6	-89.6	-89.6
-1.5	-74.6	-74.6	-74.6	-79.6	-84.6	-84.6	-84.6	-84.6	-84.6
-1.4	-69.6	-69.6	-69.6	-74.6	-79.6	-79.6	-79.6	-79.6	-79.6
-1.3	-64.6	-64.6	-64.6	-69.6	-74.6	-74.6	-74.6	-74.6	-74.6
-1.2	-59.6	-59.6	-59.6	-64.6	-69.6	-69.6	-69.6	-69.6	-69.6
-1.1	-54.6	-54.6	-54.6	-59.6	-64.6	-64.6	-64.6	-64.6	-64.6
-1.0	-49.6	-49.6	-49.6	-54.6	-59.6	-59.6	-59.6	-59.6	-59.6
-0.9	-44.6	-44.6	-44.6	-49.6	-54.6	-54.6	-54.6	-54.6	-54.6
-0.8	-39.6	-39.6	-39.6	-44.6	-49.6	-49.6	-49.6	-49.6	-49.6
-0.7	-34.6	-34.6	-34.6	-39.6	-44.6	-44.6	-44.6	-44.6	-44.6
-0.6	-29.6	-29.6	-29.6	-34.6	-39.6	-39.6	-39.6	-39.6	-39.6
-0.5	-24.6	-24.6	-24.6	-29.6	-34.6	-34.6	-34.6	-34.6	-34.6
-0.4	-19.6	-19.6	-19.6	-24.6	-29.6	-29.6	-29.6	-29.6	-29.6
-0.3	-14.6	-14.6	-14.6	-19.6	-24.6	-24.6	-24.6	-24.6	-24.6
-0.2	-9.6	-9.6	-9.6	-14.6	-19.6	-19.6	-19.6	-19.6	-19.6
-0.1	**-7.6**	**-7.6**	**-7.6**	-9.6	-14.6	-14.6	-14.6	-14.6	-14.6
0.0	-8.6	-8.6	-8.6	**-7.6**	-9.6	-9.6	-9.6	-9.6	-9.6
0.1	-9.6	-9.6	-9.6	-8.6	**-7.6**	**-7.6**	**-7.6**	**-7.6**	**-7.6**
0.2	-10.6	-10.6	-10.6	-9.6	-8.6	-8.6	-8.6	-8.6	-8.6
0.3	-11.6	-11.6	-11.6	-10.6	-9.6	-9.6	-9.6	-9.6	-9.6
0.4	-12.6	-12.6	-12.6	-11.6	-10.6	-10.6	-10.6	-10.6	-10.6
0.5	-13.6	-13.6	-13.6	-12.6	-11.6	-11.6	-11.6	-11.6	-11.6
0.6	-14.6	-14.6	-14.6	-13.6	-12.6	-12.6	-12.6	-12.6	-12.6
0.7	-15.6	-15.6	-15.6	-14.6	-13.6	-13.6	-13.6	-13.6	-13.6
0.8	-16.6	-16.6	-16.6	-15.6	-14.6	-14.6	-14.6	-14.6	-14.6
0.9	-17.6	-17.6	-17.6	-16.6	-15.6	-15.6	-15.6	-15.6	-15.6
1.0	-18.6	-18.6	-18.6	-17.6	-16.6	-16.6	-16.6	-16.6	-16.6
1.1	-19.6	-19.6	-19.6	-18.6	-17.6	-17.6	-17.6	-17.6	-17.6
1.2	-20.6	-20.6	-20.6	-19.6	-18.6	-18.6	-18.6	-18.6	-18.6
1.3	-21.6	-21.6	-21.6	-20.6	-19.6	-19.6	-19.6	-19.6	-19.6
1.4	-22.6	-22.6	-22.6	-21.6	-20.6	-20.6	-20.6	-20.6	-20.6
1.5	-23.6	-23.6	-23.6	-22.6	-21.6	-21.6	-21.6	-21.6	-21.6
1.6	-24.6	-24.6	-24.6	-23.6	-22.6	-22.6	-22.6	-22.6	-22.6
1.7	-25.6	-25.6	-25.6	-24.6	-23.6	-23.6	-23.6	-23.6	-23.6
1.8	-26.6	-26.6	-26.6	-25.6	-24.6	-24.6	-24.6	-24.6	-24.6
1.9	-27.6	-27.6	-27.6	-26.6	-25.6	-25.6	-25.6	-25.6	-25.6
2.0	-28.6	-28.6	-28.6	-27.6	-26.6	-26.6	-26.6	-26.6	-26.6
3.6	-44.6	-44.6	-44.6	-43.6	-42.6	-42.6	-42.6	-42.6	-42.6
$OAL_{O,sh}-UOL_{O,sh}$	0.0	0.0	0.0	0.0	0.0	0.0	0.0	0.0	0.0

Table VII - Spectral Directivity Relations for Inner Stream Shock Noise
(a) Corrected Directivity Angle, $\theta_{l,sh,cor}$, from 0 to 90 deg

	Normalized sound pressure level, $SPL_{l,sh}-UOL_{l,sh}$, dB vs. corrected directivity angle									
Frequency parameter	Corrected effective directivity angle, $\theta_{l,sh,cor}$, deg									
$\log S_{l,sh}$	0	10	20	30	40	50	60	70	80	90
-3.6	-181.0	-181.0	-181.0	-181.0	-181.0	-181.5	-182.0	-182.5	-178.0	-178.4
-2.2	-111.0	-111.0	-111.0	-111.0	-111.0	-111.5	-112.0	-112.5	-108.0	-108.4
-2.1	-106.0	-106.0	-106.0	-106.0	-106.0	-106.5	-107.0	-107.5	-103.0	-103.4
-2.0	-101.0	-101.0	-101.0	-101.0	-101.0	-101.5	-102.0	-102.5	-98.0	-98.4
-1.9	-96.0	-96.0	-96.0	-96.0	-96.0	-96.5	-97.0	-97.5	-93.0	-93.4
-1.8	-91.0	-91.0	-91.0	-91.0	-91.0	-91.5	-92.0	-92.5	-88.0	-88.4
-1.7	-86.0	-86.0	-86.0	-86.0	-86.0	-86.5	-87.0	-87.5	-83.0	-83.4
-1.6	-81.0	-81.0	-81.0	-81.0	-81.0	-81.5	-82.0	-82.5	-78.0	-78.4
-1.5	-76.0	-76.0	-76.0	-76.0	-76.0	-76.5	-77.0	-77.5	-73.0	-73.4
-1.4	-71.0	-71.0	-71.0	-71.0	-71.0	-71.5	-72.0	-72.5	-68.0	-68.4
-1.3	-66.0	-66.0	-66.0	-66.0	-66.0	-66.5	-67.0	-67.5	-63.0	-63.4
-1.2	-61.0	-61.0	-61.0	-61.0	-61.0	-61.5	-62.0	-62.5	-58.0	-58.4
-1.1	-56.0	-56.0	-56.0	-56.0	-56.0	-56.5	-57.0	-57.5	-53.0	-53.4
-1.0	-51.0	-51.0	-51.0	-51.0	-51.0	-51.5	-52.0	-52.5	-48.0	-48.4
-0.9	-46.0	-46.0	-46.0	-46.0	-46.0	-46.5	-47.0	-47.5	-43.0	-43.4
-0.8	-41.0	-41.0	-41.0	-41.0	-41.0	-41.5	-42.0	-42.5	-38.0	-38.4
-0.7	-36.0	-36.0	-36.0	-36.0	-36.0	-36.5	-37.0	-37.5	-33.0	-33.4
-0.6	-31.0	-31.0	-31.0	-31.0	-31.0	-31.5	-32.0	-32.5	-28.0	-28.4
-0.5	-26.0	-26.0	-26.0	-26.0	-26.0	-26.5	-27.0	-27.5	-23.0	-23.4
-0.4	-21.0	-21.0	-21.0	-21.0	-21.0	-21.5	-22.0	-22.5	-18.0	-18.4
-0.3	-16.0	-16.0	-16.0	-16.0	-16.0	-16.5	-17.0	-17.5	-13.0	-13.4
-0.2	-11.0	-11.0	-11.0	-11.0	-11.0	-11.5	-12.0	-12.5	-8.0	-8.4
-0.1	-6.0	-6.0	-6.0	-6.0	-6.0	-6.5	-7.0	-7.5	**-6.0**	**-6.4**
0.0	**-4.0**	**-4.0**	**-4.0**	**-4.0**	**-4.0**	**-4.5**	**-5.0**	**-5.5**	-7.5	-7.9
0.1	-5.5	-5.5	-5.5	-5.5	-5.5	-6.0	-6.5	-7.0	-9.5	-9.4
0.2	-7.5	-7.5	-7.5	-7.5	-7.5	-8.0	-8.5	-9.0	-11.5	-10.9
0.3	-9.5	-9.5	-9.5	-9.5	-9.5	-10.0	-10.5	-11.0	-13.5	-12.4
0.4	-11.5	-11.5	-11.5	-11.5	-11.5	-12.0	-12.5	-13.0	-15.5	-13.9
0.5	-13.5	-13.5	-13.5	-13.5	-13.5	-14.0	-14.5	-15.0	-17.5	-15.4
0.6	-15.5	-15.5	-15.5	-15.5	-15.5	-16.0	-16.5	-17.0	-19.5	-16.9
0.7	-17.5	-17.5	-17.5	-17.5	-17.5	-18.0	-18.5	-19.0	-21.5	-18.4
0.8	-19.5	-19.5	-19.5	-19.5	-19.5	-20.0	-20.5	-21.0	-23.5	-19.9
0.9	-21.5	-21.5	-21.5	-21.5	-21.5	-22.0	-22.5	-23.0	-25.5	-21.4
1.0	-23.5	-23.5	-23.5	-23.5	-23.5	-24.0	-24.5	-25.0	-27.5	-22.9
1.1	-25.5	-25.5	-25.5	-25.5	-25.5	-26.0	-26.5	-27.0	-29.5	-24.4
1.2	-27.5	-27.5	-27.5	-27.5	-27.5	-28.0	-28.5	-29.0	-31.5	-25.9
1.3	-29.5	-29.5	-29.5	-29.5	-29.5	-30.0	-30.5	-31.0	-33.5	-27.4
1.4	-31.5	-31.5	-31.5	-31.5	-31.5	-32.0	-32.5	-33.0	-35.5	-28.9
1.5	-33.5	-33.5	-33.5	-33.5	-33.5	-34.0	-34.5	-35.0	-37.5	-30.4
1.6	-35.5	-35.5	-35.5	-35.5	-35.5	-36.0	-36.5	-37.0	-39.5	-31.9
1.7	-37.5	-37.5	-37.5	-37.5	-37.5	-38.0	-38.5	-39.0	-41.5	-33.4
1.8	-39.5	-39.5	-39.5	-39.5	-39.5	-40.0	-40.5	-41.0	-43.5	-34.9
1.9	-41.5	-41.5	-41.5	-41.5	-41.5	-42.0	-42.5	-43.0	-45.5	-36.4
2.0	-43.5	-43.5	-43.5	-43.5	-43.5	-44.0	-44.5	-45.0	-47.5	-37.9
3.6	-71.5	-71.5	-71.5	-71.5	-71.5	-72.0	-72.5	-73.0	-75.5	-65.9
$OAL_{l,sh}-UOL_{l,sh}$	1.8	1.8	1.8	1.8	1.8	1.3	0.8	0.3	-0.2	0.0

Table VII (Concluded) - Spectral Directivity Relations for Inner Stream Shock Noise
(b) Corrected Directivity Angle, $\theta_{I,sh,cor}$, from 90 to 180 deg

Frequency parameter — Normalized sound pressure level, $SPL_{I,sh}-UOL_{I,sh}$, dB vs. corrected directivity angle
Corrected effective directivity angle, $\theta_{O,sh,cor}$, deg

$\log S_{I,sh}$	100	110	120	130	140	150	160	170	180
-3.6	-178.6	-178.8	-179.0	-179.2	-179.4	-179.6	-179.8	-180.0	-180.2
-2.2	-108.6	-108.8	-109.0	-109.2	-109.4	-109.6	-109.8	-110.0	-110.2
-2.1	-103.6	-103.8	-104.0	-104.2	-104.4	-104.6	-104.8	-105.0	-105.2
-2.0	-98.6	-98.8	-99.0	-99.2	-99.4	-99.6	-99.8	-100.0	-100.2
-1.9	-93.6	-93.8	-94.0	-94.2	-94.4	-94.6	-94.8	-95.0	-95.2
-1.8	-88.6	-88.8	-89.0	-89.2	-89.4	-89.6	-89.8	-90.0	-90.2
-1.7	-83.6	-83.8	-84.0	-84.2	-84.4	-84.6	-84.8	-85.0	-85.2
-1.6	-78.6	-78.8	-79.0	-79.2	-79.4	-79.6	-79.8	-80.0	-80.2
-1.5	-73.6	-73.8	-74.0	-74.2	-74.4	-74.6	-74.8	-75.0	-75.2
-1.4	-68.6	-68.8	-69.0	-69.2	-69.4	-69.6	-69.8	-70.0	-70.2
-1.3	-63.6	-63.8	-64.0	-64.2	-64.4	-64.6	-64.8	-65.0	-65.2
-1.2	-58.6	-58.8	-59.0	-59.2	-59.4	-59.6	-59.8	-60.0	-60.2
-1.1	-53.6	-53.8	-54.0	-54.2	-54.4	-54.6	-54.8	-55.0	-55.2
-1.0	-48.6	-48.8	-49.0	-49.2	-49.4	-49.6	-49.8	-50.0	-50.2
-0.9	-43.6	-43.8	-44.0	-44.2	-44.4	-44.6	-44.8	-45.0	-45.2
-0.8	-38.6	-38.8	-39.0	-39.2	-39.4	-39.6	-39.8	-40.0	-40.2
-0.7	-33.6	-33.8	-34.0	-34.2	-34.4	-34.6	-34.8	-35.0	-35.2
-0.6	-28.6	-28.8	-29.0	-29.2	-29.4	-29.6	-29.8	-30.0	-30.2
-0.5	-23.6	-23.8	-24.0	-24.2	-24.4	-24.6	-24.8	-25.0	-25.2
-0.4	-18.6	-18.8	-19.0	-19.2	-19.4	-19.6	-19.8	-20.0	-20.2
-0.3	-13.6	-13.8	-14.0	-14.2	-14.4	-14.6	-14.8	-15.0	-15.2
-0.2	-8.6	-8.8	-9.0	-9.2	-9.4	-9.6	-9.8	-10.0	-10.2
-0.1	**-6.6**	**-6.8**	**-7.0**	**-7.2**	**-7.4**	**-7.6**	**-7.8**	**-8.0**	**-8.2**
0.0	-8.1	-8.3	-8.5	-8.7	-8.9	-9.1	-9.3	-9.5	-9.7
0.1	-9.6	-9.8	-10.0	-10.2	-10.4	-10.6	-10.8	-11.0	-11.2
0.2	-11.1	-11.3	-11.5	-11.7	-11.9	-12.1	-12.3	-12.5	-12.7
0.3	-12.6	-12.8	-13.0	-13.2	-13.4	-13.6	-13.8	-14.0	-14.2
0.4	-14.1	-14.3	-14.5	-14.7	-14.9	-15.1	-15.3	-15.5	-15.7
0.5	-15.6	-15.8	-16.0	-16.2	-16.4	-16.6	-16.8	-17.0	-17.2
0.6	-17.1	-17.3	-17.5	-17.7	-17.9	-18.1	-18.3	-18.5	-18.7
0.7	-18.6	-18.8	-19.0	-19.2	-19.4	-19.6	-19.8	-20.0	-20.2
0.8	-20.1	-20.3	-20.5	-20.7	-20.9	-21.1	-21.3	-21.5	-21.7
0.9	-21.6	-21.8	-22.0	-22.2	-22.4	-22.6	-22.8	-23.0	-23.2
1.0	-23.1	-23.3	-23.5	-23.7	-23.9	-24.1	-24.3	-24.5	-24.7
1.1	-24.6	-24.8	-25.0	-25.2	-25.4	-25.6	-25.8	-26.0	-26.2
1.2	-26.1	-26.3	-26.5	-26.7	-26.9	-27.1	-27.3	-27.5	-27.7
1.3	-27.6	-27.8	-28.0	-28.2	-28.4	-28.6	-28.8	-29.0	-29.2
1.4	-29.1	-29.3	-29.5	-29.7	-29.9	-30.1	-30.3	-30.5	-30.7
1.5	-30.6	-30.8	-31.0	-31.2	-31.4	-31.6	-31.8	-32.0	-32.2
1.6	-32.1	-32.3	-32.5	-32.7	-32.9	-33.1	-33.3	-33.5	-33.7
1.7	-33.6	-33.8	-34.0	-34.2	-34.4	-34.6	-34.8	-35.0	-35.2
1.8	-35.1	-35.3	-35.5	-35.7	-35.9	-36.1	-36.3	-36.5	-36.7
1.9	-36.6	-36.8	-37.0	-37.2	-37.4	-37.6	-37.8	-38.0	-38.2
2.0	-38.1	-38.3	-38.5	-38.7	-38.9	-39.1	-39.3	-39.5	-39.7
3.6	-66.1	-66.3	-66.5	-66.7	-66.9	-67.1	-67.3	-67.5	-67.7
$OAL_{I,sh}-UOL_{I,sh}$	-0.2	-0.4	-0.6	-0.8	-1.0	-1.2	-1.4	-1.6	-1.8
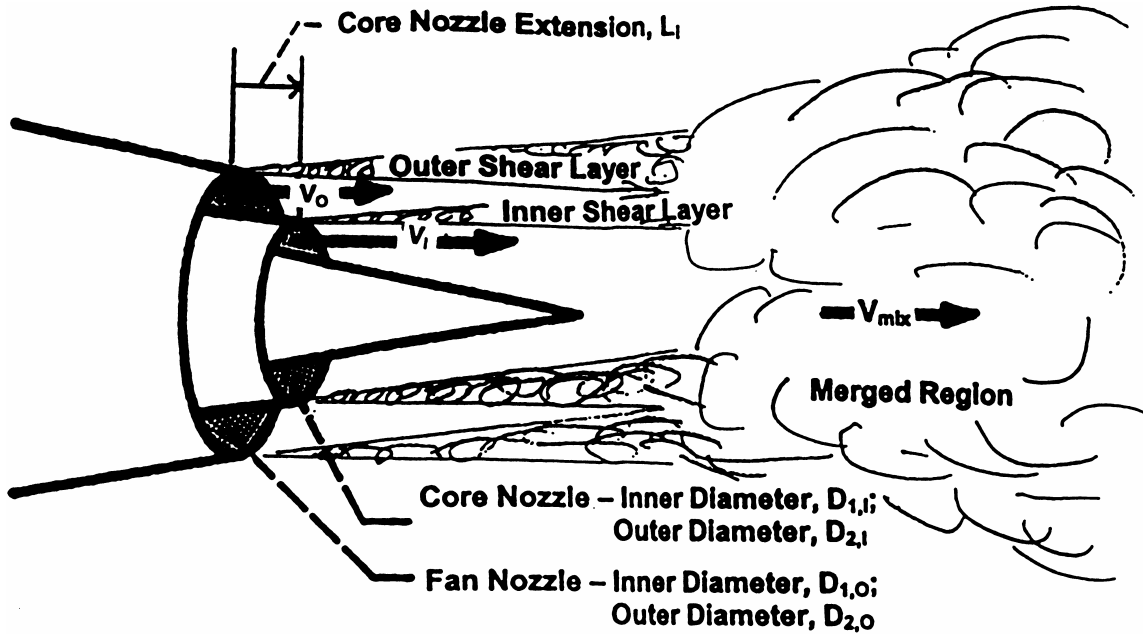
Figure 1 – Separate-Flow Coannular Plug Nozzle Geometry and Mixing Noise Generation Regions
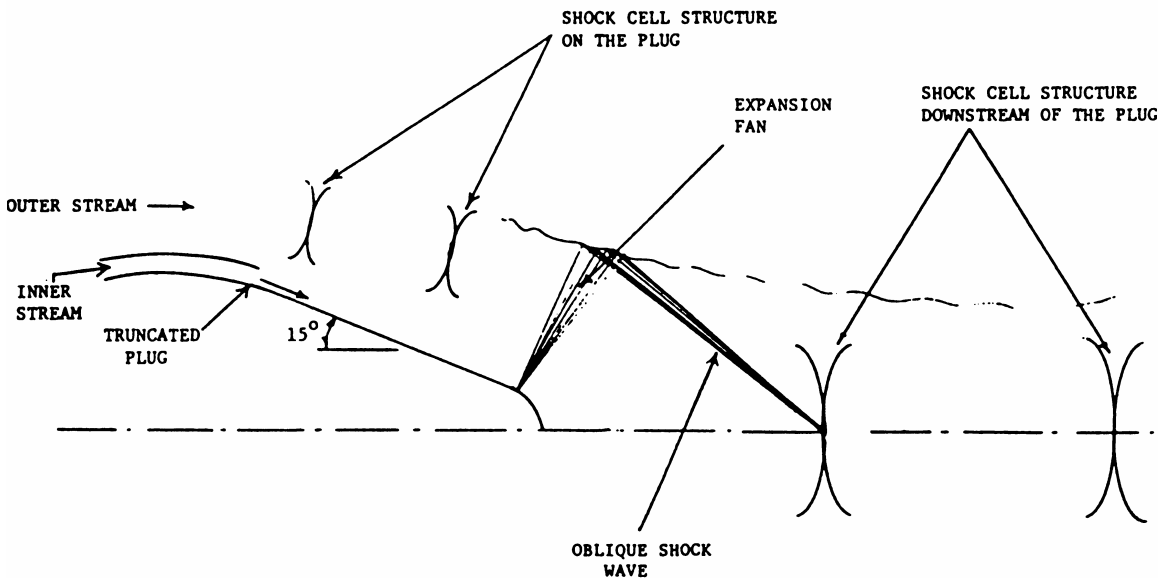
Figure 2 – Schematic Representation of Supersonic Flow from a Separate Flow Coannular Plug Nozzle (from Ref. 23)
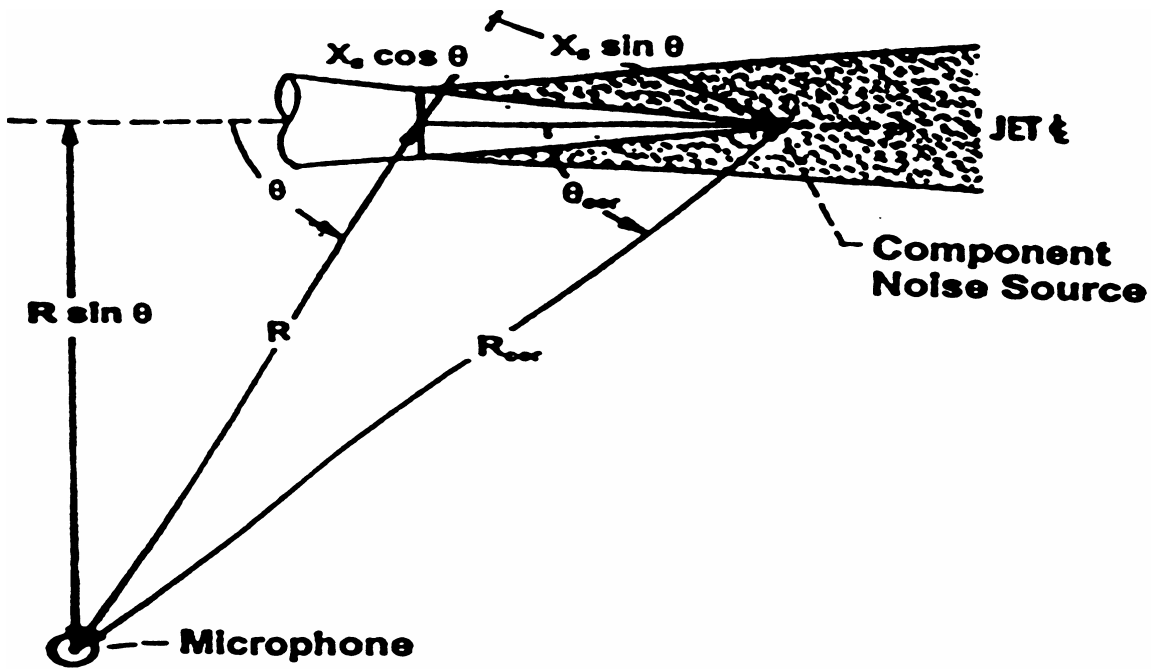
Figure 3 – Noise Source and Microphone Location Geometry
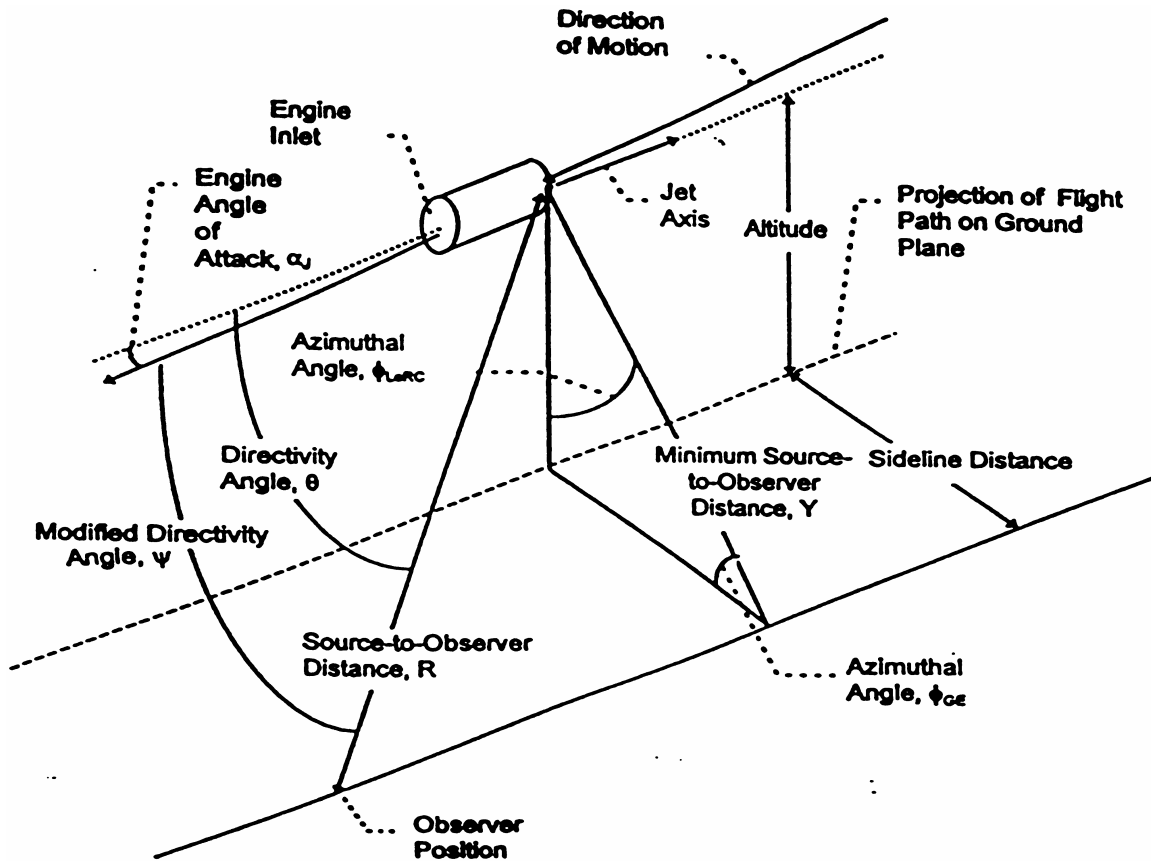
Figure 4 – Aircraft Flyover Geometry
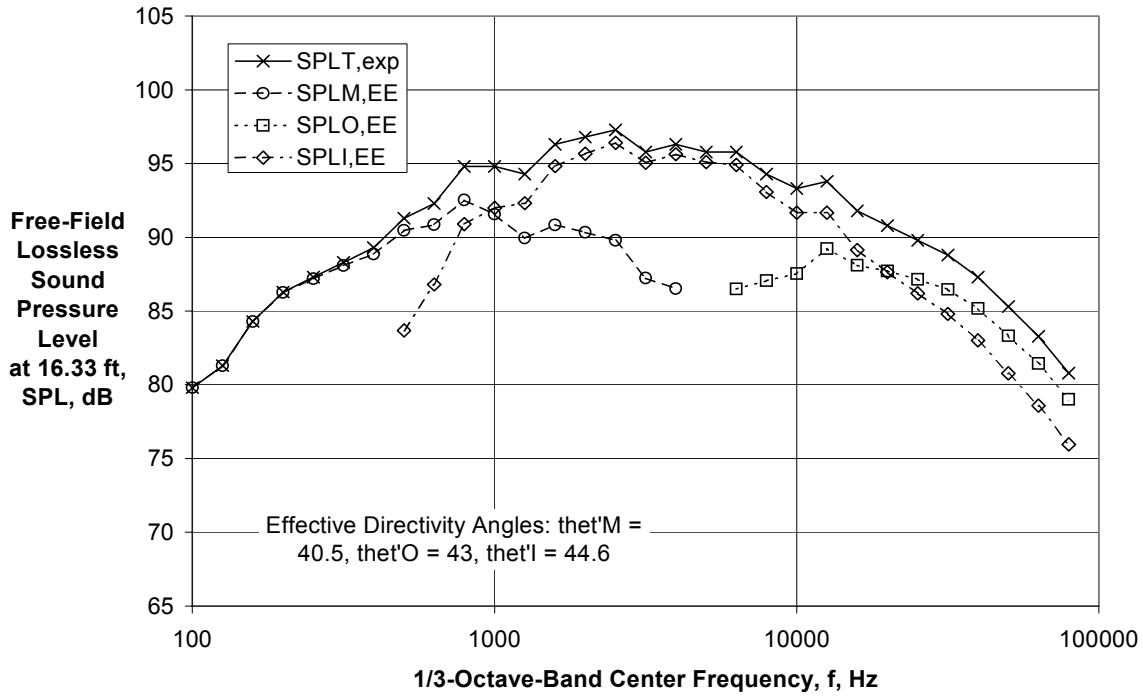
(a) Directivity Angle = 46 deg
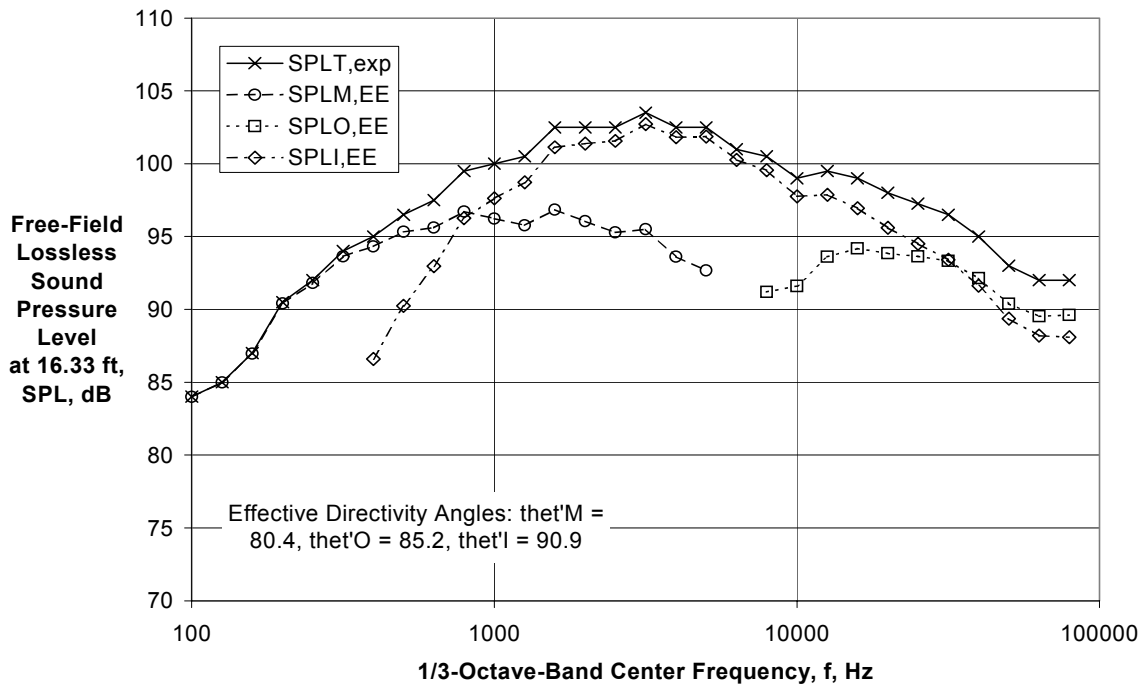
(b) Directivity Angle = 95 deg

Figure 5 - Component Extraction Using First Generation Spectral Directivities and Experimental Coefficients for CVP Coplanar Nozzle with A_I/A_O = 1.94, V_{mix}/c_{amb} = 0.938, M_f = 0.0 (Ref. 25, Rdg. 05)
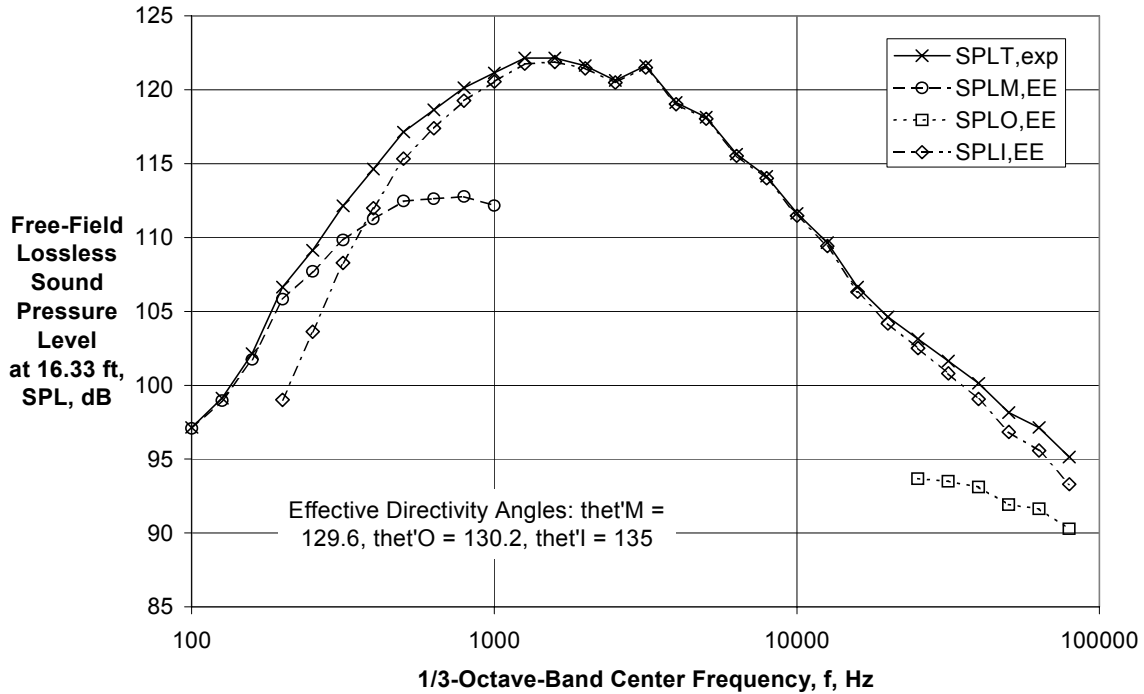
(c) Directivity Angle = 139 deg

Figure 5 (Concluded) - Component Extraction Using First Generation Spectral Directivities and Experimental Coefficients for CVP Coplanar Nozzle with $A_I/A_O = 1.94$, $V_{mix}/c_{amb} = 0.938$, $M_f = 0.0$ (Ref. 25, Rdg. 05)
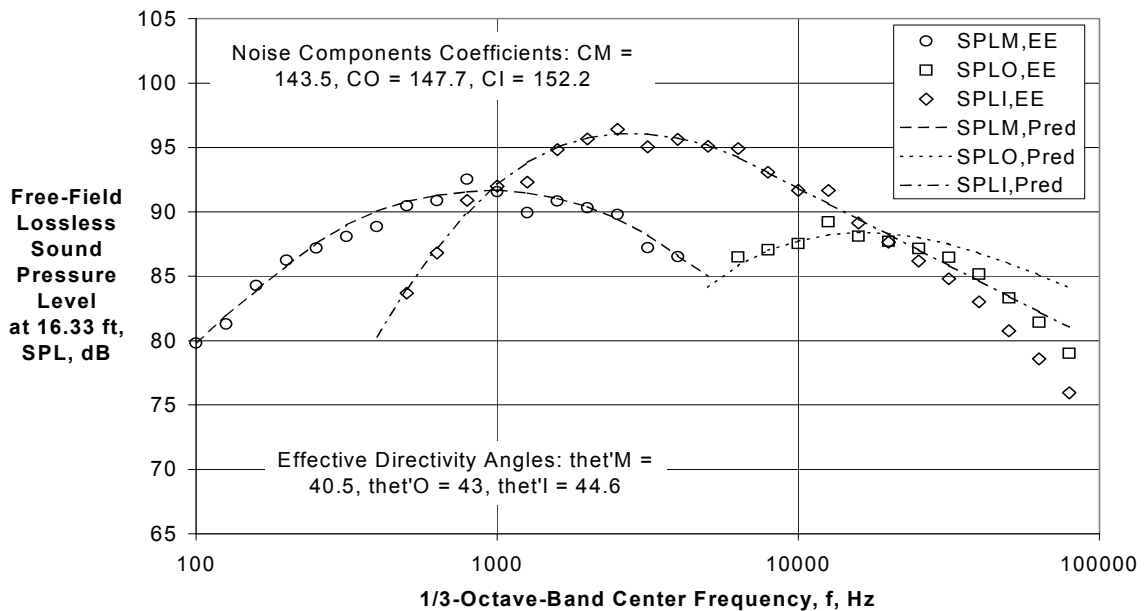
(a) Directivity Angle = 46 deg

Figure 6 – Comparison of Extracted Component Spectral Directivities with Predicted for CVP Coplanar Nozzle with $A_I/A_O = 1.94$, $V_{mix}/c_{amb} = 0.938$, $M_f = 0.0$ (Ref. 25, Rdg. 05)
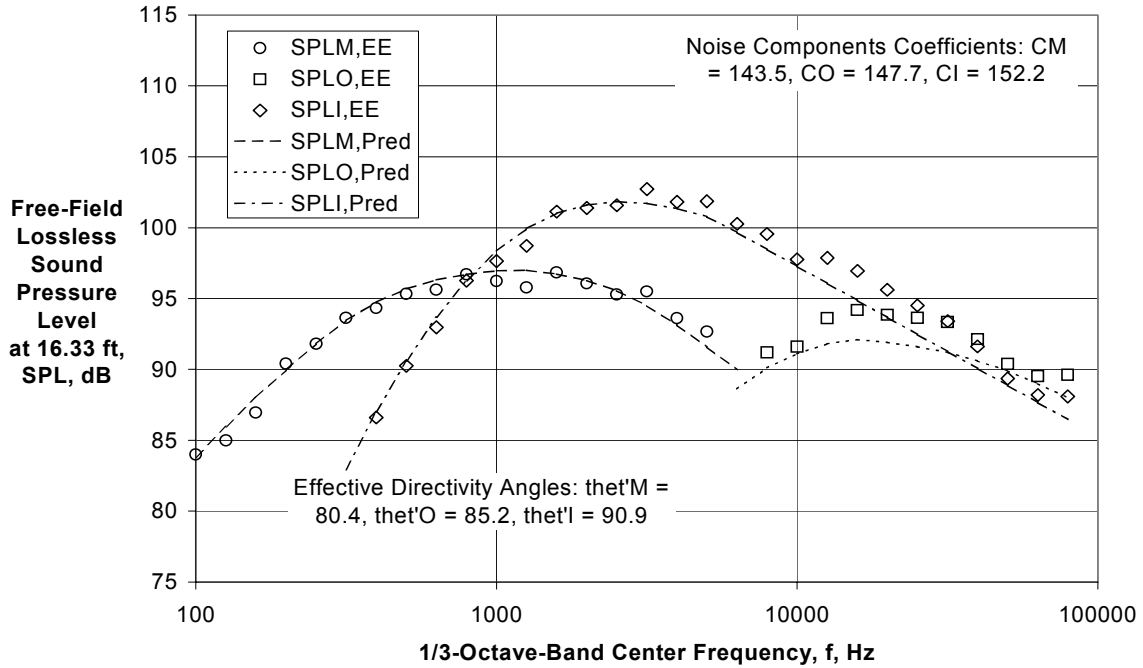
(b) Directivity Angle = 95 deg
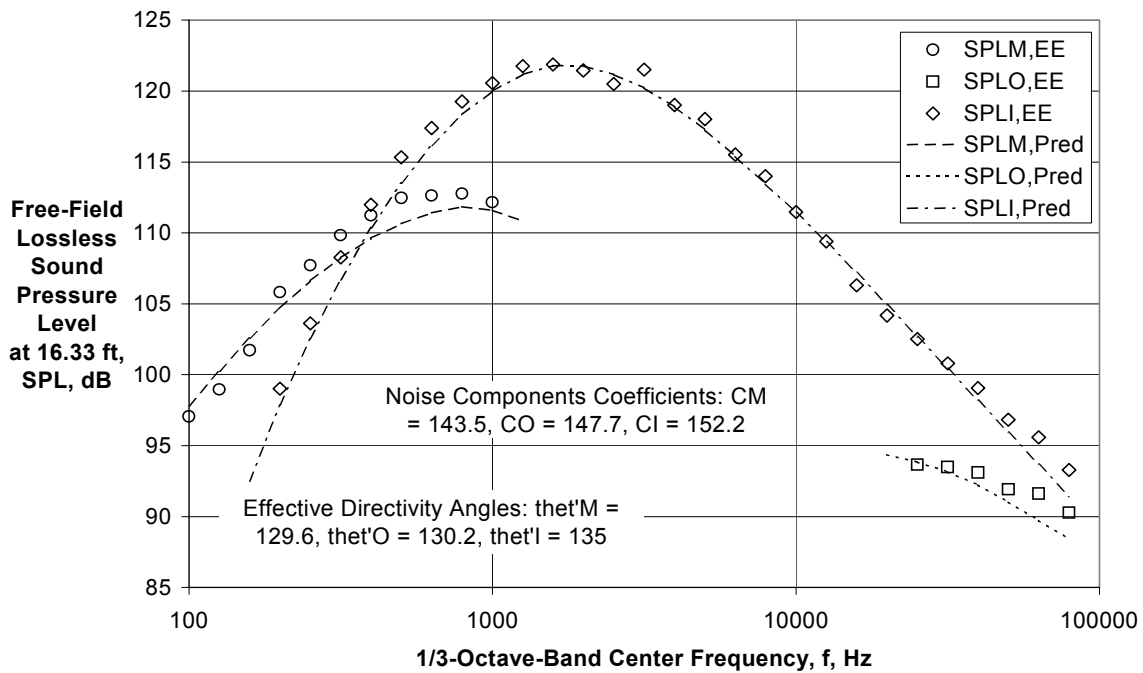
(c) Directivity Angle = 139 deg

Figure 6 (Concluded) – Comparison of Extracted Component Spectral Directivities with Predicted for CVP Coplanar Nozzle with A_I/A_O = 1.94, V_{mix}/c_{amb} = 0.938, M_f = 0.0 (Ref. 25, Rdg. 05)

(a) Directivity Angle = 60 deg

(b) Directivity Angle = 90 deg
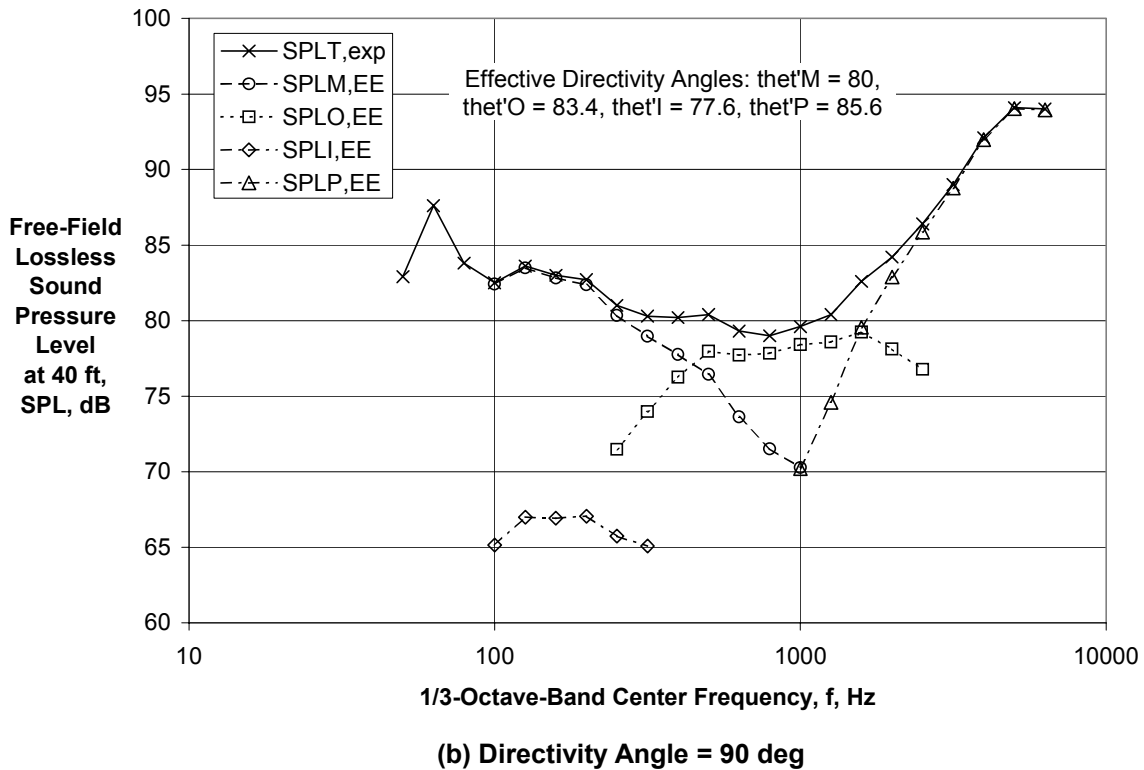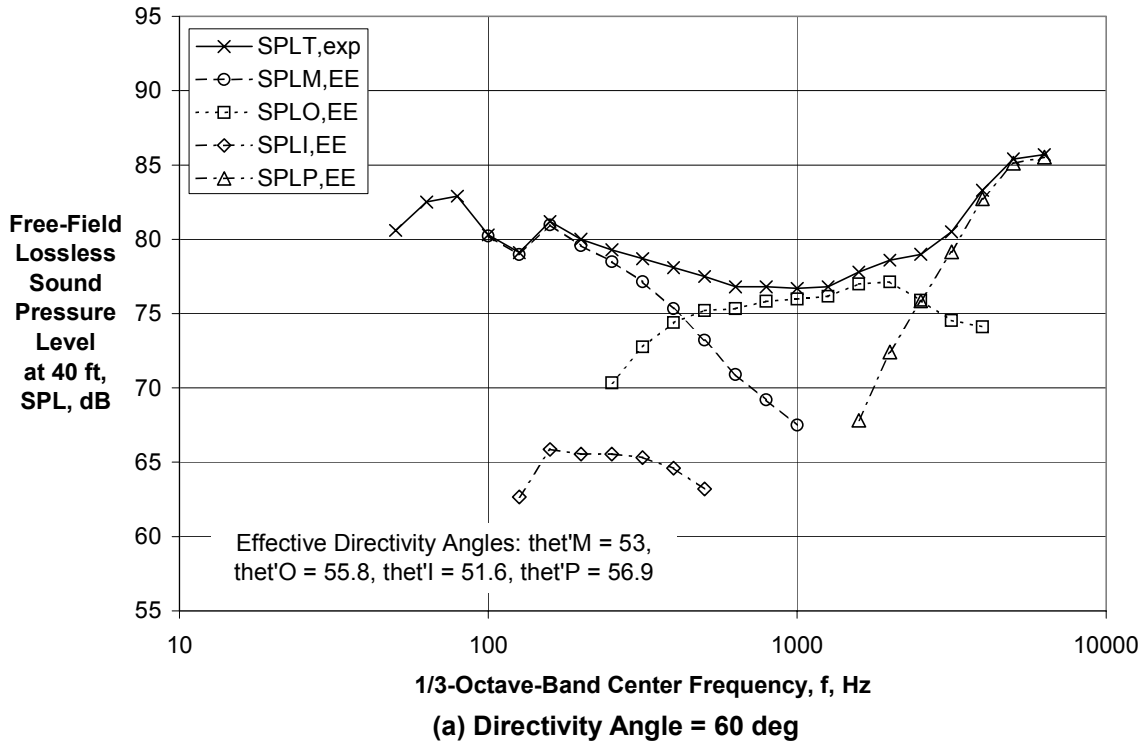
Figure 7 - Component Extraction Using First Generation Spectral Directivities and Experimental Coefficients for CVP Extended Core Nozzle with A_I/A_O = 6.53, V_{mix}/c_{amb} = 0.591, M_f = 0.20 (Ref. 24, Rdg. 1262)
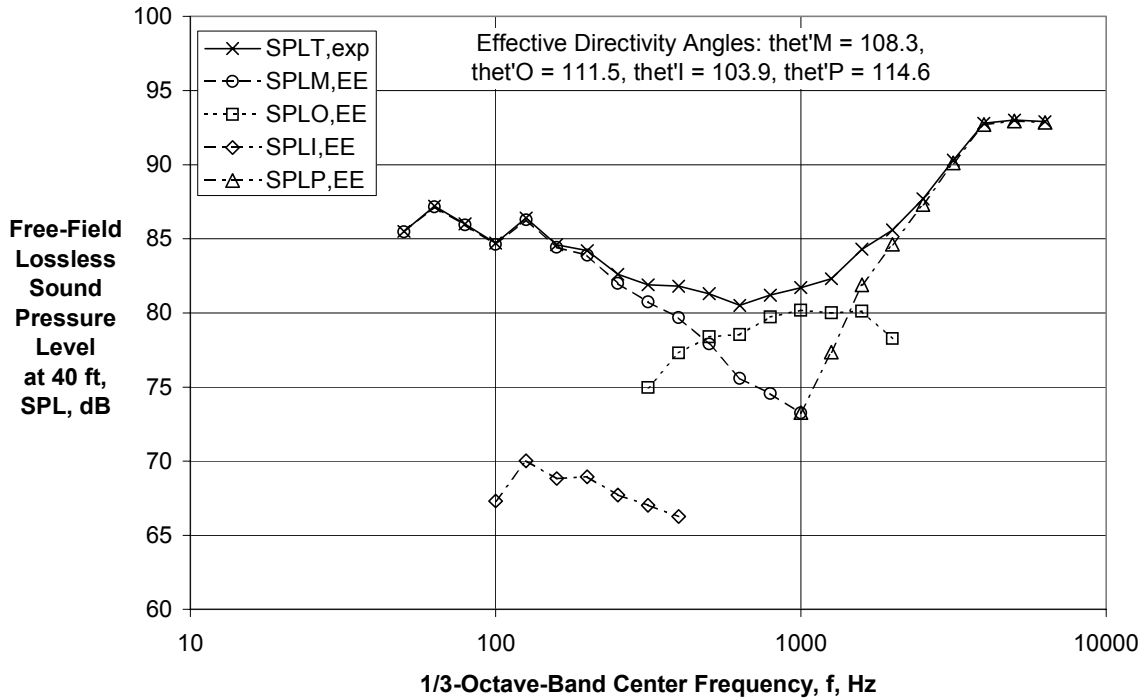
(c) Directivity Angle = 120 deg
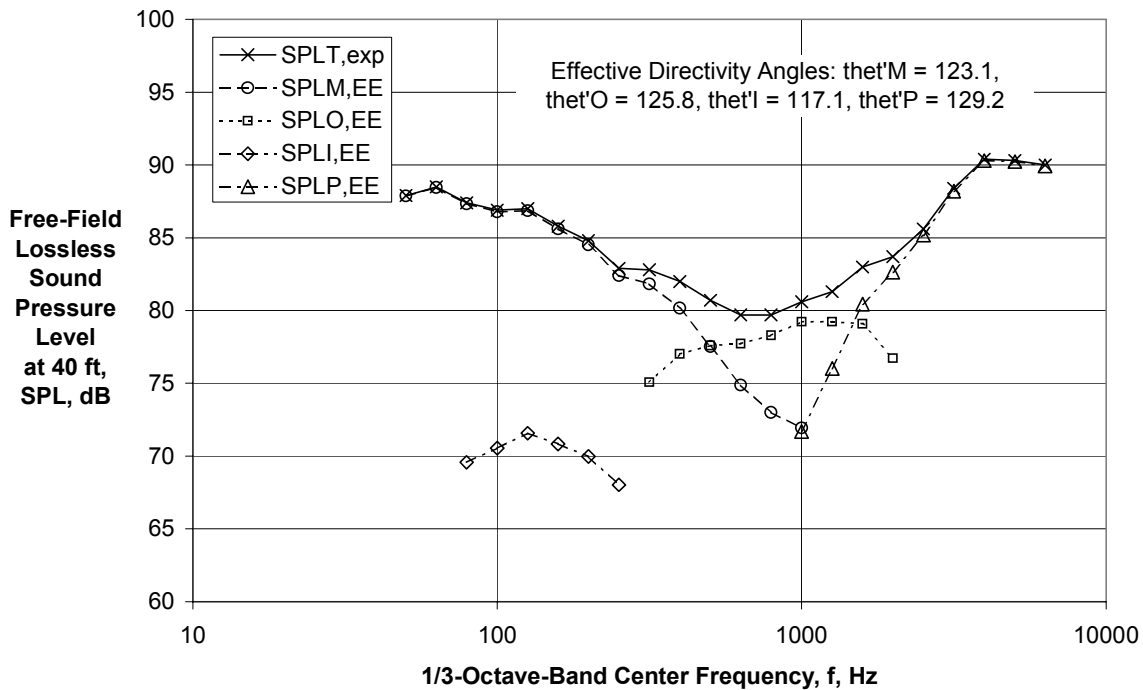
(d) Directivity Angle = 135 deg

Figure 7 (Continued) - Component Extraction Using First Generation Spectral Directivities and Experimental Coefficients for CVP Extended Core Nozzle with A_I/A_O = 6.53, V_{mix}/c_{amb} = 0.591, M_f = 0.20 (Ref. 24, Rdg. 1262)
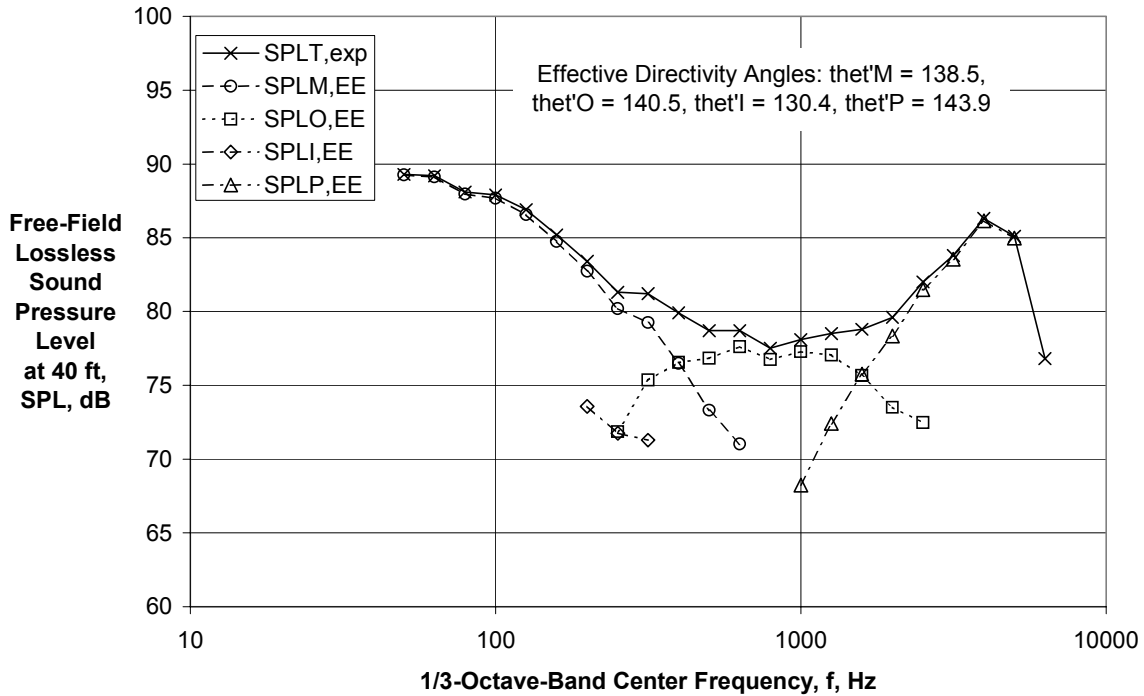
(e) Directivity Angle = 150 deg
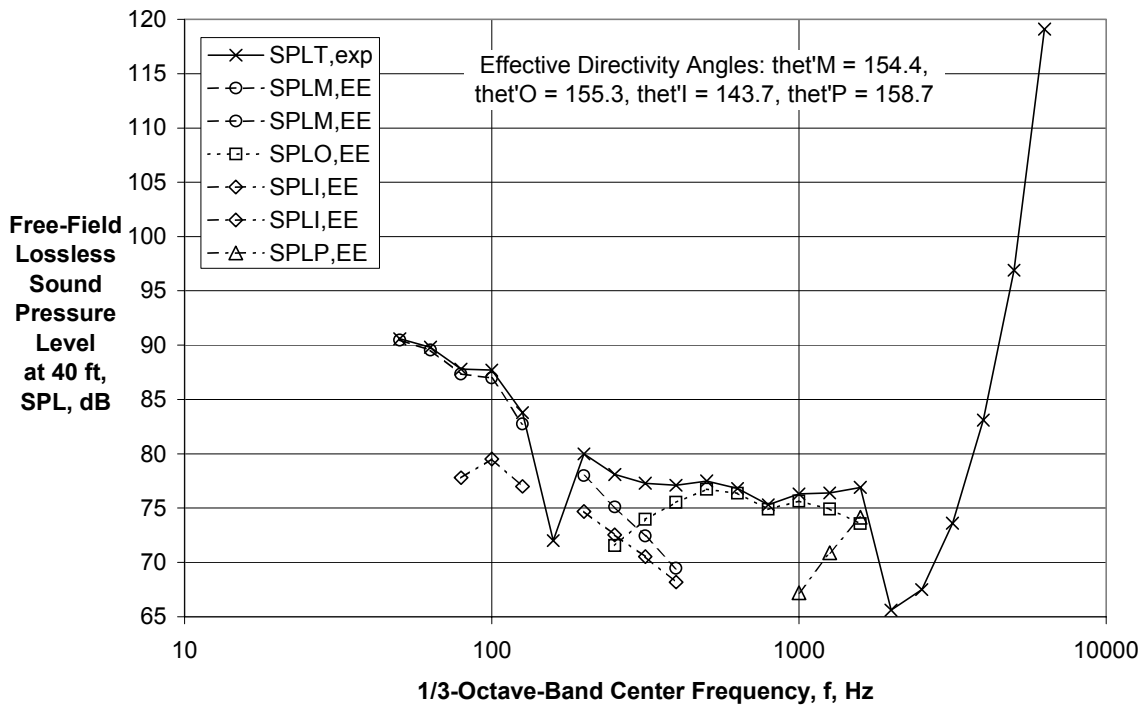
(f) Directivity Angle = 165 deg

Figure 7 (Concluded) - Component Extraction Using First Generation Spectral Directivities and Experimental Coefficients for CVP Extended Core Nozzle with A_I/A_O = 6.53, V_{mix}/c_{amb} = 0.591, M_f = 0.20 (Ref. 24, Rdg. 1262)
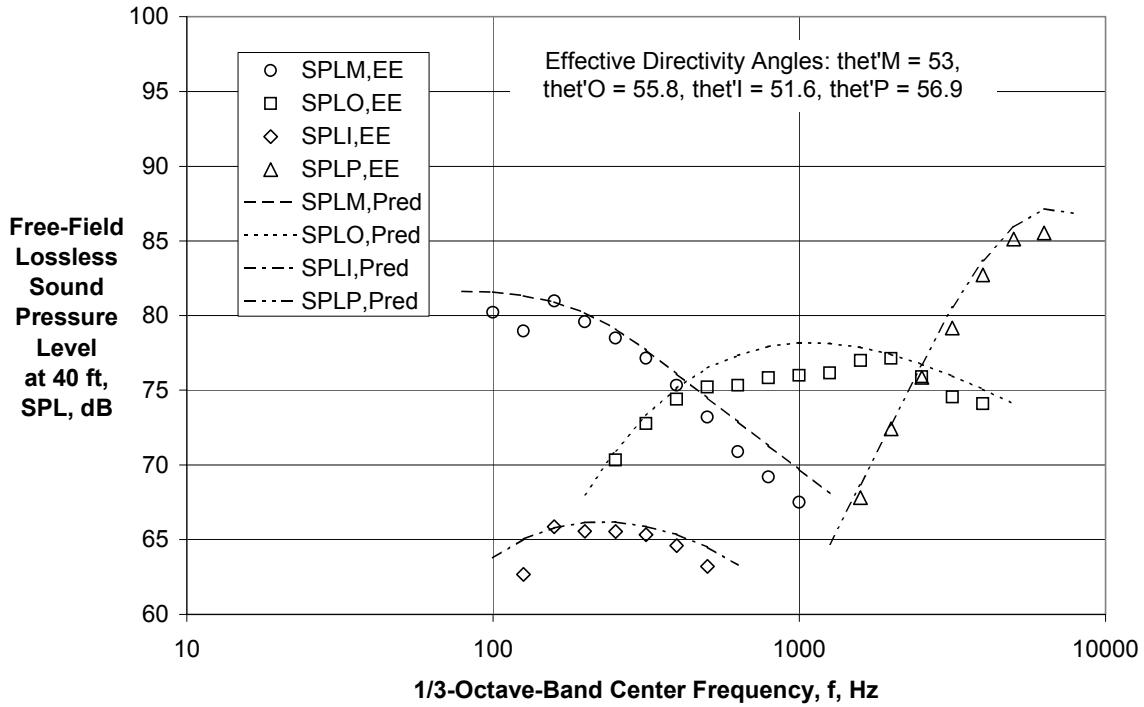
(a) Directivity Angle = 60 deg
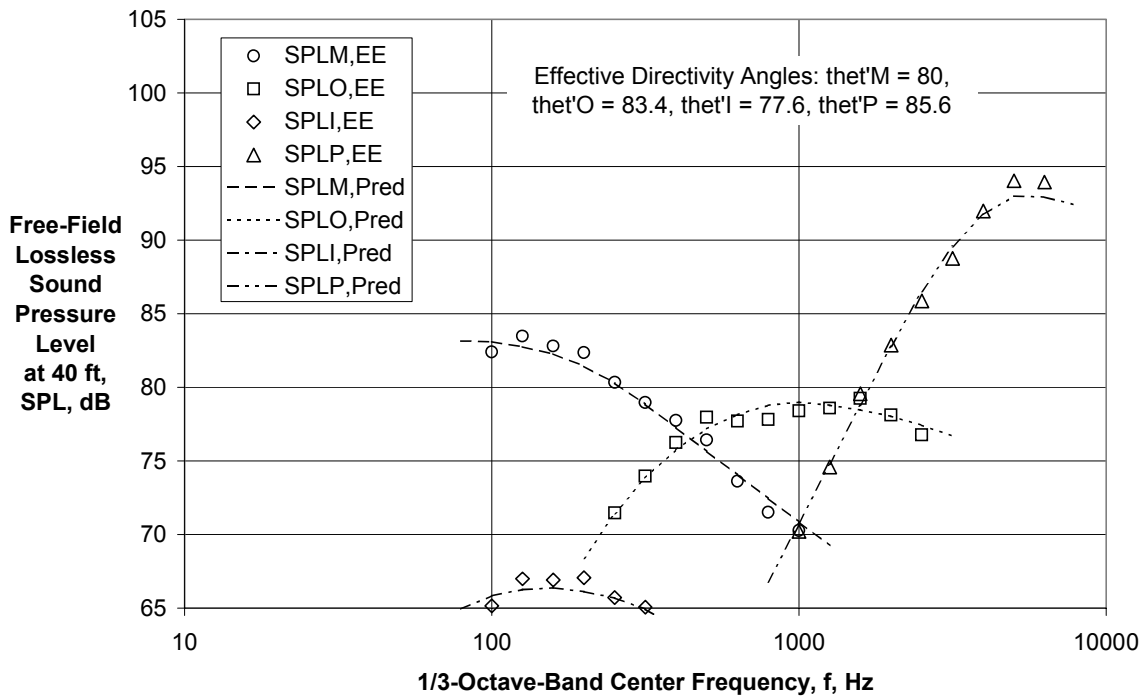
(b) Directivity Angle = 90 deg

Figure 8 – Comparison of Extracted Component Spectral Directivities with Predicted for CVP Extended Core Nozzle with A_I/A_O = 6.53, V_{mix}/c_{amb} = 0.591, M_f = 0.20 (Ref. 24, Rdg. 1262)
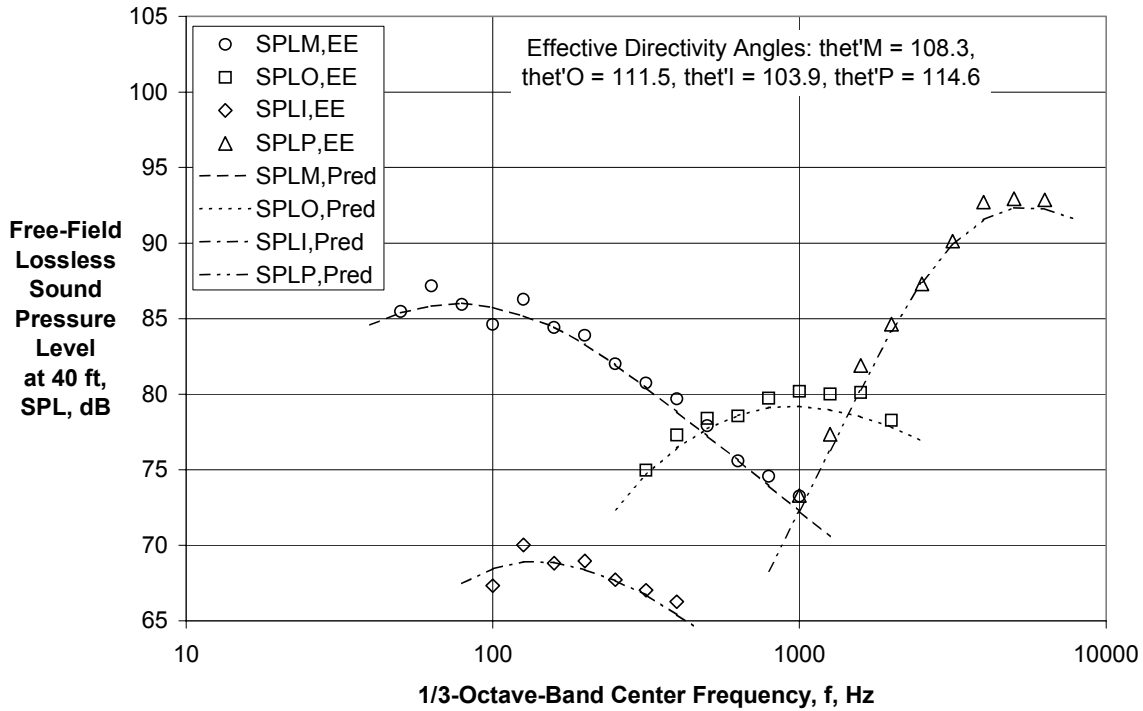
(c) Directivity Angle = 120 deg
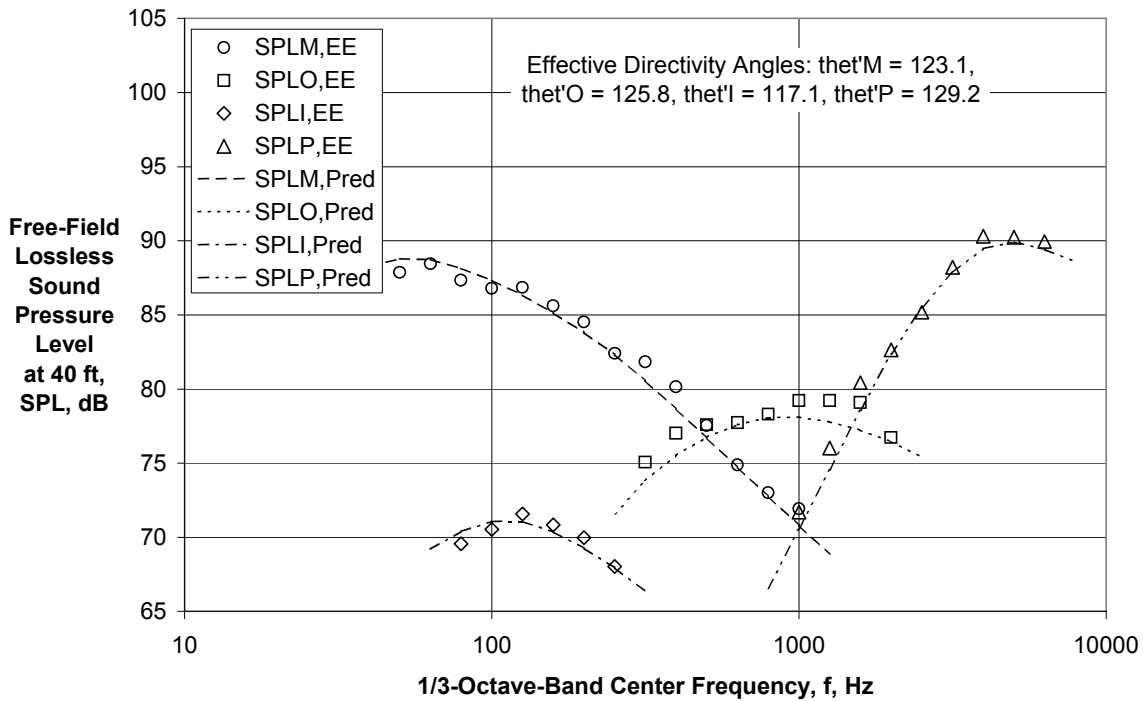
(d) Directivity Angle = 135 deg

Figure 8 (Continued) – Comparison of Extracted Component Spectral Directivities with Predicted for CVP Extended Core Nozzle with A_I/A_O = 6.53, V_{mix}/c_{amb} = 0.591, M_f = 0.20 (Ref. 24, Rdg. 1262)
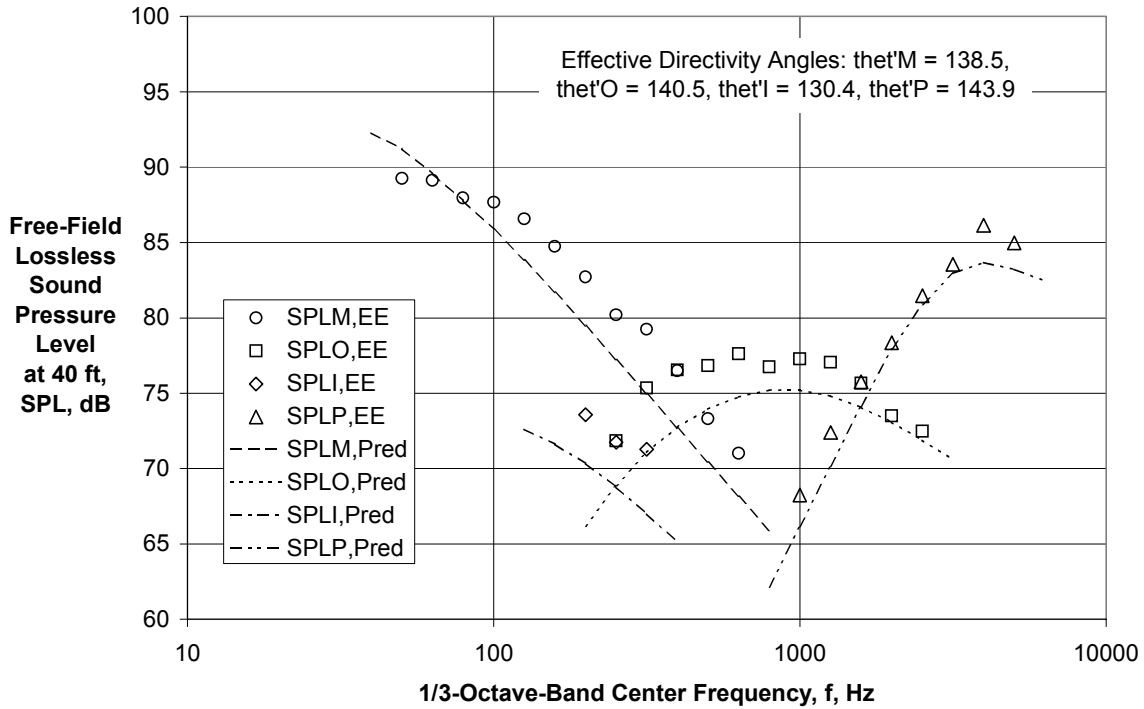
(e) Directivity Angle = 150 deg
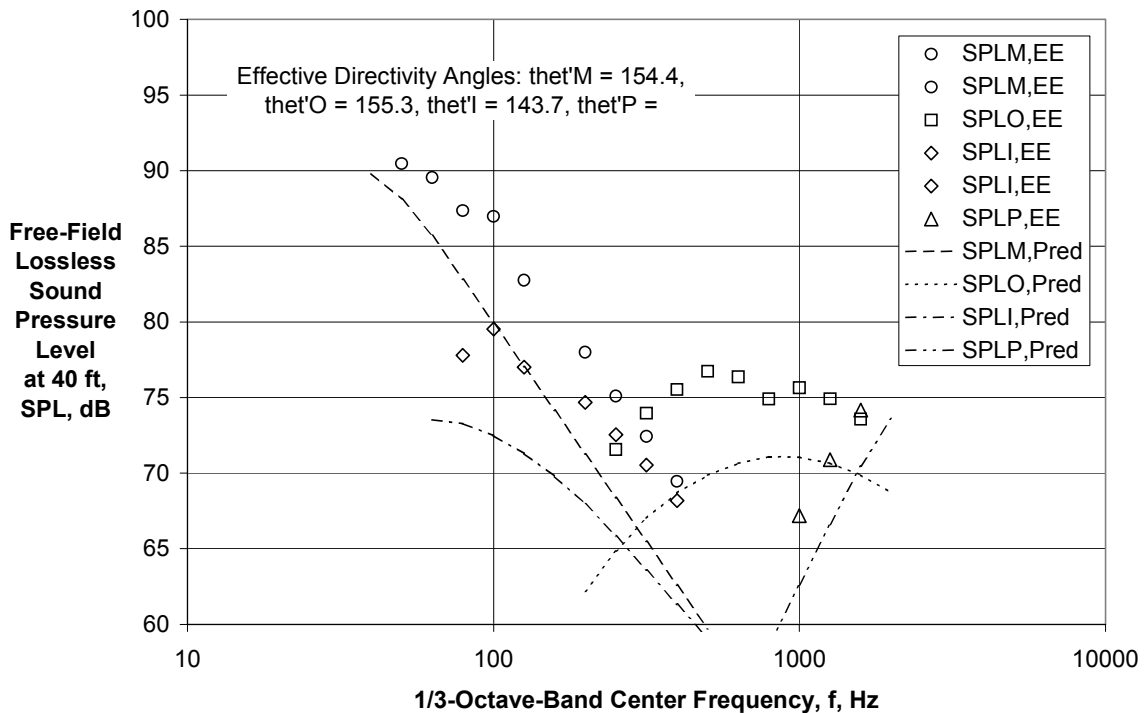
(f) Directivity Angle = 165 deg

Figure 8 (Concluded) – Comparison of Extracted Component Spectral Directivities with Predicted for CVP Extended Core Nozzle with A_I/A_O = 6.53, V_{mix}/c_{amb} = 0.591, M_f = 0.20 (Ref. 24, Rdg. 1262)
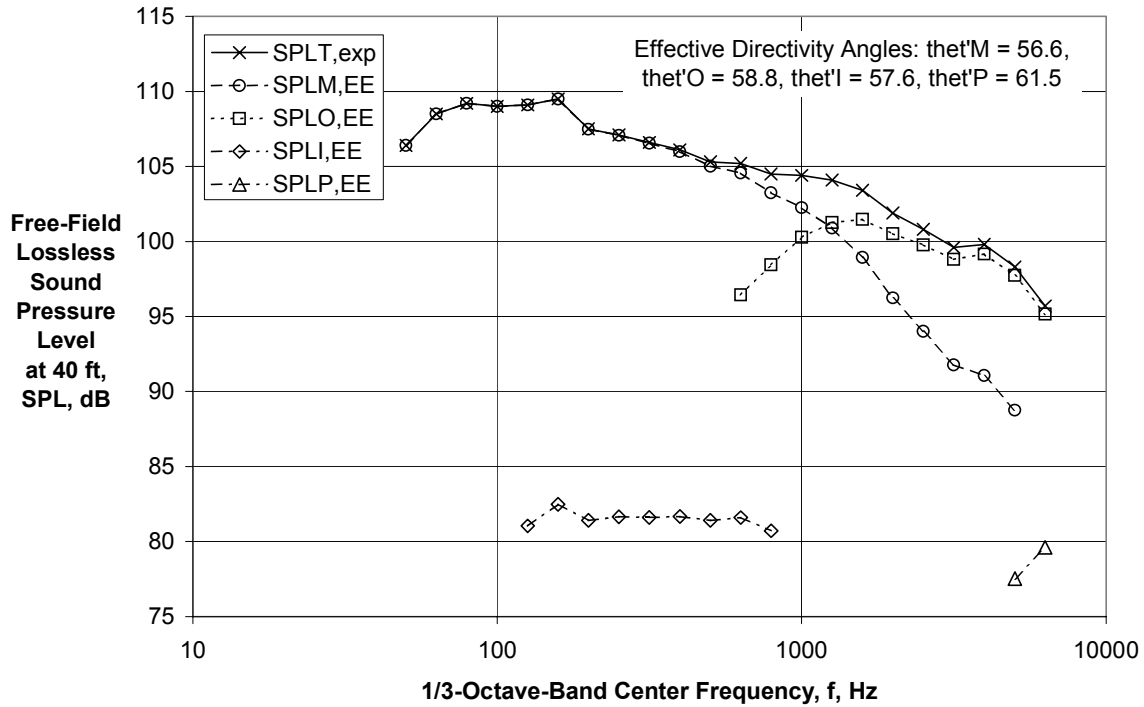
(a) Directivity Angle = 60 deg
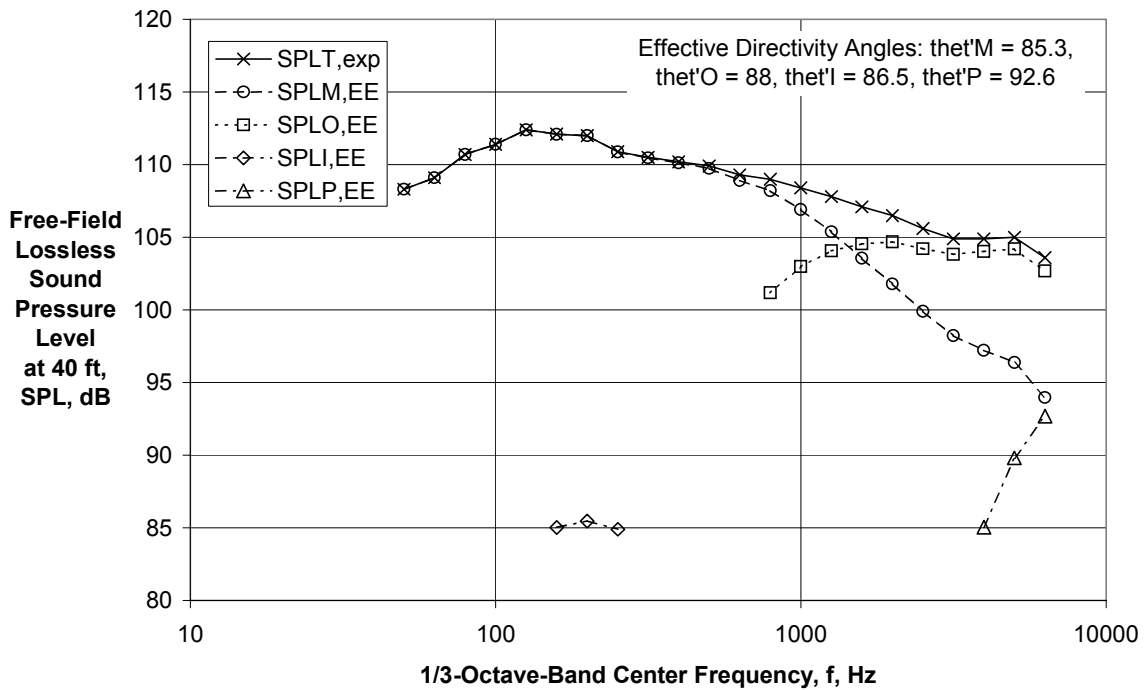
(b) Directivity Angle = 90 deg

Figure 9 - Component Extraction Using First Generation Spectral Directivities and Experimental Coefficients for CVP Extended Core Nozzle with A_I/A_O = 2.75, V_{mix}/c_{amb} = 1.088, M_f = 0.0 (Ref. 24, Rdg. 383)
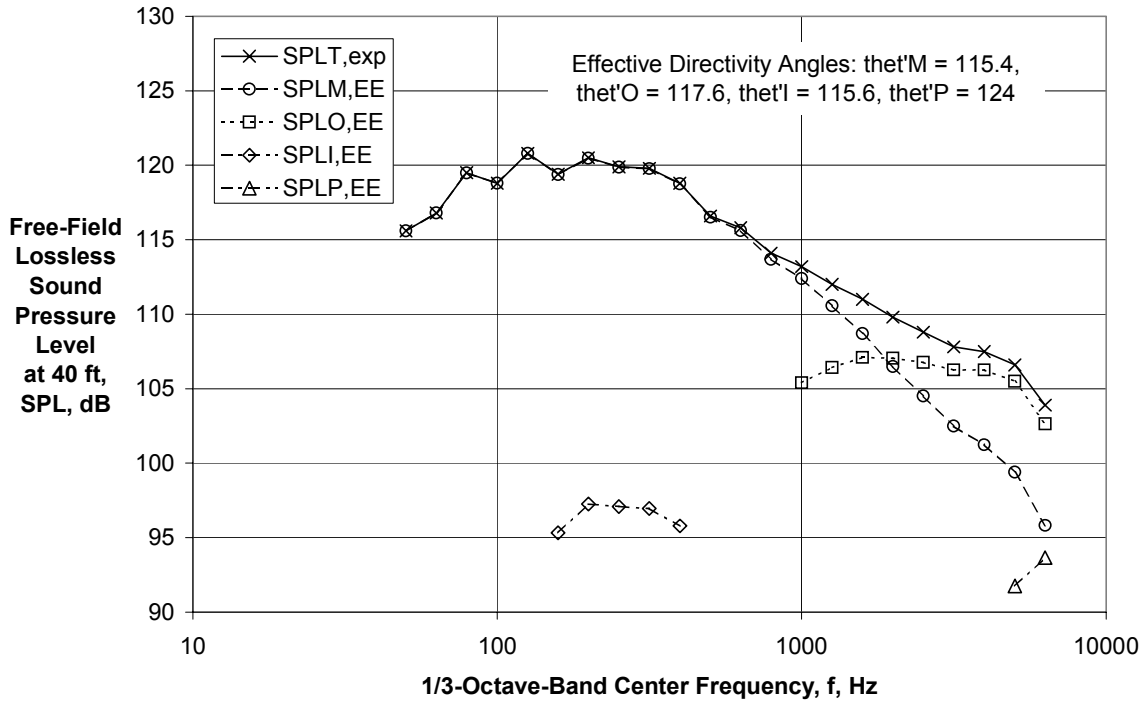
(c) Directivity Angle = 120 deg
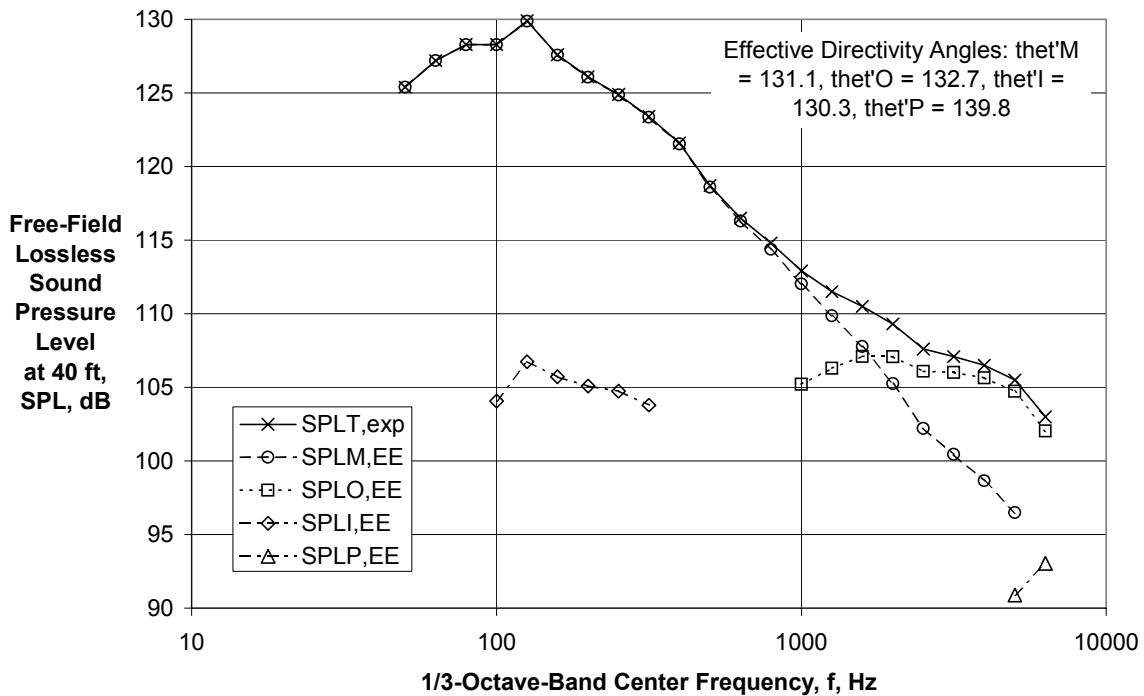
(d) Directivity Angle = 135 deg

Figure 9 (Continued) - Component Extraction Using First Generation Spectral Directivities and Experimental Coefficients CVP Extended Core Nozzle with A_I/A_O = 2.75, V_{mix}/c_{amb} = 1.088, M_f = 0.0 (Ref. 24, Rdg. 383)
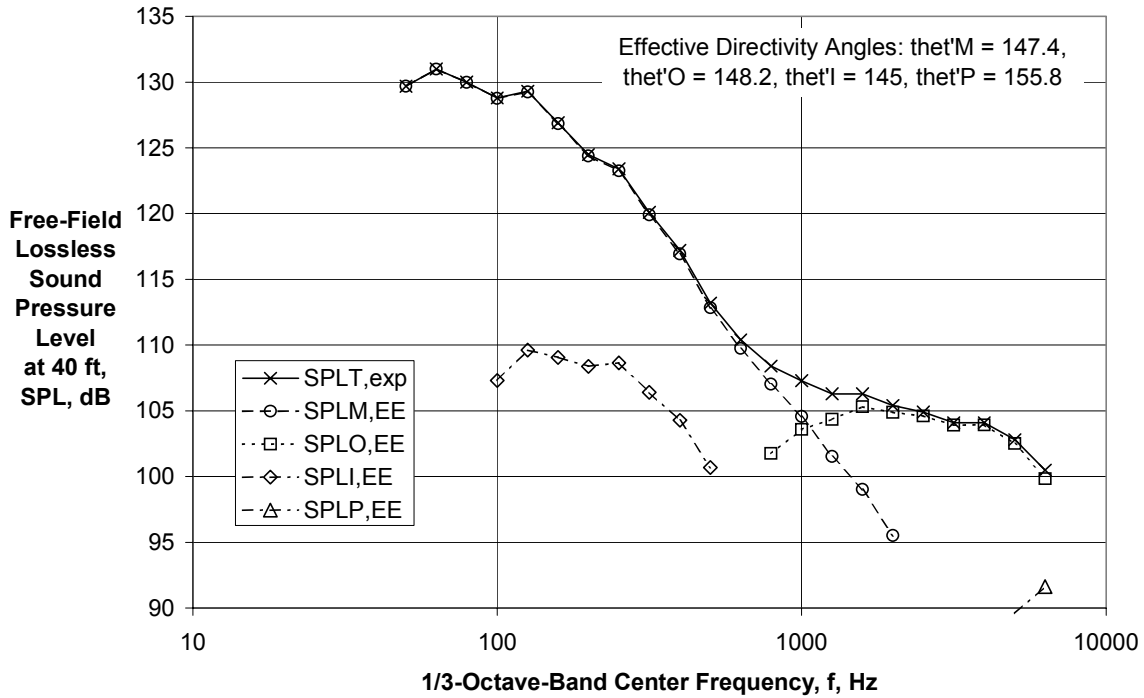
(e) Directivity Angle = 150 deg
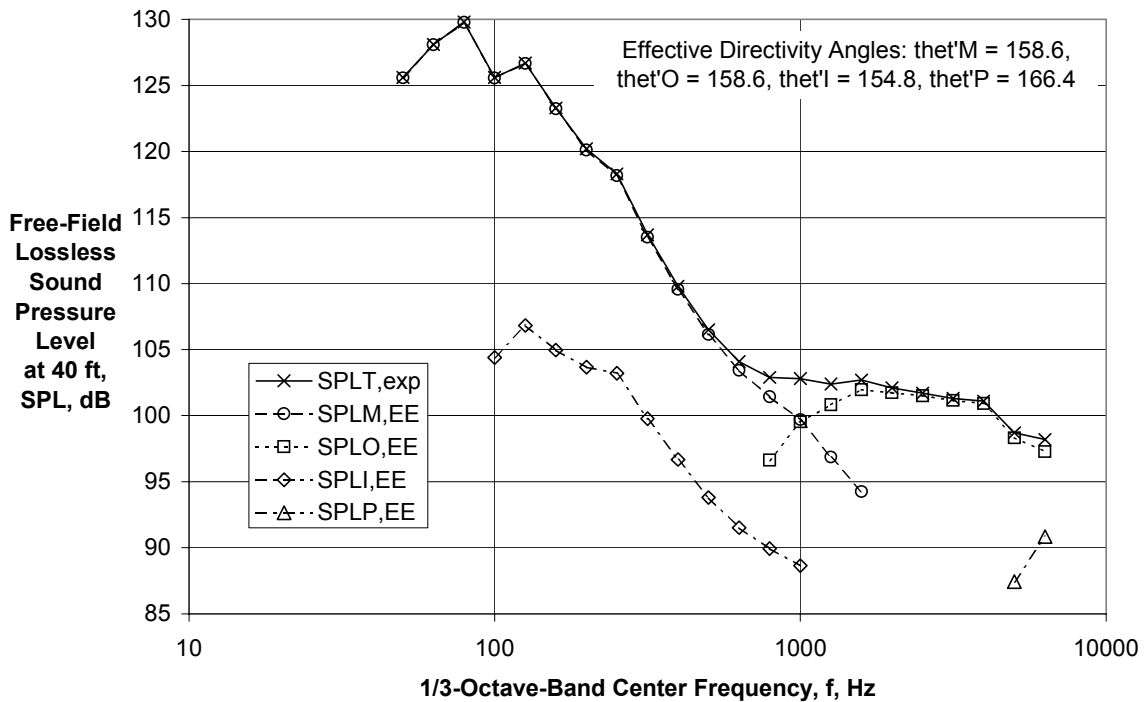
(f) Directivity Angle = 160 deg

Figure 9 (Concluded) - Component Extraction Using First Generation Spectral Directivities and Experimental Coefficients for CVP Extended Core Nozzle with A_I/A_O = 2.75, V_{mix}/c_{amb} = 1.088, M_f = 0.0 (Ref. 24, Rdg. 383)
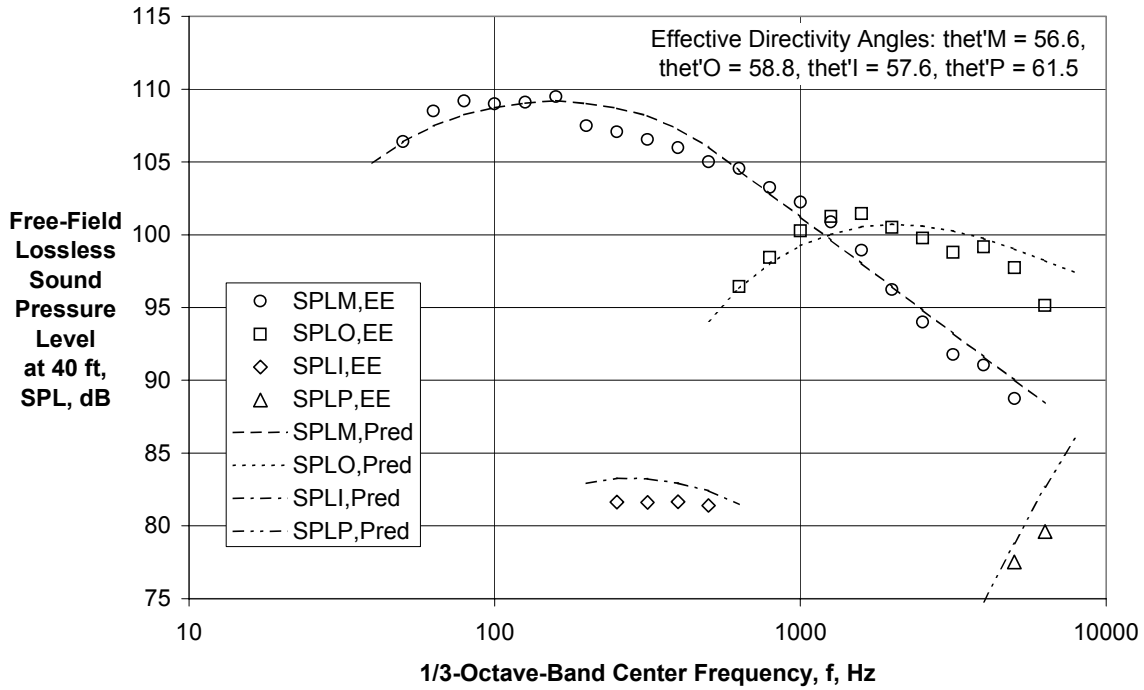
(a) Directivity Angle = 60 deg
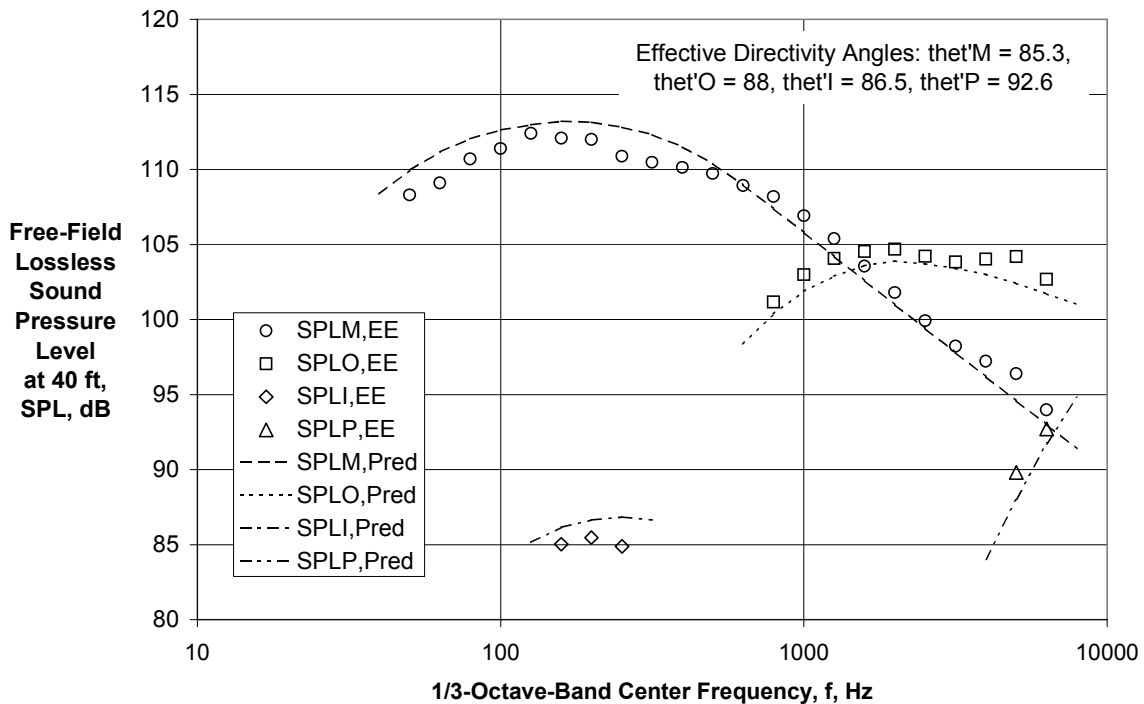
(b) Directivity Angle = 90 deg

Figure 10 - Comparison of Extracted Component Spectral Directivities with Predicted for CVP Extended Core Nozzle with A_I/A_O = 2.75, V_{mix}/c_{amb} = 1.088, M_f = 0.0 (Ref. 24, Rdg. 383)
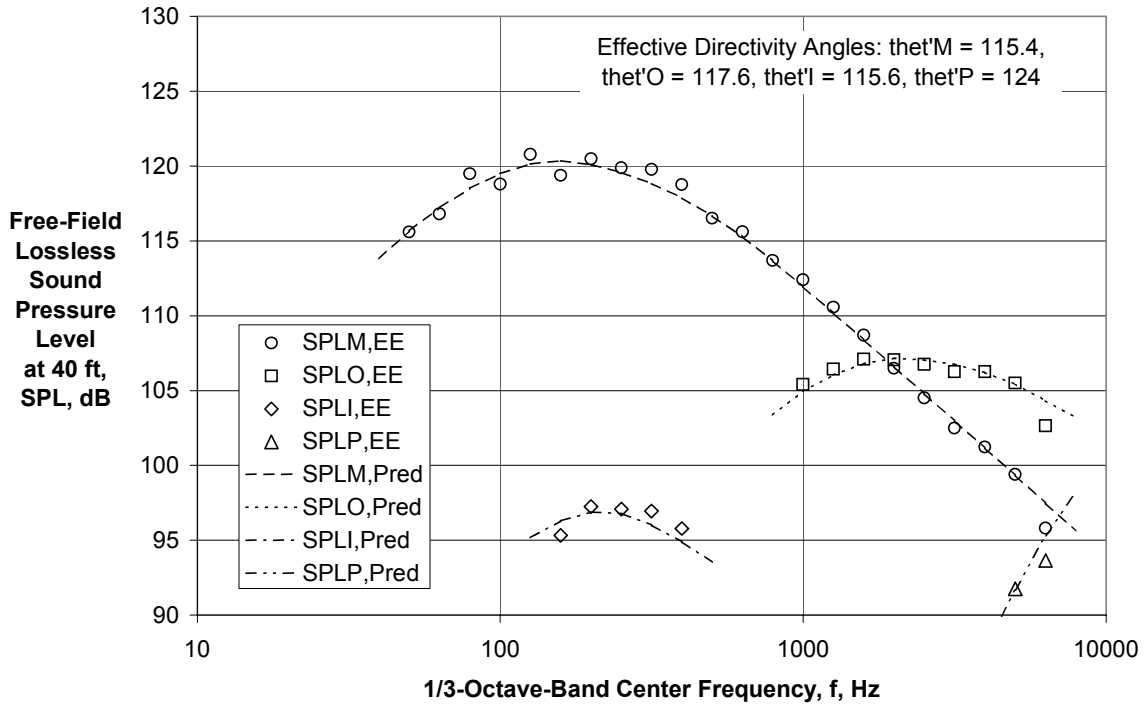
(c) Directivity Angle = 120 deg
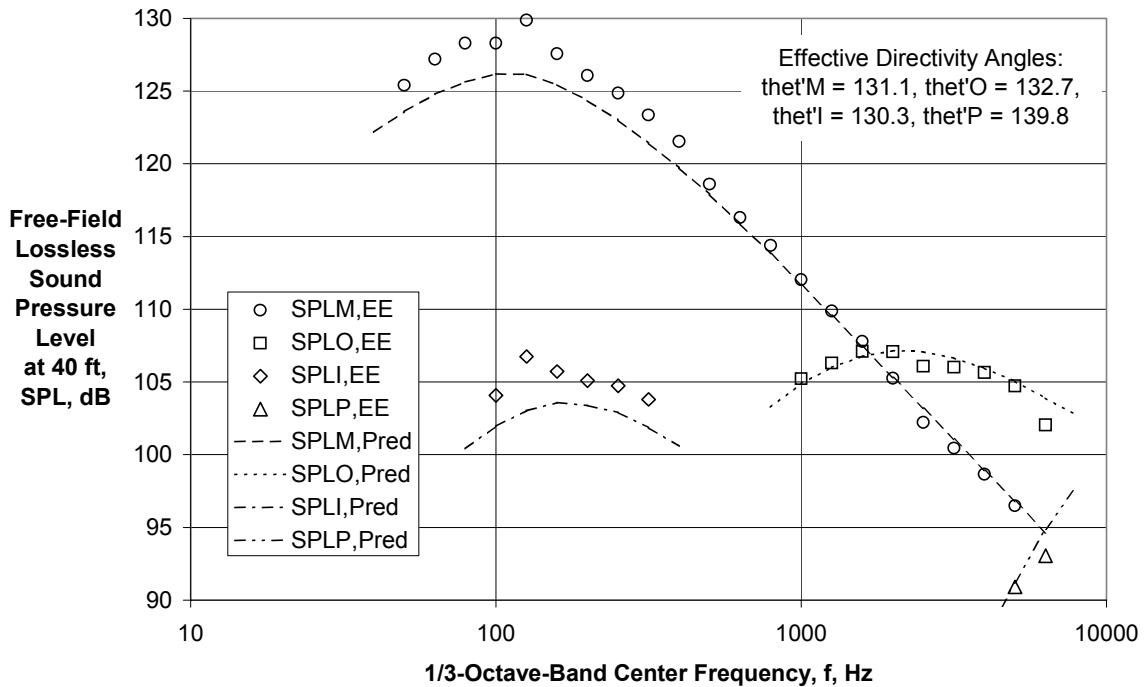
(d) Directivity Angle = 135 deg

Figure 10 (Continued) - Comparison of Extracted Component Spectral Directivities with Predicted for CVP Extended Core Nozzle with A_I/A_O = 2.75, V_{mix}/c_{amb} = 1.088, M_f = 0.0 (Ref. 24, Rdg. 383)
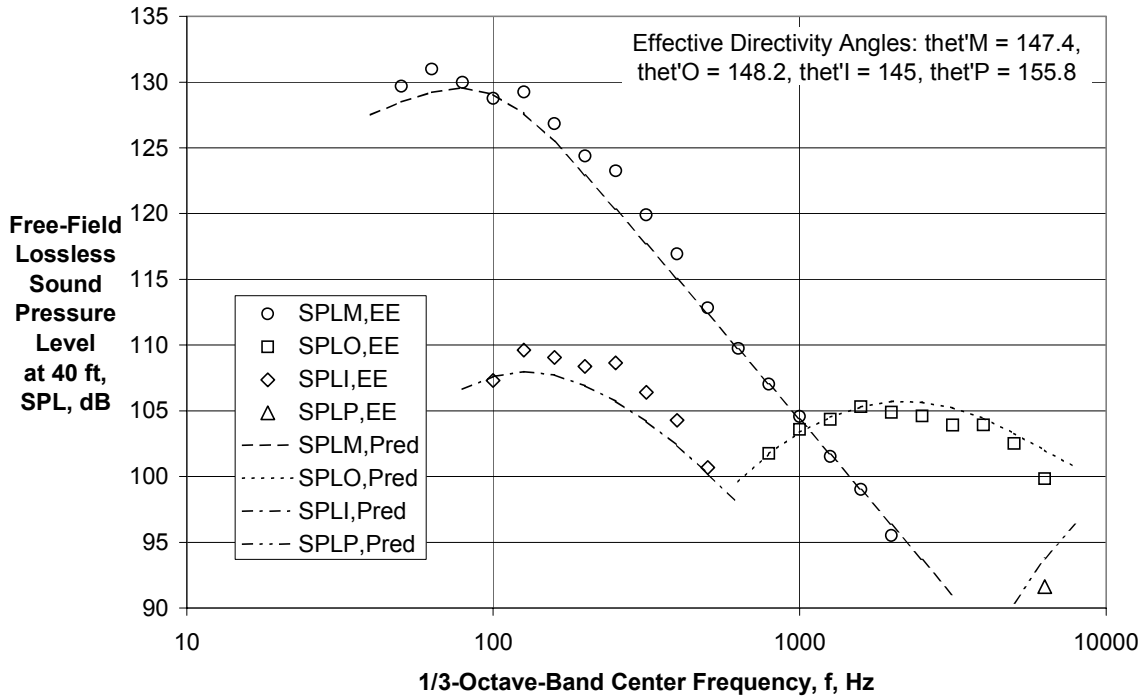
(e) Directivity Angle = 150 deg
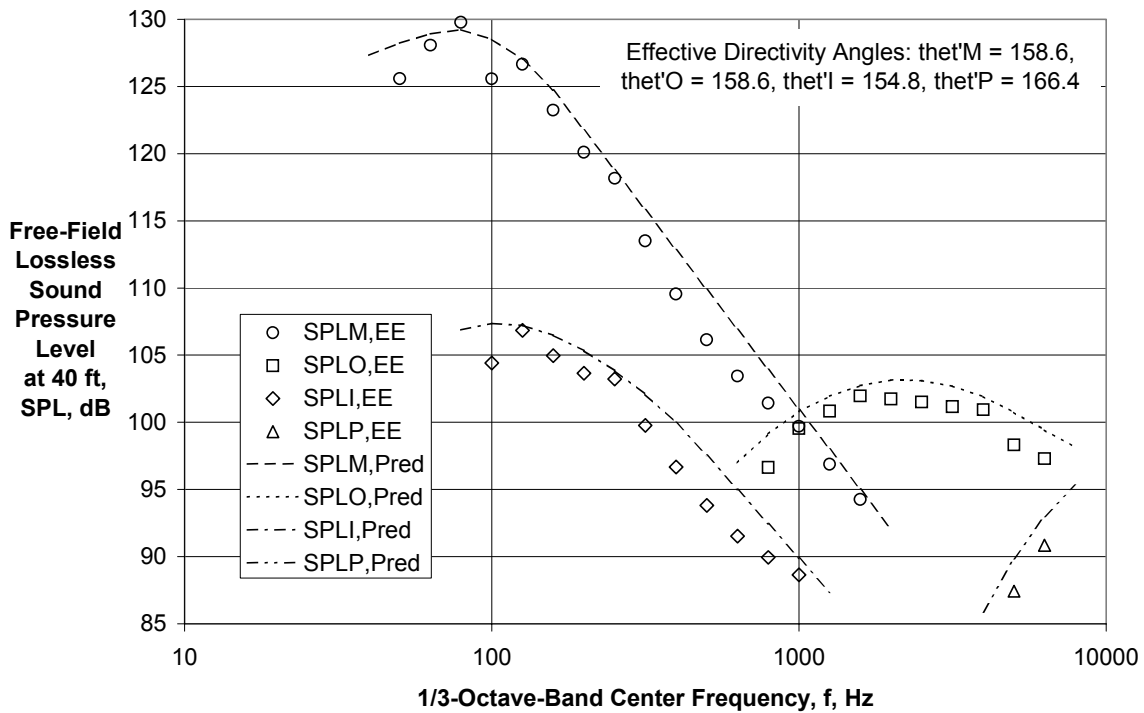
(f) Directivity Angle = 160 deg

Figure 10 (Concluded) - Comparison of Extracted Component Spectral Directivities with Predicted for CVP Extended Core with A_I/A_O = 2.75, V_{mix}/c_{amb} = 1.088, M_f = 0.0 (Ref. 24, Rdg. 383)
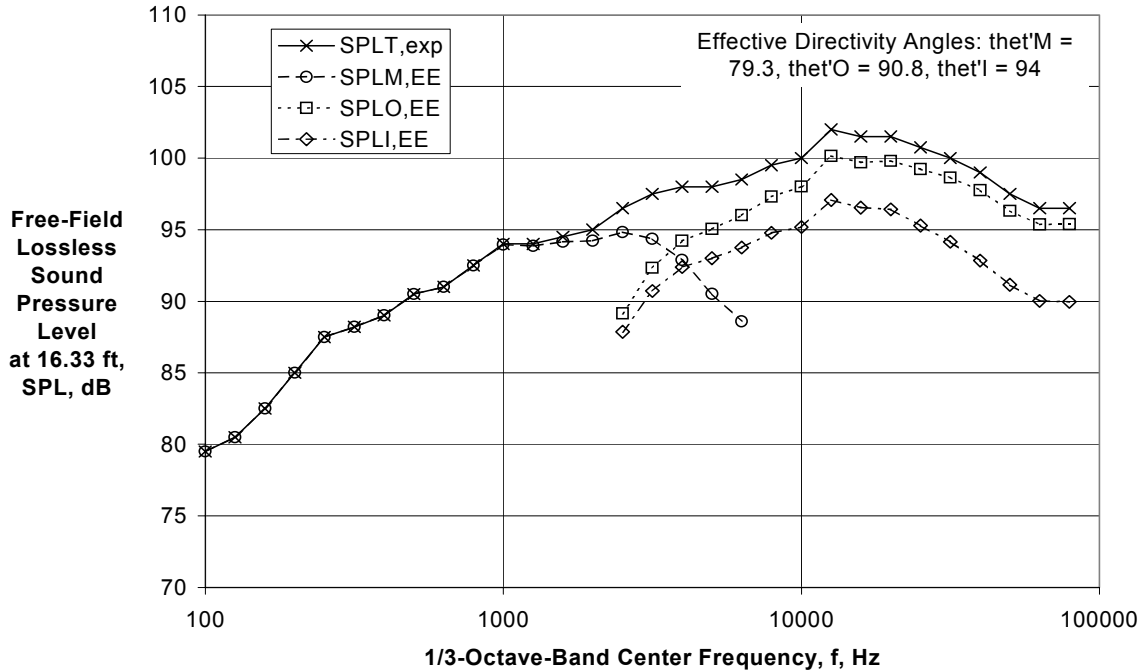
(a) Directivity Angle = 95 deg
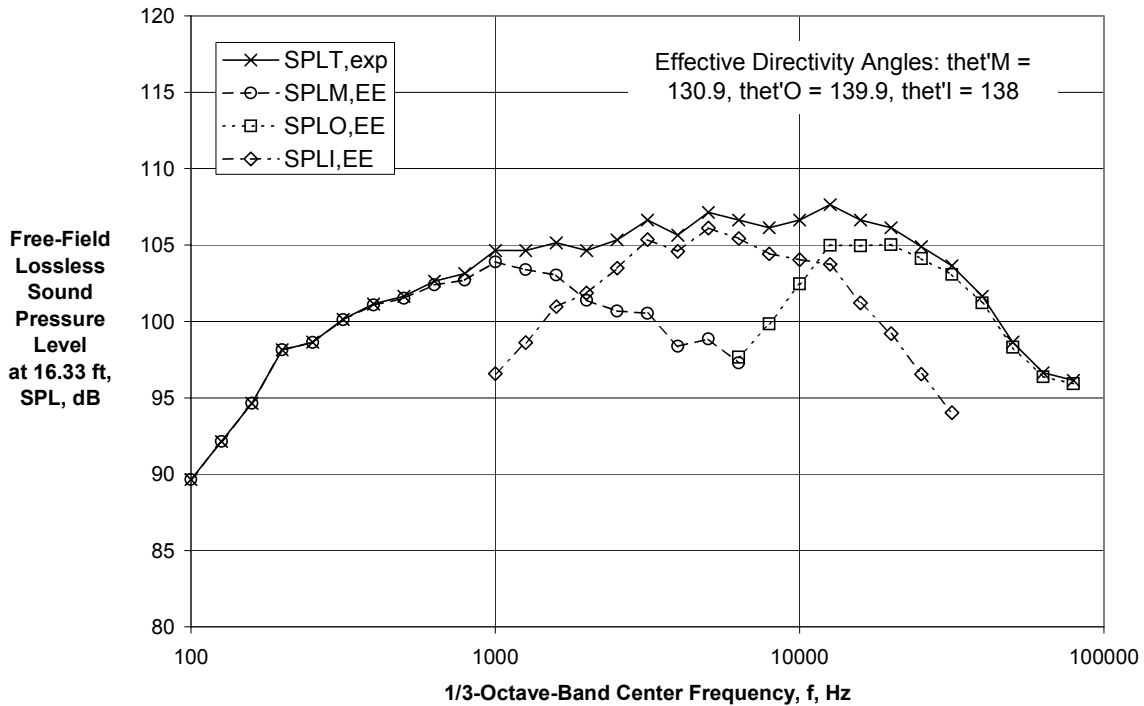
(b) Directivity Angle = 139 deg

Figure 11 - Component Extraction Using First Generation Spectral Directivities and Experimental Coefficients for IVP Extended Core Nozzle with A_I/A_O = 1.26, V_{mix}/c_{amb} = 1.168, M_f = 0.0 (Ref. 25, Rdg. 15)
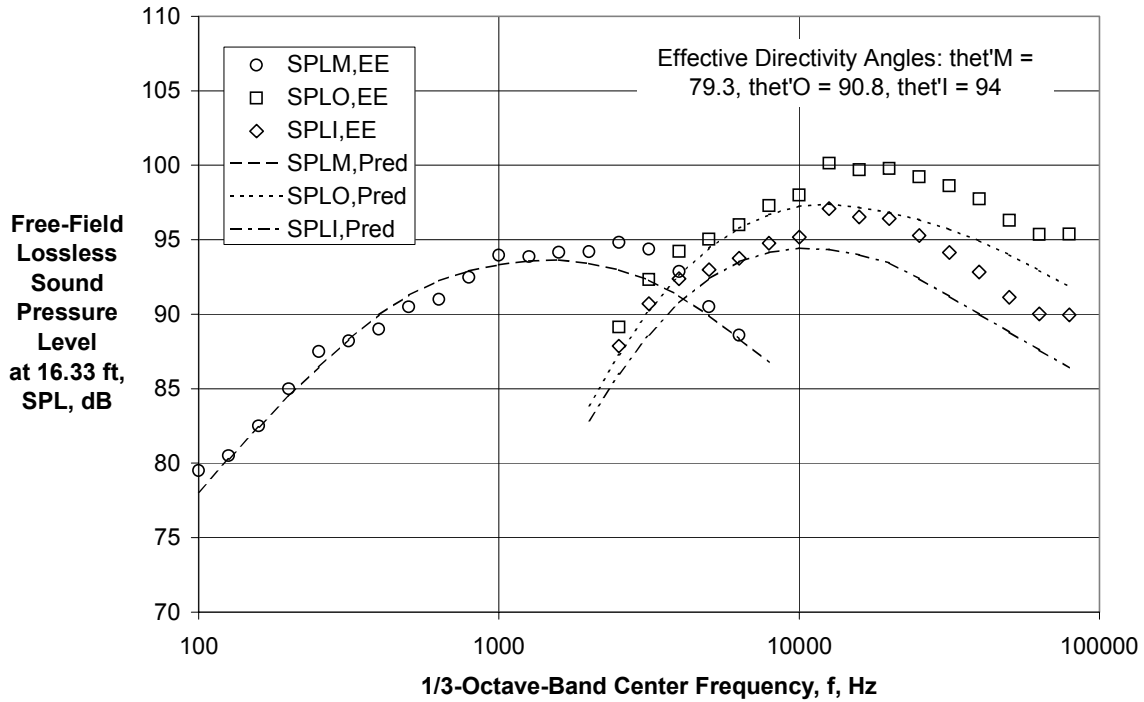
(a) Directivity Angle = 95 deg
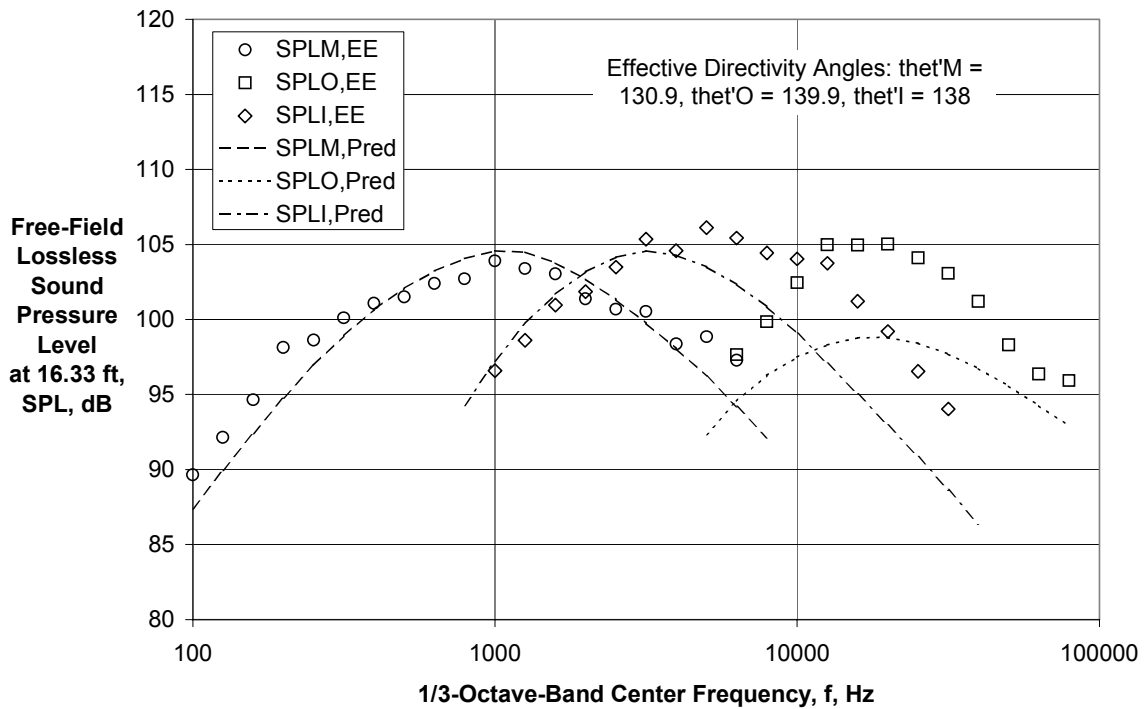
(b) Directivity Angle = 139 deg

Figure 12 - Comparison of Extracted Component Spectral Directivities with Predicted for IVP Extended Core Nozzle with A_I/A_O = 1.26, V_{mix}/c_{amb} = 1.168, M_f = 0.0 (Ref. 25, Rdg. 15)
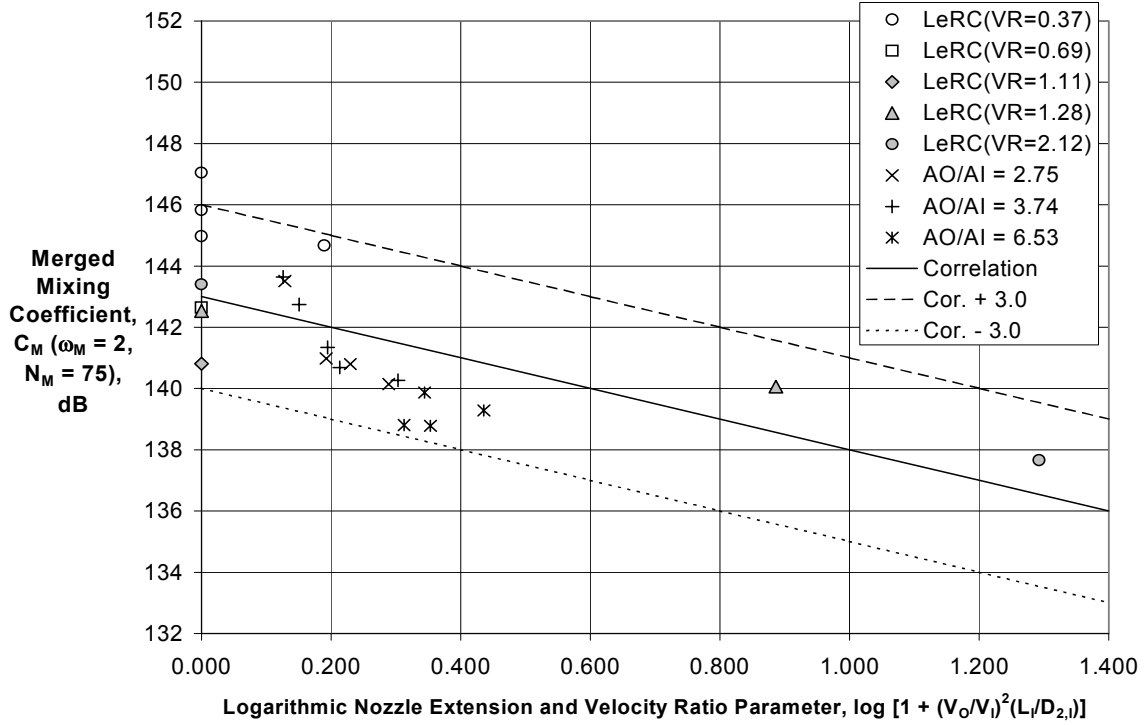
Figure 13 – First Generation Correlation of Merged Mixing Noise Coefficients for Density Exponent ω_M = 2.0 and Slope N_M = 75 as Function of Inner Nozzle Extension and Velocity Ratio
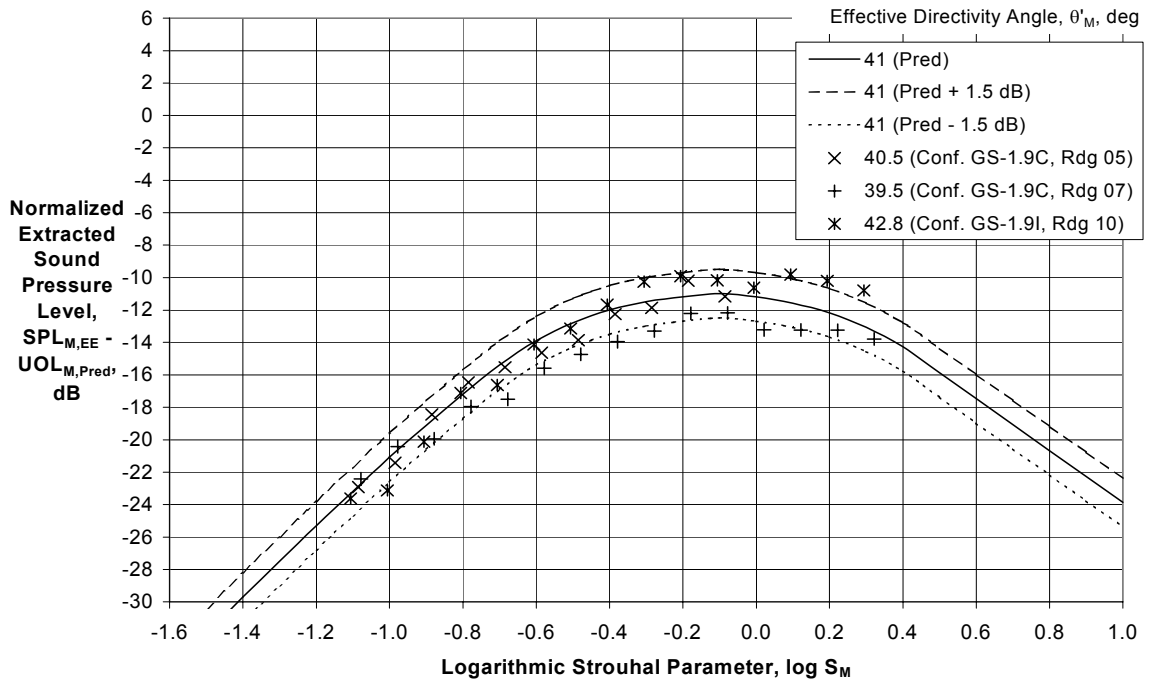
(a) Effective Directivity Angle, 39.5 < θ'_M < 42.8 deg

Figure 14 – First Generation Merged Mixing Noise Spectral Directivity Correlation
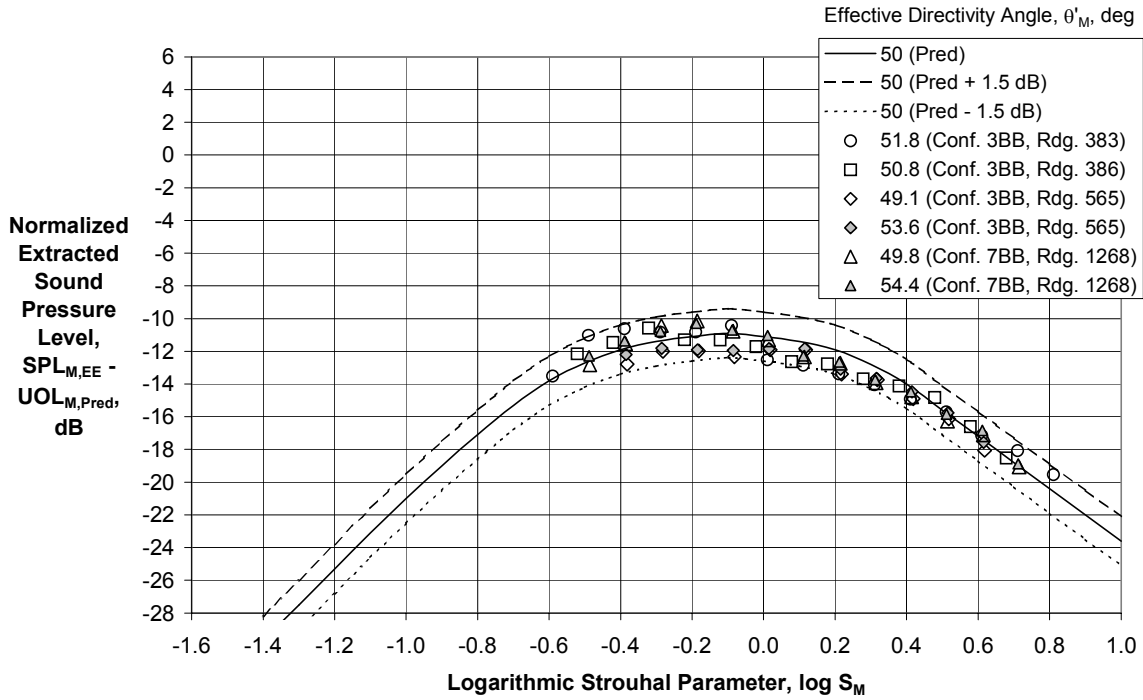
(b) Effective Directivity Angle, 49.1 < θ'M < 54.4 deg
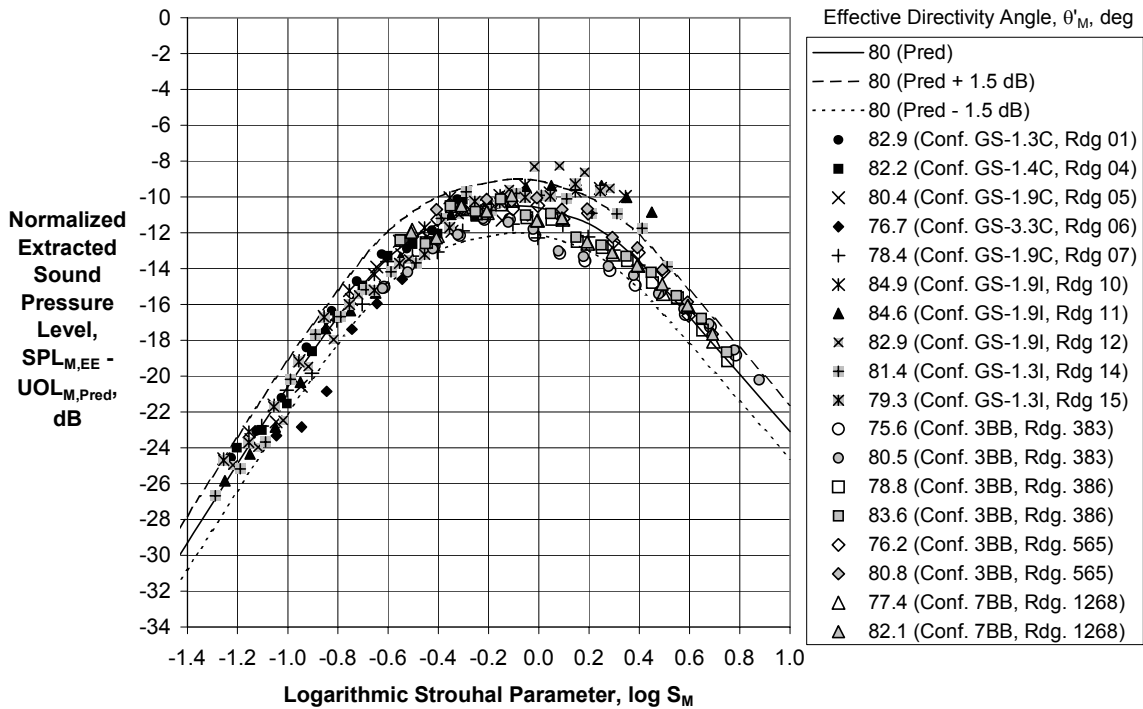
(c) Effective Directivity Angle, 75.6 < θ'M < 84.9 deg

Figure 14 (Continued) – First Generation Merged Mixing Noise Spectral Directivity Correlation
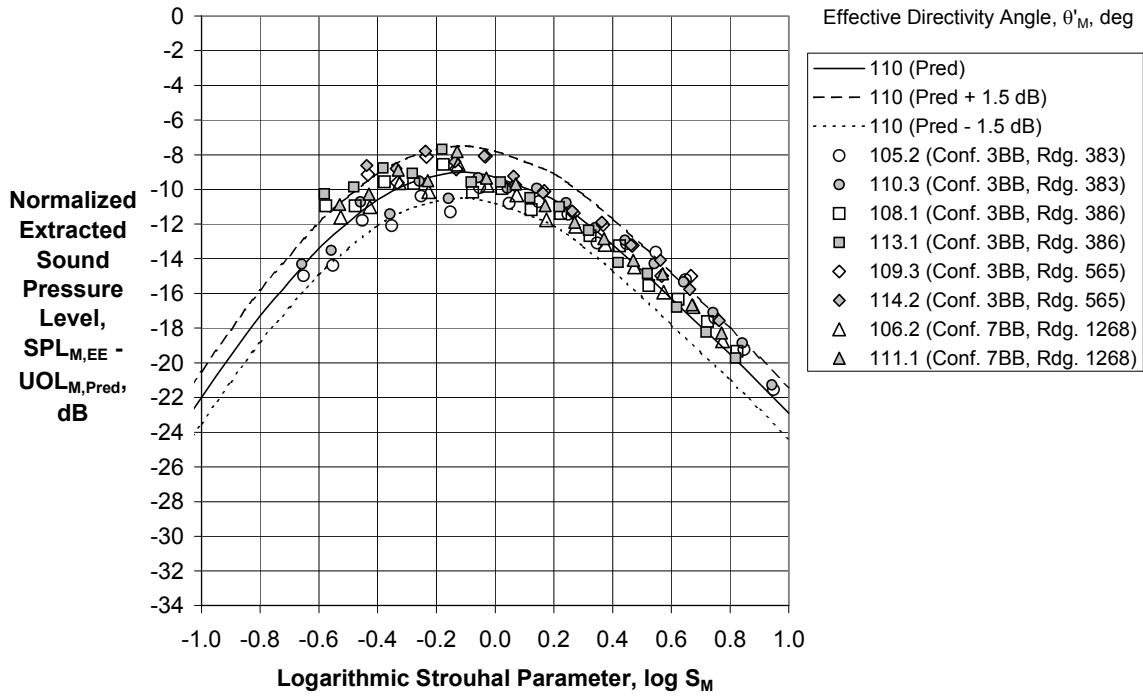
(d) Effective Directivity Angle, 105.2 < θ'$_M$ < 114.2 deg
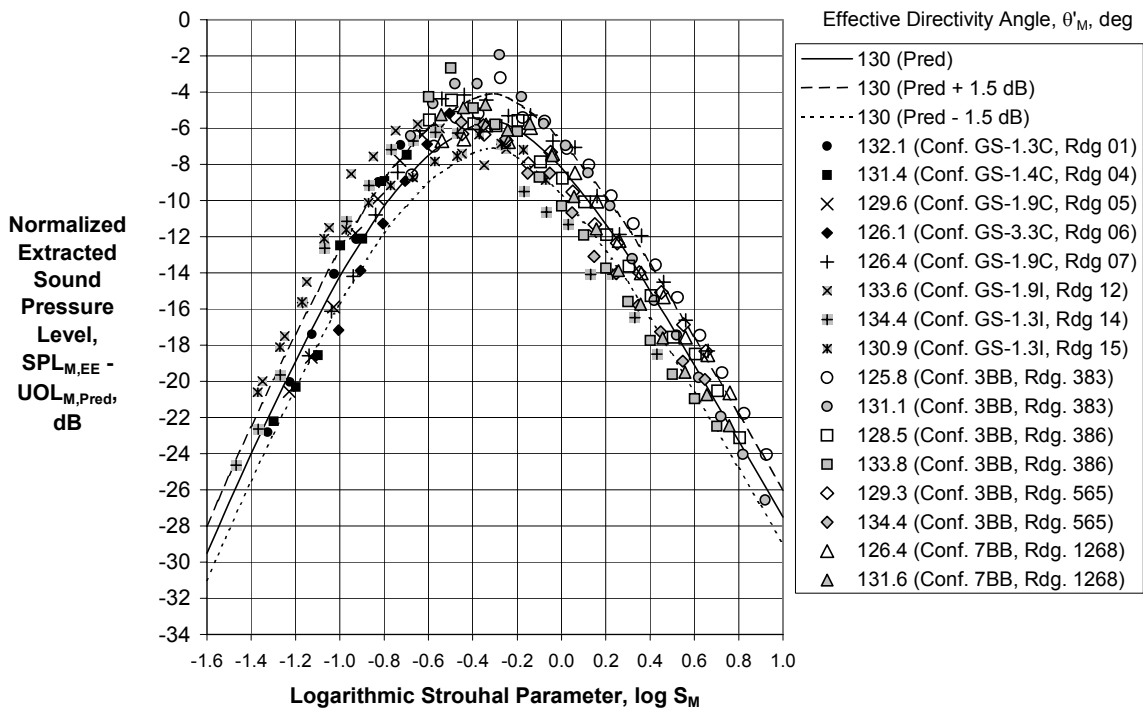
(e) Effective Directivity Angle, 125.8 < θ'$_M$ < 134.4 deg

Figure 14 (Continued) – First Generation Merged Mixing Noise Spectral Directivity Correlation
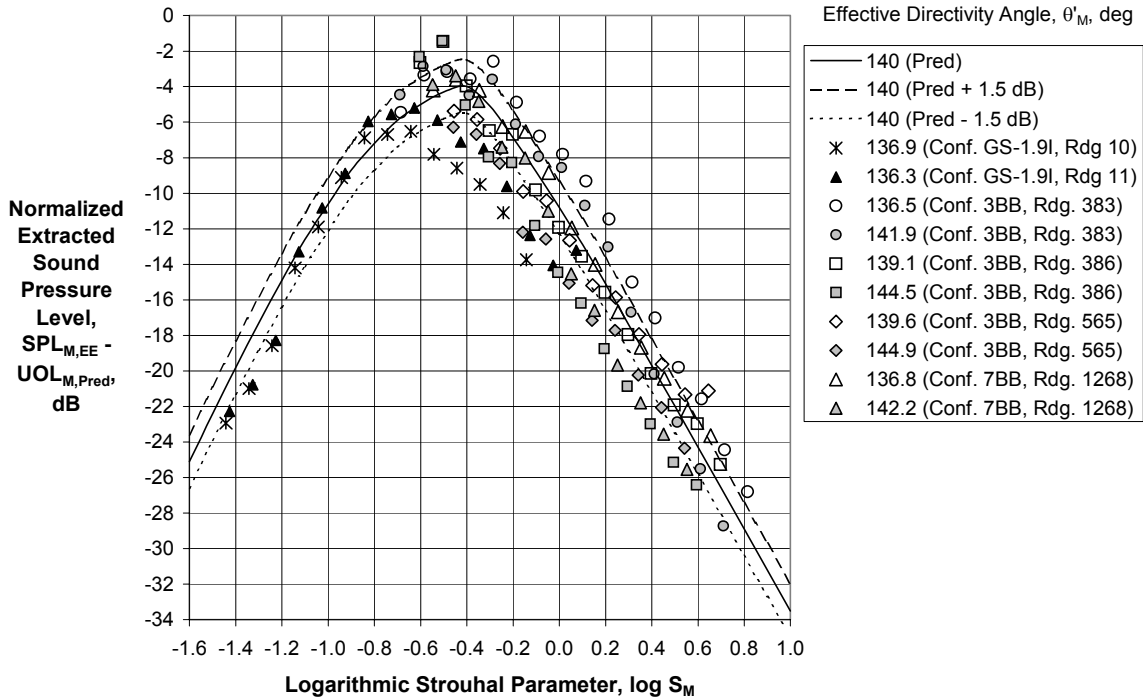
(f) Effective Directivity Angle, 136.3 < θ'_M < 144.9 deg
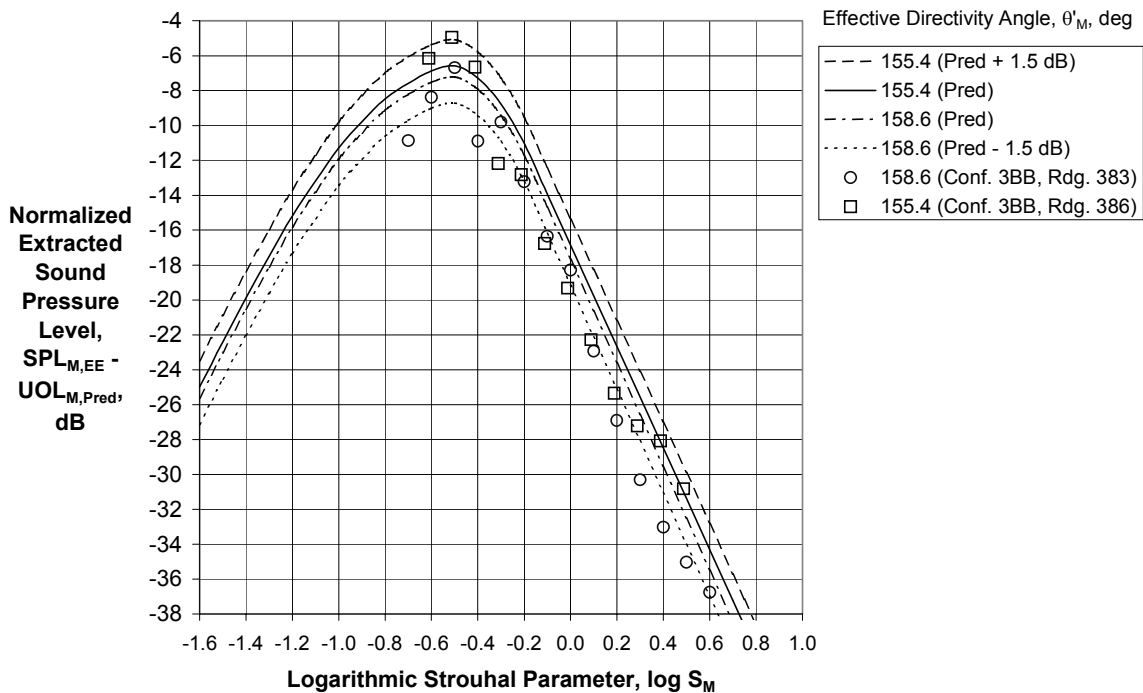
(g) Effective Directivity Angle, 155.4 < θ'_M < 158.6 deg

Figure 14 (Concluded) – First Generation Merged Mixing Noise Spectral Directivity Correlation
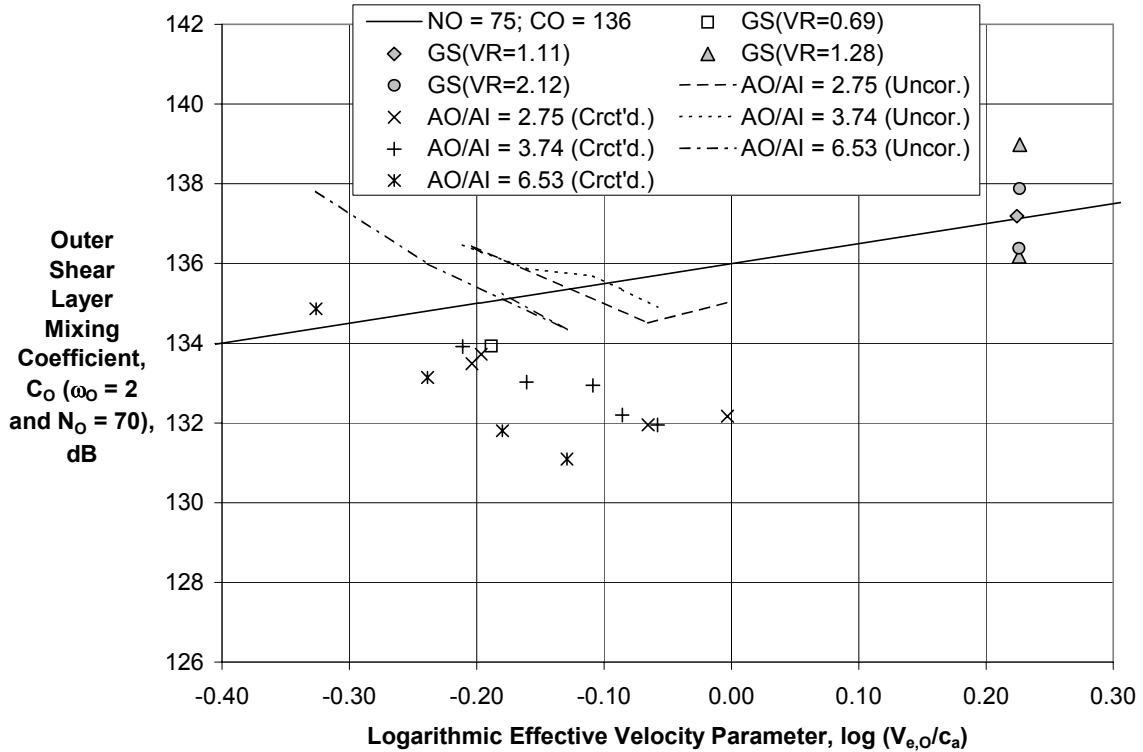
Figure 15 – First Generation Correlation of Outer Shear Layer Mixing Noise Coefficients for Density Exponent ω_O = 2.0 and Assumed Slope N_O = 70.
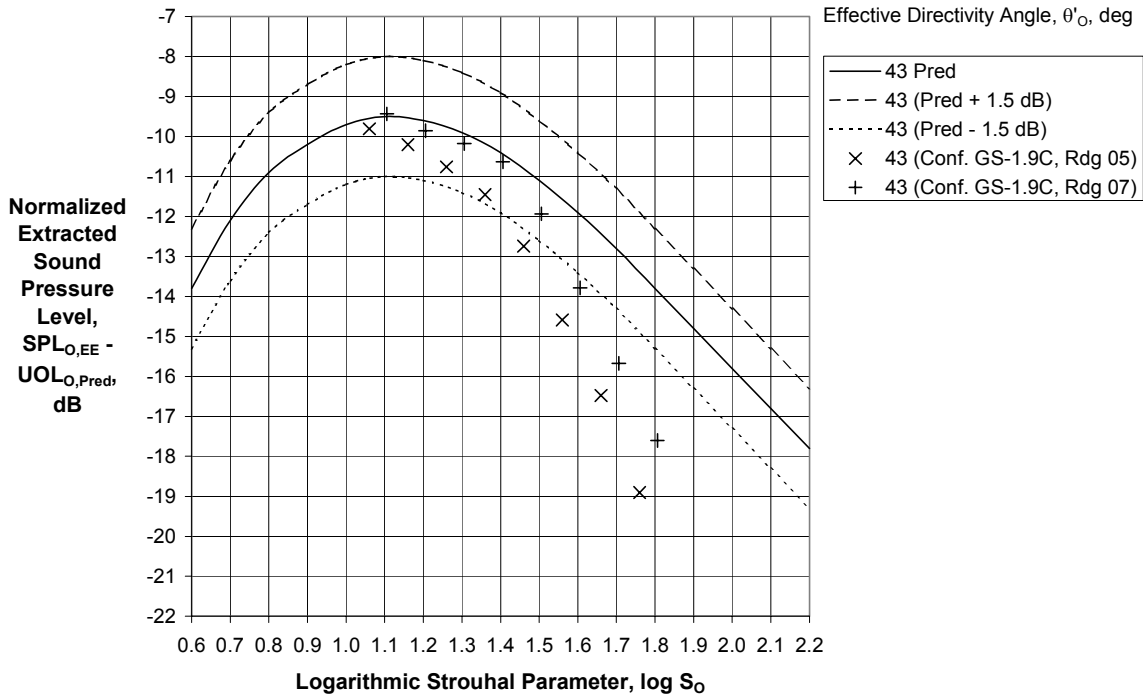
(a) Effective Directivity Angle, θ'_O = 43.0 deg

Figure 16 – First Generation Outer Shear Layer Mixing Noise Spectral Directivity Correlation
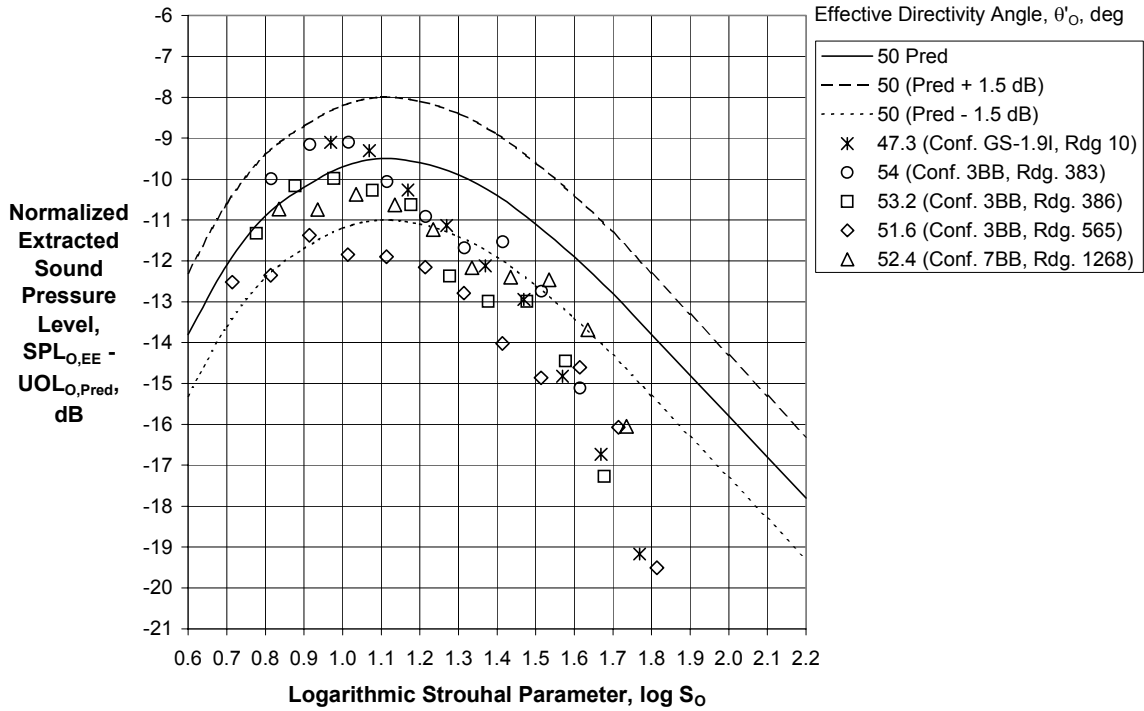
(b) Effective Directivity Angle, 47.3 < θ'$_O$ < 54.0 deg
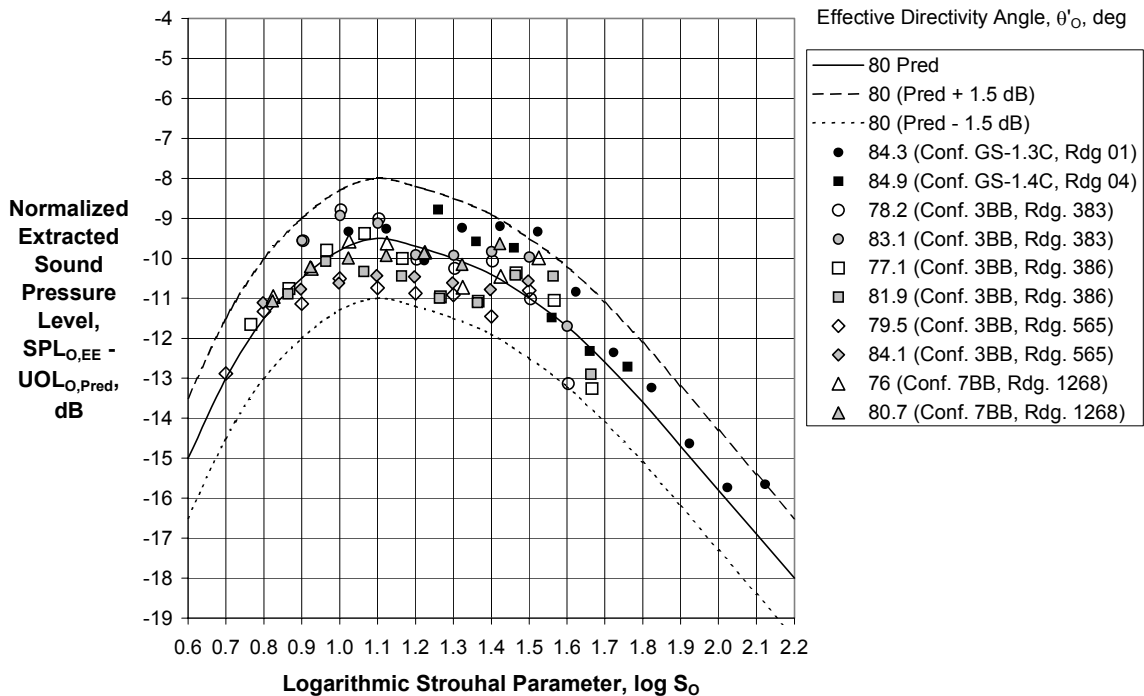
(c) Effective Directivity Angle, 76.0 < θ'$_O$ < 84.9 deg

Figure 16 (Continued) – First Generation Outer Shear Layer Mixing Noise Spectral Directivity Correlation
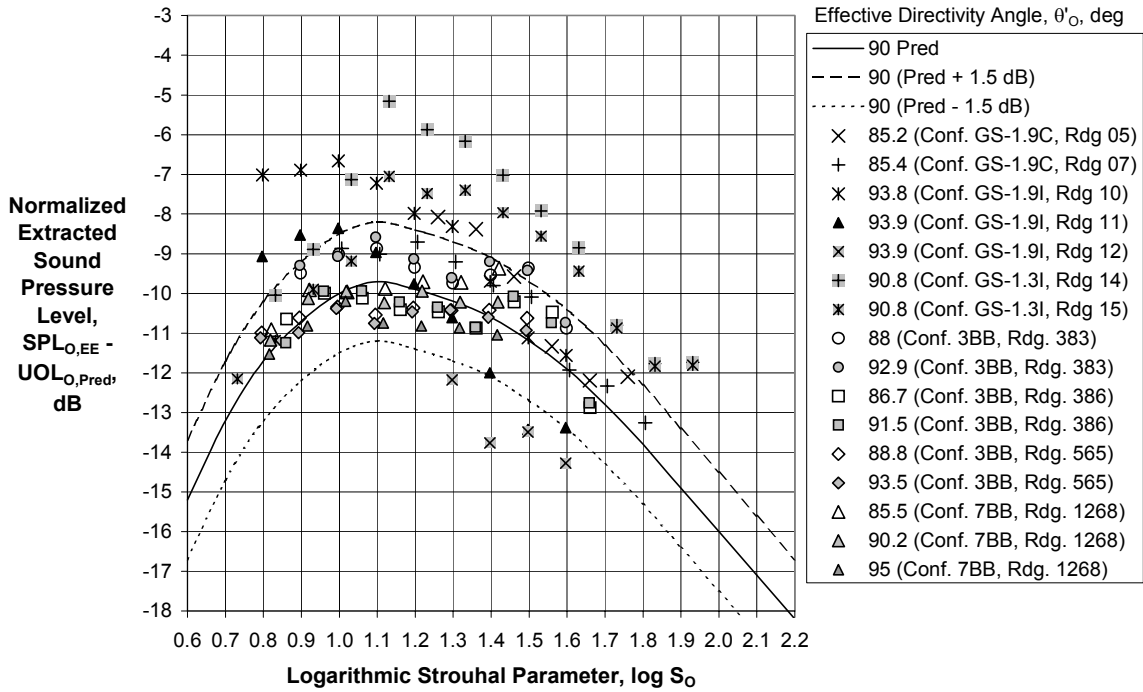
(d) Effective Directivity Angle, 85.2 < θ'$_O$ < 95.0 deg
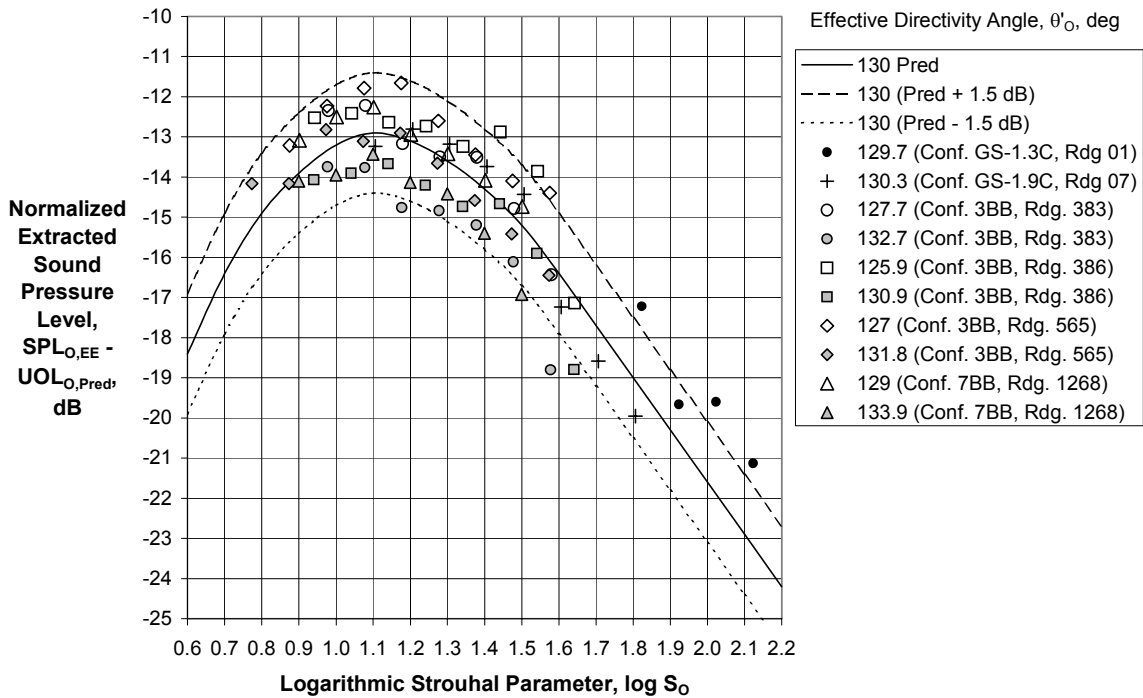
(e) Effective Directivity Angle, 125.9 < θ'$_O$ < 133.9 deg

Figure 16 (Continued) – First Generation Outer Shear Layer Mixing Noise Spectral Directivity Correlation
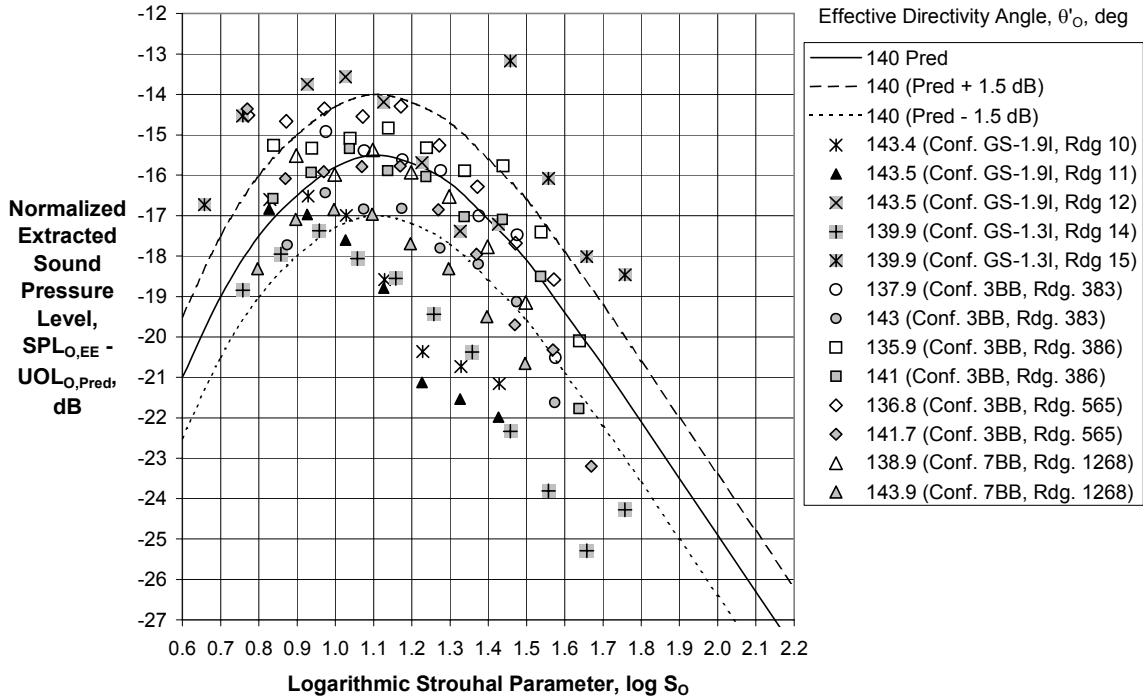
(f) Effective Directivity Angle, 135.9 < θ'ₒ < 143.9 deg
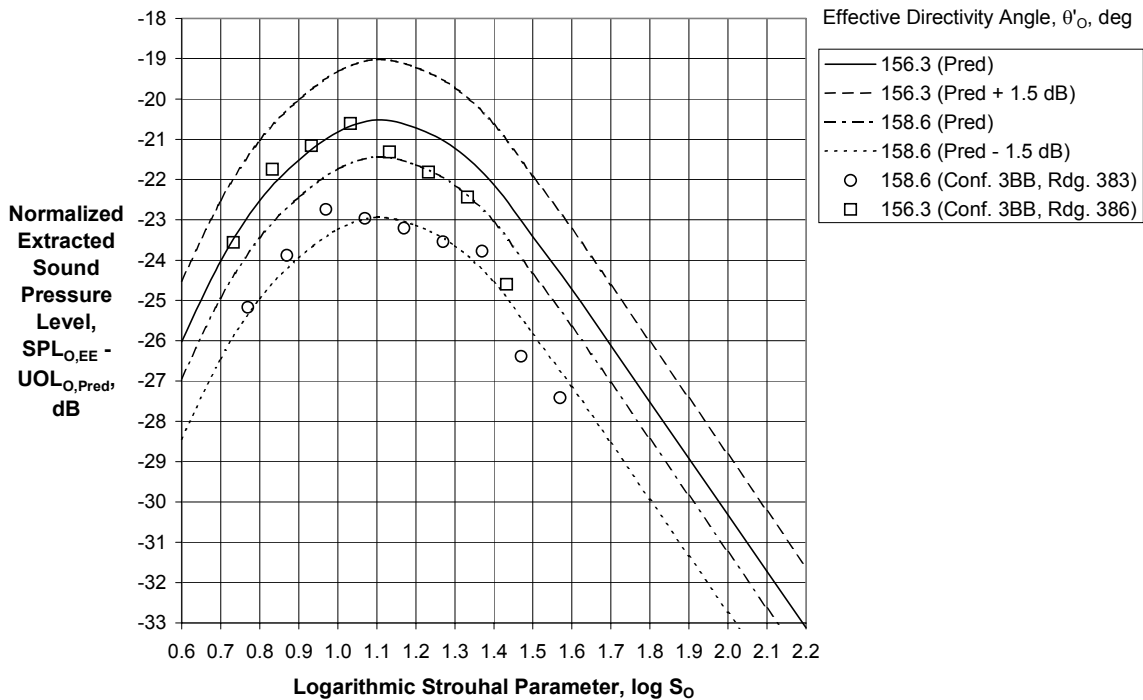
(g) Effective Directivity Angle, 156.3 < θ'ₒ < 158.6 deg

Figure 16 (Concluded) – First Generation Outer Shear Layer Mixing Noise Spectral Directivity Correlation
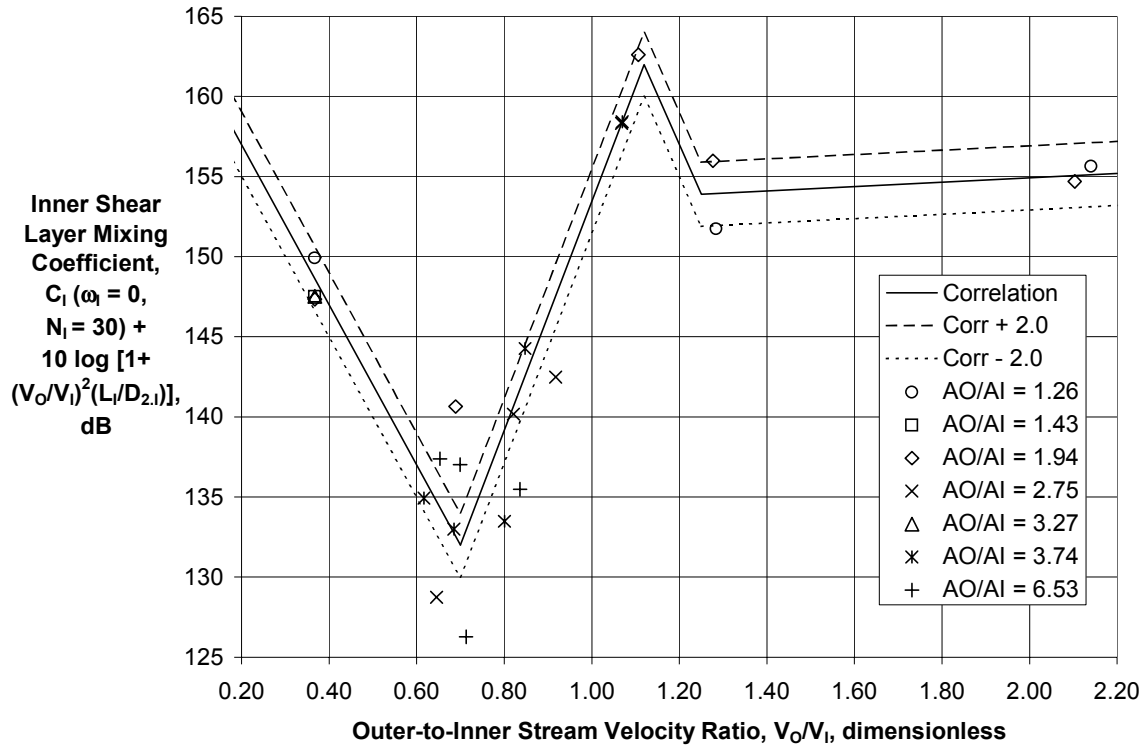
Figure 17 – First Generation Correlation of Inner Stream Mixing Coefficients for ω_I = 0.0 and Slope N_I = 30
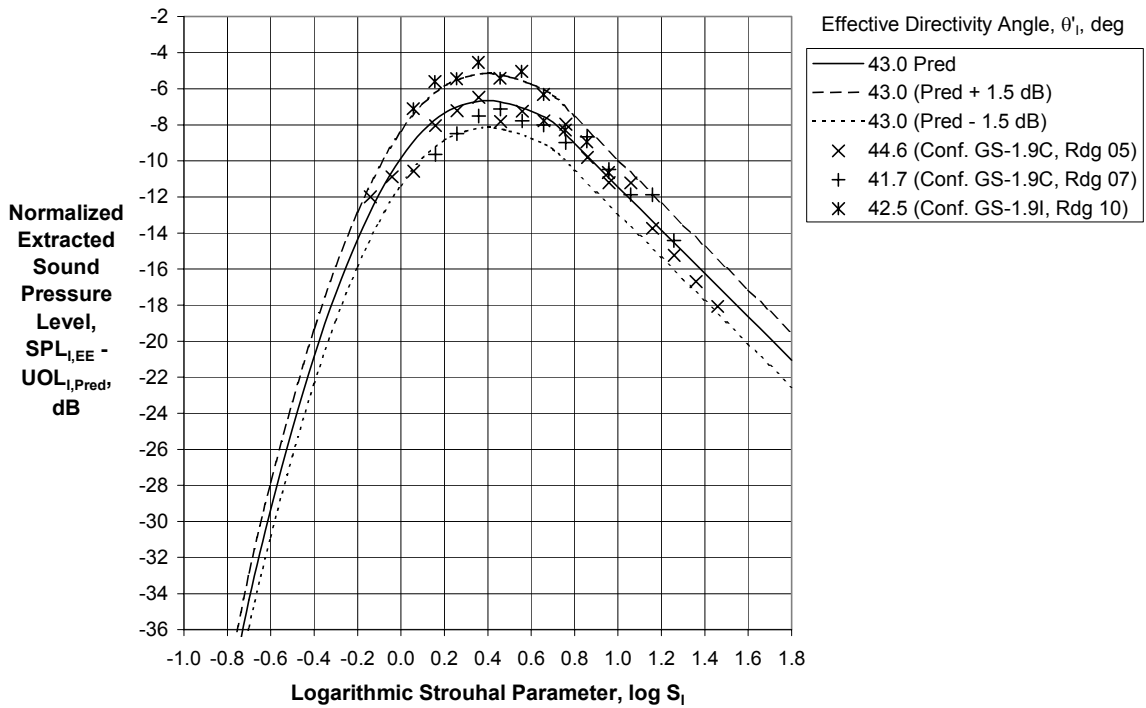
(a) Effective Directivity Angle, 41.7 < θ'_I < 44.6 deg

Figure 18 – First Generation Inner Stream Mixing Noise Spectral Directivity Correlation
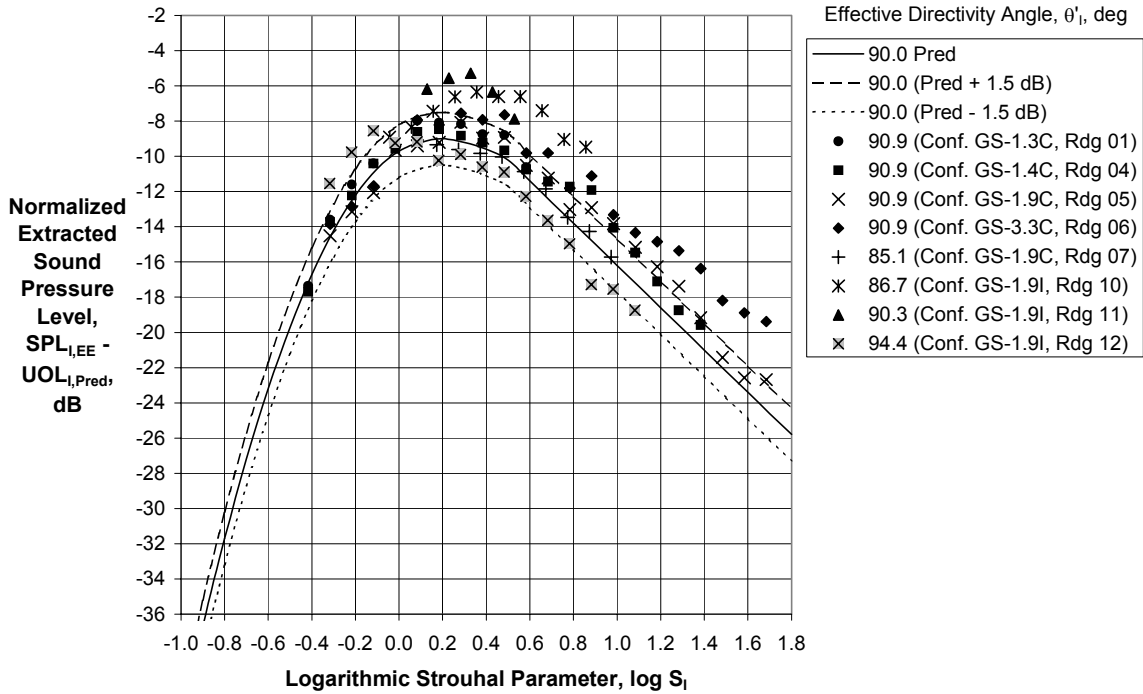
(b) Effective Directivity Angle, 85.1 < θ'$_I$ < 94.4 deg
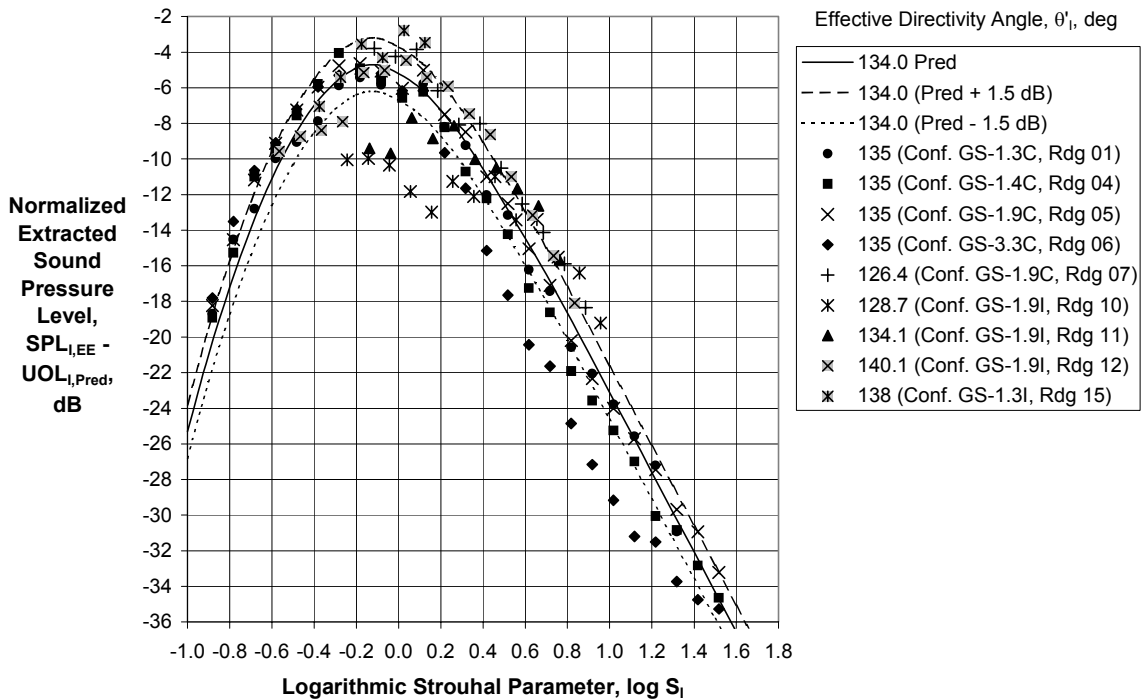
(c) Effective Directivity Angle, 126.4 < θ'$_I$ > 140.1 deg

Figure 18 (Concluded) – First Generation Inner Stream Mixing Noise Spectral Directivity Correlation
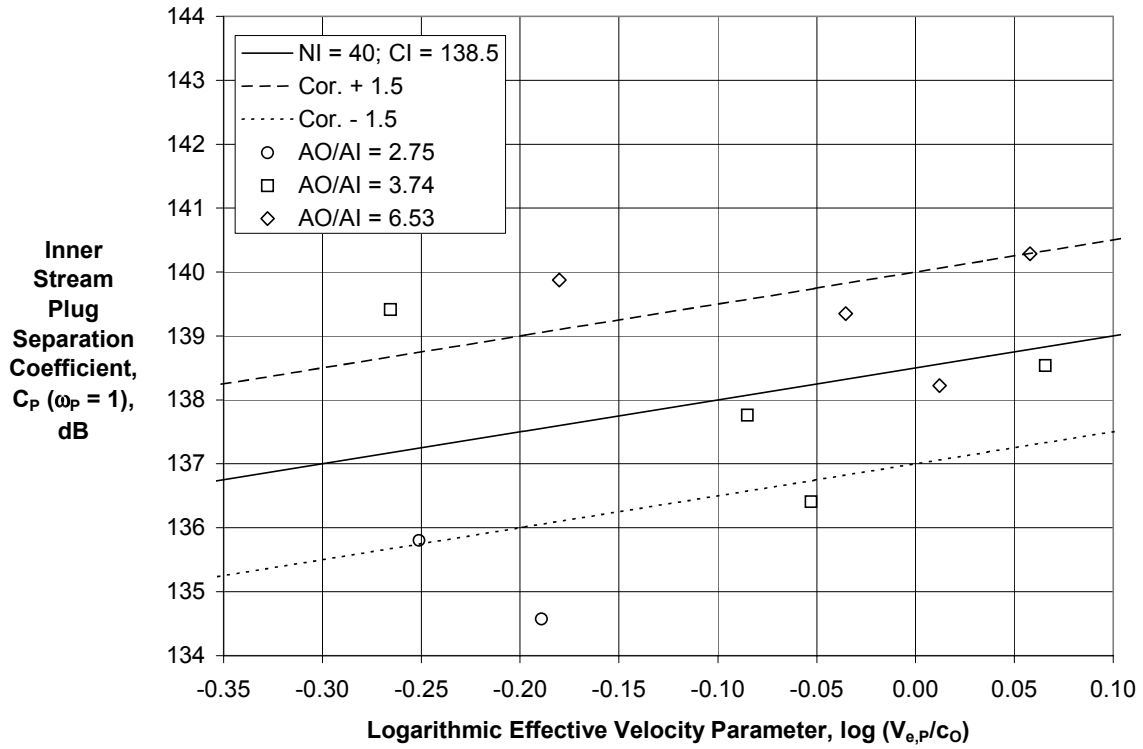
Figure 19 - First Generation Correlation of Inner Stream Plug Separation Coefficients for $\omega_P = 1.0$ and Slope $N_P = 35$
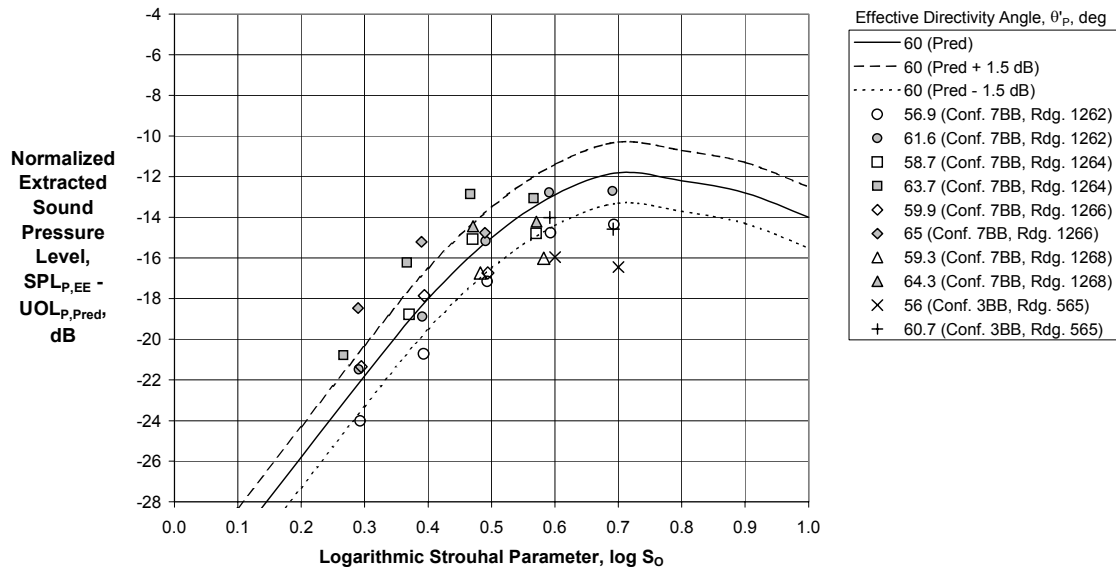
(a) Effective Directivity Angle, $56.0 < \theta'_P < 65.0$ deg

Figure 20 – First Generation Inner Stream Plug Separation Noise Spectral Directivity Correlation
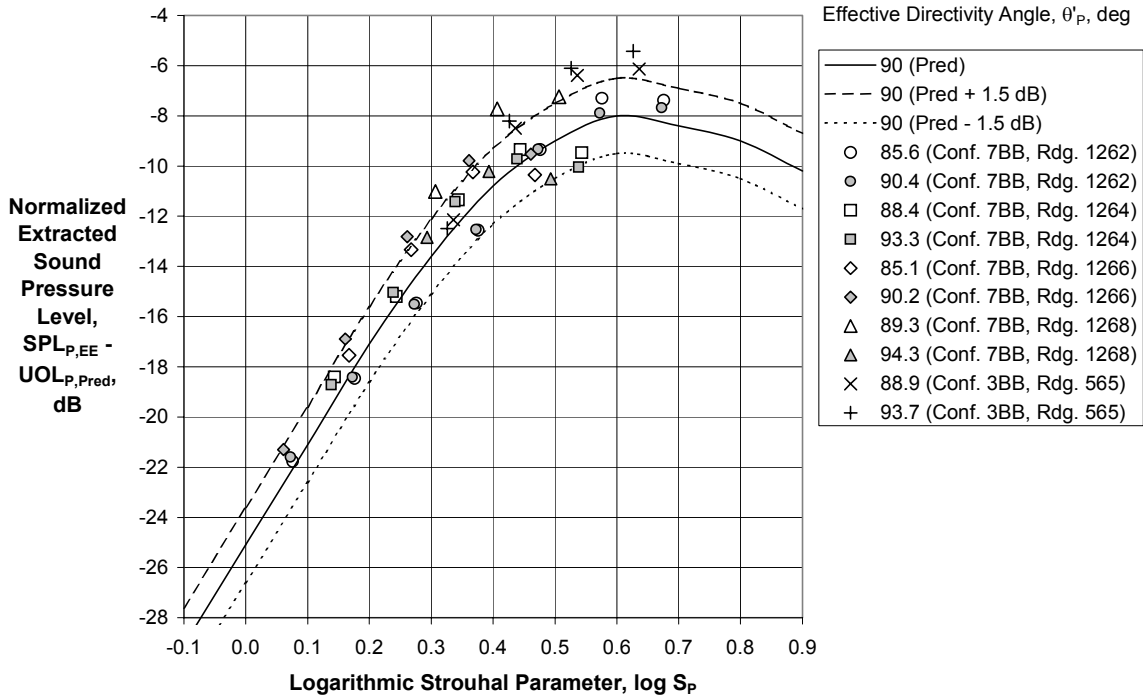
(b) Effective Directivity Angle, 85.6 < θ'_P < 93.7 deg
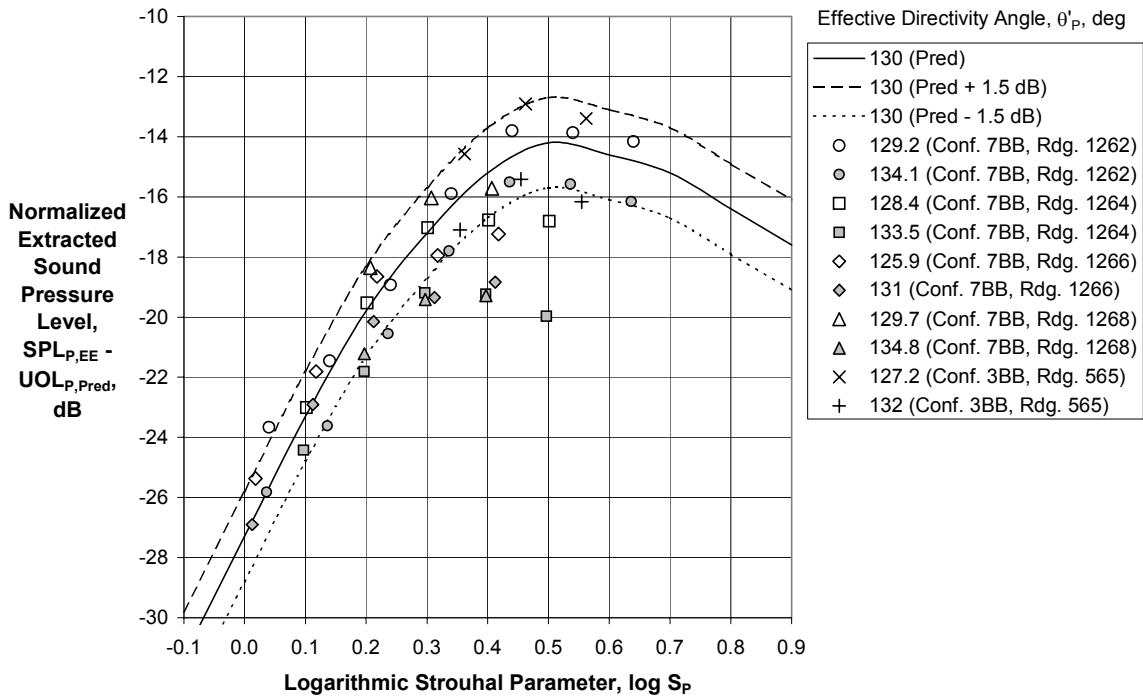
(c) Effective Directivity Angle, 125.9 < θ'_P < 134.8 deg

Figure 20 (Continued) – First Generation Inner Stream Plug Separation Noise Spectral Directivity Correlation
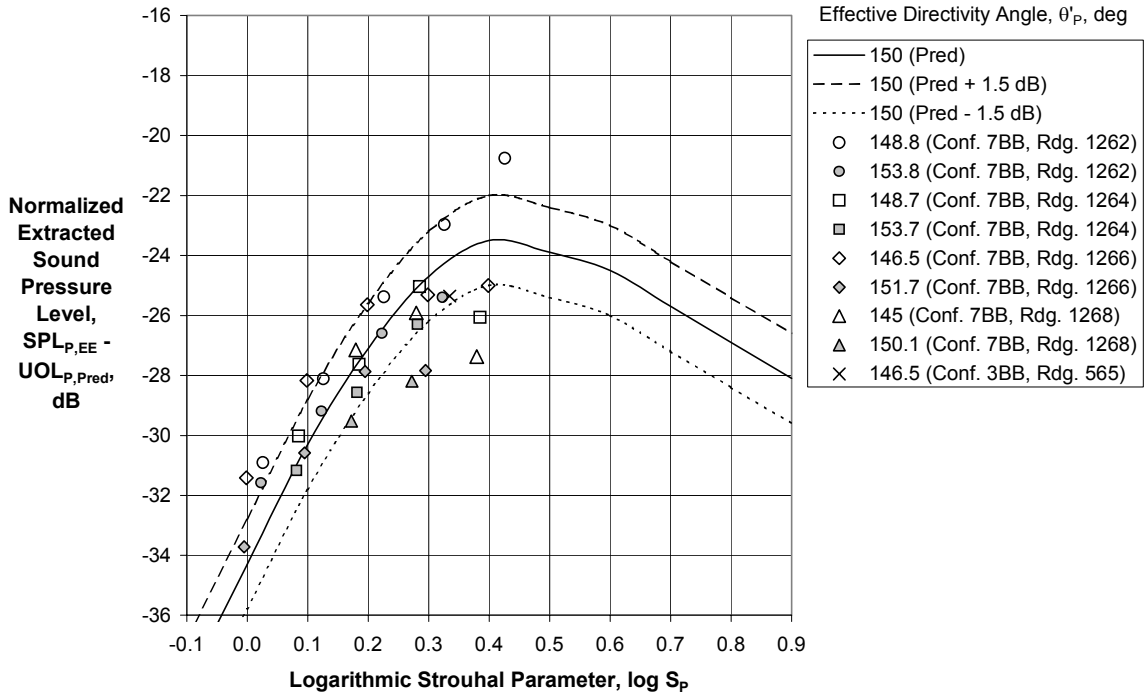
(d) Effective Directivity Angle, 145.0 < θ'$_P$ < 153.8 deg

Figure 20 (Concluded) – First Generation Inner Stream Plug Separation Noise Spectral Directivity Correlation
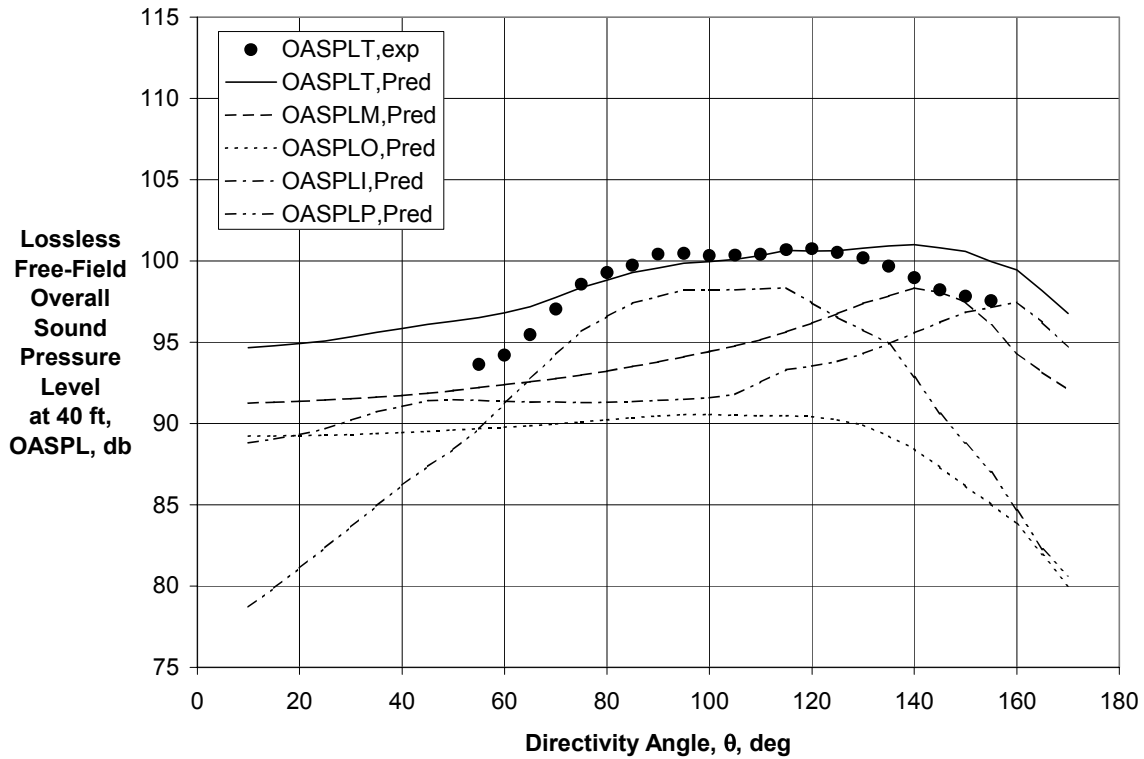
Figure 21 – Comparison of Experimental and First Generation Predicted Directivities for V$_{mix}$/c$_{amb}$ = 0.591, M$_f$ = 0.20 (A$_O$/A$_I$ = 6.53, Ref. 24, Rdg. 1262)
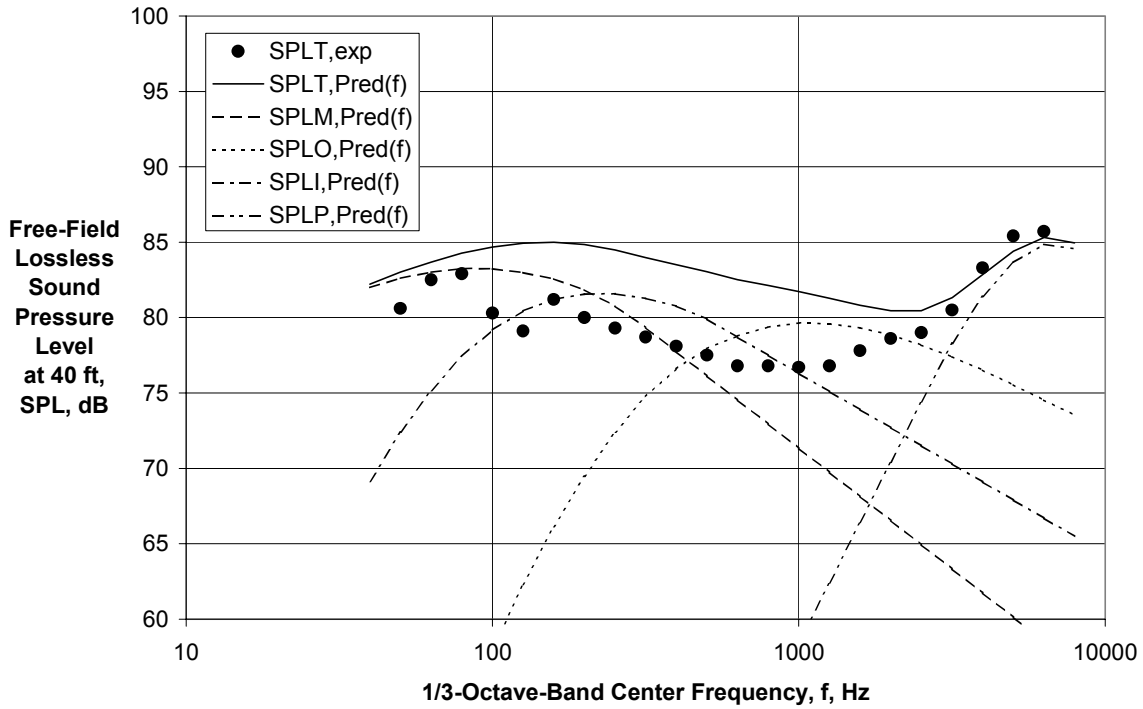
(a) Directivity Angle = 60 deg
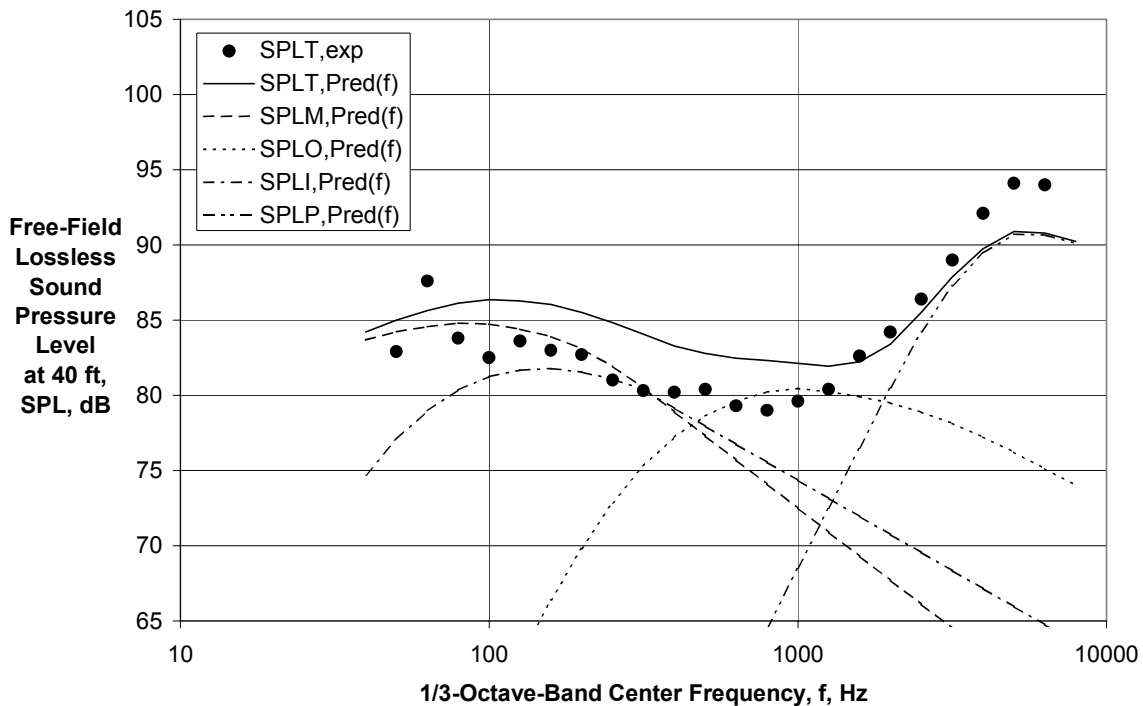
(b) Directivity Angle = 90 deg

Figure 22 – Comparison of Experimental and First Generation Predicted Spectra for V_{mix}/c_{amb} = 0.591, M_f = 0.20 (A_O/A_I = 6.53, Ref. 24, Rdg. 1262)
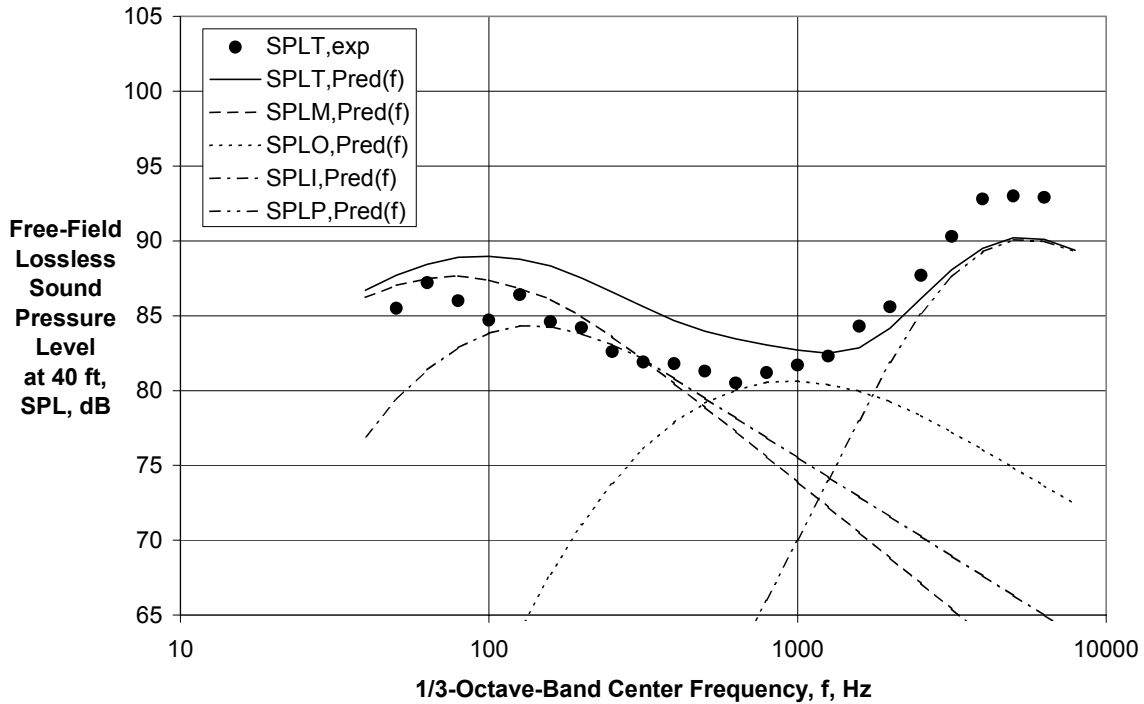
(c) Directivity Angle = 120 deg
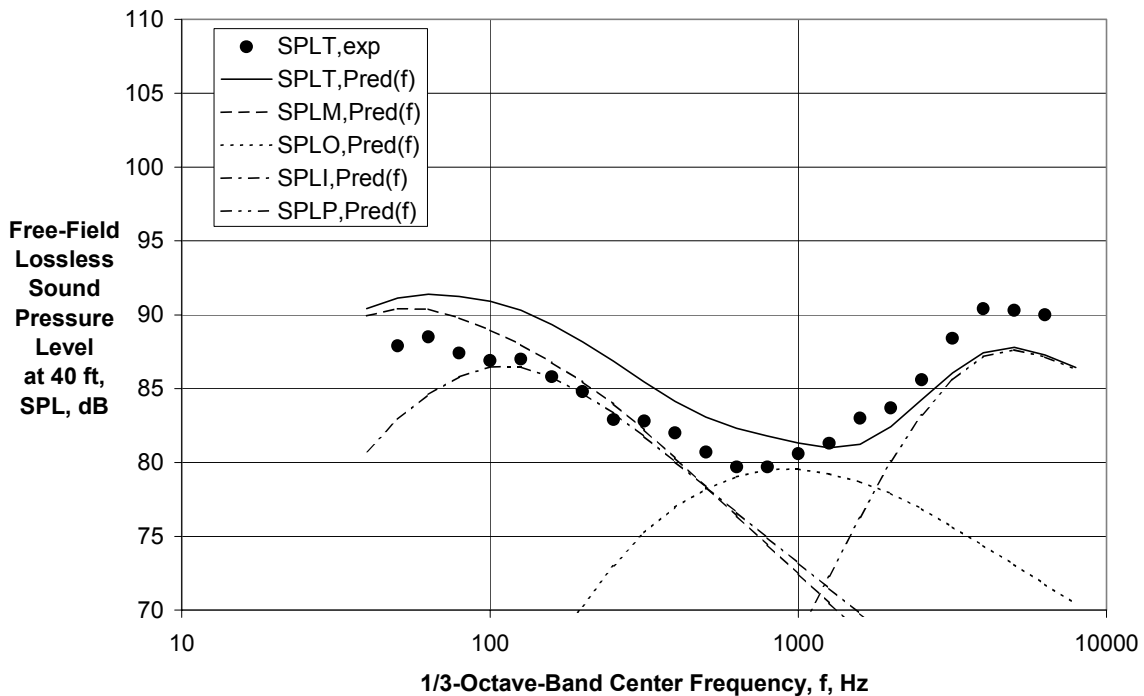
(d) Directivity Angle = 135 deg

Figure 22 (Continued) – Comparison of Experimental and First Generation Predicted Spectra for V_{mix}/c_{amb} = 0.591, M_f = 0.20 (A_O/A_I = 6.53, Ref. 24, Rdg. 1262)
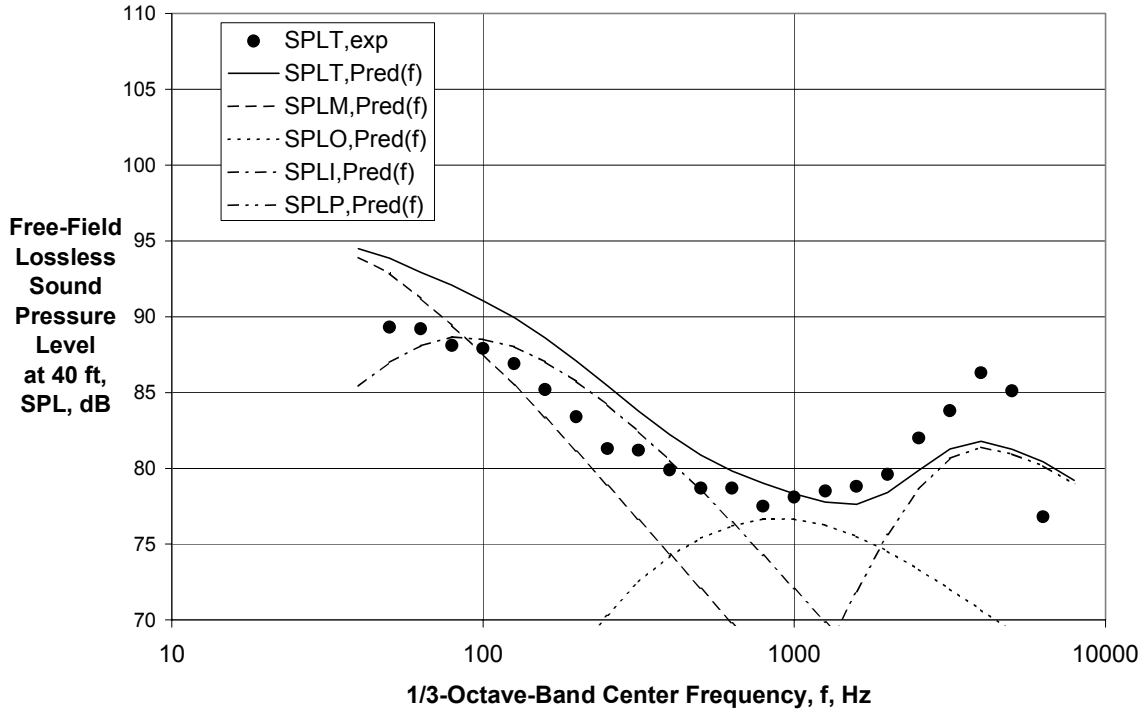
(e) Directivity Angle = 150 deg
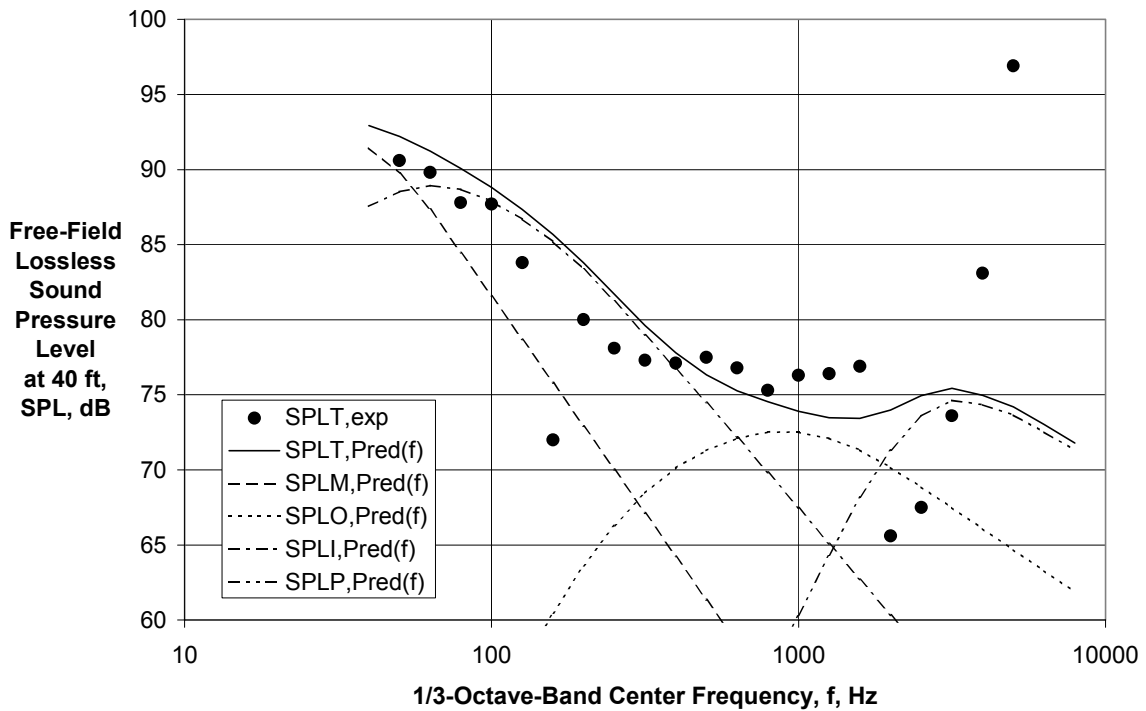
(f) Directivity Angle = 165 deg

Figure 22 (Concluded) – Comparison of Experimental and First Generation Predicted Spectra for V_{mix}/c_{amb} = 0.591, M_f = 0.20 (A_O/A_I = 6.53, Ref. 24, Rdg. 1262)
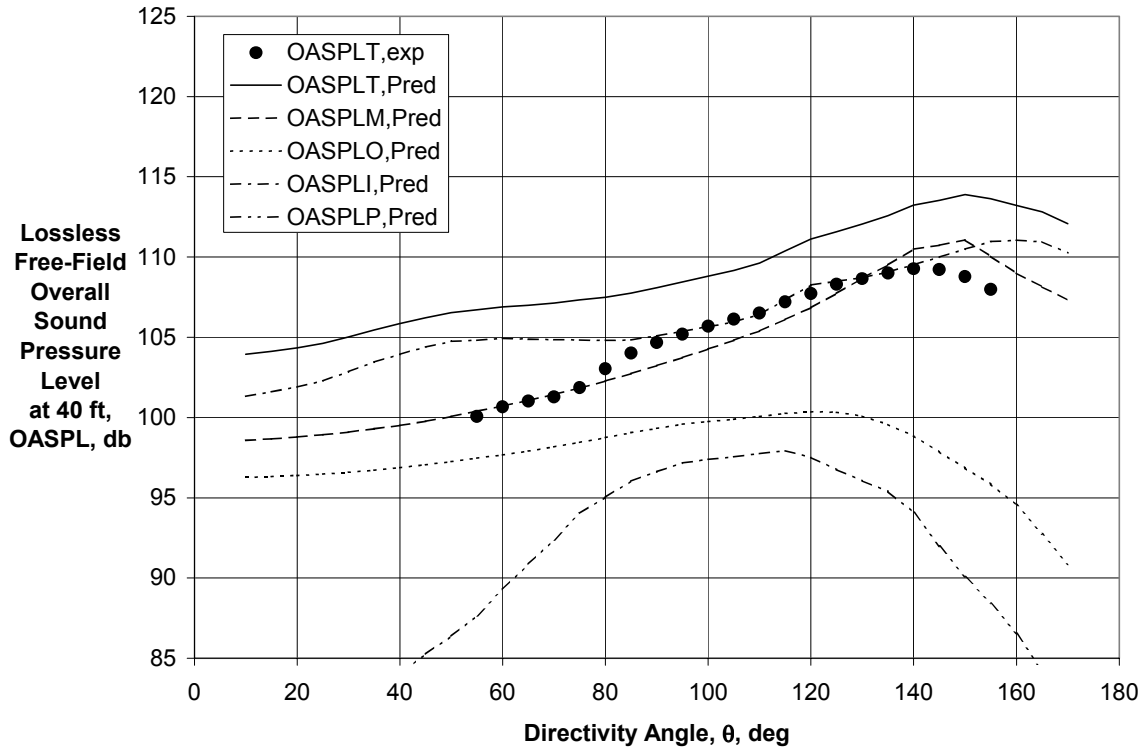
Figure 23– Comparison of Experimental and First Generation Predicted Directivities for V_{mix}/c_{amb} = 0.633, M_f = 0.0 (A_O/A_I = 2.75, Ref. 24, Rdg. 565)
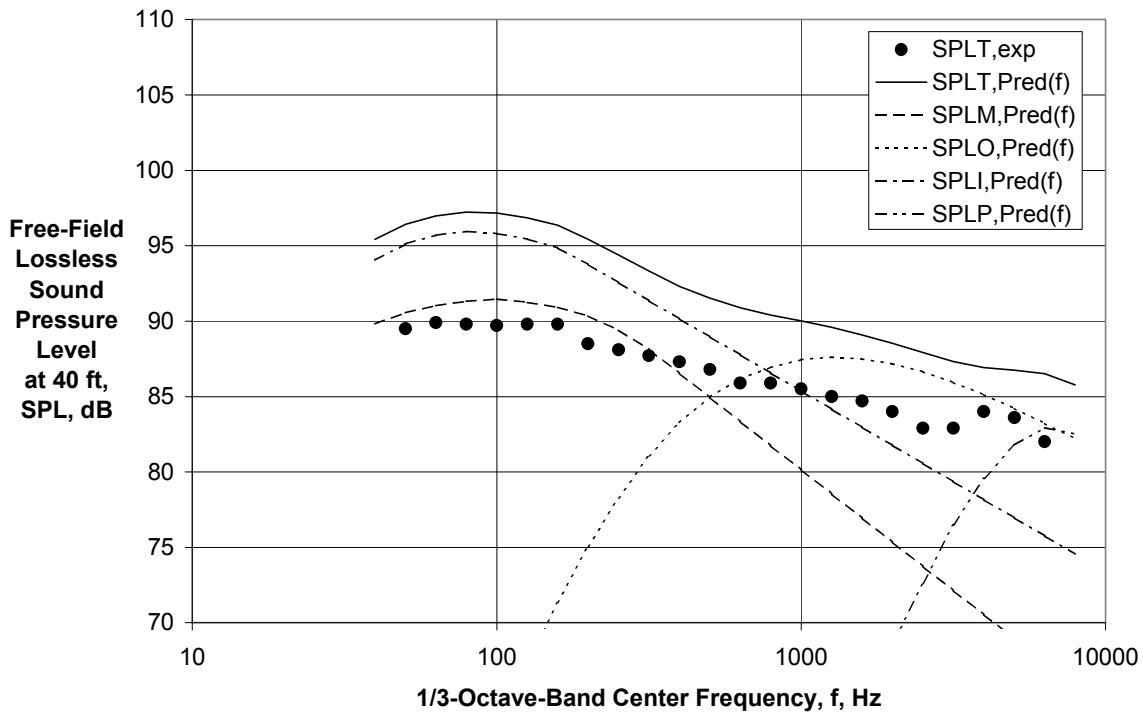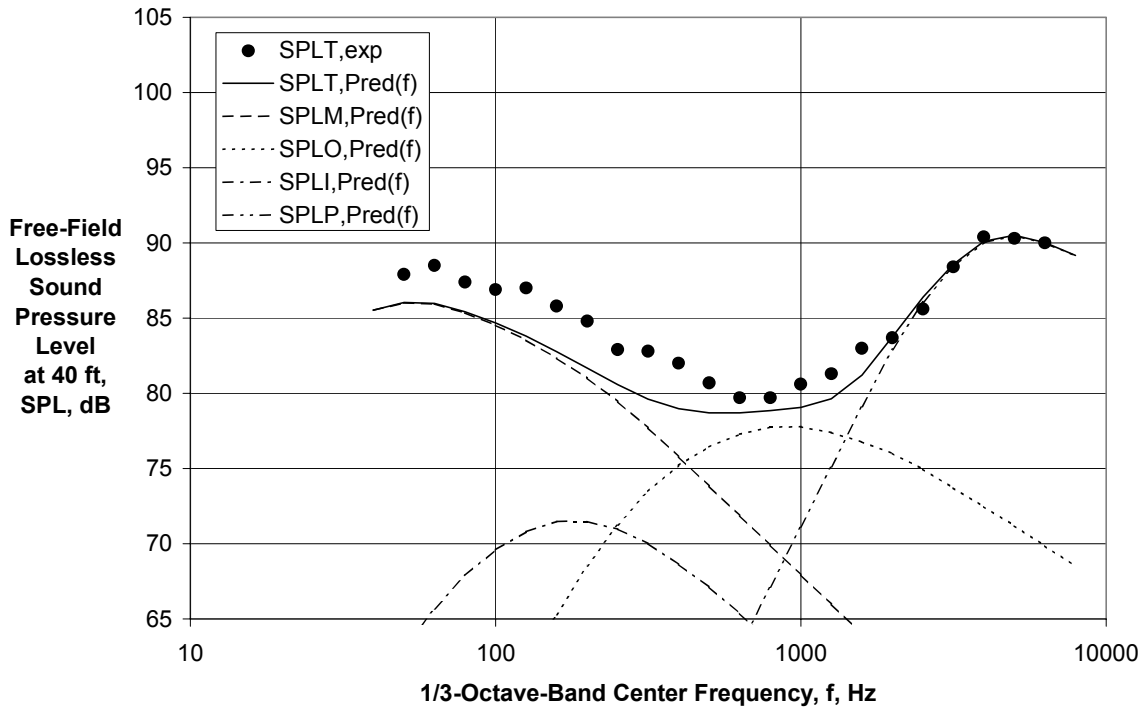

(a) Directivity Angle = 60 deg

Figure 24 – Comparison of Experimental and First Generation Predicted Spectra for V_{mix}/c_{amb} = 0.633, M_f = 0.0 (A_O/A_I = 2.75, Ref. 24, Rdg. 565)
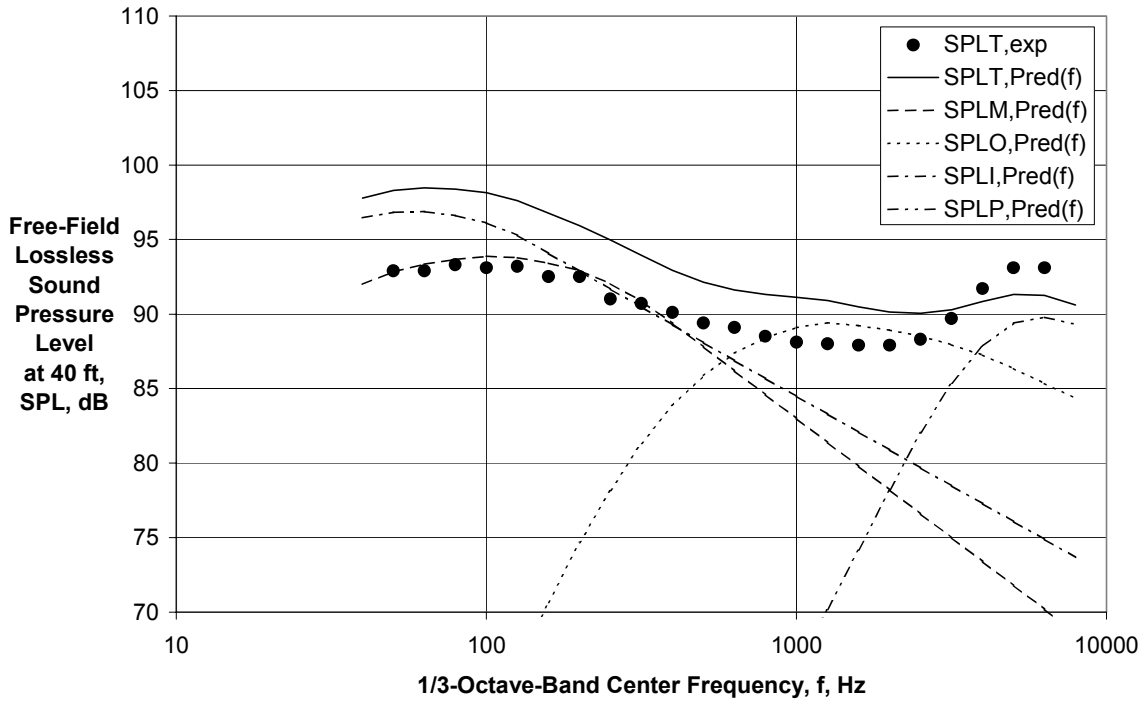
(b) Directivity Angle = 90 deg
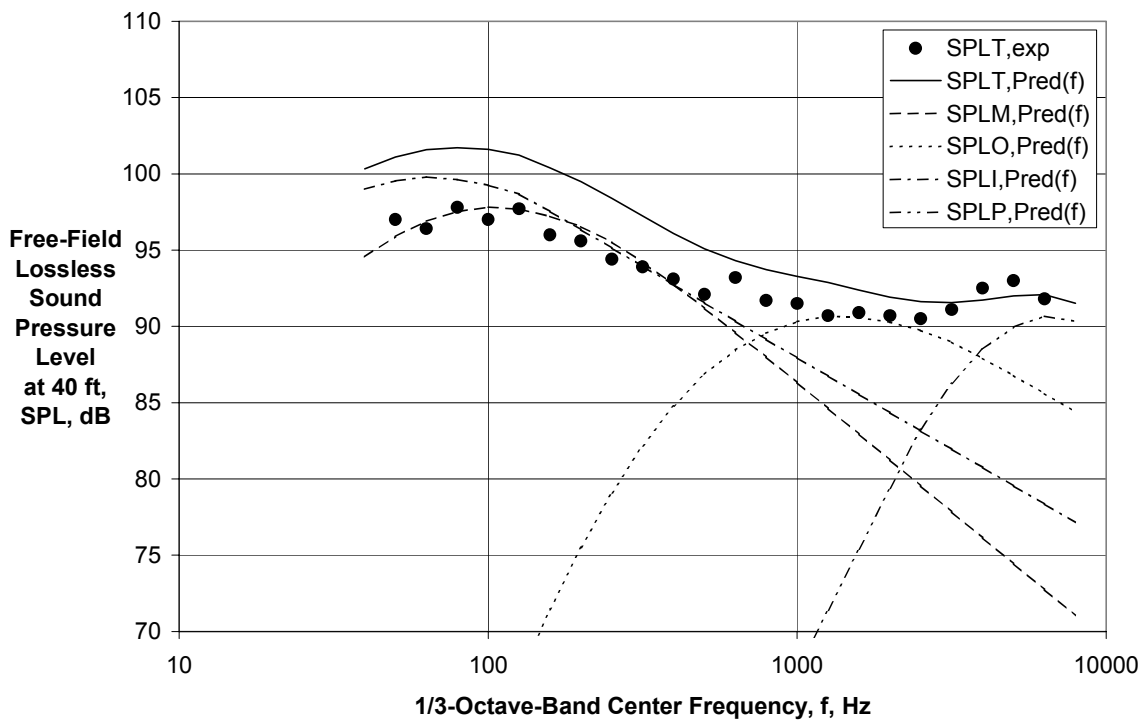
(c) Directivity Angle = 120 deg

Figure 24 (Continued) – Comparison of Experimental and First Generation Predicted Spectra for V_{mix}/c_{amb} = 0.633, M_f = 0.0 (A_O/A_I = 2.75, Ref. 24, Rdg. 565)
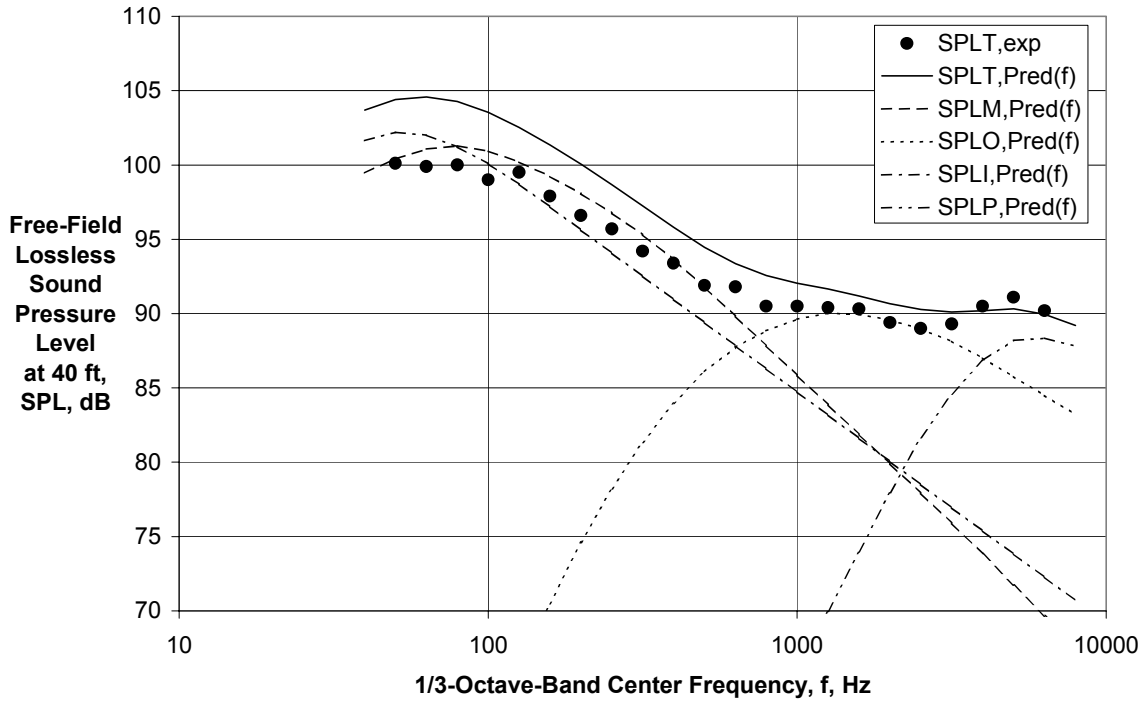
(d) Directivity Angle = 135 deg
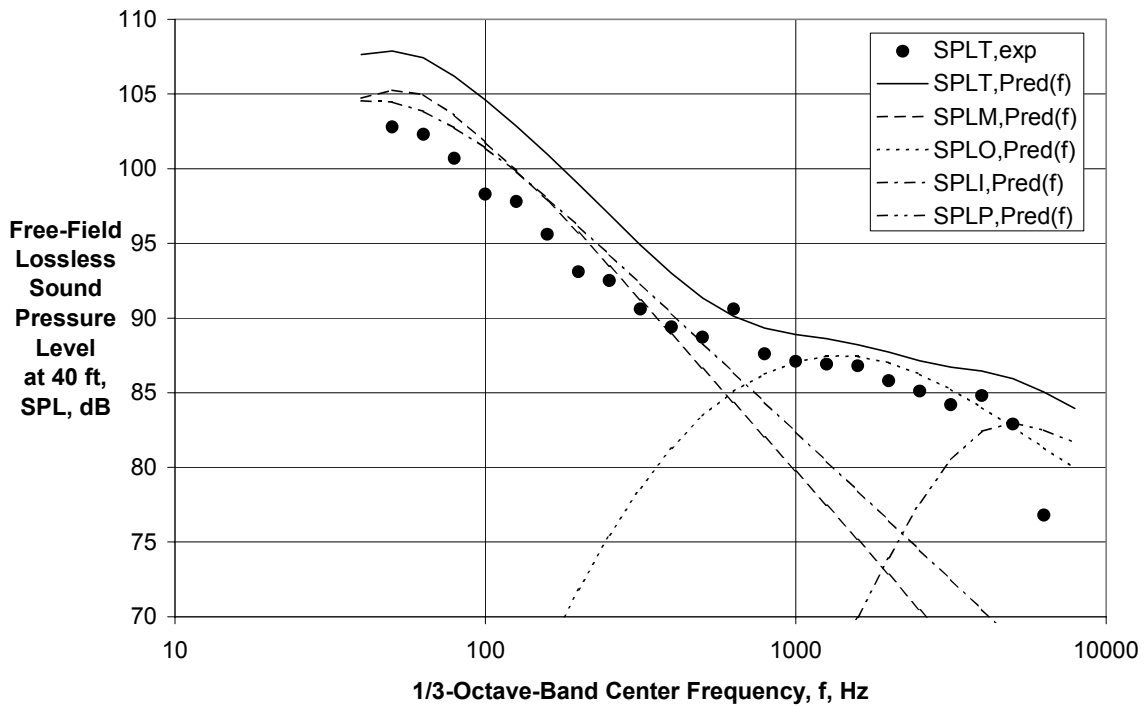
(e) Directivity Angle = 150 deg

Figure 24 (Continued) – Comparison of Experimental and First Generation Predicted Spectra for V_{mix}/c_{amb} = 0.633, M_f = 0.0 (A_O/A_I = 2.75, Ref. 24, Rdg. 565)
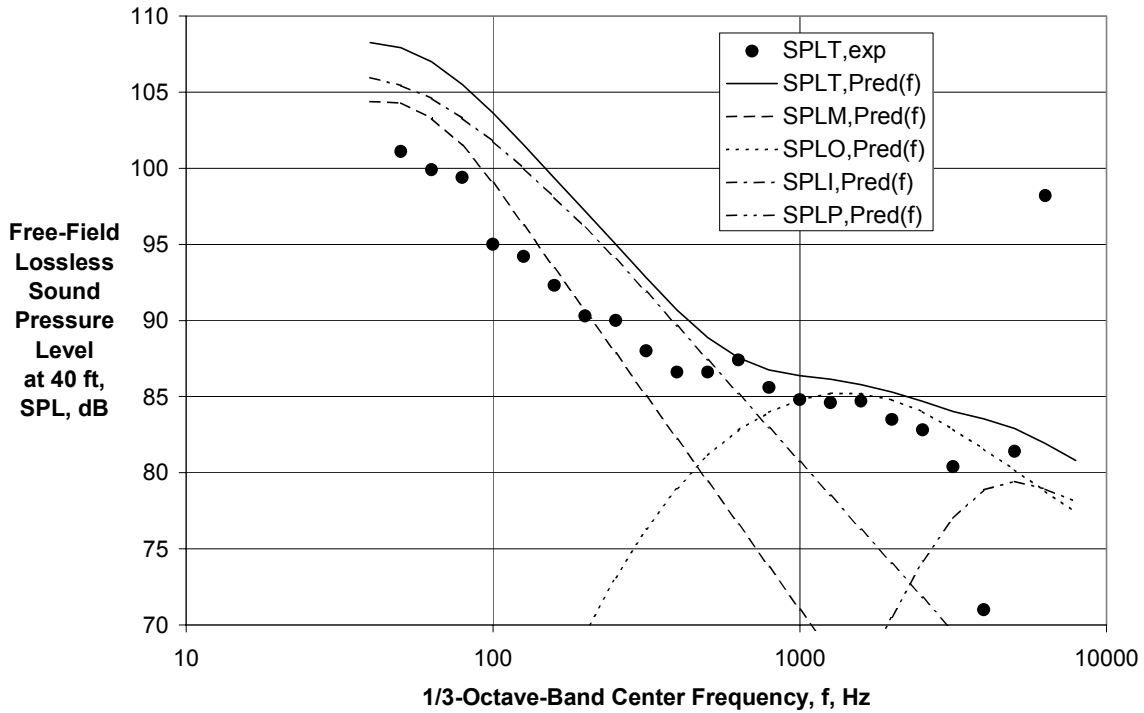
(f) Directivity Angle = 160 deg

Figure 24 (Concluded) – Comparison of Experimental and First Generation Predicted Spectra for V_{mix}/c_{amb} = 0.633, M_f = 0.0 (A_O/A_I = 2.75, Ref. 24, Rdg. 565)
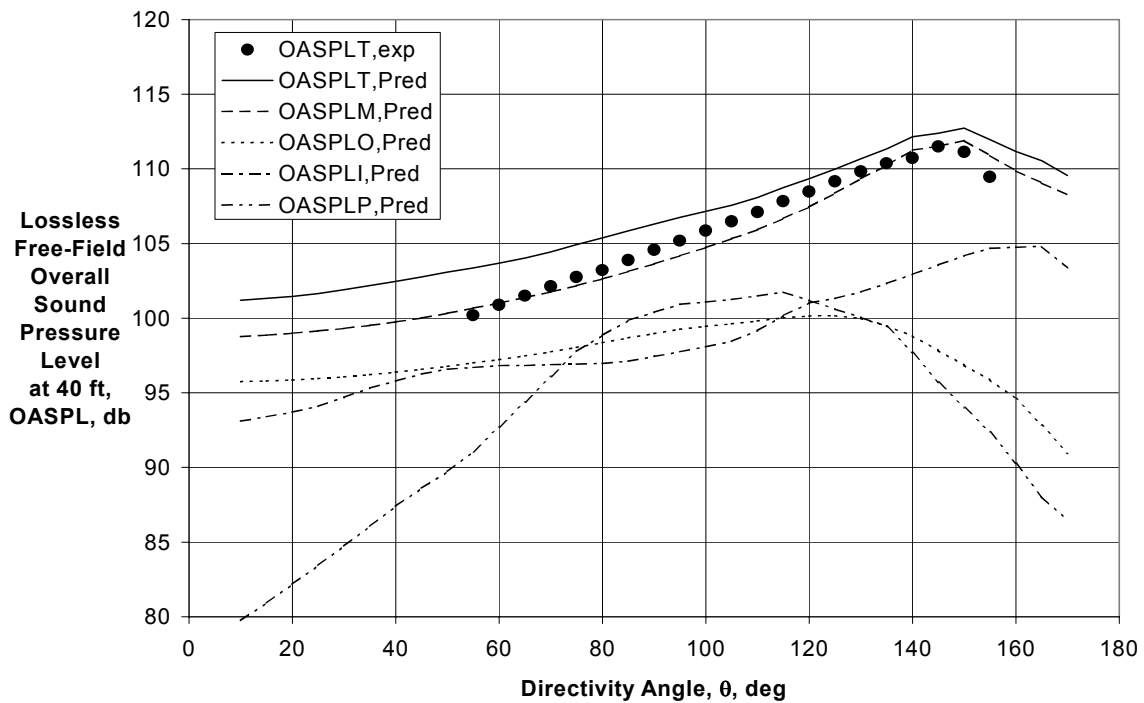
Figure 25 - Comparison of Experimental and First Generation Predicted Directivities for V_{mix}/c_{amb} = 0.635, M_f = 0.0 (A_O/A_I = 2.75, Ref. 24, Rdg. 378)
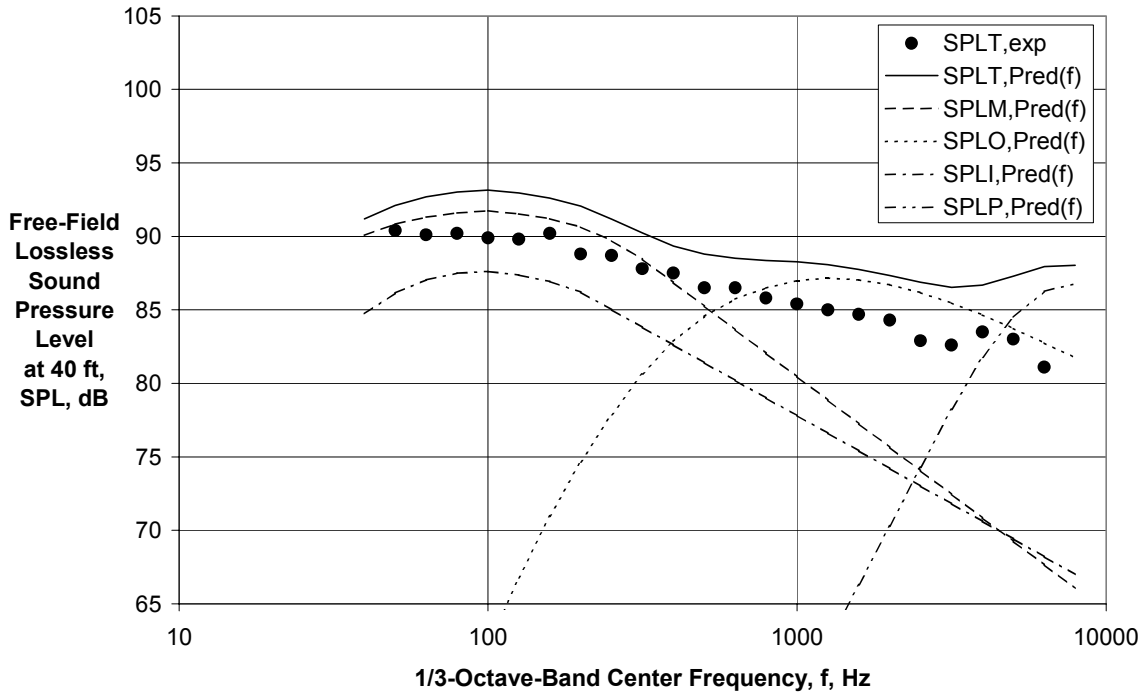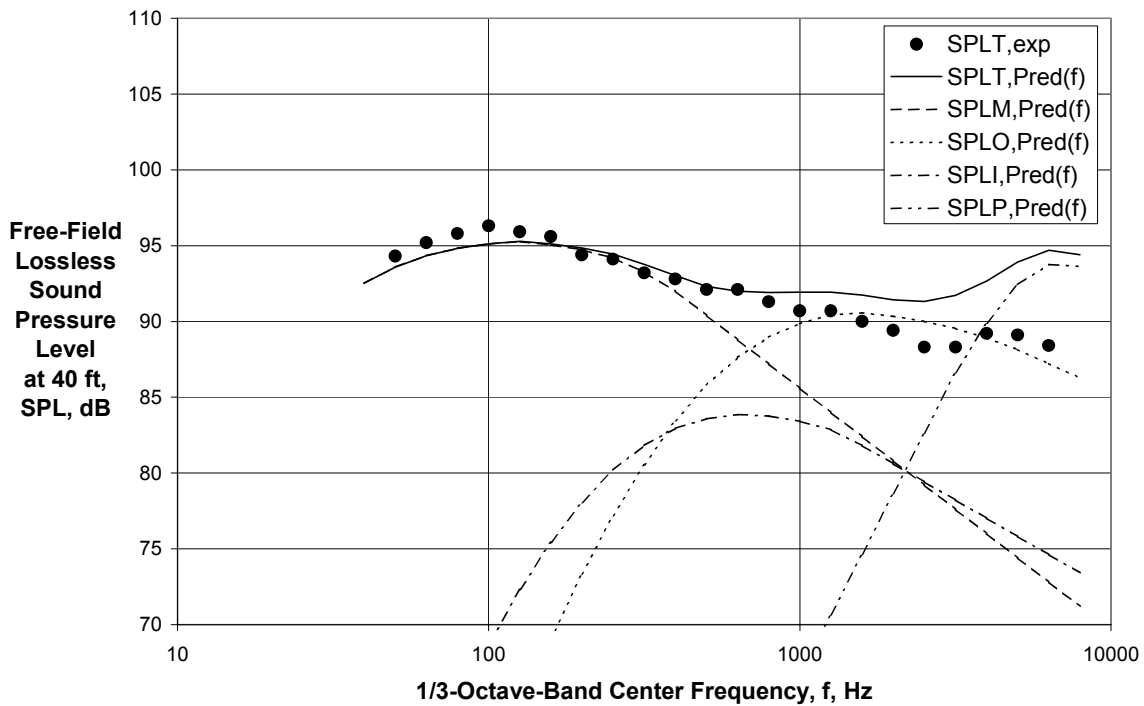
(a) Directivity Angle = 60 deg
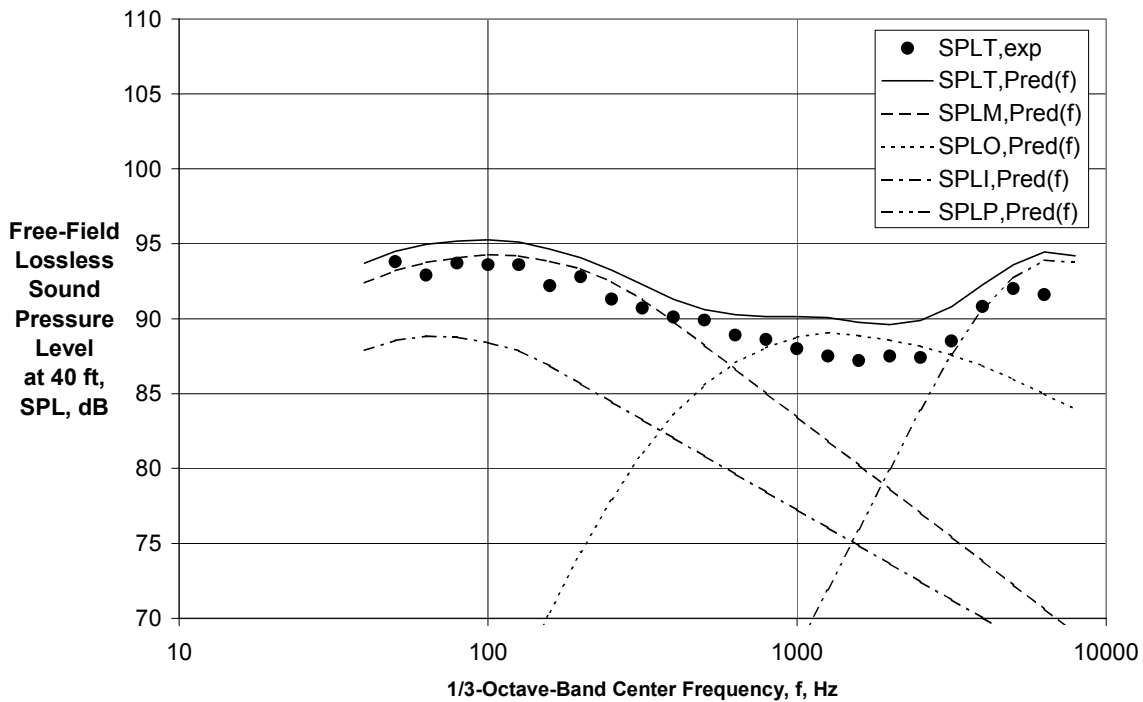
(b) Directivity Angle = 90 deg

Figure 26 - Comparison of Experimental and First Generation Predicted Spectra for V_{mix}/c_{amb} = 0.635, M_f = 0.0 (A_O/A_I = 2.75, Ref. 24, Rdg. 378)
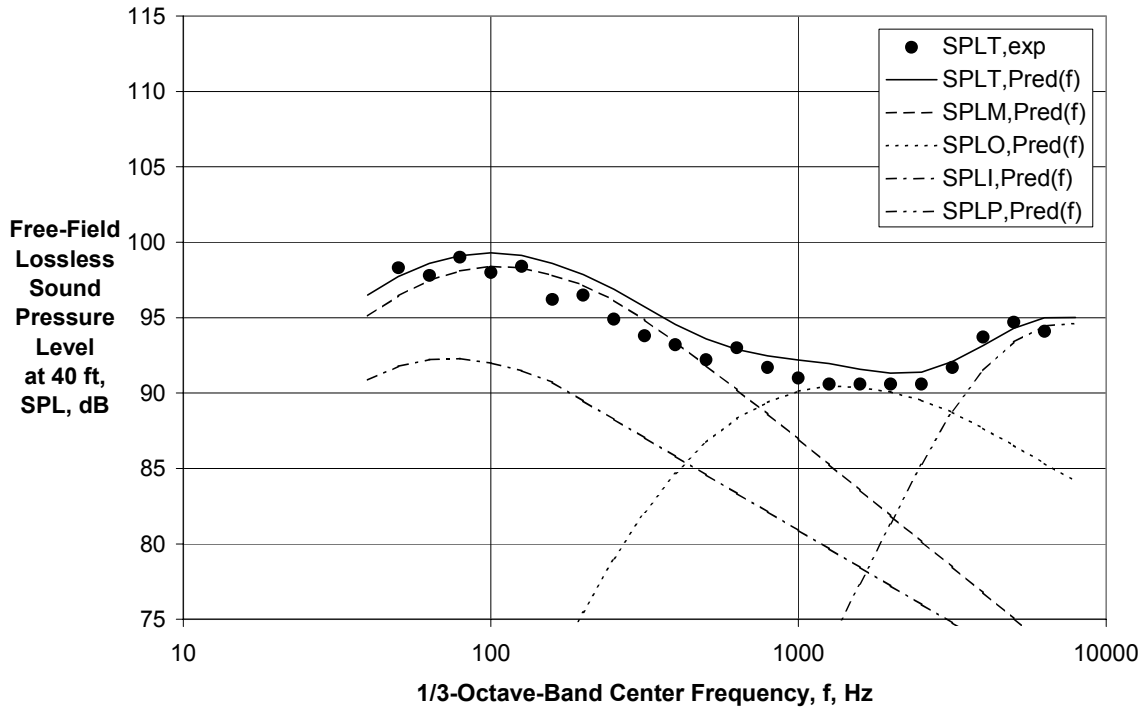
(c) Directivity Angle = 120 deg
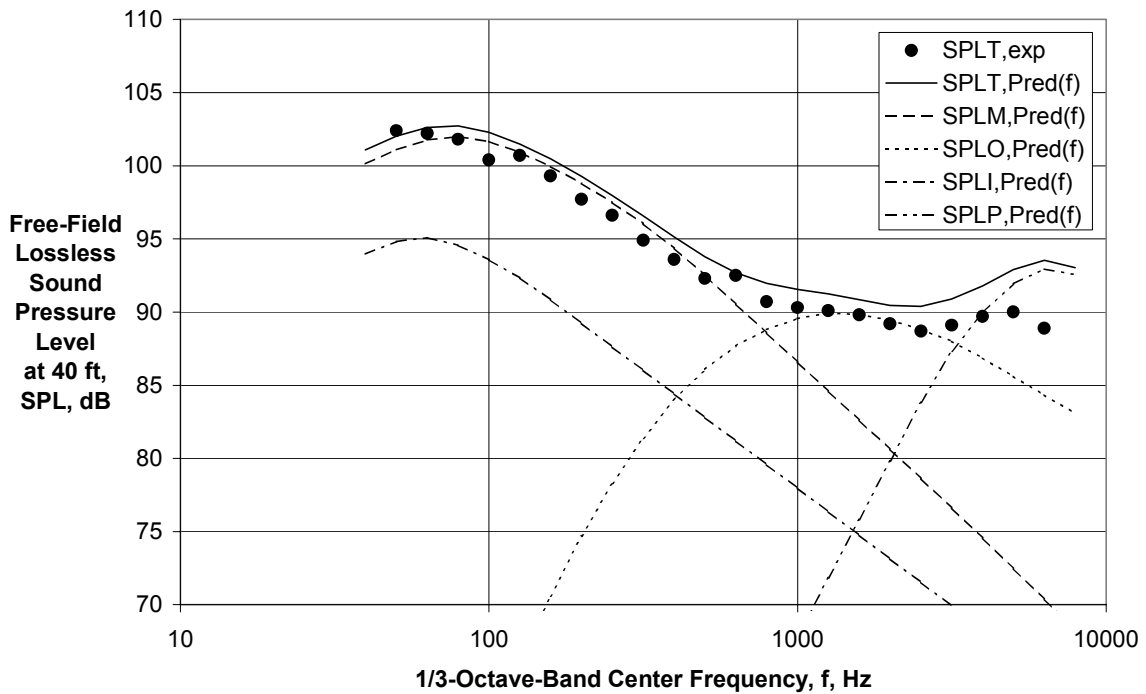
(d) Directivity Angle = 135 deg

Figure 26 (Continued) - Comparison of Experimental and First Generation Predicted Spectra for V_{mix}/c_{amb} = 0.635, M_f = 0.0 (A_O/A_I = 2.75, Ref. 24, Rdg. 378)
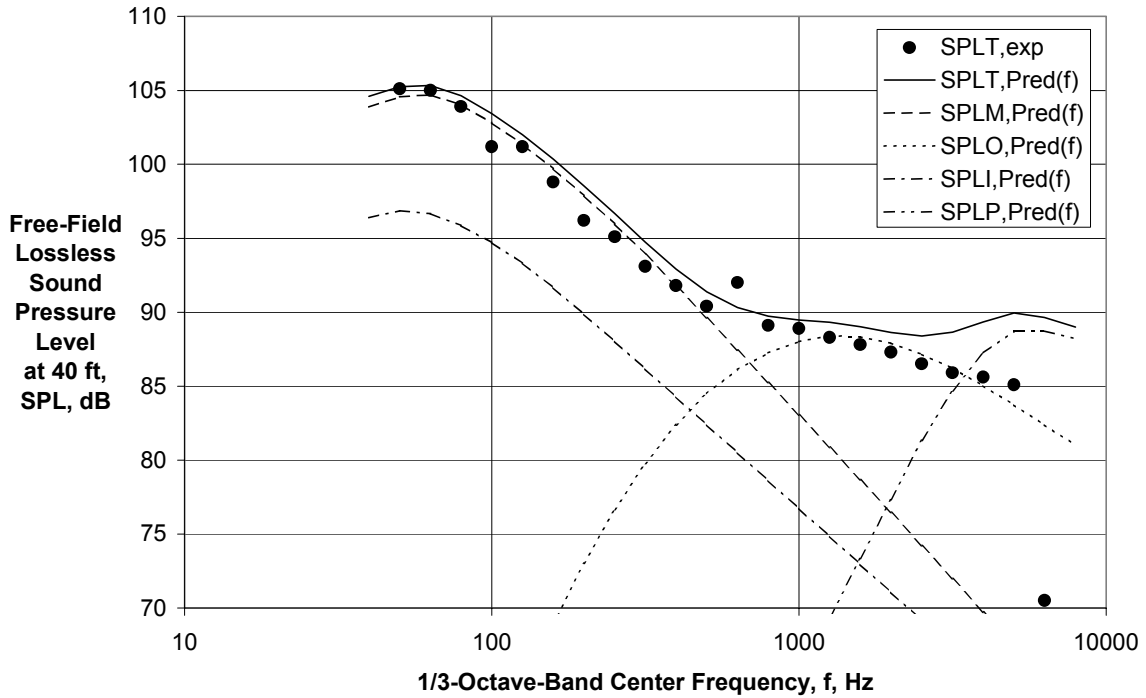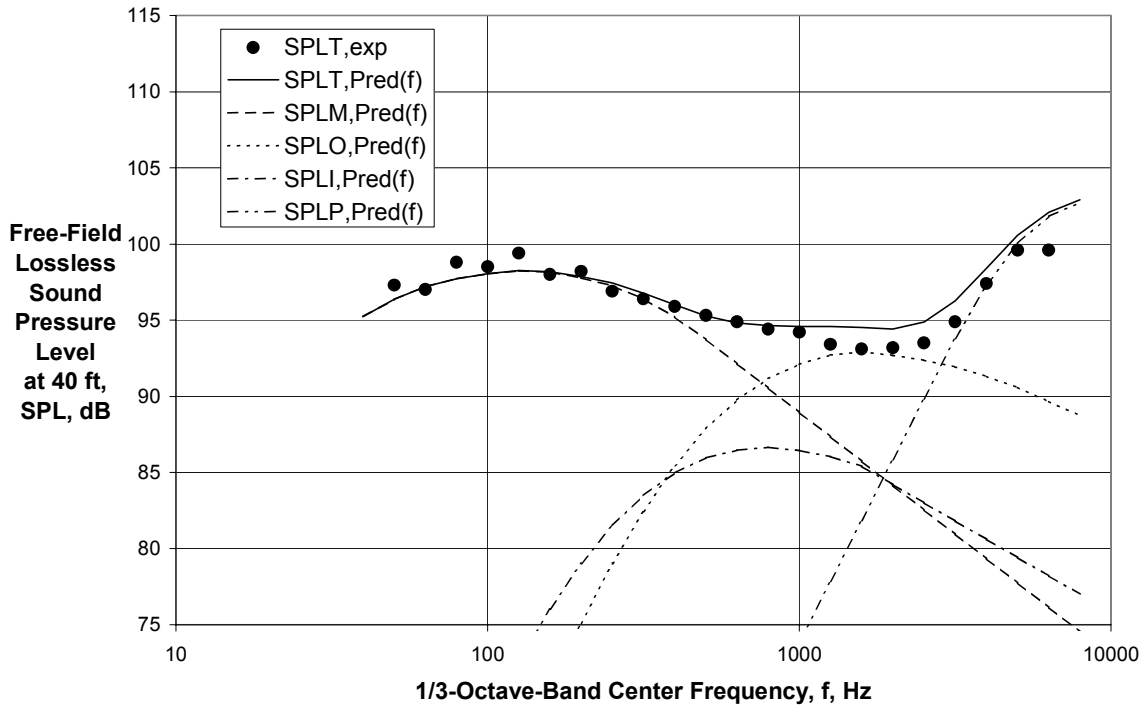
(e) Directivity Angle = 145 deg
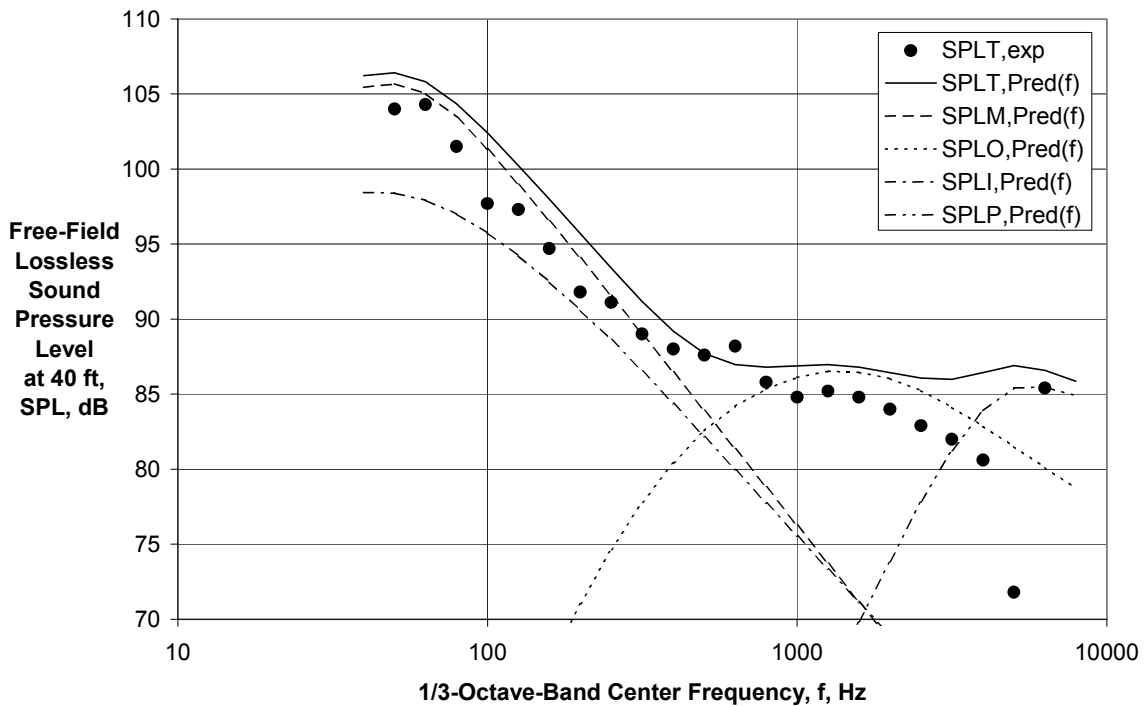
(f) Directivity Angle = 155 deg

Figure 26 (Concluded) - Comparison of Experimental and First Generation Predicted Spectra for V_{mix}/c_{amb} = 0.635, M_f = 0.0 (A_O/A_I = 2.75, Ref. 24, Rdg. 378)
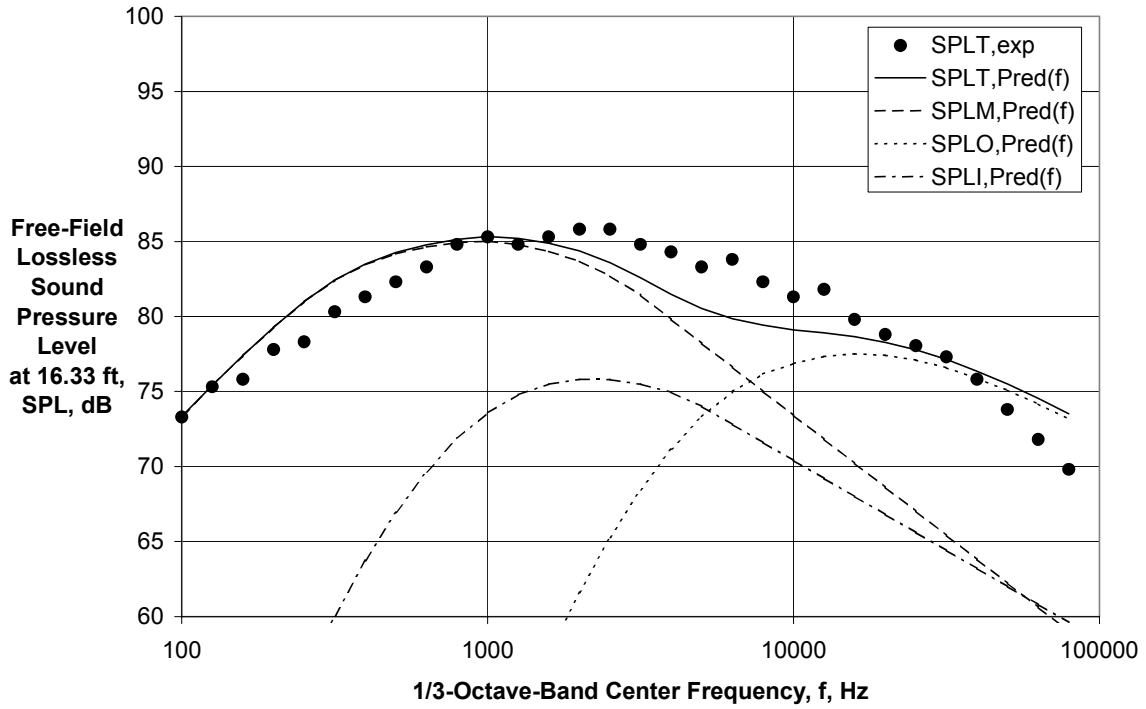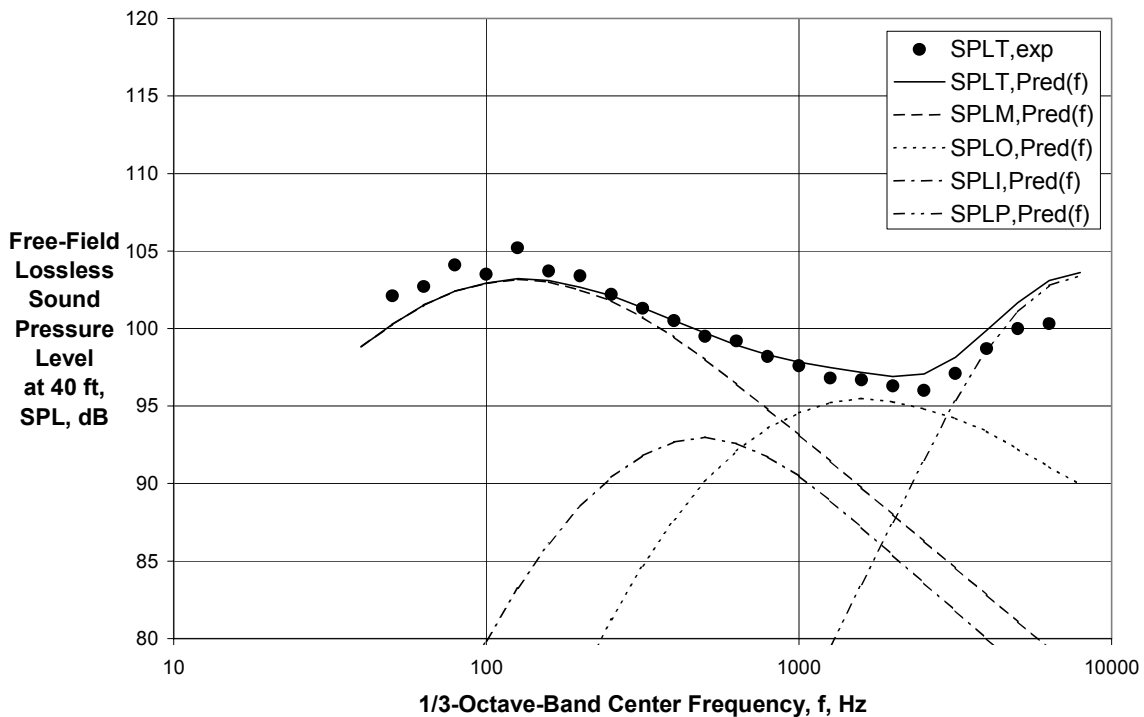
(a) Directivity Angle = 46 deg
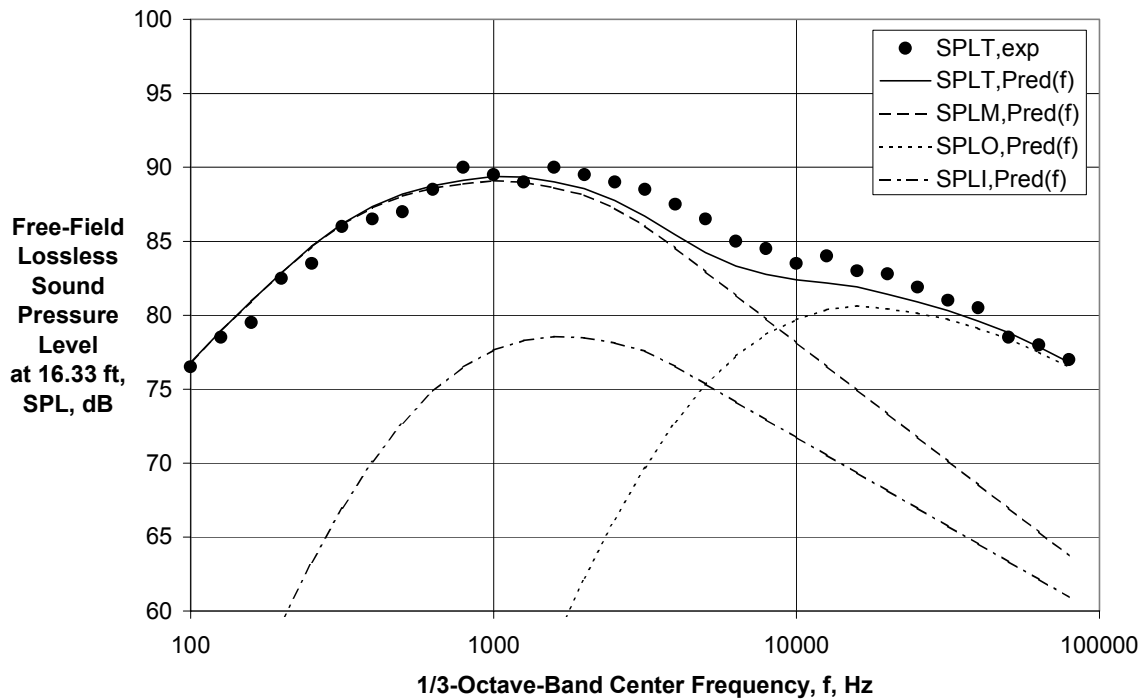
(b) Directivity Angle = 95 deg

Figure 27 - Comparison of Experimental and First Generation Predicted Spectra for V_{mix}/c_{amb} = 0.725, M_f = 0.0 (A_O/A_I = 1.94, Ref. 25, Rdg. 07)
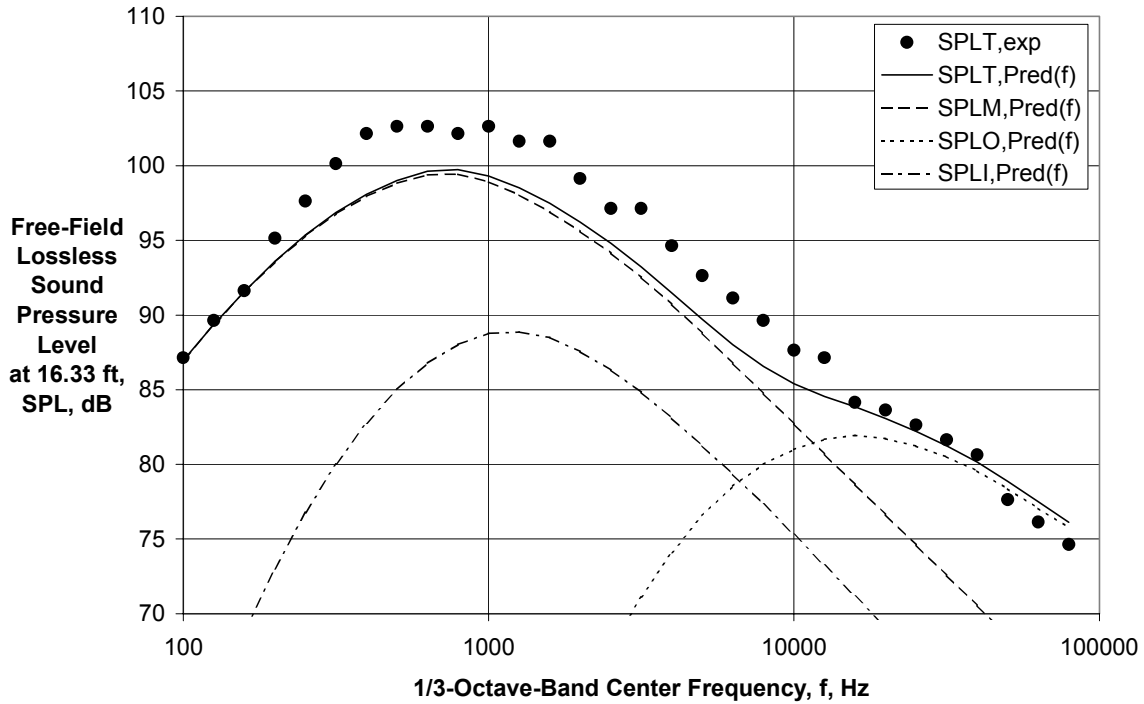
(c) Directivity Angle = 139 deg

Figure 27 (Concluded) - Comparison of Experimental and First Gen. Pred. Spectra for V_{mix}/c_{amb} = 0.725, M_f = 0.0 (A_O/A_I = 1.94, Ref. 25, Rdg. 07)
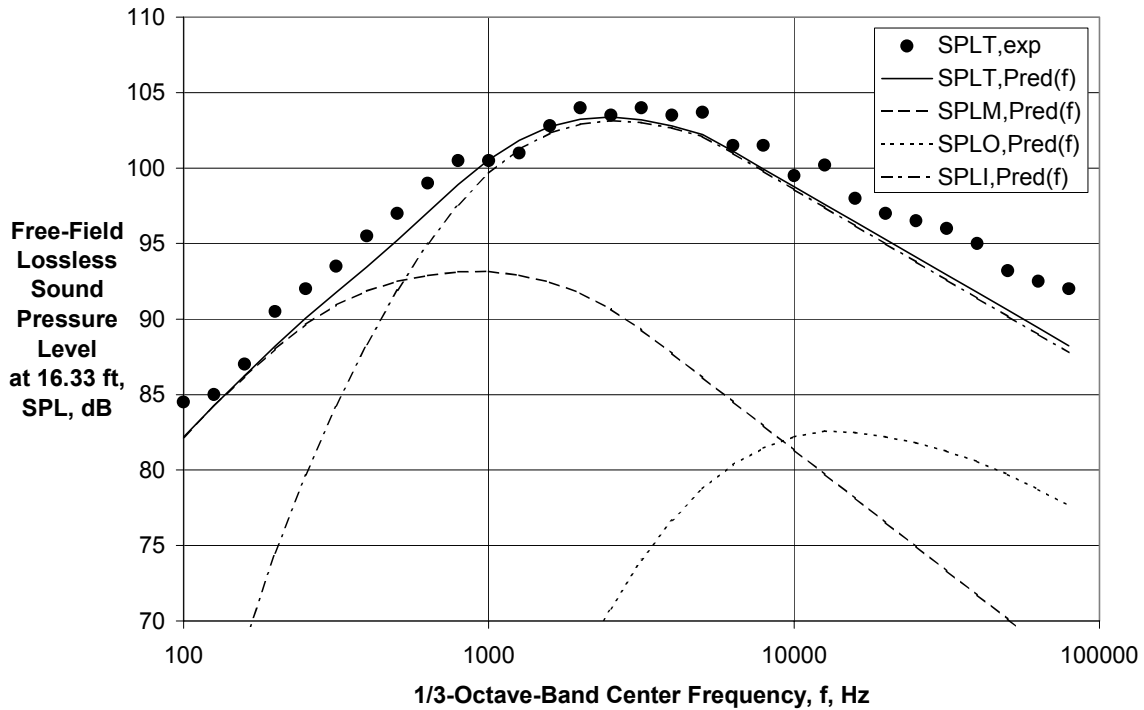
(a) Directivity Angle = 95 deg

Figure 28 - Comparison of Experimental and First Generation Predicted Spectra for V_{mix}/c_{amb} = 0.839, M_f = 0.0 (A_O/A_I = 3.27, Ref. 25, Rdg. 06)
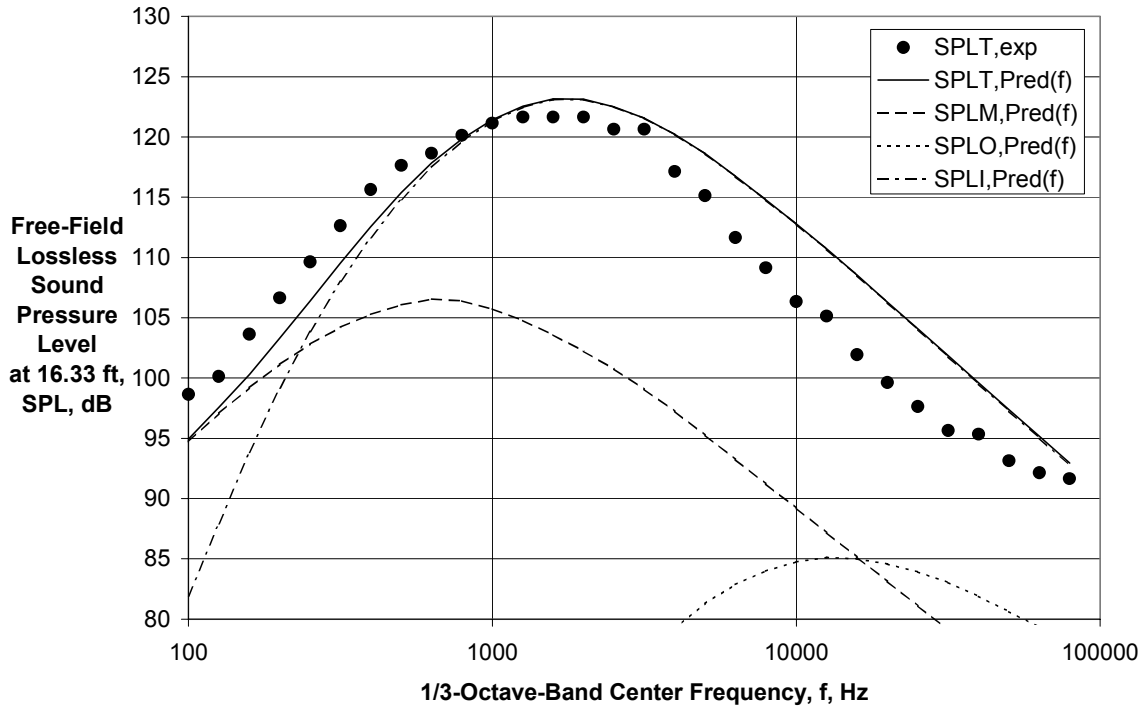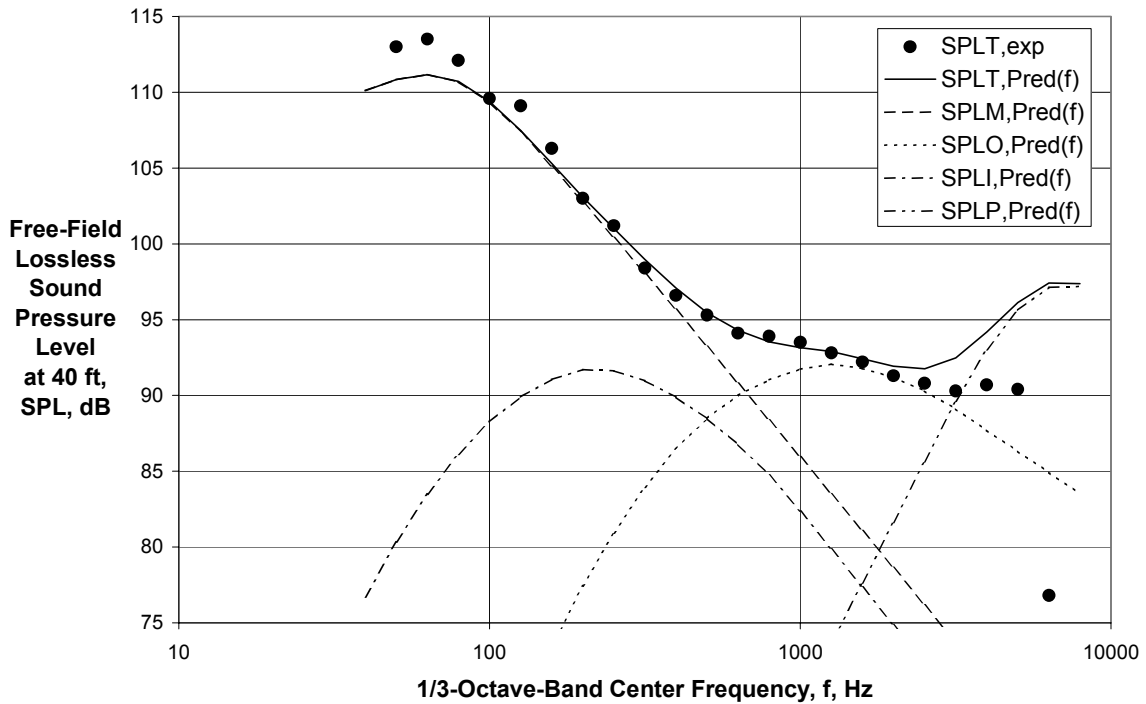
(b) Directivity Angle = 139 deg

Figure 28 (Concluded) - Comparison of Experimental and First Gen. Pred. Spectra for $V_{mix}/c_{amb} = 0.839$, $M_f = 0.0$ ($A_O/A_I = 3.27$, Ref. 25, Rdg. 06)
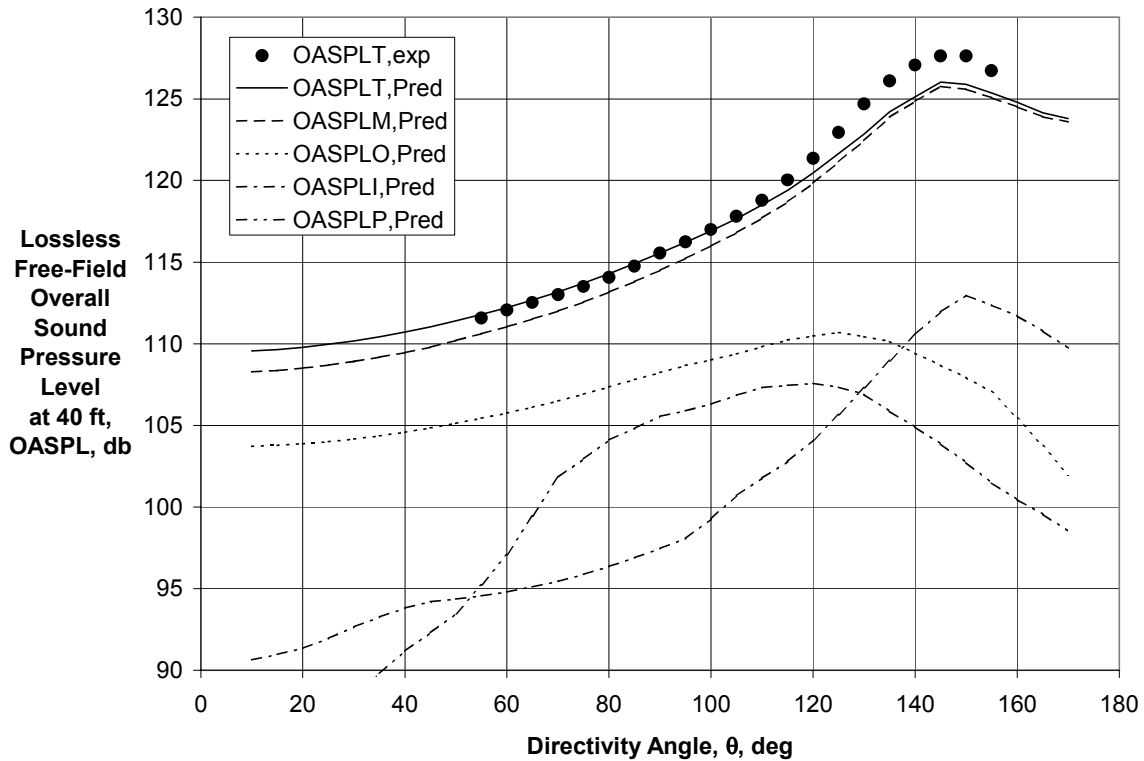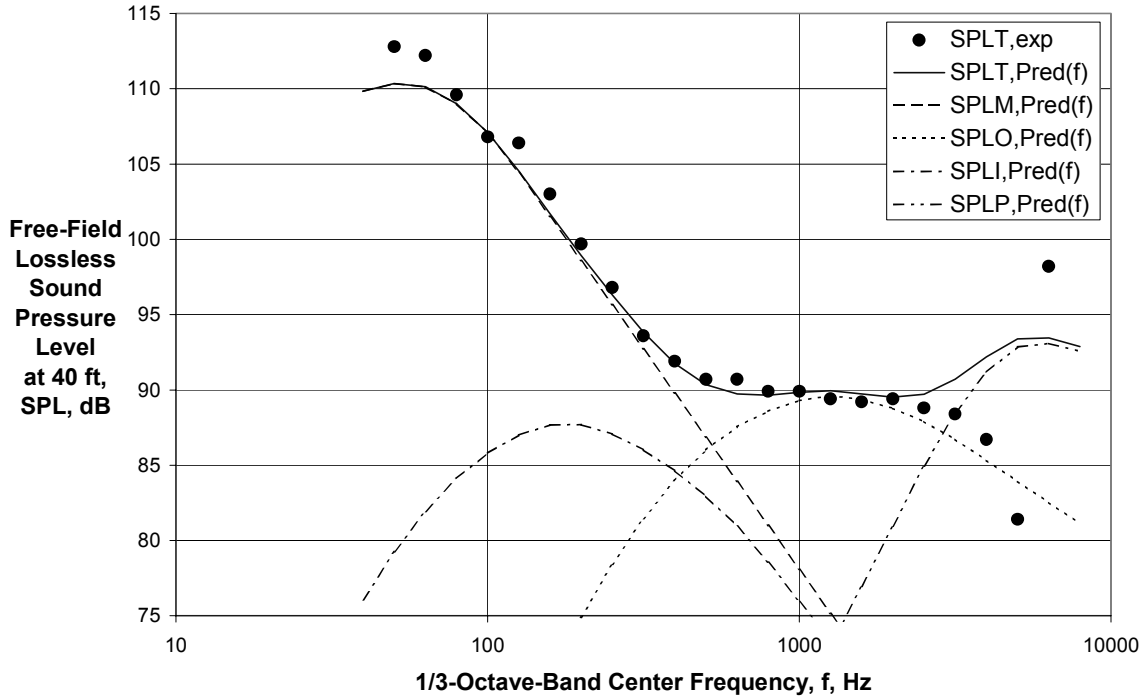

Figure 29 - Comparison of Experimental and First Generation Predicted Directivities for $V_{mix}/c_{amb} = 0.870$, $M_f = 0.0$ ($A_O/A_I = 3.74$, Ref. 24, Rdg. 1015)
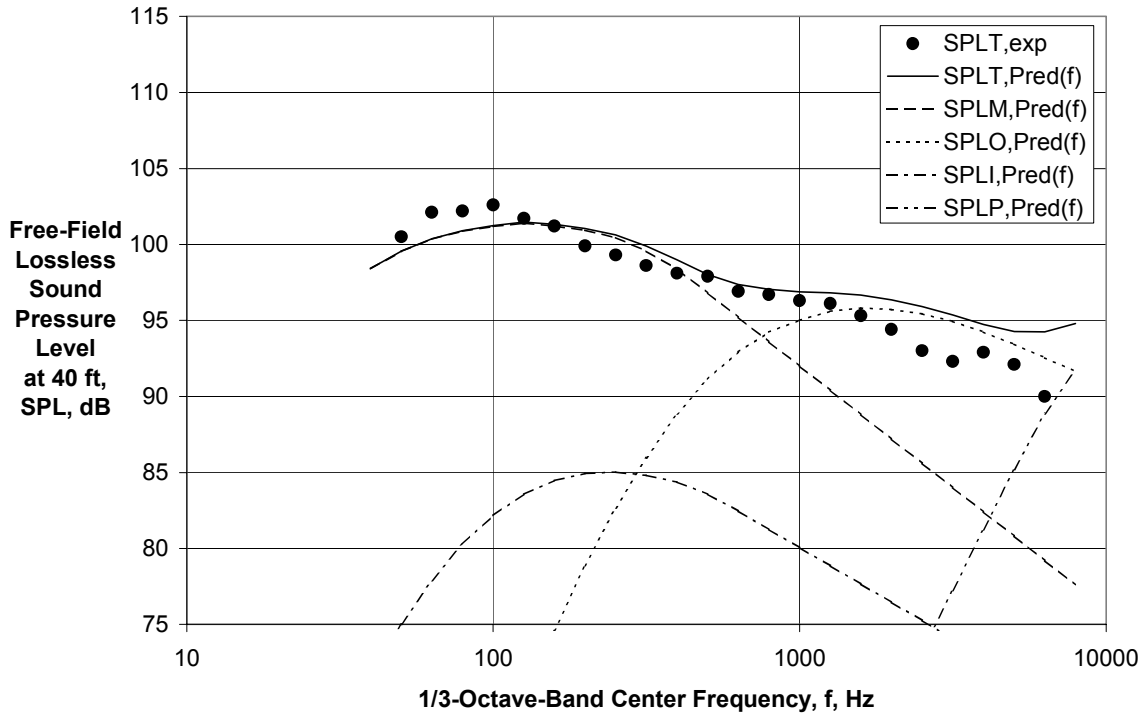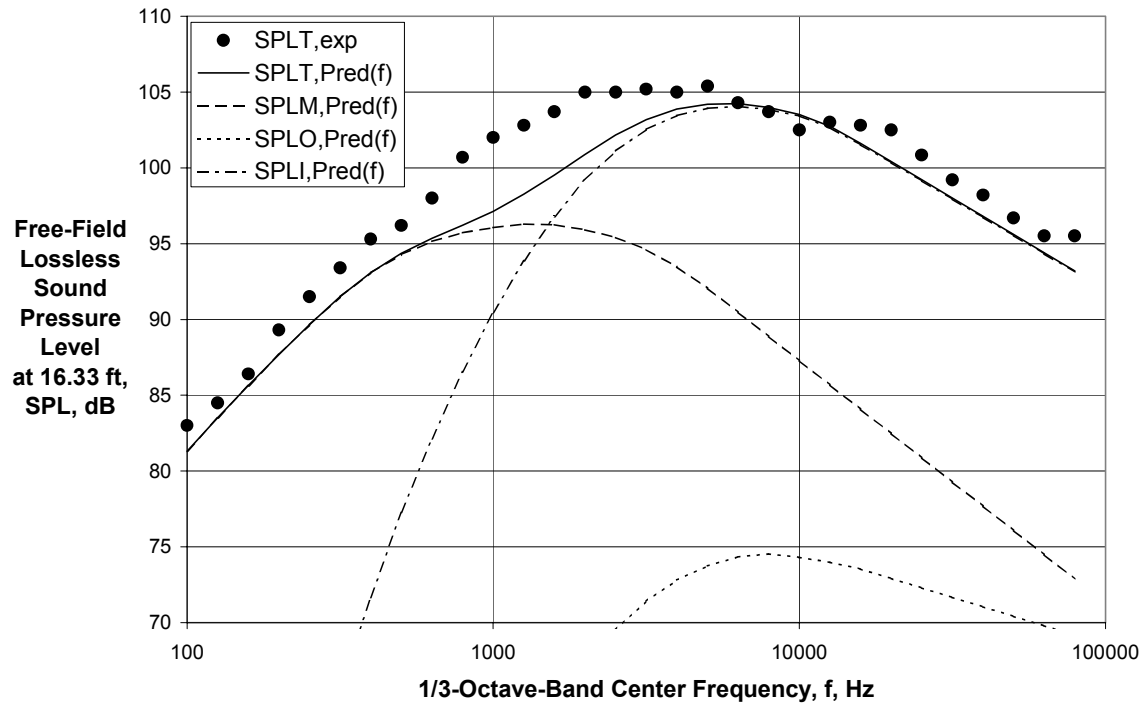
(a) Directivity Angle = 60 deg
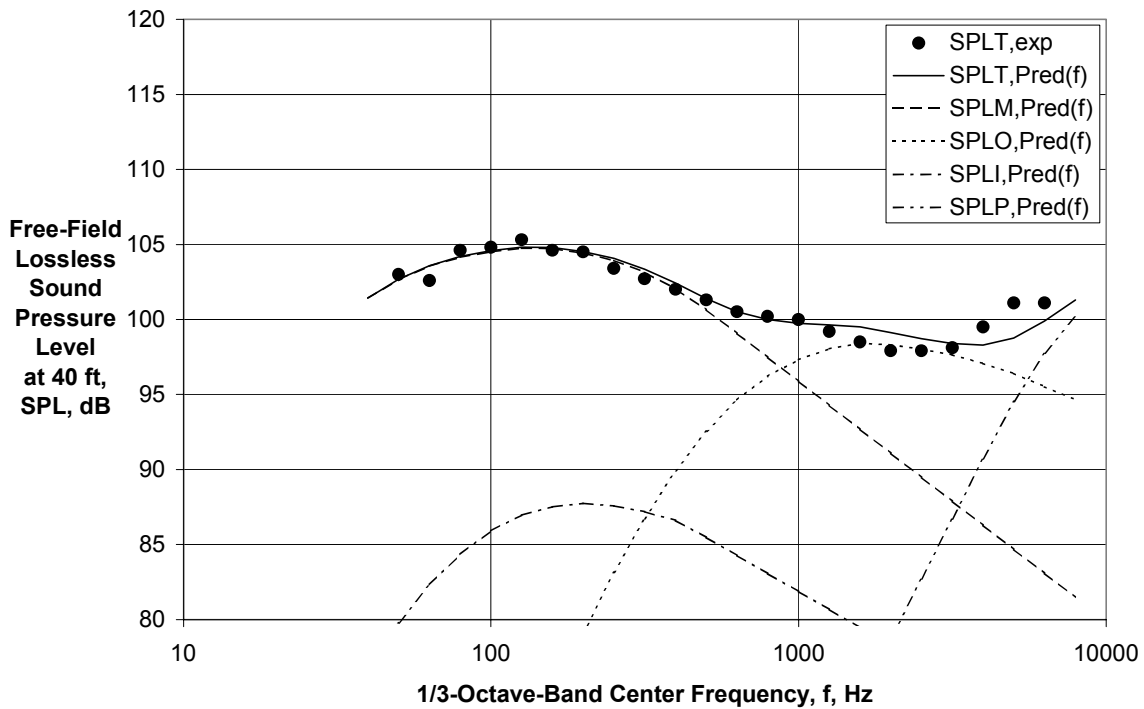
(b) Directivity Angle = 90 deg

Figure 30 - Comparison of Experimental and First Generation Predicted Spectra for V_{mix}/c_{amb} = 0.870, M_f = 0.0 (A_O/A_I = 3.74, Ref. 24, Rdg. 1015)
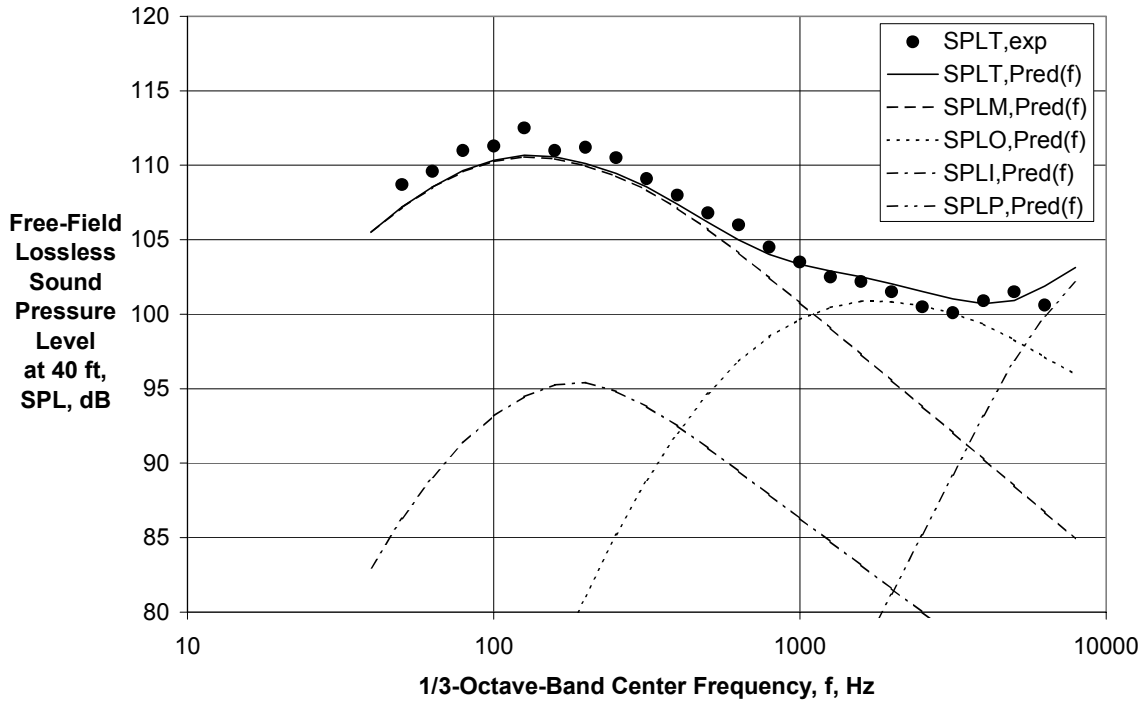
(c) Directivity Angle = 120 deg
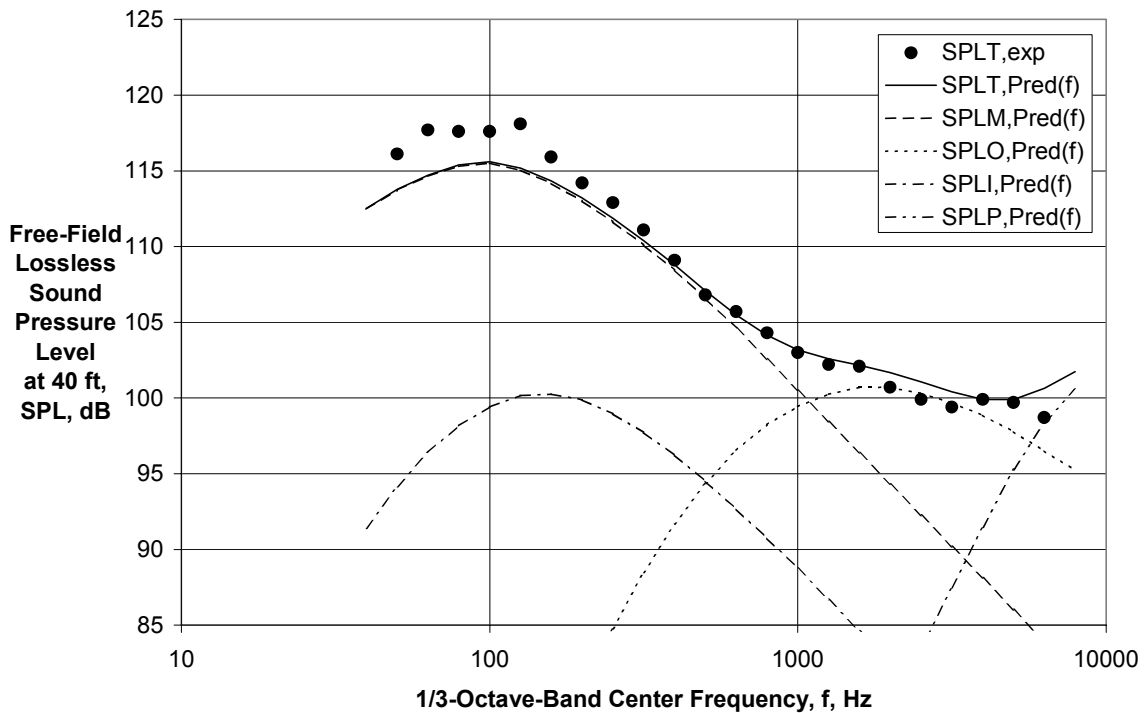
(d) Directivity Angle = 135 deg

Figure 30 (Continued) - Comparison of Experimental and First Generation Predicted Spectra for V_{mix}/c_{amb} = 0.870, M_f = 0.0 (A_O/A_I = 3.74, Ref. 24, Rdg. 1015)
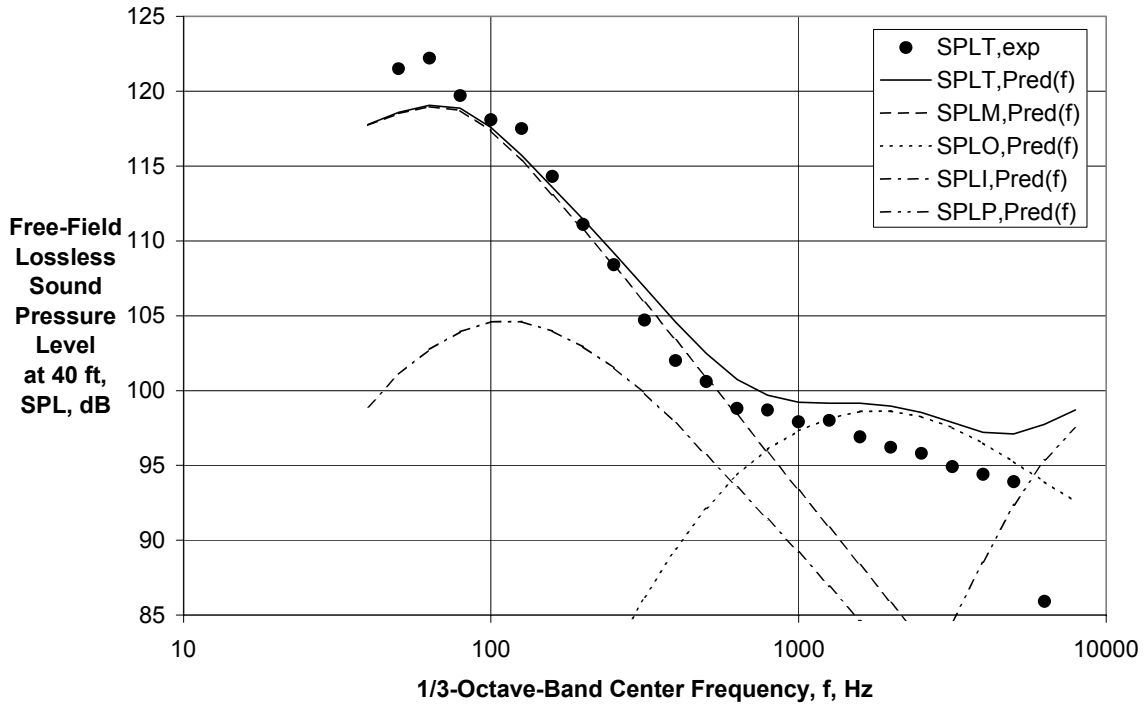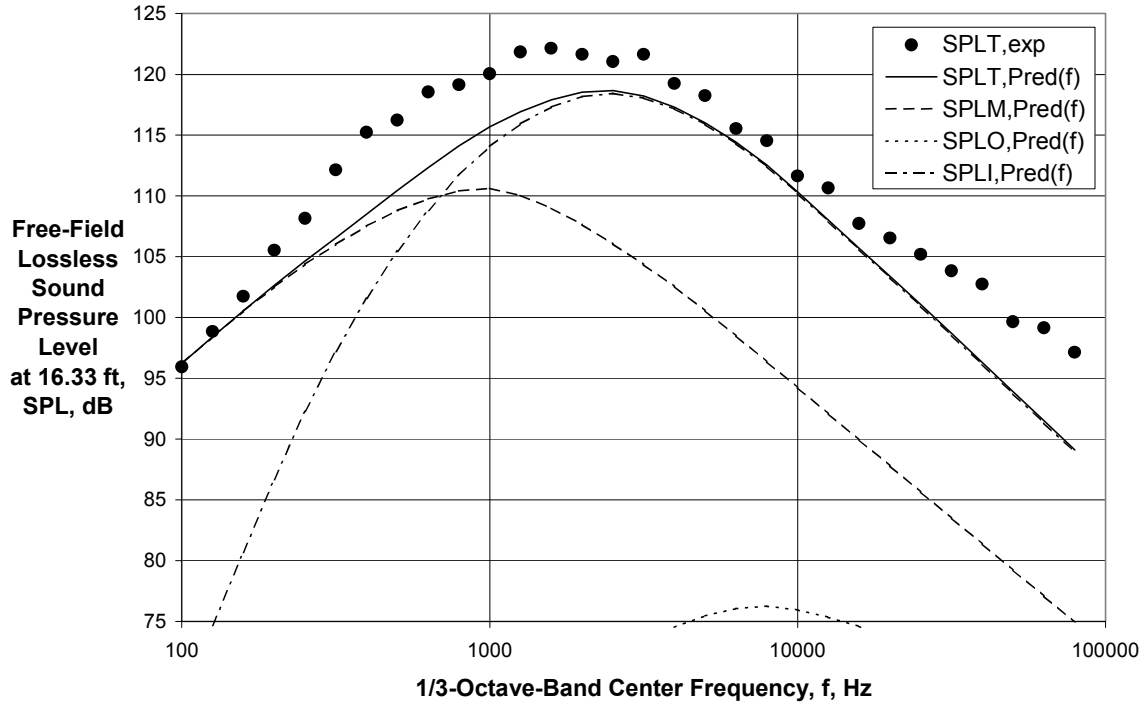
(e) Directivity Angle = 150 deg
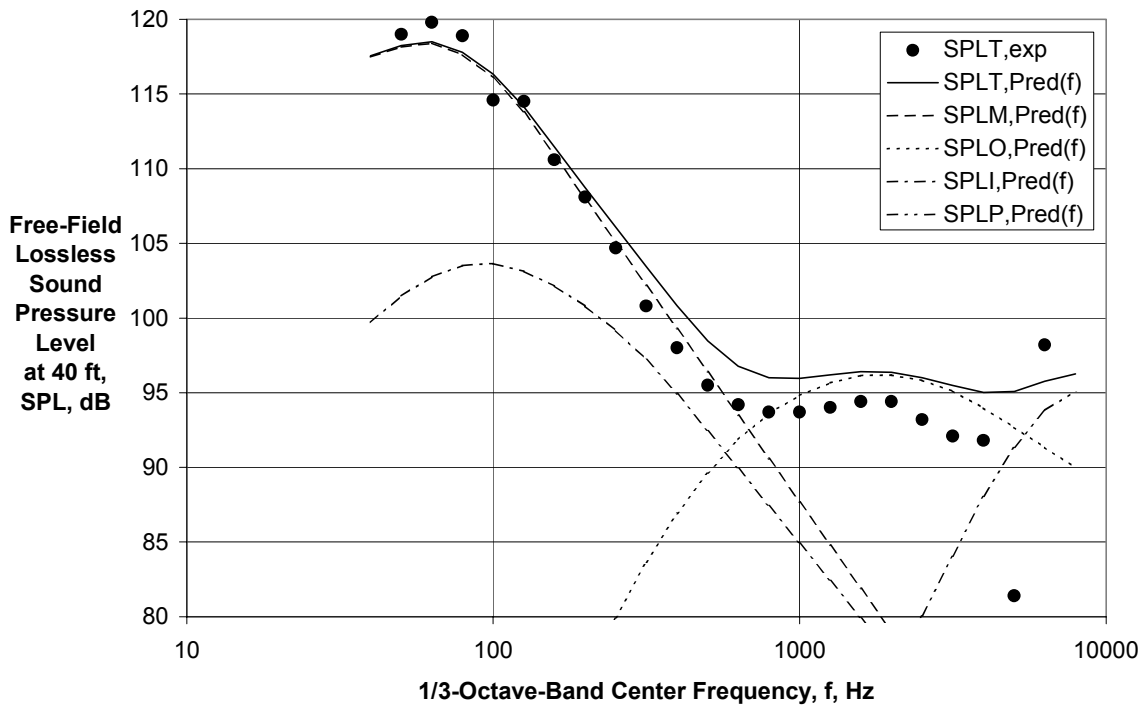
(f) Directivity Angle = 160 deg

Figure 30 (Concluded) - Comparison of Experimental and First Generation Predicted Spectra for V_{mix}/c_{amb} = 0.870, M_f = 0.0 (A_O/A_I = 3.74, Ref. 24, Rdg. 1015)
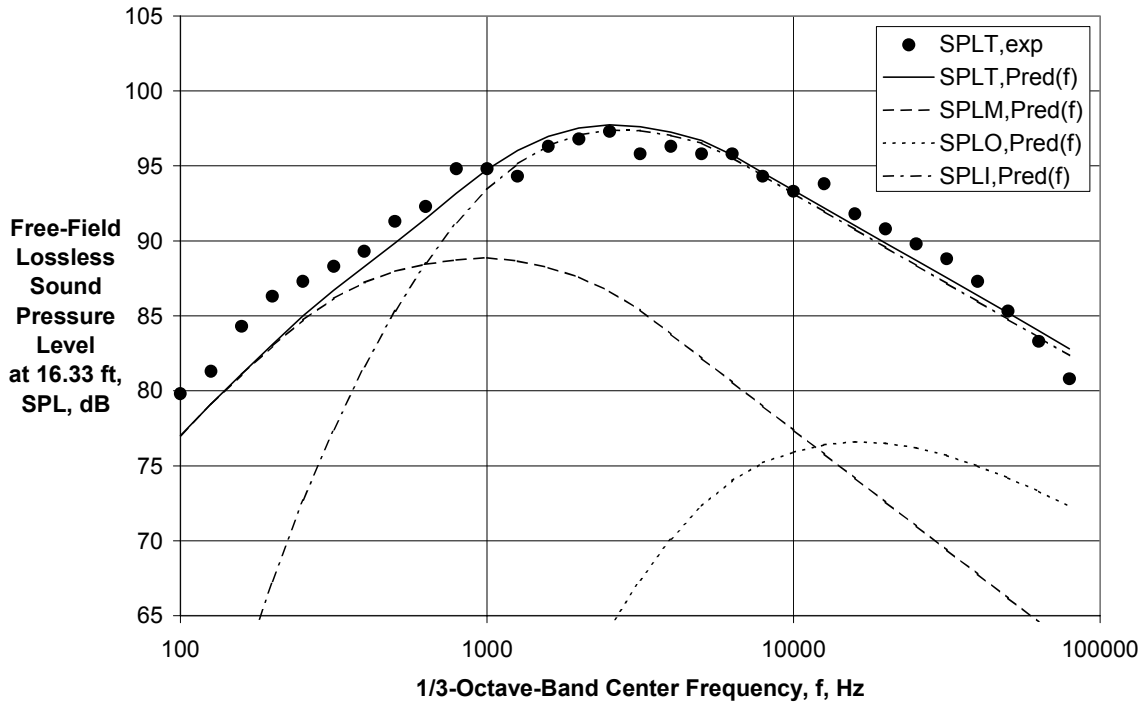
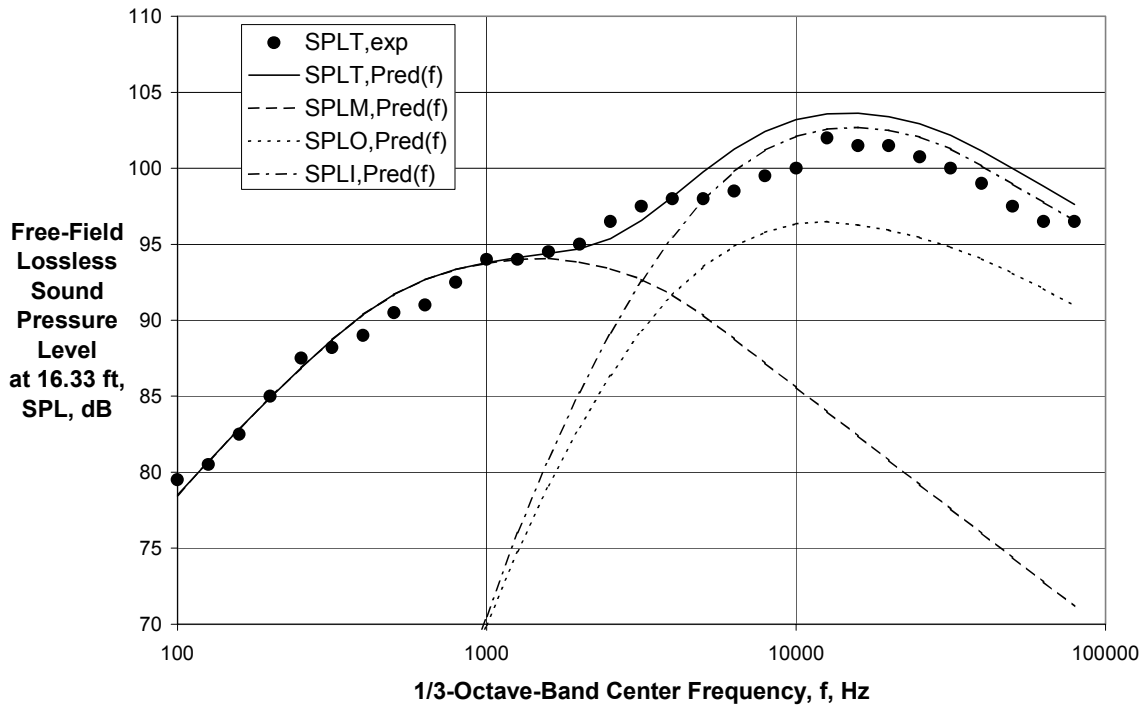**(a) Directivity Angle = 46 deg**
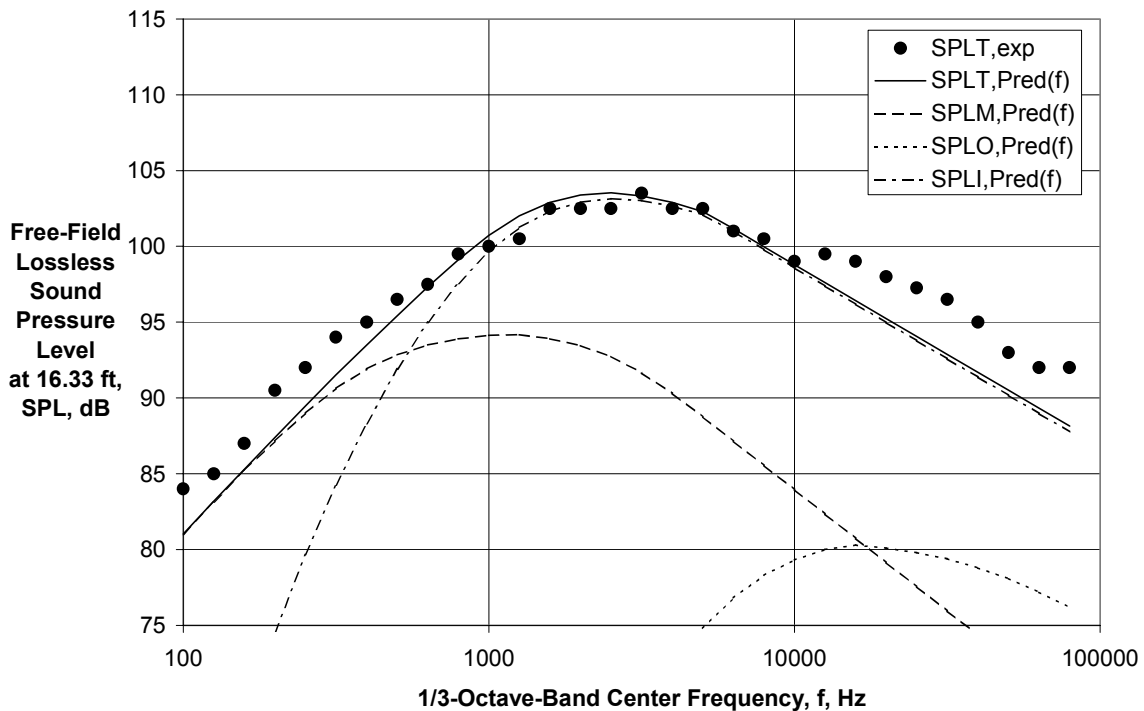
(b) Directivity Angle = 95 deg

Figure 31 - Comparison of Experimental and First Generation Predicted Spectra for V_{mix}/c_{amb} = 0.938, M_f = 0.0 (A_O/A_I = 1.94, Ref. 25, Rdg. 05)
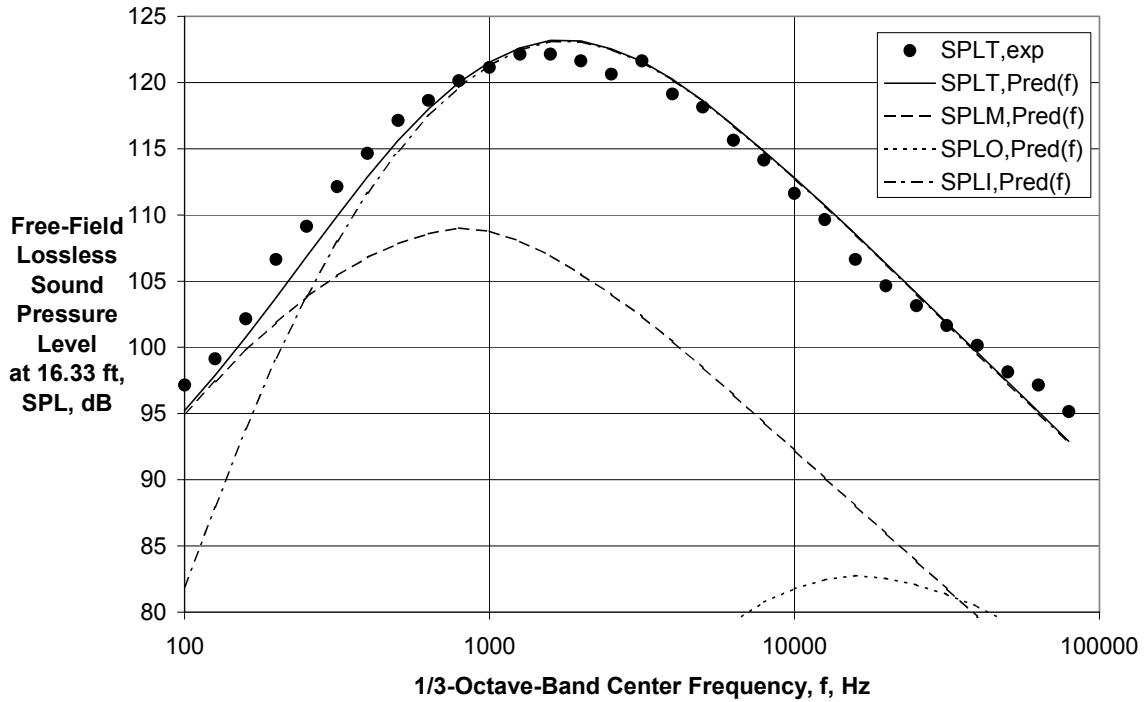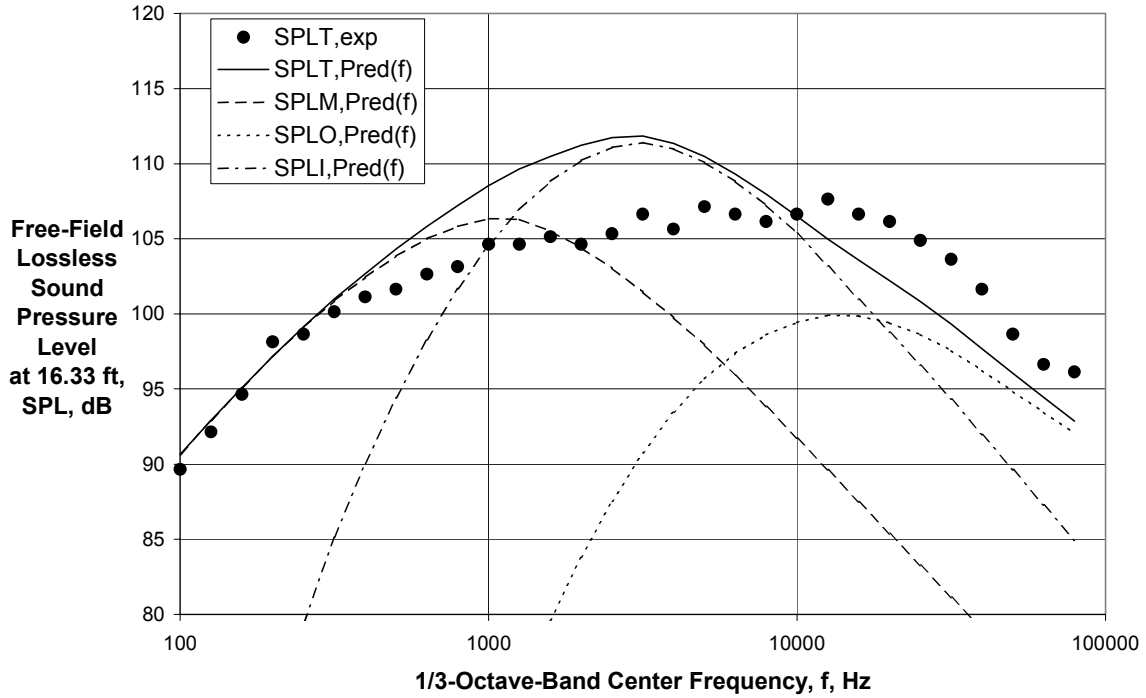
(c) Directivity Angle = 139 deg

Figure 31 (Concluded) - Comparison of Experimental and First Gen. Pred. Spectra for V_{mix}/c_{amb} = 0.938, M_f = 0.0 (A_O/A_I = 1.94, Ref. 25, Rdg. 05)
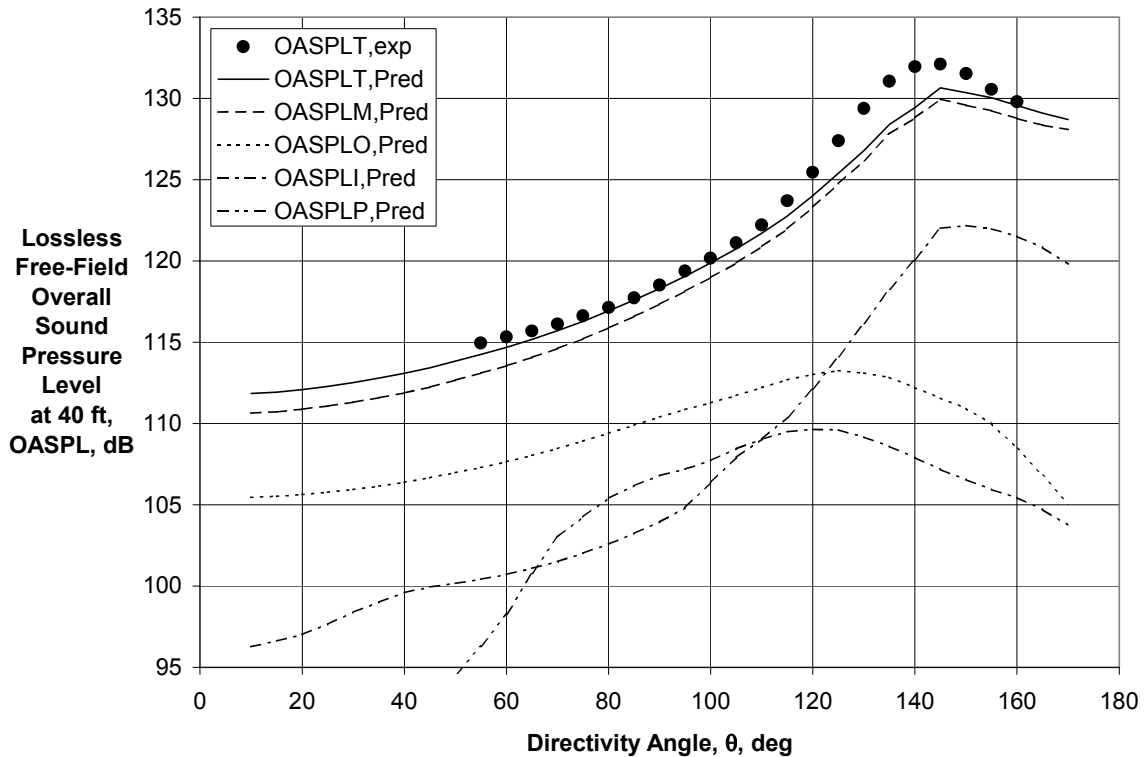
Figure 32 - Comparison of Experimental and First Generation Predicted Directivities for V_{mix}/c_{amb} = 0.949, M_f = 0.0 (A_O/A_I = 3.74, Ref. 24, Rdg. 1017)

(a) Directivity Angle = 60 deg

(b) Directivity Angle = 90 deg
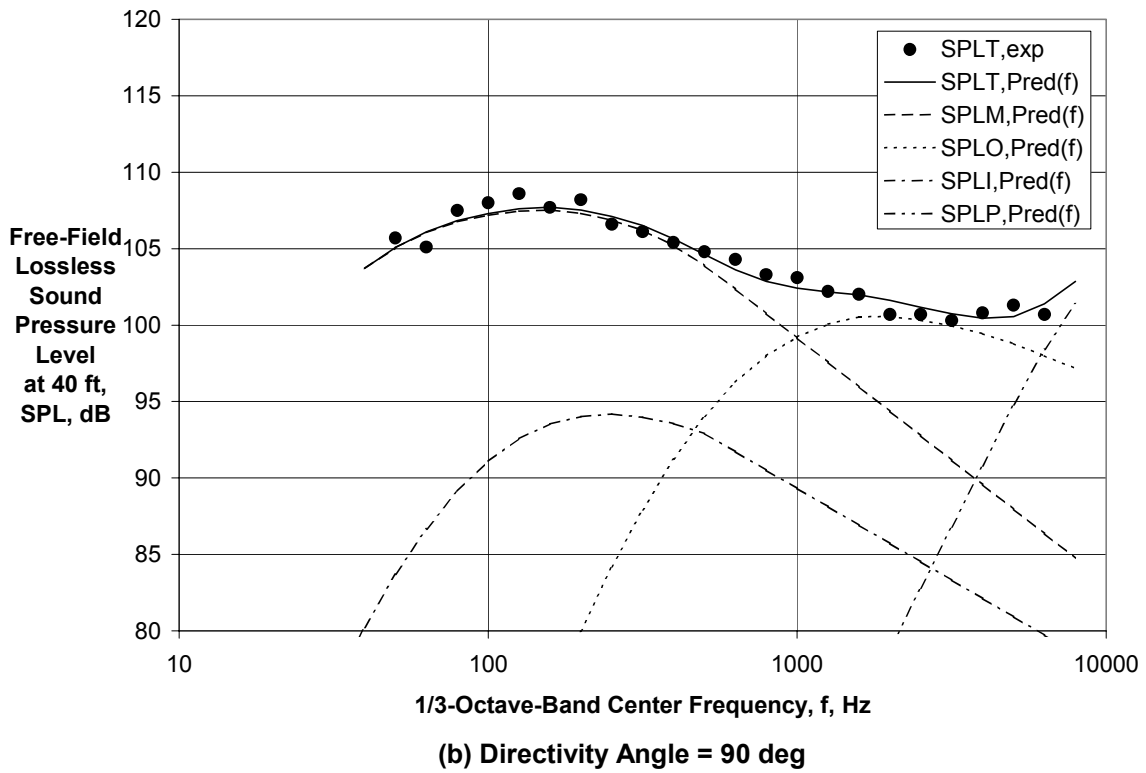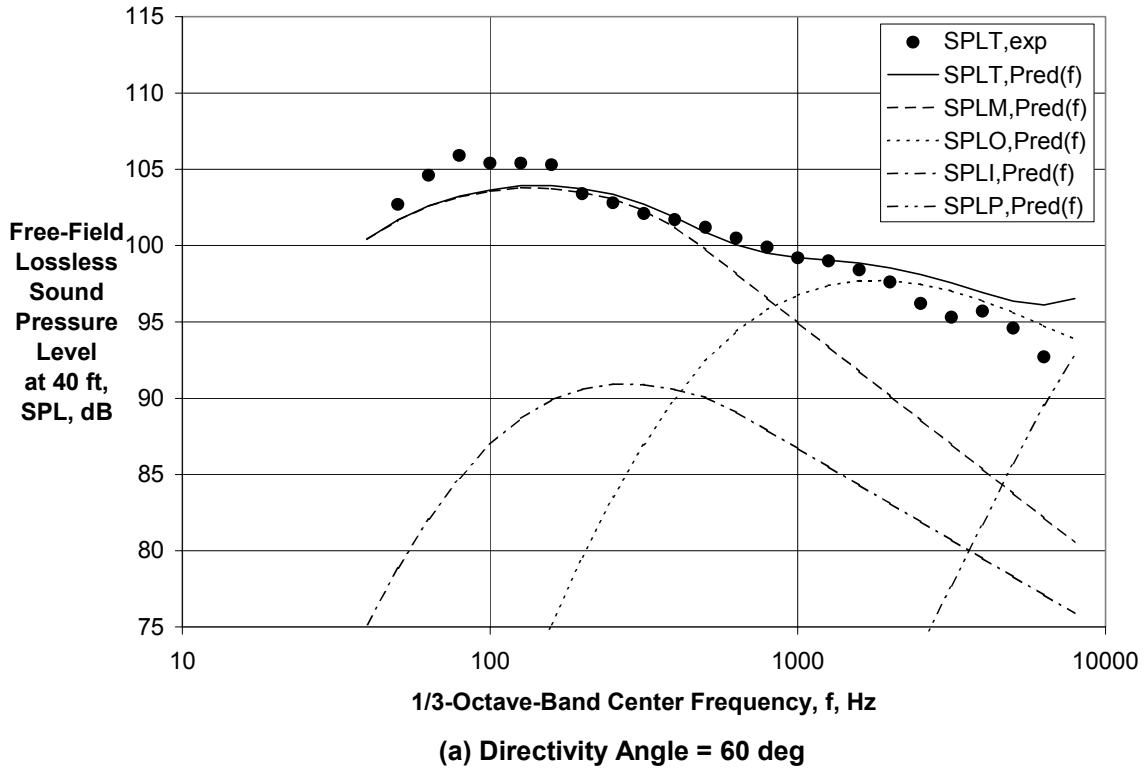
Figure 33 - Comparison of Experimental and First Generation Predicted Spectra for V_{mix}/c_{amb} = 0.949, M_f = 0.0 (A_O/A_I = 3.74, Ref. 24, Rdg. 1017)
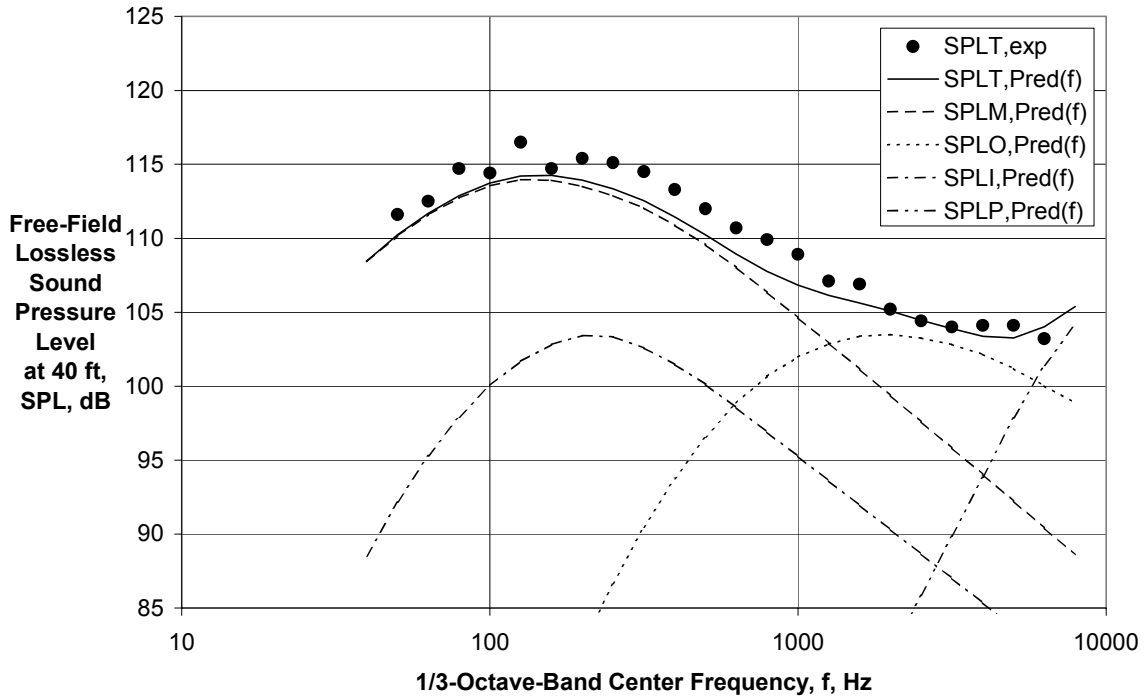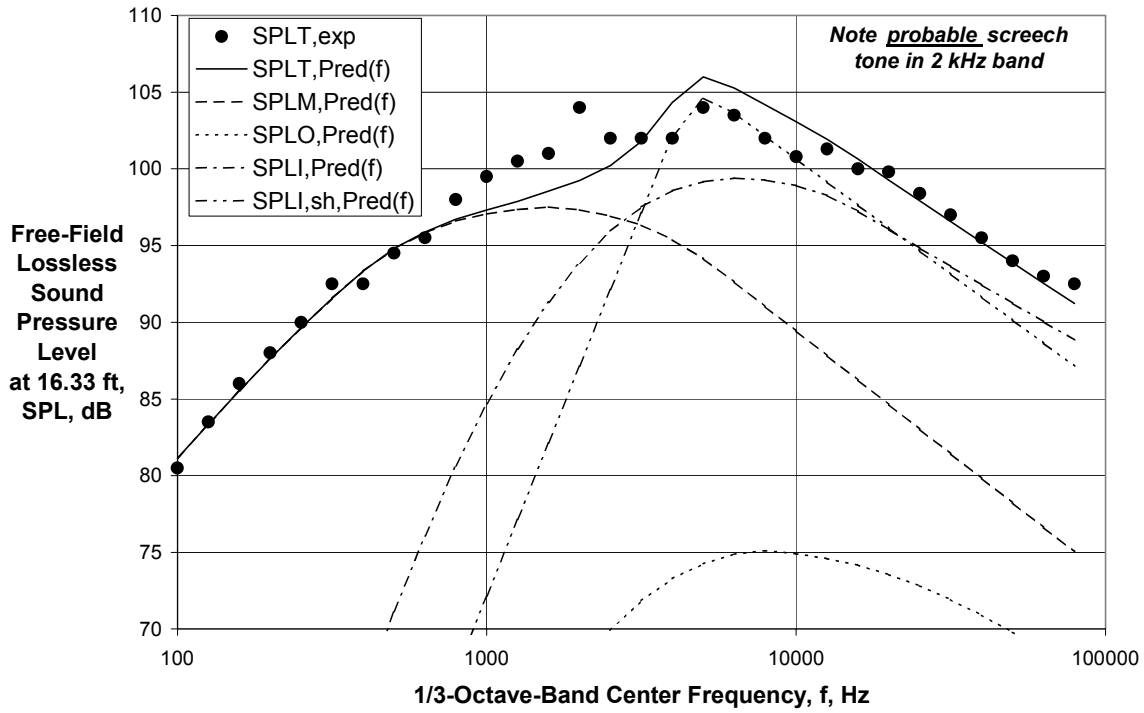
(c) Directivity Angle = 120 deg
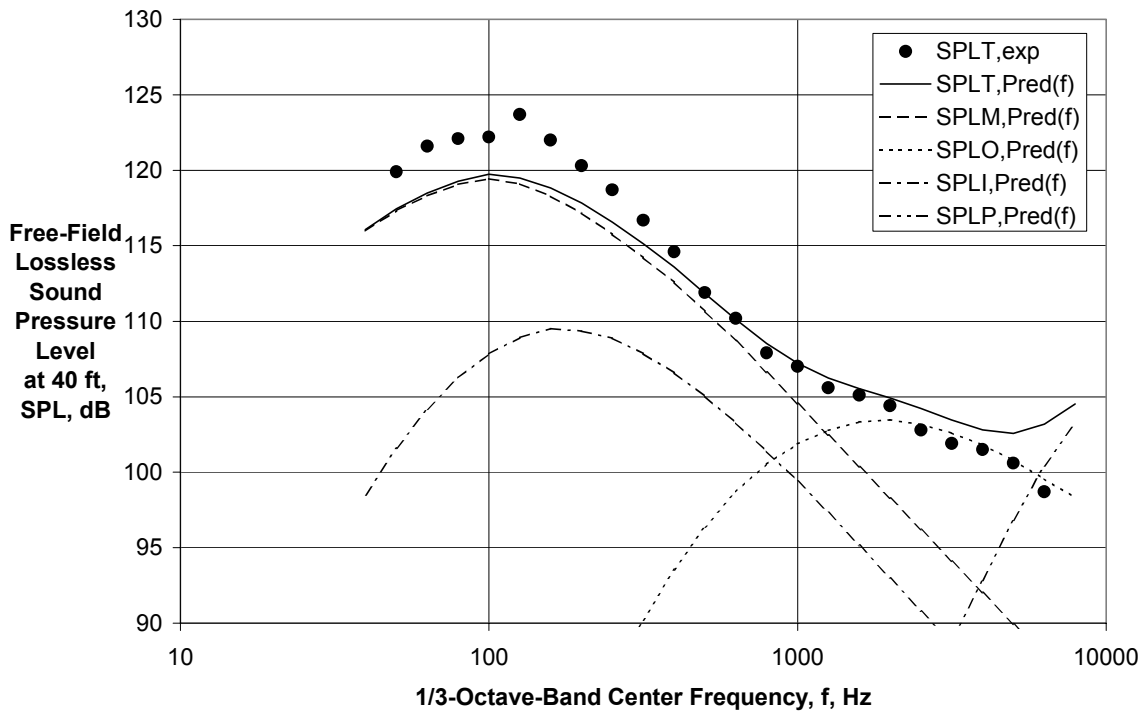
(d) Directivity Angle = 135 deg

Figure 33 (Continued) - Comparison of Experimental and First Generation Predicted Spectra for V_{mix}/c_{amb} = 0.949, M_f = 0.0 (A_O/A_I = 3.74, Ref. 24, Rdg. 1017)
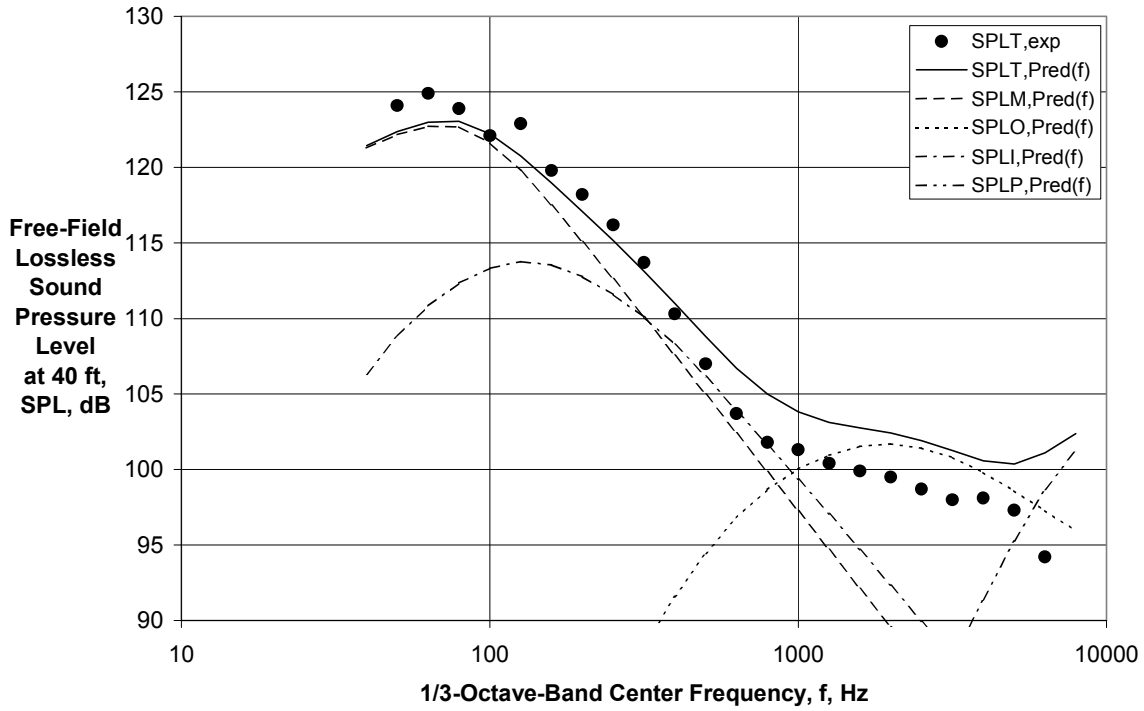
(e) Directivity Angle = 150 deg
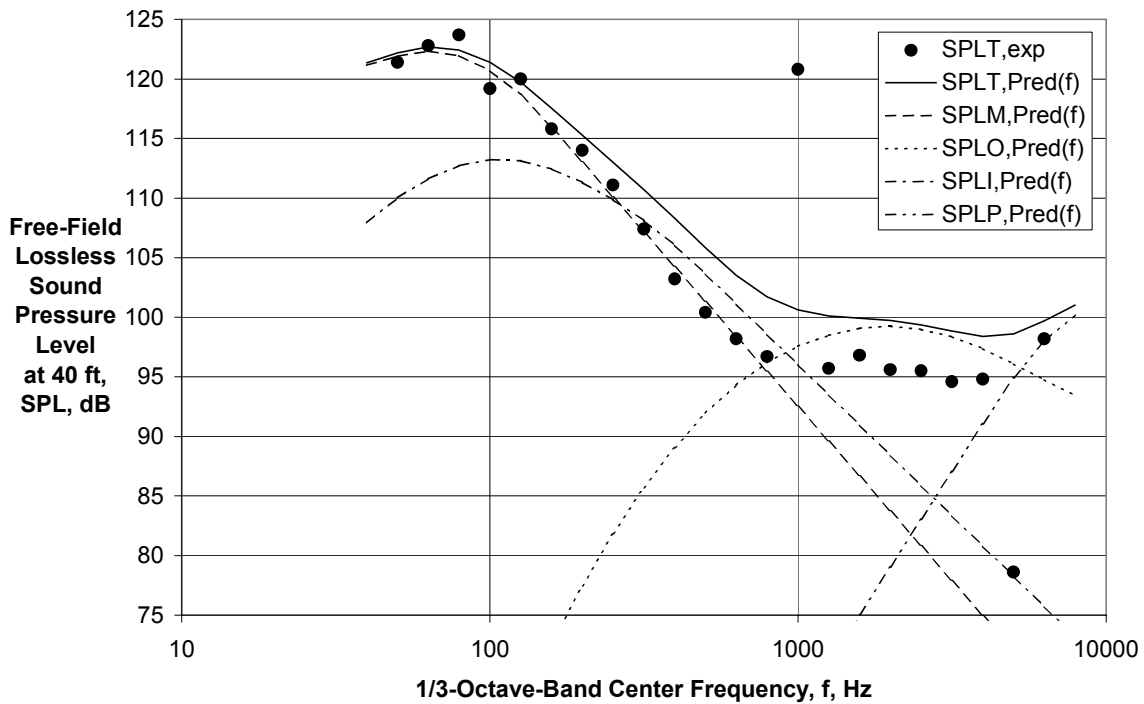
(f) Directivity Angle = 160 deg

Figure 33 (Concluded) - Comparison of Experimental and First Generation Predicted Spectra for V_{mix}/c_{amb} = 0.949, M_f = 0.0 (A_O/A_I = 3.74, Ref. 24, Rdg. 1017)
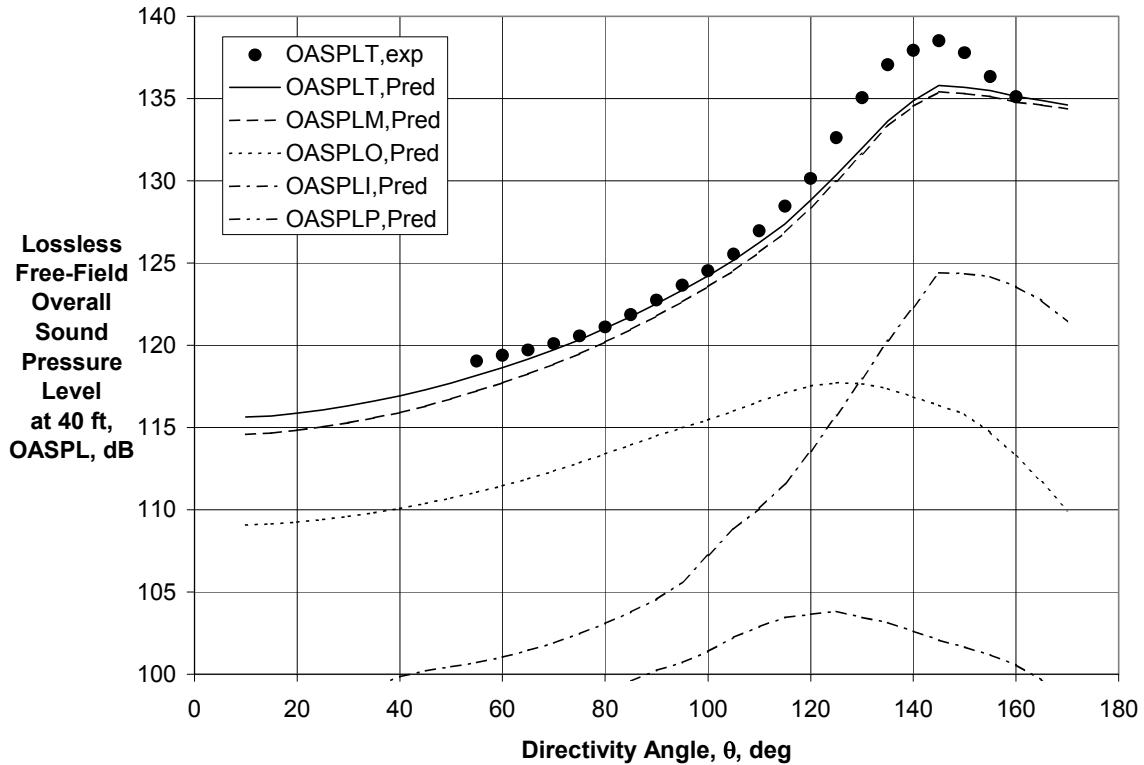
Figure 34 - Comparison of Experimental and First Generation Predicted Directivities for V_{mix}/c_{amb} = 1.09, M_f = 0.0 (A_O/A_I = 2.75, Ref. 24, Rdg. 383)
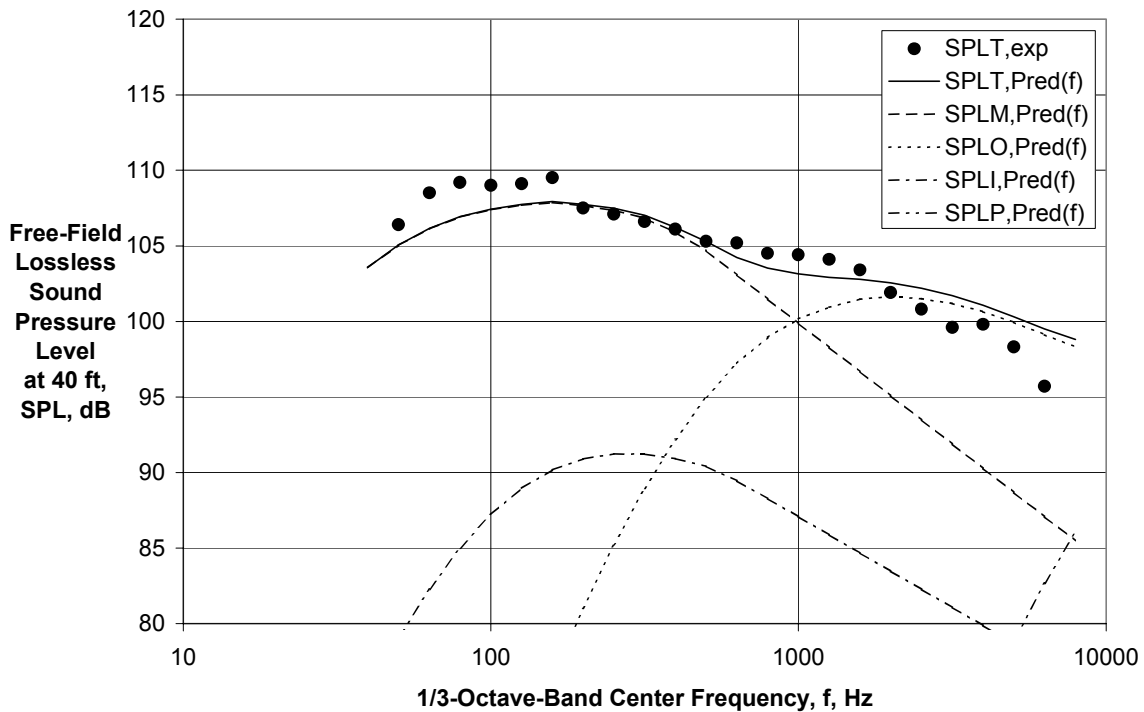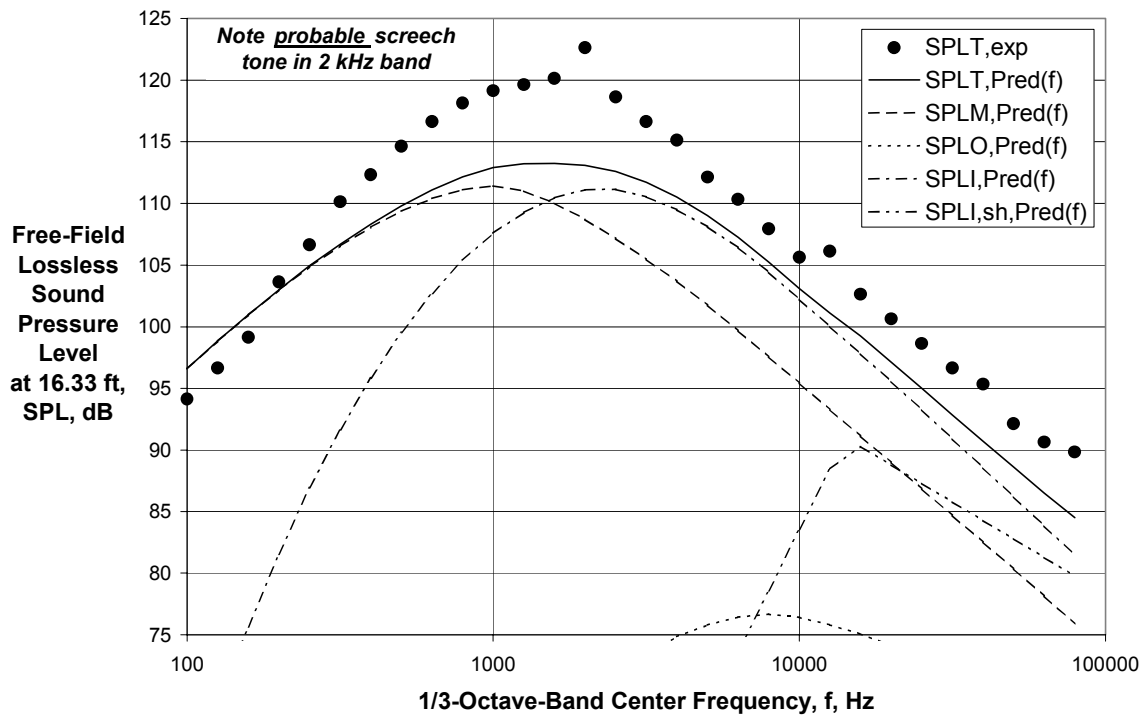

(a) Directivity Angle = 60 deg

Figure 35 - Comparison of Experimental and First Generation Predicted Spectra for V_{mix}/c_{amb} = 1.09, M_f = 0.0 (A_O/A_I = 2.75, Ref. 24, Rdg. 383)
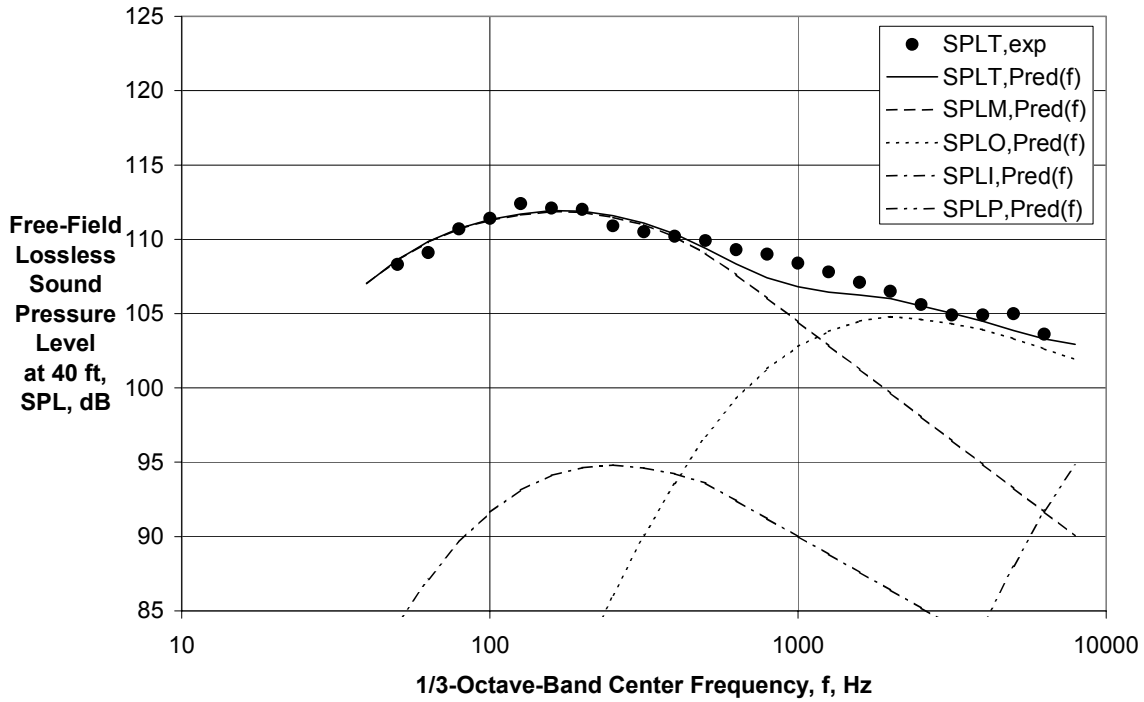
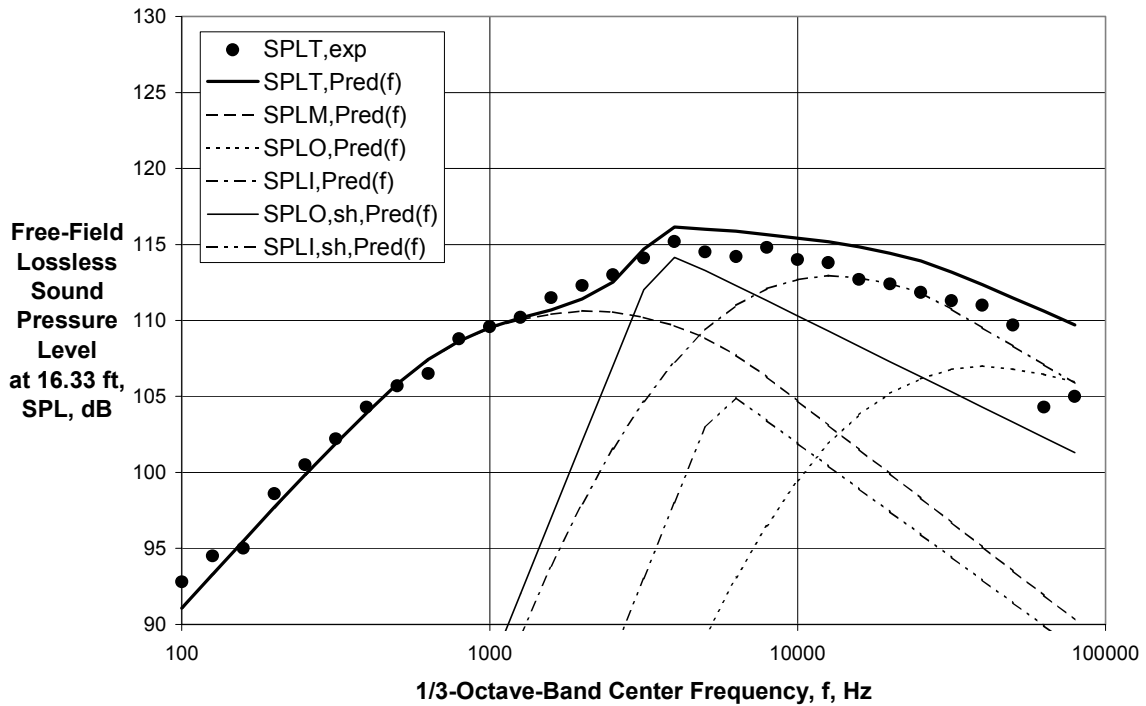**(b) Directivity Angle = 90 deg**
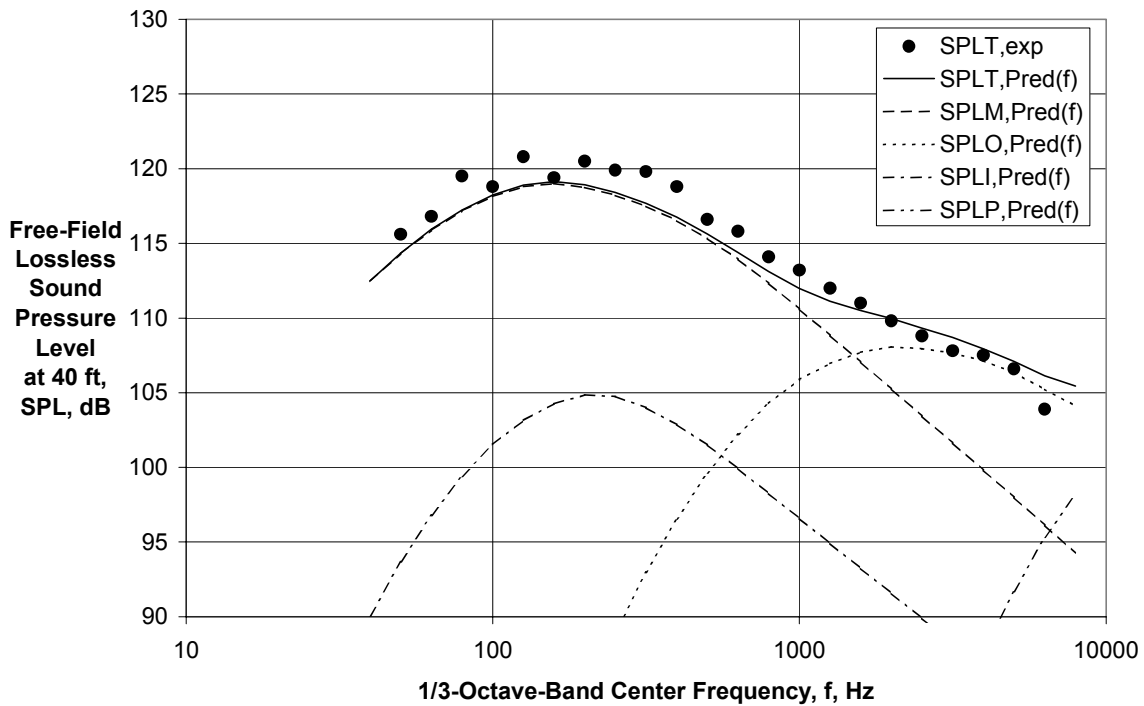
(c) Directivity Angle = 120 deg

Figure 35 (Continued) - Comparison of Experimental and First Generation Predicted Spectra for V_{mix}/c_{amb} = 1.09, M_f = 0.0 (A_O/A_I = 2.75, Ref. 24, Rdg. 383)
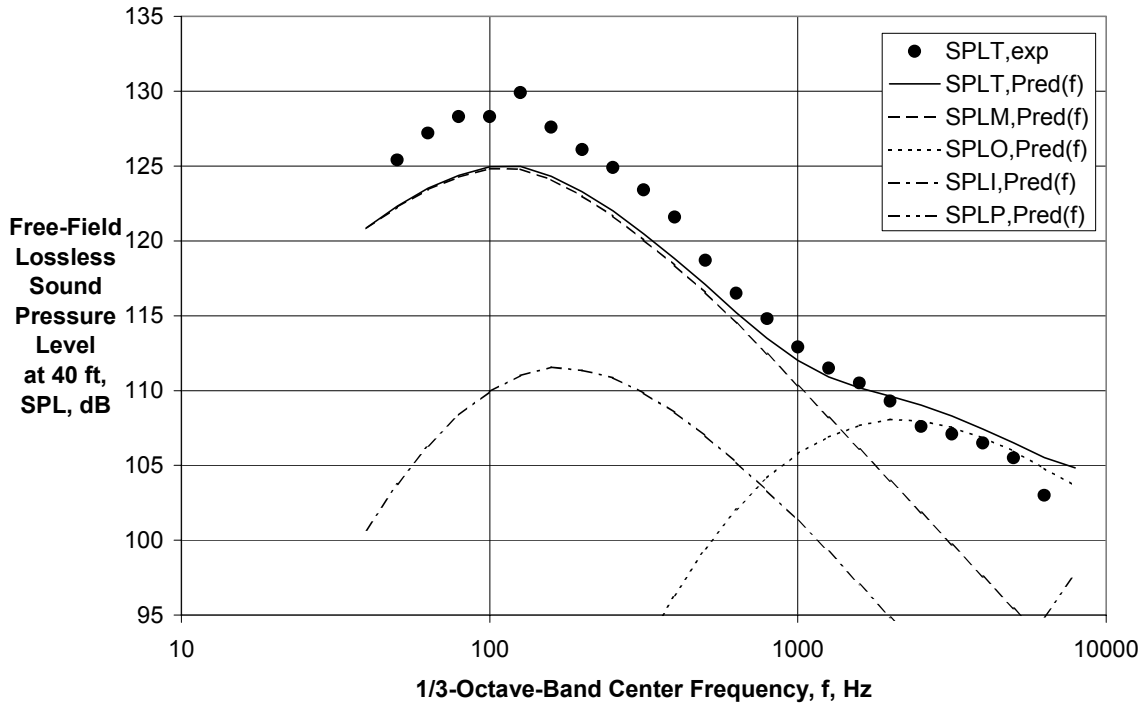
(d) Directivity Angle = 135 deg
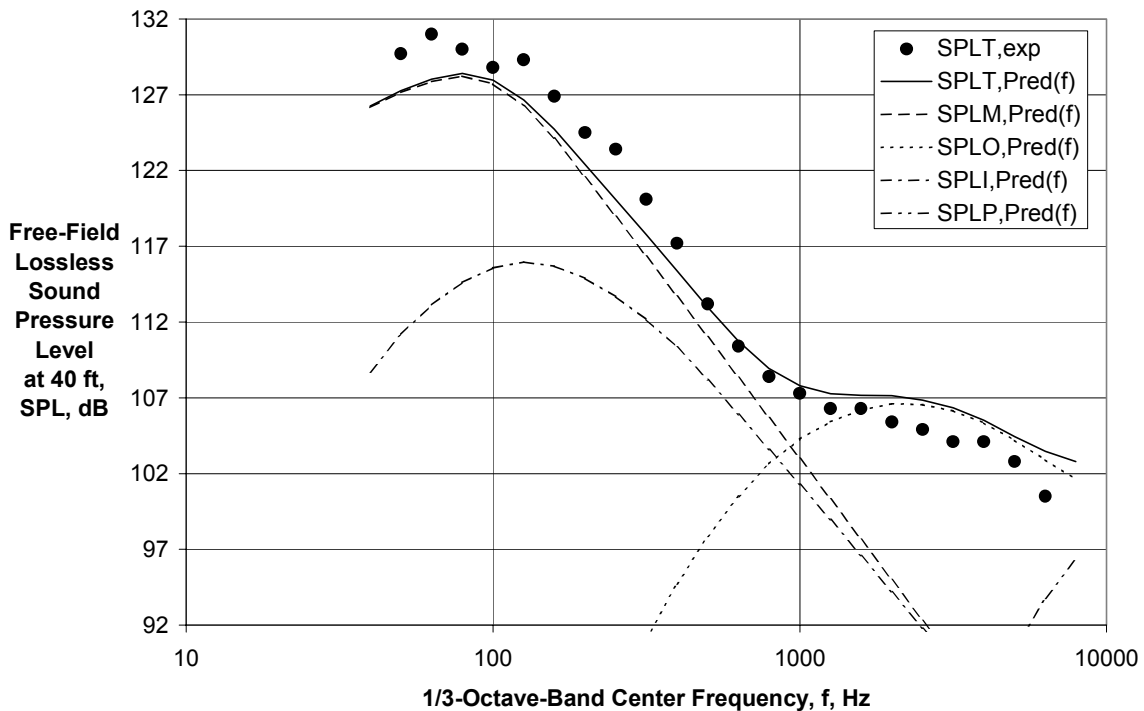
(e) Directivity Angle = 150 deg

Figure 35 (Continued) - Comparison of Experimental and First Generation Predicted Spectra for V_{mix}/c_{amb} = 1.09, M_f = 0.0 (A_O/A_I = 2.75, Ref. 24, Rdg. 383)
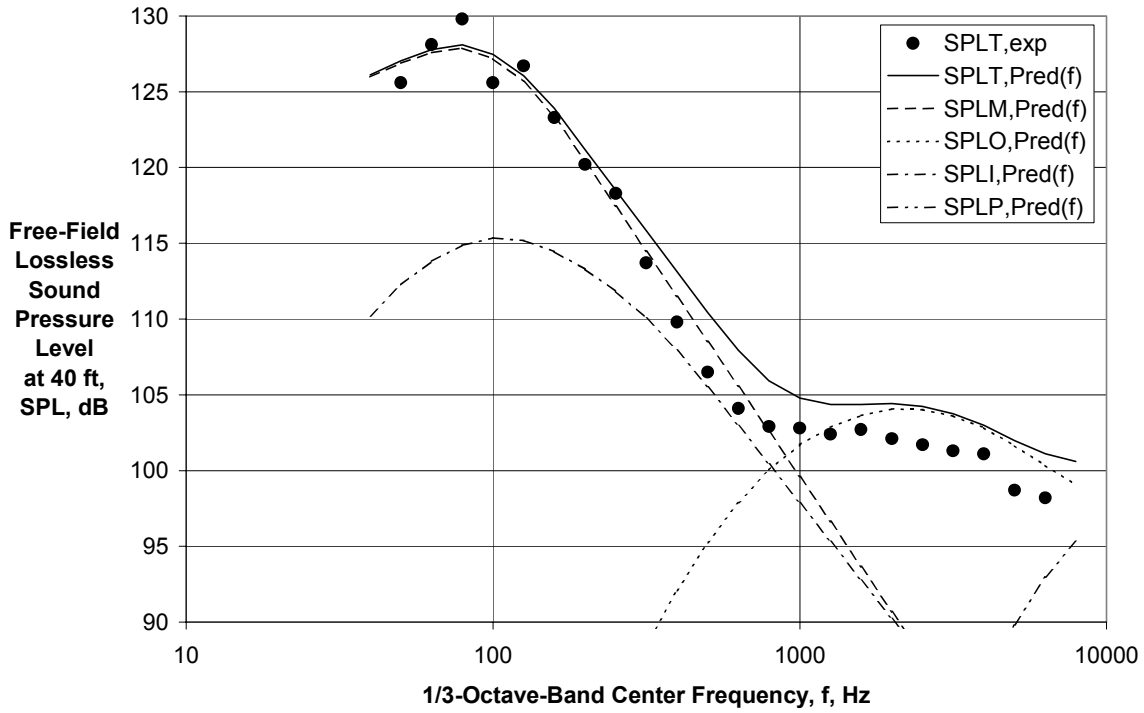
(f) Directivity Angle = 160 deg

Figure 35 (Concluded) - Comparison of Exp. and First Generation Predicted Spectra for V_{mix}/c_{amb} = 1.09, M_f = 0.0 (A_O/A_I = 2.75, Ref. 24, Rdg. 383)
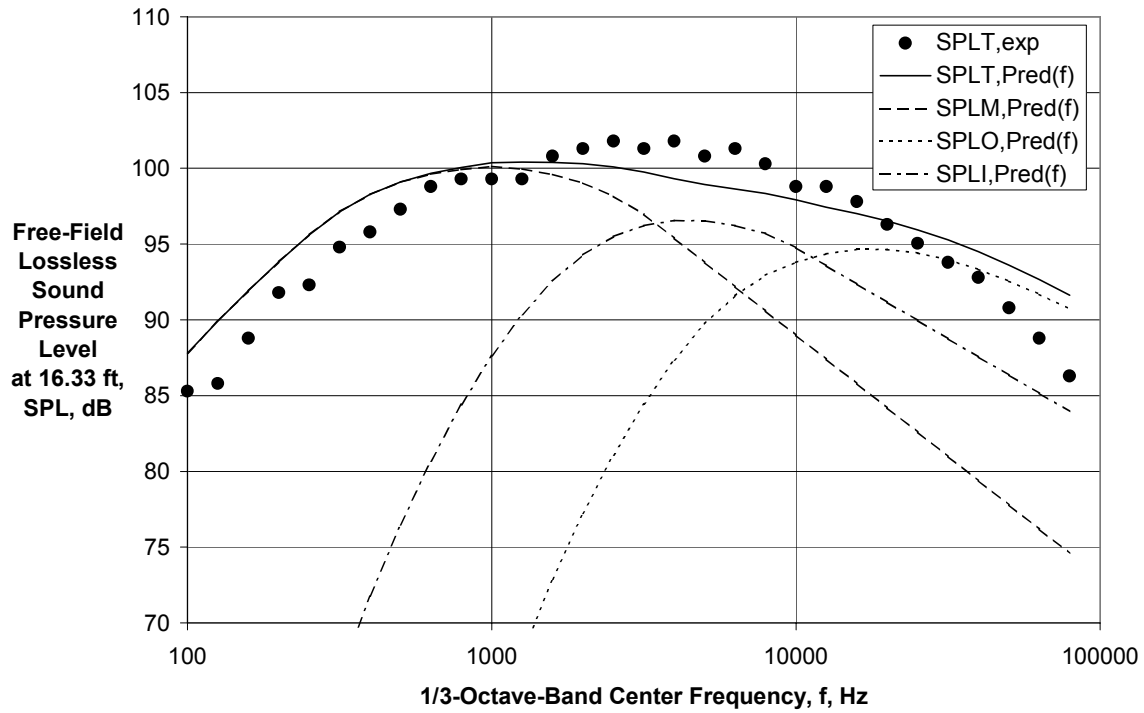
(a) Directivity Angle = 46 deg

Figure 36 - Comparison of Experimental and First Generation Predicted Spectra for V_{mix}/c_{amb} = 1.63, M_f = 0.0 (A_O/A_I = 1.94, Ref. 25, Rdg. 10)
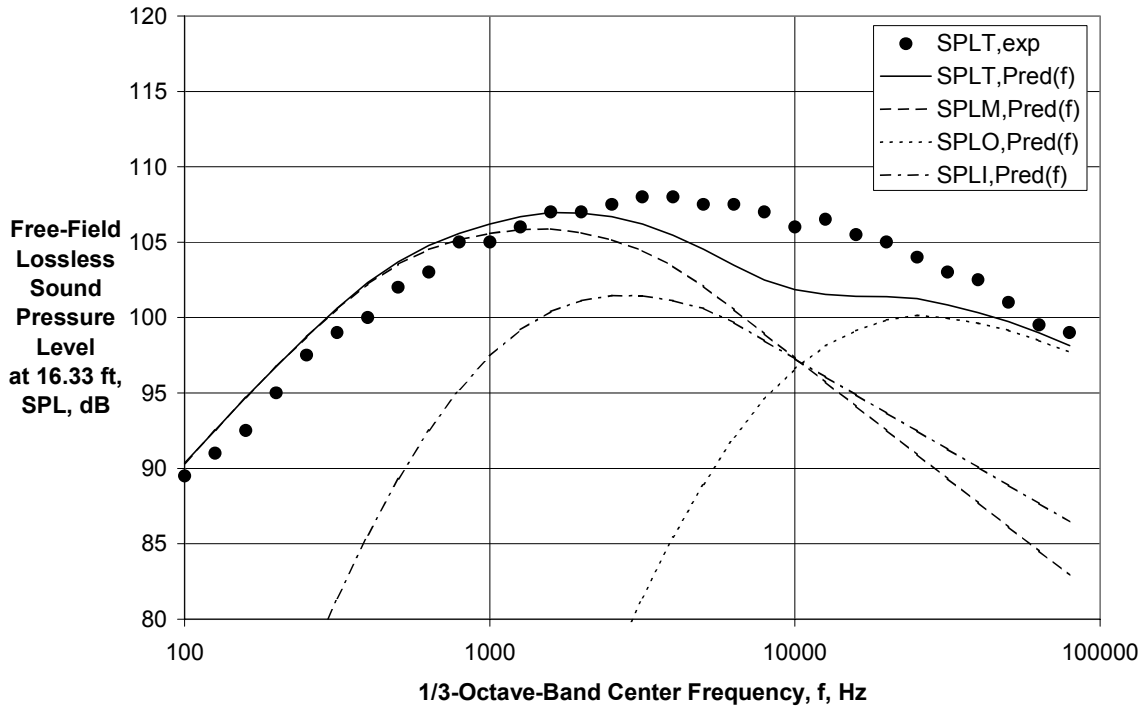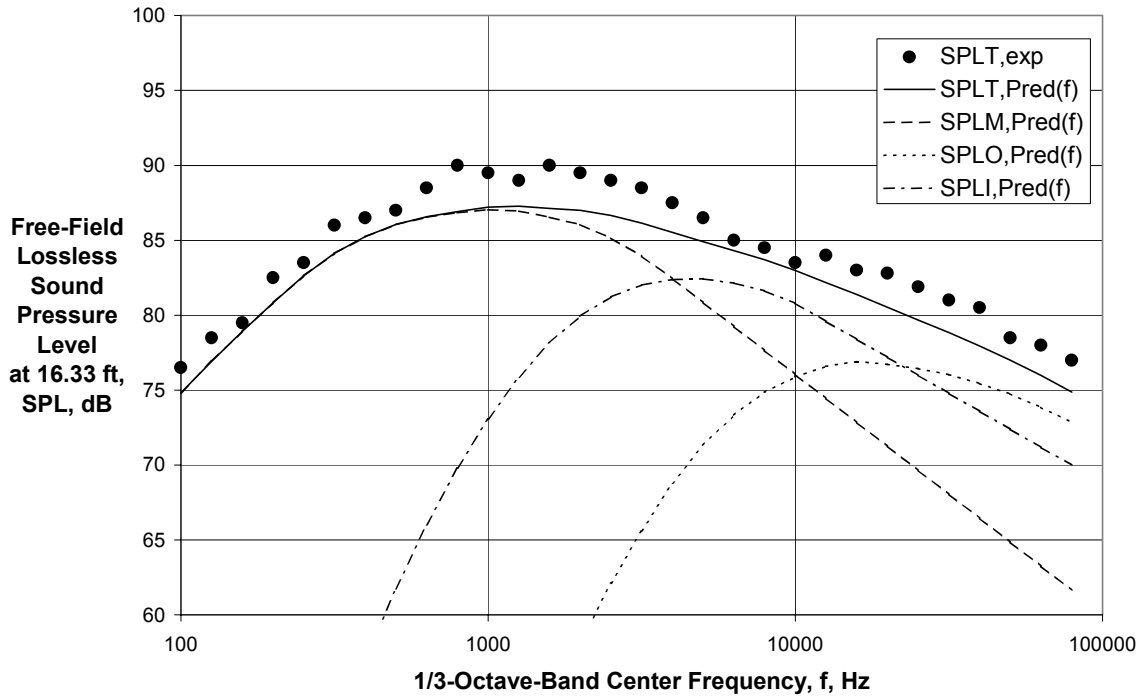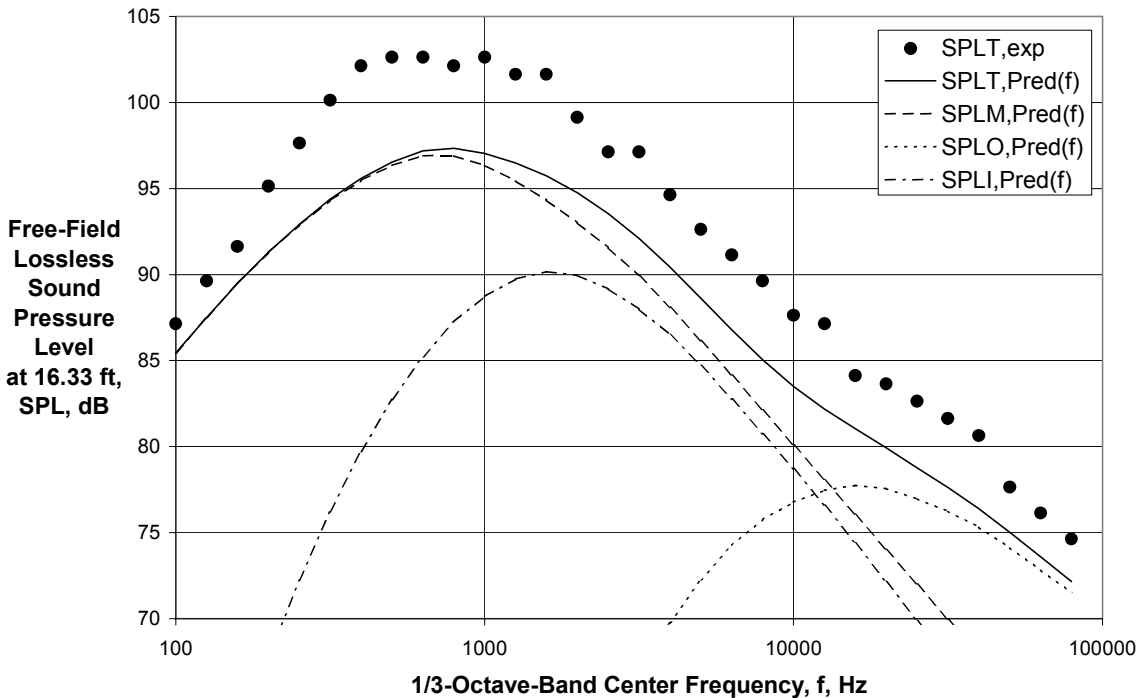
(b) Directivity Angle = 95 deg
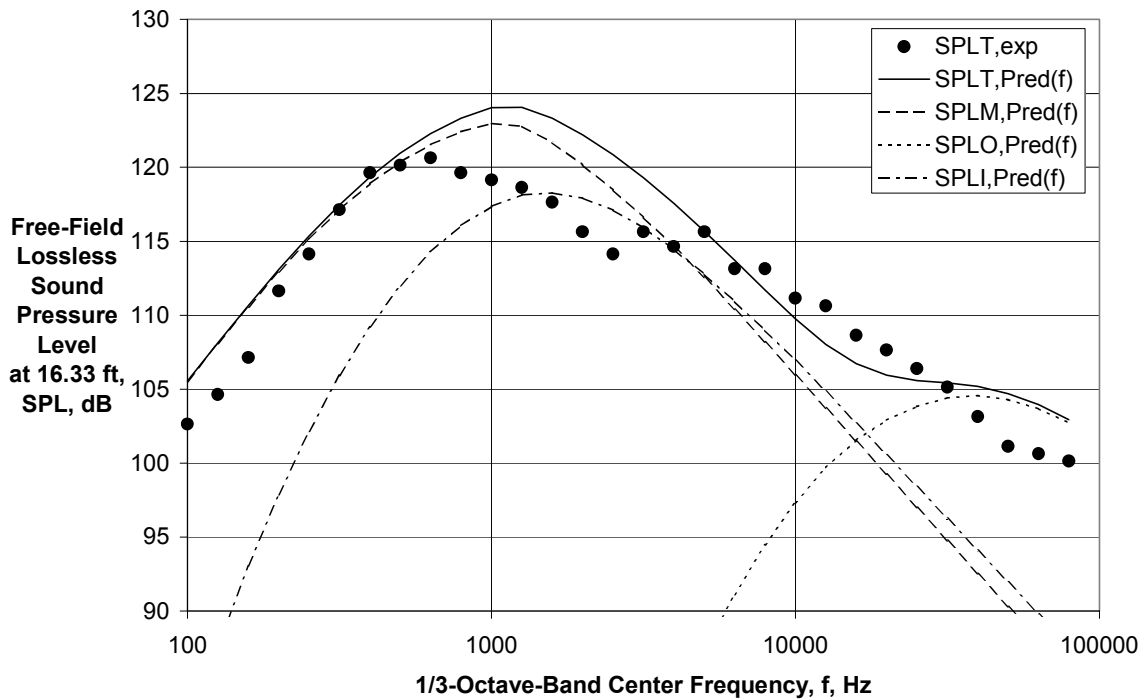
(c) Directivity Angle = 139 deg

Figure 36 (Concluded) - Comparison of Experimental and First Generation Predicted Spectra for V_{mix}/c_{amb} = 1.63, M_f = 0.0 (A_O/A_I = 1.94, Ref. 25, Rdg. 10)
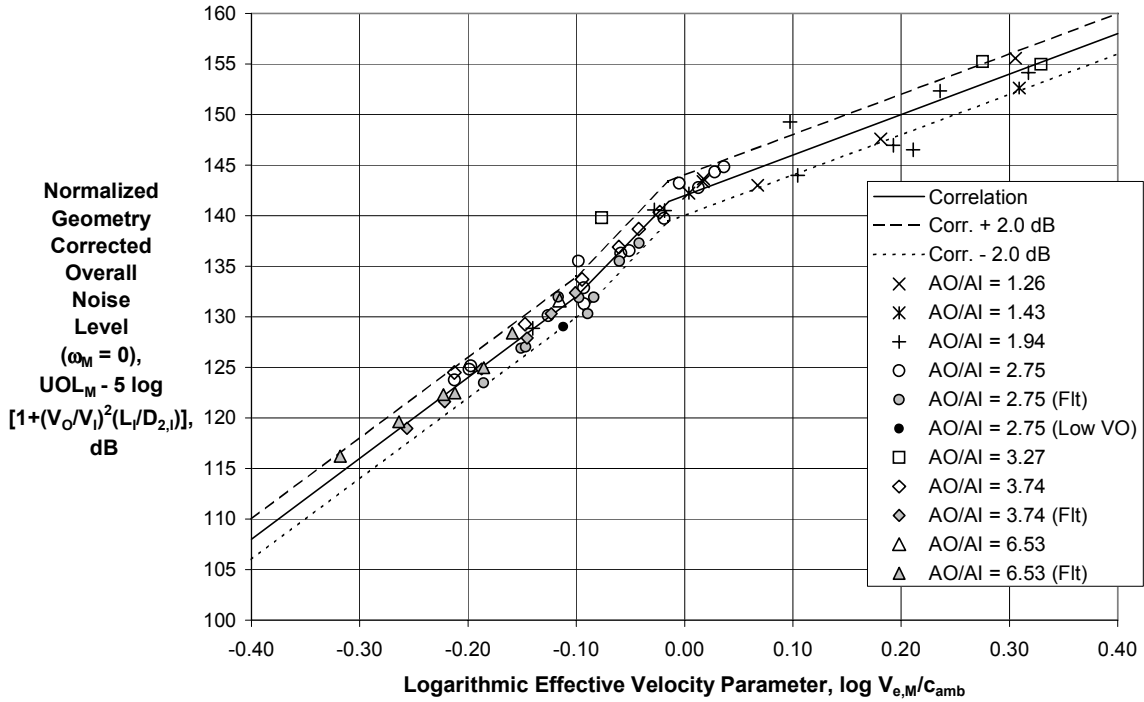
(a) No Density Effect, $\omega_M = 0.0$
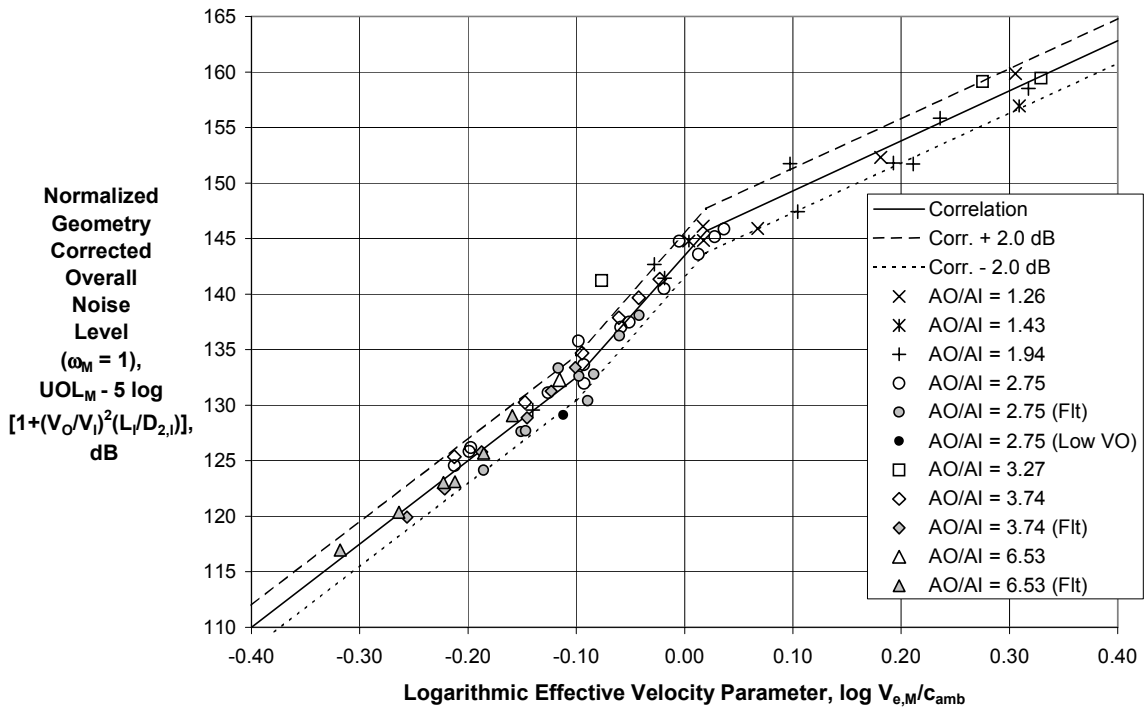
(b) Constant Density Exponent, $\omega_M = 1.00$

Figure 37 – Merged Mixing Noise Correlation with Inner Nozzle Extension Effect
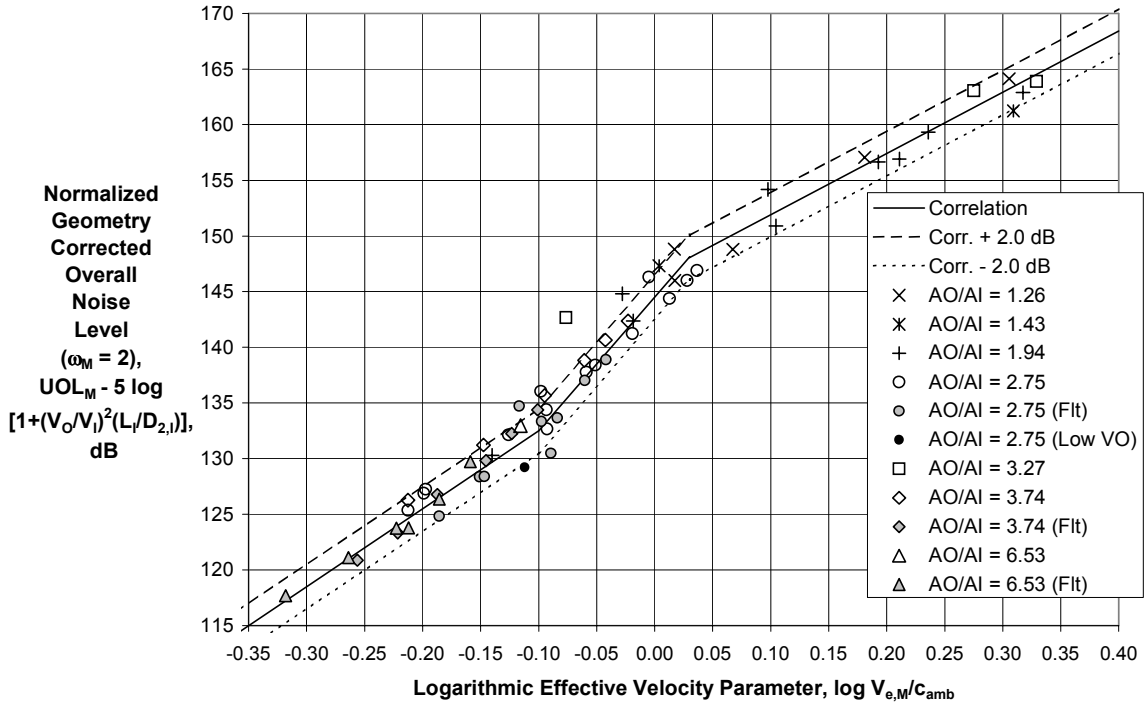
(c) Constant Density Exponent ω_M = 2.00
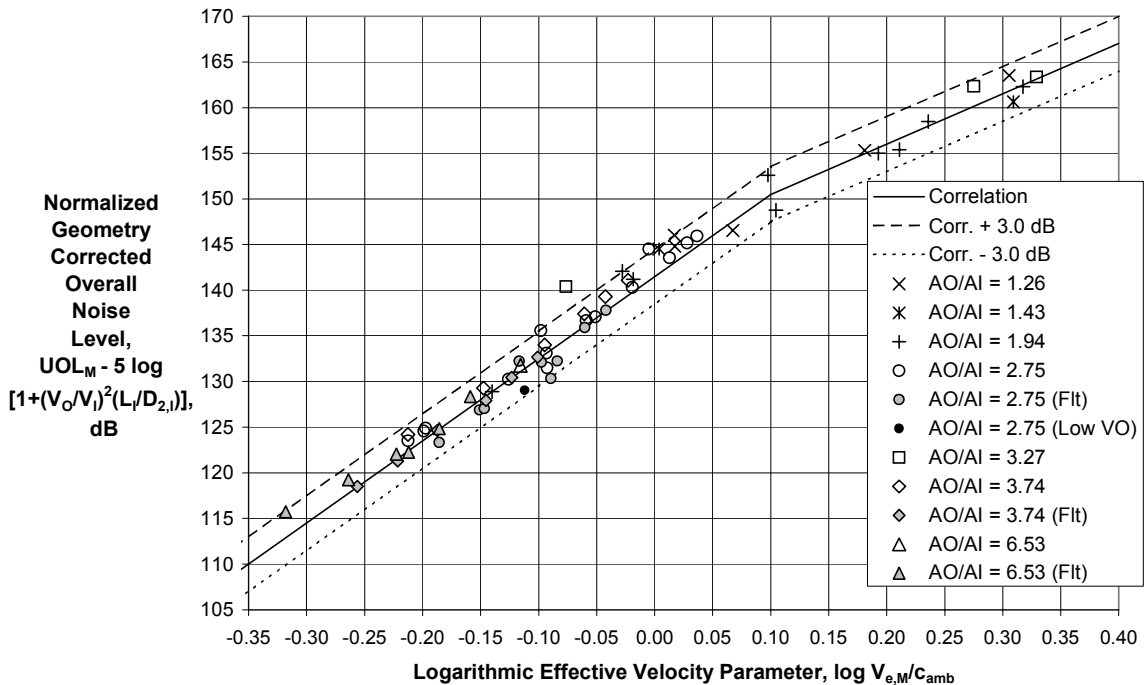
(d) Variable Density Exponent ω_M

Figure 37 (Concluded) – Merged Mixing Noise Correlation with Inner Nozzle Extension Effect
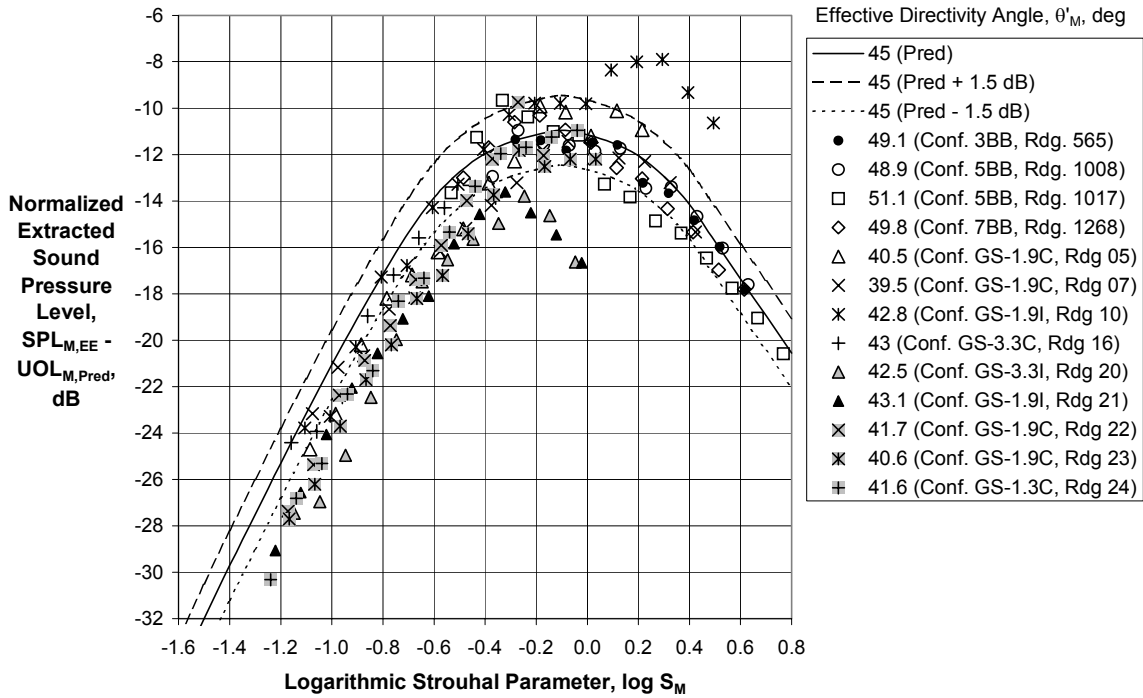
(a) Effective Directivity Angle, 39.5 < θ'_M < 51.1 deg
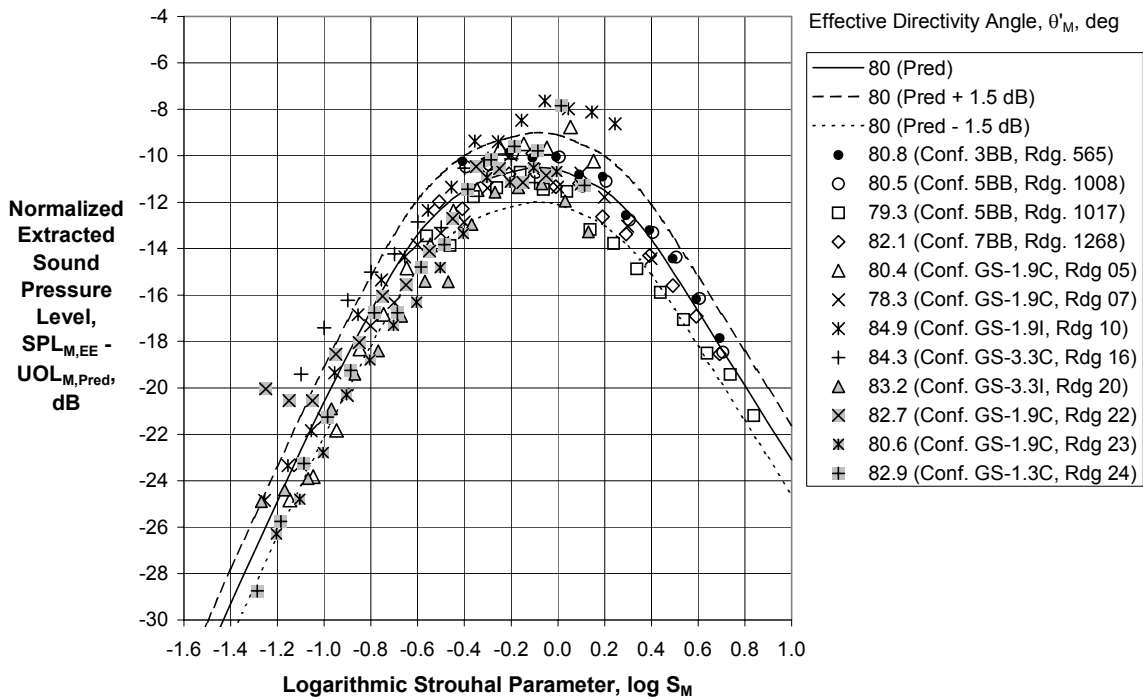
(b) Effective Directivity Angle, 75.9 < θ'_M < 84.9 deg

Figure 38 – Merged Mixing Noise Spectral Directivity Correlation
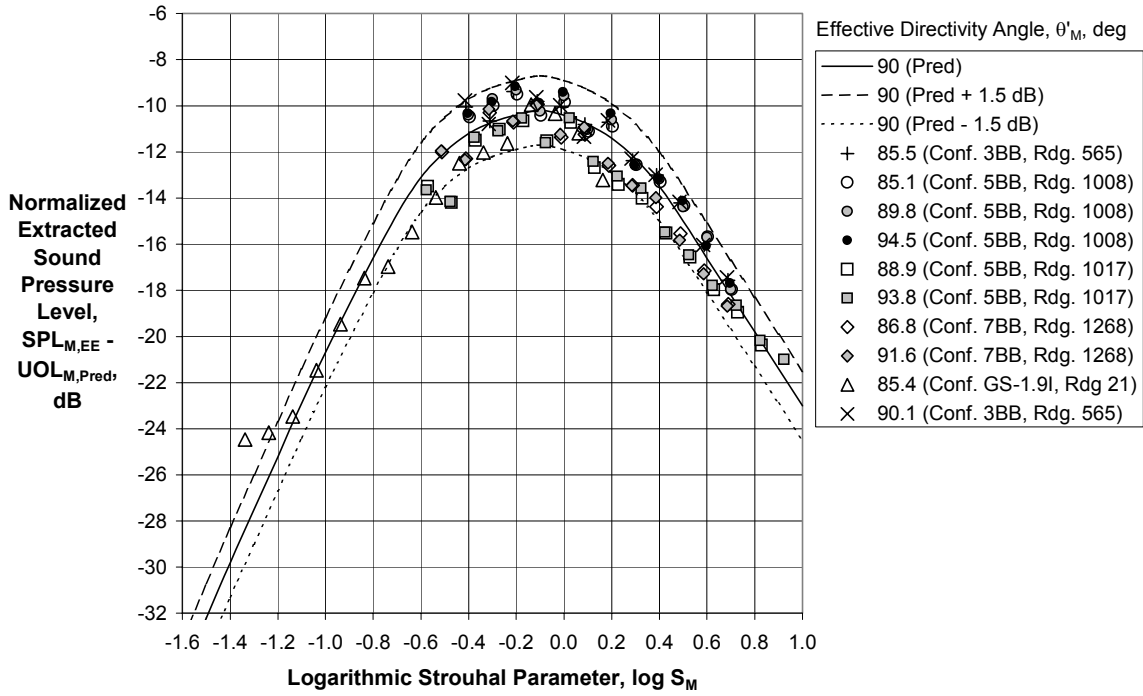
(c) Effective Directivity Angle, 85.1 < θ'$_M$ < 94.5 deg
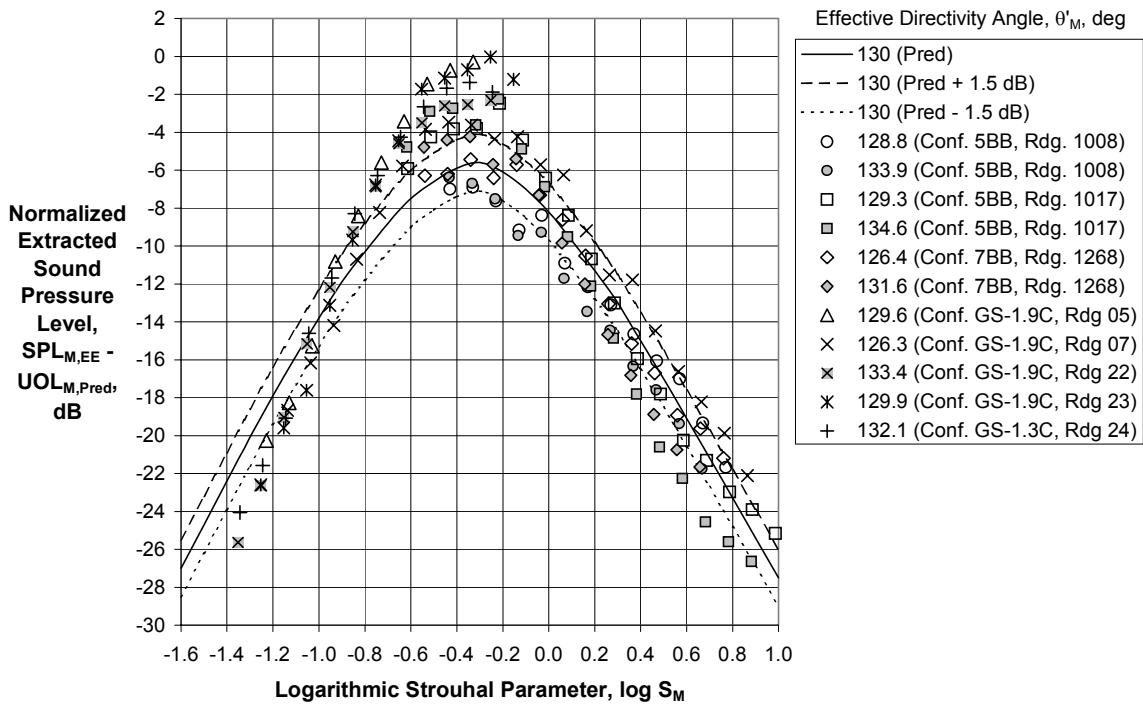
(d) Effective Directivity Angle, 126.3 < θ'$_M$ < 134.6 deg

Figure 38 (Continued) – Merged Mixing Noise Spectral Directivity Correlation
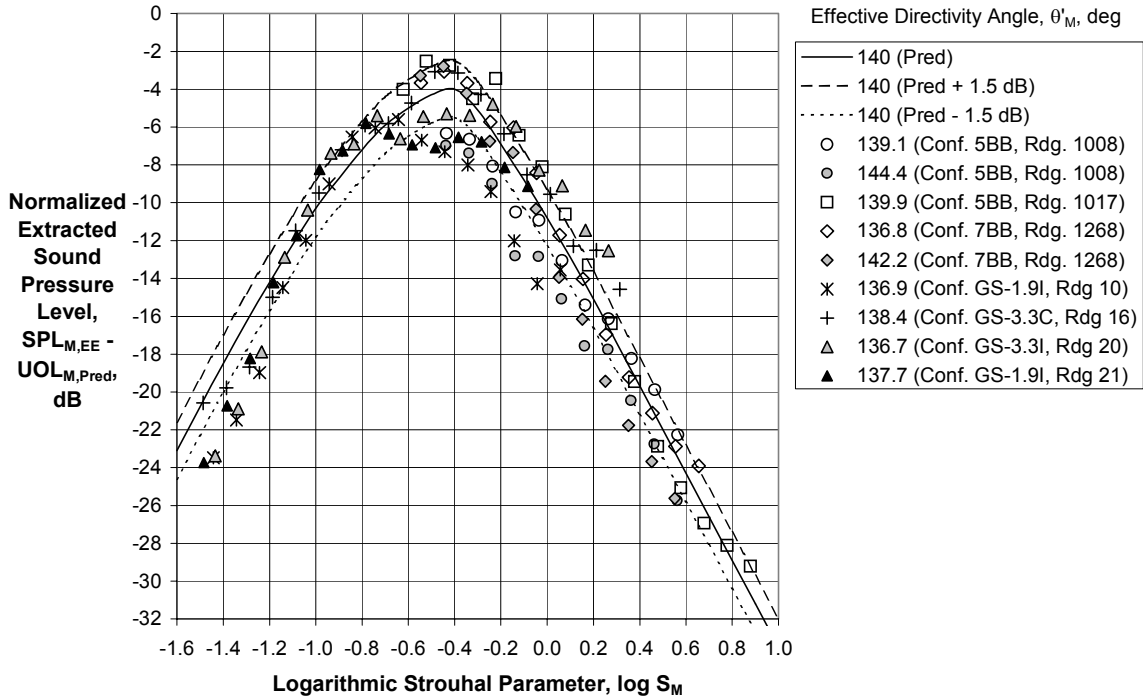
(e) Effective Directivity Angle, 136.7 < θ'$_M$ < 144.4 deg

Figure 38 (Concluded) – Merged Mixing Noise Spectral Directivity Correlation
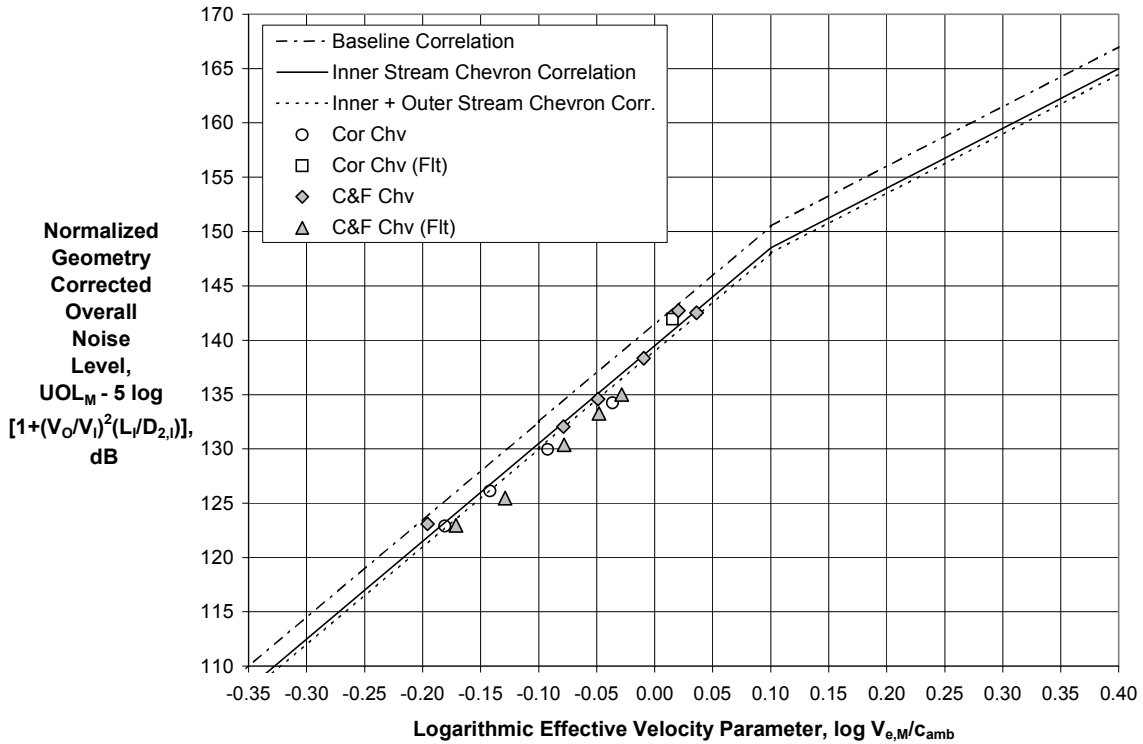
Figure 39 – Effect of Chevrons on Merged Mixing Noise Correlation with Inner Nozzle Extension Effect and Variable Density Exponent ω$_M$
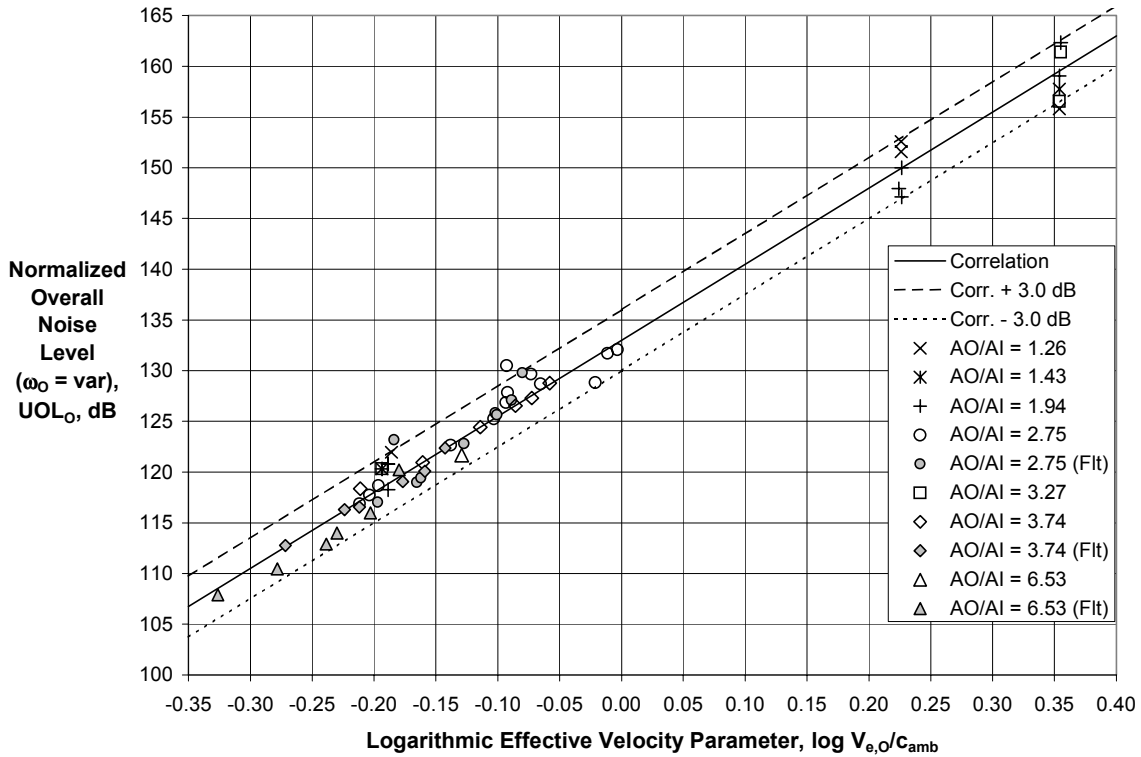
Figure 40 – Outer Shear Layer Mixing Noise Correlation with Variable Density Exponent
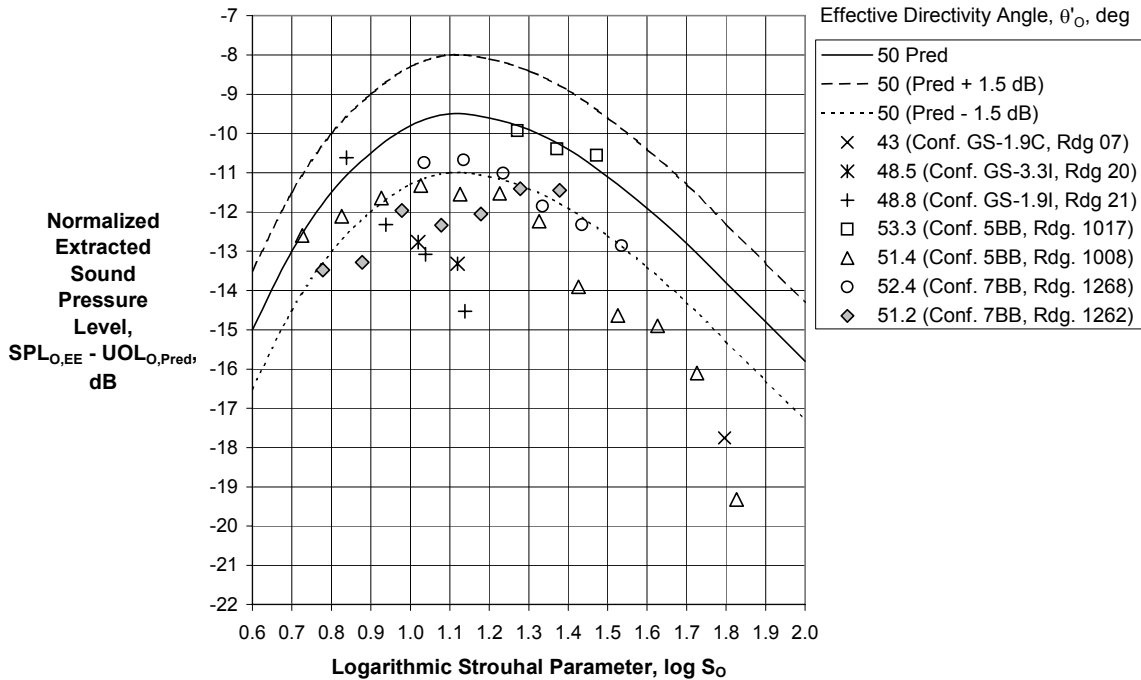
(a) Effective Directivity Angle, 48.5 < θ'_O < 53.3 deg

Figure 41 – Outer Shear Layer Mixing Noise Spectral Directivity Correlation
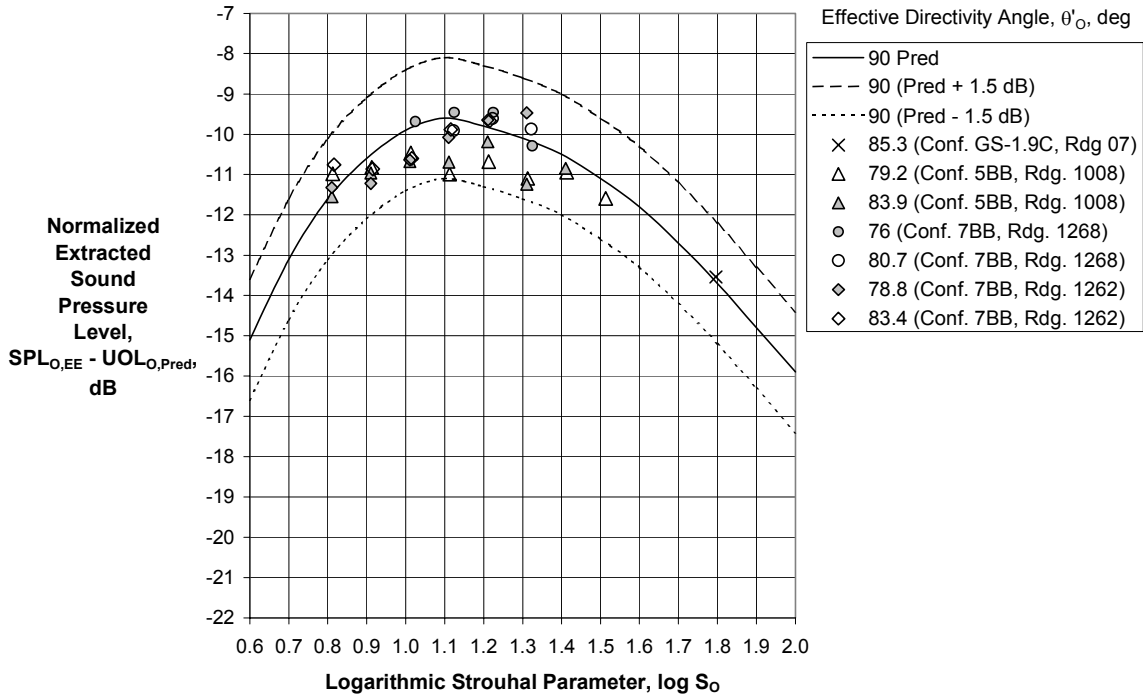
(b) Effective Directivity Angle, 76.0 < θ'_O < 85.3 deg
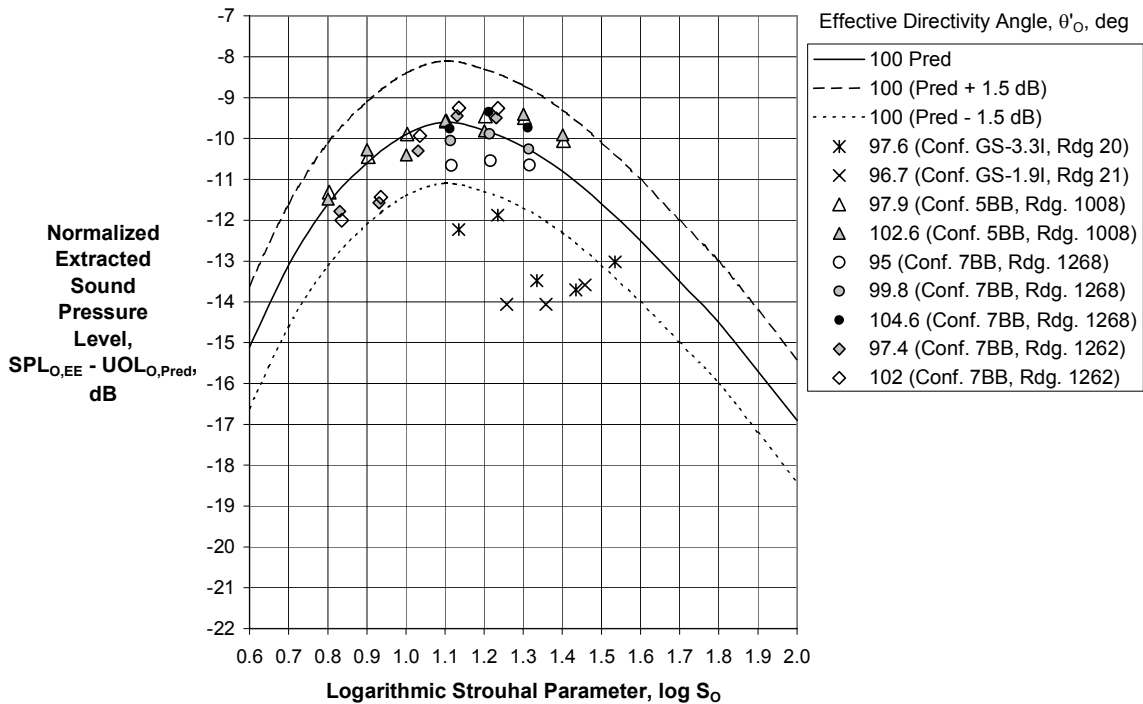
(c) Effective Directivity Angle, 95.0 < θ'_O < 104.6 deg

Figure 41 (Continued) – Outer Shear Layer Mixing Noise Spectral Directivity Correlation
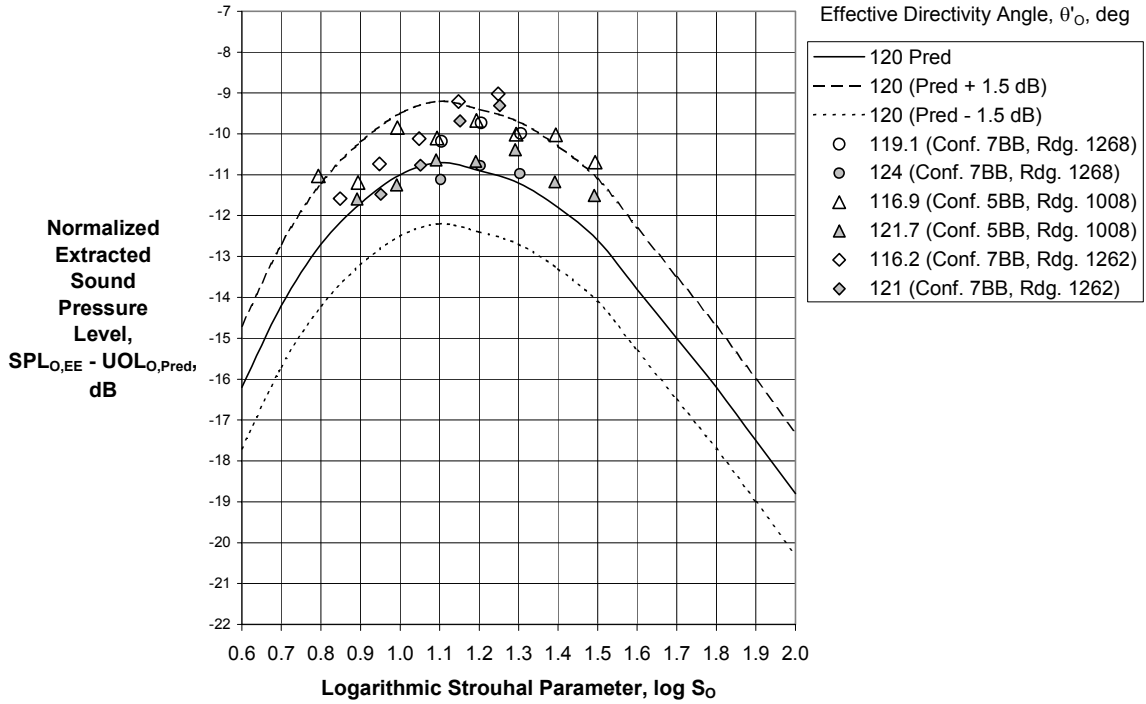
(d) Effective Directivity Angle, 116.9 < θ'$_O$ < 124.0 deg
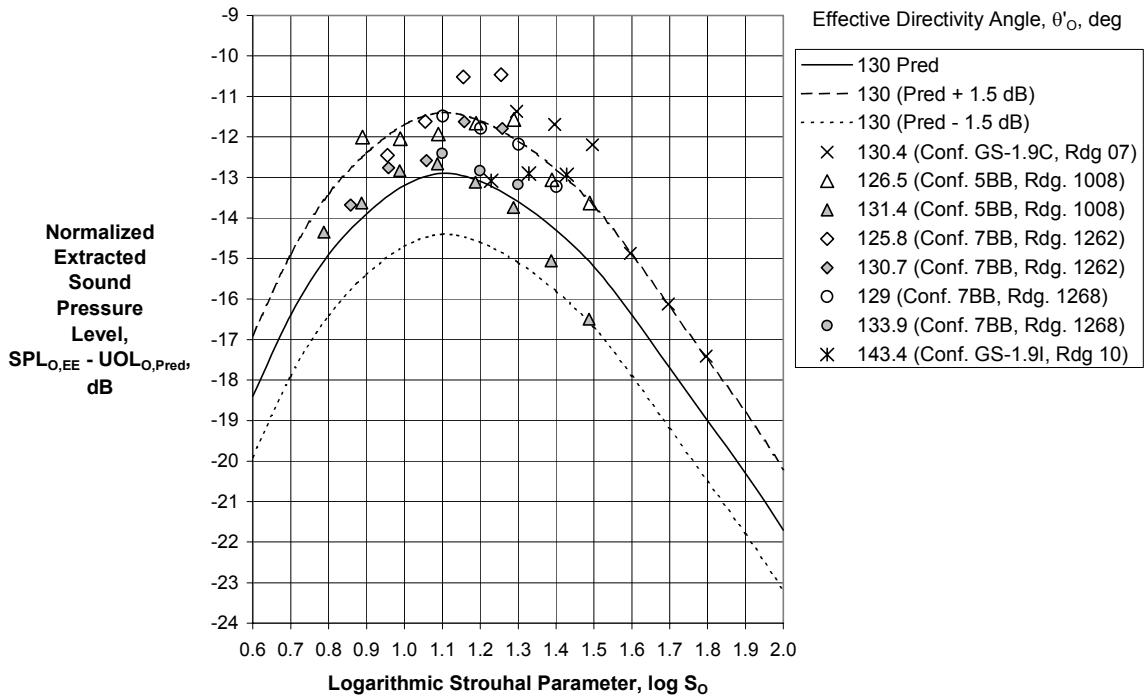
(e) Effective Directivity Angle, 126.5 < θ'$_O$ < 131.4 deg

Figure 41 (Continued) – Outer Shear Layer Mixing Noise Spectral Directivity Correlation
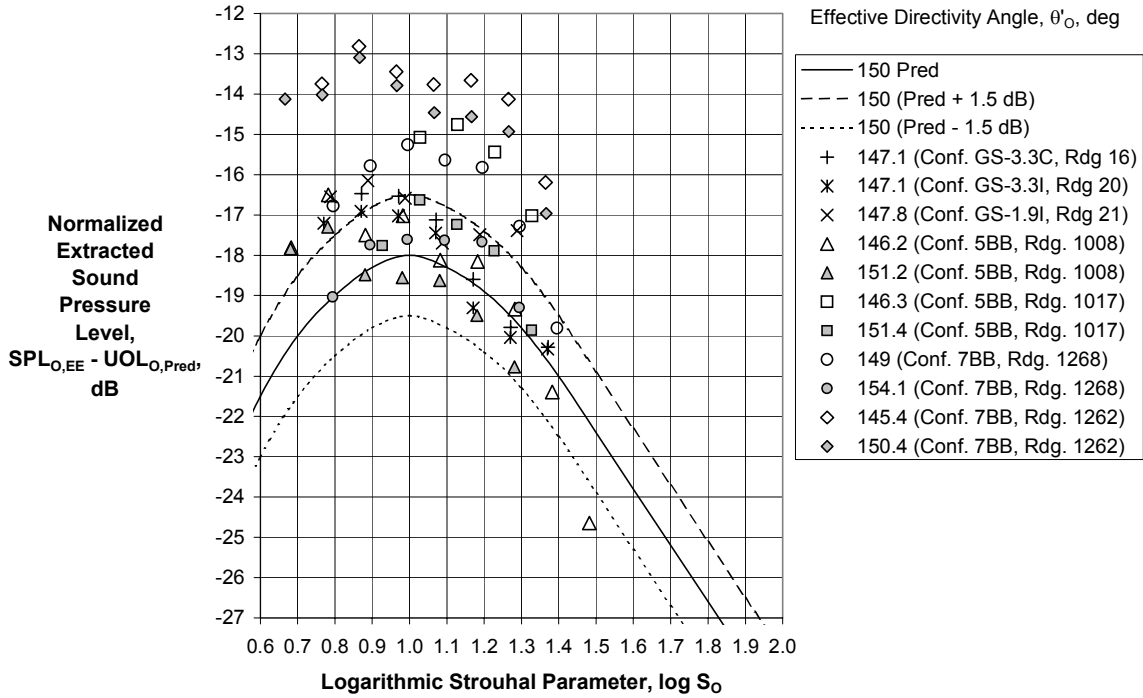
(f) Effective Directivity Angle, 145.4 < θ'$_O$ < 154.1 deg

Figure 41 (Concluded) – Outer Shear Layer Mixing Noise Spectral Directivity Correlation
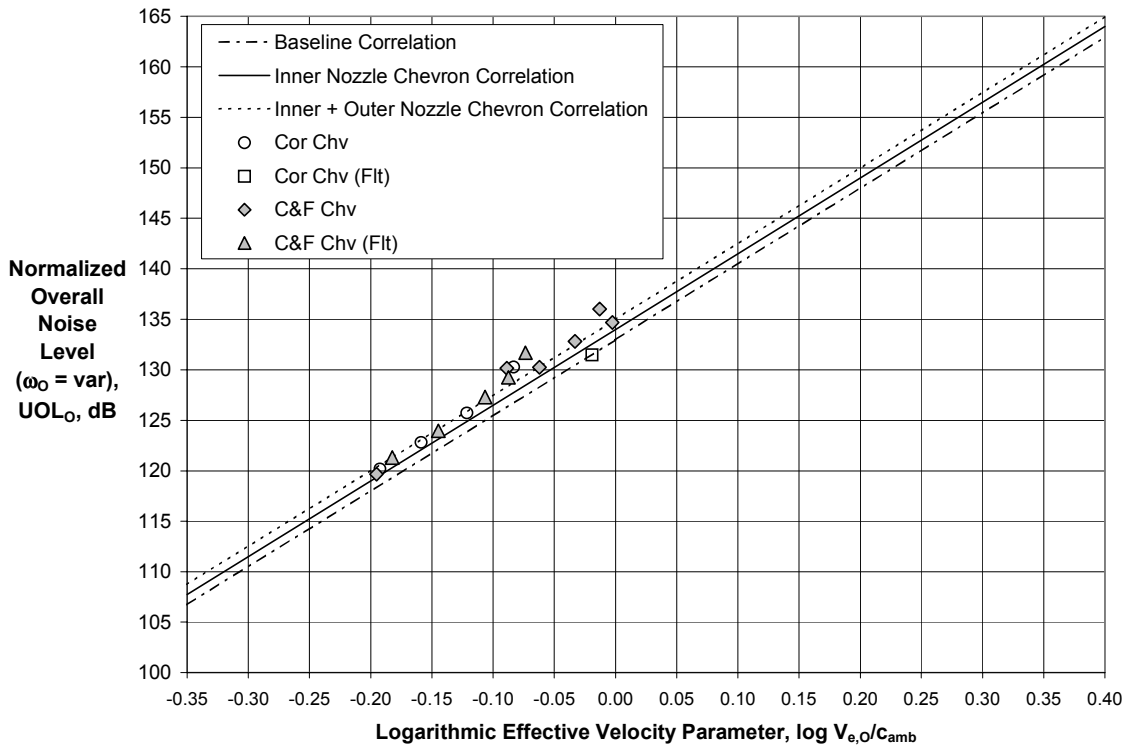
Figure 42 – Effect of Chevrons on Outer Shear Layer Mixing Noise Correlation with Variable Density Exponent
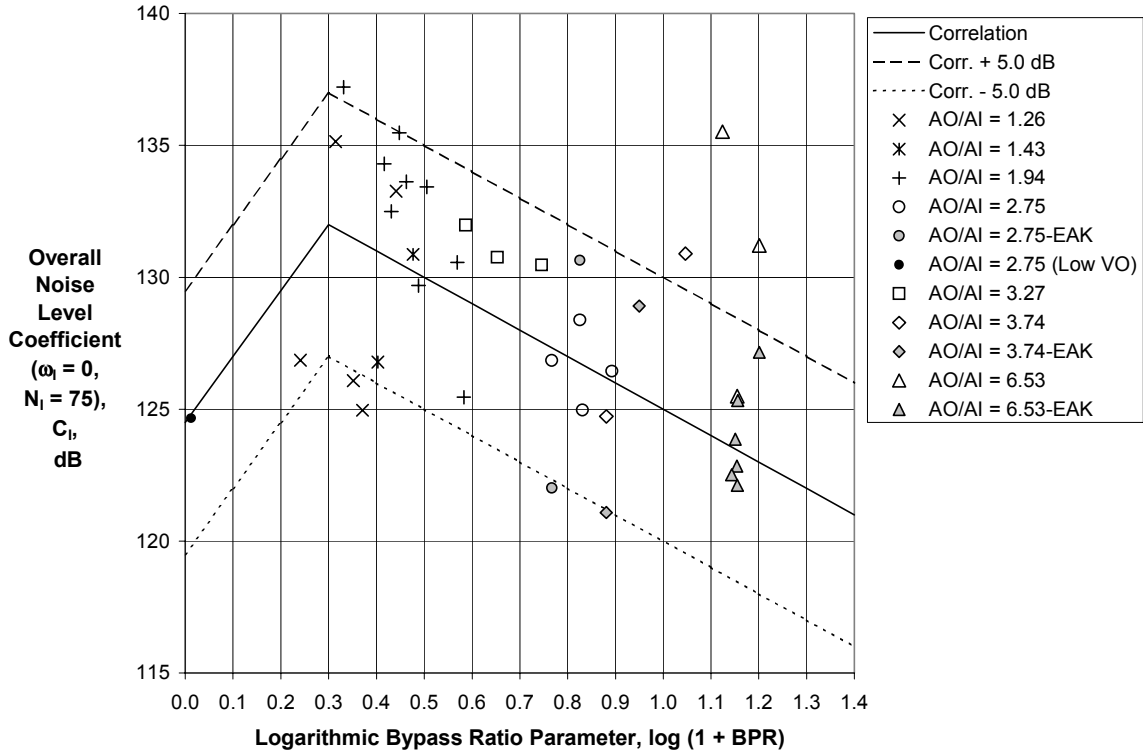
Figure 43 – Final Inner Stream Mixing Noise Correlation as Function of Bypass Ratio with Density Exponent ω_I = 0.0 and Slope N_I = 75
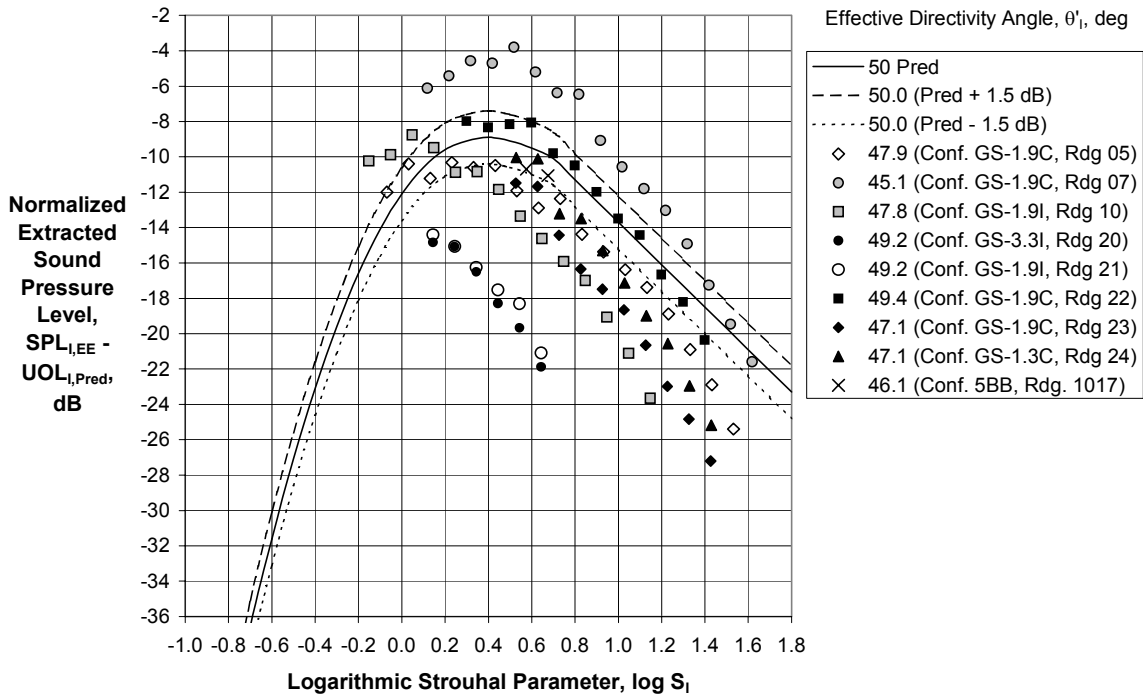
(a) Effective Directivity Angle, 45.1 < θ'_I < 49.4 deg

Figure 44 – Inner Stream Mixing Noise Spectral Directivity Correlation
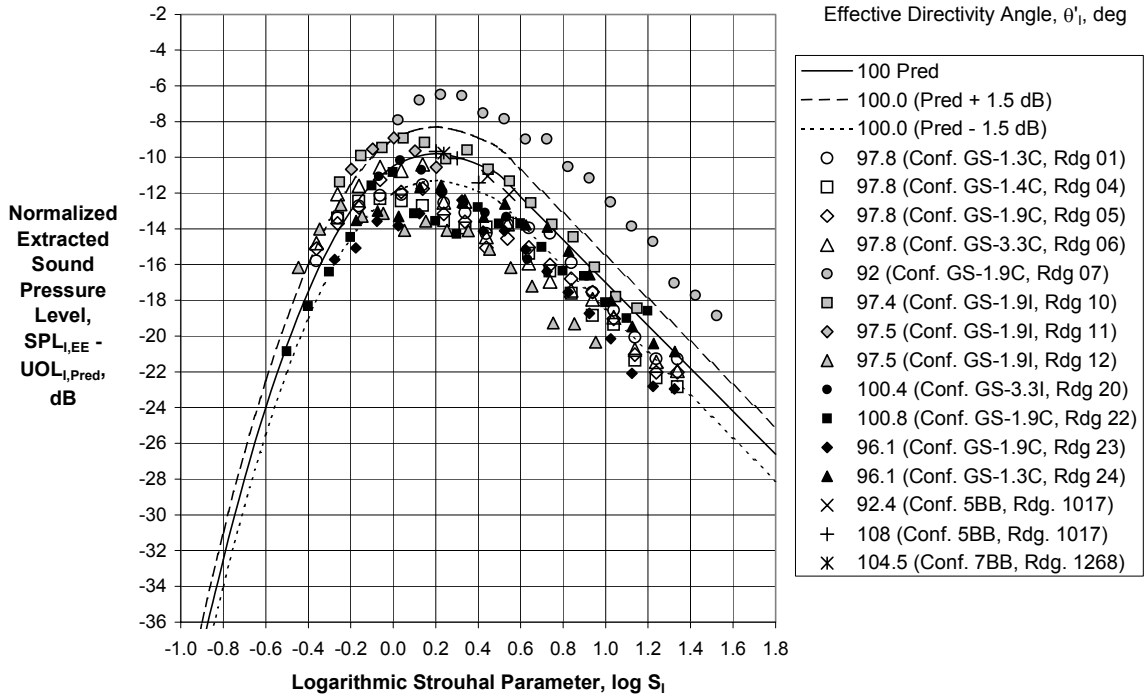
(b) Effective Directivity Angle, 92.0 < θ'₁ < 108.0 deg
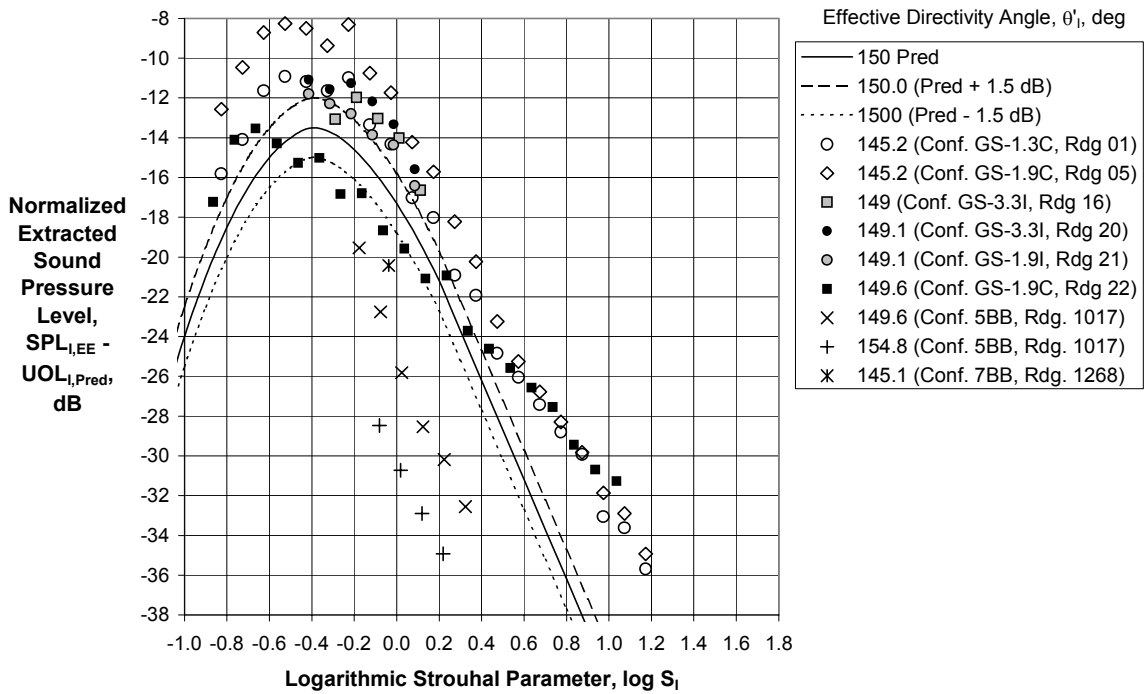
(c) Effective Directivity Angle, 145.1 < θ'₁ < 154.8 deg

Figure 44 (Concluded) – Inner Stream Mixing Noise Spectral Directivity Correlation
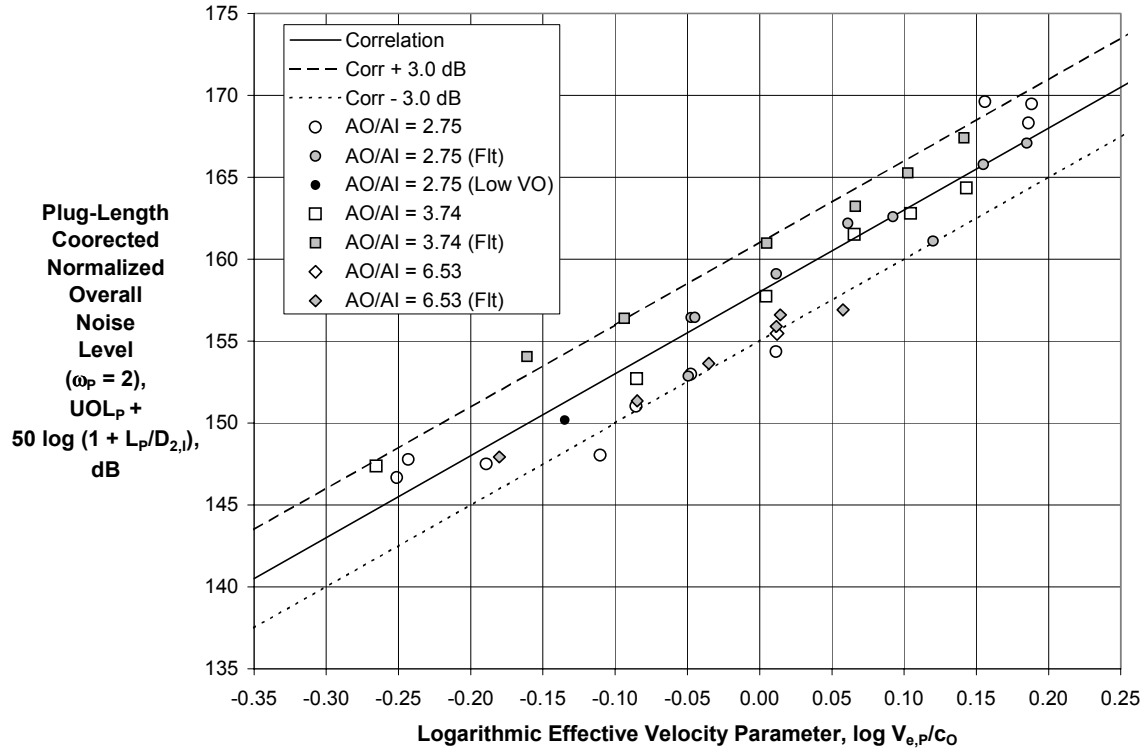
Figure 45 – Final Inner Stream Plug Separation Noise Correlation with Density Exponent $\omega_P = 2.0$ and Nondimensionalized Plug Length Effect
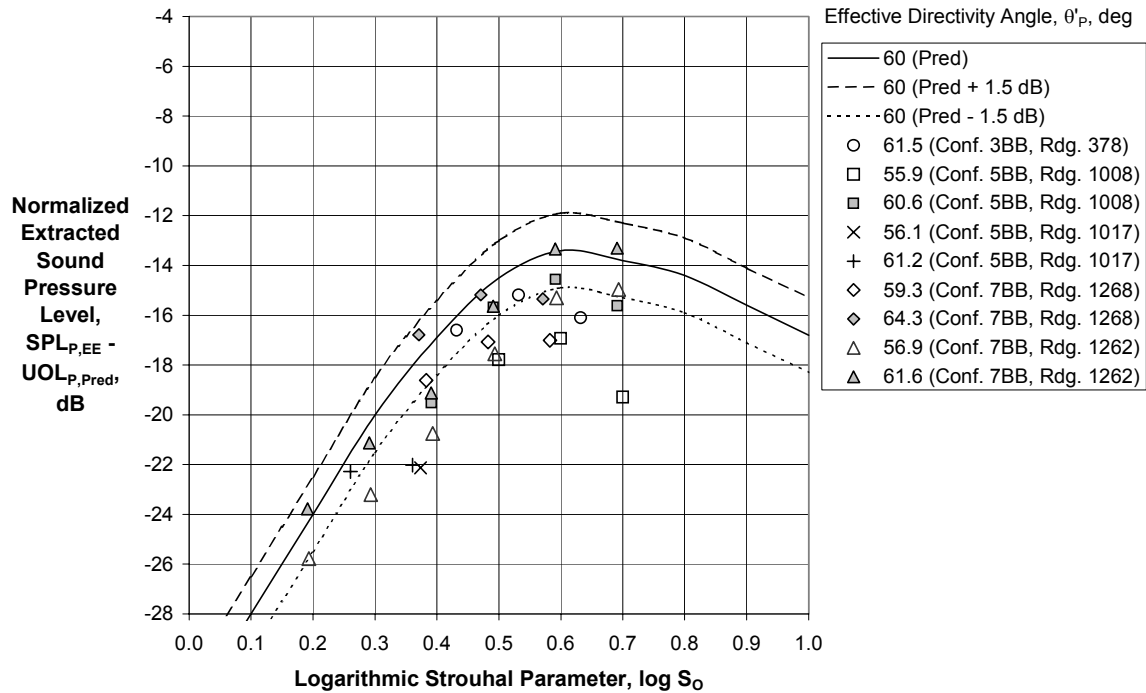
(a) Effective Directivity Angle, $55.9 < \theta'_P < 64.3$ deg

Figure 46 - Inner Stream Plug Separation Noise Spectral Directivity Correlation
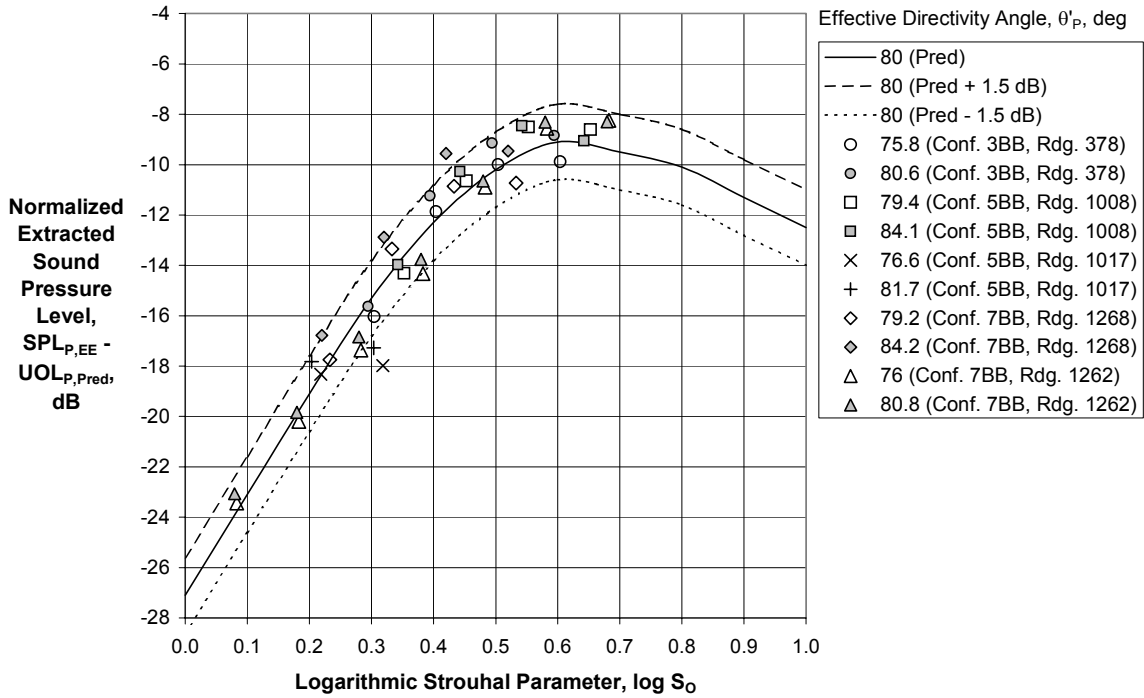
(b) Effective Directivity Angle, 76.0 < θ'$_P$ < 84.2 deg
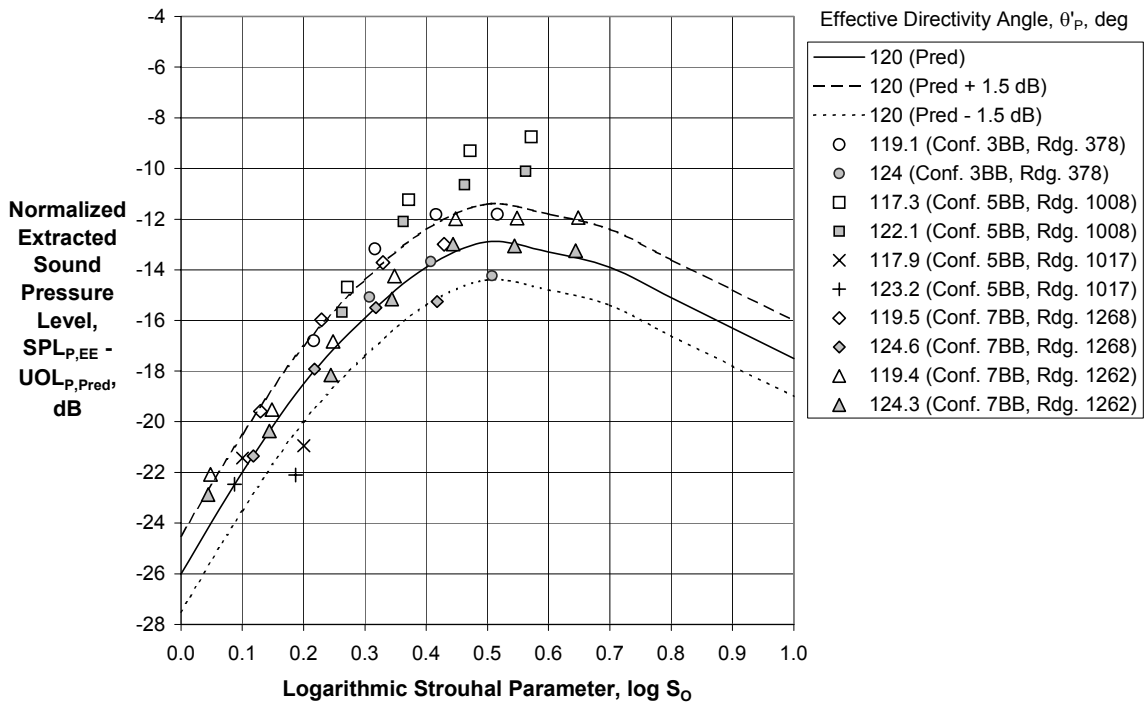
(c) Effective Directivity Angle, 117.3 < θ'$_P$ < 124.6 deg

Figure 46 (Continued) - Inner Stream Plug Separation Noise Spectral Directivity Correlation
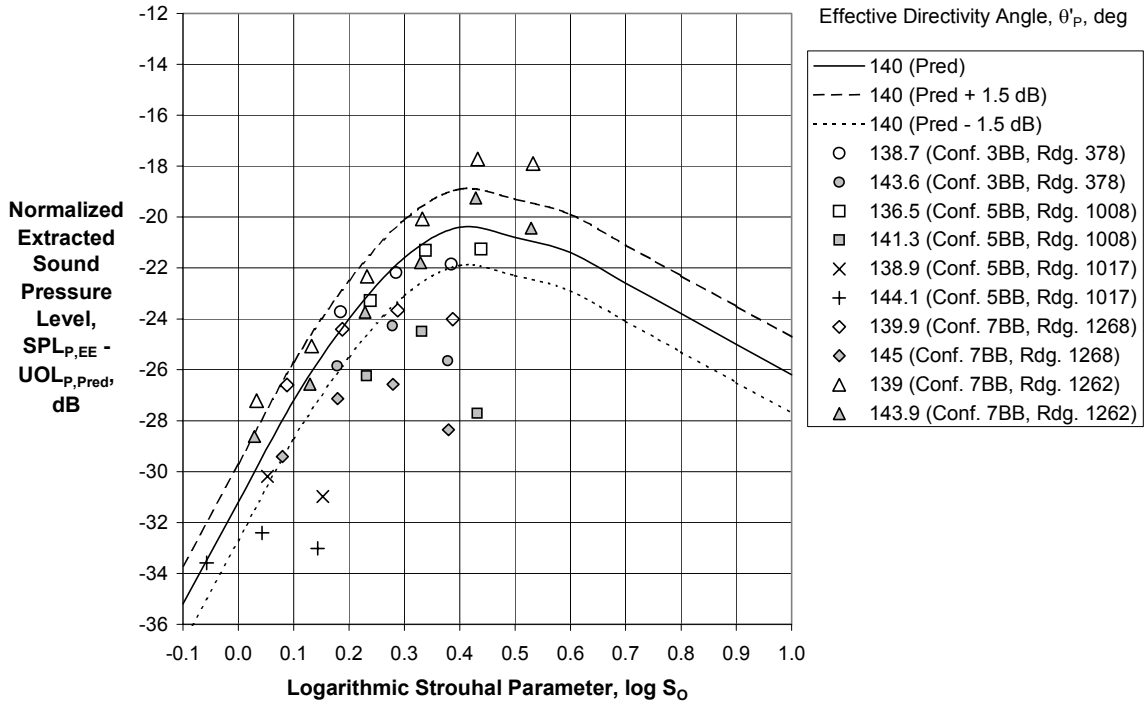
(d) Effective Directivity Angle, $136.5 < \theta'_P < 145.0$ deg

Figure 46 (Concluded) - Inner Stream Plug Separation Noise Spectral Directivity Correlation
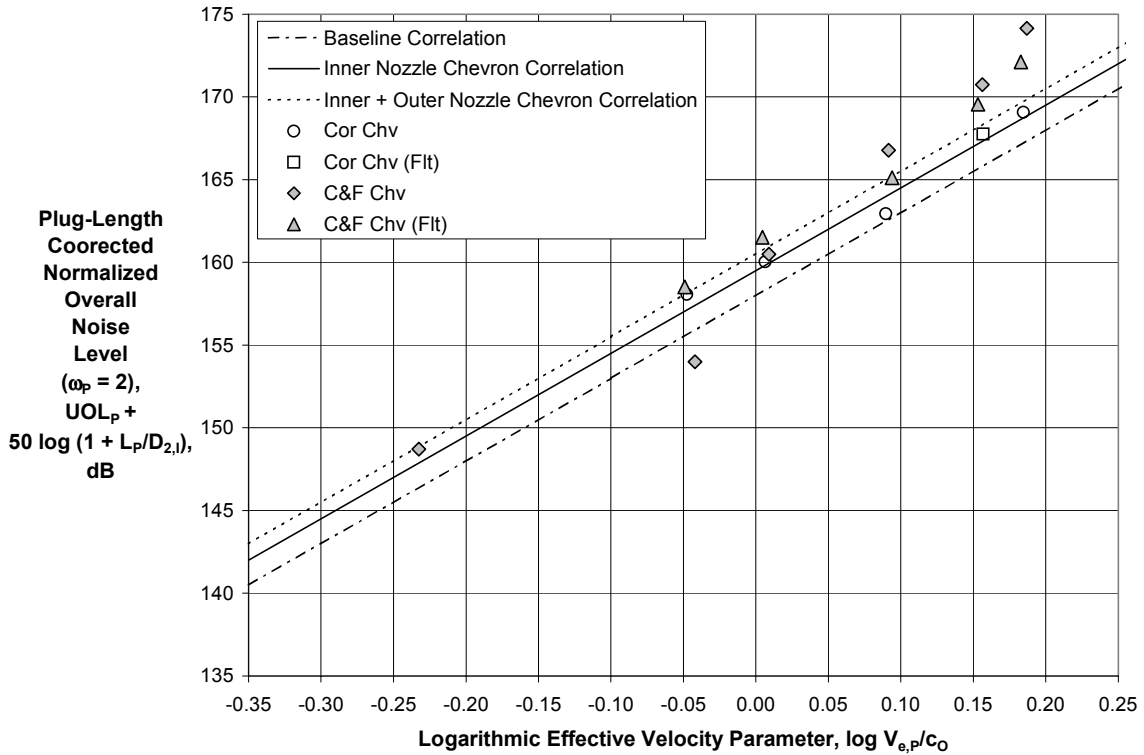
Figure 47 – Effect of Chevrons on Inner Stream Plug Separation Noise Correlation with Density Exponent $\omega_P = 2.0$ and Nondim. Plug Length Effect
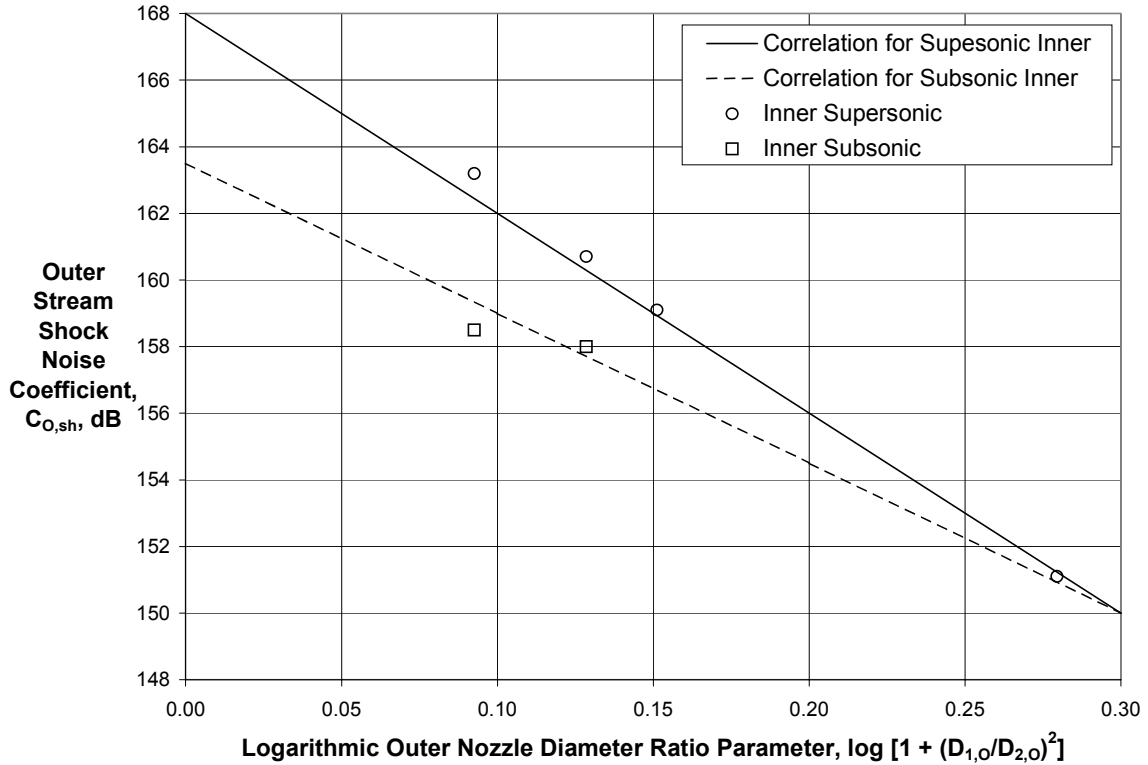
Figure 48 – Correlation of Outer Stream Shock Noise Coefficient with Outer Stream Diameter Ratio
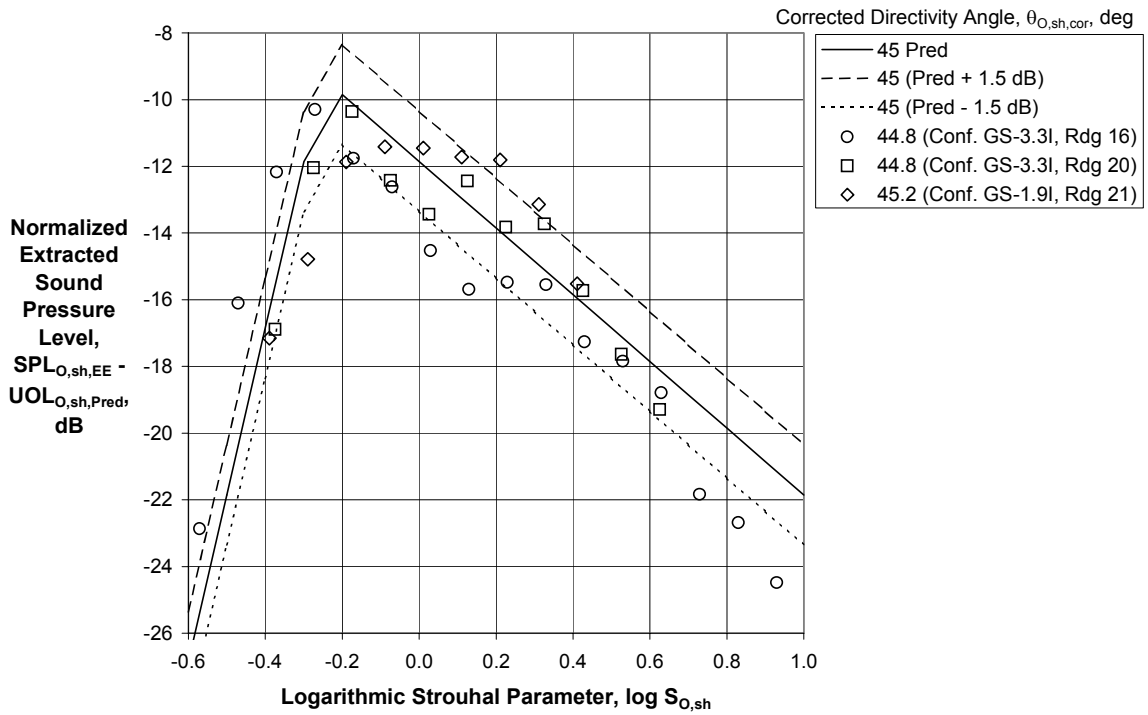
(a) Corrected Directivity Angle, 44.8 < $\theta_{O,sh,cor}$ < 45.2 deg

Figure 49 – Outer Stream Shock Noise Spectral Directivity Correlation
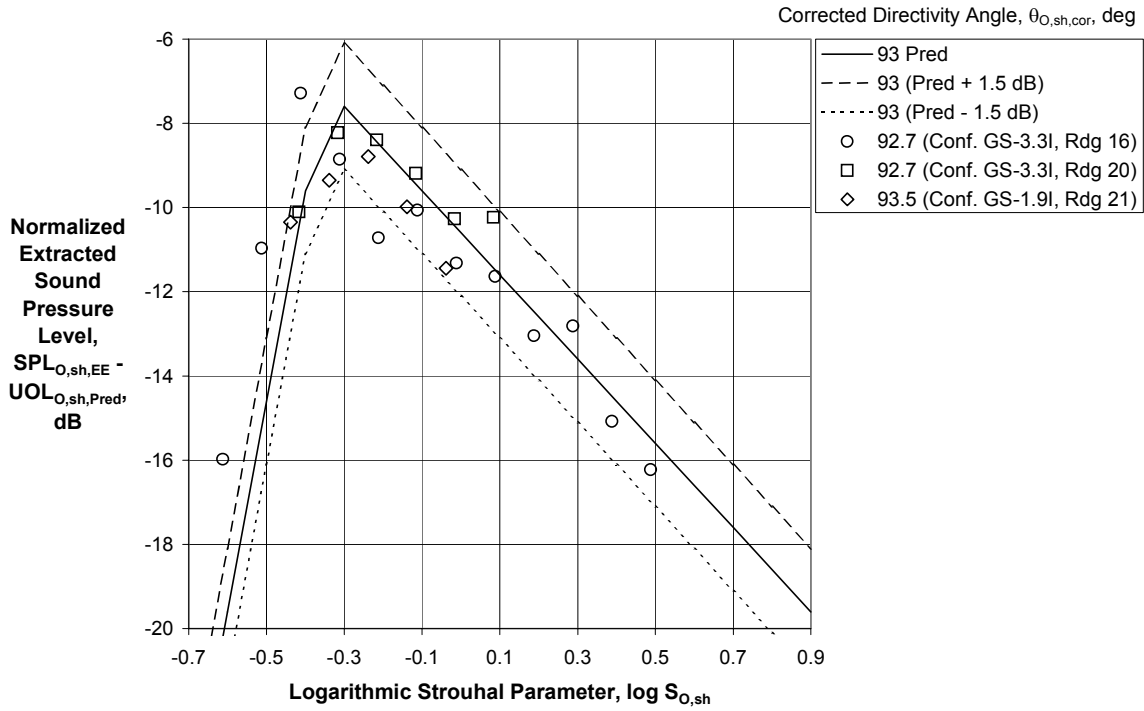
(b) Corrected Directivity Angle, 92.7 < θ_O,sh,cor < 93.5 deg

Figure 49 (Concluded) – Outer Stream Shock Noise Spectral Directivity Correlation
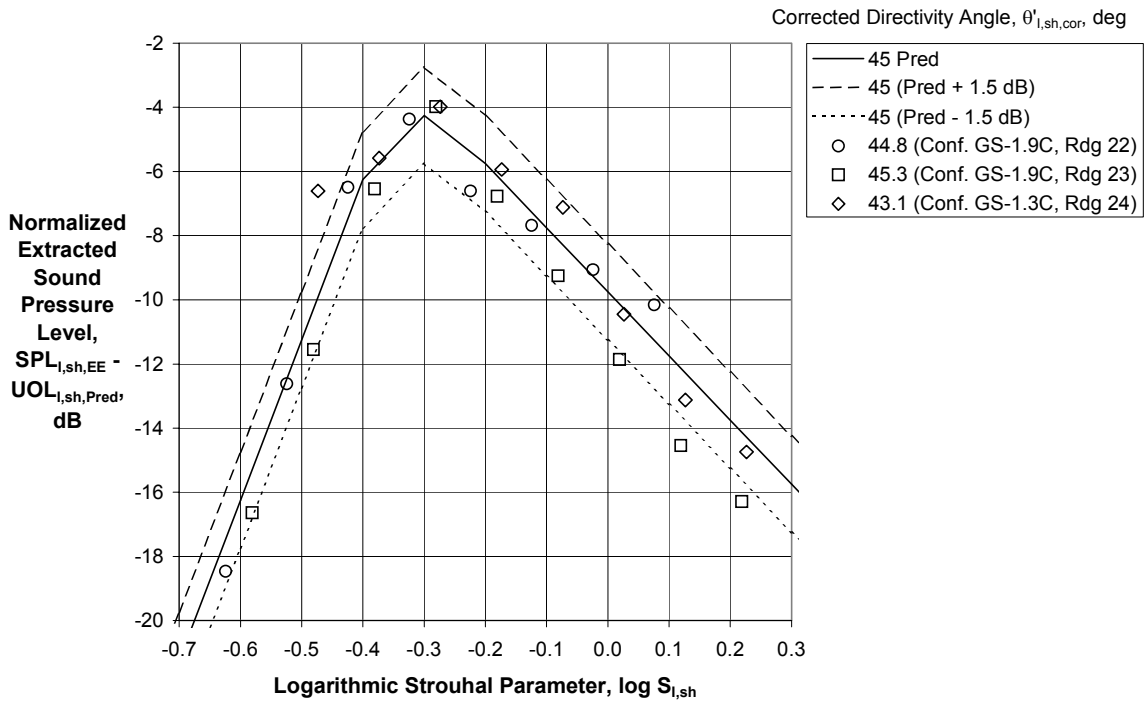
(a) Corrected Directivity Angle, 43.1 < θ_I,sh,cor < 45.3 deg

Figure 50 – Inner Stream Shock Noise Spectral Directivity Correlation
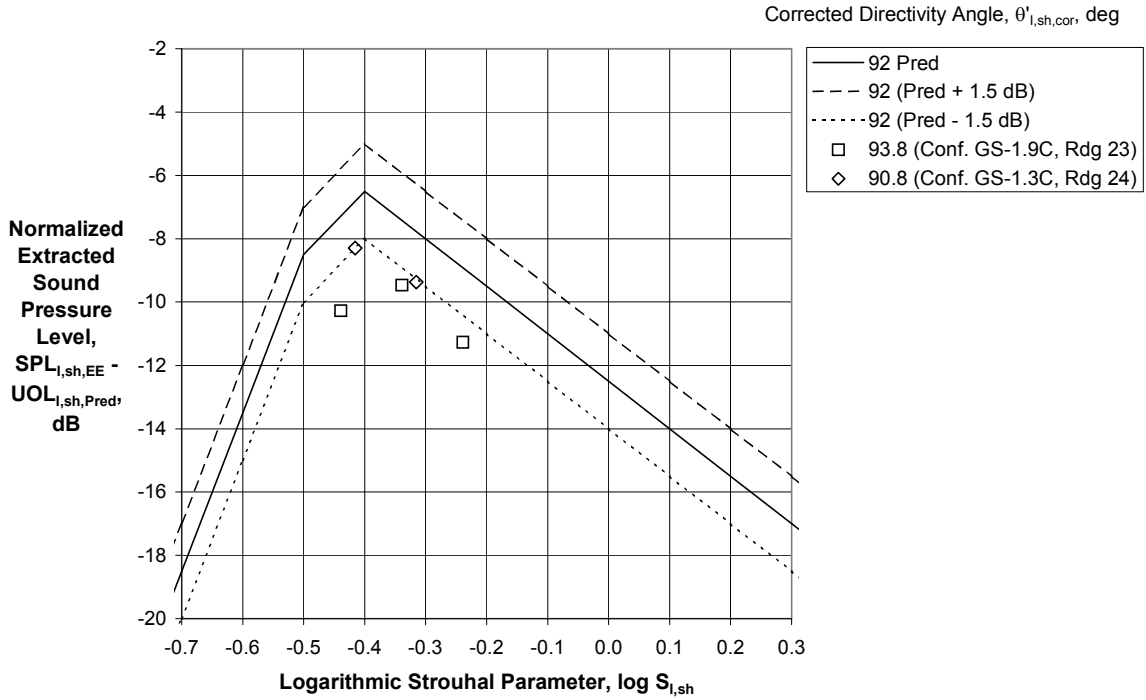
(b) Corrected Directivity Angle, 90.8 < $\theta_{l,sh,cor}$ < 93.8 deg

Figure 50 (Concluded) – Inner Stream Shock Noise Spectral Directivity Correlation
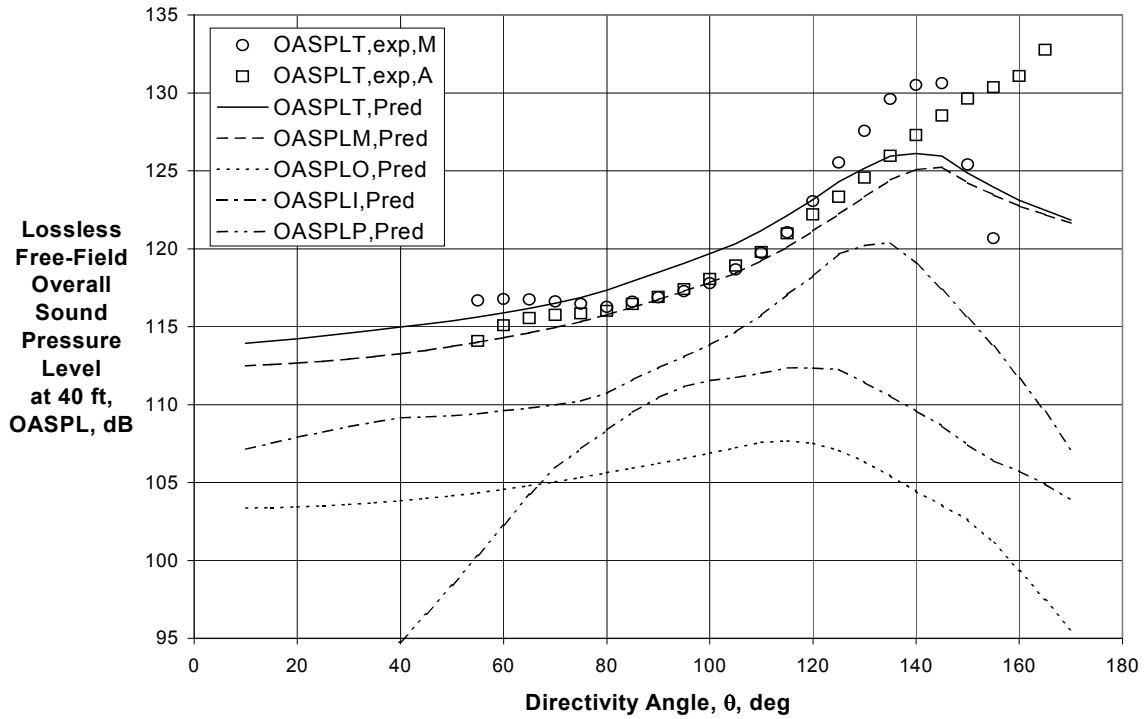
Figure 51 – Impact of Flight Transformation Methodology on Comparison of Experimental and Final Predicted Directivities for V_{mix}/c_{amb} = 1.087, M_f = 0.28 (A_O/A_I = 2.75, Ref. 24, Rdg. 396)
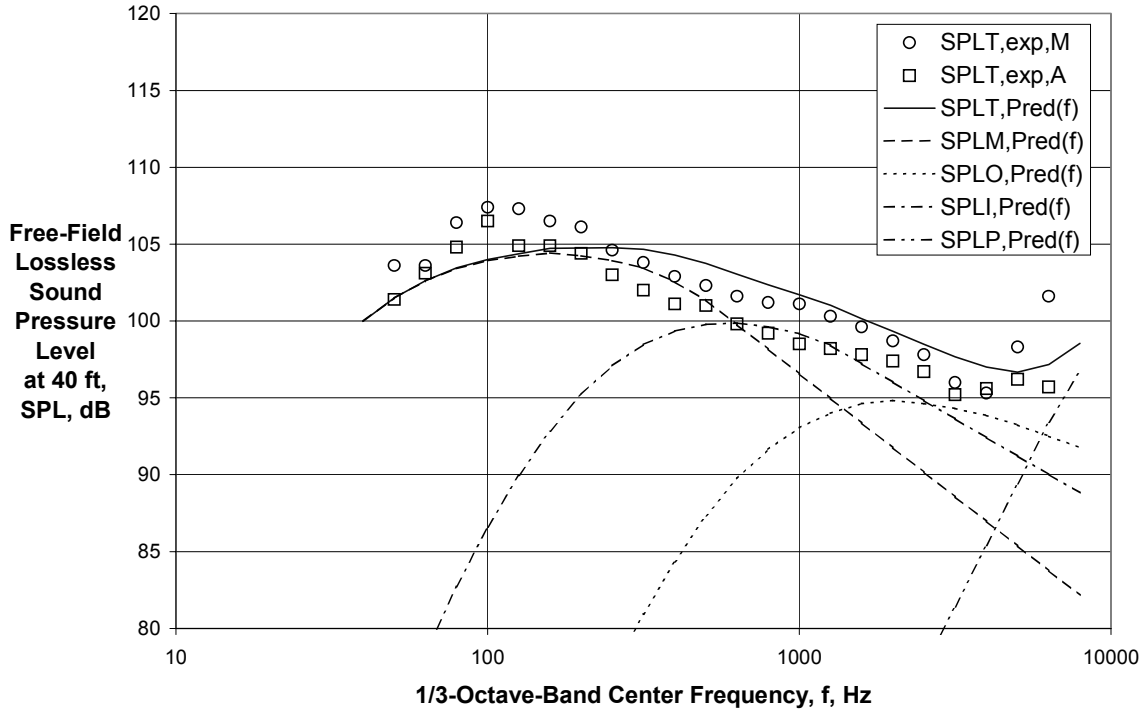
(a) Directivity Angle = 60 deg
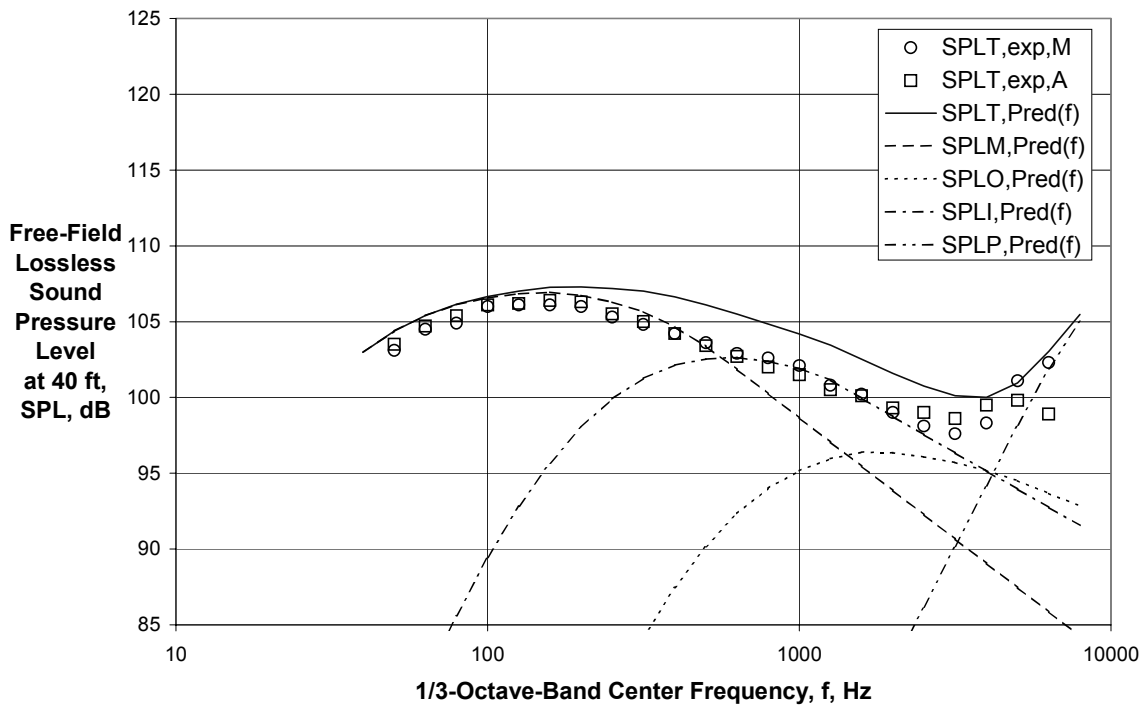
(b) Directivity Angle = 90 deg

Figure 52 - Impact of Flight Transformation Methodology on Comparison of Experimental and Final Predicted Spectra for V_{mix}/c_{amb} = 1.087, M_f = 0.28 (A_O/A_I = 2.75, Ref. 24, Rdg. 396)
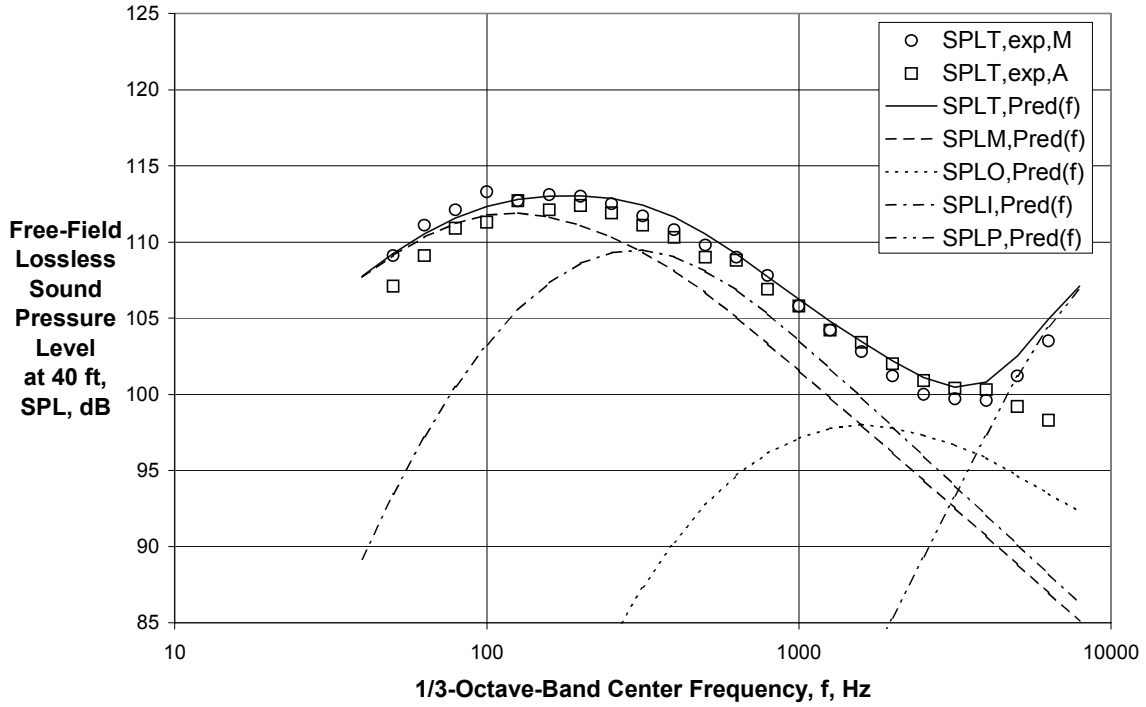
(c) Directivity Angle = 120 deg
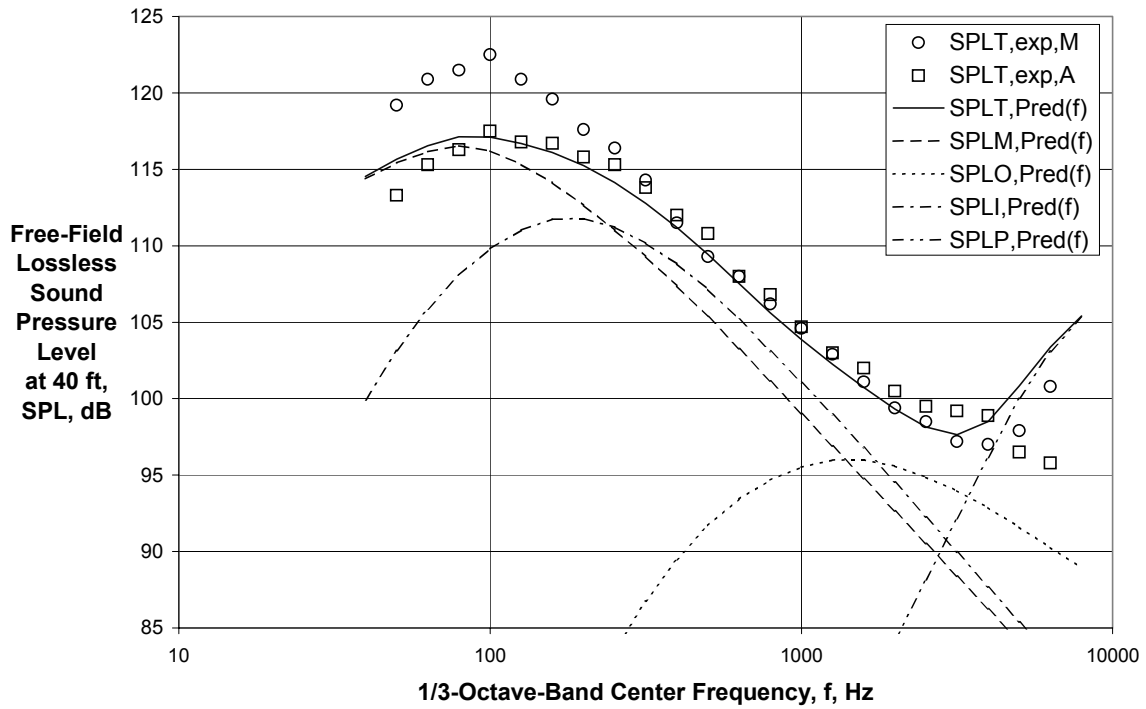
(d) Directivity Angle = 135 deg

Figure 52 (Continued) - Impact of Flight Transformation Methodology on Comparison of Experimental and Final Predicted Spectra for V_{mix}/c_{amb} = 1.087, M_f = 0.28 (A_O/A_I = 2.75, Ref. 24, Rdg. 396)
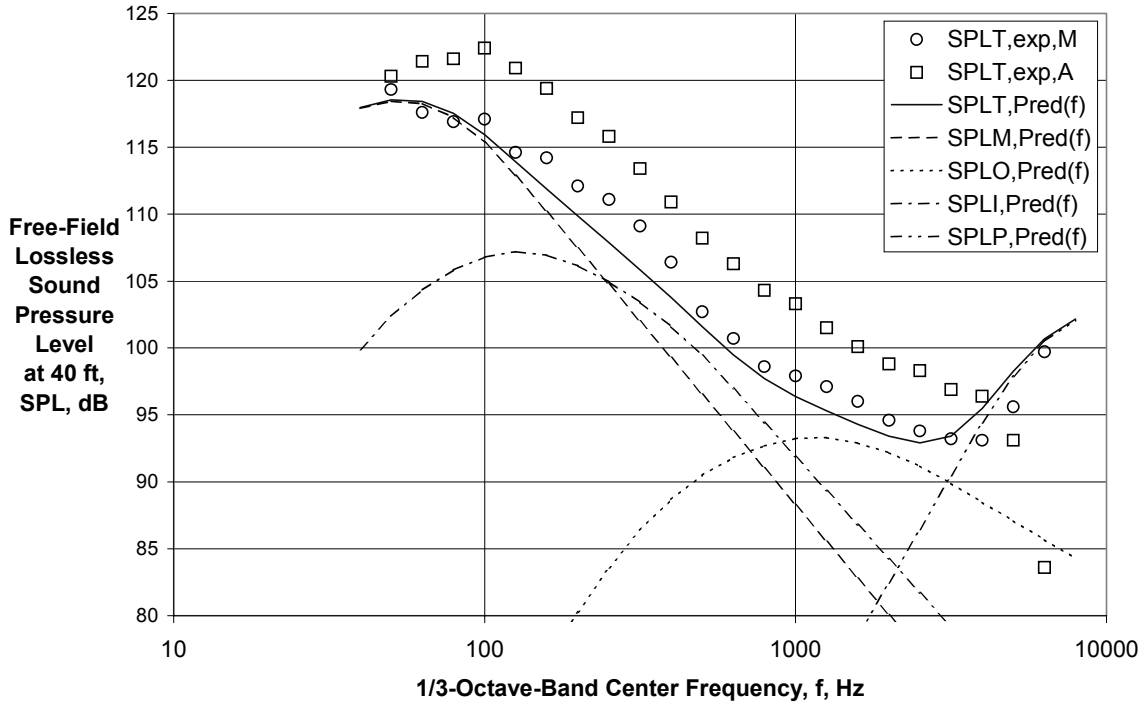
(e) Directivity Angle = 150 deg
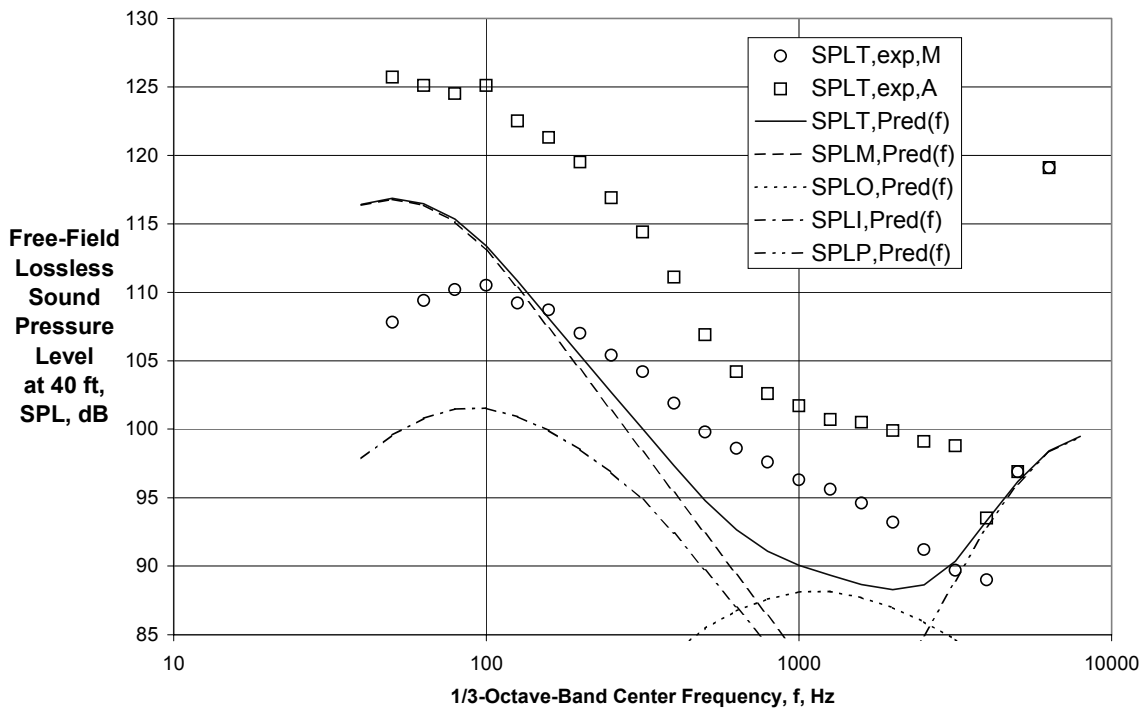
(f) Directivity Angle = 165 deg

Figure 52 (Concluded) - Impact of Flight Transformation Methodology on Comparison of Experimental and Final Predicted Spectra for V_{mix}/c_{amb} = 1.087, M_f = 0.28 (A_O/A_I = 2.75, Ref. 24, Rdg. 396)
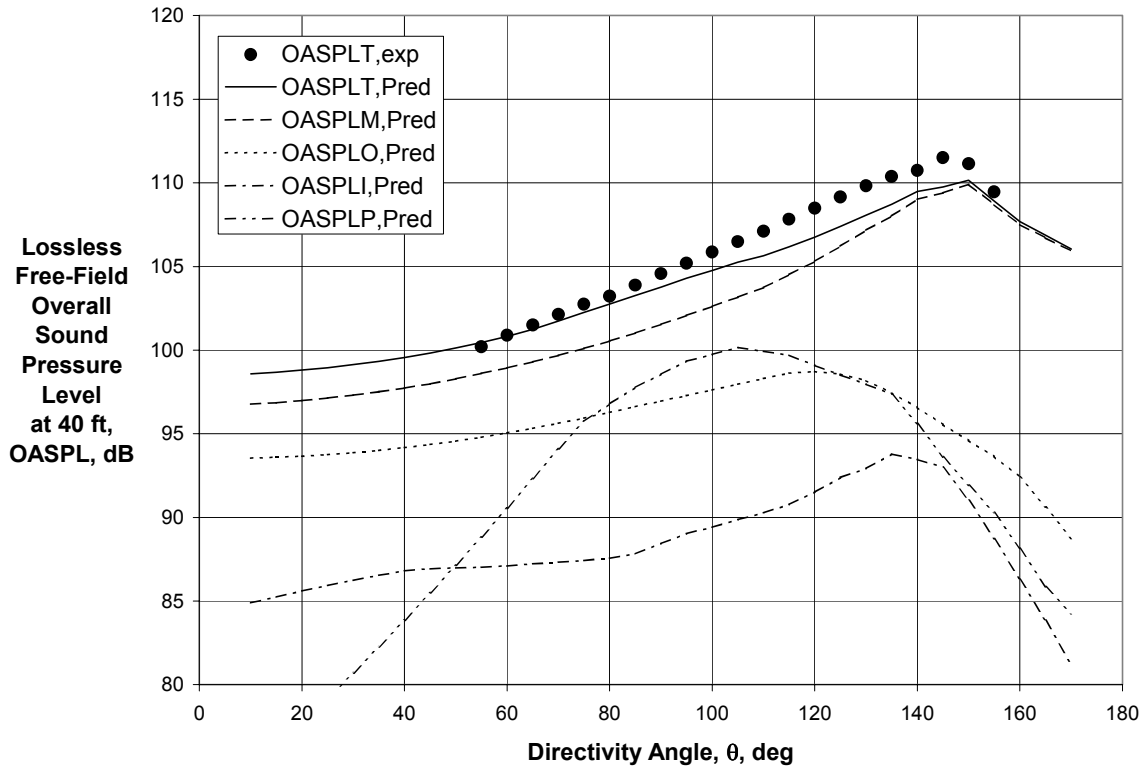
Figure 53 - Comparison of Experimental and Final Predicted Directivities for V_{mix}/c_{amb} = 0.635, M_f = 0.0 (A_O/A_I = 2.75, Ref. 24, Rdg. 378)
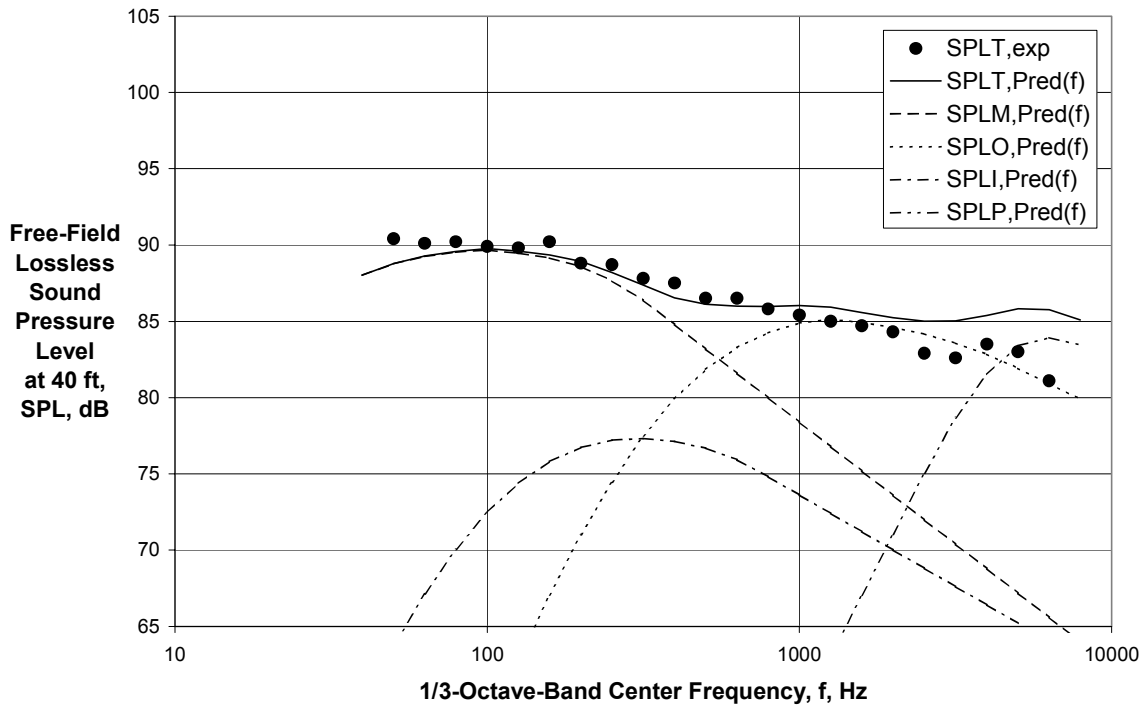
(a) Directivity Angle = 60 deg

Figure 54 - Comparison of Experimental and Final Predicted Spectra for V_{mix}/c_{amb} = 0.635, M_f = 0.0 (A_O/A_I = 2.75, Ref. 24, Rdg. 378)
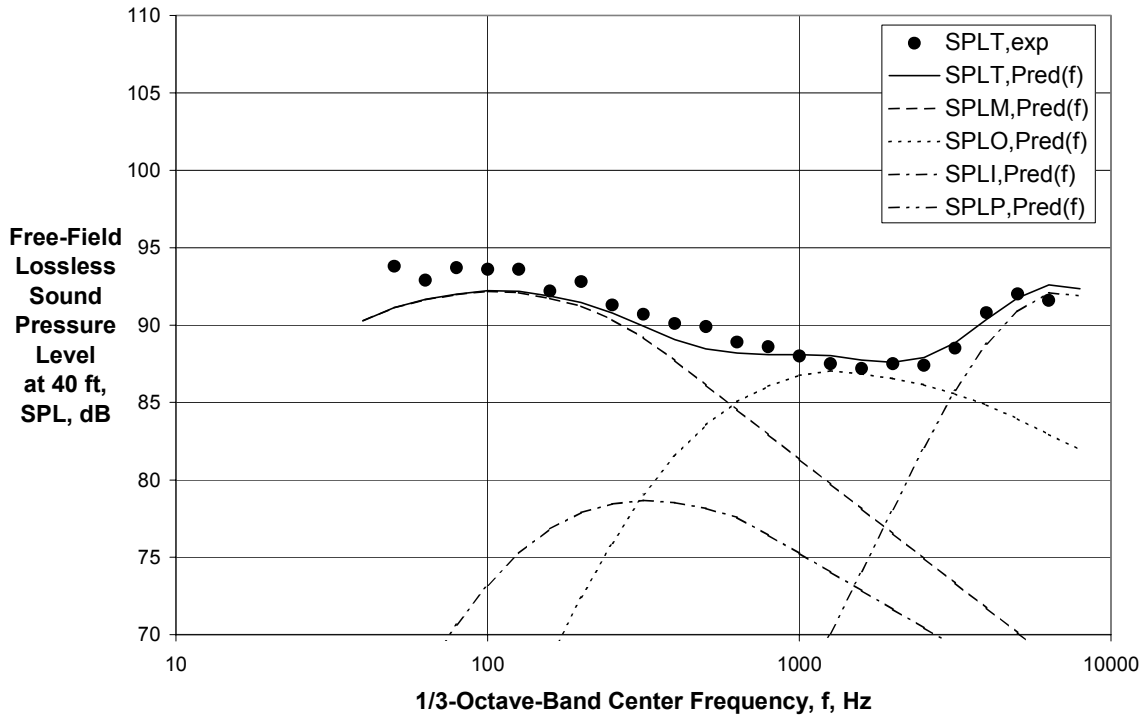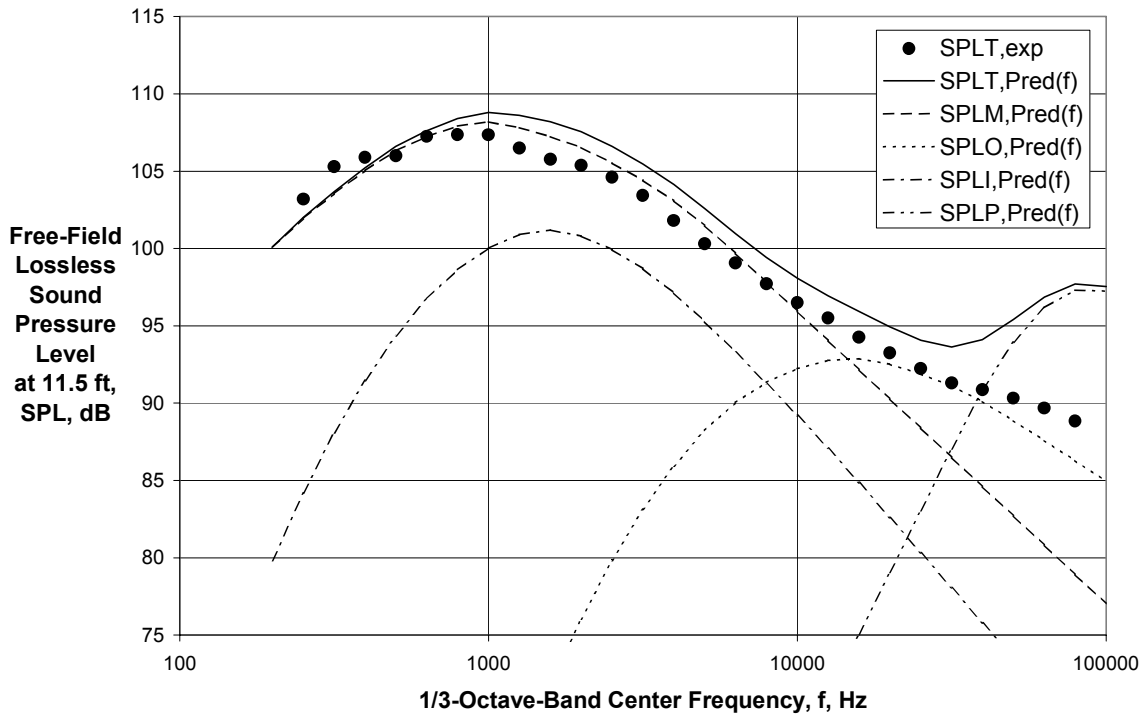
(b) Directivity Angle = 90 deg
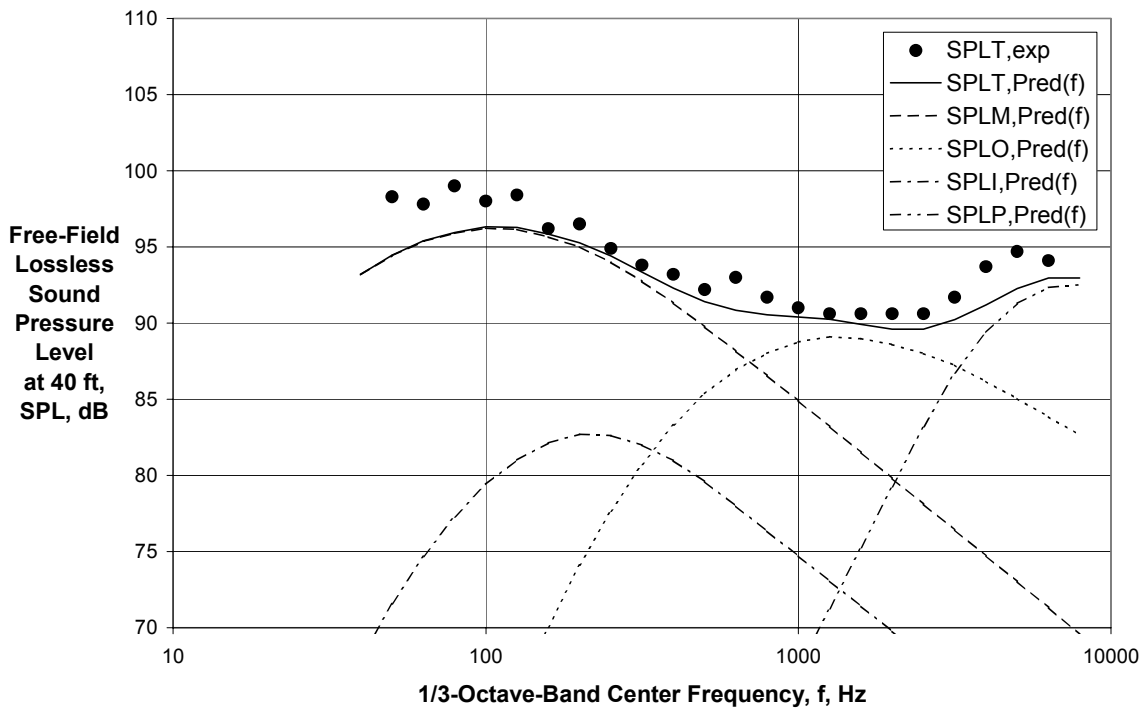
(c) Directivity Angle = 120 deg

Figure 54 (Continued) - Comparison of Experimental and Final Predicted Spectra for V_{mix}/c_{amb} = 0.635, M_f = 0.0 (A_O/A_I = 2.75, Ref. 24, Rdg. 378)
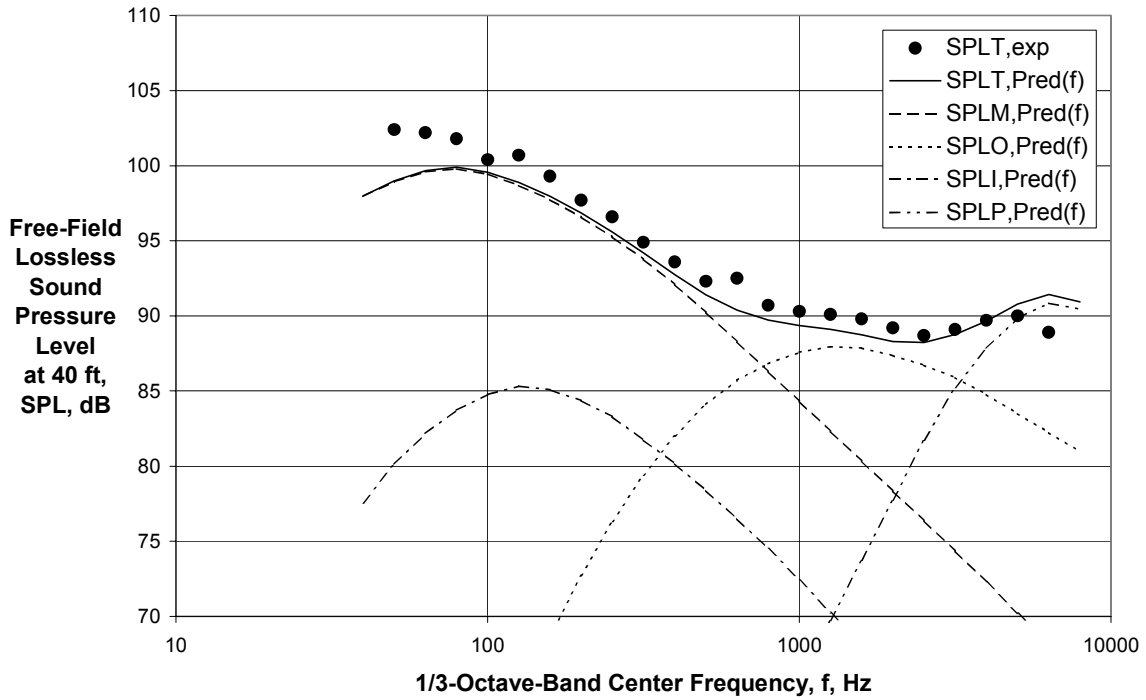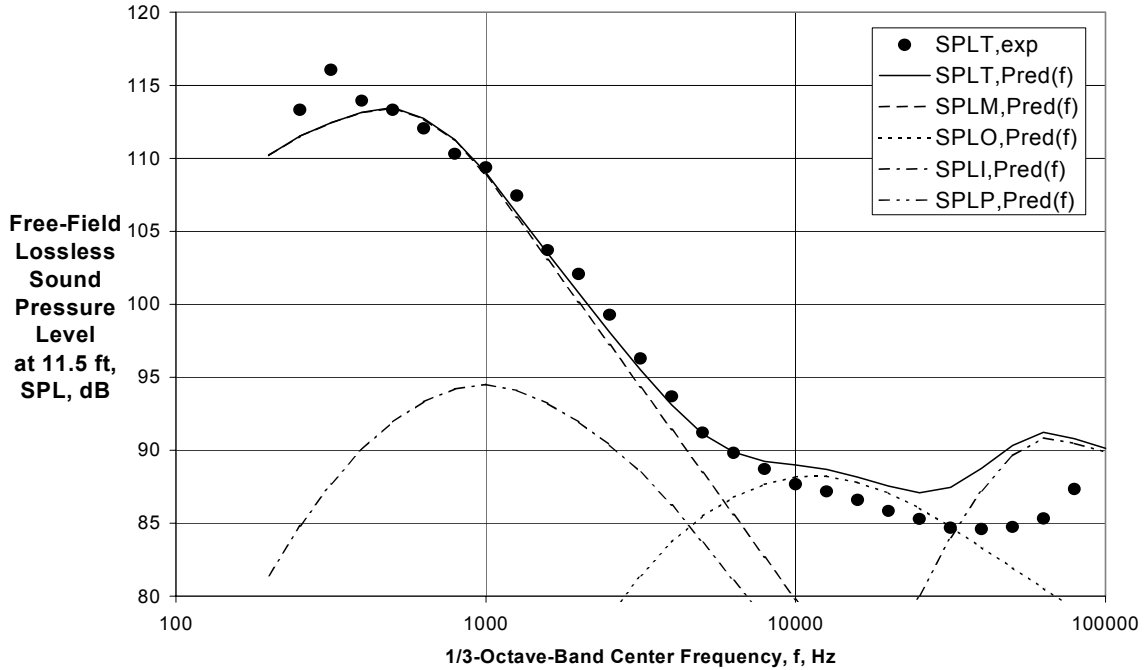
(d) Directivity Angle = 135 deg
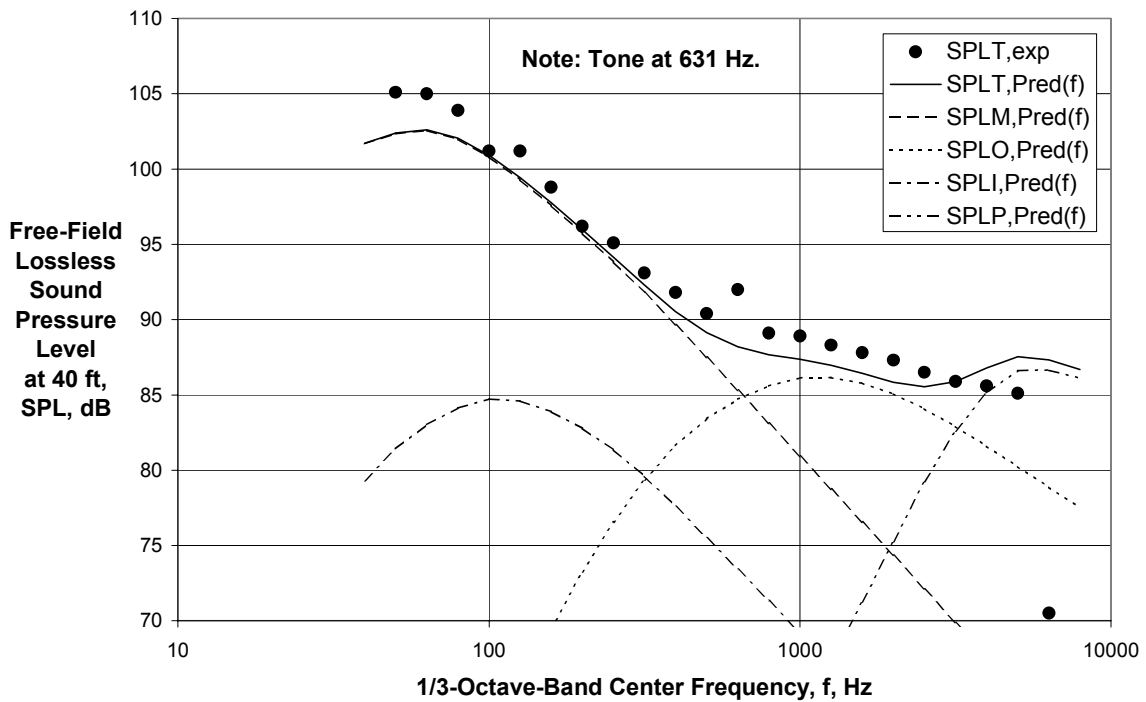
(e) Directivity Angle = 145 deg

Figure 54 (Continued) - Comparison of Experimental and Final Predicted Spectra for V_{mix}/c_{amb} = 0.635, M_f = 0.0 (A_O/A_I = 2.75, Ref. 24, Rdg. 378)

Note: tone at 631 Hz and bad data at 5 & 6.3 kHz.
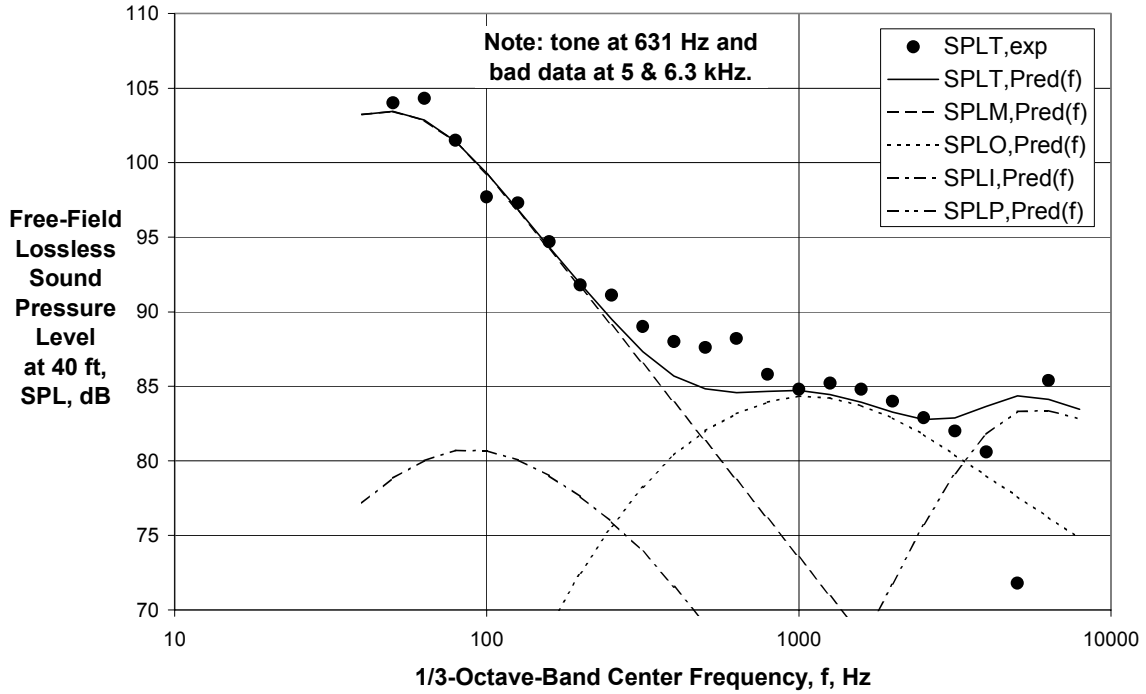
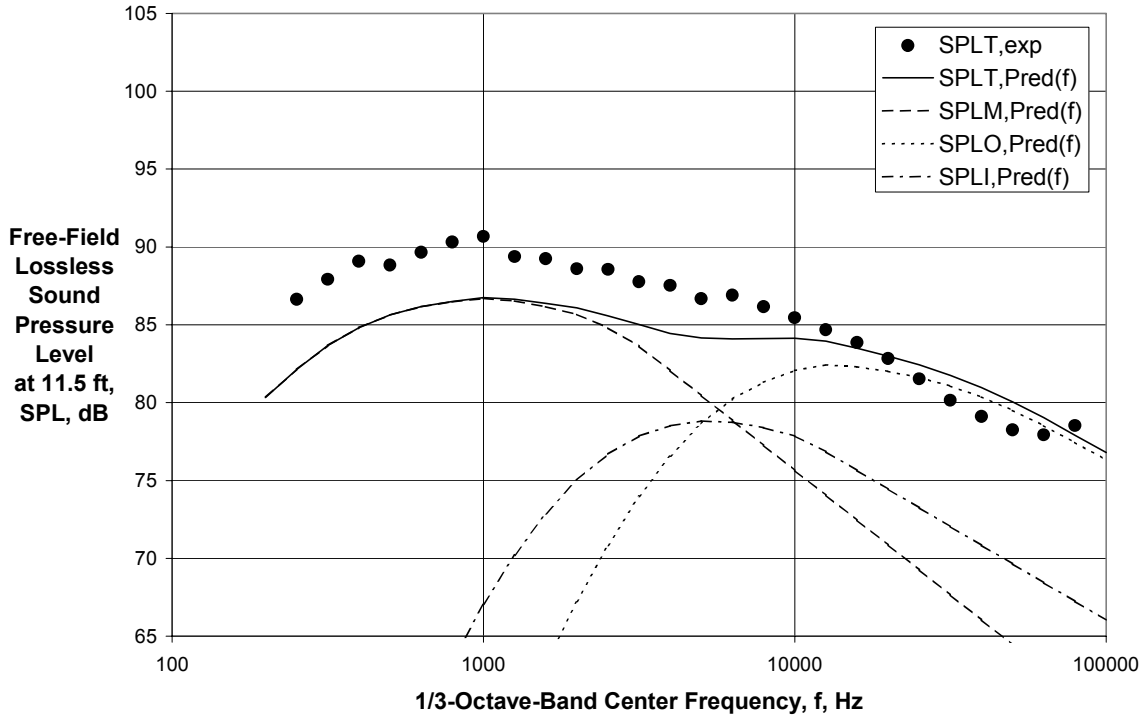**(f) Directivity Angle = 155 deg**

Figure 54 (Concluded) - Comparison of Experimental and Final Predicted Spectra for V_{mix}/c_{amb} = 0.635, M_f = 0.0 (A_O/A_I = 2.75, Ref. 24, Rdg. 378)
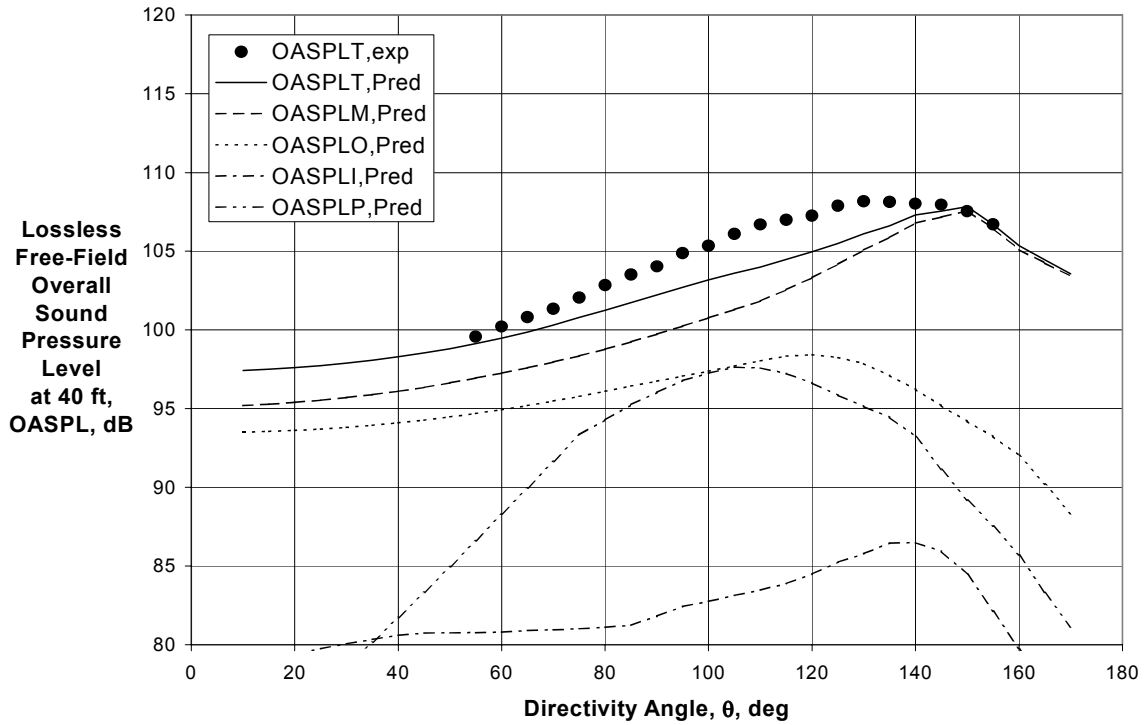
Figure 55 - Comparison of Experimental and Final Predicted Directivities for V_{mix}/c_{amb} = 0.613, M_f = 0.0 (A_O/A_I = 3.74, Ref. 24, Rdg. 1008)
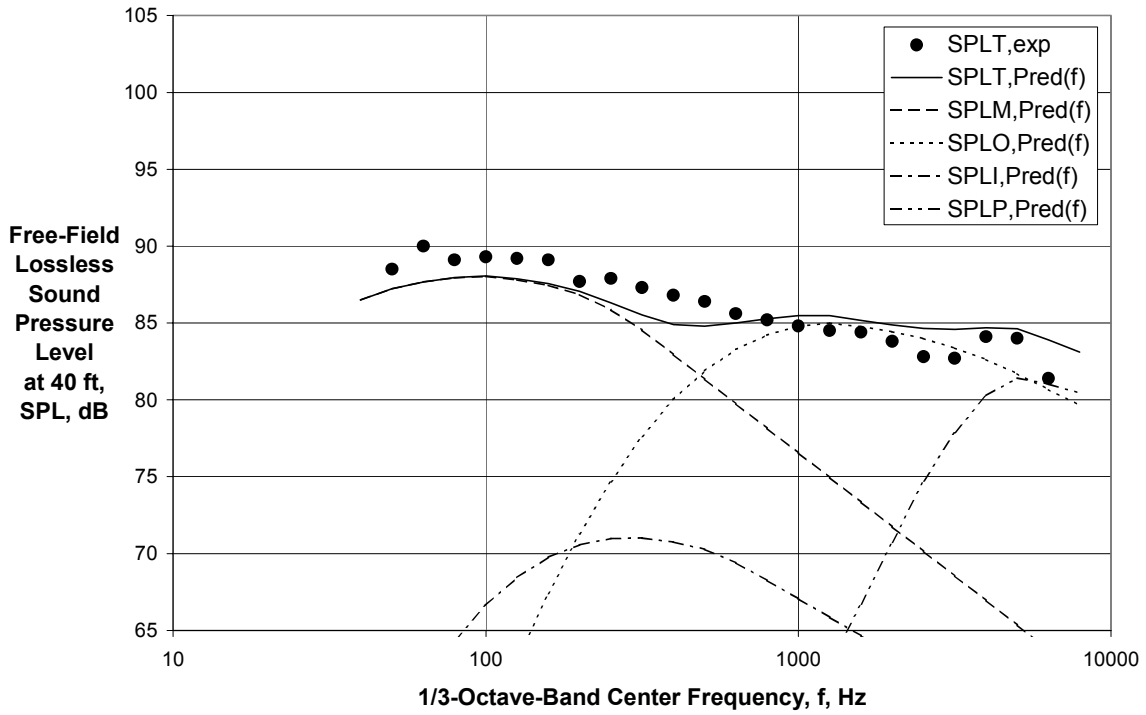
(a) Directivity Angle = 60 deg
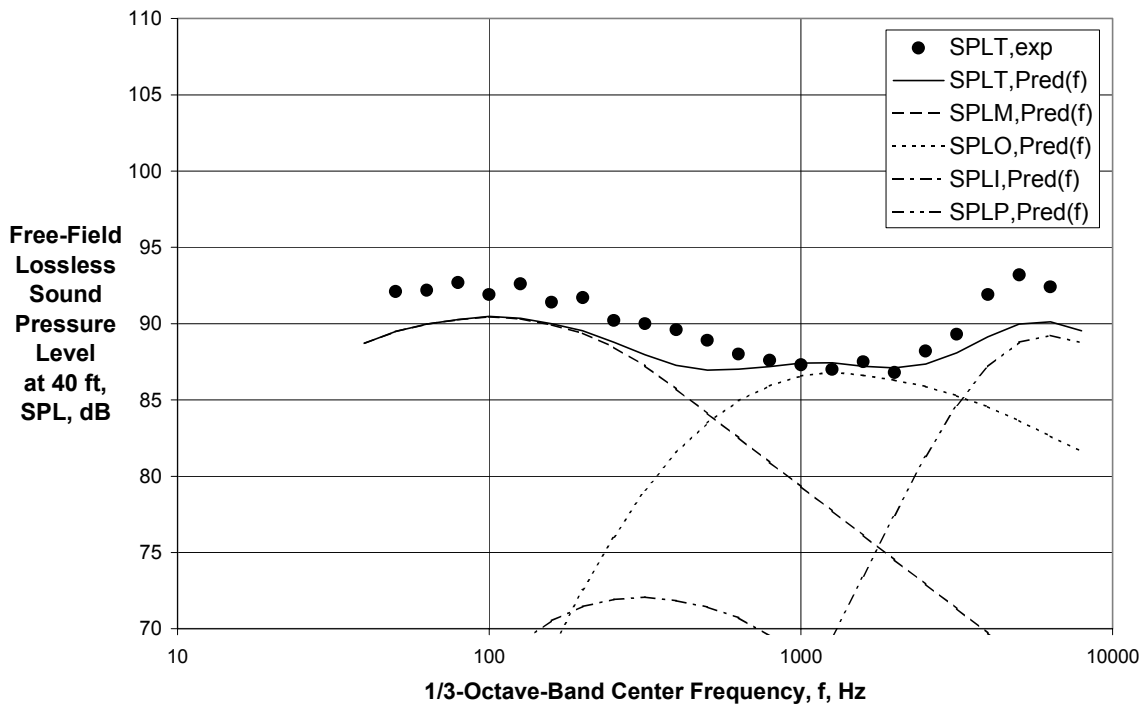
(b) Directivity Angle = 90 deg

Figure 56 - Comparison of Experimental and Final Predicted Spectra for
$V_{mix}/c_{amb} = 0.613$, $M_f = 0.0$ ($A_O/A_I = 3.74$, Ref. 24, Rdg. 1008)
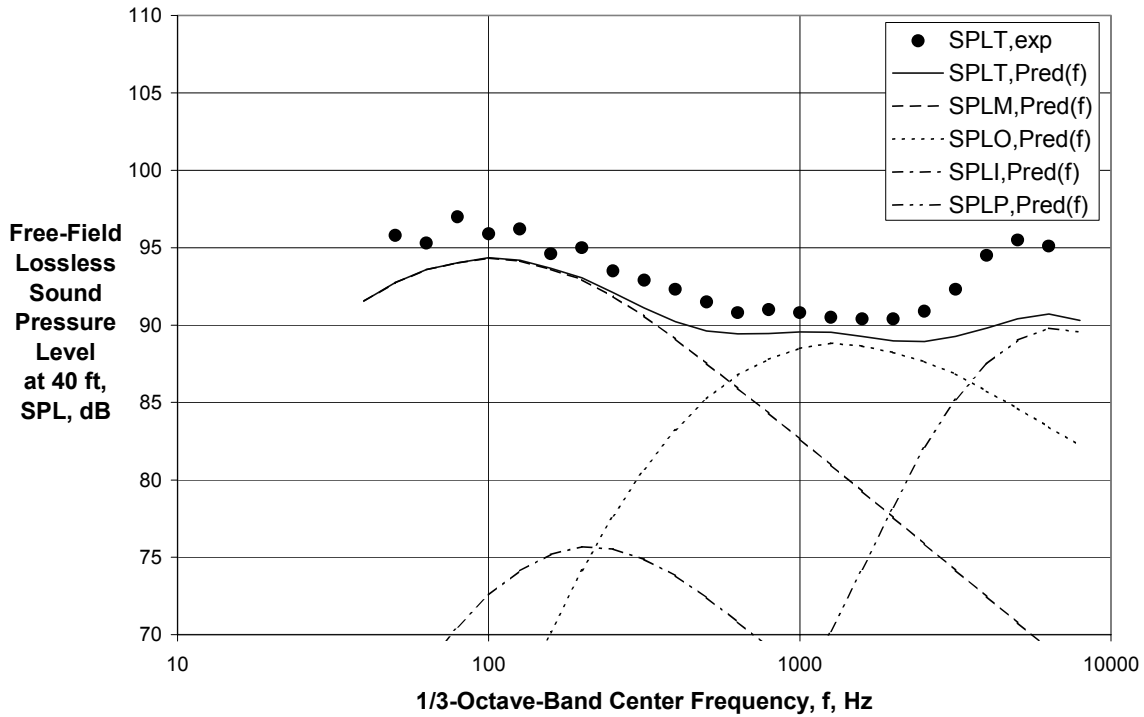
(c) Directivity Angle = 120 deg
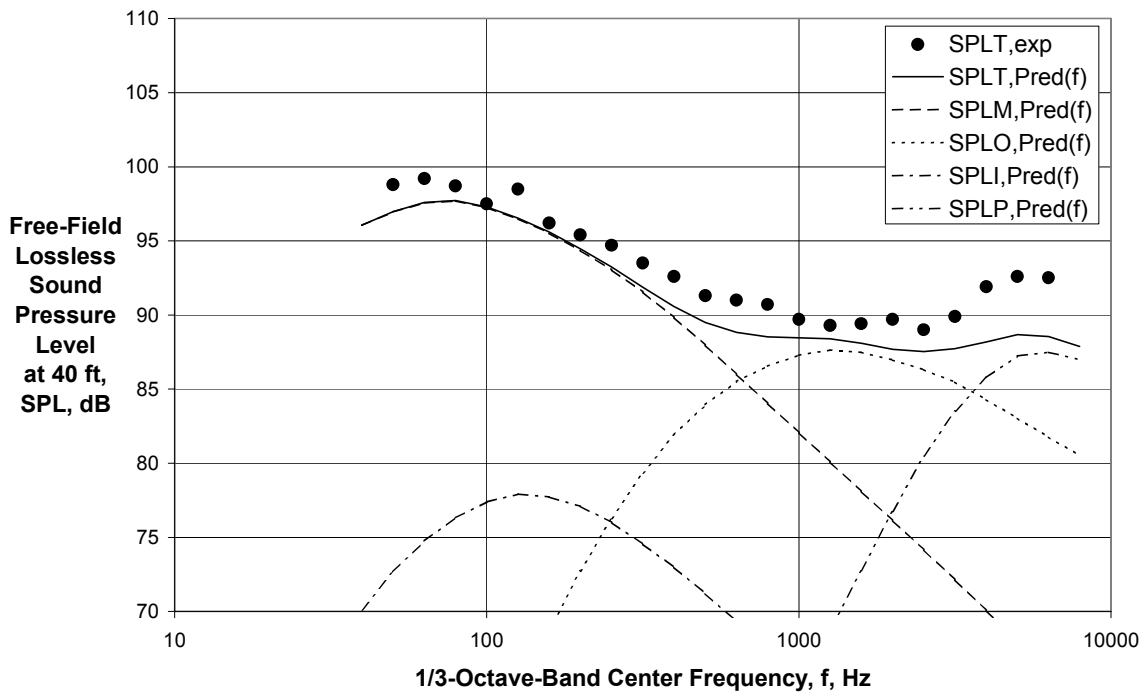
(d) Directivity Angle = 135 deg

Figure 56 (Continued) - Comparison of Experimental and Final Predicted Spectra for V_{mix}/c_{amb} = 0.613, M_f = 0.0 (A_O/A_I = 3.74, Ref. 24, Rdg. 1008)
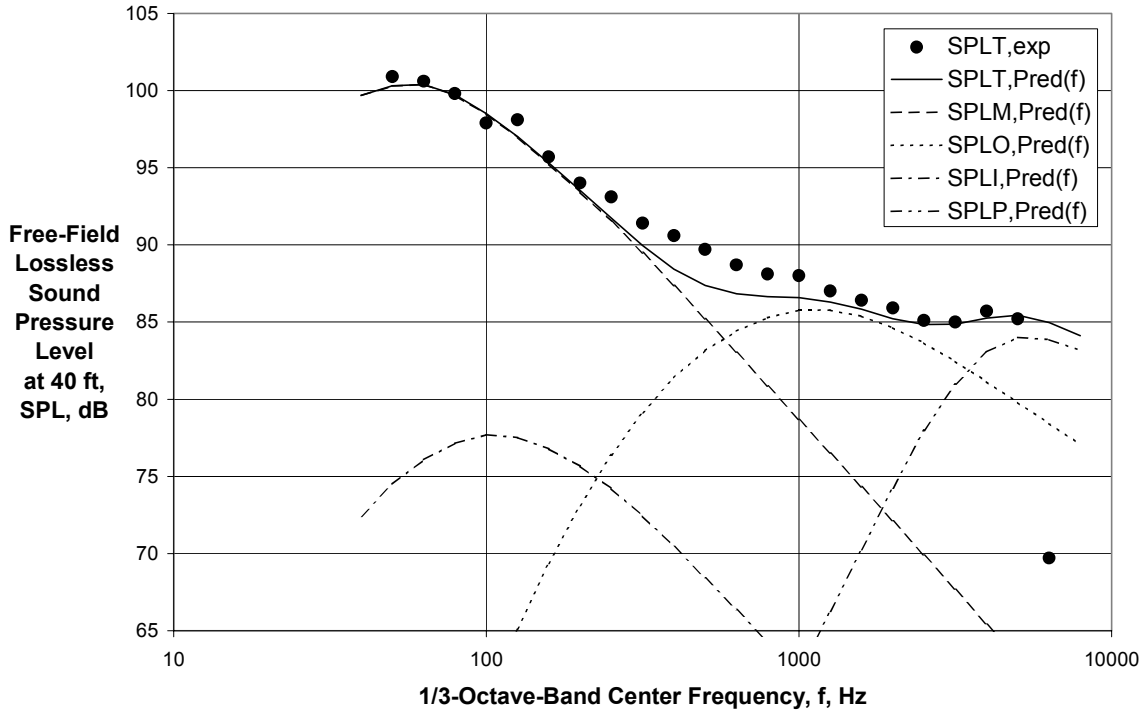
(e) Directivity Angle = 145 deg
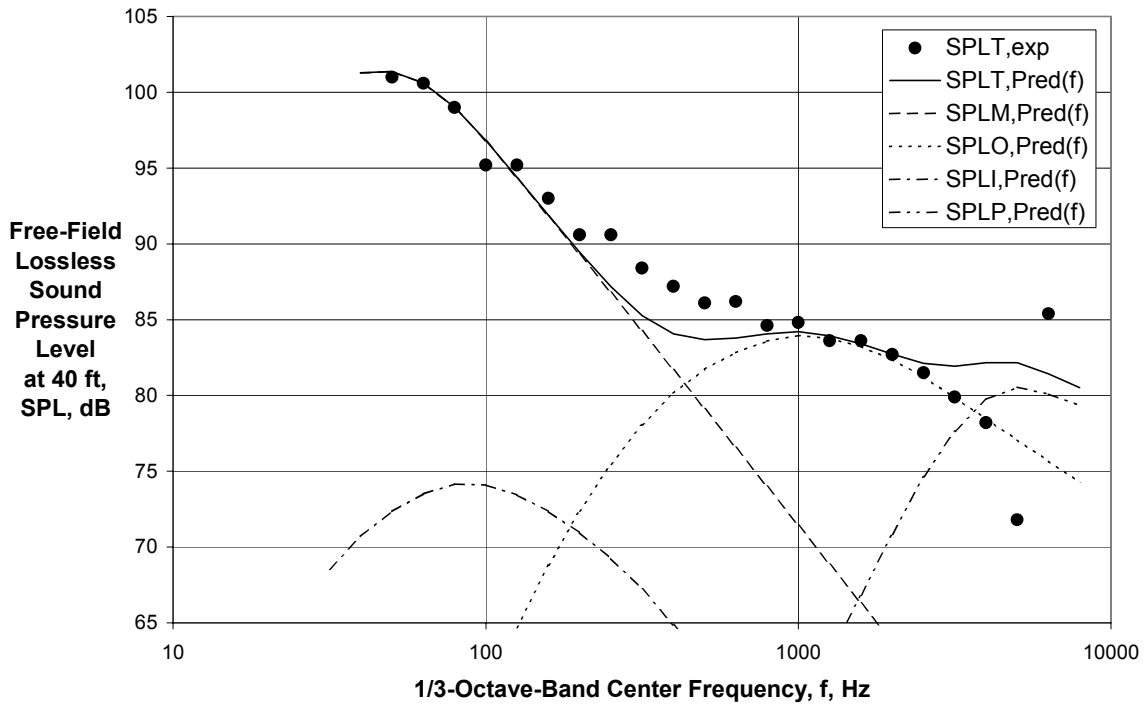
(f) Directivity Angle = 155 deg

Figure 56 (Concluded) - Comparison of Experimental and Final Predicted Spectra for V_{mix}/c_{amb} = 0.613, M_f = 0.0 (A_O/A_I = 3.74, Ref. 24, Rdg. 1008)
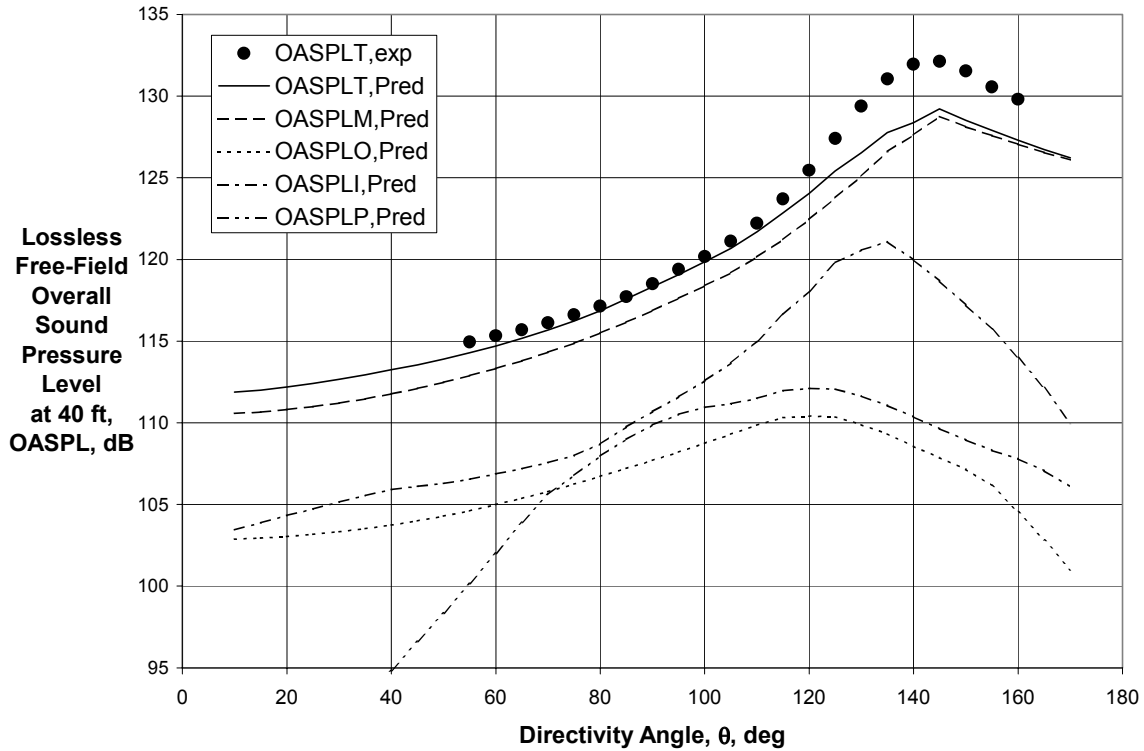
Figure 57 - Comparison of Experimental and Final Predicted Directivities for $V_{mix}/c_{amb} = 0.949$, $M_f = 0.0$ ($A_O/A_I = 3.74$, Ref. 24, Rdg. 1017)
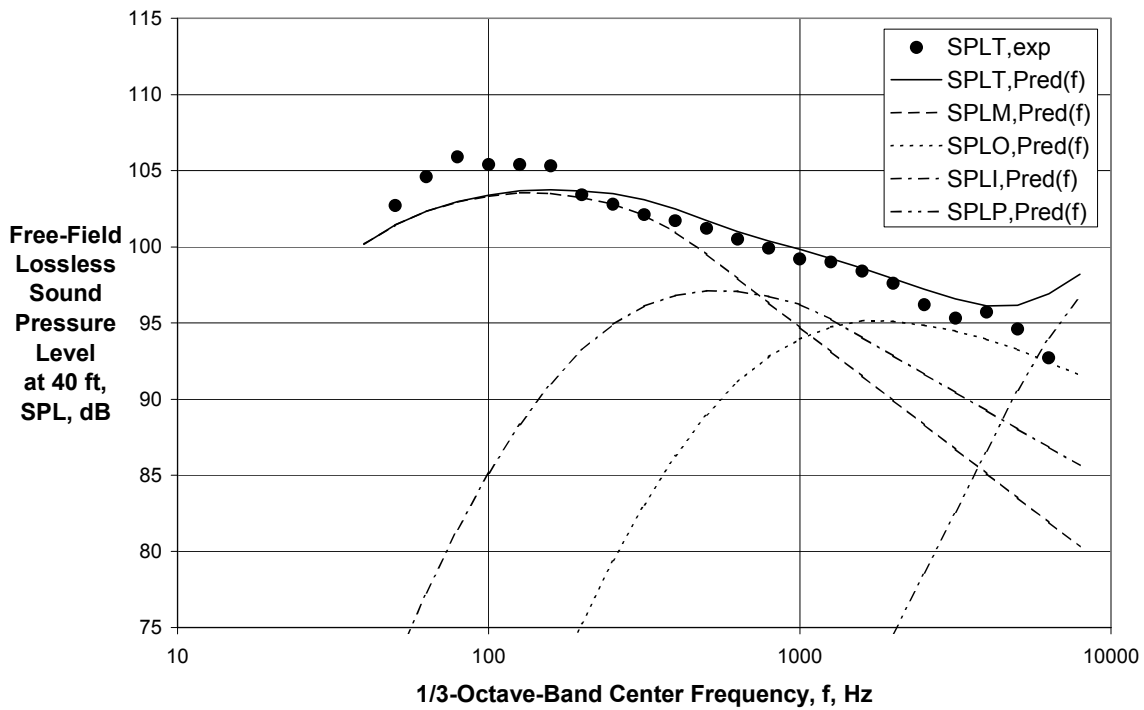
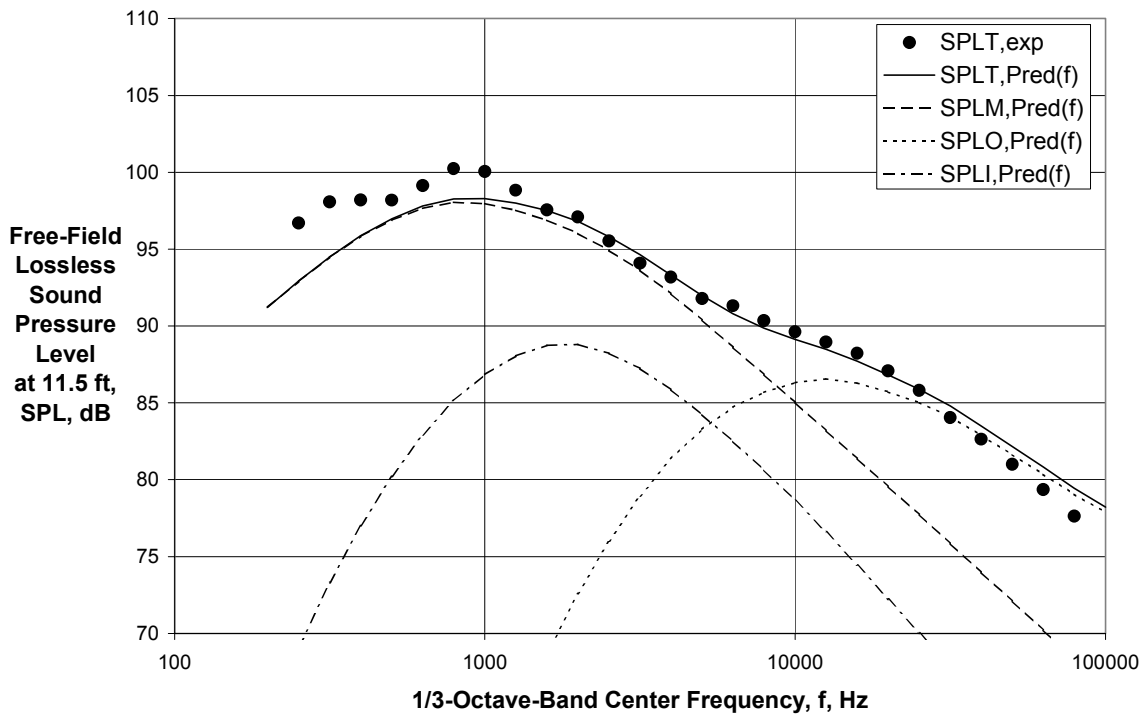**(a) Directivity Angle = 60 deg**

Figure 58 - Comparison of Experimental and Final Predicted Spectra for $V_{mix}/c_{amb} = 0.949$, $M_f = 0.0$ ($A_O/A_I = 3.74$, Ref. 24, Rdg. 1017)
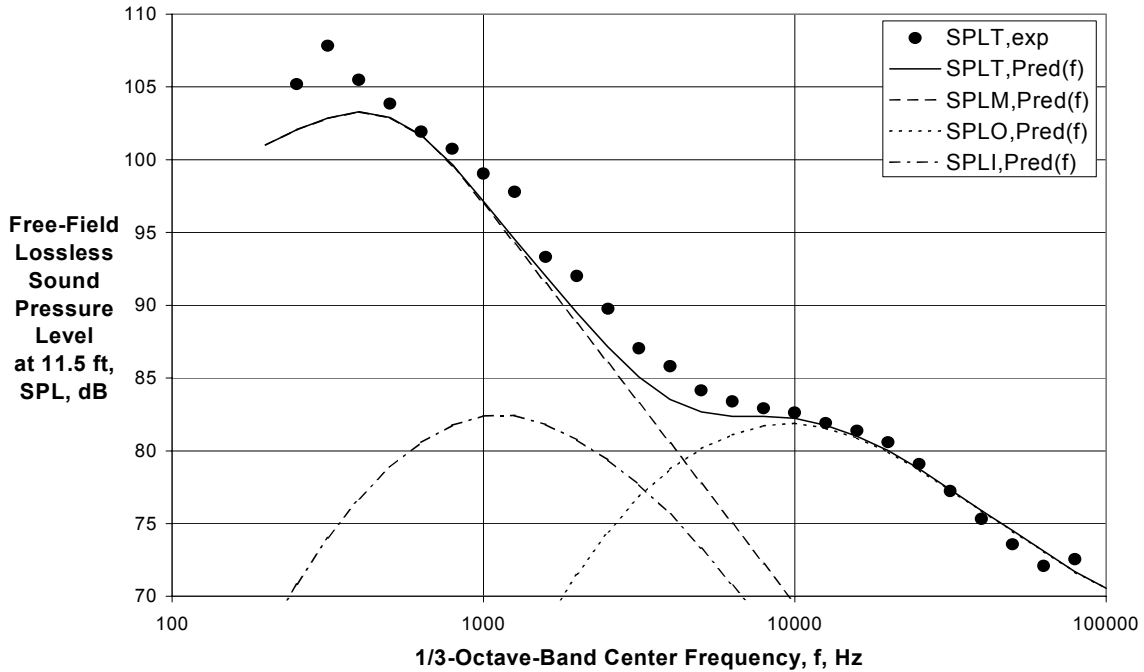
(b) Directivity Angle = 90 deg

(c) Directivity Angle = 120 deg
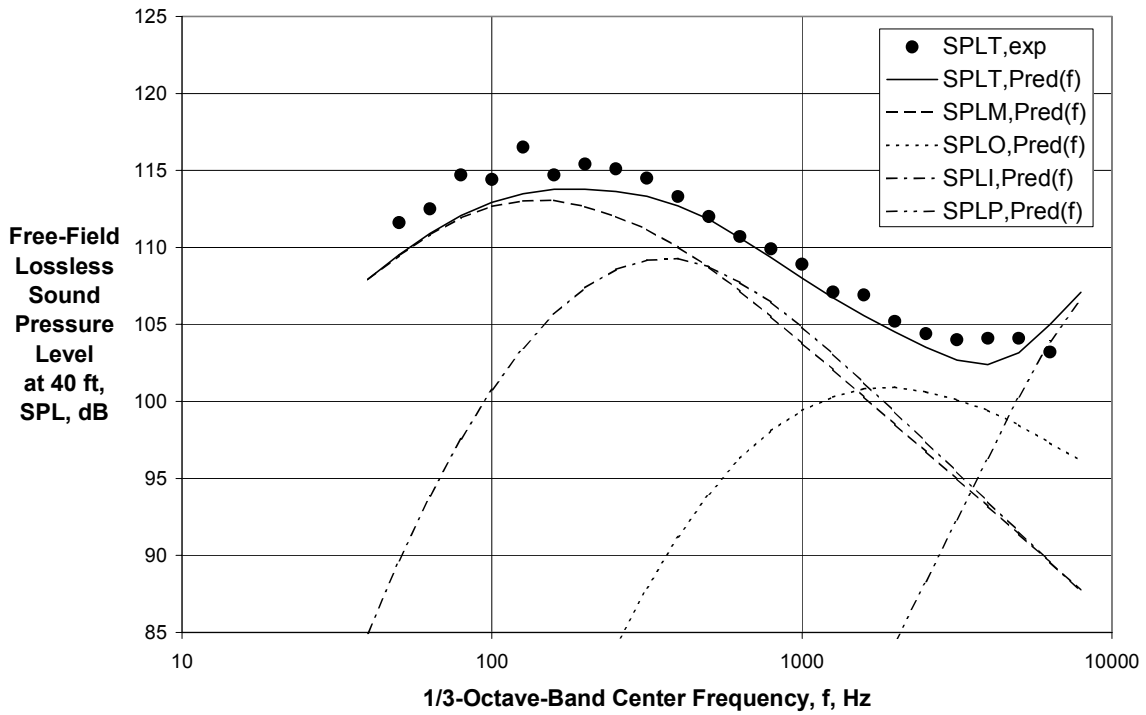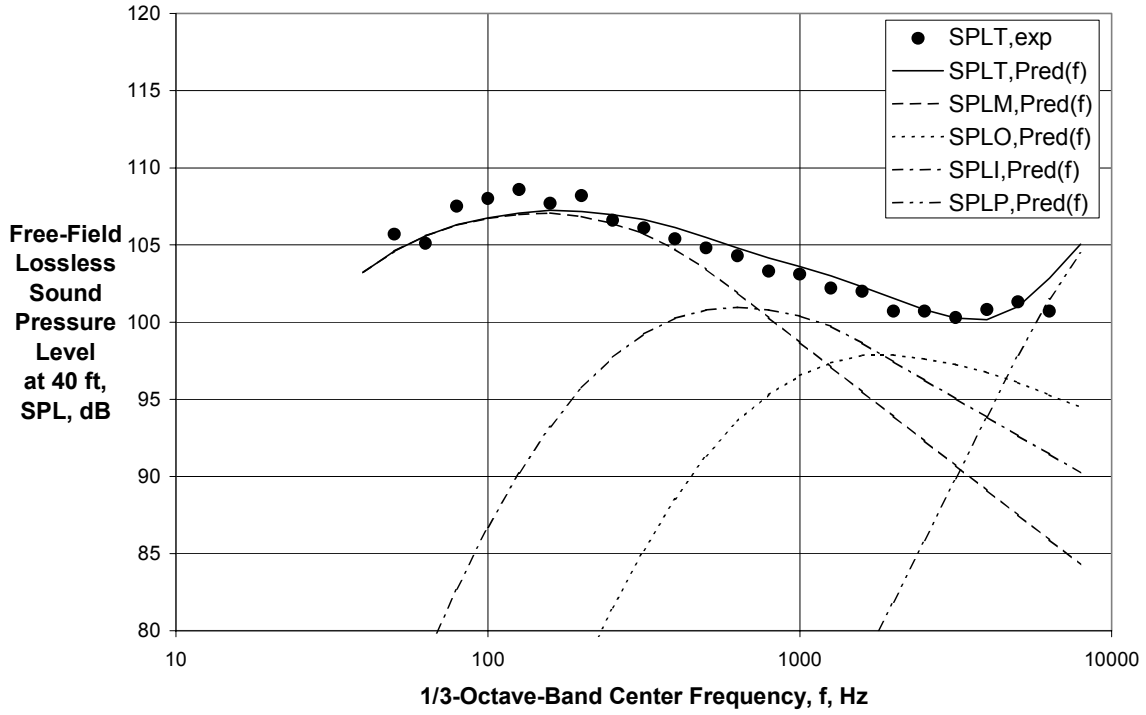
Figure 58 (Continued) - Comparison of Experimental and Final Predicted Spectra for V_{mix}/c_{amb} = 0.949, M_f = 0.0 (A_O/A_I = 3.74, Ref. 24, Rdg. 1017)
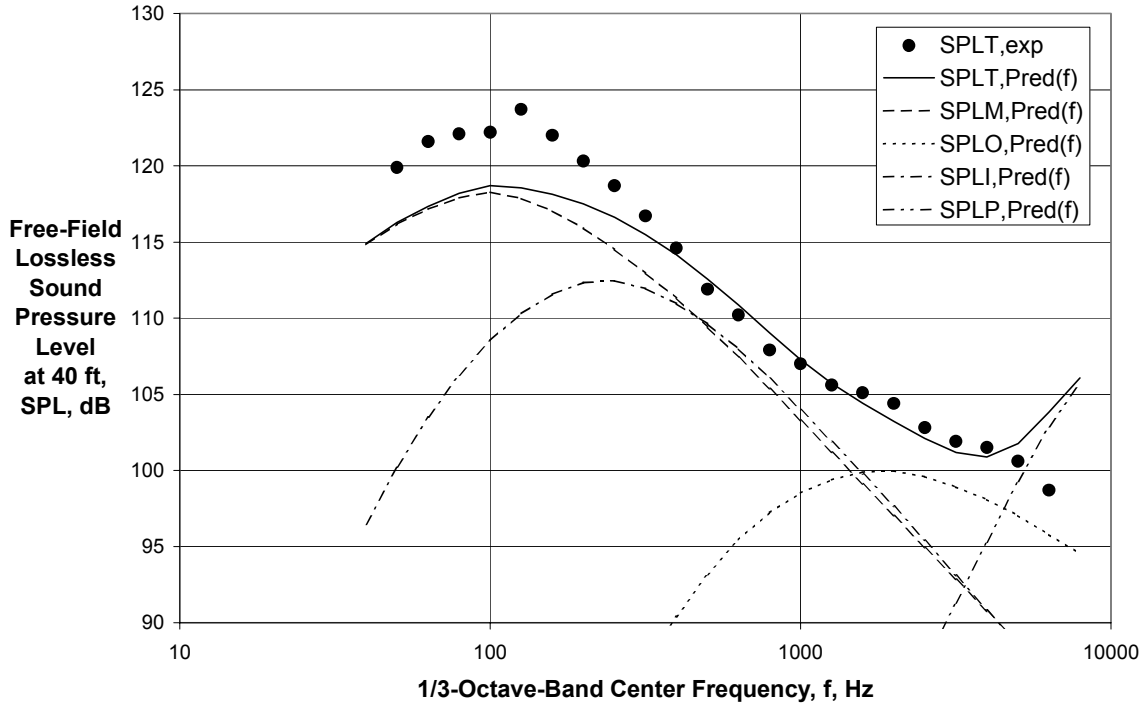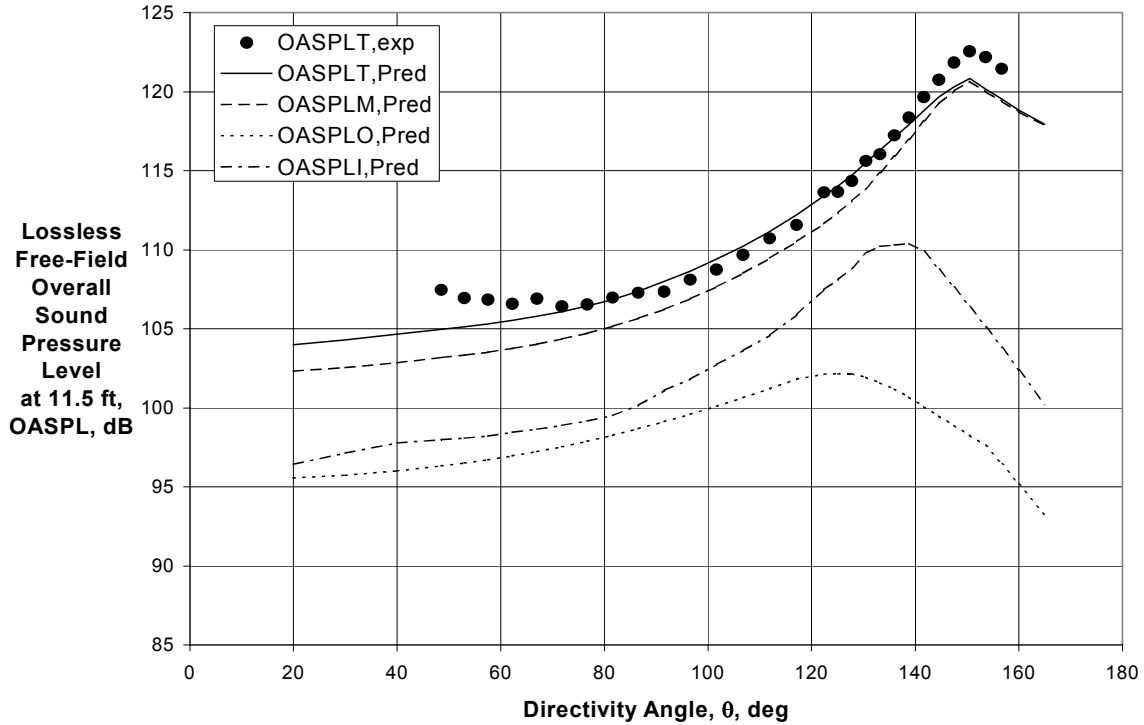
(d) Directivity Angle = 135 deg
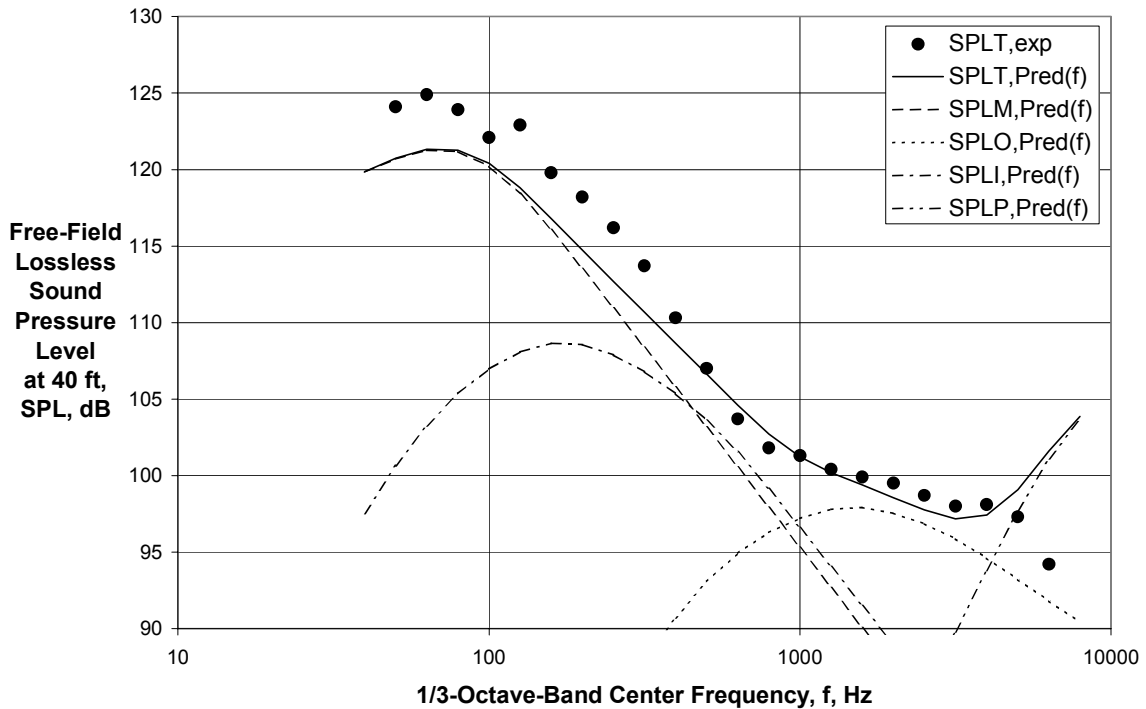
(e) Directivity Angle = 150 deg

Figure 58 (Continued) - Comparison of Experimental and Final Predicted Spectra for V_{mix}/c_{amb} = 0.949, M_f = 0.0 (A_O/A_I = 3.74, Ref. 24, Rdg. 1017)
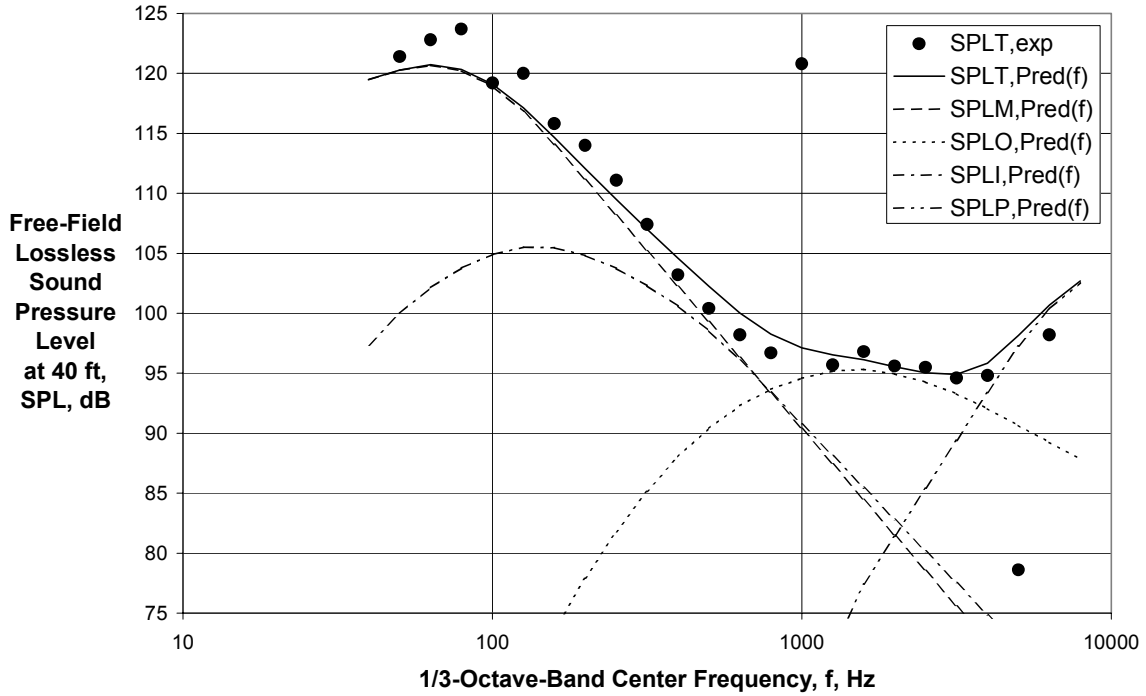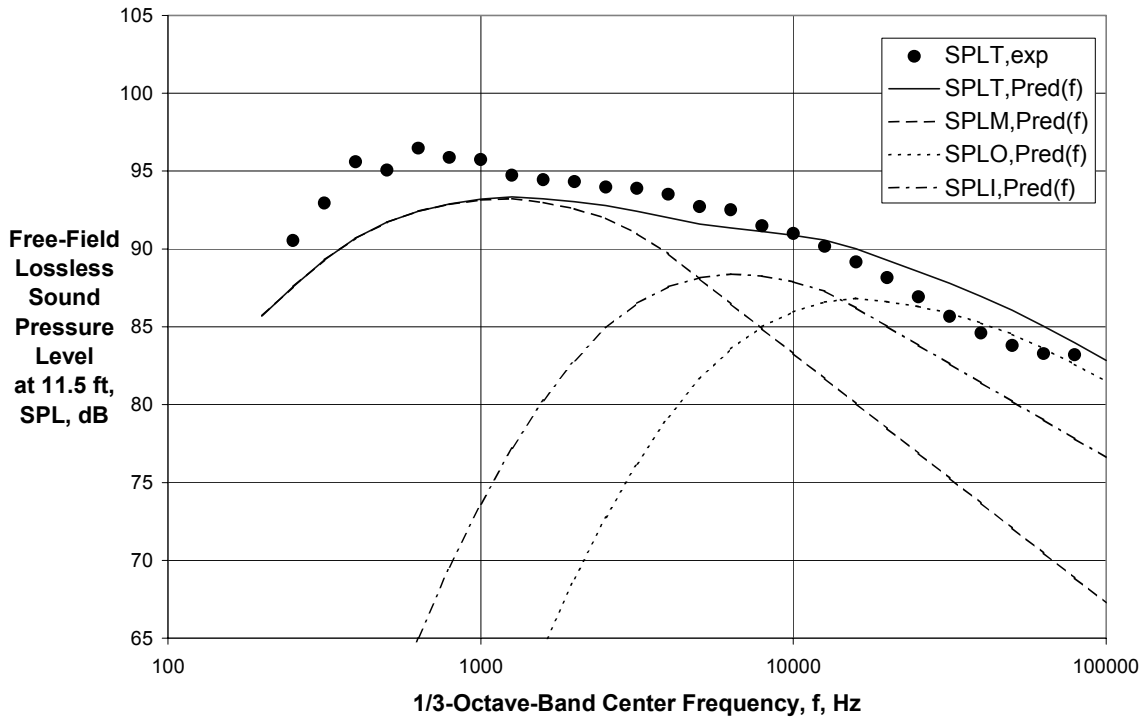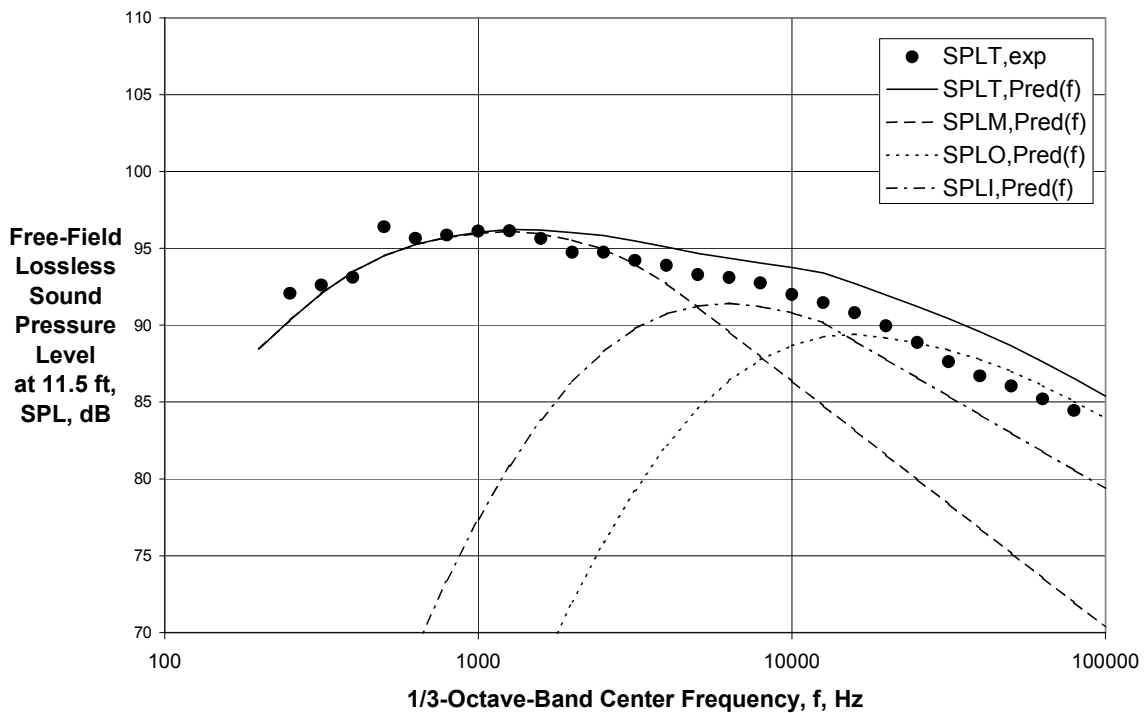
(f) Directivity Angle = 160 deg

Figure 58 (Concluded) - Comparison of Experimental and Final Predicted Spectra for V_{mix}/c_{amb} = 0.949, M_f = 0.0 (A_O/A_l = 3.74, Ref. 24, Rdg. 1017)
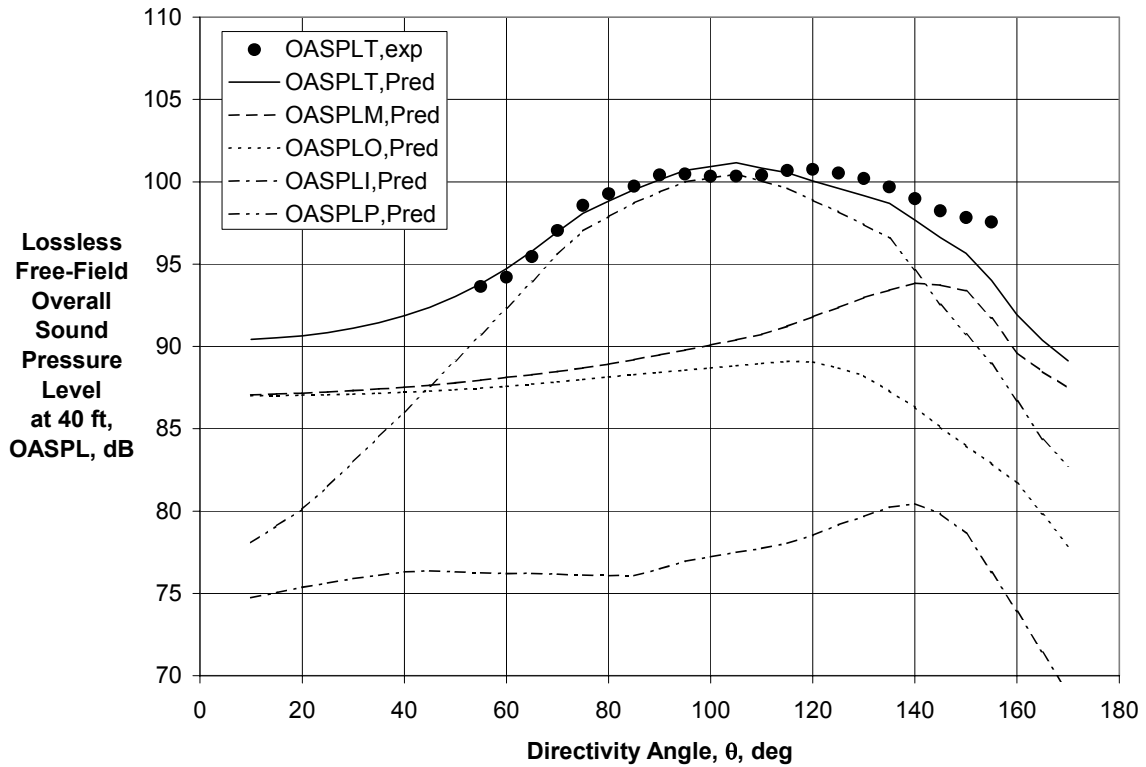
Figure 59 - Comparison of Experimental and Final Predicted Directivities for V_{mix}/c_{amb} = 0.591, M_f = 0.20 (A_O/A_l = 6.53, Ref. 24, Rdg. 1262)
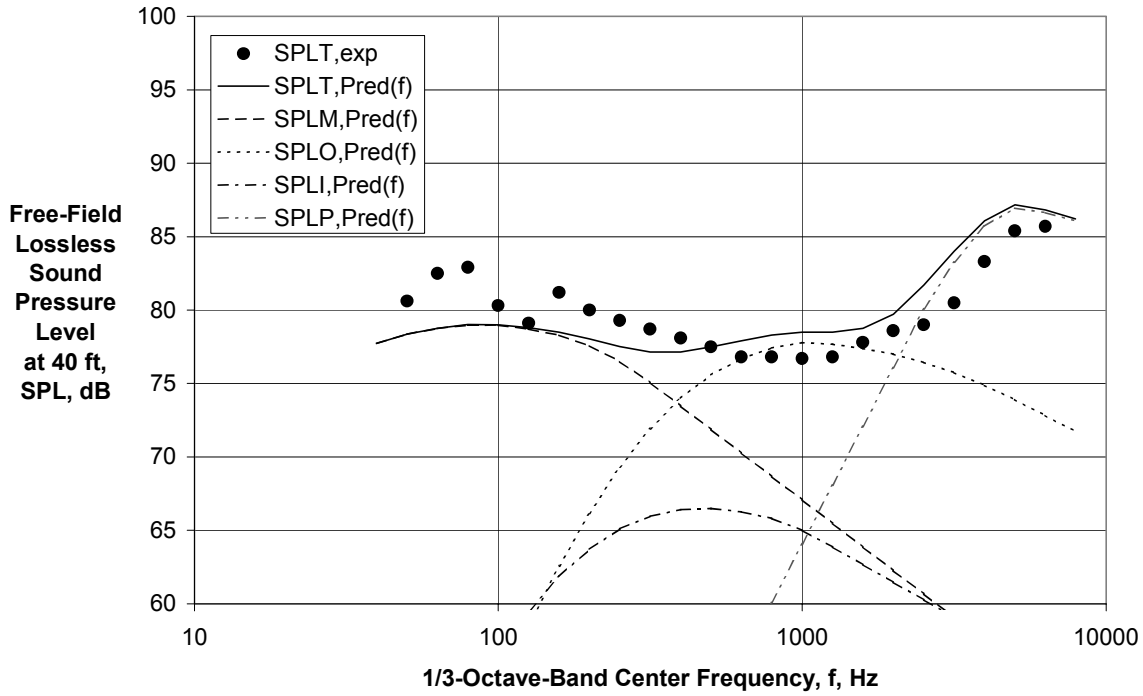
(a) Directivity Angle = 60 deg
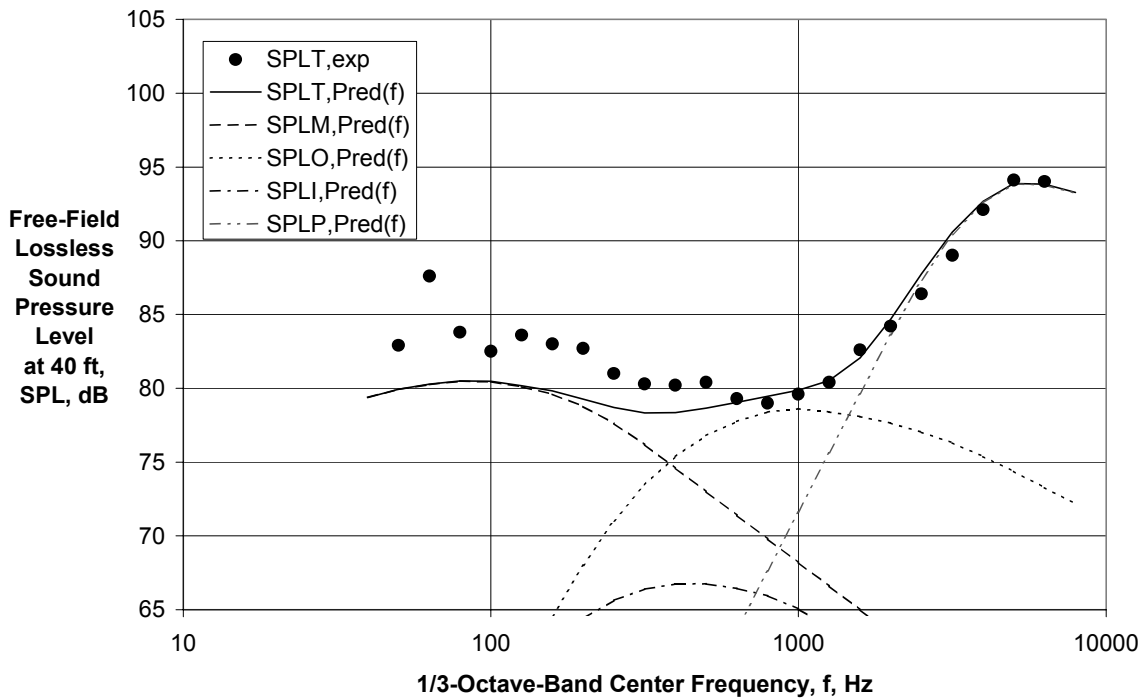
(b) Directivity Angle = 90 deg

Figure 60 - Comparison of Experimental and Final Predicted Spectra for
V_{mix}/c_{amb} = 0.591, M_f = 0.20 (A_O/A_I = 6.53, Ref. 24, Rdg. 1262)
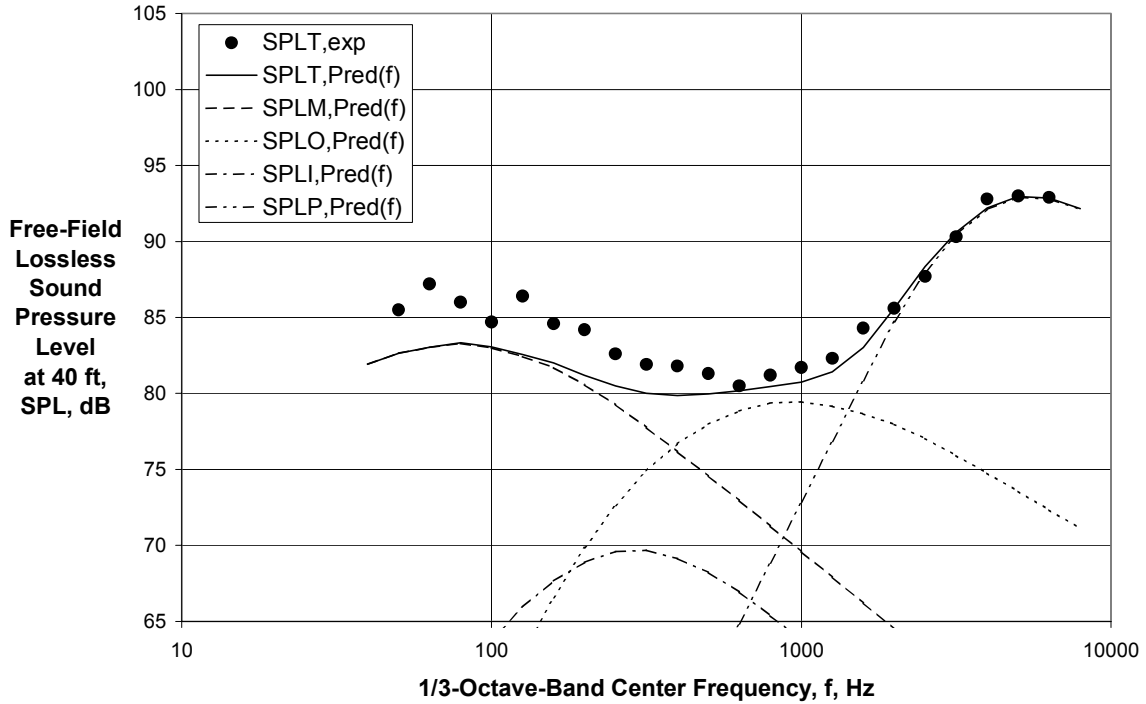
(c) Directivity Angle = 120 deg

(d) Directivity Angle = 135 deg

Figure 60 (Continued) - Comparison of Experimental and Final Predicted Spectra for V_{mix}/c_{amb} = 0.591, M_f = 0.20 (A_O/A_I = 6.53, Ref. 24, Rdg. 1262)
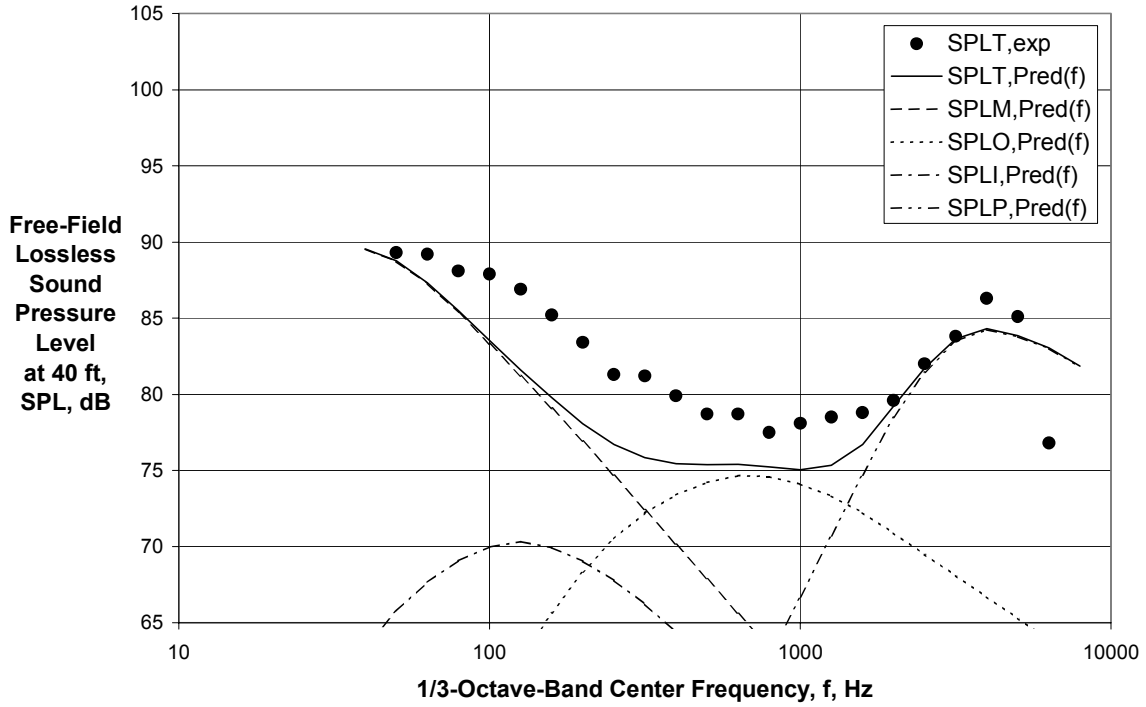
(e) Directivity Angle = 150 deg
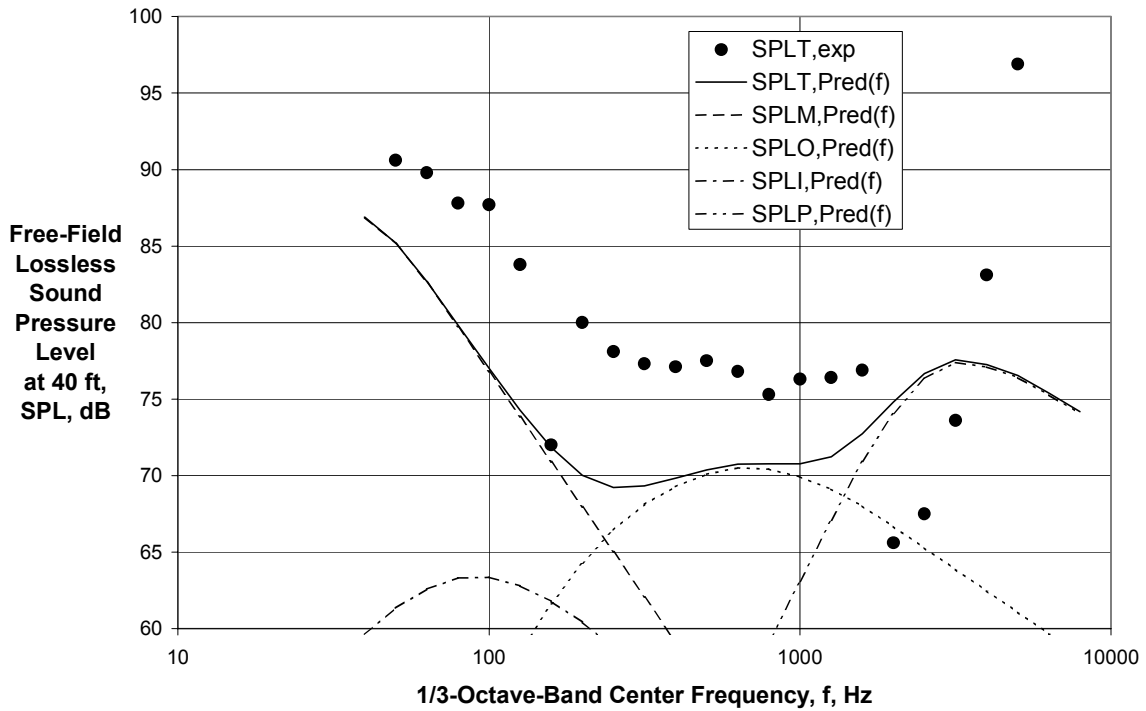
(f) Directivity Angle = 165 deg

Figure 60 (Concluded) - Comparison of Experimental and Final Predicted Spectra for $V_{mix}/c_{amb} = 0.591$, $M_f = 0.20$ ($A_O/A_I = 6.53$, Ref. 24, Rdg. 1262)
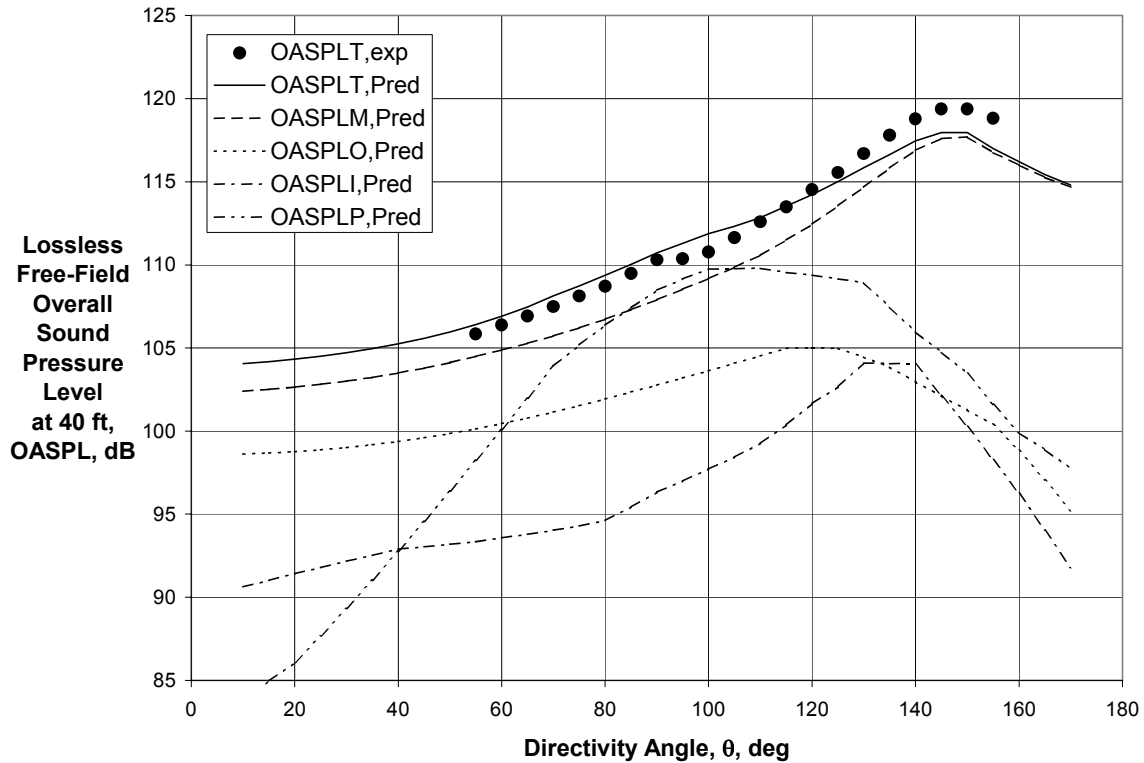
Figure 61 - Comparison of Experimental and Final Predicted Directivities for $V_{mix}/c_{amb} = 0.766$, $M_f = 0.0$ ($A_O/A_I = 6.53$, Ref. 24, Rdg. 1268)

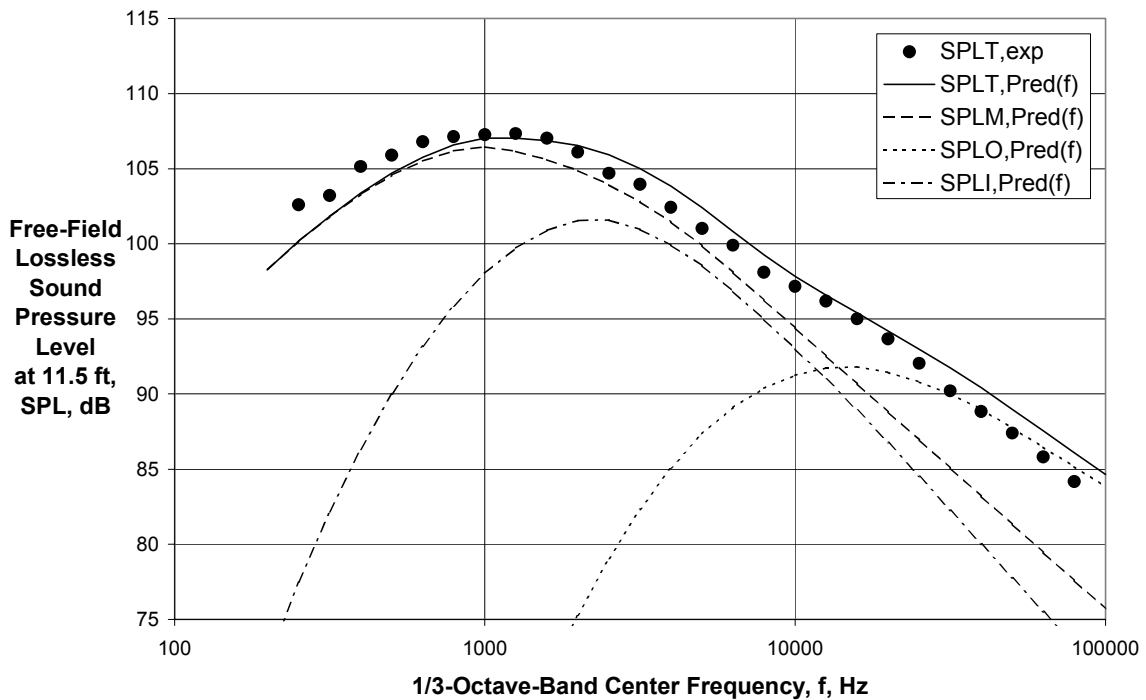**(a) Directivity Angle = 60 deg**

Figure 62 - Comparison of Experimental and Final Predicted Spectra for $V_{mix}/c_{amb} = 0.766$, $M_f = 0.0$ ($A_O/A_I = 6.53$, Ref. 24, Rdg. 1268)
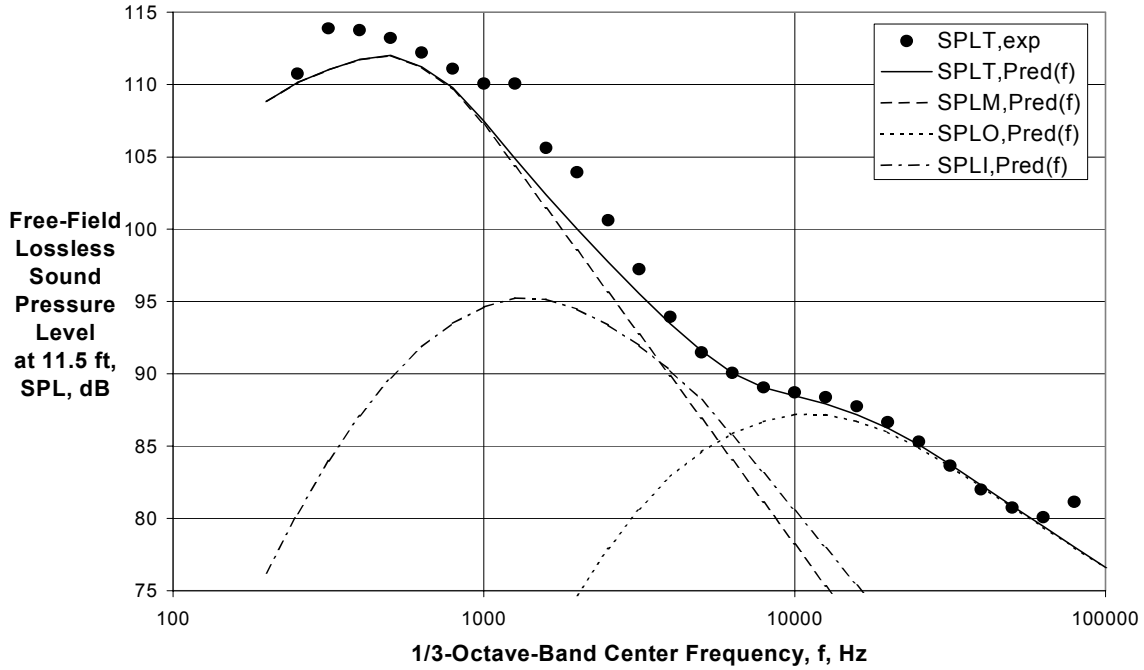
(b) Directivity Angle = 90 deg

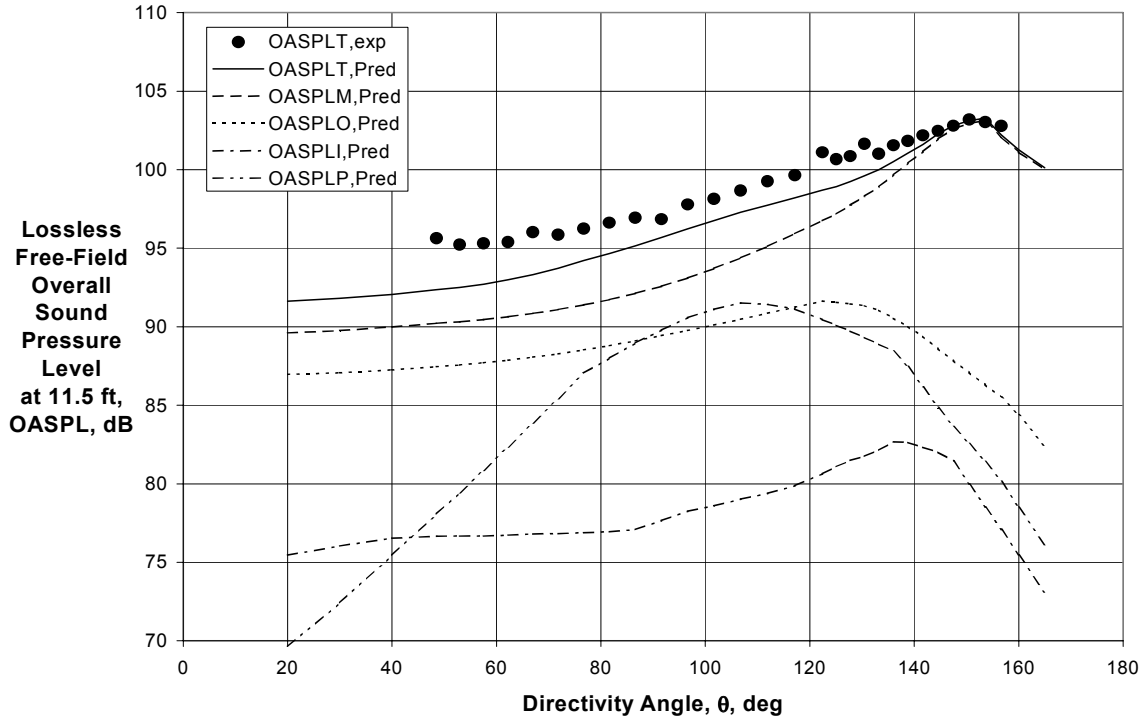**(c) Directivity Angle = 120 deg**

Figure 62 (Continued) - Comparison of Experimental and Final Predicted Spectra for V_{mix}/c_{amb} = 0.766, M_f = 0.0 (A_O/A_I = 6.53, Ref. 24, Rdg. 1268)
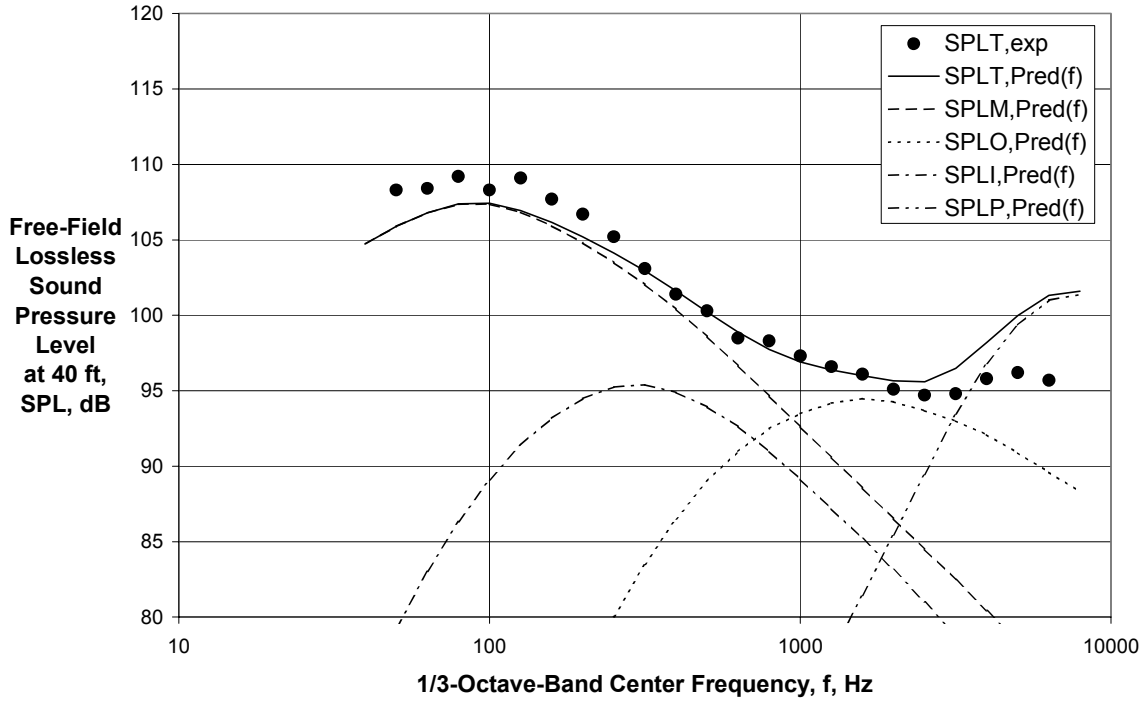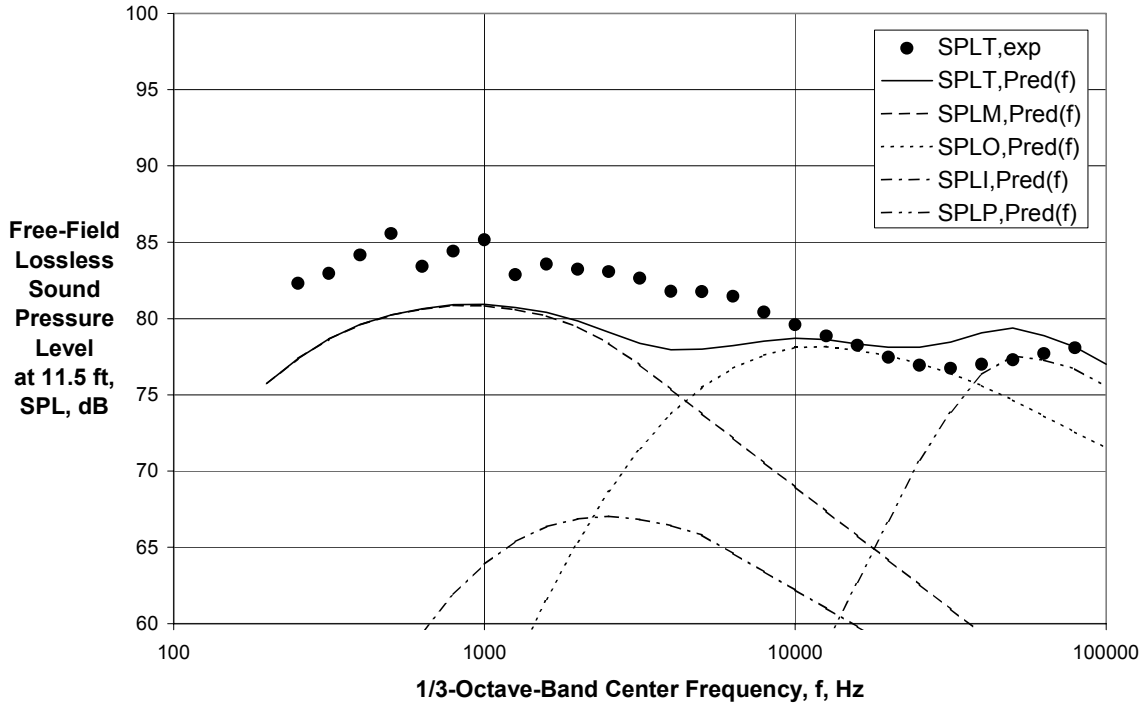
(d) Directivity Angle = 135 deg

(e) Directivity Angle = 150 deg

Figure 62 (Continued) - Comparison of Experimental and Final Predicted Spectra for V_{mix}/c_{amb} = 0.766, M_f = 0.0 (A_O/A_I = 6.53, Ref. 24, Rdg. 1268)
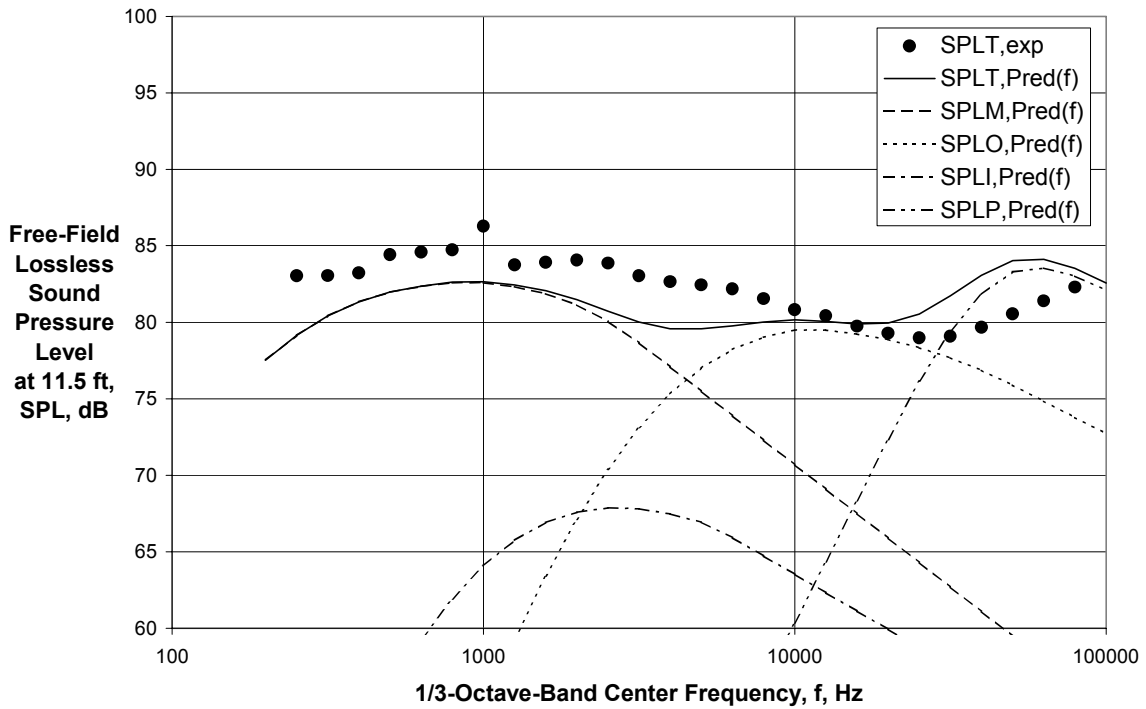
(f) Directivity Angle = 160 deg

Figure 62 (Concluded) - Comparison of Experimental and Final Predicted Spectra for V_{mix}/c_{amb} = 0.766, M_f = 0.0 (A_O/A_I = 6.53, Ref. 24, Rdg. 1268)

(a) Directivity Angle = 95 deg

Figure 63 - Comparison of Experimental and Final Predicted Spectra for V_{mix}/c_{amb} = 1.04, M_f = 0.0 (A_O/A_I = 1.26, Ref. 25, Rdg. 01)

(b) Directivity Angle = 139 deg

Figure 63 (Concluded) - Comparison of Experimental and Final Predicted Spectra for V_{mix}/c_{amb} = 1.04, M_f = 0.0 (A_O/A_I = 1.26, Ref. 25, Rdg. 01)

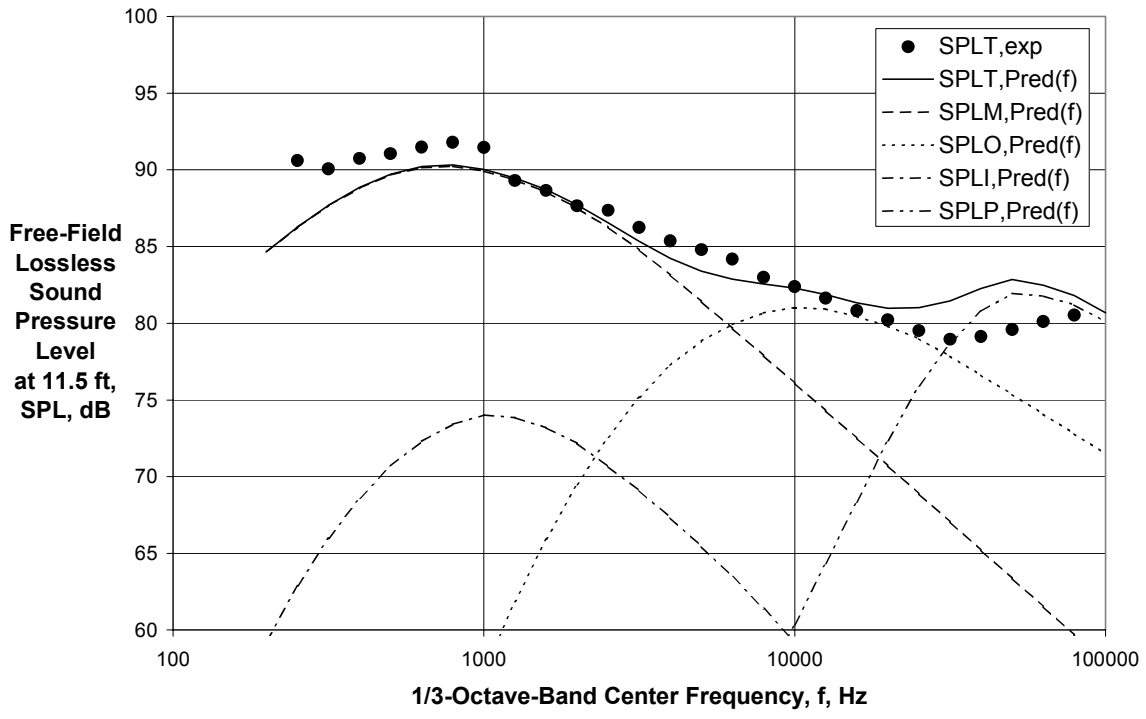**(a) Directivity Angle = 95 deg**

Figure 64 - Comparison of Experimental and Final Predicted Spectra for V_{mix}/c_{amb} = 1.17, M_f = 0.0 (A_O/A_I = 1.26, Ref. 25, Rdg. 15)

(b) Directivity Angle = 139 deg

Figure 64 (Concluded) - Comparison of Experimental and Final Predicted Spectra for V_{mix}/c_{amb} = 1.17, M_f = 0.0 (A_O/A_I = 1.26, Ref. 25, Rdg. 15)
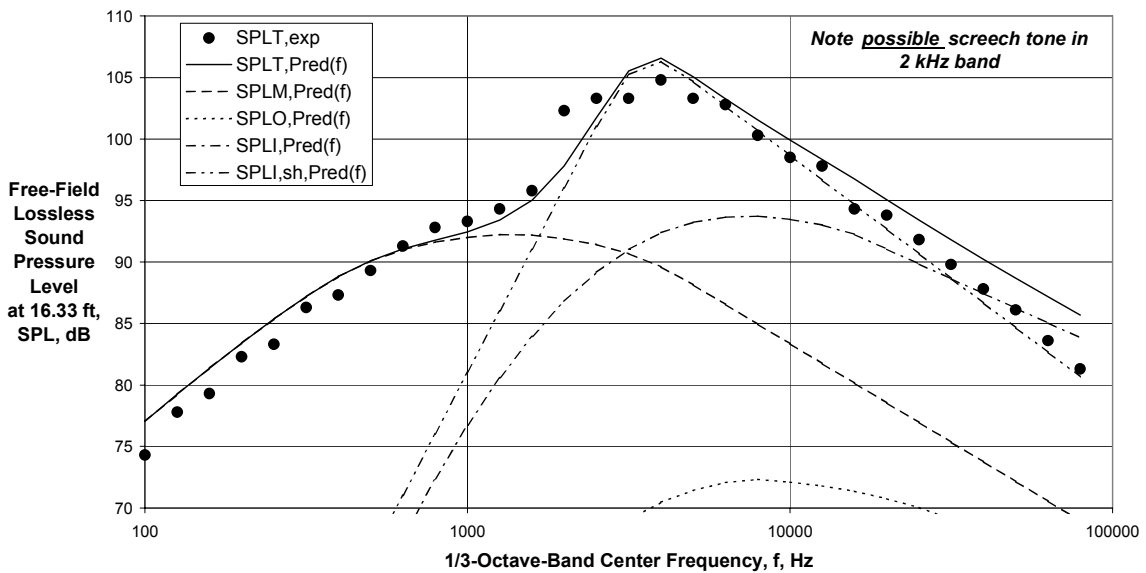
(a) Directivity Angle = 46 deg

Figure 65 - Comparison of Experimental and Final Predicted Spectra for V_{mix}/c_{amb} = 1.04, M_f = 0.0 (A_O/A_I = 1.26, Ref. 25, Rdg. 24)
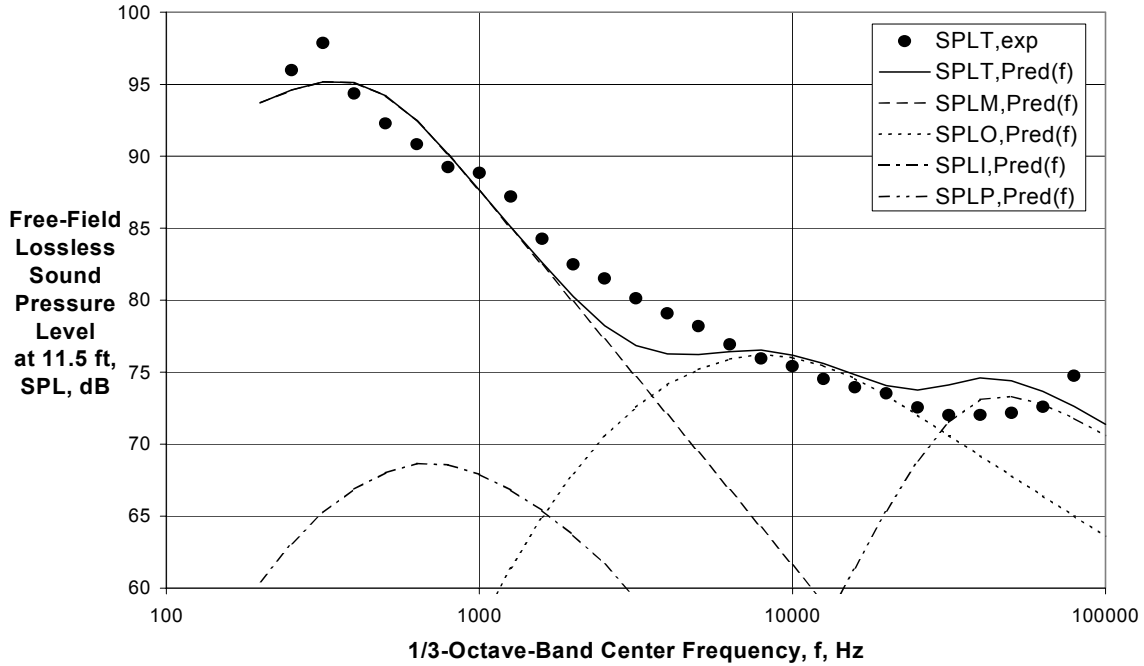
(b) Directivity Angle = 95 deg

(c) Directivity Angle = 139 deg

Figure 65 (Concluded) - Comparison of Experimental and Final Predicted Spectra for V_{mix}/c_{amb} = 1.04, M_f = 0.0 (A_O/A_I = 1.26, Ref. 25, Rdg. 24)
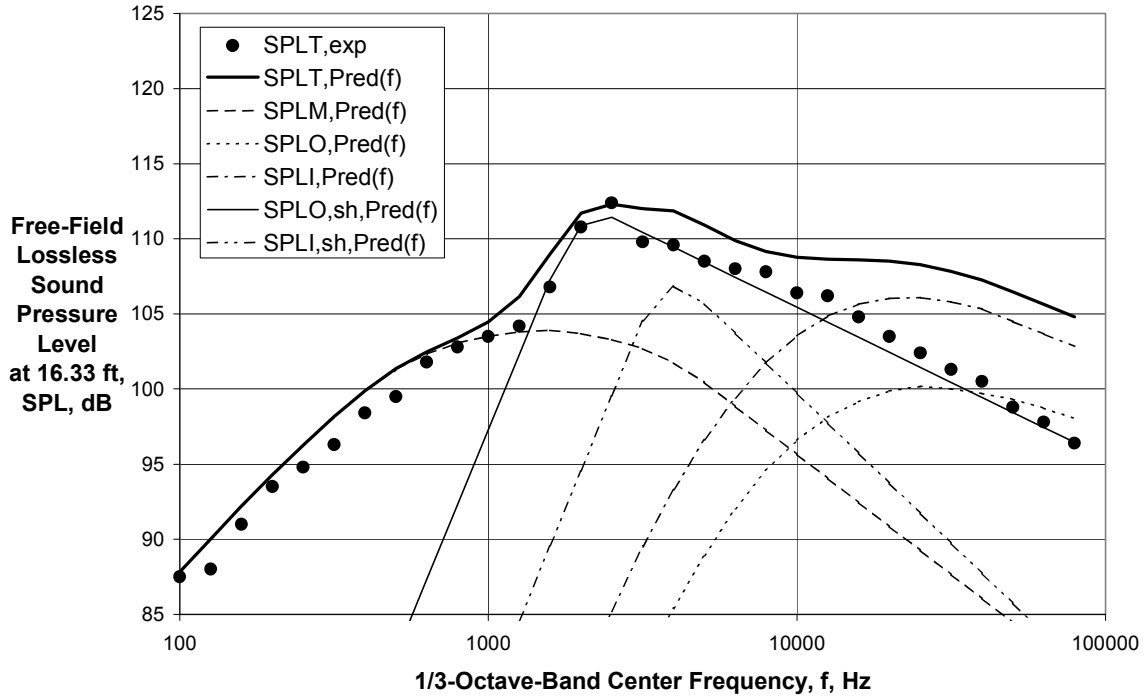
(a) Directivity Angle = 46 deg

(b) Directivity Angle = 95 deg

Figure 66 - Comparison of Experimental and Final Predicted Spectra for
V_{mix}/c_{amb} **= 2.04, M_f = 0.0 (A_O/A_I = 1.43, Ref. 25, Rdg. 18)**
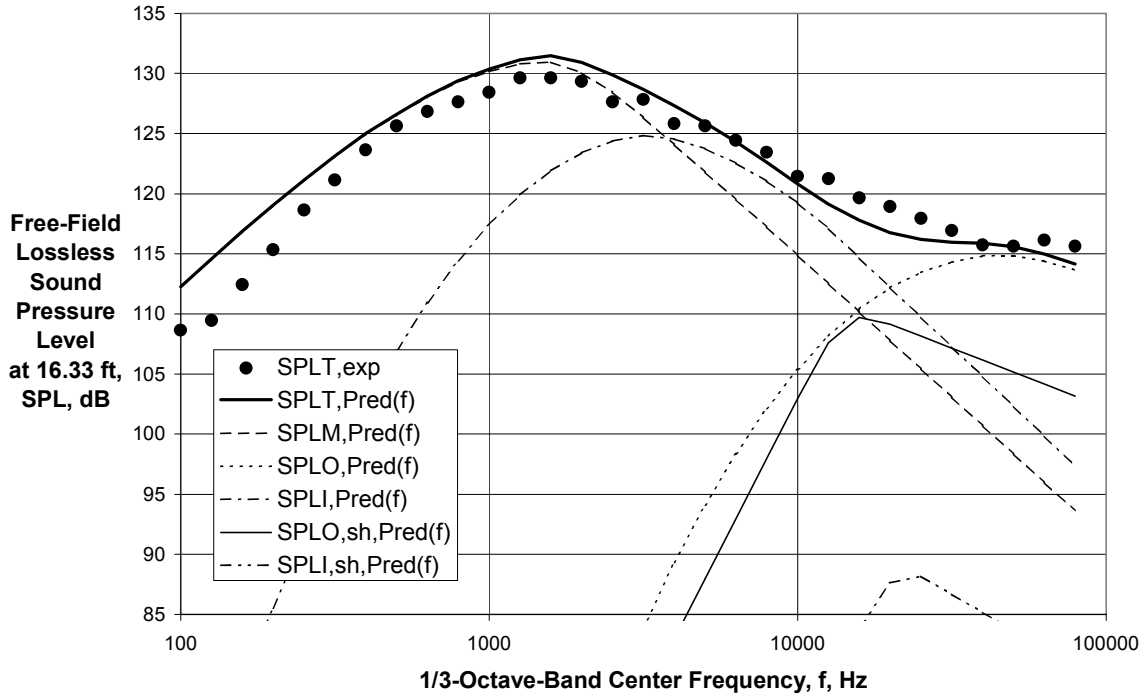
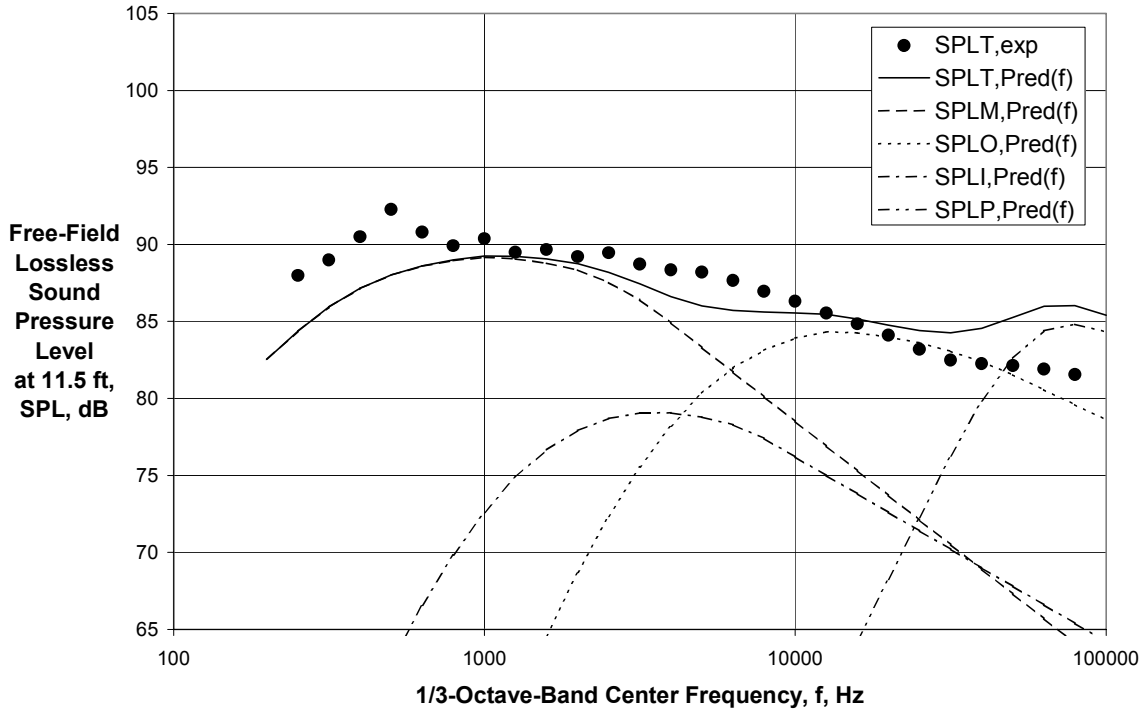**(c) Directivity Angle = 139 deg**

Figure 66 (Concluded) - Comparison of Experimental and Final Predicted Spectra for V_{mix}/c_{amb} = 2.04, M_f = 0.0 (A_O/A_I = 1.43, Ref. 25, Rdg. 18)
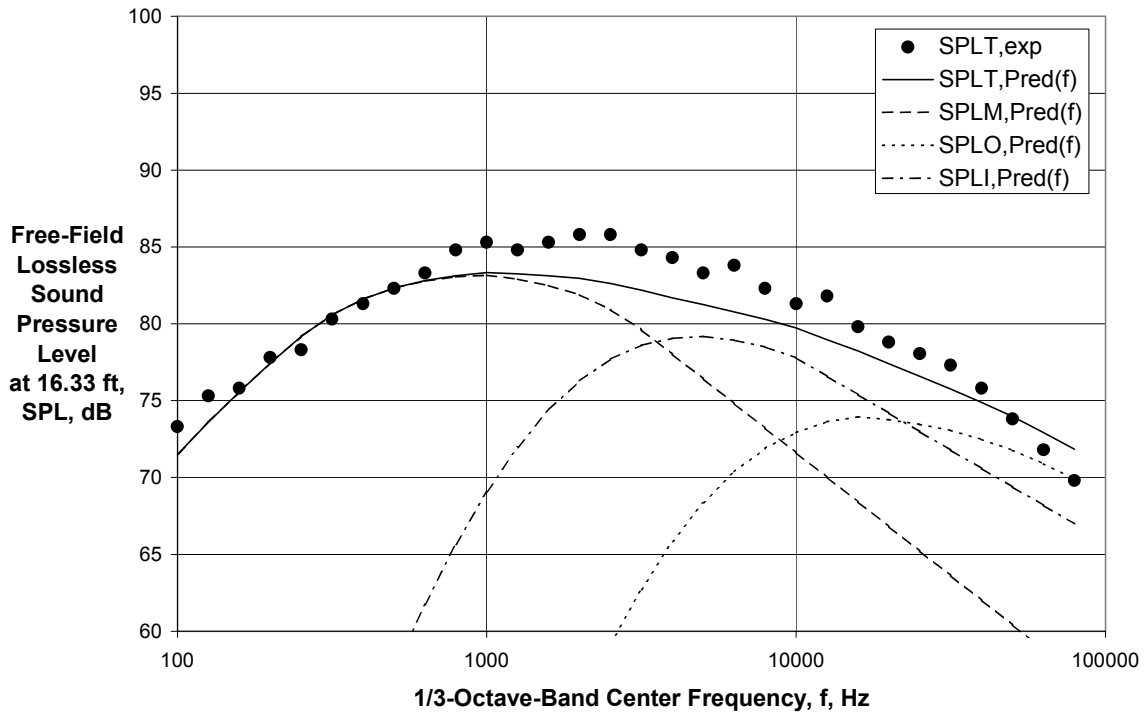
(a) Directivity Angle = 46 deg

Figure 67 - Comparison of Experimental and Final Predicted Spectra for V_{mix}/c_{amb} = 0.725, M_f = 0.0 (A_O/A_I = 1.94, Ref. 25, Rdg. 07)

(b) Directivity Angle = 95 deg

(c) Directivity Angle = 139 deg

Figure 67 (Concluded) - Comparison of Experimental and Final Predicted Spectra for V_{mix}/c_{amb} = 0.725, M_f = 0.0 (A_O/A_I = 1.94, Ref. 25, Rdg. 07)
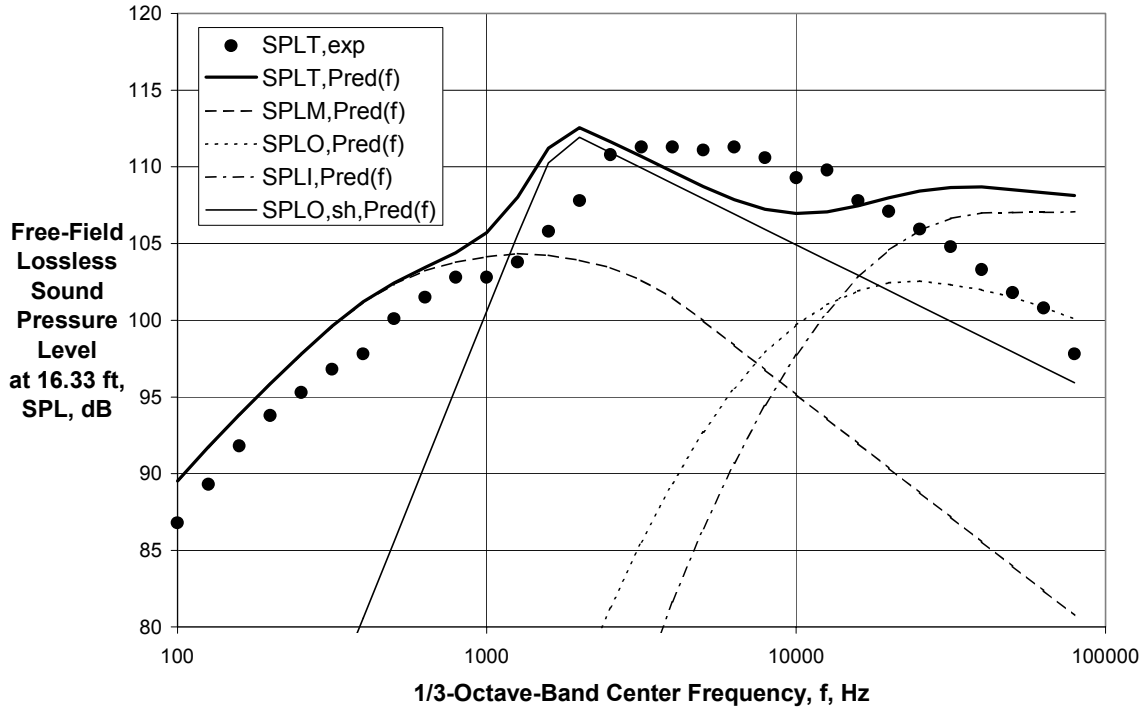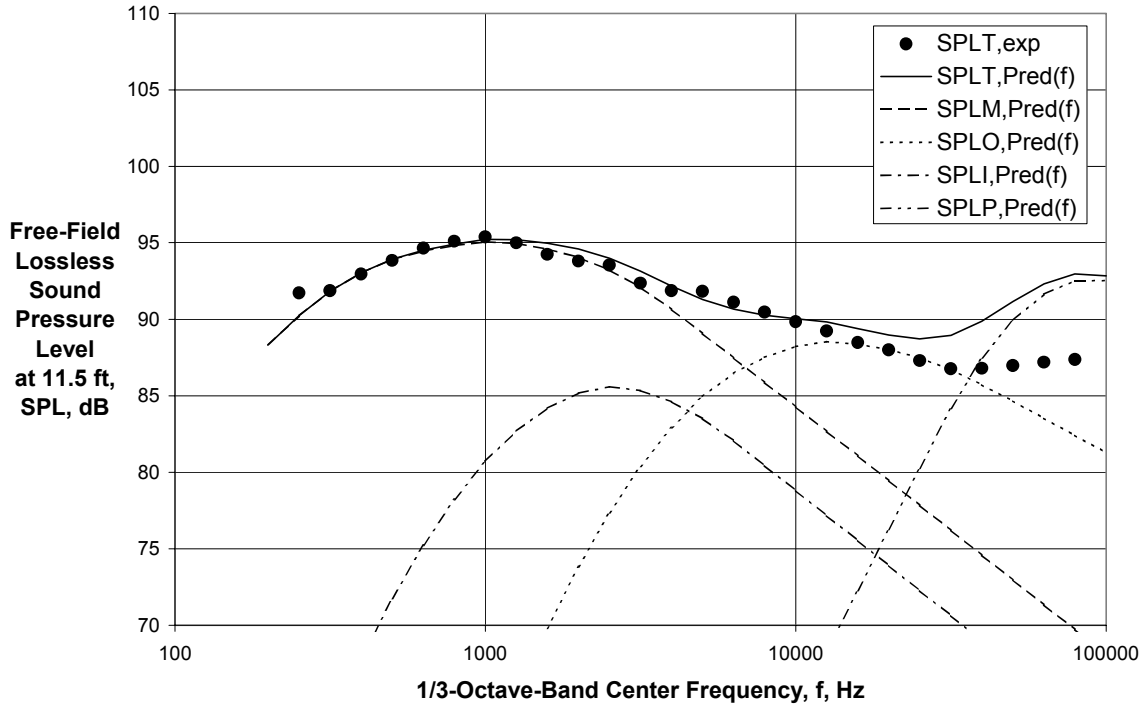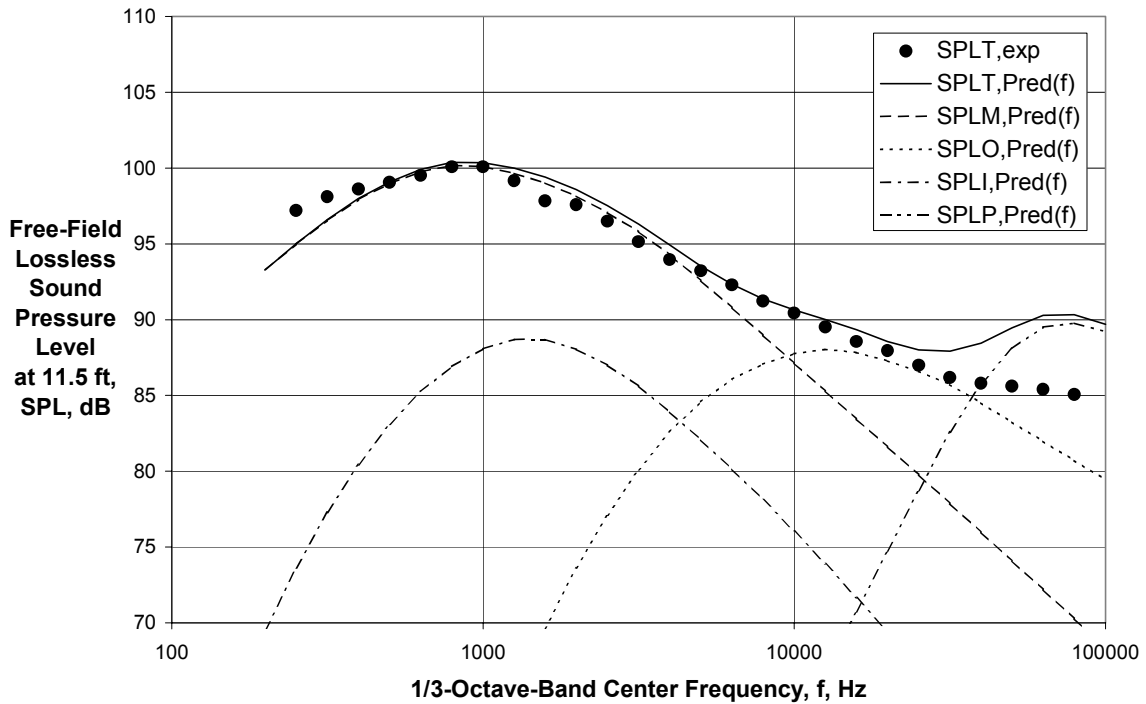
(a) Directivity Angle = 46 deg
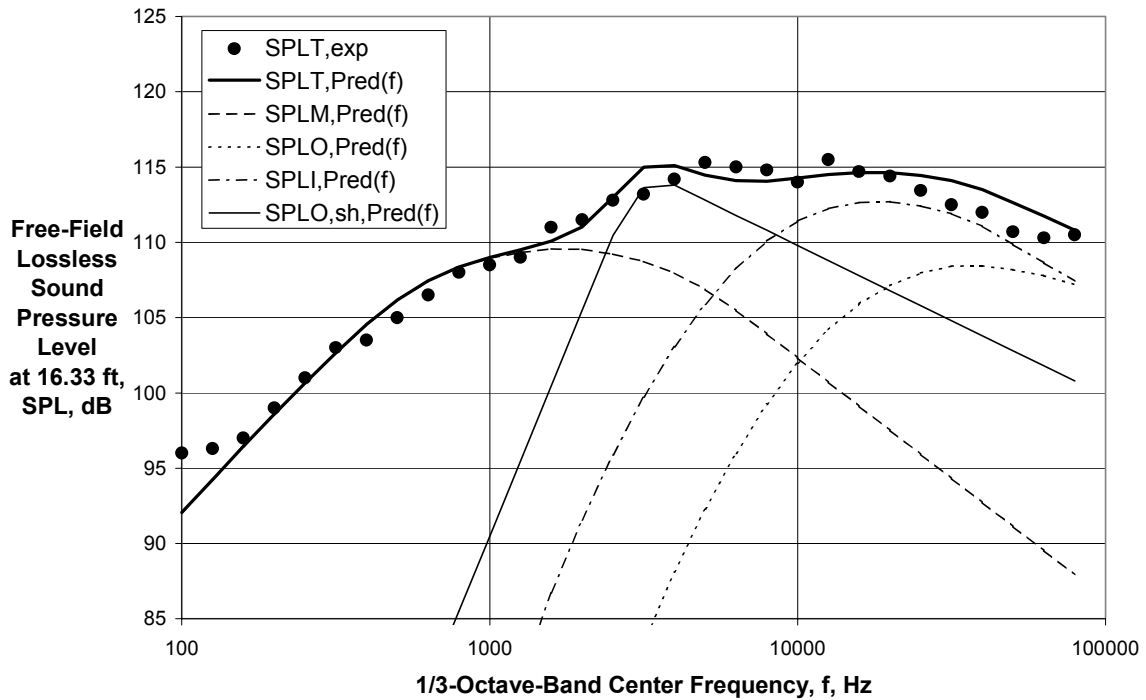
(b) Directivity Angle = 95 deg

Figure 68 - Comparison of Experimental and Final Predicted Spectra for
$V_{mix}/c_{amb} = 1.72$, $M_f = 0.0$ ($A_O/A_I = 1.94$, Ref. 25, Rdg. 21)
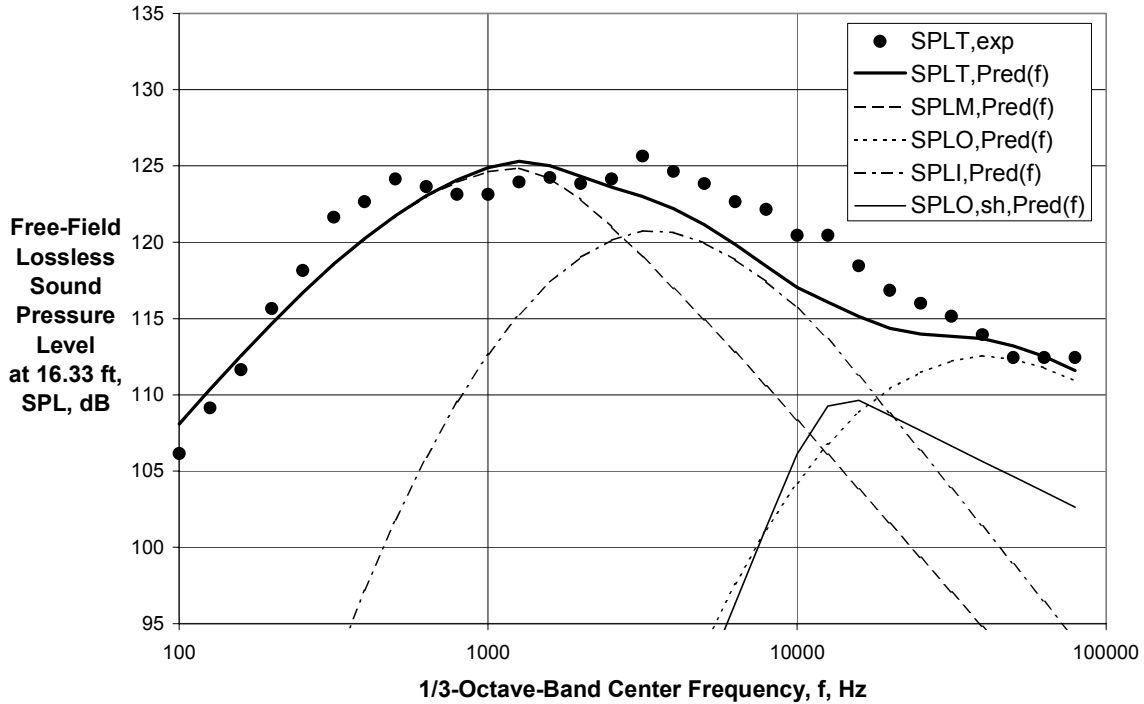
(c) Directivity Angle = 139 deg

Figure 68 (Concluded) - Comparison of Experimental and Final Predicted Spectra for V_{mix}/c_{amb} = 1.72, M_f = 0.0 (A_O/A_I = 1.94, Ref. 25, Rdg. 21)
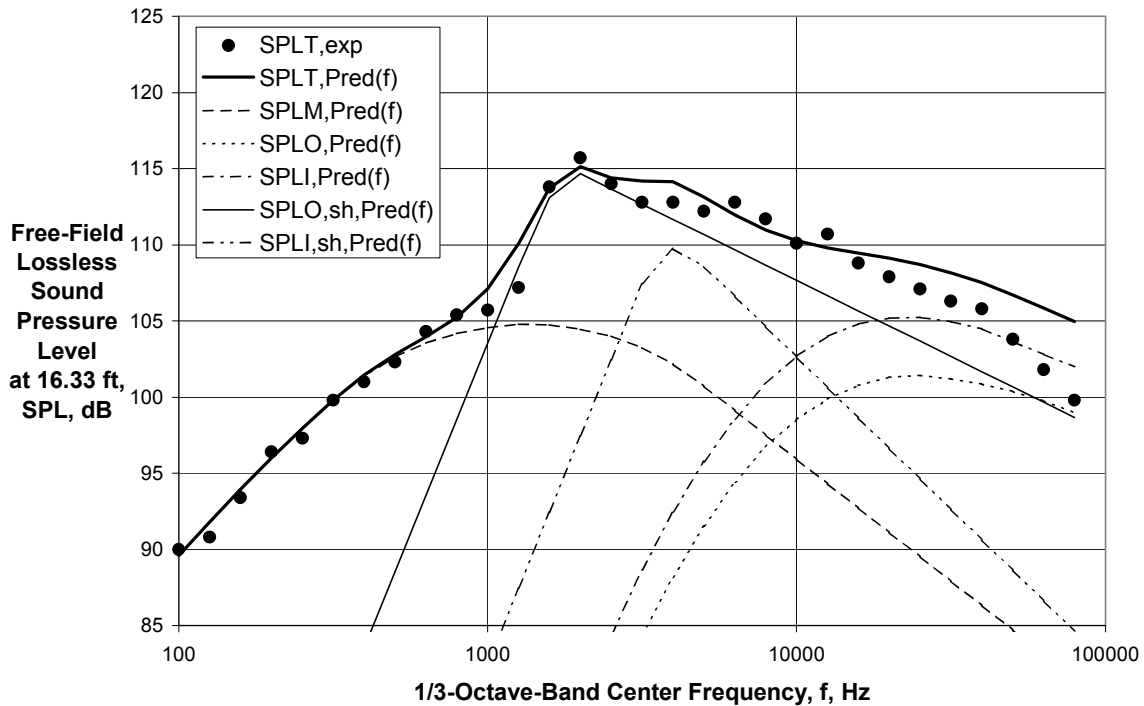
(a) Directivity Angle = 46 deg

Figure 69 - Comparison of Experimental and Final Predicted Spectra for V_{mix}/c_{amb} = 2.08, M_f = 0.0 (A_O/A_I = 1.94, Ref. 25, Rdg. 17)
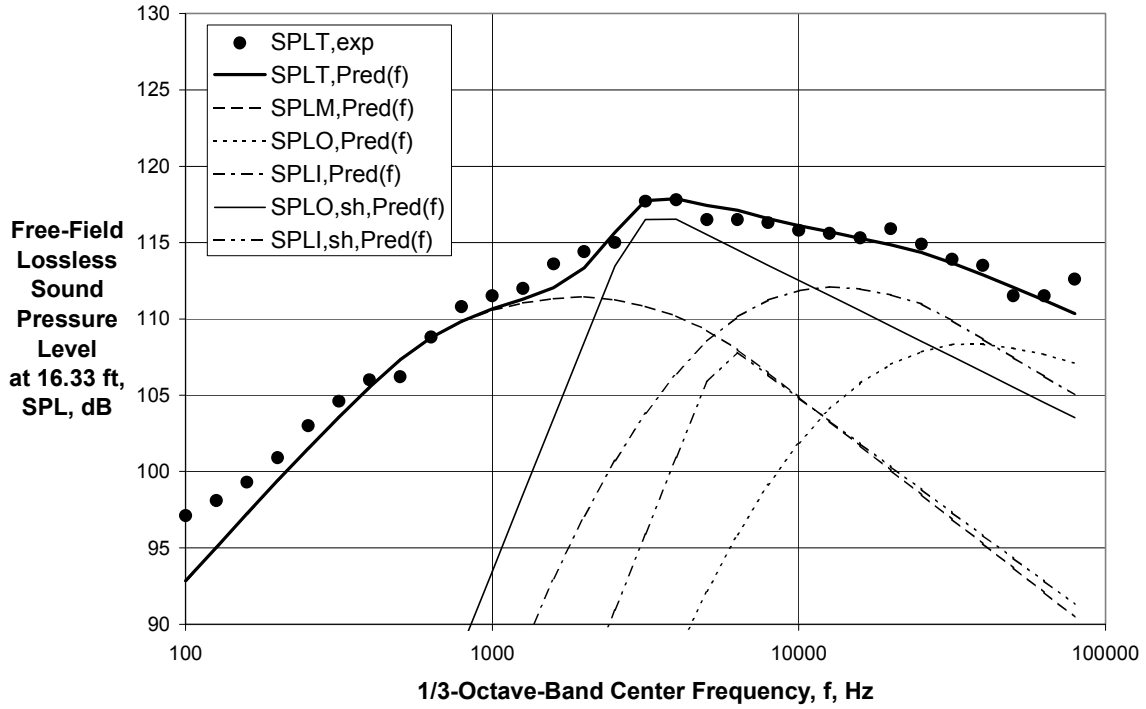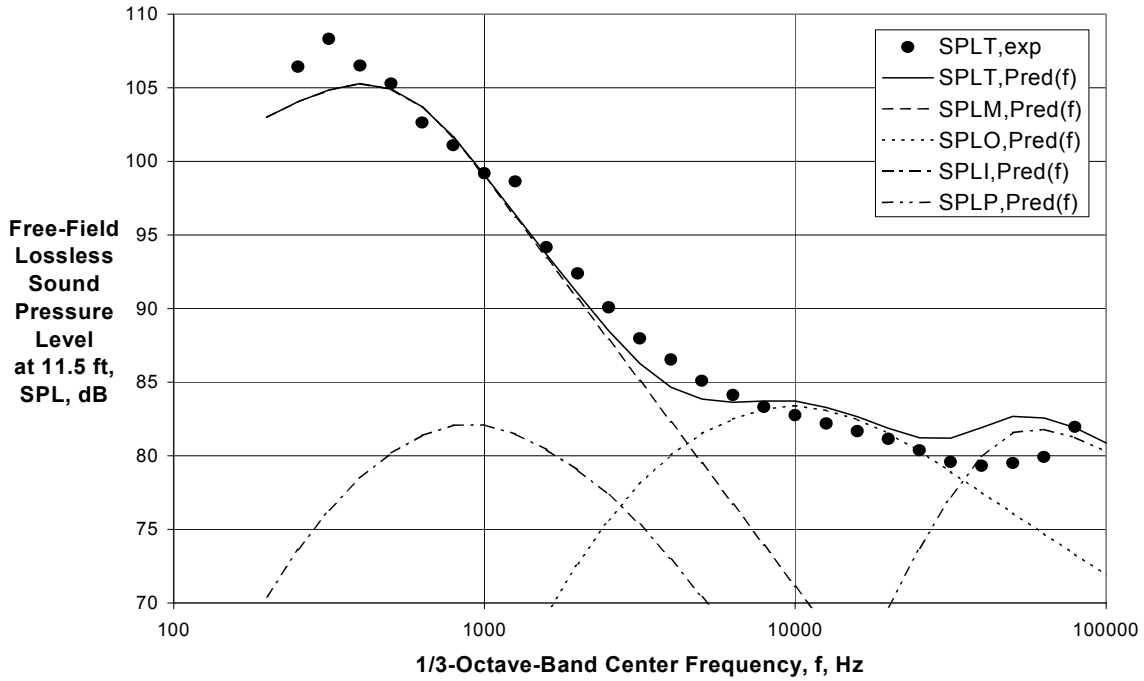
(b) Directivity Angle = 95 deg
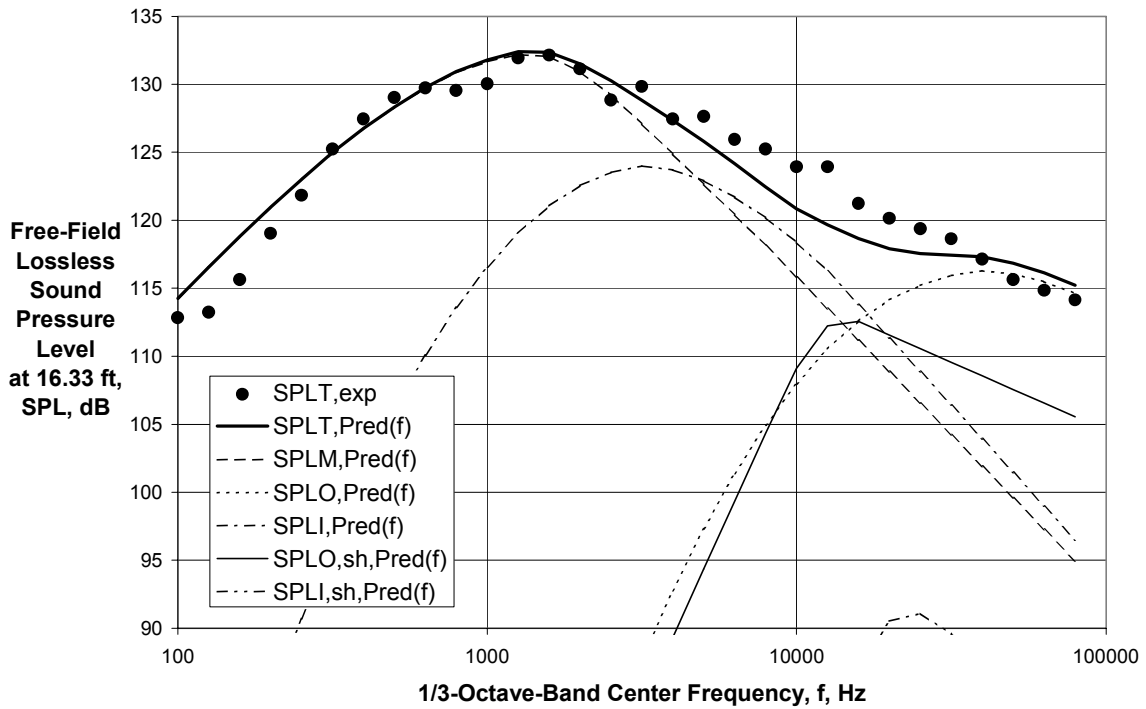
(c) Directivity Angle = 139 deg

Figure 69 (Concluded) - Comparison of Experimental and Final Predicted Spectra for V_{mix}/c_{amb} = 2.08, M_f = 0.0 (A_O/A_I = 1.94, Ref. 25, Rdg. 17)
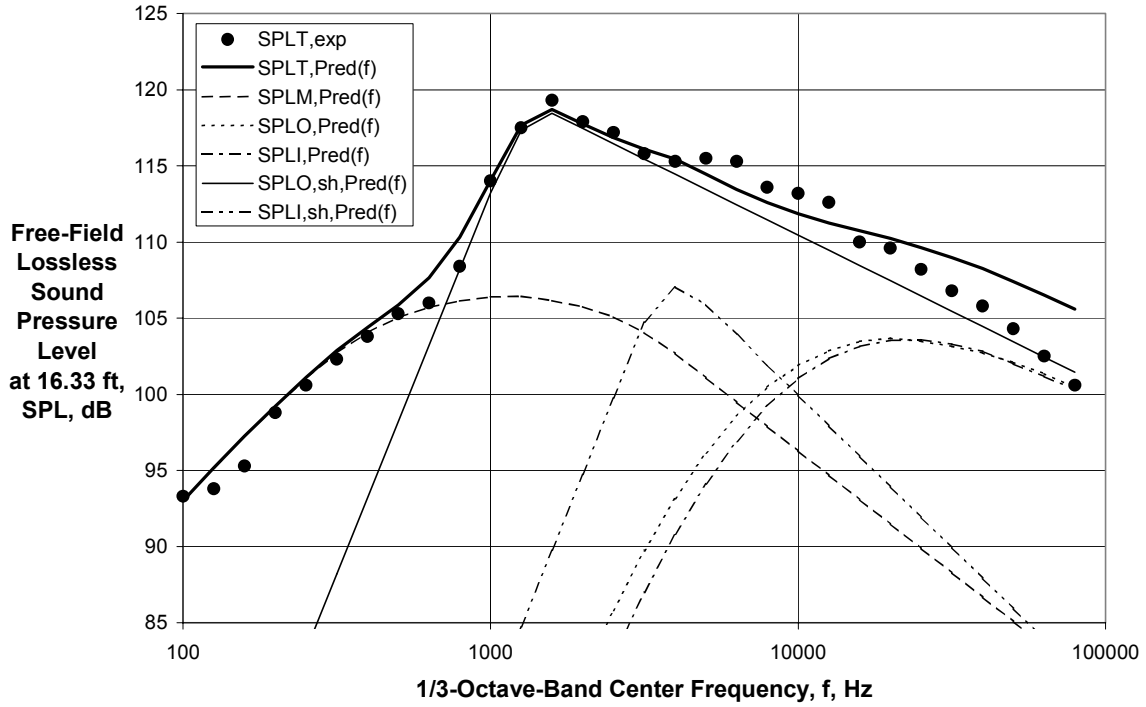
(a) Directivity Angle = 46 deg
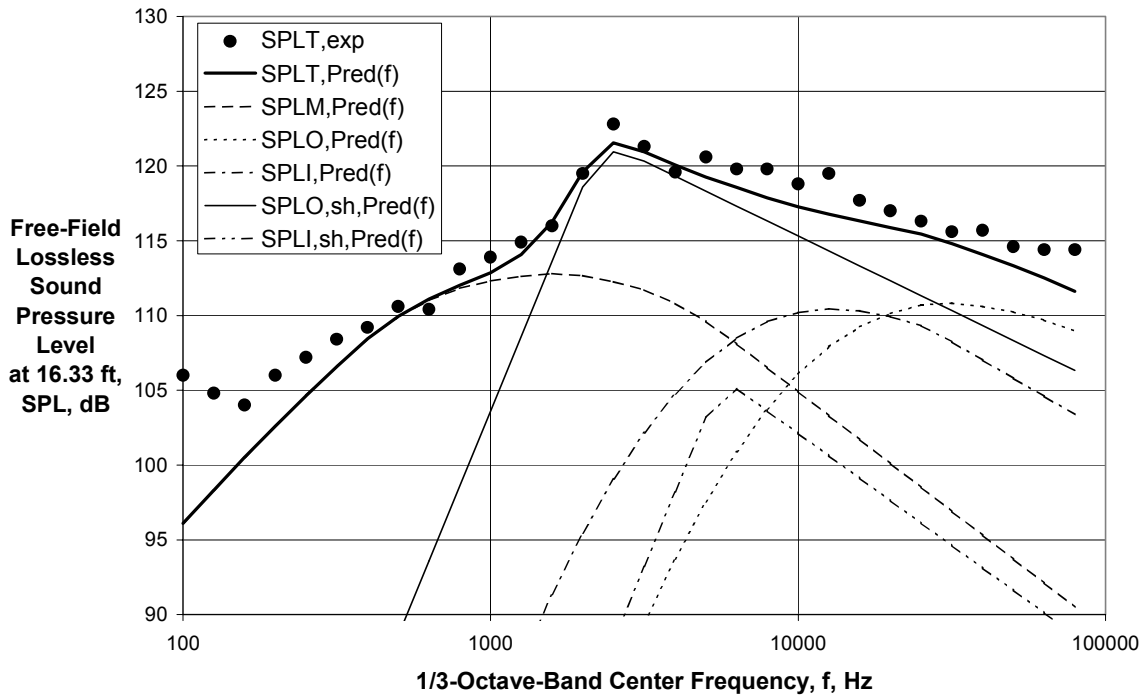
(b) Directivity Angle = 95 deg

Figure 70 - Comparison of Experimental and Final Predicted Spectra for
$V_{mix}/c_{amb} = 2.13$, $M_f = 0.0$ ($A_O/A_I = 3.27$, Ref. 25, Rdg. 16)
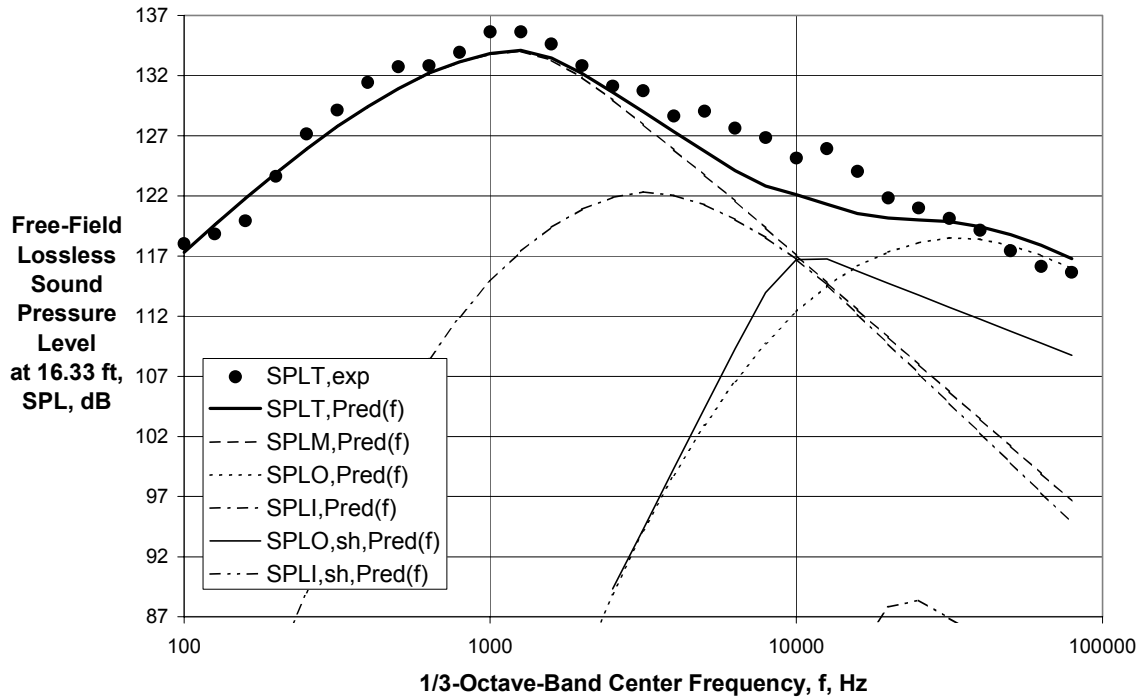
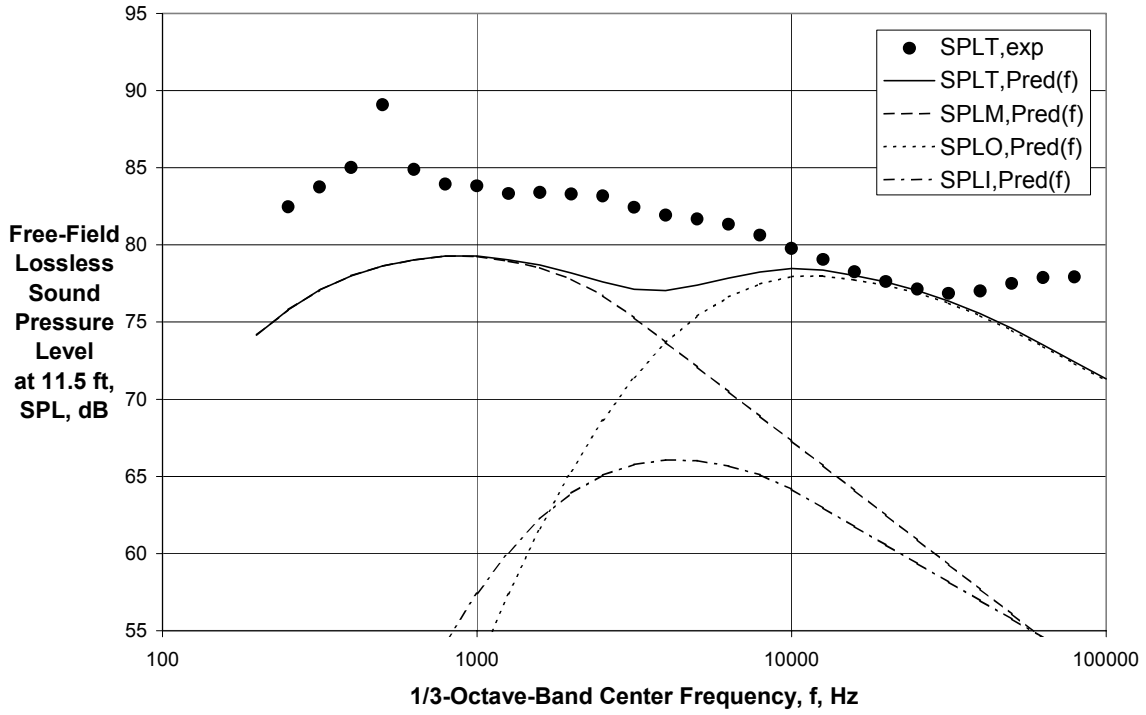**(c) Directivity Angle = 139 deg**

Figure 70 (Concluded) - Comparison of Experimental and Final Predicted Spectra for V_{mix}/c_{amb} = 2.13, M_f = 0.0 (A_O/A_I = 3.27, Ref. 25, Rdg. 16)
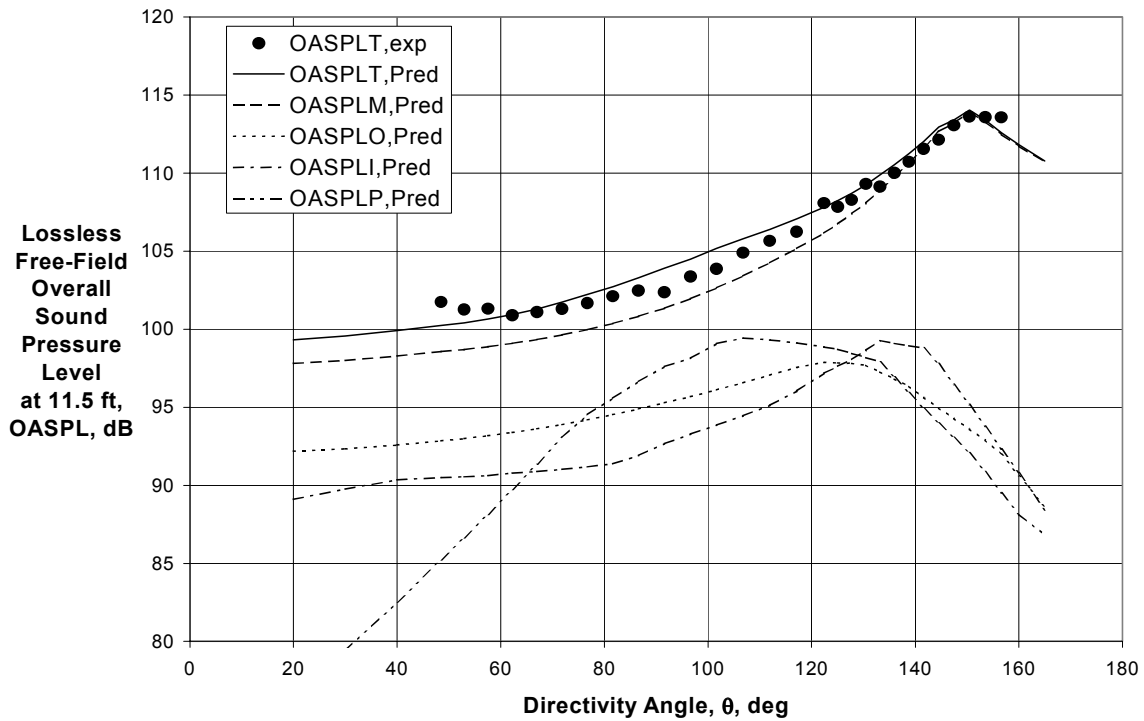
Figure 71 - Comparison of Experimental and Final Predicted Directivities for External Plug Nozzle with V_{mix}/c_{amb} = 0.835, M_f = 0.10 (A_O/A_I = 2.66, Cond. 50010, Ref. 31)
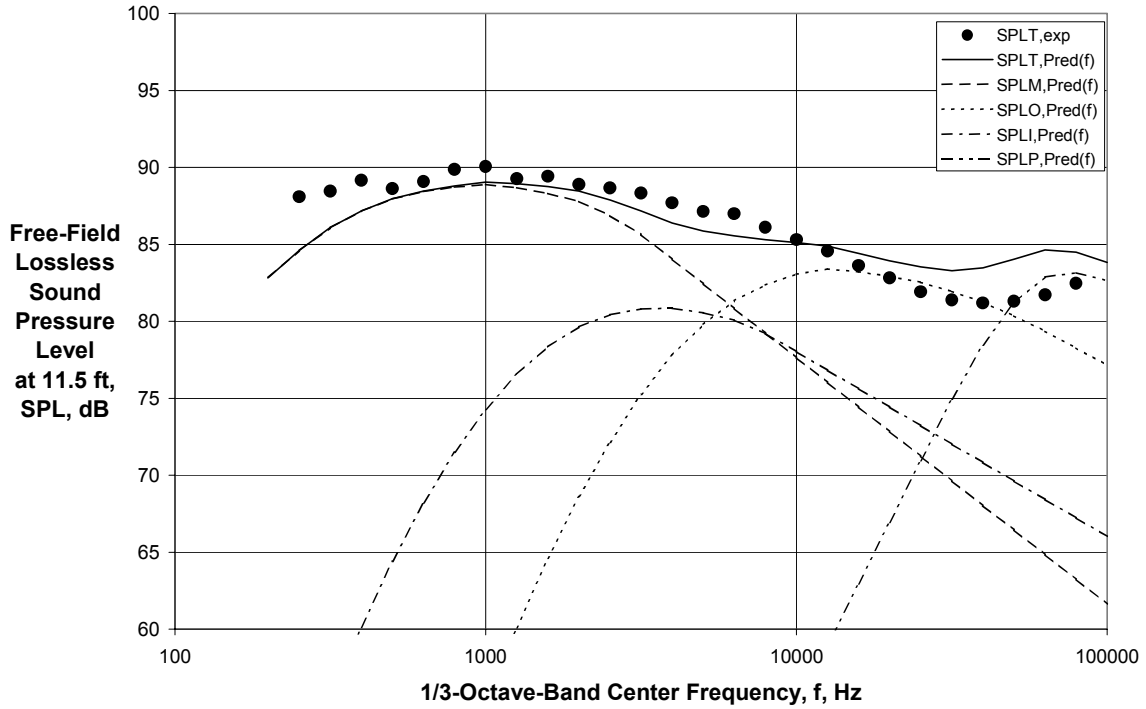
(a) Directivity Angle = 58 deg
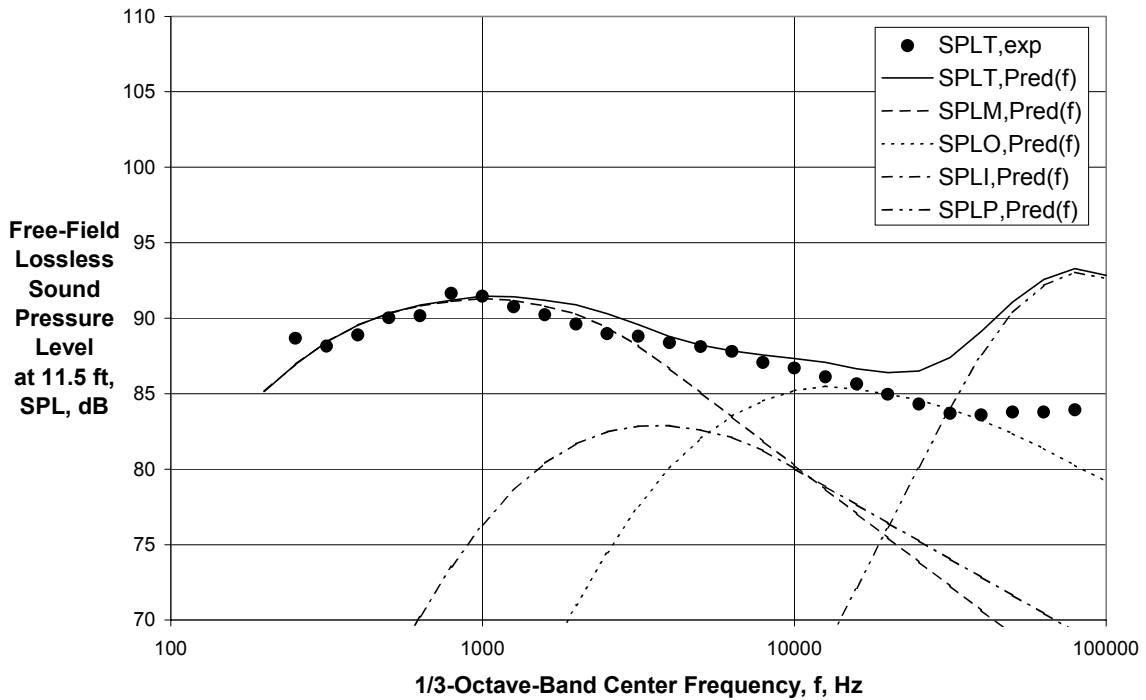
(b) Directivity Angle = 92 deg
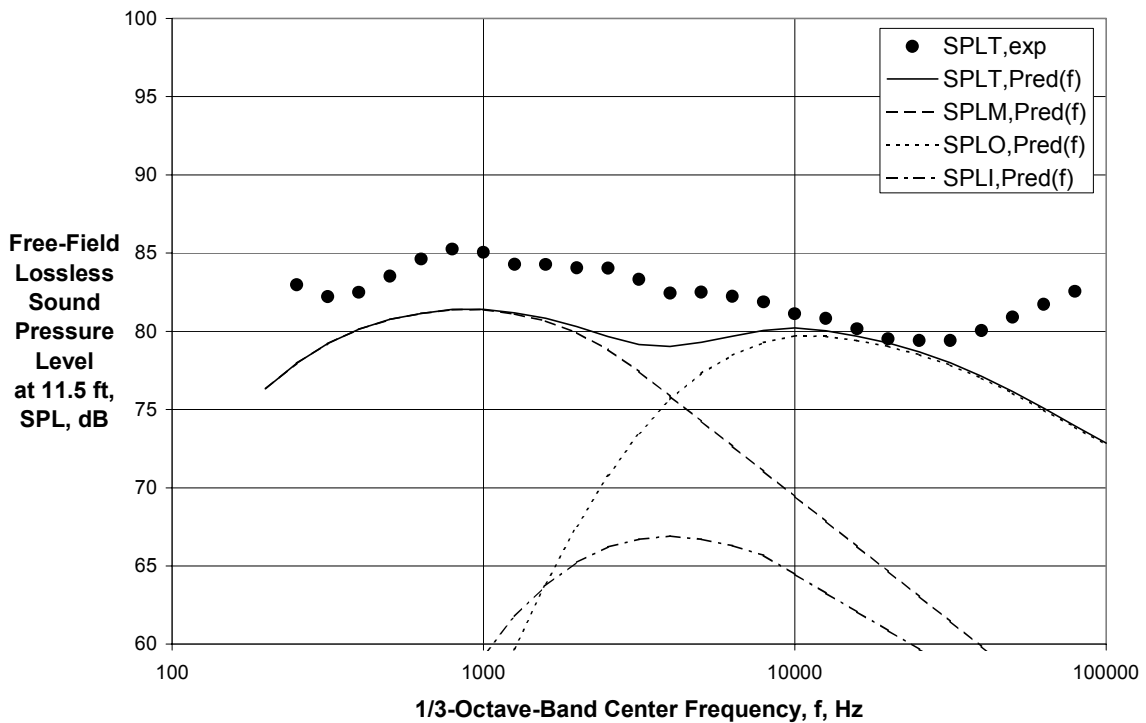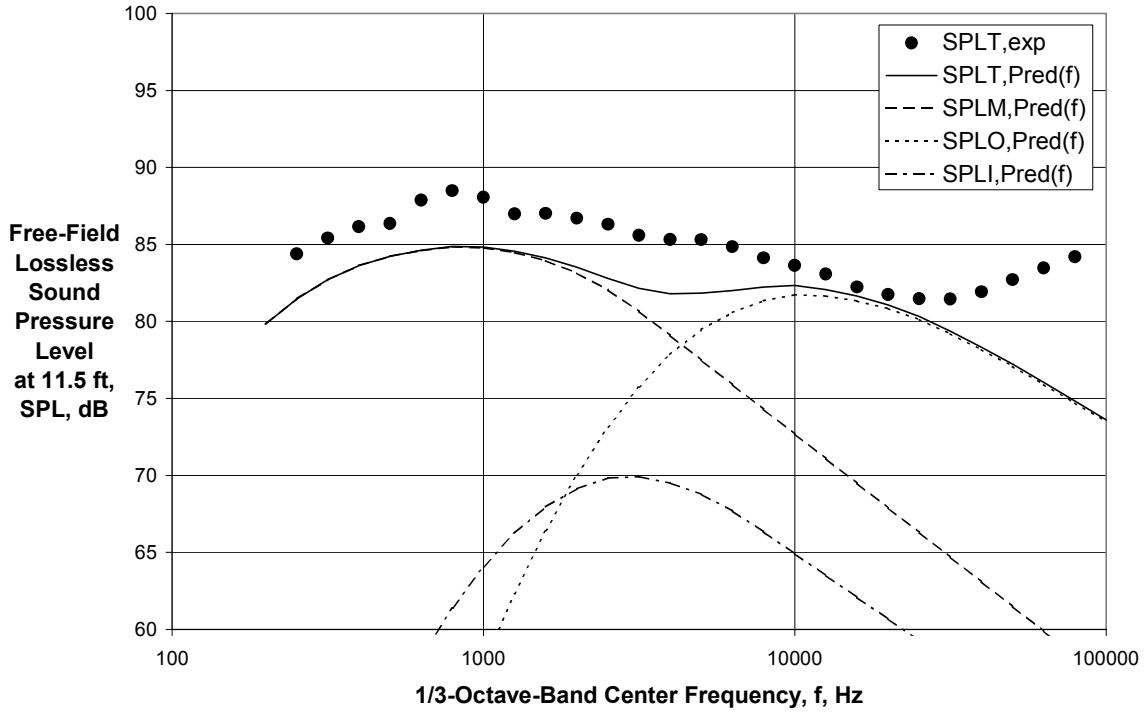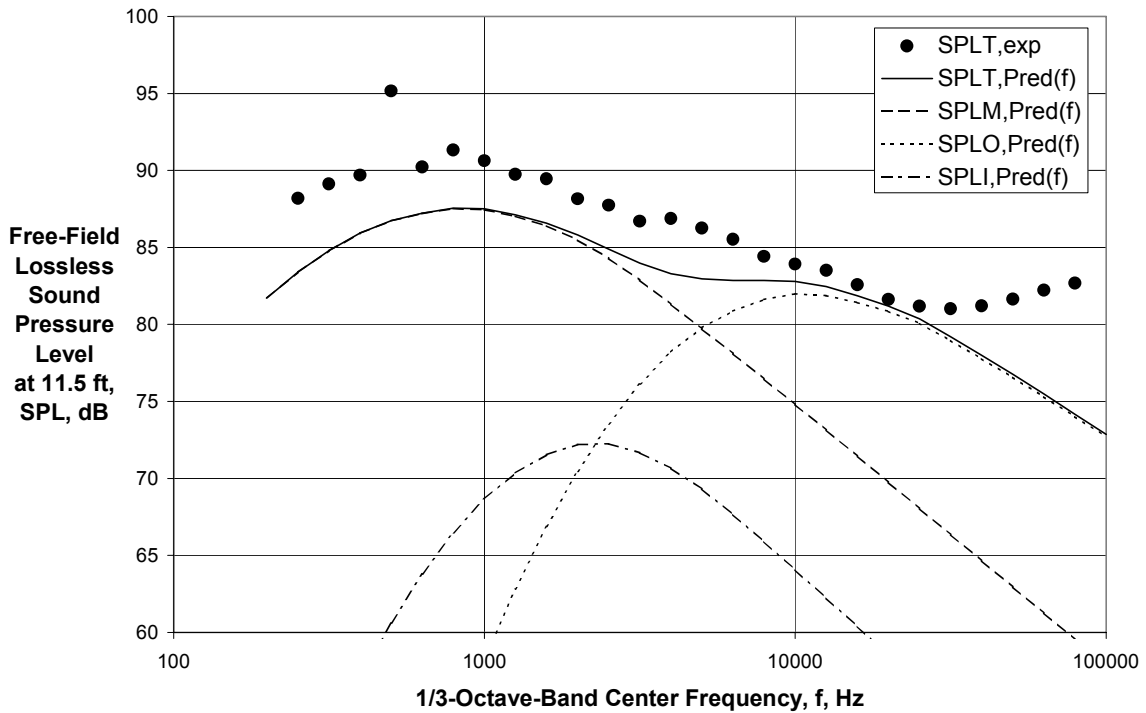
Figure 72 - Comparison of Experimental and Final Predicted Spectra for External Plug Nozzle with V_{mix}/c_{amb} = 0.835, M_f = 0.10 (A_O/A_I = 2.66, Cond. 50010, Ref. 31)
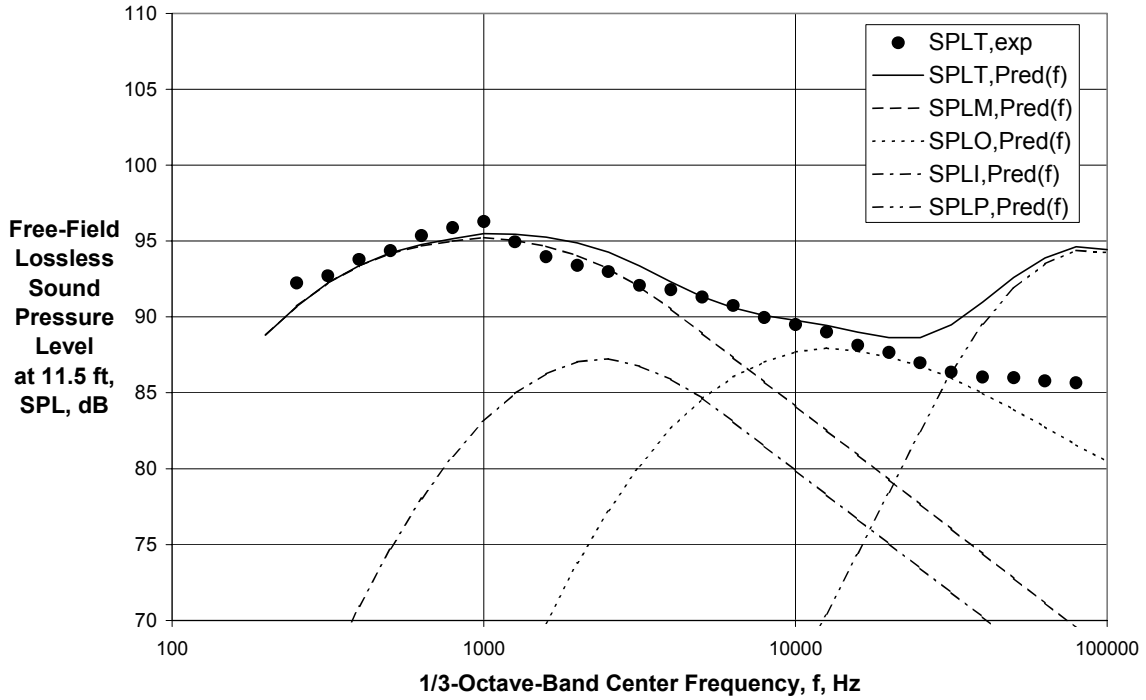
(c) Directivity Angle = 117 deg
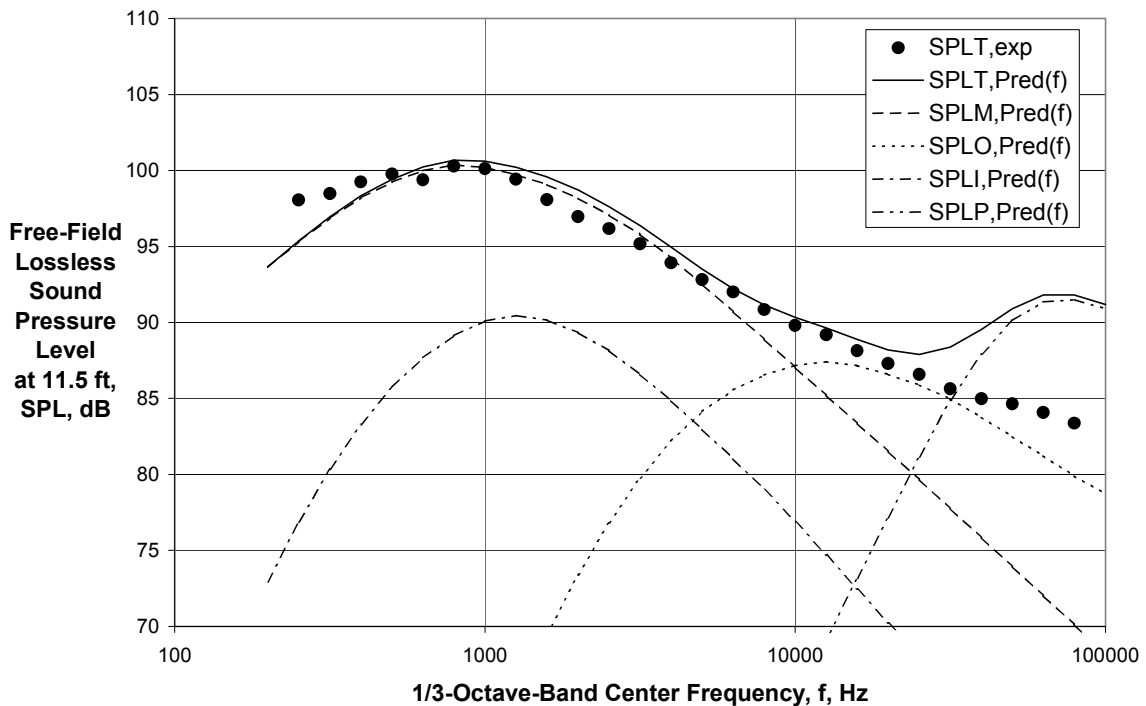
(d) Directivity Angle = 136 deg

Figure 72 (Continued) - Comparison of Experimental and Final Predicted Spectra for External Plug Nozzle with V_{mix}/c_{amb} = 0.835, M_f = 0.10 (A_O/A_I = 2.66, Cond. 50010, Ref. 31)
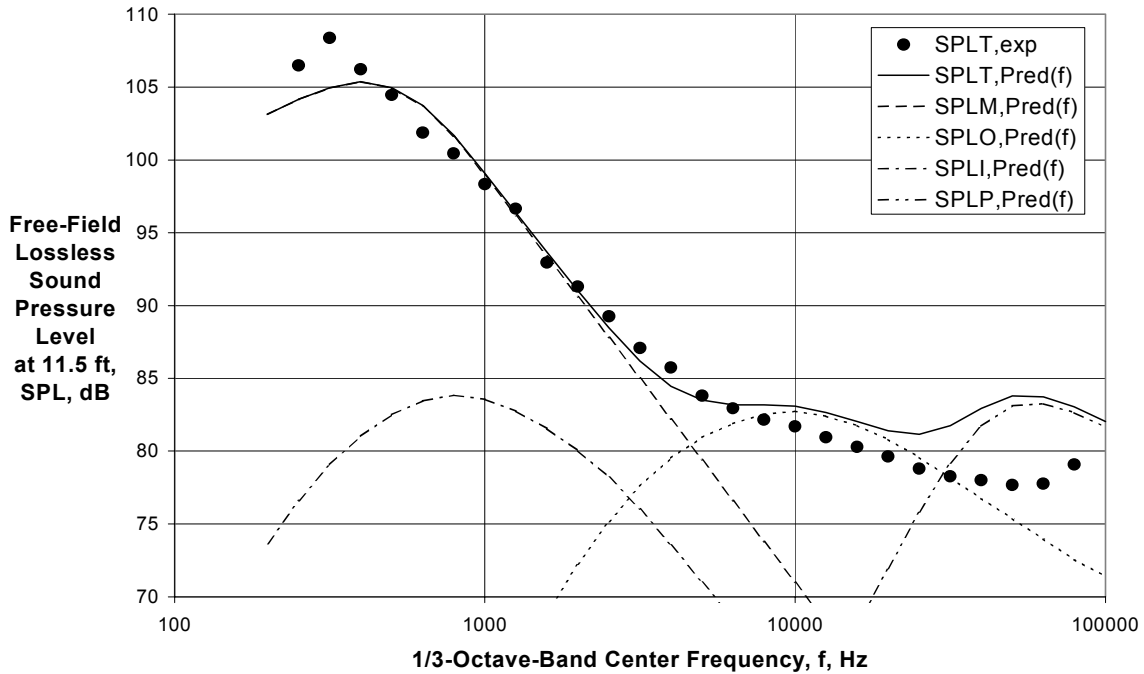
(e) Directivity Angle = 157 deg

Figure 72 (Concluded) - Comparison of Experimental and Final Predicted Spectra for External Plug Nozzle with V_{mix}/c_{amb} = 0.835, M_f = 0.10 (A_O/A_I = 2.66, Cond. 50010, Ref. 31)
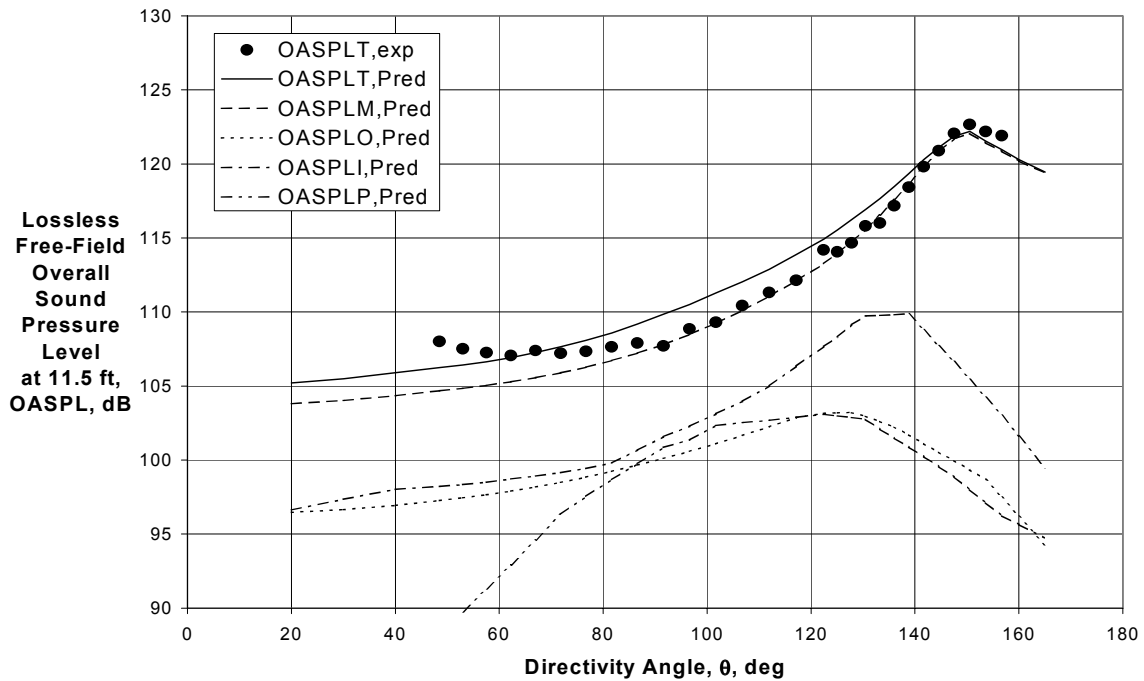
Figure 73 - Comparison of Experimental and Final Predicted Directivities for External Plug Nozzle with V_{mix}/c_{amb} = 0.989, M_f = 0.10 (A_O/A_I = 2.66, Cond. 150010, Ref. 31)
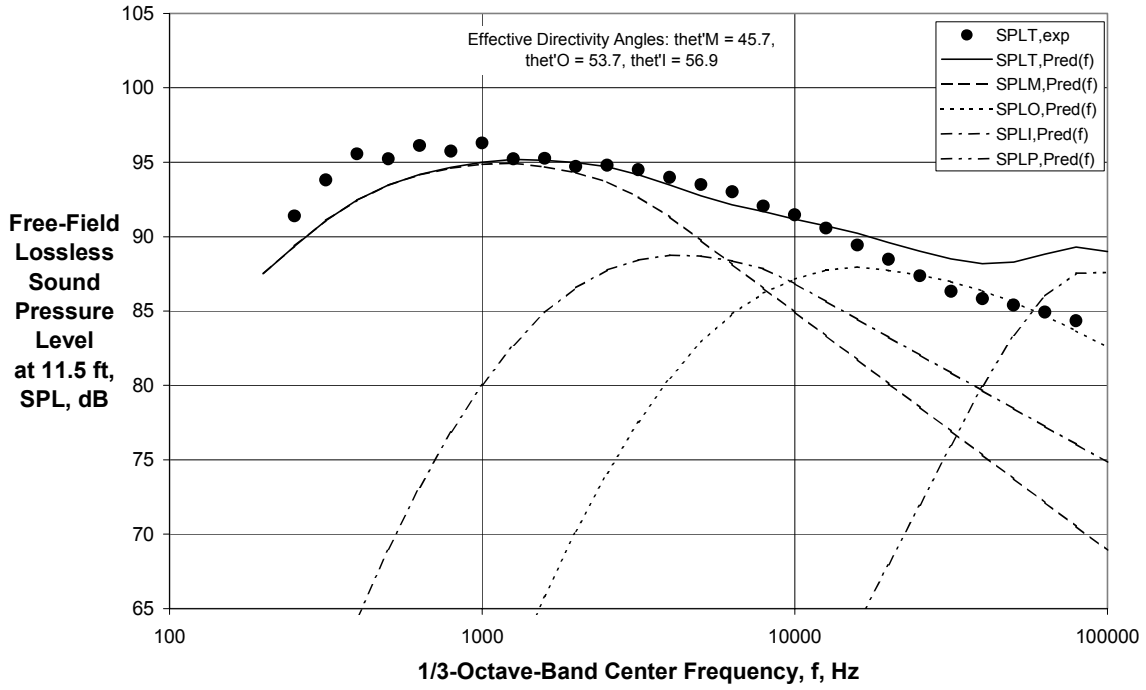
(a) Directivity Angle = 58 deg
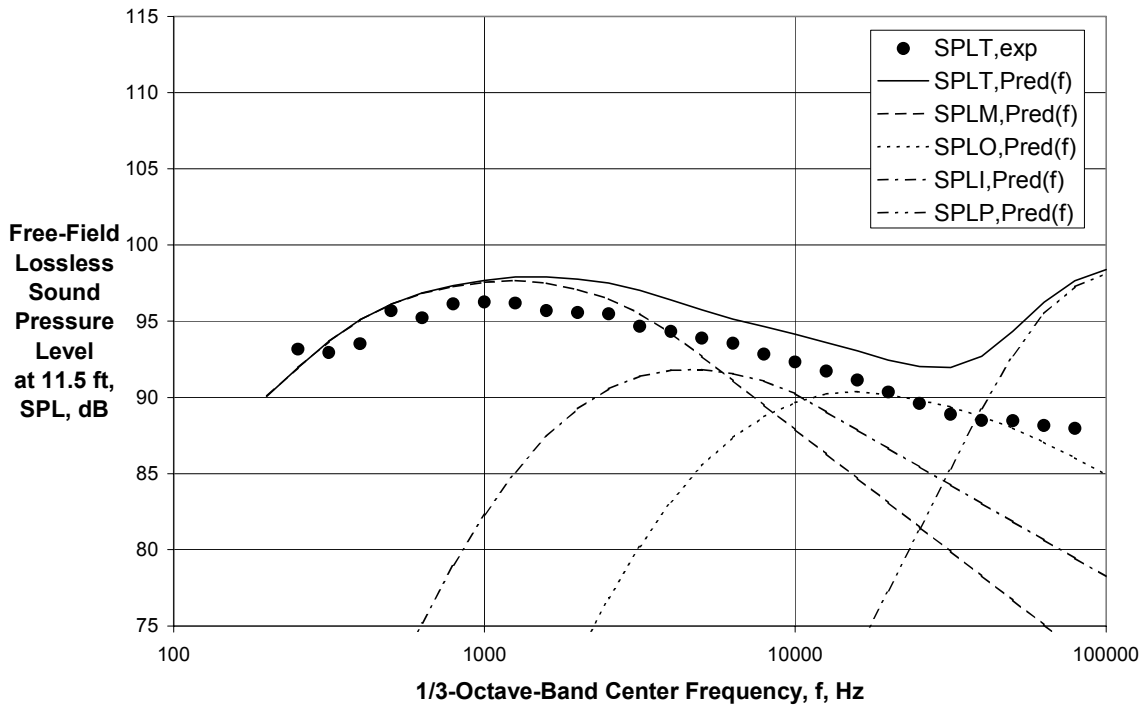
(b) Directivity Angle = 92 deg

Figure 74 - Comparison of Experimental and Final Predicted Spectra for External Plug Nozzle with V_{mix}/c_{amb} = 0.989, M_f = 0.10 (A_O/A_I = 2.66, Cond. 150010, Ref. 31)
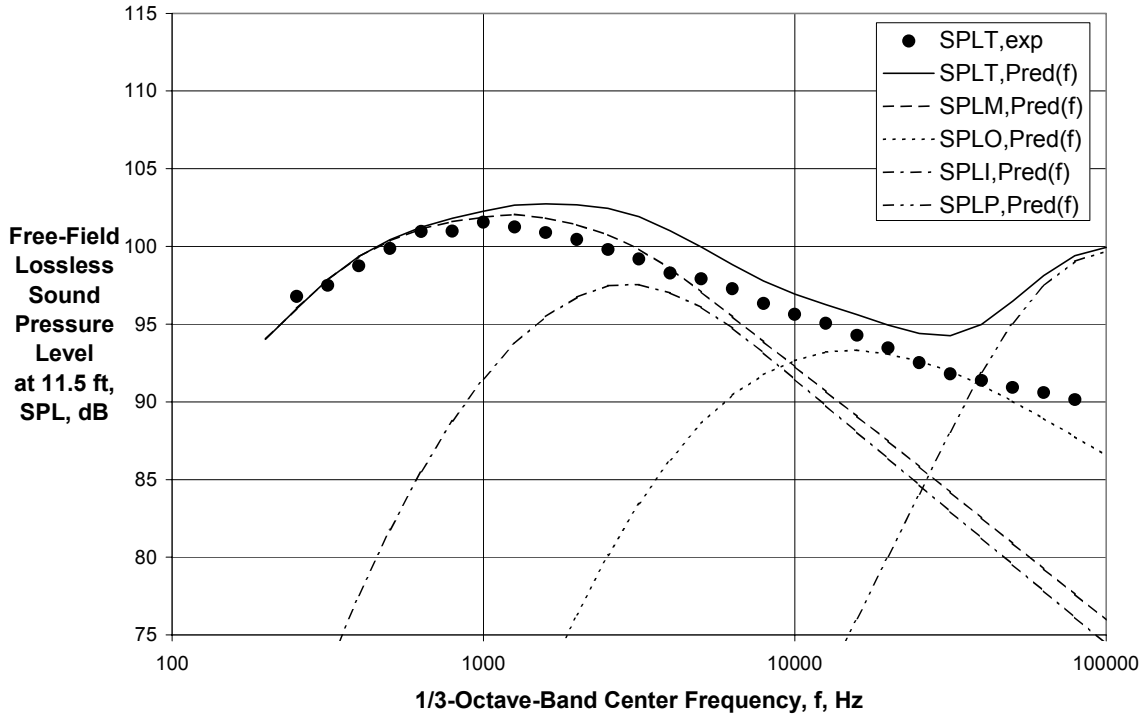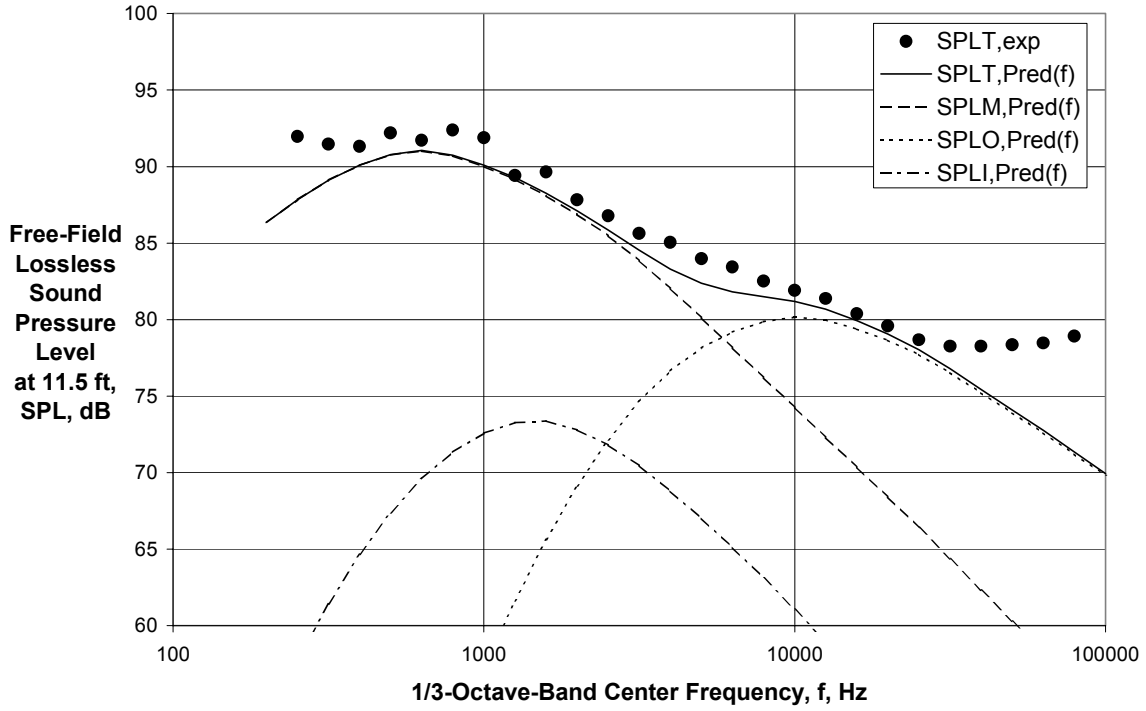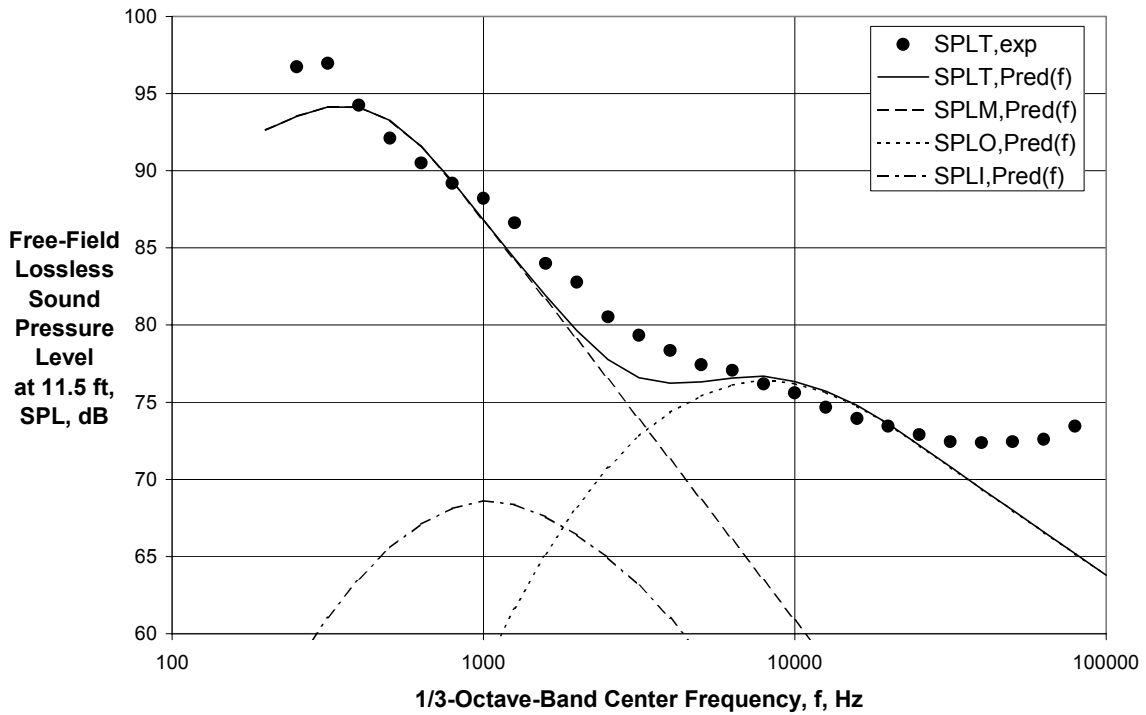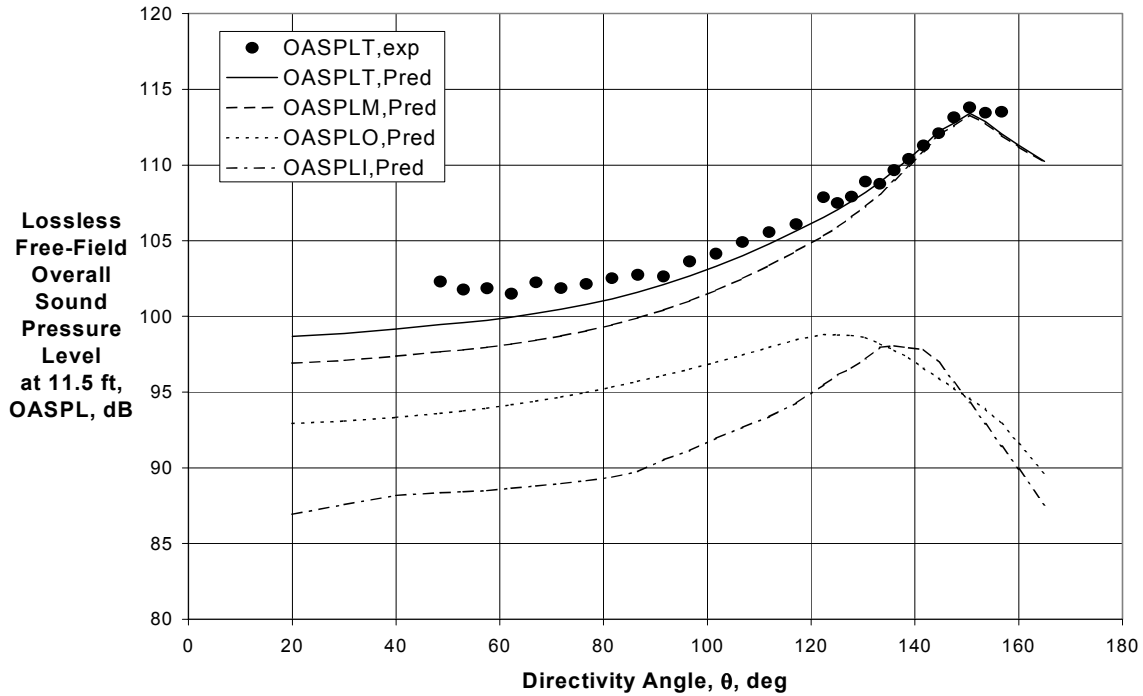
(c) Directivity Angle = 117 deg

(d) Directivity Angle = 136 deg

Figure 74 (Continued) - Comparison of Experimental and Final Predicted Spectra for External Plug Nozzle with V_{mix}/c_{amb} = 0.989, M_f = 0.10 (A_O/A_I = 2.66, Cond. 150010, Ref. 31)
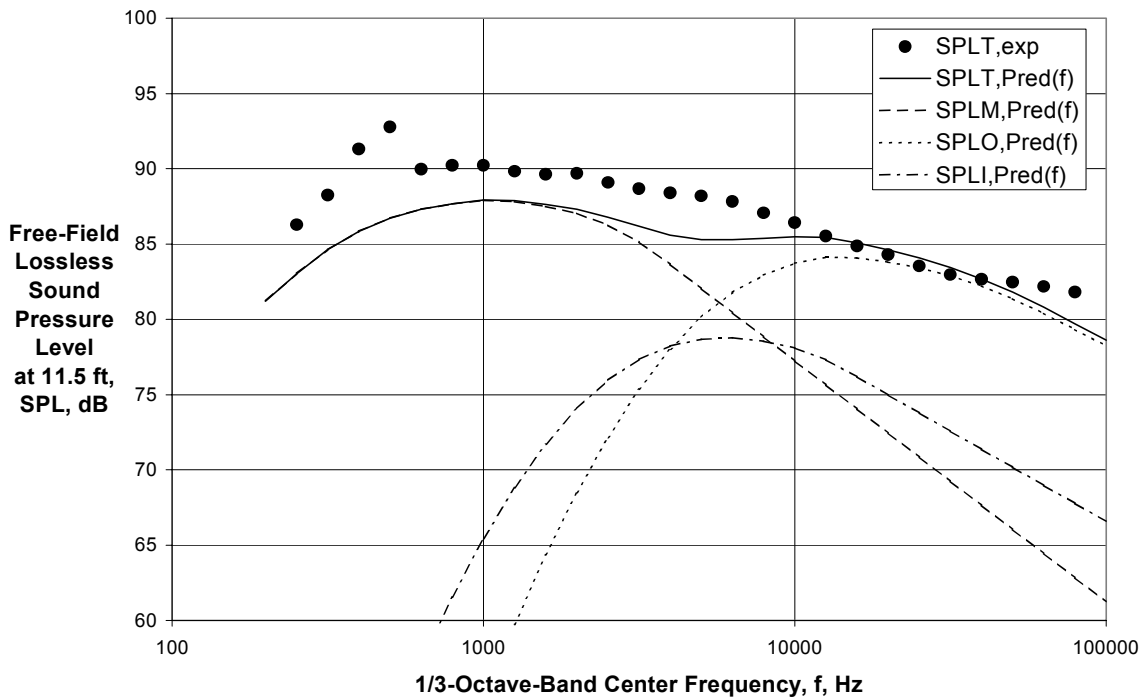
(e) Directivity Angle = 157 deg

Figure 74 (Concluded) - Comparison of Experimental and Final Predicted Spectra for External Plug Nozzle with V_{mix}/c_{amb} = 0.989, M_f = 0.10 (A_O/A_I = 2.66, Cond. 150010, Ref. 31)
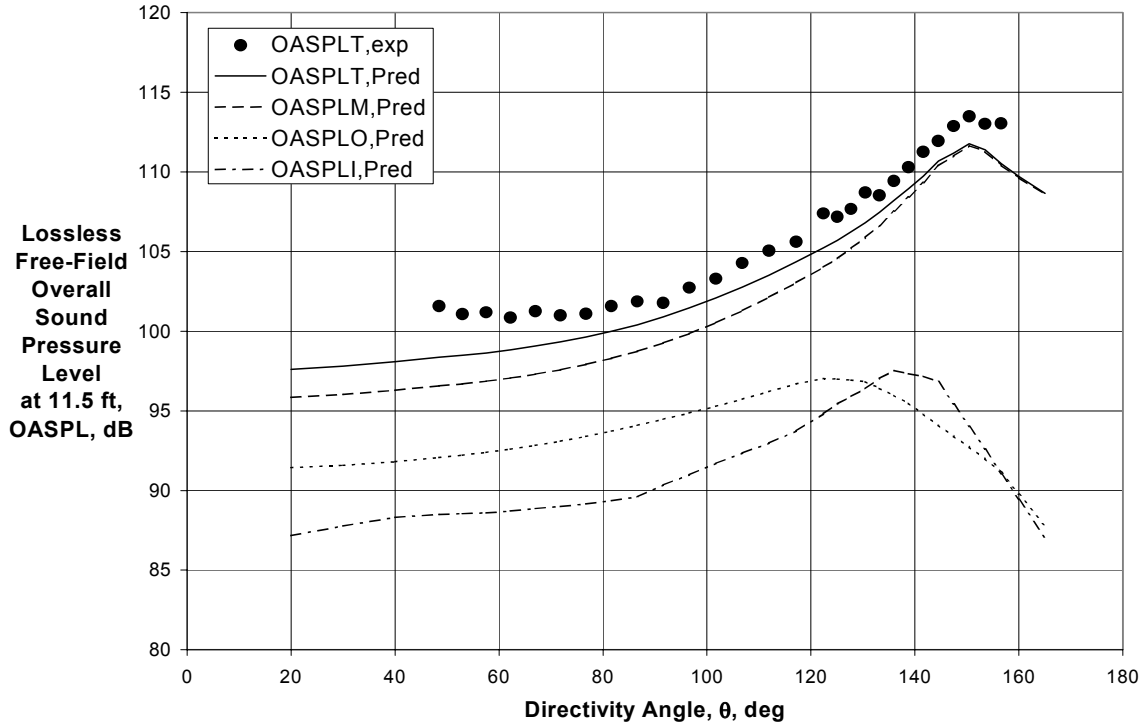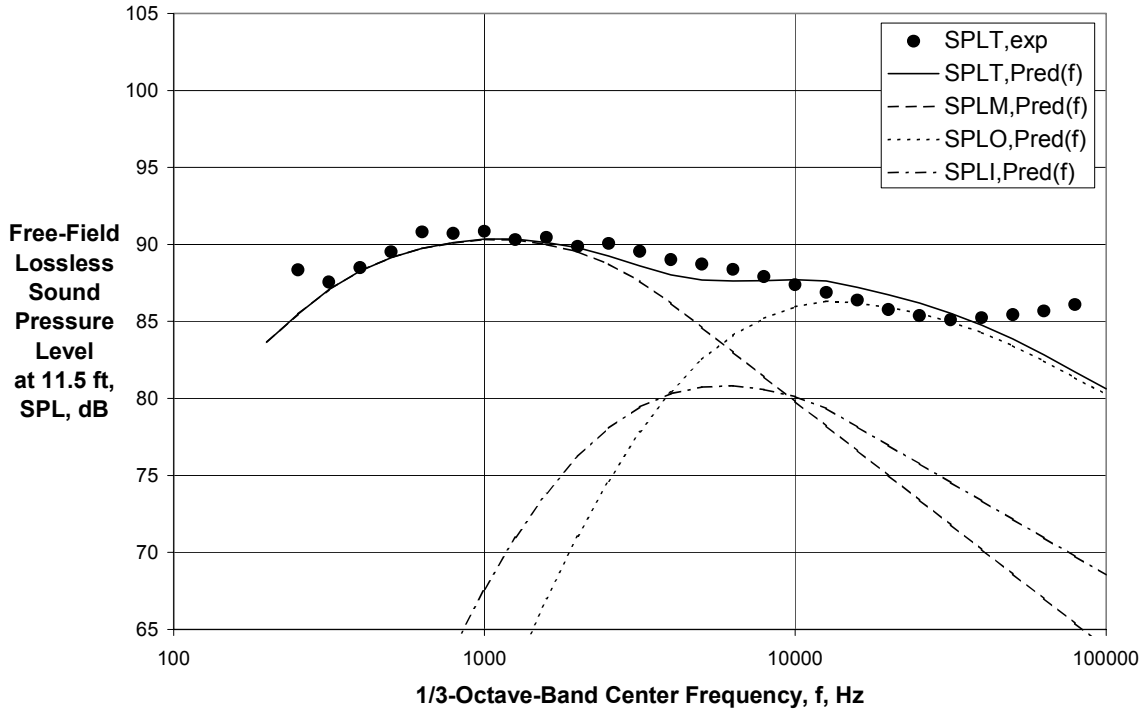

Figure 75 - Comparison of Experimental and Final Predicted Directivities for Internal Plug Nozzle with V_{mix}/c_{amb} = 0.809, M_f = 0.10 (A_O/A_I = 2.72, Cond. 50010, Ref. 31)
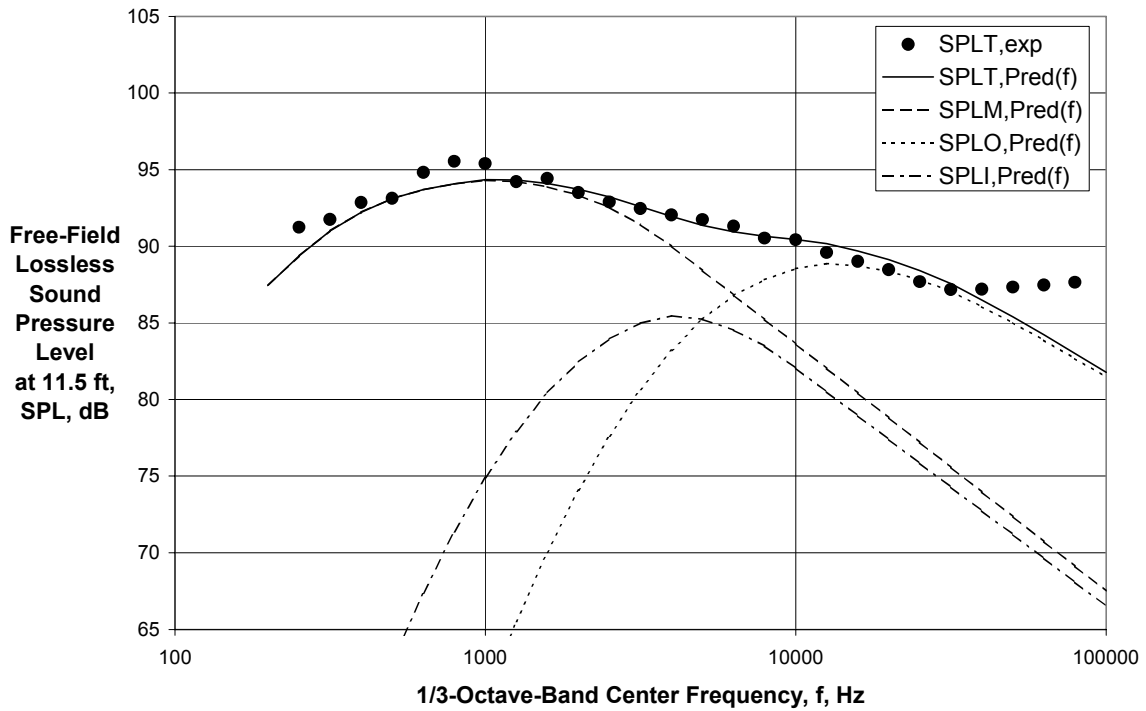
(a) Directivity Angle = 58 deg
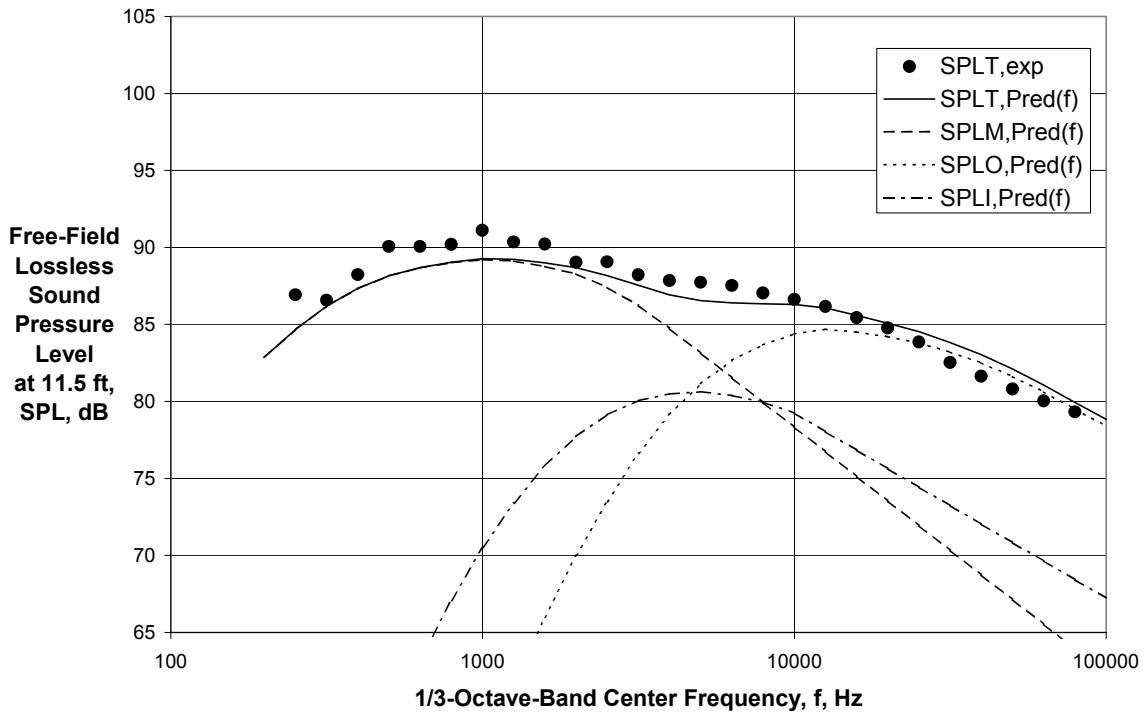
(b) Directivity Angle = 92 deg

Figure 76 - Comparison of Experimental and Final Predicted Spectra for Internal Plug Nozzle with V_{mix}/c_{amb} = 0.809, M_f = 0.10 (A_O/A_I = 2.72, Cond. 50010, Ref. 31)
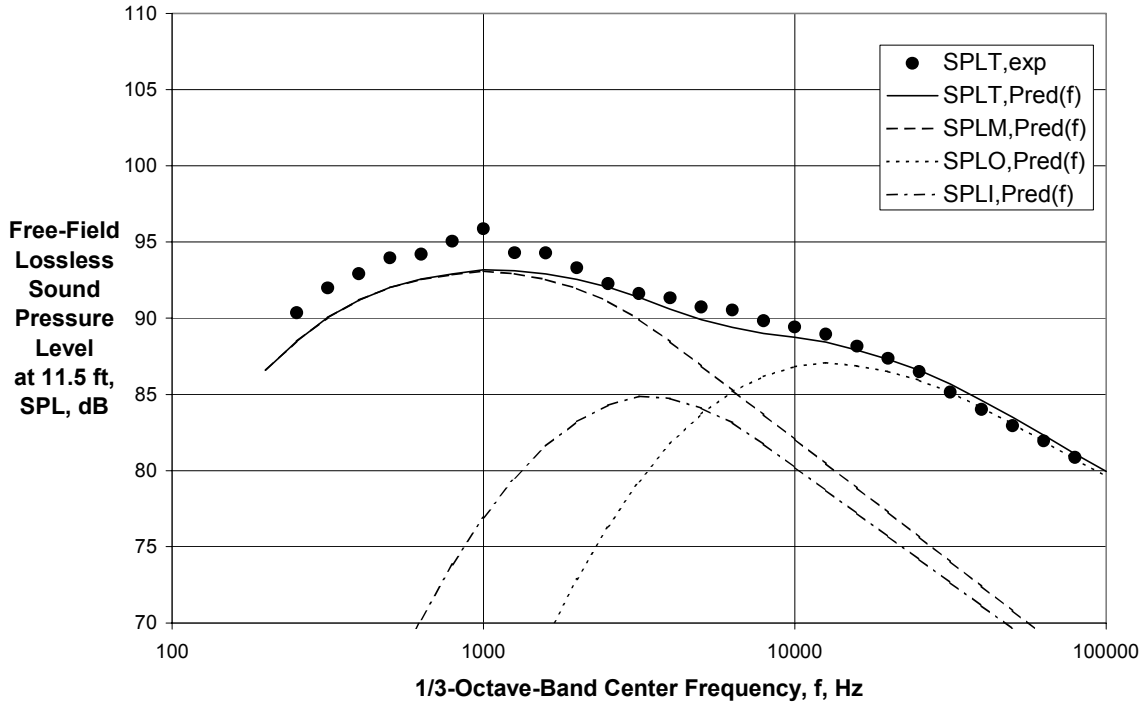
(c) Directivity Angle = 117 deg

(d) Directivity Angle = 136 deg

Figure 76 (Continued) - Comparison of Experimental and Final Predicted Spectra for Internal Plug Nozzle with V_{mix}/c_{amb} = 0.809, M_f = 0.10 (A_O/A_I = 2.72, Cond. 50010, Ref. 31)

(e) Directivity Angle = 157 deg

Figure 76 (Concluded) - Comparison of Experimental and Final Predicted Spectra for Internal Plug Nozzle with V_{mix}/c_{amb} = 0.809, M_f = 0.10 (A_O/A_I = 2.72, Cond. 50010, Ref. 31)
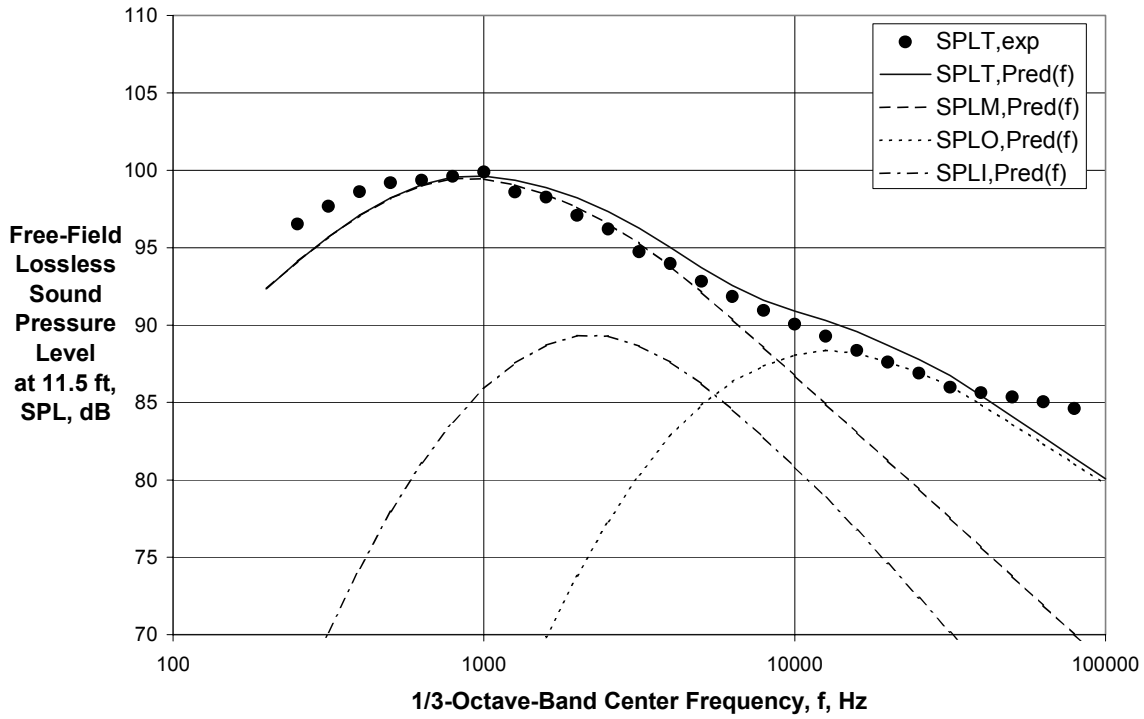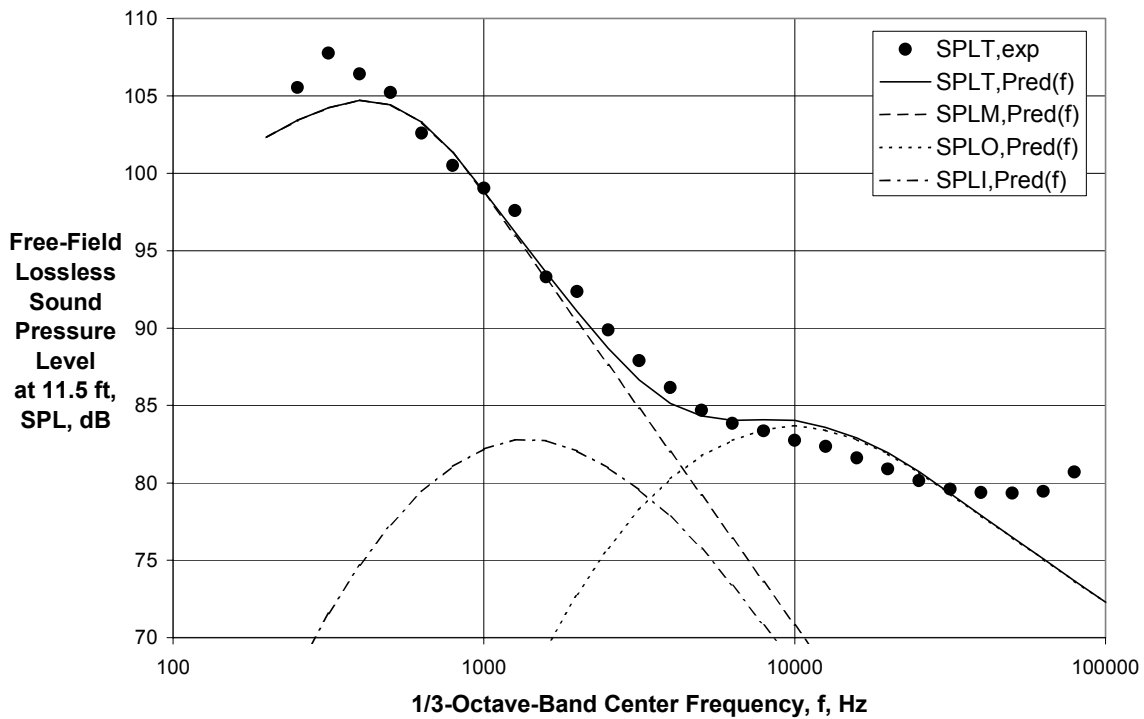

Figure 77 - Comparison of Experimental and Final Predicted Directivities for Internal Plug Nozzle with V_{mix}/c_{amb} = 0.967, M_f = 0.10 (A_O/A_I = 2.72, Cond. 150010, Ref. 31)

(a) Directivity Angle = 58 deg

(b) Directivity Angle = 92 deg

Figure 78 - Comparison of Experimental and Final Predicted Spectra for Internal Plug Nozzle with V_{mix}/c_{amb} = 0.967, M_f = 0.10 (A_O/A_I = 2.72, Cond. 150010, Ref. 31)
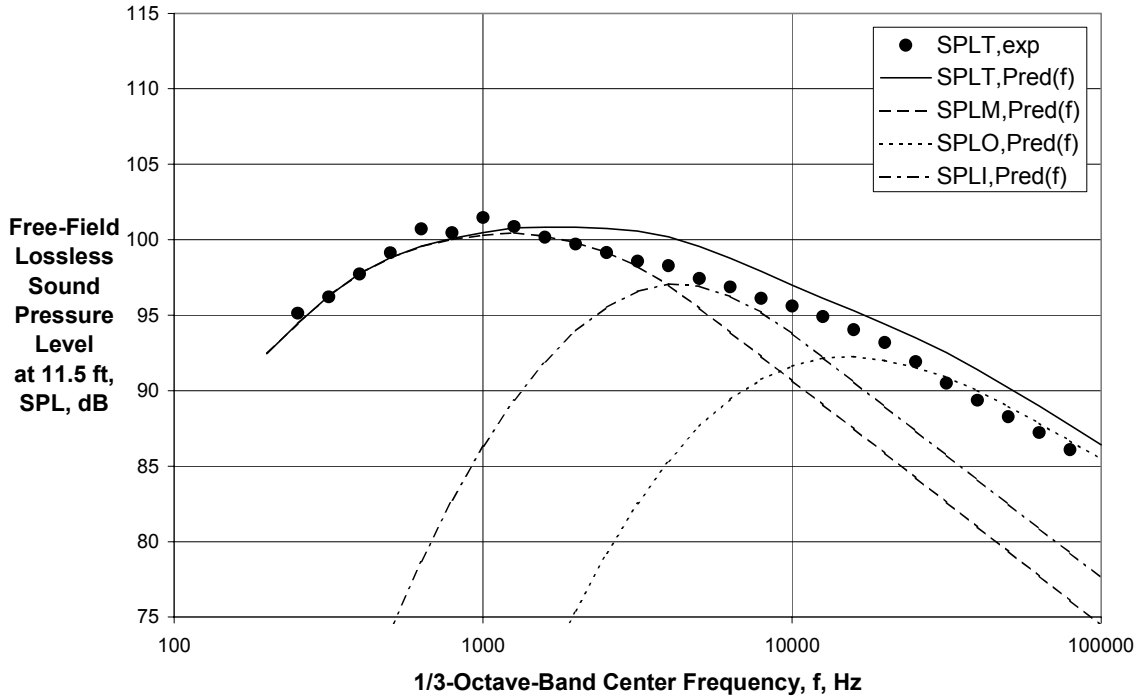
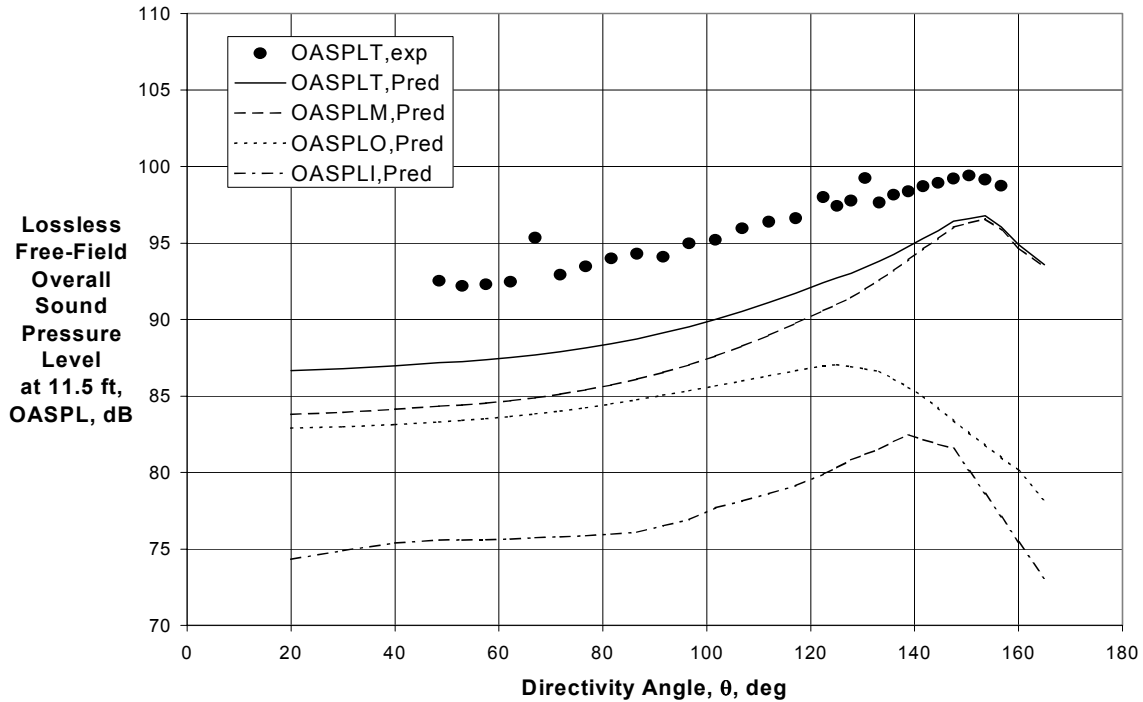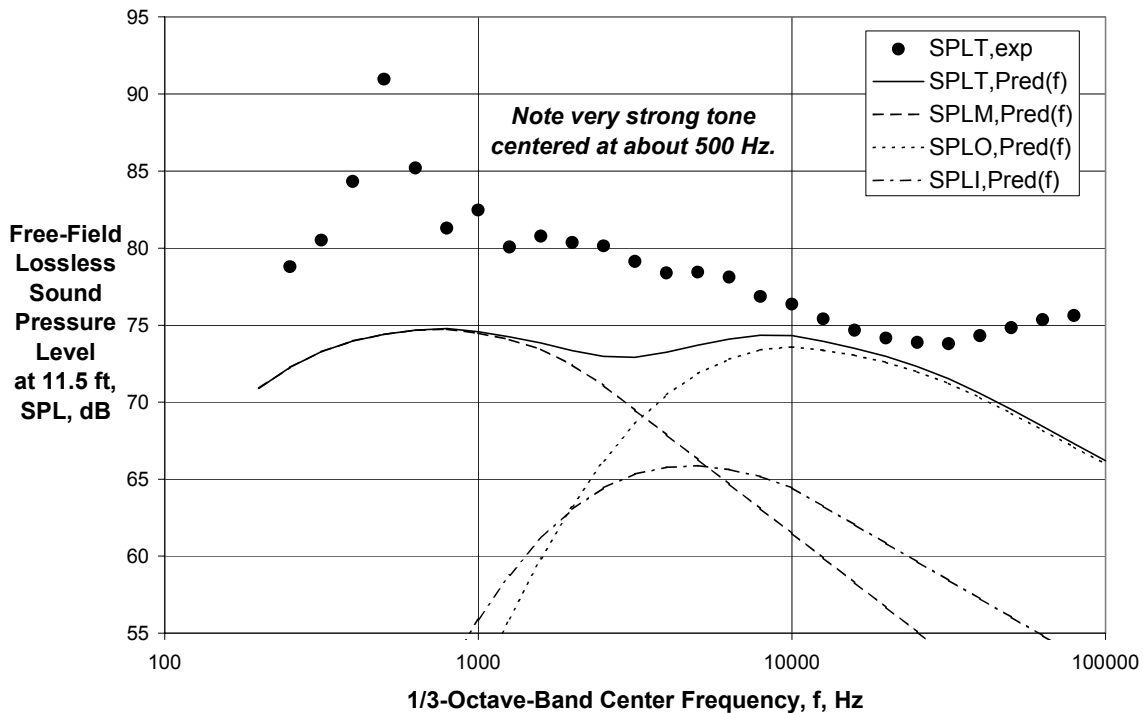**(c) Directivity Angle = 117 deg**

(d) Directivity Angle = 136 deg

Figure 78 (Continued) - Comparison of Experimental and Final Predicted Spectra for Internal Plug Nozzle with V_{mix}/c_{amb} = 0.967, M_f = 0.10 (A_O/A_I = 2.72, Cond. 150010, Ref. 31)

(e) Directivity Angle = 157 deg

Figure 78 (Concluded) - Comparison of Experimental and Final Predicted Spectra for Internal Plug Nozzle with V_{mix}/c_{amb} = 0.967, M_f = 0.10 (A_O/A_I = 2.72, Cond. 150010, Ref. 31)
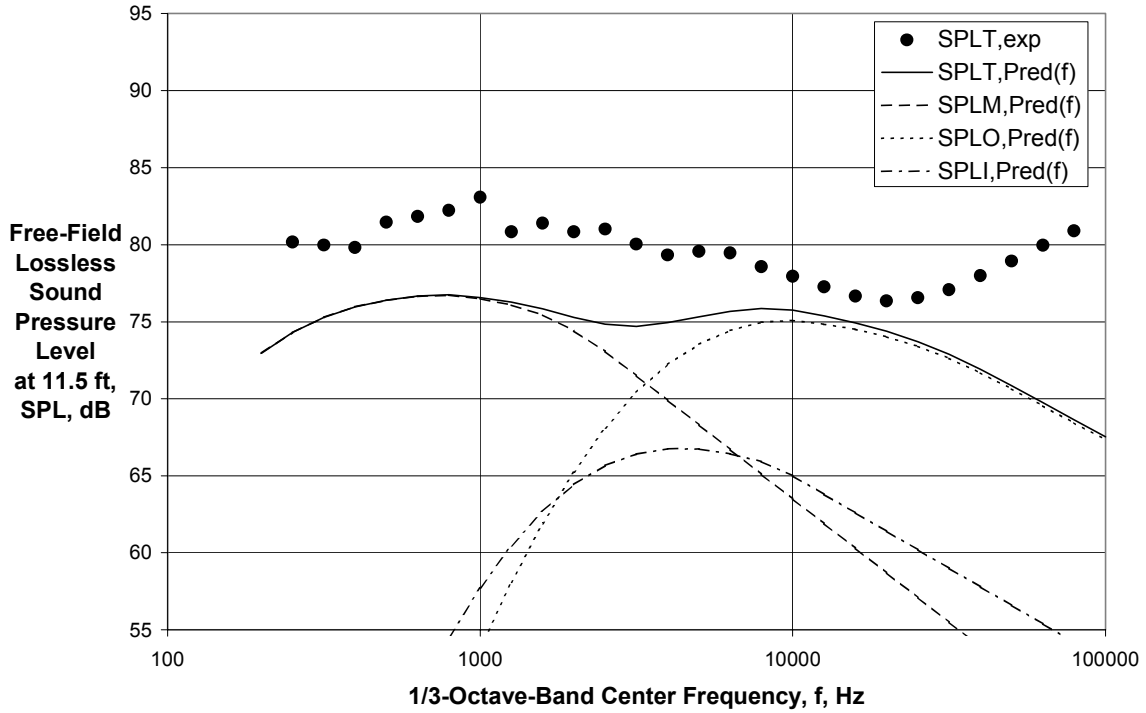

Figure 79 - Comparison of Experimental and Final Predicted Directivities for External Plug Nozzle with V_{mix}/c_{amb} = 0.671, M_f = 0.10 (A_O/A_I = 4.18, Cond. 250010, Ref. 31)
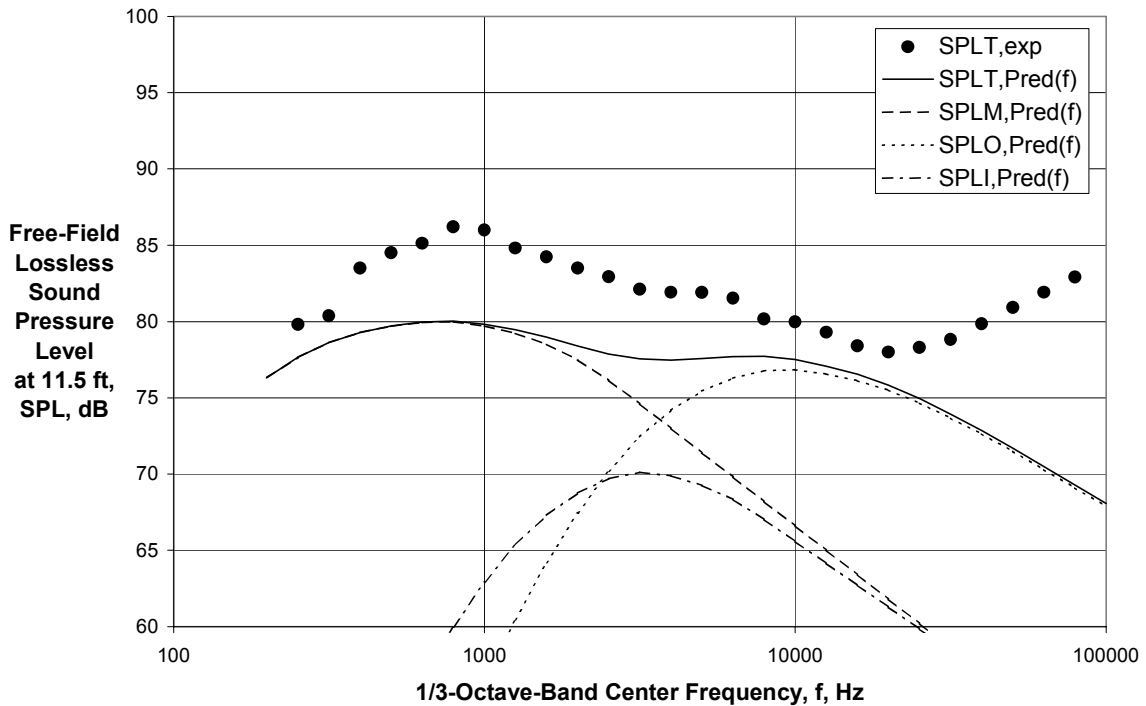
(a) Directivity Angle = 67 deg

(b) Directivity Angle = 92 deg

Figure 80 - Comparison of Experimental and Final Predicted Spectra for External Plug Nozzle with V_{mix}/c_{amb} = 0.671, M_f = 0.10 (A_O/A_I = 4.18, Cond. 250010, Ref. 31)
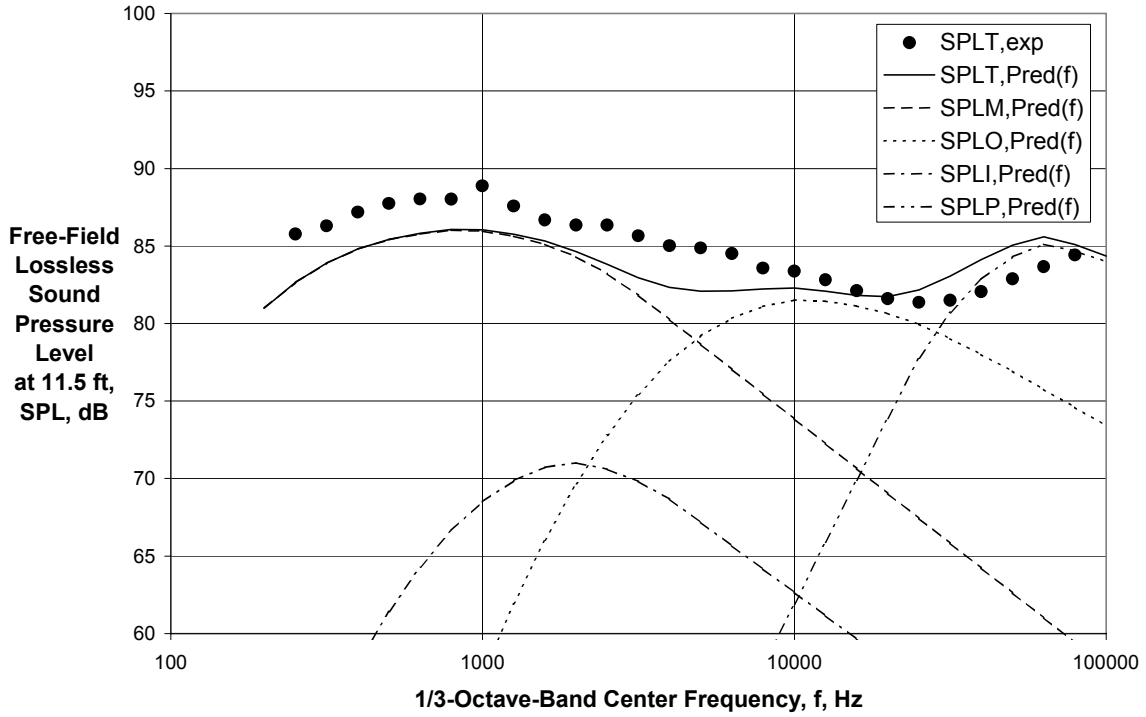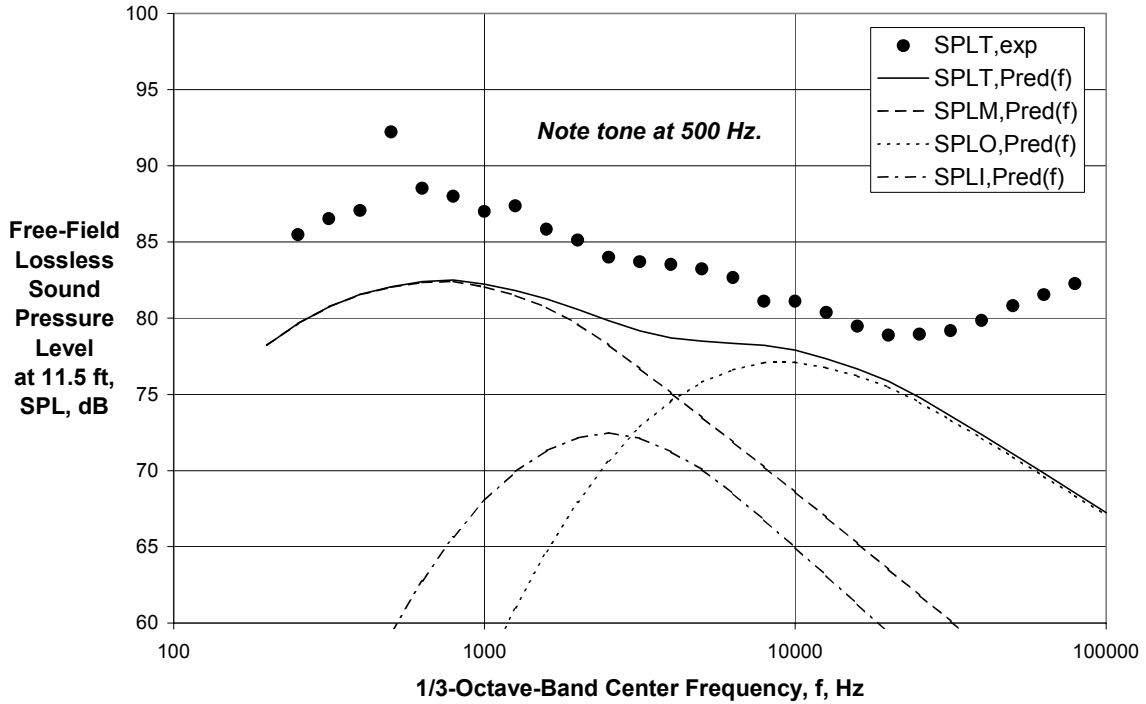
(c) Directivity Angle = 117 deg

(d) Directivity Angle = 136 deg

Figure 80 (Continued) - Comparison of Experimental and Final Predicted Spectra for External Plug Nozzle with $V_{mix}/c_{amb} = 0.671$, $M_f = 0.10$ ($A_O/A_I = 4.18$, Cond. 250010, Ref. 31)
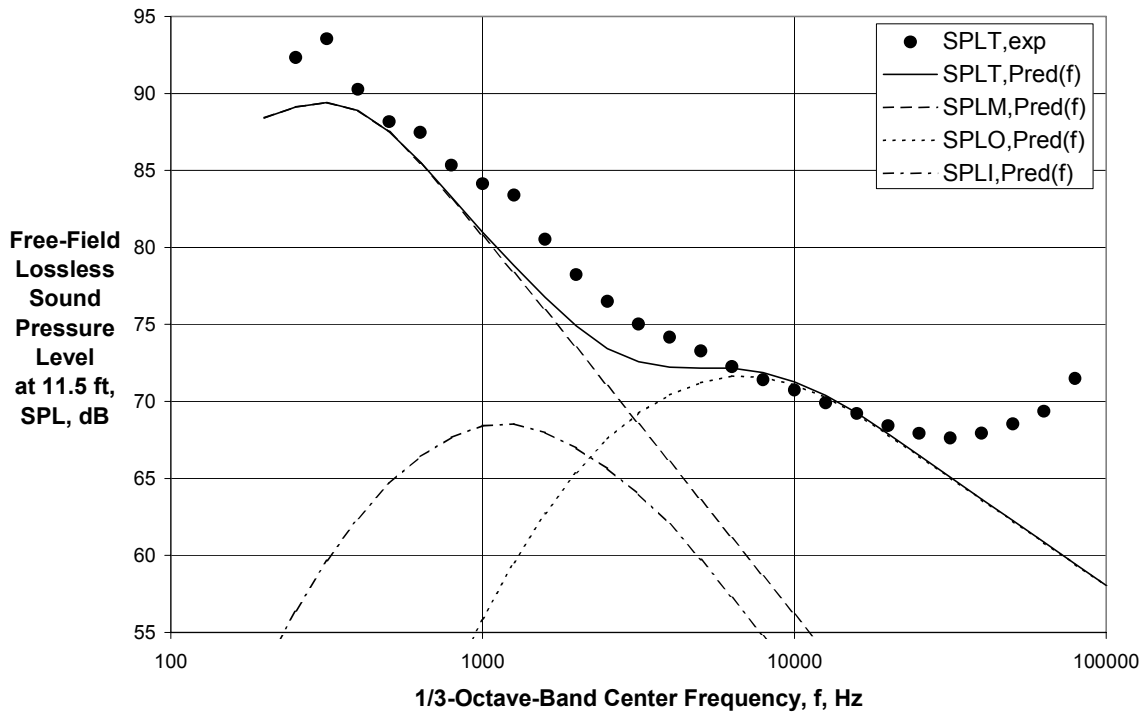
(e) Directivity Angle = 157 deg

Figure 80 (Concluded) - Comparison of Experimental and Final Predicted Spectra for External Plug Nozzle with V_{mix}/c_{amb} = 0.671, M_f = 0.10 (A_O/A_I = 4.18, Cond. 250010, Ref. 31)
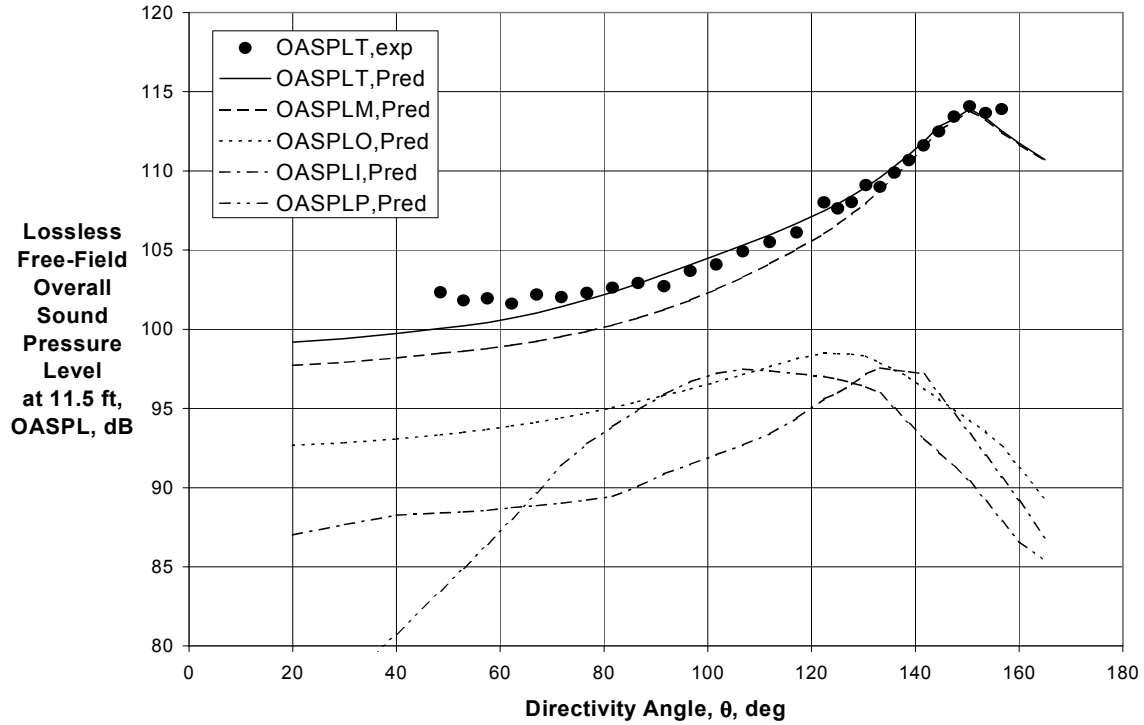
Figure 81 - Comparison of Experimental and Final Predicted Directivities for External Plug Nozzle with V_{mix}/c_{amb} = 0.828, M_f = 0.10 (A_O/A_I = 4.18, Cond. 310010, Ref. 31)

(a) Directivity Angle = 67 deg
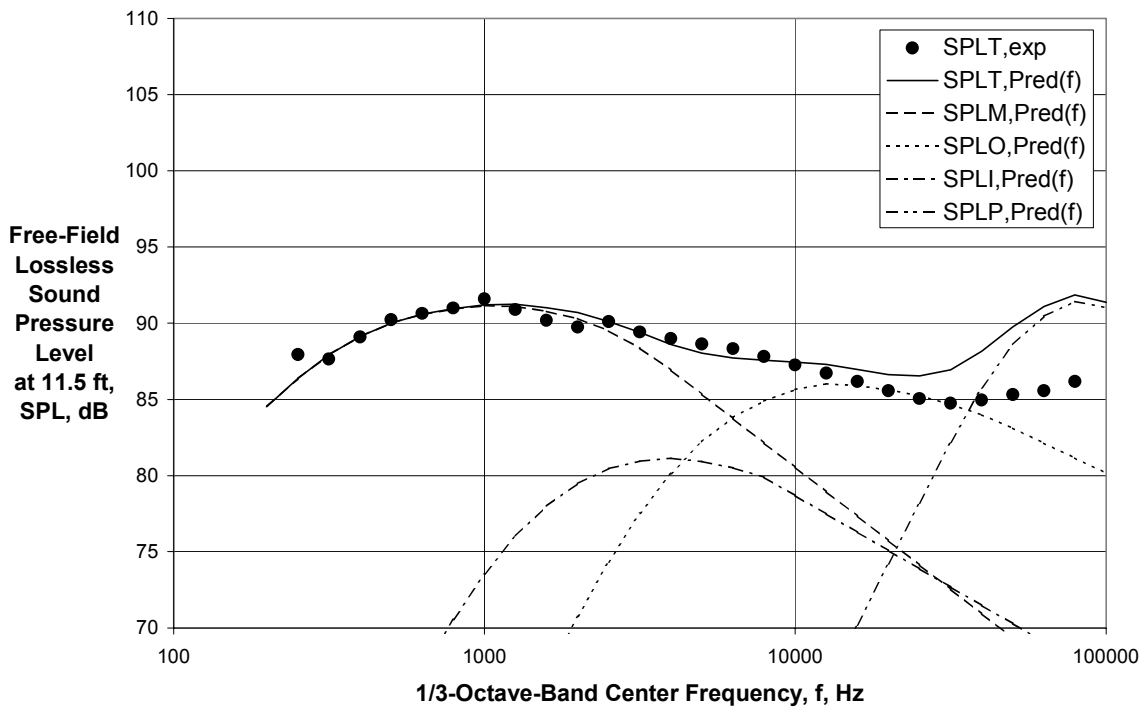
(b) Directivity Angle = 92 deg

Figure 82 - Comparison of Experimental and Final Predicted Spectra for External Plug Nozzle with V_{mix}/c_{amb} = 0.828, M_f = 0.10 (A_O/A_I = 4.18, Cond. 310010, Ref. 31)
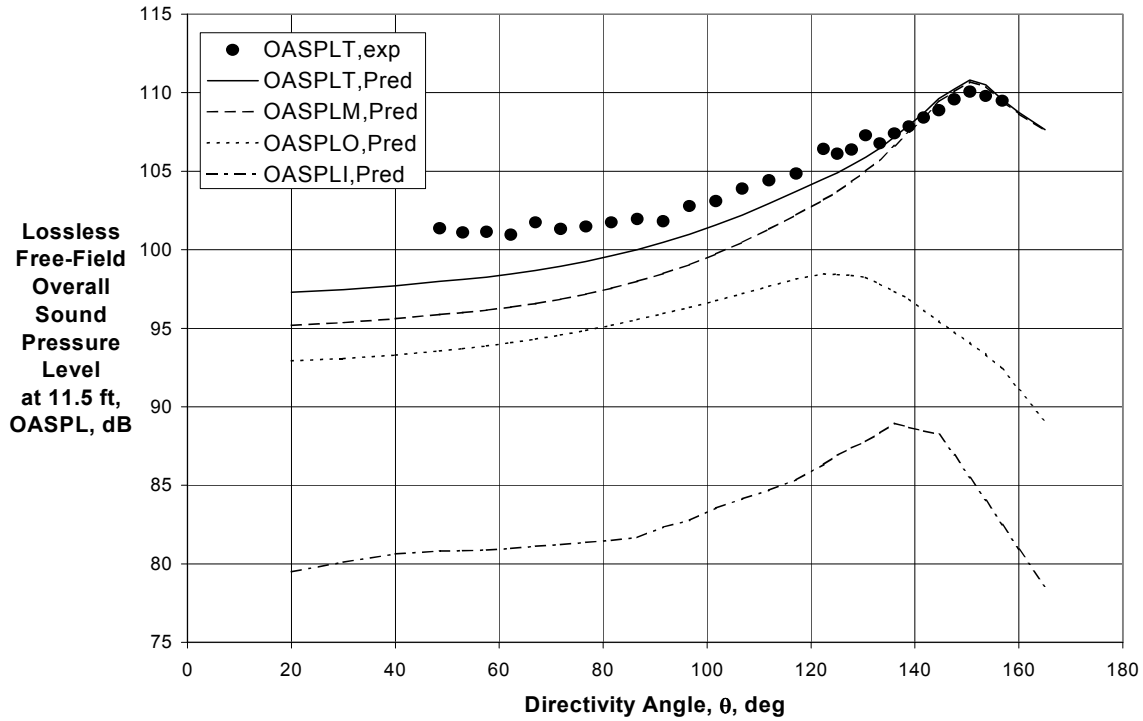
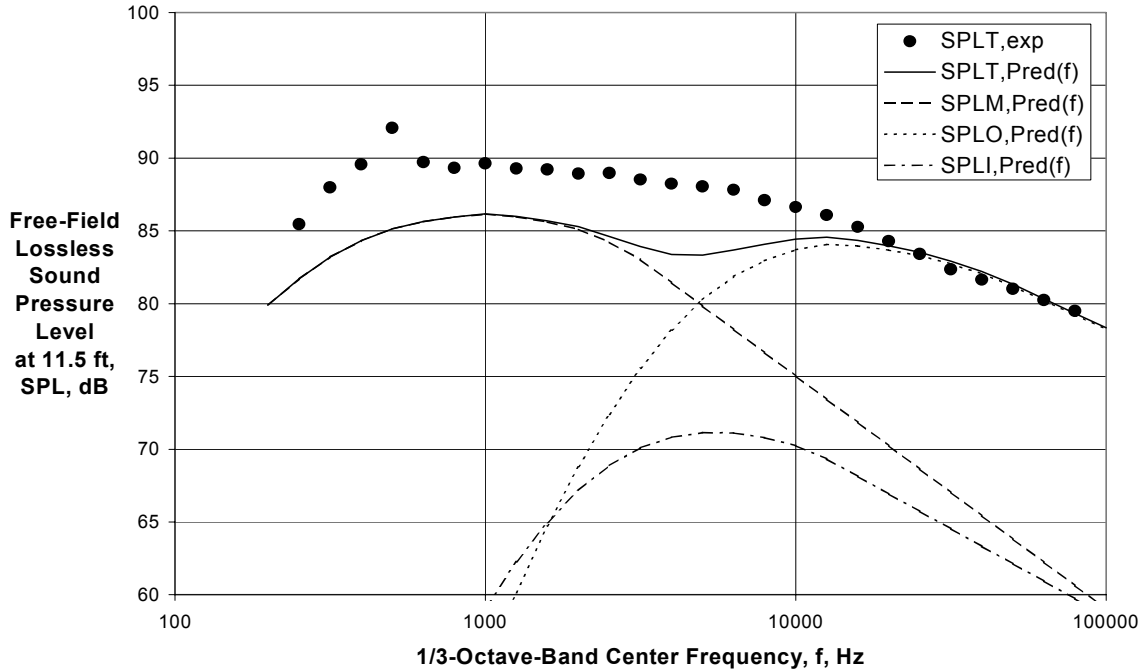**(c) Directivity Angle = 117 deg**

(d) Directivity Angle = 136 deg

Figure 82 (Continued) - Comparison of Experimental and Final Predicted Spectra for External Plug Nozzle with V_{mix}/c_{amb} = 0.828, M_f = 0.10 (A_O/A_I = 4.18, Cond. 310010, Ref. 31)

(e) Directivity Angle = 157 deg

Figure 82 (Concluded) - Comparison of Experimental and Final Predicted Spectra for External Plug Nozzle with V_{mix}/c_{amb} = 0.828, M_f = 0.10 (A_O/A_I = 4.18, Cond. 310010, Ref. 31)
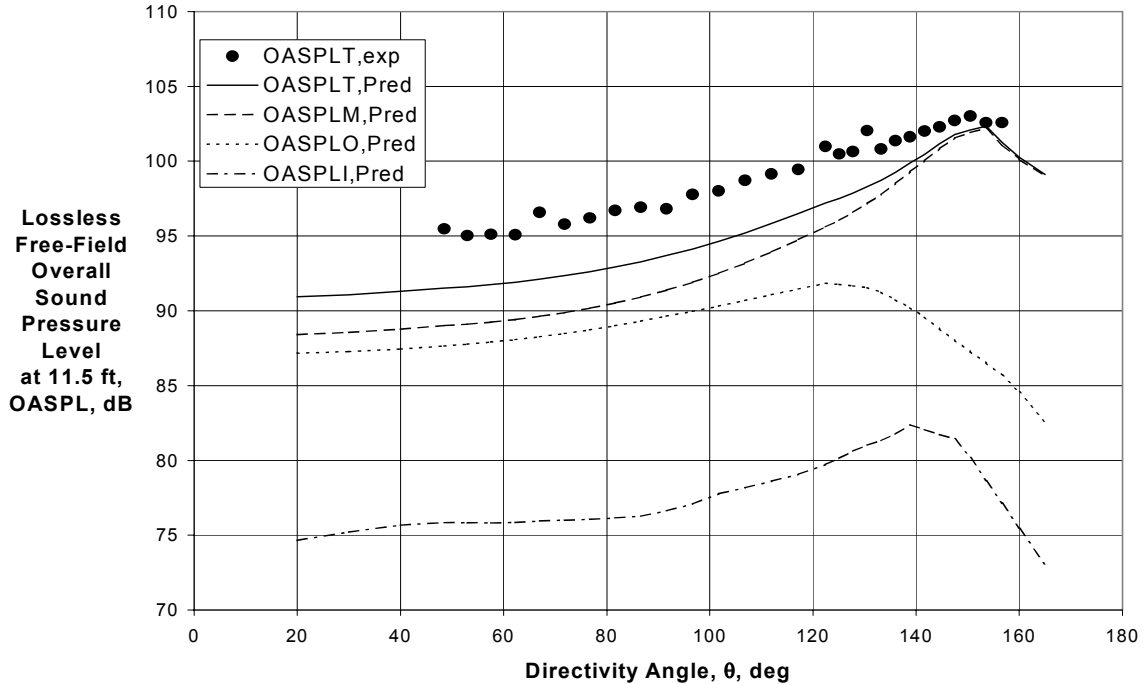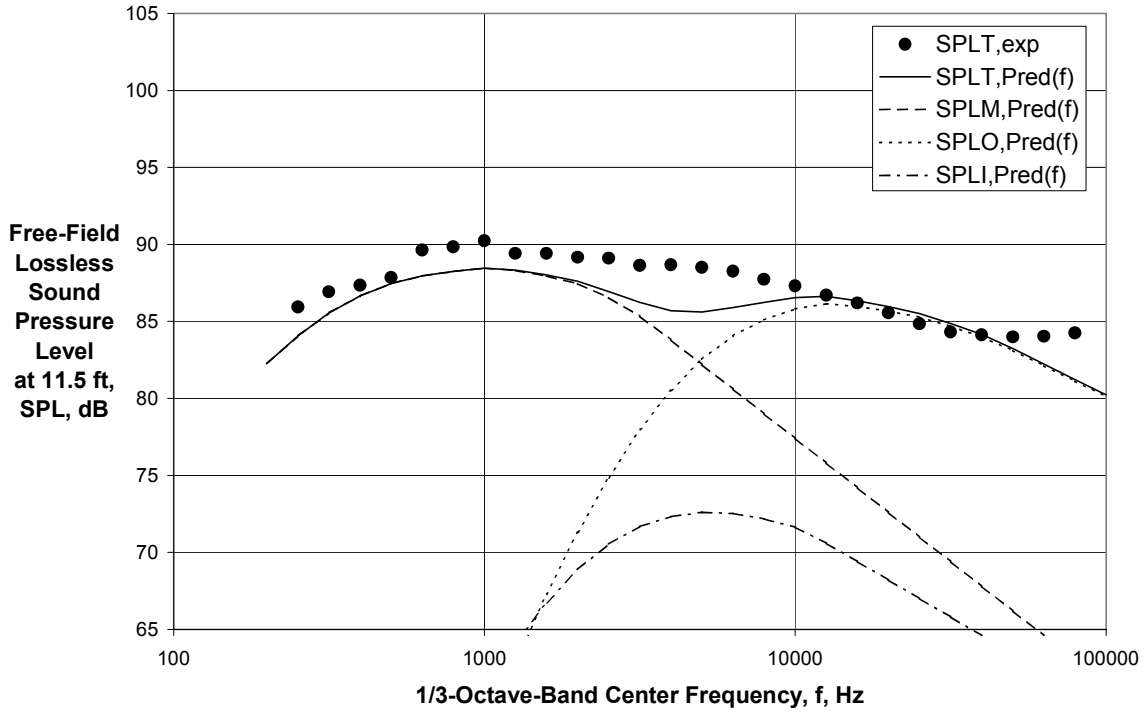

Figure 83 - Comparison of Experimental and Final Predicted Directivities for Internal Plug Nozzle with V_{mix}/c_{amb} = 0.676, M_f = 0.10 (A_O/A_I = 4.09, Cond. 250010, Ref. 31)
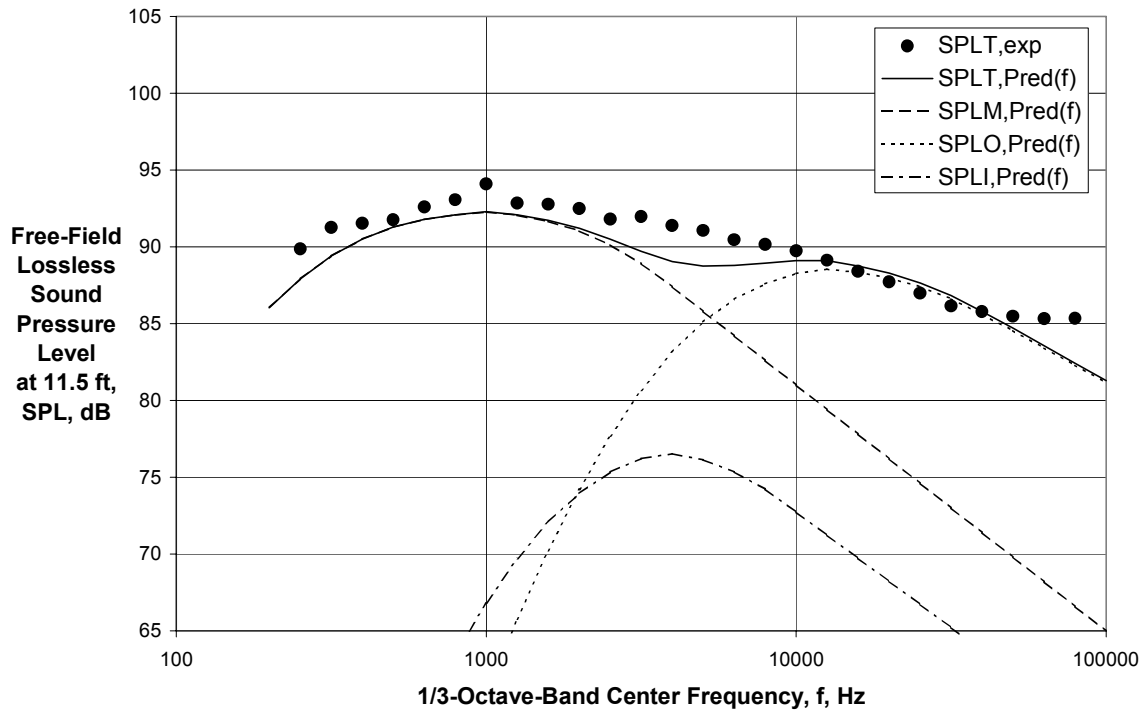
(a) Directivity Angle = 67 deg

(b) Directivity Angle = 92 deg

Figure 84 - Comparison of Experimental and Final Predicted Spectra for Internal Plug Nozzle with V_{mix}/c_{amb} = 0.676, M_f = 0.10 (A_O/A_I = 4.09, Cond. 250010, Ref. 31)

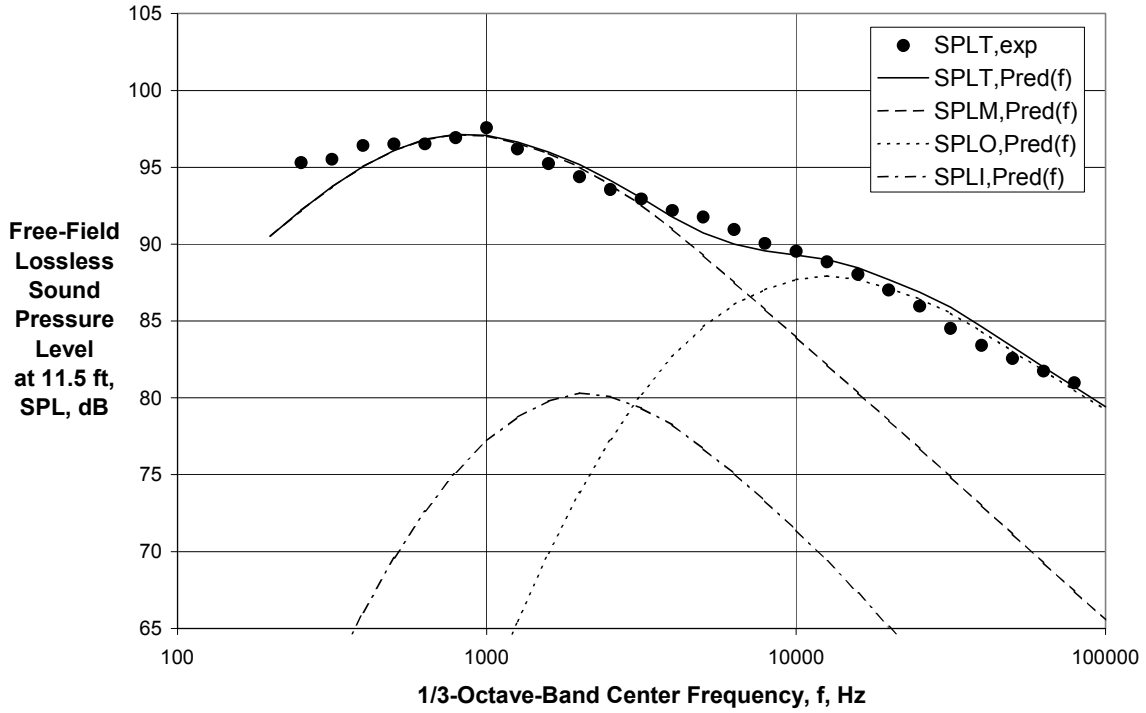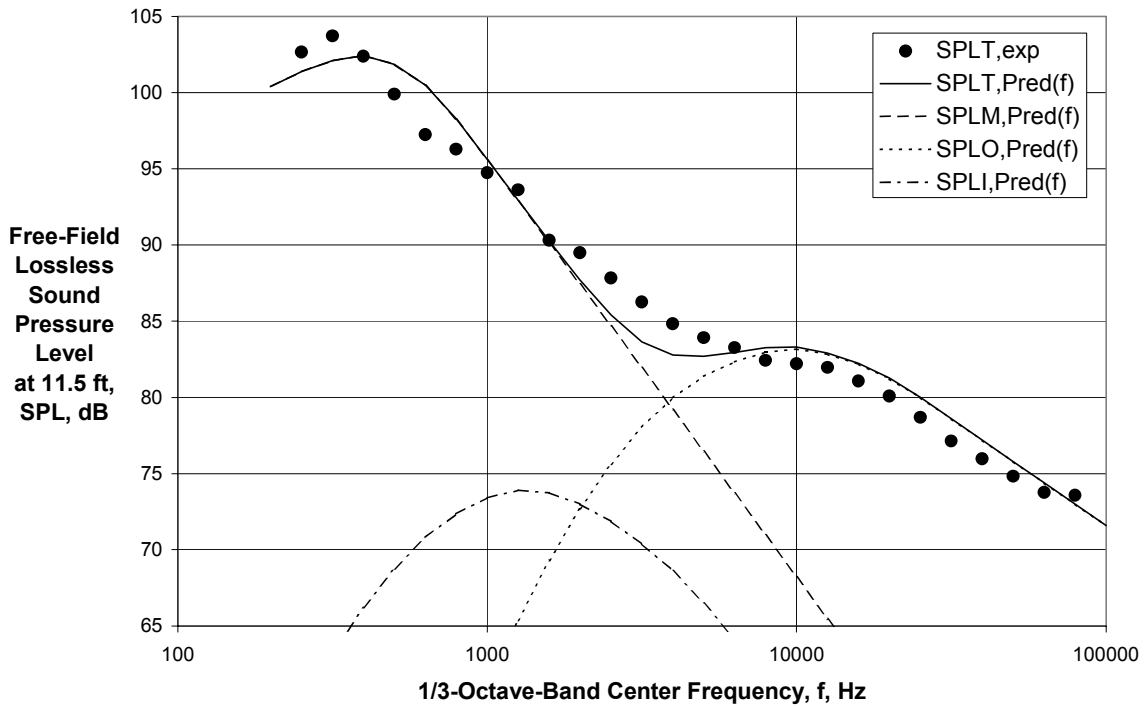**(c) Directivity Angle = 117 deg**

(d) Directivity Angle = 130 deg

Figure 84 (Continued) - Comparison of Experimental and Final Predicted Spectra for Internal Plug Nozzle with V_{mix}/c_{amb} = 0.676, M_f = 0.10 (A_O/A_I = 4.09, Cond. 250010, Ref. 31)
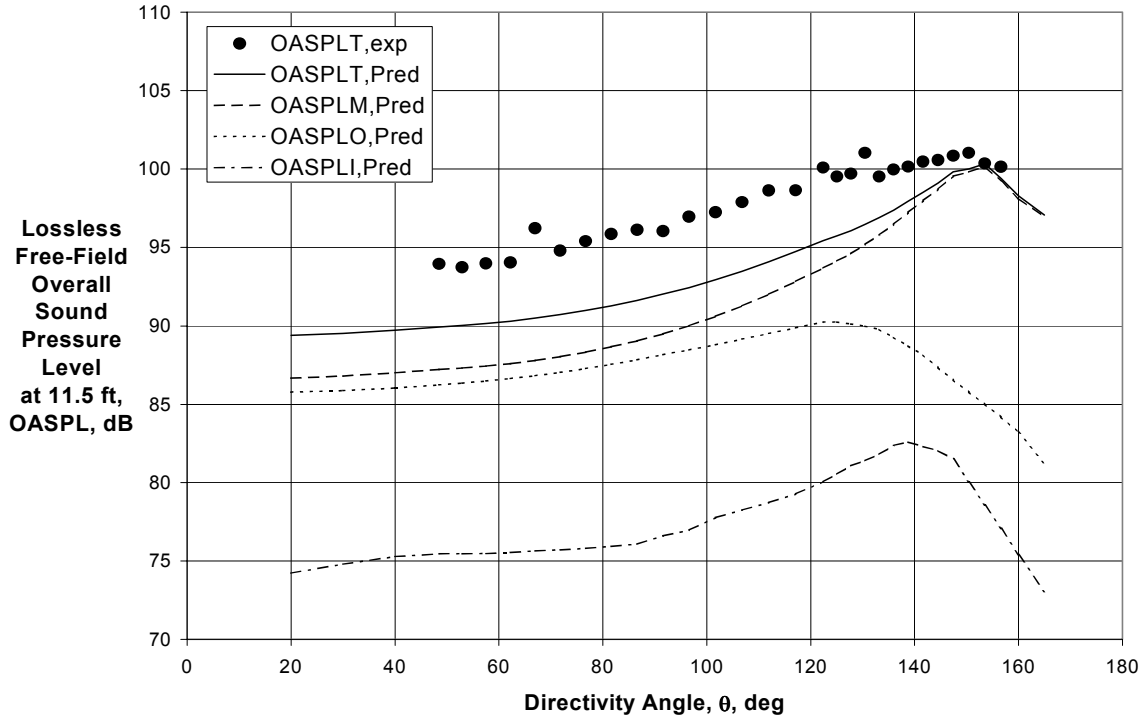
(e) Directivity Angle = 142 deg

(f) Directivity Angle = 157 deg

Figure 84 (Concluded) - Comparison of Experimental and Final Predicted Spectra for Internal Plug Nozzle with V_{mix}/c_{amb} = 0.676, M_f = 0.10 (A_O/A_I = 4.09, Cond. 250010, Ref. 31)

Figure 85 - Comparison of Experimental and Final Predicted Directivities for Internal Plug Nozzle with V_{mix}/c_{amb} = 0.840, M_f = 0.10 (A_O/A_I = 4.09, Cond. 310010, Ref. 31)

(a) Directivity Angle = 67 deg

Figure 86 - Comparison of Experimental and Final Predicted Spectra for Internal Plug Nozzle with V_{mix}/c_{amb} = 0.840, M_f = 0.10 (A_O/A_I = 4.09, Cond. 310010, Ref. 31)
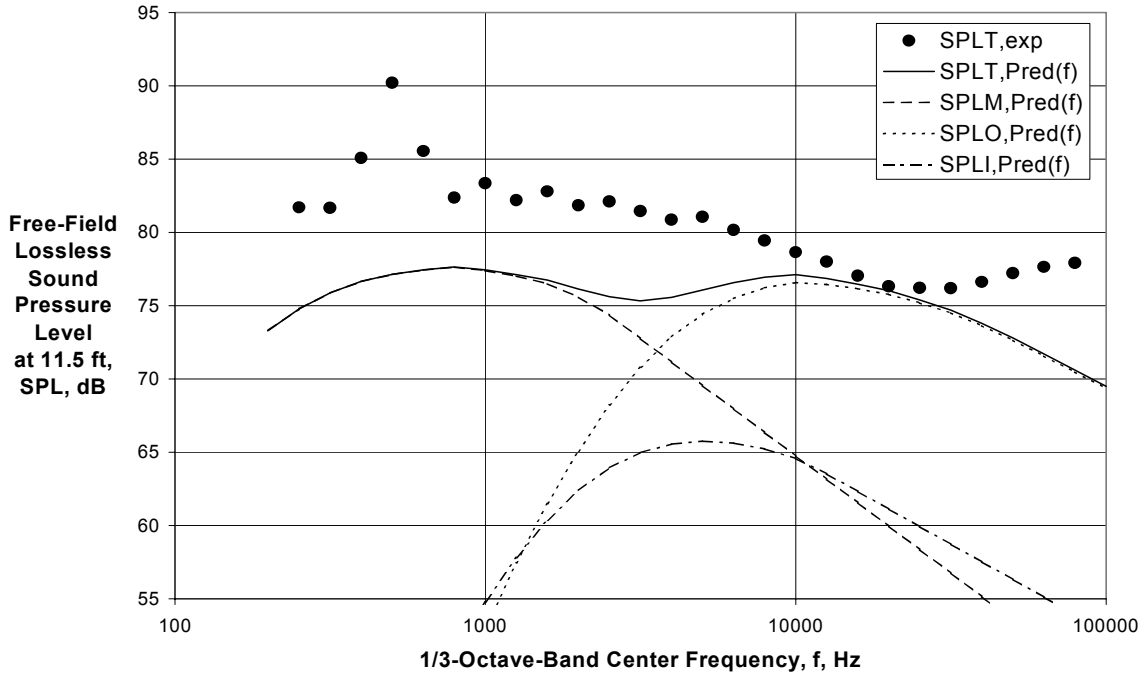
(b) Directivity Angle = 92 deg

(c) Directivity Angle = 117 deg

Figure 86 (Continued) - Comparison of Experimental and Final Predicted Spectra for Internal Plug Nozzle with V_{mix}/c_{amb} = 0.840, M_f = 0.10 (A_O/A_I = 4.09, Cond. 310010, Ref. 31)
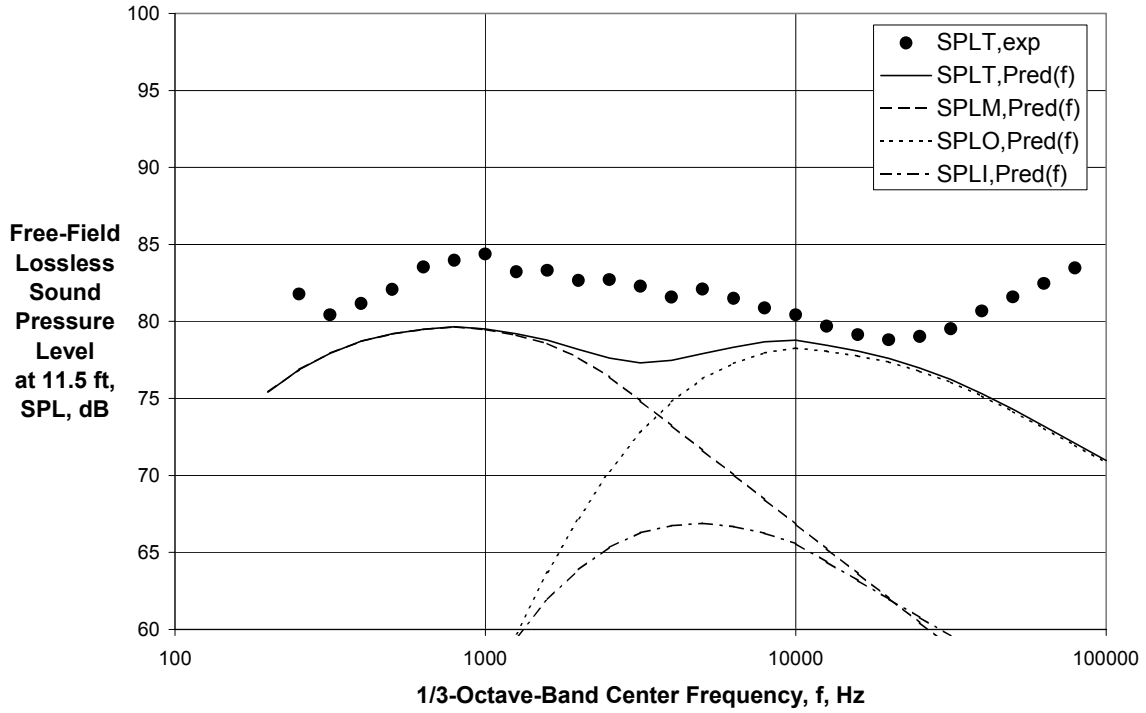
(d) Directivity Angle = 136 deg

(e) Directivity Angle = 157 deg

Figure 86 (Concluded) - Comparison of Experimental and Final Predicted Spectra for Internal Plug Nozzle with V_{mix}/c_{amb} = 0.840, M_f = 0.10 (A_O/A_I = 4.09, Cond. 310010, Ref. 31)

Figure 87 - Comparison of Experimental and Final Predicted Directivities for Internal Plug Nozzle with V_{mix}/c_{amb} = 0.592, M_f = 0.10 (A_O/A_I = 5.66, Cond. 430010, Ref. 31)
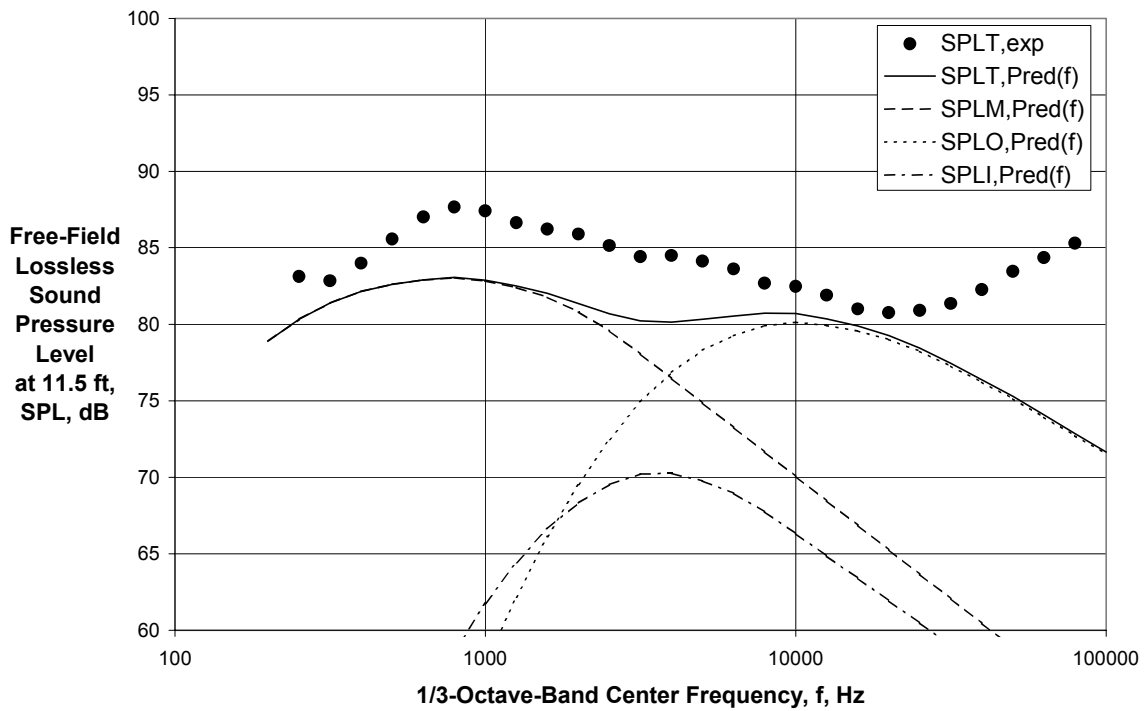

(a) Directivity Angle = 67 deg

Figure 88 - Comparison of Experimental and Final Predicted Spectra for Internal Plug Nozzle with V_{mix}/c_{amb} = 0.592, M_f = 0.10 (A_O/A_I = 5.66, Cond. 430010, Ref. 31)
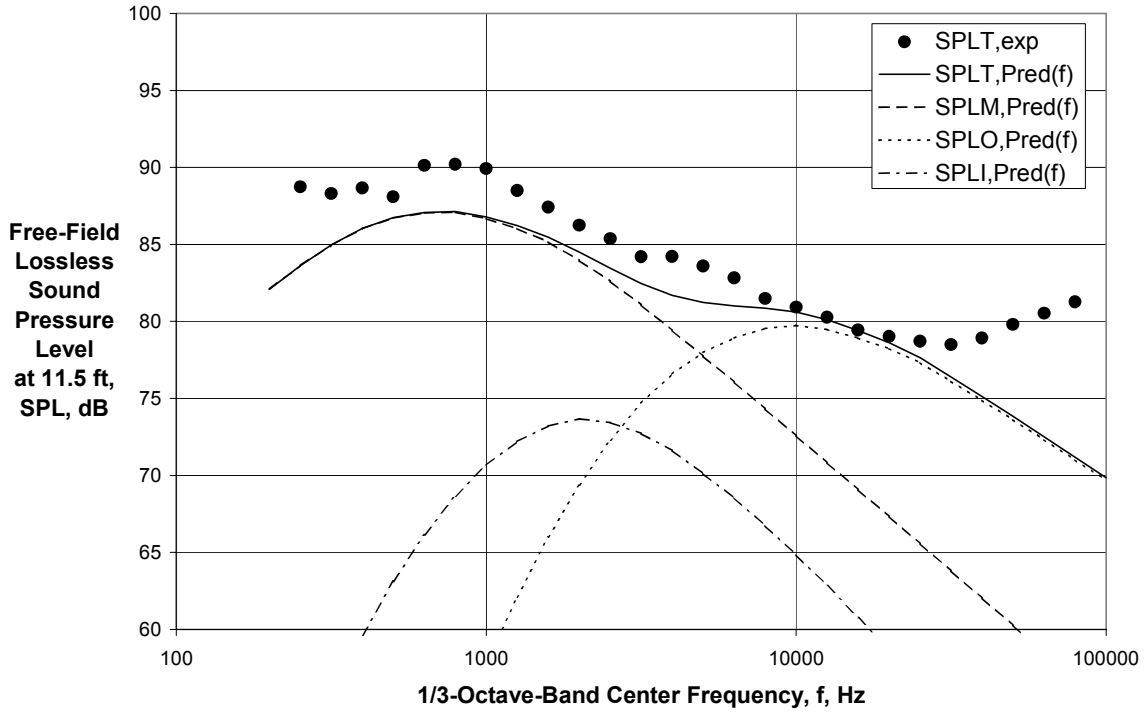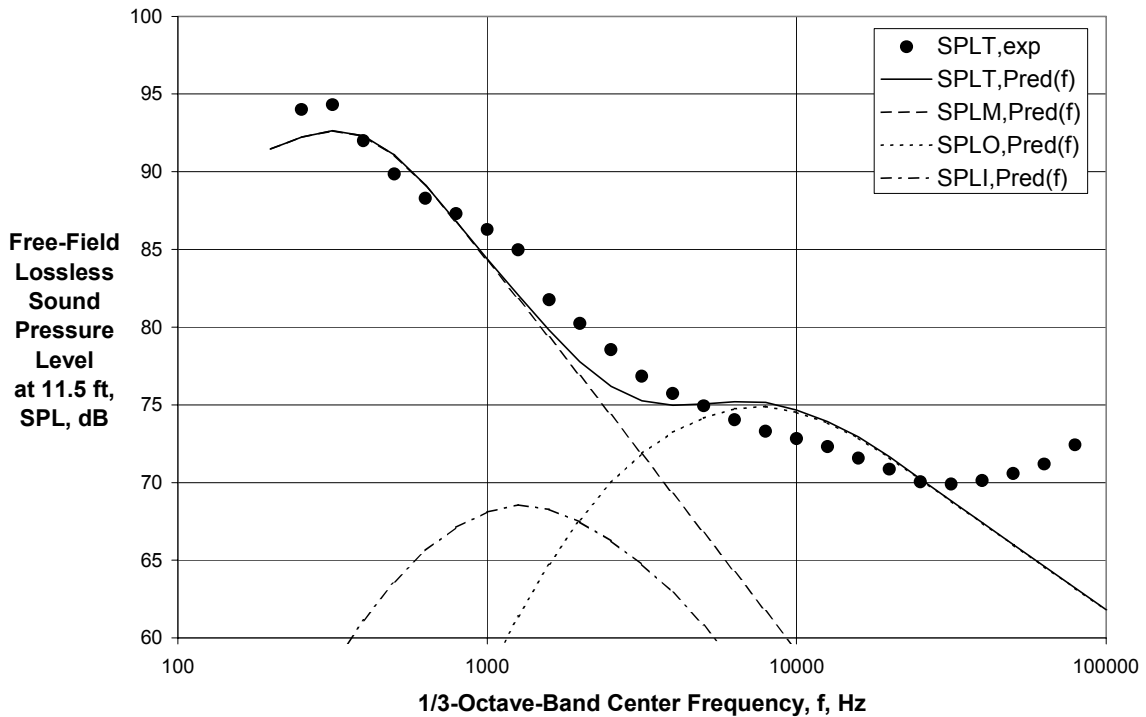
(b) Directivity Angle = 92 deg

(c) Directivity Angle = 117 deg

Figure 88 (Continued) - Comparison of Experimental and Final Predicted Spectra for Internal Plug Nozzle with V_{mix}/c_{amb} = 0.592, M_f = 0.10 (A_O/A_I = 5.66, Cond. 430010, Ref. 31)
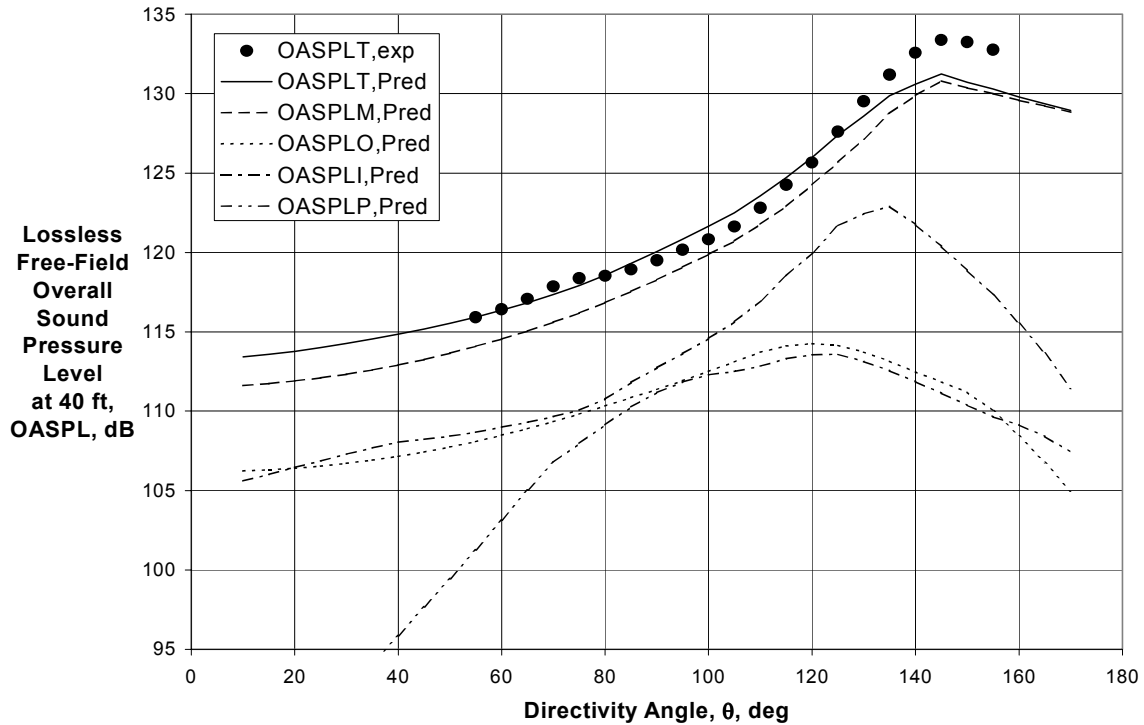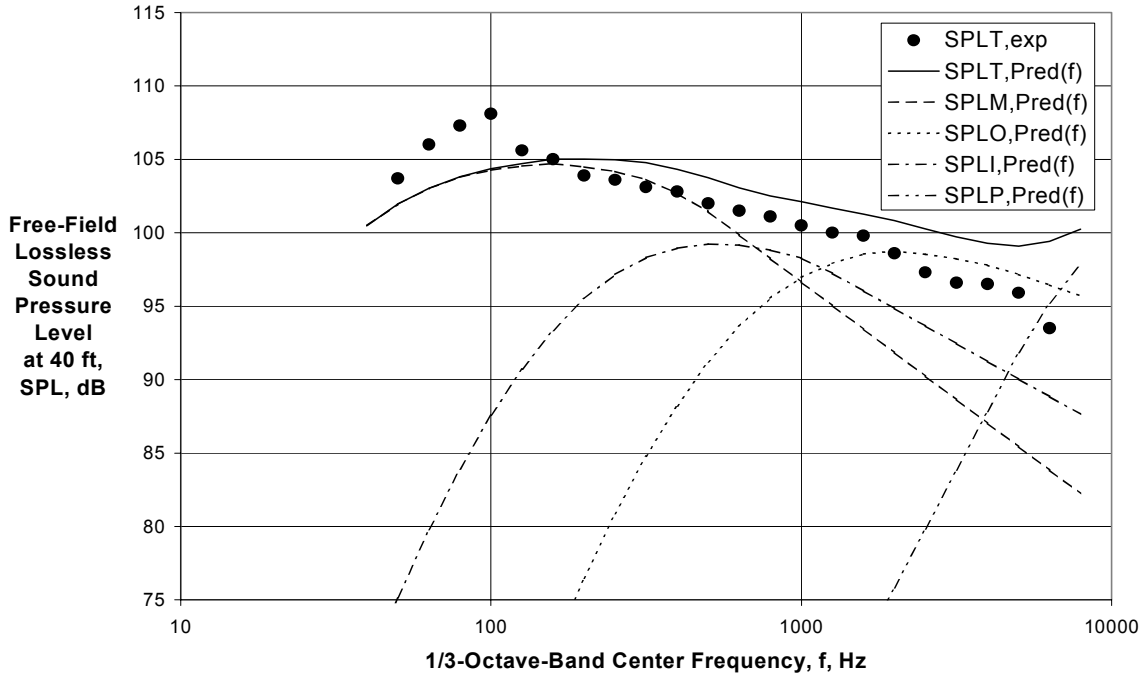
(d) Directivity Angle = 130 deg

(e) Directivity Angle = 157 deg

Figure 88 (Concluded) - Comparison of Experimental and Final Predicted Spectra for Internal Plug Nozzle with V_{mix}/c_{amb} = 0.592, M_f = 0.10 (A_O/A_I = 5.66, Cond. 430010, Ref. 31)

Figure 89 - Comparison of Experimental and Final Predicted Directivities for Internal Plug Nozzle with V_{mix}/c_{amb} = 0.800, M_f = 0.10 (A_O/A_I = 5.66, Cond. 530010, Ref. 31)

(a) Directivity Angle = 67 deg

Figure 90 - Comparison of Experimental and Final Predicted Spectra for Internal Plug Nozzle with V_{mix}/c_{amb} = 0.800, M_f = 0.10 (A_O/A_I = 5.66, Cond. 530010, Ref. 31)
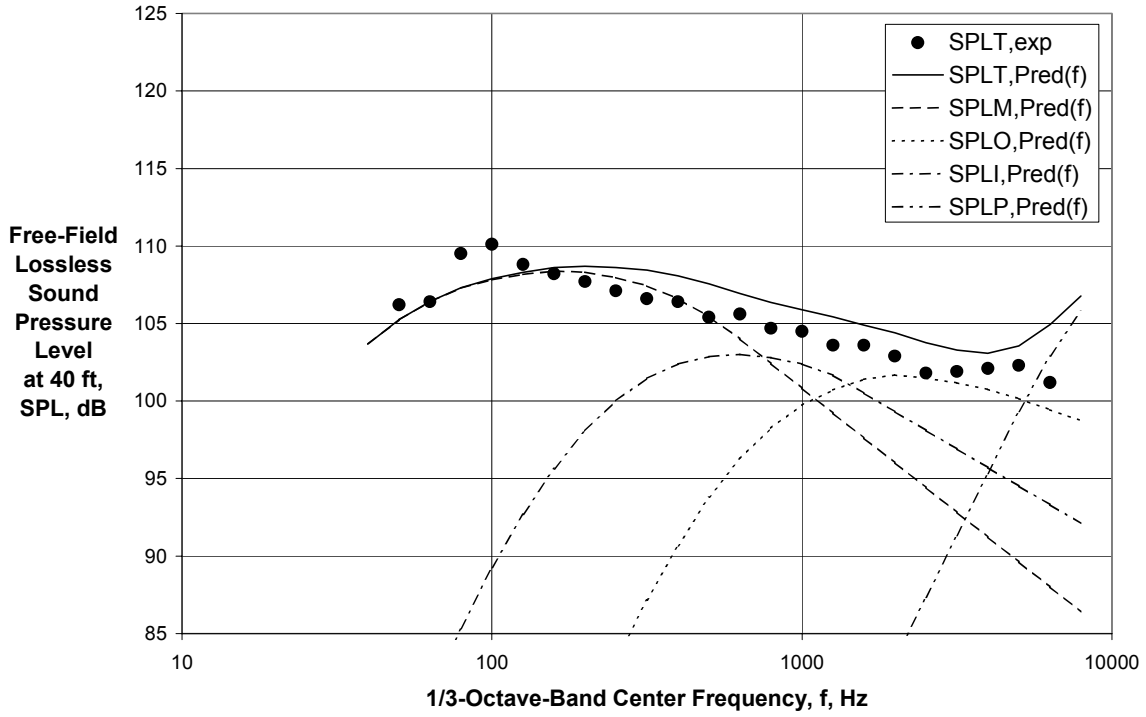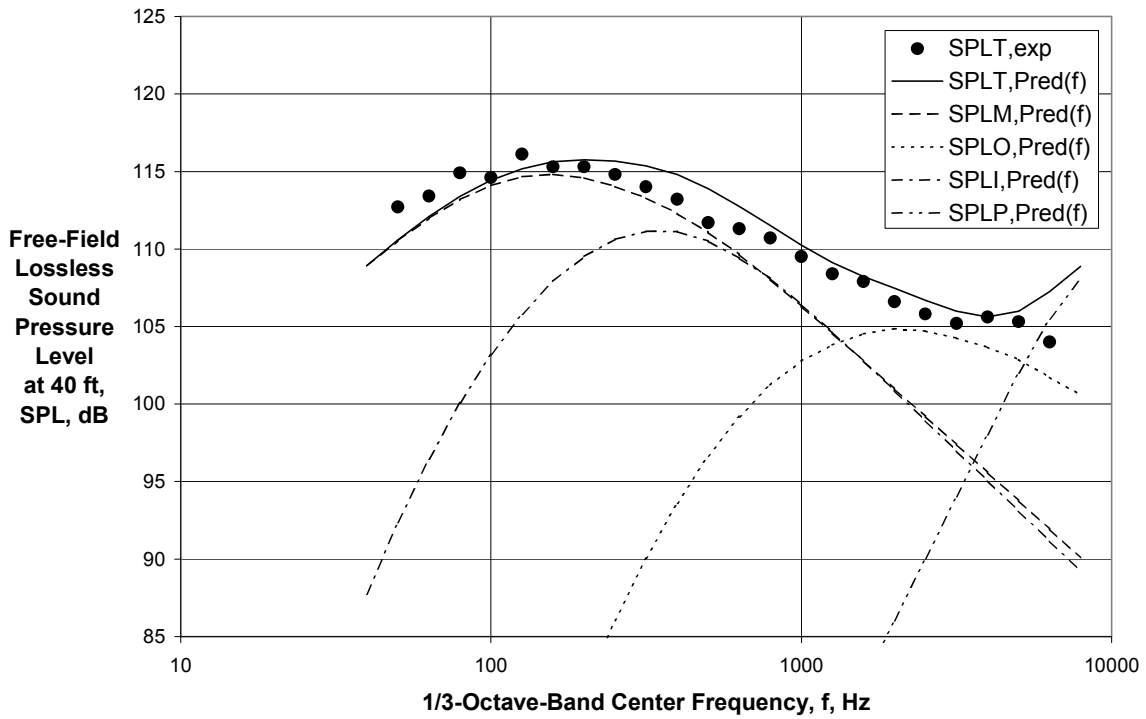
(b) Directivity Angle = 92 deg

(c) Directivity Angle = 117 deg

Figure 90 (Continued) - Comparison of Experimental and Final Predicted Spectra for Internal Plug Nozzle with V_{mix}/c_{amb} = 0.800, M_f = 0.10 (A_O/A_I = 5.66, Cond. 530010, Ref. 31)
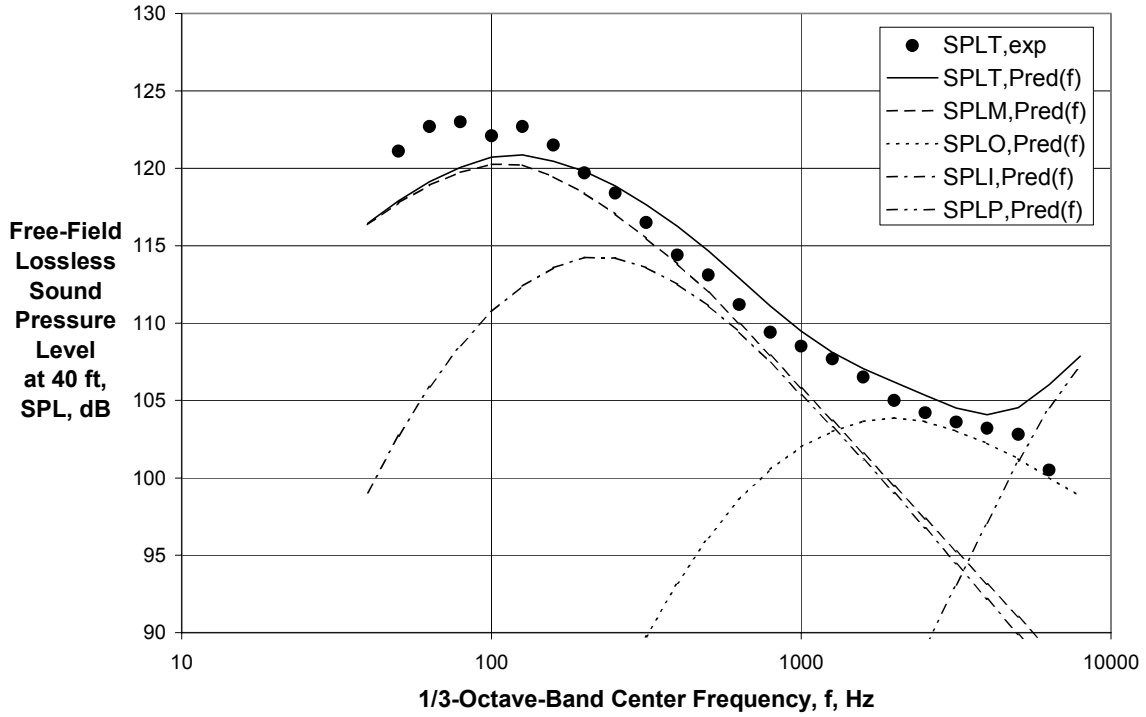
(d) Directivity Angle = 136 deg

(e) Directivity Angle = 157 deg

Figure 90 (Concluded) - Comparison of Experimental and Final Predicted Spectra for Internal Plug Nozzle with V_{mix}/c_{amb} = 0.800, M_f = 0.10 (A_O/A_I = 5.66, Cond. 530010, Ref. 31)

Figure 91 - Comparison of Experimental and Final Predicted Directivities for Internal Plug Nozzle with V_{mix}/c_{amb} = 0.635, M_f = 0.10 (A_O/A_I = 6.93, Cond. 720010, Ref. 31)

(a) Directivity Angle = 67 deg

Figure 92 - Comparison of Experimental and Final Predicted Spectra for Internal Plug Nozzle with V_{mix}/c_{amb} = 0.635, M_f = 0.10 (A_O/A_I = 6.93, Cond. 720010, Ref. 31)
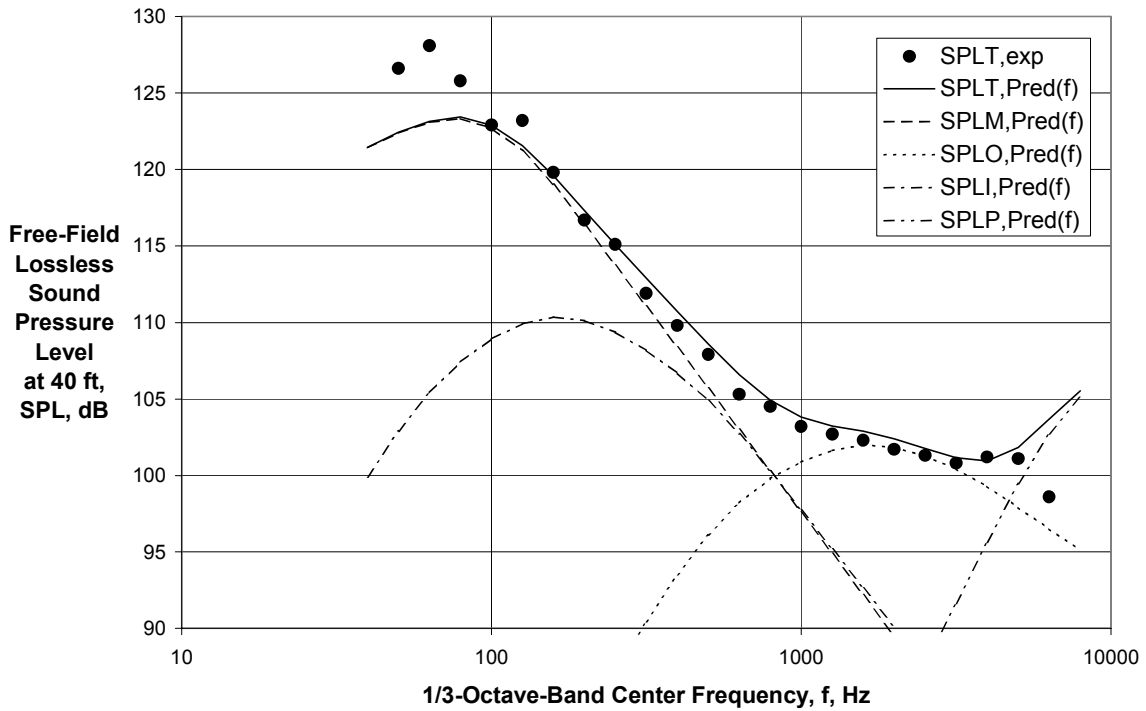
(b) Directivity Angle = 92 deg

(c) Directivity Angle = 117 deg

Figure 92 (Continued) - Comparison of Experimental and Final Predicted Spectra for Internal Plug Nozzle with V_{mix}/c_{amb} = 0.635, M_f = 0.10 (A_O/A_I = 6.93, Cond. 720010, Ref. 31)
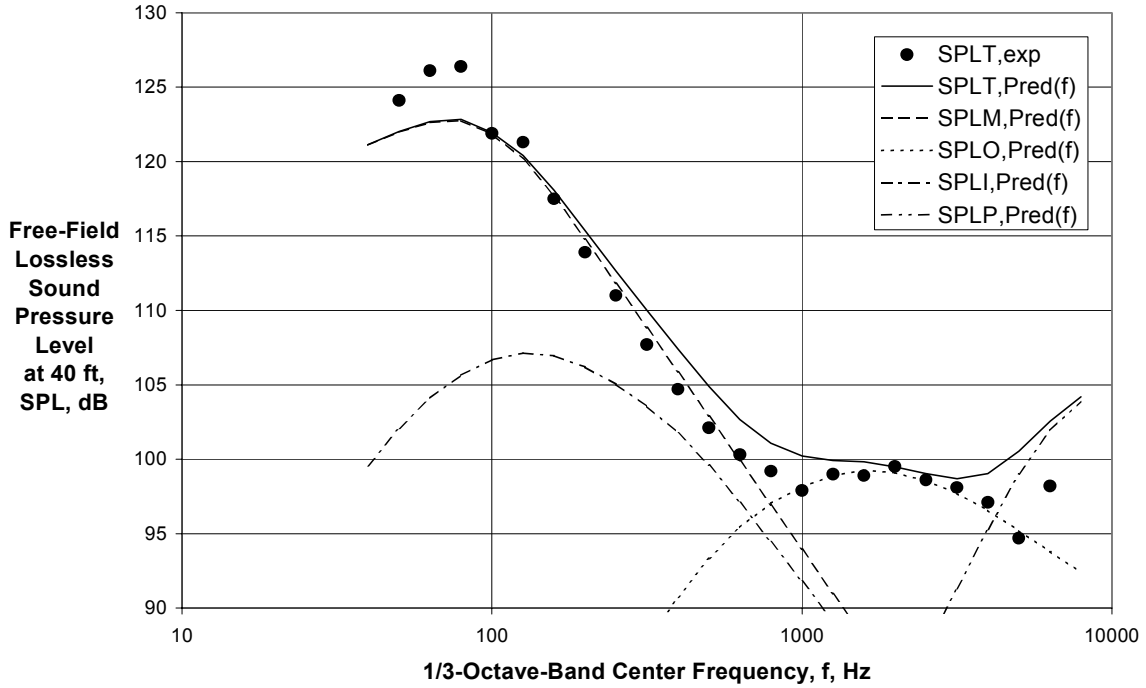
(d) Directivity Angle = 136 deg

(e) Directivity Angle = 157 deg

Figure 92 (Concluded) - Comparison of Experimental and Final Predicted Spectra for Internal Plug Nozzle with $V_{mix}/c_{amb} = 0.635$, $M_f = 0.10$ ($A_O/A_I = 6.93$, Cond. 720010, Ref. 31)

Figure 93 - Comparison of Experimental and Final Predicted Directivities for Inner-Stream Chevron Nozzle with V_{mix}/c_{amb} = 1.04, M_f = 0.0 (A_O/A_I = 2.75, Ref. 24, Rdg. 811)

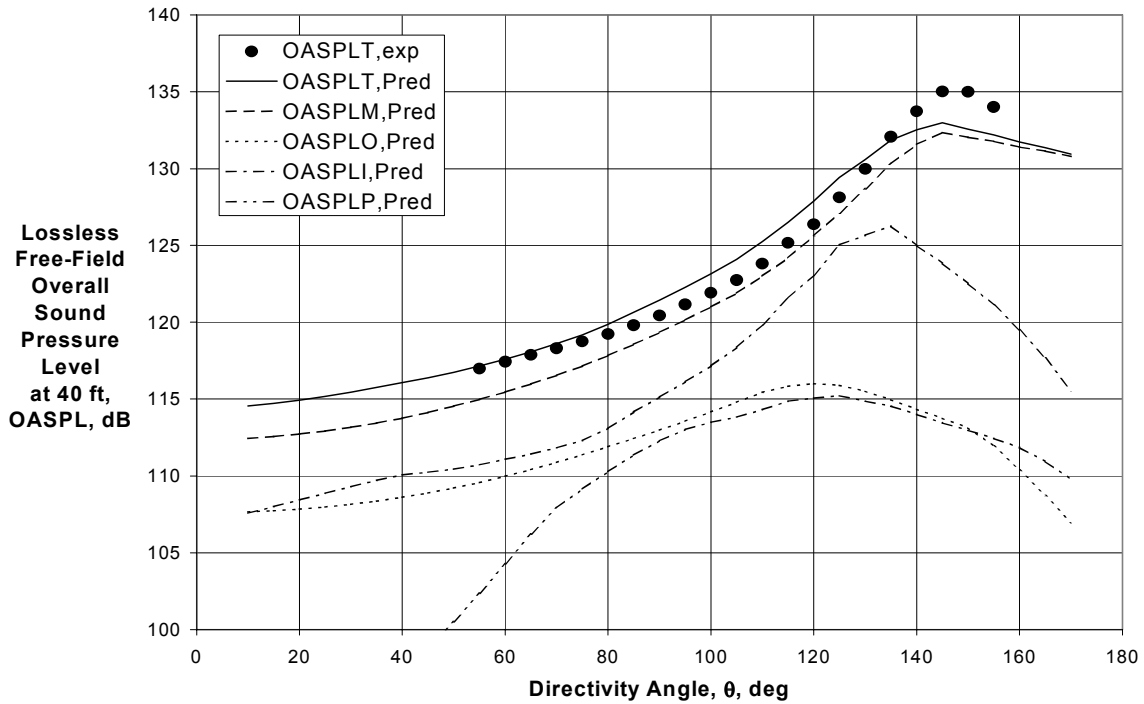**(a) Directivity Angle = 60 deg**

Figure 94 - Comparison of Experimental and Final Predicted Spectra for Inner-Stream Chevron Nozzle with V_{mix}/c_{amb} = 1.04, M_f = 0.0 (A_O/A_I = 2.75, Ref. 24, Rdg. 811)
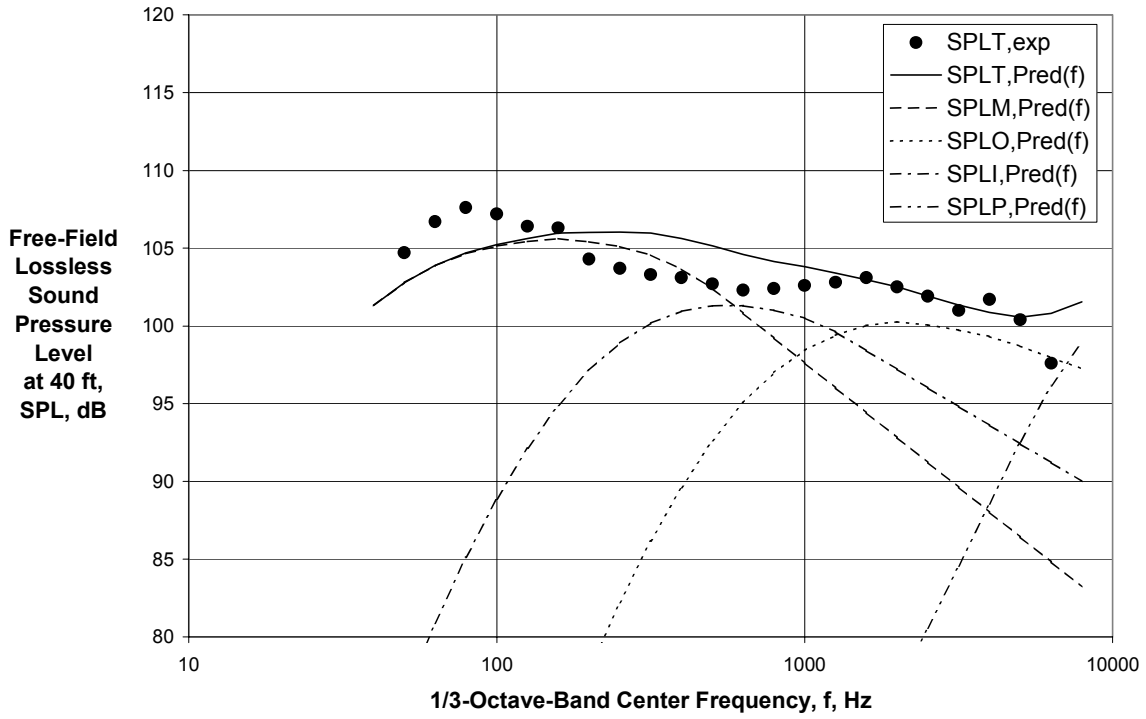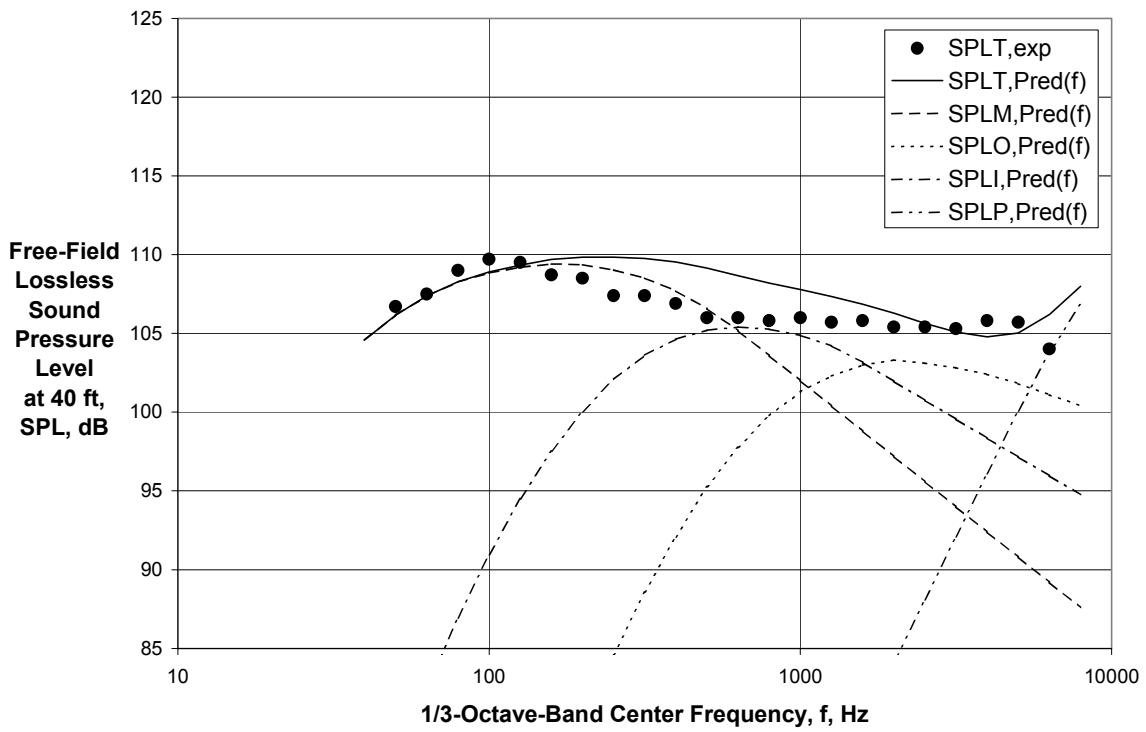
(b) Directivity Angle = 90 deg

(c) Directivity Angle = 120 deg

Figure 94 (Continued) - Comparison of Experimental and Final Predicted Spectra for Inner-Stream Chevron Nozzle with V_{mix}/c_{amb} = 1.04, M_f = 0.0 (A_O/A_I = 2.75, Ref. 24, Rdg. 811)

(d) Directivity Angle = 135 deg

(e) Directivity Angle = 150 deg

Figure 94 (Continued) - Comparison of Experimental and Final Predicted Spectra for Inner-Stream Chevron Nozzle with V_{mix}/c_{amb} = 1.04, M_f = 0.0 (A_O/A_I = 2.75, Ref. 24, Rdg. 811)

(f) Directivity Angle = 160 deg

Figure 94 (Concluded) - Comparison of Experimental and Final Predicted Spectra for Inner-Stream Chevron Nozzle with V_{mix}/c_{amb} = 1.04, M_f = 0.0 (A_O/A_I = 2.75, Ref. 24, Rdg. 811)

Figure 95 - Comparison of Experimental and Final Predicted Directivities for Combined Inner and Outer Stream Chevron Nozzle with V_{mix}/c_{amb} = 1.09, M_f = 0.0 (A_O/A_I = 2.75, Ref. 24, Rdg. 903)
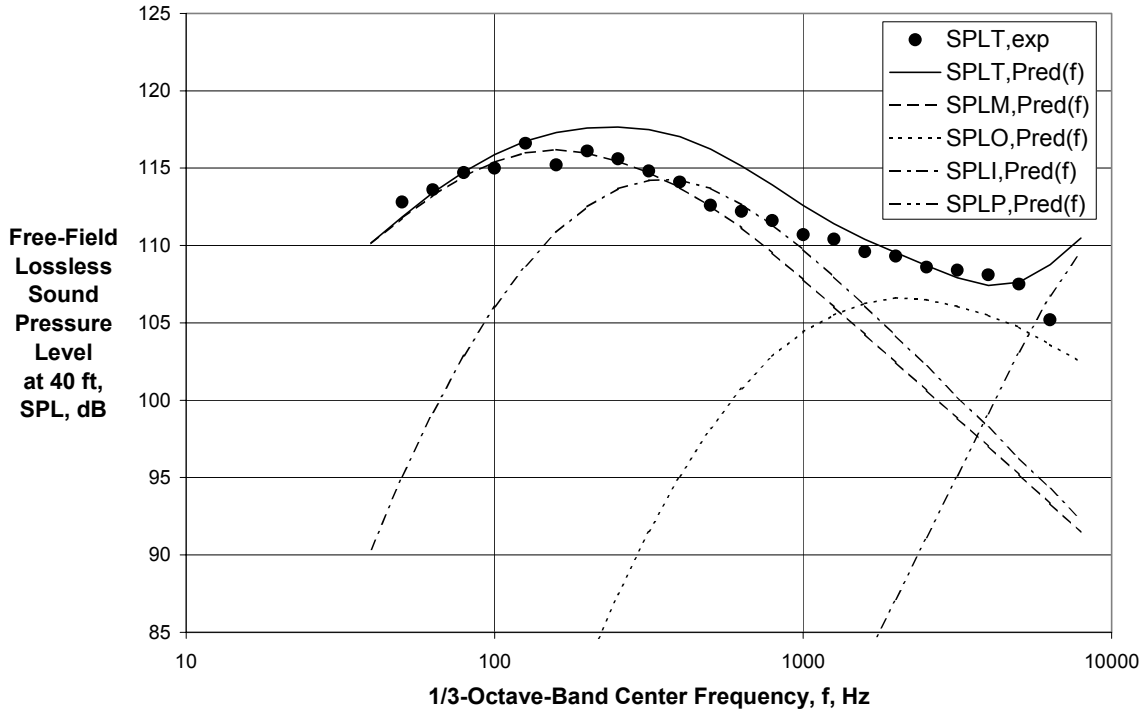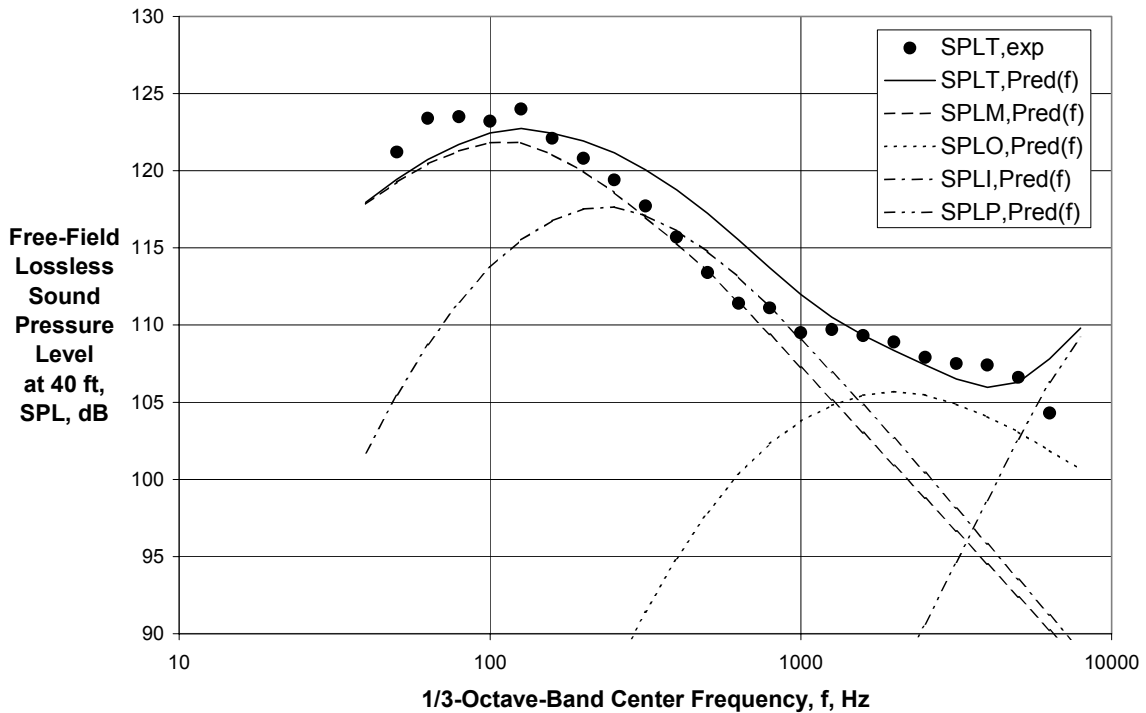
(a) Directivity Angle = 60 deg

(b) Directivity Angle = 90 deg

Figure 96 - Comparison of Experimental and Final Predicted Spectra for Combined Inner and Outer Stream Chevron Nozzle with V_{mix}/c_{amb} = 1.09, M_f = 0.0 (A_O/A_I = 2.75, Ref. 24, Rdg. 903)
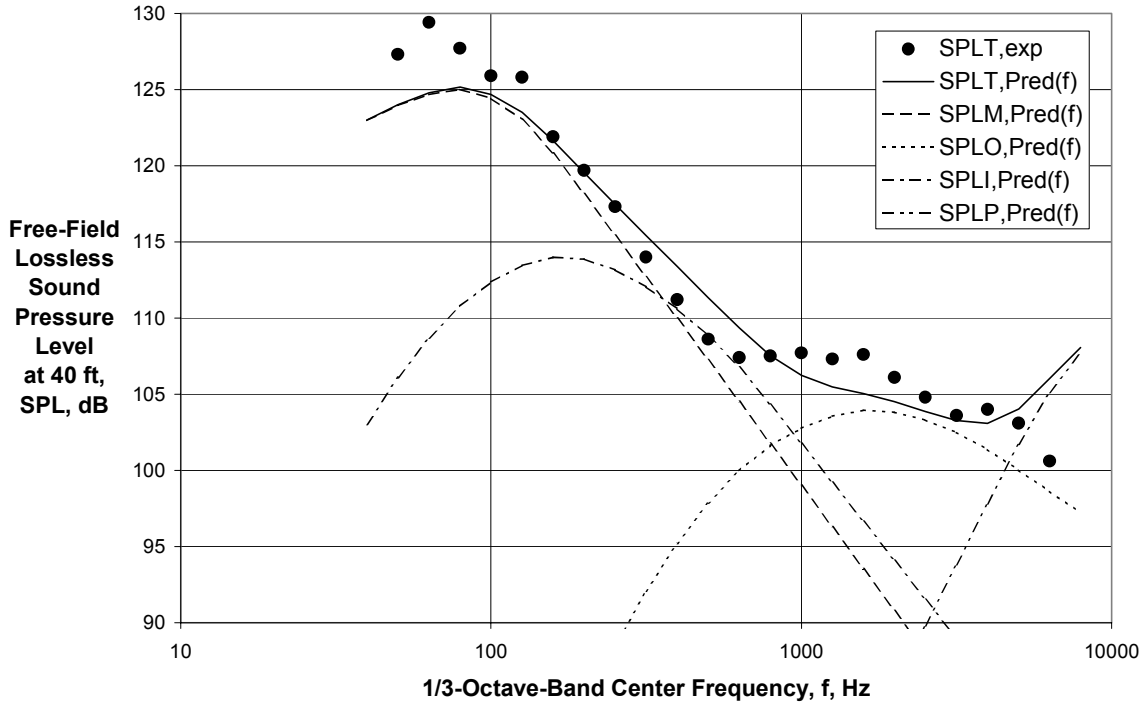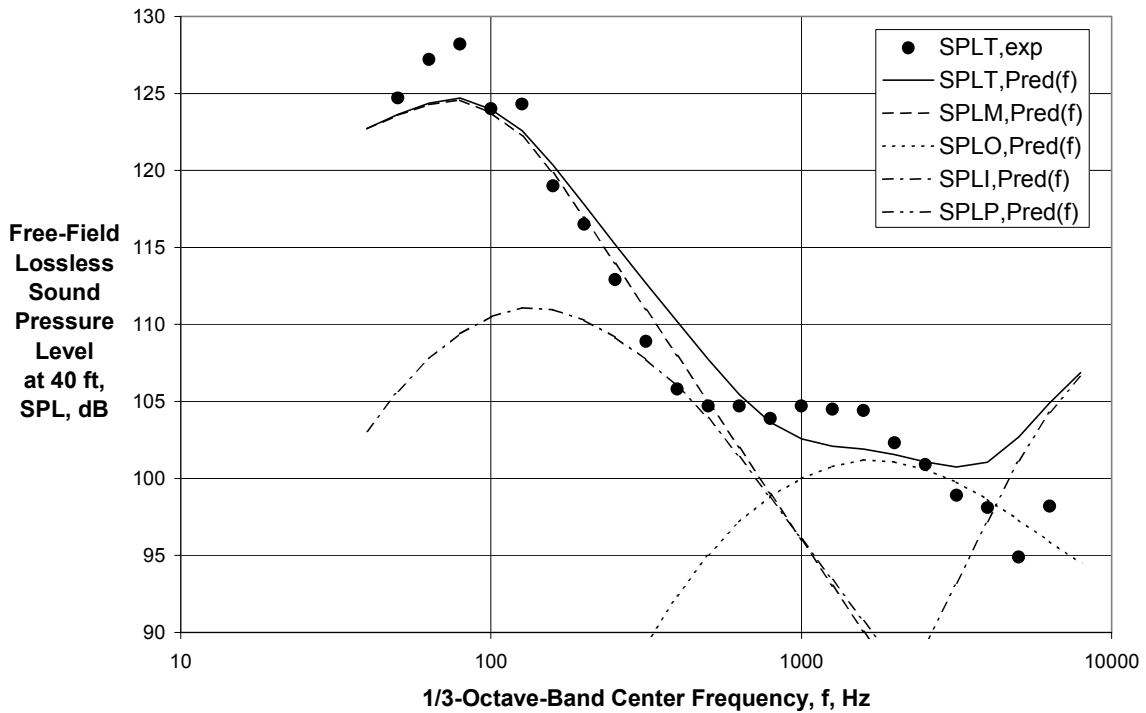
(c) Directivity Angle = 120 deg

(d) Directivity Angle = 135 deg

Figure 96 (Continued) - Comparison of Experimental and Final Predicted Spectra for Combined Inner and Outer Stream Chevron Nozzle with V_{mix}/c_{amb} = 1.09, M_f = 0.0 (A_O/A_I = 2.75, Ref. 24, Rdg. 903)

(e) Directivity Angle = 150 deg

(f) Directivity Angle = 160 deg

Figure 96 (Concluded) - Comparison of Experimental and Final Predicted Spectra for Combined Inner and Outer Stream Chevron Nozzle with V_{mix}/c_{amb} = 1.09, M_f = 0.0 (A_O/A_I = 2.75, Ref. 24, Rdg. 903)

REPORT DOCUMENTATION PAGE

1. AGENCY USE ONLY (Leave blank)	2. REPORT DATE September 2003	3. REPORT TYPE AND DATES COVERED Final Contractor Report

4. TITLE AND SUBTITLE

Jet Noise Modeling for Coannular Nozzles Including the Effects of Chevrons

5. FUNDING NUMBERS

WBS–22–781–30–12
NAS3–00178, Task Order 6

6. AUTHOR(S)

James R. Stone, Eugene A. Krejsa, and Bruce J. Clark

7. PERFORMING ORGANIZATION NAME(S) AND ADDRESS(ES)

Modern Technologies Corporation
Propulsion Systems Group
7530 Lucerne Drive, Suite 206
Middleburg Heights, Ohio 44130

8. PERFORMING ORGANIZATION REPORT NUMBER

E–14084

9. SPONSORING/MONITORING AGENCY NAME(S) AND ADDRESS(ES)

National Aeronautics and Space Administration
Washington, DC 20546–0001

10. SPONSORING/MONITORING AGENCY REPORT NUMBER

NASA CR—2003-212522

11. SUPPLEMENTARY NOTES

Project Manager, Jeffrey J. Berton, Aeronautics Directorate, NASA Glenn Research Center, organization code 2400, 216–977–7031.

12a. DISTRIBUTION/AVAILABILITY STATEMENT

Unclassified - Unlimited
Subject Categories: 05, 07, 71, and 45   Distribution: Nonstandard

Available electronically at http://gltrs.grc.nasa.gov

This publication is available from the NASA Center for AeroSpace Information, 301–621–0390.

12b. DISTRIBUTION CODE

13. ABSTRACT (Maximum 200 words)

This document describes the development of an improved predictive model for coannular jet noise, applying the approach used with great success by the Modern Technologies Corporation (MTC) in developing a noise prediction model for two-dimensional mixer ejector (2DME) nozzles under the High Speed Research Program. The end result is a more consistent and robust model than currently available in the NASA/MTC *FOOTPR* code, which is based on an interim coupling of older separate codes for conventional and inverted-velocity-profile (CVP and IVP) coannular jets. The new code also includes a limited-range prediction of the effects of mixing-enhancement nozzle-exit chevrons on jet noise. The method is programmed and transformed into an upgraded jet noise module suitable for incorporation into NASA's current aircraft system noise prediction codes. The scope of the task is in alignment with the mission of NASA's Quiet Aircraft Technology Program. The methodology recently developed (2001) by MTC for General Electric under NASA funding for coannular nozzles of bypass ratio approximately $5 \leq BPR \leq 14$ with and without mixing enhancement chevrons, based on recent (1997) static and simulated flight tests conducted at the NASA Glenn Research Center (GRC), serves as the starting point. This initial model is then extended to much lower BPR and a wide range of outer-stream to inner-stream velocity ratio, utilizing static test results from GRC's predecessor, NASA Lewis Research Center (LeRC). The development of this predictive model is heavily dependent on having good quality experimental data available to work with, and data quality is carefully considered throughout this task. Once a preliminary procedure is developed, data from another test facility, at NASA Langley Research Center (LaRC), with its own unique characteristics, are utilized to establish the validity of the new methodology over a wide range of conditions including the effects of flight, and to identify issues or areas needing further improvement. The improved finalized model is incorporated into MTC's version of the *FOOTPR* code and a users' guide is provided. MTC also supports the adaptation of this code for incorporation in the NASA LaRC *Aircraft Noise Prediction Program (ANOPP)*.

14. SUBJECT TERMS

Noise prediction (aircraft); Noise reduction; Coaxial Nozzles; Noise measurement; Jet aircraft noise

15. NUMBER OF PAGES
212

16. PRICE CODE

17. SECURITY CLASSIFICATION OF REPORT Unclassified	18. SECURITY CLASSIFICATION OF THIS PAGE Unclassified	19. SECURITY CLASSIFICATION OF ABSTRACT Unclassified	20. LIMITATION OF ABSTRACT